

Annual Research Briefs – 1994

Center for Turbulence Research

December 1994



Ames Research Center



Stanford University

CONTENTS

Preface	1
Conditional statistics in a turbulent premixed flame derived from direct numerical simulation. T. MANTEL and R. W. BILGER	3
Lewis number and Damköhler number effects in vortex-flame interactions. J.-M. SAMANIEGO	29
Fundamental mechanisms in premixed flame propagation via vortex-flame interactions - numerical simulations. T. MANTEL	45
Triple flames and flame stabilization. J. E. BROADWELL	77
Flame propagation under partially-premixed conditions. G. R. RUETSCH	79
Turbulence modeling for separated flow. P. A. DURBIN	97
Notes on rotating turbulence. O. ZEMAN	107
A dynamic localization model with stochastic backscatter. D. CARATI and S. GHOSAL	115
Large-eddy simulation of a plane wake. S. GHOSAL and M. ROGERS	127
Local dynamic subgrid-scale models in channel flow. W. CABOT	143
Unstructured-grid large-eddy simulation of flow over an airfoil. KENNETH JANSEN	161
Large-eddy simulation of flow through a plane, asymmetric diffuser. HANS-JAKOB KALTENBACH	175
Large-eddy simulation of a boundary layer with concave stream-wise curvature. T. S. LUND	185
Experimental investigations of "on-demand" vortex generators. SEYED G. SADDUGHI	197
Direct numerical simulations of "on-demand" vortex generators — break Mathematical formulation. P. KOUMOUTSAKOS	205
Drag reduction strategies. D. C. HILL	215
Optimal active control for Burgers equation. YUTAKA IKEDA	219
Acoustics of laminar boundary layer breakdown. MENG WANG	225
Small-scale behavior in distorted turbulent boundary layers at low Reynolds number. SEYED G. SADDUGHI	243
Transverse vorticity measurements in the NASA Ames 80 ft×120 ft wind tunnel boundary layer. J. F. FOSS, D. G. BOHL, F. D. BRAMKAMP, and J. G. KLEWICKI	263

Experimental and numerical study of the intermittency exponent μ . ALEXANDER PRASKOVSKY	269
On the dynamics of small-scale vorticity in isotropic turbulence. J. JIMÉNEZ and A. A. WRAY	287
Forced free-shear layer measurements. R. L. LEBOEUF	313
Numerical study of boundary layer interaction with shocks - method and code validation. N. A. ADAMS	339
Resolution requirements for velocity gradients in turbulence. J. JIMÉNEZ	357
A method for obtaining a statistically stationary turbulent free shear flow. S. F. TIMSON, S. K. LELE and R. D. MOSER	365
Direct numerical simulation of incompressible axisymmetric flows. PATRICK LOULOU	373
Database post-processing in Tensoral. ELIOT DRESSELHAUS	379
Appendix: Center for Turbulence Research 1994 Roster	391

Preface

This report contains the 1994 annual progress reports of the Research Fellows and students of the Center for Turbulence Research. A separate report documenting the findings from the fifth CTR Summer Program was published earlier this year.

Since its inception in 1987, the objective of the Center for Turbulence Research has been to advance the physical understanding of turbulence in order to develop fundamentally-based predictive methods for engineering analysis and techniques for turbulence control. We believe that the pacing item for turbulence modeling and control is new fundamental ideas, which must be motivated by engineering applications. CTR strives to create an environment conducive to generation of new ideas, and this has been the guiding principle in the appointment of the CTR Fellows. In the past eight years, CTR has been able to attract over two hundred very bright postdoctoral researchers and established experts in turbulence and related fields for research, for the Summer Programs, and for other technical exchanges. From their research and interactions between them, a number of important new ideas for turbulence modeling and simulation have emerged, and several have already been implemented in engineering codes. CTR contributions include new models for compressibility effects in high-speed flows, the elliptic relaxation method for treatment of flow inhomogeneities and solid boundaries, the dynamic subgrid-scale modeling approach for large-eddy simulation, structure-based turbulence modeling, new methods for computation of aerodynamic sound, and new insights into the physics and modeling of chemically reacting turbulence obtained through a combination of experiments and direct numerical simulations.

Last year CTR hosted thirteen resident Postdoctoral Fellows, three Research Associates, and five Senior Research Fellows, and it supported two doctoral students and four short-term visitors. In addition, CTR sponsored its fifth Summer Program in July 1994 with thirty participants. The major portion of Stanford's doctoral research program in turbulence is sponsored by the United States Air Force Office of Scientific Research and the Office of Naval Research. Many students supported by these programs also conduct their research at the CTR. This report includes work only for those students who were directly supported by the CTR.

The first group of reports in this volume are directed towards turbulence combustion. A notable progress in this area was the successful completion of an experimental and numerical study designed for validation of simple chemical mechanisms for prediction codes. The second and the largest group of reports are concerned with the prediction of turbulent flows. A significant fraction of CTR's effort in large-eddy simulation and Reynolds-averaged turbulence modeling was focused on the *application* of models developed at the CTR to complex, unsteady separated flows. The remaining articles are devoted to experimental and numerical studies of turbulence control, physics of turbulence and sound generation, and simulation techniques. The last report is on the advanced postprocessing project, which has

now produced functioning software for the analysis of the database of numerical simulations of turbulence.

The CTR roster for 1994 is provided in the Appendix. Also listed are the members of the Advisory Committee, which meets annually to review the Center's program, and the Steering Committee, which acts on Fellowship applications.

It is a great pleasure to thank Debra Spinks, the Center's Administrative Assistant, for her skillful compilation of this report.

Parviz Moin
William C. Reynolds

Conditional statistics in a turbulent premixed flame derived from direct numerical simulation

By T. Mantel & R. W. Bilger¹

1. Motivation and objectives

In premixed turbulent combustion modeling, the most common approach is based on averaged transport equations for statistical moments (mean, variance) of thermochemical variables. Most of the recent developments are for systems in the flamelet regime and consider infinitely fast chemical reactions compared to the turbulent mixing (Bray 1980, Peters 1986). Under this assumption, the turbulent flame can be represented as a collection of laminar flamelets stretched and convected by the turbulent flow field. Thus, several authors have proposed to describe the turbulent flame by a transport equation for the surface flame area per unit of volume Σ (Bideaux *et al.* 1994, Candel & Poinso 1990, Pope 1985-a, Trouvé & Poinso 1994) or by a transport equation for an arbitrary scalar field (concentration, temperature) $G(x_k, t) = G_0$ which describes the flame sheet as an infinitely thin interface separating fresh and burnt gases (Kerstein *et al.* 1988, Peters 1992, Williams 1985-b). Another possibility is to derive a transport equation for the dissipation of the fluctuations of the concentration leading, in the limit of high Damköhler number, to a balance equation for Σ (Mantel & Borghi 1994).

Another general approach consists of directly calculating the probability density function (pdf) of the thermochemical variables through its transport equation (Borghi 1988, O'Brien 1985, Pope 1985-b). This method avoids the modeling of the chemical reaction rate and can more easily take into account reduced chemical schemes or complete chemical schemes as well (Vervisch 1991). However, the limitation of these models is the high computational cost of the Monte-Carlo method used and the sub-models for the molecular mixing terms.

Recently, Bilger (1993-a,b) has proposed an alternative method based on conditional moment closure (CMC) applied to turbulent reacting flows for both non-premixed and premixed systems. This technique goes beyond the zone conditioning methods developed and applied to non reacting flows in the case of a two-dimensional mixing layer by Libby (1975) and extended to the turbulent mixing of scalars by Dopazo (1977). Like pdf approaches, the CMC method is valid in the different regimes of combustion and can take into account reduced or complete chemical schemes. Moreover, the chemical reaction term can be decomposed using a Taylor expansion (Bilger 1993-b) and can be estimated without modeling. Although CMC methods in turbulent reacting flows are of recent origin and still under development, applications to real configurations for non-premixed combustion have

¹ University of Sydney, Australia

been already performed using detailed chemistry (Smith *et al.* 1992). Comparisons with experimental data obtained for a turbulent jet-flame show encouraging results (Smith *et al.* 1993). As in classical flamelet models (Bray 1980), the dissipation rate of a conserved scalar appears in the CMC approach and is a crucial quantity which must be modeled. To validate models for the conditional dissipation rate, Mell *et al.* (1994) use results from direct numerical simulation of a reacting mixture in homogeneous turbulence whereas Li & Bilger (1993) utilize experimental results in a reactive scalar mixing layer. Conditional statistics concerning the dissipation of temperature fluctuations in a non-reacting system are also available (Jayesh & Warhaft 1992).

Nevertheless, for premixed systems only theoretical developments exist (Bilger 1993-b) and certain problems are still unresolved. This is particularly the case for the conditional mean velocity and the conditional mean scalar dissipation rate. This last term characterizes the molecular mixing (or the rate of dissipation of the scalar fluctuations) and must be treated carefully in turbulent premixed combustion as has been shown in Borghi (1990) and Mantel & Borghi (1994).

But, unlike diffusion flames, scalar dissipation is a quantity difficult to measure in premixed flames because of the weak spatial resolution of experimental devices (Bilger 1993-c). Experimental results for the scalar dissipation have not yet been published. Since for premixed systems no data are available, another possibility consists of analyzing results of DNS of turbulent premixed flames. Among the available databases, we cite the pioneering work of Trouvé & Poinso (1994) who have simulated the interaction between a premixed flame and a three-dimensional isotropic decaying turbulent flow field with realistic heat release. The analysis of these numerical results will provide new information concerning the conditional statistics in turbulent premixed flames and eventually lead to new models for these unclosed terms.

The objective of this paper is to briefly introduce CMC methods for premixed systems and to derive the transport equation for the conditional species mass fraction conditioned on the progress variable based on the enthalpy. Our statistical analysis will be based on the 3-D DNS database of Trouvé & Poinso (1994) available at the Center for Turbulence Research. The initial conditions and characteristics (turbulence, thermo-diffusive properties) as well as the numerical method utilized in the DNS of Trouvé & Poinso (1994) are presented, and some details concerning our statistical analysis are also given. From the analysis of DNS results, the effects of the position in the flame brush, of the Damköhler and Lewis numbers on the conditional mean scalar dissipation, and conditional mean velocity are presented and discussed. Information concerning unconditional turbulent fluxes are also presented. The anomaly found in previous studies (Libby & Bray 1981, Moss 1980) of counter-gradient diffusion for the turbulent flux of the progress variable is investigated.

2. Accomplishments

2.1 Equation for the conditional average of the species mass fraction

The transport equation for the conditional average of the mass fraction of a reactive species has been derived by Bilger (1993-b) from the balance equations for the species mass fraction Y_i for the species i and for the progress variable c based on the enthalpy which will be defined below. Its derivation is similar to that used for non-premixed flames (Bilger 1993-a). Klimenko (1990) has a different approach which has not been implemented in premixed flames.

The balance equation for the mass fraction Y_i is:

$$\rho \frac{\partial Y_i}{\partial t} + \rho U_k \frac{\partial Y_i}{\partial x_k} = \frac{\partial}{\partial x_k} (\rho \mathcal{D}_i \frac{\partial Y_i}{\partial x_k}) + \dot{w}_i \quad (1)$$

where \mathcal{D}_i is the molecular mass diffusivity for the species i , ρ the mass density, U_k the velocity vector, and \dot{w}_i the chemical reaction rate.

For the progress variable c , we use the special definition proposed by Bilger (1993-b):

$$c = \frac{h^s - h_u^s - 2h + 2h_u}{\Delta h^s} \quad (2)$$

Here, h is the total enthalpy, h^s represents the sensible enthalpy, and the subscript u characterizes the unburnt gases. The sensible enthalpy rise Δh^s is given by the adiabatic burnt value less the unburnt value. Thus, the progress variable c varies to 0 in the fresh gases to 1 in the fully burnt gases for adiabatic flames. For non-adiabatic flames c can go beyond unity, this being considered useful for studying NO formation and CO burnt out.

The transport equation for h and h^s are respectively:

$$\rho \frac{\partial h}{\partial t} + \rho U_k \frac{\partial h}{\partial x_k} = \frac{\partial}{\partial x_k} (\rho \alpha \frac{\partial h}{\partial x_k}) + \frac{\partial p}{\partial t} - \Phi_R \quad (3)$$

$$\rho \frac{\partial h^s}{\partial t} + \rho U_k \frac{\partial h^s}{\partial x_k} = \frac{\partial}{\partial x_k} (\rho \alpha \frac{\partial h^s}{\partial x_k}) + \frac{\partial p}{\partial t} - \Phi_R + \sum_{i=1}^N \dot{w}_i \Delta h_i^f \quad (4)$$

where α represents the thermal diffusivity of the mixture, p the pressure, Φ_R the radiative heat flux, and Δh_i^f the heat of formation for the species i .

According to its definition given in Eq. (2), the equation for c is directly obtained by combining Eqs. (3) and (4):

$$\rho \frac{\partial c}{\partial t} + \rho U_k \frac{\partial c}{\partial x_k} = \frac{\partial}{\partial x_k} (\rho \alpha \frac{\partial c}{\partial x_k}) + \frac{1}{\Delta h^s} \sum_{i=1}^N \dot{w}_i \Delta h_i^f \quad (5)$$

Here, the pressure rise and the radiative heat losses have been neglected.

The conditional average of the species mass fraction Y_i conditioned on the progress variable $c(x_k, t)$ being at a chosen value ζ can be defined:

$$Q_i(\zeta, x_k, t) \equiv \langle Y_i(x_k, t) \mid c(x_k, t) = \zeta \rangle = \langle Y_i \mid \zeta \rangle \quad (6)$$

From this definition and from Eqs. (1) and (5), Bilger (1993-a) has obtained the balance equation for Q_i :

$$\begin{aligned} \langle \rho | \zeta \rangle \frac{\partial Q_i}{\partial t} + \langle \rho | \zeta \rangle \langle U_k | \zeta \rangle \frac{\partial Q_i}{\partial x_k} &= \frac{1}{Le_i} \langle \rho | \zeta \rangle \langle \alpha \frac{\partial c}{\partial x_k} \frac{\partial c}{\partial x_k} | \zeta \rangle \frac{\partial^2 Q_i}{\partial \zeta^2} + \langle \dot{w}_i | \zeta \rangle \\ &+ e_Q + e_y - \frac{1}{\Delta h^s} \left(\sum_{i=1}^N \Delta h_i^f \langle \dot{w}_i | \zeta \rangle \right) \frac{\partial Q_i}{\partial \zeta} \end{aligned} \quad (7)$$

with

$$Le_i = \frac{\alpha}{D_i} \quad (8)$$

$$e_Q = \frac{\partial}{\partial x_k} (\rho D_i \frac{\partial Q_i}{\partial x_k}) + \langle \{ \rho D_i \frac{\partial Q_{i,c}}{\partial x_k} \frac{\partial c}{\partial x_k} + \frac{\partial}{\partial x_k} (\rho D_i (1 - Le_i) \frac{\partial c}{\partial x_k}) \} | \zeta \rangle \quad (9)$$

$$e_y \approx -\frac{1}{P_c(\zeta)} \frac{\partial}{\partial x_k} (\langle \rho u_k y_i | \zeta \rangle P_c(\zeta)) \quad (10)$$

Here, Le_i represents the Lewis number for the species i , u_k and y_i are the fluctuating parts of respectively U_k and Y_i about their conditional means, and $Q_{i,c}$ is the derivative of Q with regards to c . The probability density function of c defined at $c = \zeta$ is given by $P_c(\zeta)$.

If the Reynolds number of the flow is sufficiently high, the molecular diffusion fluxes present in e_Q are negligible compared to the turbulent flux (Bilger 1993-a). The conditional turbulent flux e_y has been observed negligible in the case of a reacting mixing layer (Bilger 1993-a) and can probably be neglected in premixed flames.

The conditional mean chemical reaction rate can be approximated using a Taylor expansion for $\langle \dot{w}_i | \zeta \rangle$ (Bilger 1993-b). This technique has been used by Smith *et al.* (1992) for the prediction of radicals and NO in a turbulent diffusion jet flame and comparisons with experimental data lead to satisfying agreements.

Even after these approximations, some terms of Eq. (7) remain unclosed and need to be modeled. Our attention will be focused principally on the conditional mean velocity $\langle U_k | \zeta \rangle$ and on the conditional mean scalar dissipation N_ζ defined by:

$$N_\zeta = \langle \alpha \frac{\partial c}{\partial x_k} \frac{\partial c}{\partial x_k} | \zeta \rangle \quad (11)$$

These two terms are also crucial quantities in models using pdf methods. They appear explicitly in the transport equation for the pdf $P(\zeta)$:

$$\langle \rho | \zeta \rangle \frac{\partial P}{\partial t} + \langle \rho | \zeta \rangle \langle U_k | \zeta \rangle \frac{\partial P}{\partial x_k} = \frac{\partial}{\partial \zeta} (\langle \dot{w}_c | \zeta \rangle P) + \frac{\partial^2}{\partial \zeta^2} (\langle \rho | \zeta \rangle N_\zeta P) \quad (12)$$

where \dot{w}_c is the last term appearing on the right hand side of Eq. (7).

2.2 The numerical experiment of Trouvé & Poinso (1994)

Since measurements in premixed flames are limited due to spatial resolution problems (Bilger 1993-c), DNS offers the possibility of having access to specific quantities of statistical interest such as unconditional and conditional moments (mean, variance, etc). The numerical results used in the present analysis come from the DNS of turbulent premixed flames performed by Trouvé and Poinso (1994). These authors have studied the interaction between an initially planar premixed laminar flame with realistic heat release and a three-dimensional decaying isotropic turbulent flow field. Their code fully resolves the compressible Navier-Stokes equations using a sixth order spatial scheme (Lele 1992) and a third order temporal scheme (Wray 1992). Due to the heat release and the resulting gas expansion, the boundary conditions in the direction of propagation of the flame are inflow/outflow non-reflecting (Poinso and Lele 1992), whereas periodicity is used in the two other directions.

The chemistry is described by a single-step irreversible reaction using a classical Arrhenius law. Following the notation of Williams (1985-a), the reaction rate for the deficient species (subscript R) can be expressed:

$$\dot{\omega}_R = \Lambda \rho Y_R \exp\left(-\frac{\beta(1-\Theta)}{1-\varphi(1-\Theta)}\right) \quad (13)$$

where:

$$\begin{aligned} \Theta &= (T - T_u)/(T_b - T_u) \text{ is the reduced temperature} \\ \varphi &= (T_b - T_u)/T_b \text{ represents the heat release parameter} \\ \beta &= \varphi E_a/R^0 T_b \text{ is the Zel'dovich number} \\ \Lambda &= B \exp(-\beta/\varphi) \text{ is the pre-exponential factor} \end{aligned}$$

The subscripts u and b represent respectively the unburnt and burnt gases and E_a the activation energy of the reaction, R^0 being the universal gas constant.

Moreover, in the simulations, the temperature dependence of the transport coefficients is taken into account by a power law:

$$\frac{\mu}{\mu_u} = \left(\frac{T}{T_u}\right)^b \quad (14)$$

where μ represents the dynamic viscosity and b is a constant equal to 0.76. The thermal conductivity and molecular diffusivity of the reactants are determined by considering constant Prandtl and Schmidt numbers.

Different simulations have been performed for various Lewis number (0.8, 1.0, 1.2), the other physical parameters being the same for all the configurations. At time $t = 0$, the turbulent Reynolds number based on the Taylor microscale λ is $Re_\lambda = 50$ and the initial Damköhler number (defined by $Da = (\lambda/u')/(\alpha_u/S_{L_0}^2)$) is $Da = 0.4$. Here, α_u represents the thermo-diffusivity in the fresh gases, S_{L_0} the laminar flame speed and u' the rms turbulent velocity. These initial conditions

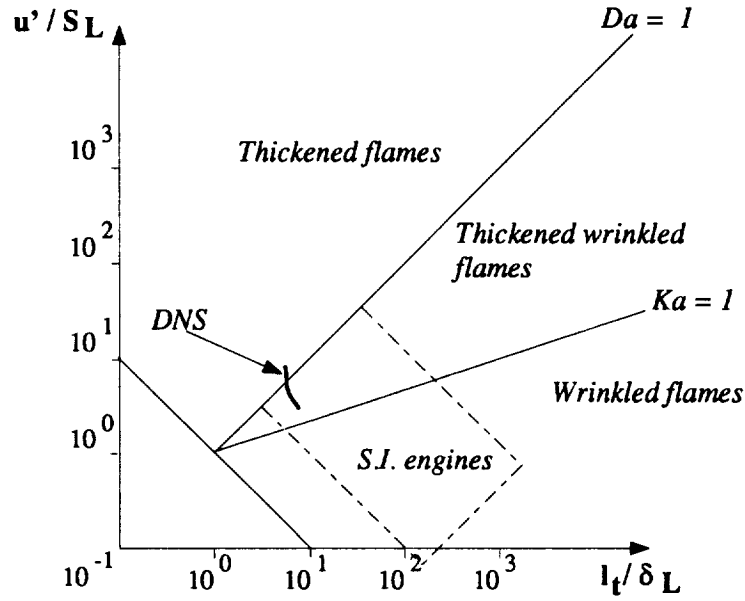


FIGURE 1. Evolution of the DNS in the diagram of premixed turbulent flames - comparisons with the operating domain of classical experimental devices and S. I. engines.

correspond to the ratios $u'/S_{L_0} = 10$ and $l_t/\delta_F = 5.2$ (l_t is the integral length scale of the turbulence and δ_F the laminar flame thickness defined by $\delta_F = \alpha_u/S_{L_0}$).

The flames investigated in the DNS evolve in the thickened wrinkled flames regime of the Borghi diagram for turbulent premixed flames (Borghi 1985) as is shown in Fig. 1. Also schematically shown in this diagram is the operating domain of classical experimental devices and S. I. engines (Abraham 1985).

In the following analysis, all of the cited turbulence quantities are obtained from a simulation of 3-D decaying isotropic turbulence with no combustion. All cases have been performed using a 129^3 computational domain.

2.3 Statistical analysis

In our analysis, since radiative heat losses and pressure rise are neglected and the specific heat is constant, the progress variable c defined in Eq. (2) is equivalent to $c = (T - T_u)/(T_b - T_u)$ and is equal to 0 in the fresh gases and to 1 in the fully burnt gases. In the calculation of the scalar dissipation $N = \alpha(\partial c/\partial x_k)(\partial c/\partial x_k)$, the thermo-diffusivity α is temperature dependent according to the relation (14) and by using the constant Prandtl number ($Pr = 0.75$).

In the determination of the conditional statistics, the progress variable space ζ is divided into 100 sub-domains. In each point of the computational domain, the variables of interest are calculated and stored in arrays corresponding to the sub-domain of ζ at this point. Conditional averages are then obtained by dividing the variable contained in the arrays by the number of samples of each sub-domain.

Since in the DNS the direction of propagation of the flame front is following the x direction, only $\langle U_1 | \zeta \rangle$ is of interest and will be investigated in the present analysis.

For the unconditional statistics, since we have access to only one realization, the problem is assumed to be homogeneous in the $y-z$ directions (x being the direction of propagation of the flame front). Then, the computational domain is divided into slices perpendicular to the x direction, and statistics are calculated for each plane through the turbulent flame front. The averaging of a variable Q varying spatially and temporarily is then estimated as it is proposed by Trouvé & Poinso (1994):

$$\langle Q(x, t) \rangle = \frac{1}{L_y L_z} \int Q(x, y, z, t) dy dz \quad (15)$$

where L_y and L_z are the size of the computational box in the y and z directions.

Through the flame brush \tilde{c} , the density weighted mean of c increases monotonically with x . Consequently, the results will be presented using the mean progress variable \tilde{c} instead of the x coordinate.

2.4 Results

2.4.1 The conditional dissipation rate N_ζ

Because it represents the small scale mixing or molecular dissipation of a scalar (concentration, temperature), the dissipation rate of the progress variable N is a crucial quantity in turbulent combustion (Borghgi 1990, Bray 1980, Mantel & Borghi 1994). In the case of turbulent premixed combustion, the mean reaction rate is directly proportional to \tilde{N} as has been demonstrated by Bray (1980) in the limit of high Damköhler numbers. Often, this term is modeled utilizing the dissipation time scale of the turbulent kinetic energy and a suitable constant, so that $\tilde{N} \propto \tilde{c}''^2 / \tau_t$ (Bray 1980, Spalding 1971). However, further studies have shown that the proportionality constant depends on at least two parameters describing the structure of the premixed flame such as the Damköhler and turbulence Reynolds numbers (Mantel & Borghi 1994, Said & Borghi 1988). In those studies, it appears that the ratio of the two dissipation time scales $R = \tau_t / \tau_c$ (τ_c represents the dissipation time scale of the scalar) is a function of the ratio $k^{1/2} / S_{L_0}$, which can also be defined by $k^{1/2} / S_{L_0} \propto (Re_t / Da)^{1/2}$ (k represents the turbulent kinetic energy). Said & Borghi (1988) proposed an algebraic formula for R whereas Mantel & Borghi (1994) have derived a transport equation for \tilde{N} .

For the conditional dissipation rate, few theoretical developments exist, and experimental and numerical data are only available for non-premixed combustion or non-reacting flows. Both Mell *et al.* (1994) in their numerical simulations and Li & Bilger (1993) in their experimental study have modeled the conditional dissipation of a conserved scalar N_η using the unconditional one and a frequency related to the large scales of the turbulence:

$$N_\eta \approx \tilde{N}_\zeta = R \tilde{Z}''^2 \frac{\epsilon}{k} \quad (16)$$

where R is the time scale ratio assumed to be constant, ϵ represents the dissipation of the turbulent kinetic energy, Z is the mixture fraction in the physical space, and η the mixture fraction in the domain of phase. These authors conclude that this classical closure gives good predictions for their experimental and numerical results, although more detailed modeling of N_ζ is better (Mell *et al.* 1994).

However, this kind of closure apparently valid for non-premixed systems cannot be applied for premixed flames because the turbulent mixing is not the only cause of scalar variance annihilation. Chemical reaction is also involved and has to be considered in the modeling of N_ζ . This is illustrated in Fig. 2 which shows the evolution of R across the flame brush. The ratio R varies significantly through the flame brush ranging from 0.3 to 1.5. This is consistent with the values found by Beguier *et al.* (1978) in the case of non-reacting flows. Only a slight effect of the Lewis number is observed on R (see Fig. 2-a). As the time goes on, we note in Fig. 2-b that R is less than unity in the most part of the turbulent flame front ($0.1 \leq \tilde{c} \leq 0.9$). This indicates that the turbulence dissipates more rapidly than the fluctuations of \tilde{c} . In such a case, it clearly appears that the well-known Eddy Break-Up model will significantly overestimate the mean reaction rate since $\tilde{w}_{ebu} \propto \tilde{c}(1 - \tilde{c})/\tau_t$.

Fig. 3 shows the form of $\hat{N}_{\zeta_{lam}} = N_{\zeta_{lam}} \tau_{ch}$ (τ_{ch} represents a chemical time scale defined by $\tau_{ch} = \alpha_u/S_{L_0}^2$) in a planar laminar flame front for different Lewis numbers. As expected, $\hat{N}_{\zeta_{lam}}$ is insensitive to the Lewis number since the progress variable is expressed in terms of temperature instead of the concentration of fuel, for instance. Unlike Bilger (1993-b), \hat{N}_ζ does not have a symmetric shape, but has a maximum value towards the burnt gases. This asymmetry is due to the high activation energy for the kinetics, whereas Bilger (1993-b) is for a full kinetic mechanism. We can note the quadratic behavior of $\hat{N}_{\zeta_{lam}}$ in the preheat zone ($\zeta < 0.6$) as given by the convection diffusion balance:

$$\rho_u S_{L_0} \frac{dc}{dx} = \frac{d}{dx} \left(\rho \alpha \frac{dc}{dx} \right) \quad (17)$$

which leads directly to $\hat{N}_{\zeta_{lam}} = (T/T_u)^{1-b} \cdot \zeta^2$.

Fig. 4 shows the evolution of N_ζ (normalized by the laminar value $N_{\zeta_{lam}}$) for the turbulent flame with $Le = 1.0$ versus ζ for different times (t/τ_0 ranges from 1.4 to 4.5, τ_0 being the eddy turn-over time). At the earliest time results are shown after one eddy turn-over time, and thus the flame has had the time needed to adapt itself to all the spectrum of the turbulence. Since in the DNS positive stretch occurs (on average) more often than negative stretch (Trouvé & Poinsot 1994), the profiles of concentration and temperature are steepened, and we can expect higher values for N_ζ than in the laminar case. At earlier times, this enhanced mixing appears to be very strong in the preheat zone but also may be dependent on the Damköhler number. Since the Damköhler number is low, the instantaneous flame front does not respond immediately to the turbulent flow field, and in the preheat zone, N_ζ is 2 or 3 times greater than the laminar value. The reaction zone, however remains almost unaffected by the turbulent mixing, and we observe an only slight increase

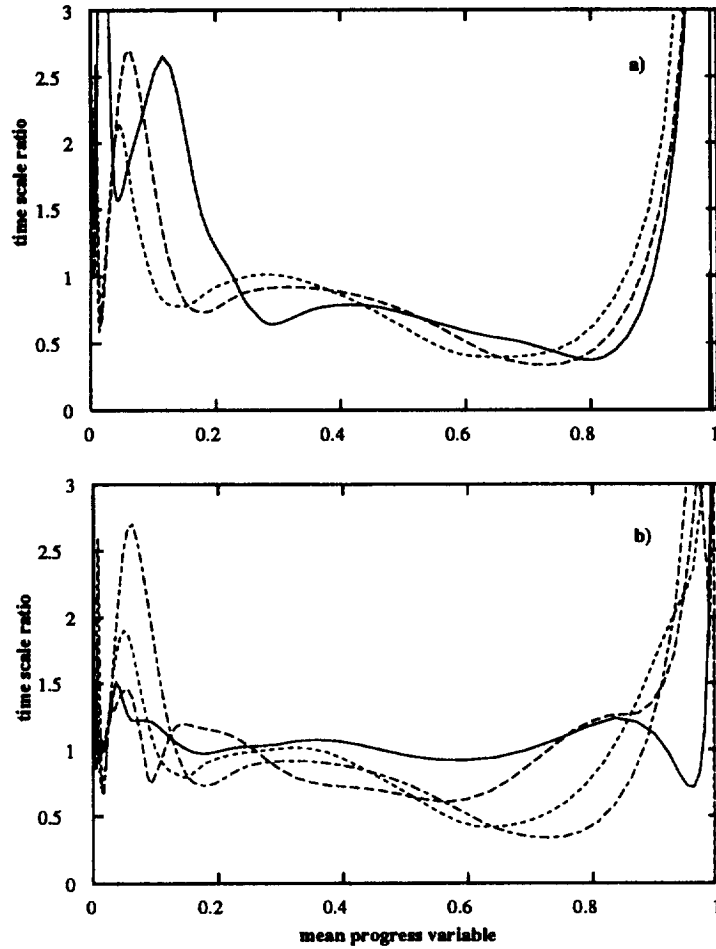


FIGURE 2. Profiles of $R = \tau_t / \tau_c$ versus \tilde{c} . a) for different Lewis number at $t/\tau_0 = 4.5$: $Le = 0.8$: —; $Le = 1.0$: ----; $Le = 1.2$: - · - · -. b) for different times and $Le = 1.0$: $t/\tau_0 = 1.4 - Re_t = 50 - Da = 0.5$: —; $t/\tau_0 = 2.7 - Re_t = 33 - Da = 0.6$: ----; $t/\tau_0 = 3.6 - Re_t = 29 - Da = 0.8$: - · - · -; $t/\tau_0 = 4.5 - Re_t = 25 - Da = 1.0$: - - - -

of N_ζ of approximately 20%. As the time goes on, the Damköhler number increases due to the decay of the turbulence. Thus, the turbulent flame comes more into the flamelet regime and N_ζ behaves more and more as in the laminar case. At this point, there is no distinction between the preheat zone, and the reaction zone and $N_\zeta / N_{\zeta_{lam}}$ is almost constant and close to unity in all of the domain of ζ .

The variation of $N_\zeta / N_{\zeta_{lam}}$ across the flame brush is represented in Fig. 5 for different values of ζ . It appears that $N_\zeta / N_{\zeta_{lam}}$ is almost constant through the turbulent flame front and is only weakly dependent on \tilde{c} . Thus, conditional statistics for N_ζ can be extracted from all the computational domain rather than in $y - z$ planes.

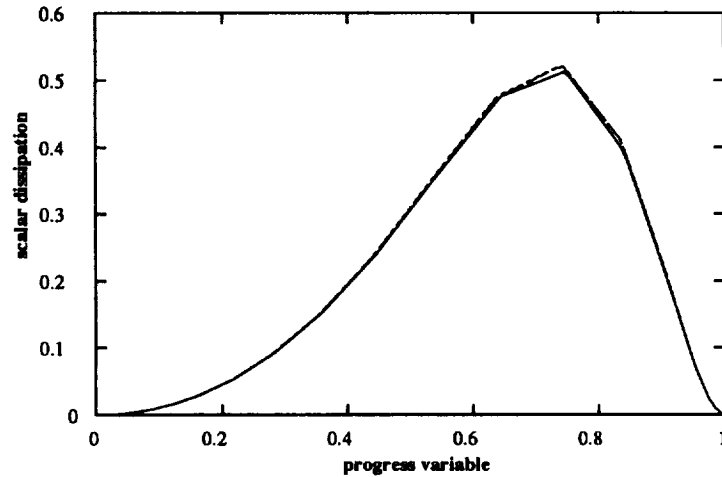


FIGURE 3. Profiles of \hat{N}_ζ for laminar flame versus ζ given by DNS. $Le = 0.8$: — ; $Le = 1.0$: - - - ; $Le = 1.2$: - · - · -

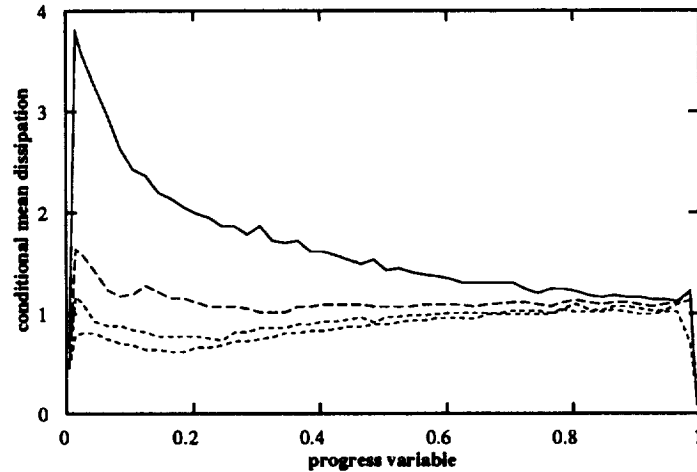


FIGURE 4. Profiles of $N_\zeta/N_{\zeta_{lam}}$ versus ζ for $Le = 1.0$. $t/\tau_0 = 1.4$: — ; $t/\tau_0 = 2.7$: - - - ; $t/\tau_0 = 3.6$: - · - · - ; $t/\tau_0 = 4.5$: - - - - . See Fig. 2 for the corresponding Damköhler numbers.

The influence of the Lewis number on N_ζ is also investigated and presented in Fig. 6 for 2 different times of the interaction. At time $t/\tau_0 = 1.4$ (corresponding to $Da = 0.5$), we notice a significant effect of the Lewis number in the reaction zone ($\zeta > 0.7$). In the preheat zone, no effect of the Lewis number is observed. The turbulent mixing predominates and diffusivities (of species and temperature) are too slow compared to the chemistry to allow the profile of c to behave like in the laminar case. In the reaction zone, the end of the temperature profile seems to be affected, illustrating an effect of the Lewis number. The gradients of c are

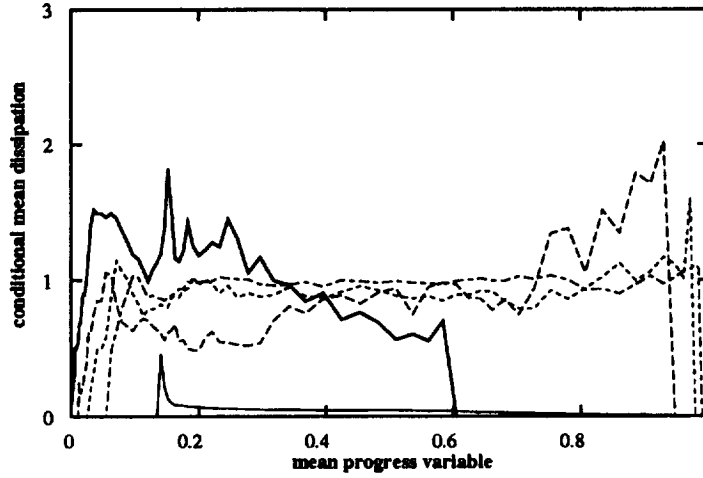


FIGURE 5. Evolution of $N_{\zeta}/N_{\zeta_{lamin}}$ versus \tilde{c} for different values of ζ at $t/\tau_0 = 4.5$ and $Le = 1.0$. $\zeta = 0.0$: — ; $\zeta = 0.25$: - - - ; $\zeta = 0.5$: ····· ; $\zeta = 0.75$: - · - · ; $\zeta = 1.0$: ———

steeper for $Le = 0.8$ and flatter for $Le = 1.2$ (for $Le = 1.2$, we can note that N_{ζ} decreases significantly below the laminar value). There is no clear explanation for such behavior. We can argue that for a positive stretch, the local reaction rate increases (decreases) when the Lewis number is smaller (greater) than unity and affects the end of the temperature profile increasing (decreasing) the gradients of c .

For time $t/\tau_0 = 4.5$ (which corresponds to $Da = 1.0$), N_{ζ} is affected uniformly by the Lewis number and no distinct behaviors exist between the preheat and reaction zones. The gradients of c are steeper everywhere in the ζ space for $Le = 0.8$ and weakly flatter (especially in the reaction zone) for $Le = 1.2$. This result is quite surprising because we can expect that when the Damköhler number increases, the turbulent flame behaves more and more in the flamelet regime. Thus locally the flame should have the structure of a laminar flame, and consequently the 3 curves of Fig. 6-b should merge together. This comment concerns mainly the case $Le = 0.8$ for which the gradients of c are significantly higher than the two others cases. Since in this case the Lewis number is smaller than unity, we can hypothesize that thermo-diffusive instabilities have become non-negligible and provoke additional stretch that is not present in the cases $Le = 1.0$ and $Le = 1.2$.

In conclusion, from the Fig. 6, it appears that the ratio $N_{\zeta}/N_{\zeta_{lamin}}$ depends strongly on the Damköhler number, particularly in the preheat zone. At this point, we cannot make a conclusion on the dependency on Lewis number since we are not able to separate the effects of the turbulence and the effects of thermo-diffusive instabilities.

In order to get more information on the role of the mixing on the structure of the flame, the product $\tilde{P}(\zeta; \tilde{c}) \cdot N_{\zeta}$ is extracted from the DNS for $Le = 1.0$ at $t/\tau_0 = 4.5$. Fig. 7 shows $\tilde{P}(\zeta; \tilde{c}) \cdot N_{\zeta}$ (non-dimensionalized by τ_{ch}) as a function of ζ

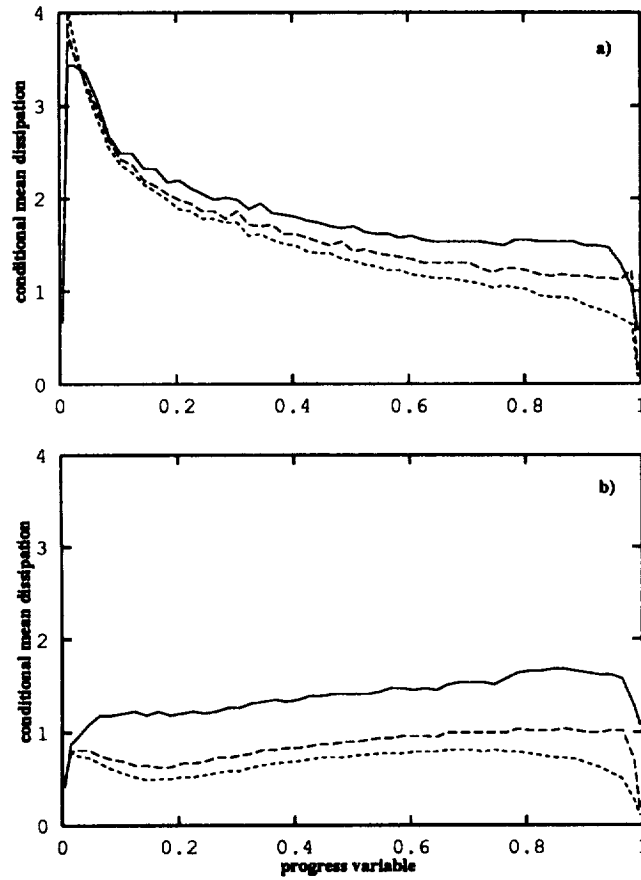


FIGURE 6. Profiles of $N_{\zeta}/N_{\zeta_{flam}}$ versus ζ . a) $t/\tau_0 = 1.4$ - b) $t/\tau_0 = 4.5$ $Le = 0.8$: — ; $Le = 1.0$: - - - - ; $Le = 1.2$: ·····

at different locations across the flame front. It appears that the dissipation occurs almost everywhere in the progress variable space, but most of it takes place in the reaction zone associated with values of ζ comprised between 0.6 and 0.9. Higher dissipation occurring in the preheat zone is only observed in regions of the turbulent flame located near the fresh gases.

The density-weighted pdf $\tilde{P}(\zeta)$ is shown in Fig. 8 for different sections of the flame brush at different instants and Lewis number. For all the cases studied here, the pdf $\tilde{P}(\zeta)$ exhibits a strong bimodal shape corresponding to fresh and fully burnt gases. However, $\tilde{P}(\zeta)$ is not purely bimodal and a broad peak on the fresh gas side (which characterizes regions of the flame brush where instantaneous flame fronts are thickened) is observed. Between these two peaks (for $0.3 \leq \zeta \leq 0.9$), the shape of $\tilde{P}(\zeta)$ is rather flat and ranges from 0.2 to 0.8. This represents intermediate events occurring in the instantaneous flame fronts. This behavior can be expected according to the schematical description given in Fig. 1 concerning the regime of

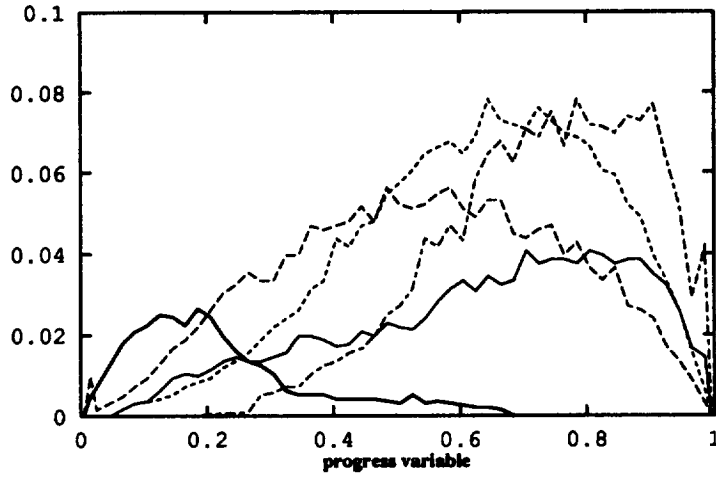


FIGURE 7. Evolution of $\tilde{P}(\zeta) \cdot N_\zeta$ (non-dimensionalized by τ_{ch}) versus ζ across the flame front at $t/\tau_0 = 4.5$ and $Le = 1.0$. $\tilde{c} = 0.05$: — ; $\tilde{c} = 0.25$: - - - - ; $\tilde{c} = 0.5$: - · - · - ; $\tilde{c} = 0.75$: - - - - ; $\tilde{c} = 0.95$: —

propagations of these flames.

Since most of the available data for turbulent premixed combustion are obtained using unconditional statistics, it is of interest to calculate unconditional variables from their conditional values. The unconditional statistics for a variable Q can be directly obtained from the conditional value $\langle Q | \zeta \rangle$ and the probability density function $\tilde{P}(\zeta)$:

$$\tilde{Q} = \int_0^1 \langle Q | \zeta \rangle \tilde{P}(\zeta) d\zeta \quad (18)$$

If $\langle Q | \zeta \rangle$ is known, it appears that the pdf $\tilde{P}(\zeta)$ has to be carefully estimated. As we said in the introduction, the pdf $\tilde{P}(\zeta)$ can be directly obtained by solving its transport equation (an expression for $\tilde{P}(\zeta)$ can be found in Borghi 1988, Pope 1985-b) or estimated by assuming realistic shapes for $\tilde{P}(\zeta)$ (Borghi 1988, Bray 1980) and predicting only its first two moments, \tilde{c} and \tilde{c}''^2 .

A way to estimate $\tilde{P}(\zeta)$ is to choose a β function as proposed by Janicka & Kollmann (1978):

$$\tilde{P}(\zeta) = \frac{\zeta^{a-1} (1-\zeta)^{b-1}}{\int_0^1 \zeta^{a-1} (1-\zeta)^{b-1} d\zeta} \quad (19)$$

with $a = \tilde{c} \left(\frac{\tilde{c}(1-\tilde{c})}{\tilde{c}''^2} - 1 \right)$ and $b = a \frac{1-\tilde{c}}{\tilde{c}}$. Fig. 9 represents the comparison between the pdf $\tilde{P}(\zeta)$ given by the DNS and the pdf estimated from Eq. (19) for different positions across the turbulent flame brush. The parameters a and b are calculated using \tilde{c} and \tilde{c}''^2 extracted from the DNS. The agreement between the

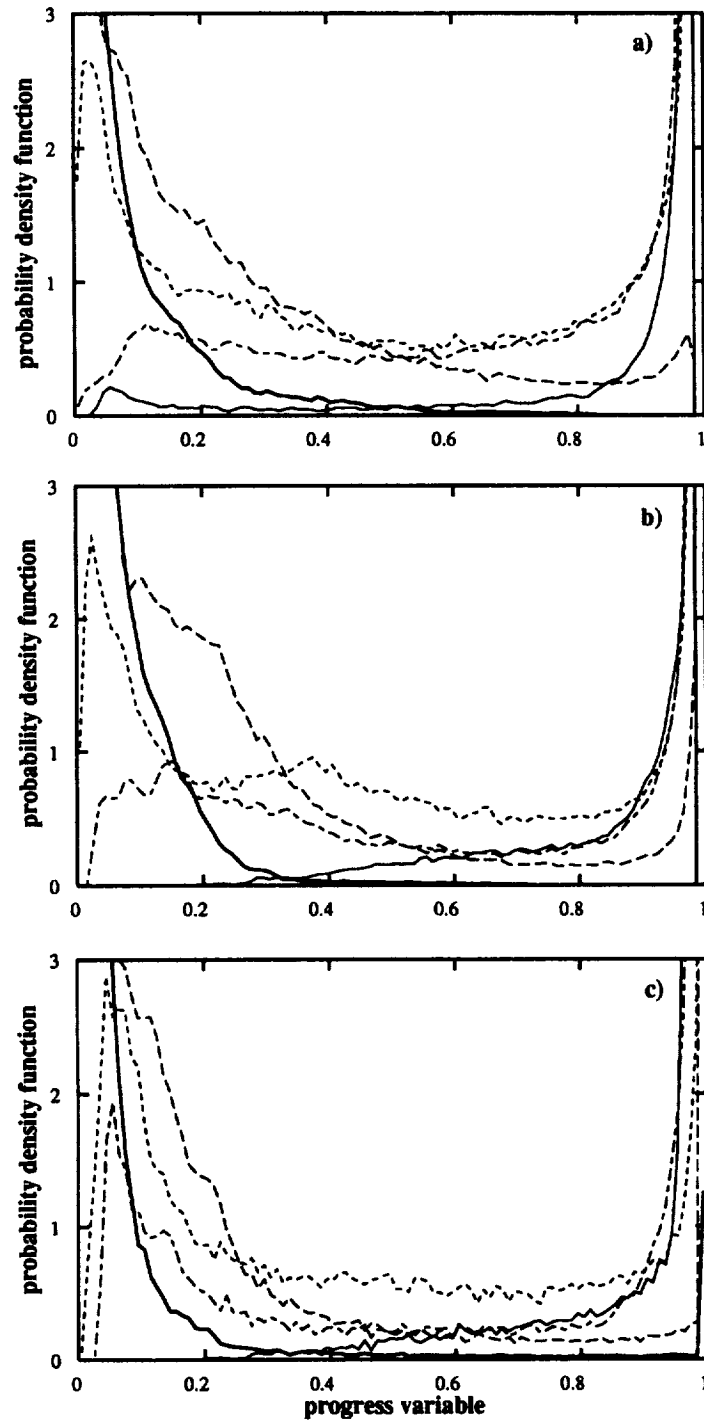


FIGURE 8. The pdf $\tilde{P}(\zeta)$ versus ζ at: a) $Le = 1.0 - t/\tau_0 = 1.4$, b) $Le = 1.0 - t/\tau_0 = 4.5$, c) $Le = 0.8 - t/\tau_0 = 4.5$. $\tilde{c} = 0.05$: — ; $\tilde{c} = 0.25$: - - - ; $\tilde{c} = 0.5$: ····· ; $\tilde{c} = 0.75$: - · - · ; $\tilde{c} = 0.95$: ———

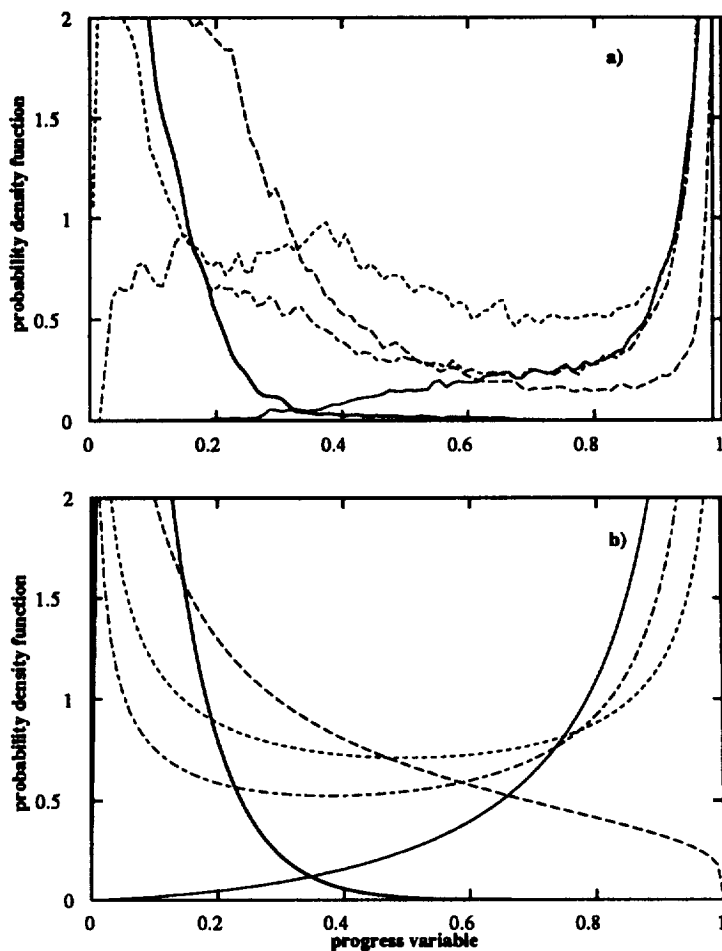


FIGURE 9. Profiles of the pdf $\tilde{P}(\zeta)$ versus ζ across the turbulent flame front at $Le = 1.0$ and $t/\tau_0 = 4.5$. a): DNS ; b): β function. $\tilde{c} = 0.05$: — ; $\tilde{c} = 0.25$: ---- ; $\tilde{c} = 0.5$: ; $\tilde{c} = 0.75$: - · - · - ; $\tilde{c} = 0.95$: ———

DNS and the model of Eq. (19) is relatively satisfying for each of the five sections studied across the turbulent flame front. The β function constitutes an interesting approach to estimating $\tilde{P}(\zeta)$ in a presumed pdf approach applied to turbulent premixed combustion.

As we have already mentioned, the pdf $\tilde{P}(\zeta)$ appears strongly bimodal, but a significant fraction of events occurs between the two spikes located at $\zeta = 0$ and $\zeta = 1$. This is probably a consequence of the low Damköhler number. Thus, the pdf present between $\zeta = 0$ and $\zeta = 1$ can become a crucial quantity in the estimation of some terms which are equal to 0 for $\zeta = 0$ and $\zeta = 1$. This is particularly the case for the conditional dissipation rate for which we have $\langle N_\zeta | \zeta = 0 \rangle = \langle N_\zeta | \zeta = 1 \rangle = 0$.

The unconditional dissipation rate defined by:

$$\tilde{N} = \int_0^1 \langle N_\zeta | \zeta \rangle \tilde{P}(\zeta) d\zeta \quad (20)$$

is strongly dependent on the value of $\tilde{P}(\zeta)$ between the two spikes, especially when Da is low as in this DNS.

In order to estimate how far we are from a purely bimodal combustion regime, we have also studied the fluctuation level parameter g defined by Bray (1980):

$$g = \frac{\widetilde{c'^{1/2}}}{\tilde{c}(1 - \tilde{c})} \quad (21)$$

This parameter varies from 0 for no fluctuation to 1, the maximum possible value corresponding to a purely bimodal pdf. In this last case, only fully burnt or fresh gases are present in the flow.

The results in Fig. 10 show that even if the level of fluctuations is high, g is significantly below the maximum value of 1.0. Thus, in some regions of the flow, intermediate states occurs quite frequently as has already been shown in Fig. 10-a where the pdf shows a plateau of about 0.5 when $\tilde{c} = 0.5$.

Because different models for turbulent premixed combustion relate directly the mean reaction rate to $\tilde{c}(1 - \tilde{c})$ and a suitable frequency, this result is important from a modeling point of view. In cases such as this, these models will overestimate the mean reaction rate. This is particularly the case in the Eddy Break-up formulation (Spalding 1971) and for the BML approach (Bray & Libby 1986). An alternative possibility is to directly calculate $\widetilde{c'^{1/2}}$ from its transport equation. However, this approach requires a good model for the dissipation rate \tilde{N} , which is not an easy task. We have already discussed the difficulties and the different possibilities of estimating this quantity (Mantel & Borghi 1994, Said & Borghi 1988).

2.4.2 The conditional mean velocity

Like the conditional dissipation rate N_ζ , the conditional mean velocity $\langle U_k | \zeta \rangle$ appearing in Eq. (7) has to be modeled. Since very little is known concerning $\langle U_k | \zeta \rangle$, information from experimental data or from DNS is of interest in order to propose realistic closure for this term.

The conditional mean velocity $\langle U_k | \zeta \rangle$ can be obtained from the conditional pdf $P(V_k | \zeta)$ of U_k and c :

$$\langle U_k | \zeta \rangle = \int_{-\infty}^{\infty} V_k P(V_k | \zeta) dV_k \quad (22)$$

where V_k represents the stochastic vector variable related to the velocity vector $U_k(x_k, t)$. According to Bayes theorem, $P(V_k | \zeta)$ is obtained from the joint pdf of V_k and ζ $P(V_k; \zeta)$ and the pdf for ζ $P(\zeta)$:

$$P(V_k | \zeta) = P(V_k; \zeta) / P(\zeta) \quad (23)$$

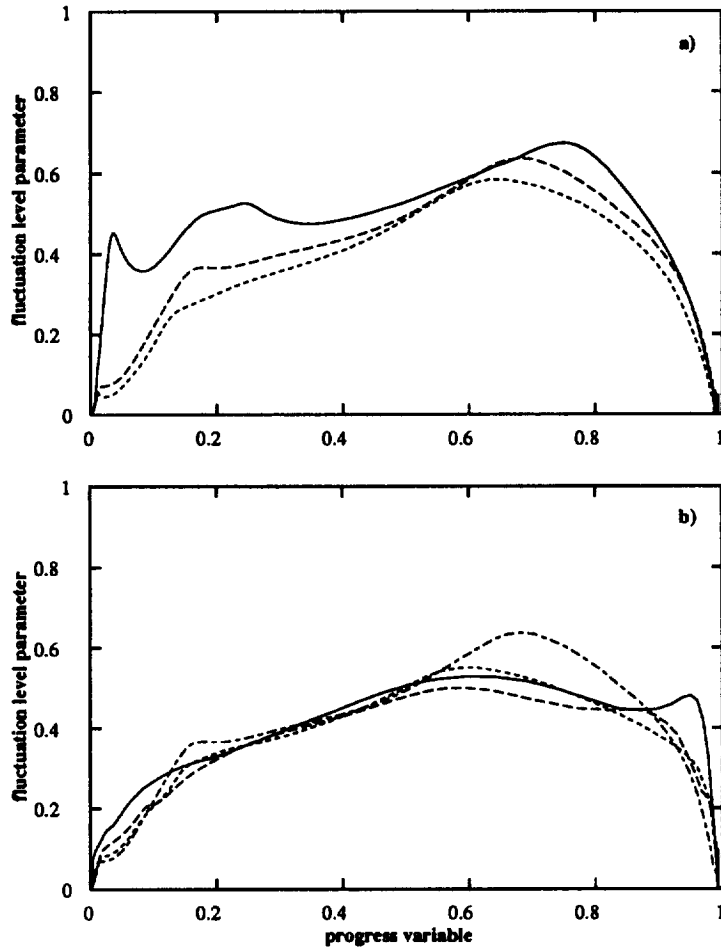


FIGURE 10. Variation of the fluctuation level parameter g versus \tilde{z} . Same legend as in Fig. 2.

The joint pdf of V_k and ζ can be modeled by presuming realistic shapes for P (Borghini & Dutoya 1978) or by calculating its transport equation (see Pope 1981-1985 for the derivation and the modeling of this equation).

The conditional mean velocity can be extracted from the DNS for the different available cases. Since in the y and z directions the conditional mean advection term is zero from homogeneity, only the conditional mean velocity in the direction of propagation of the flame (x direction) is investigated.

Fig. 11 represents the variation of the conditional velocity $\langle U_1 | \zeta \rangle$ across the turbulent flame front for different values of ζ . During the simulation, the velocity conditioned on the fresh gases is higher than the one conditioned in the burnt gases. Thus, the slip velocity (which is the difference between the mean velocity conditioned in the burnt gases and the mean velocity conditioned in the fresh gases) is always negative and indicates that the flame displacement is strongly correlated

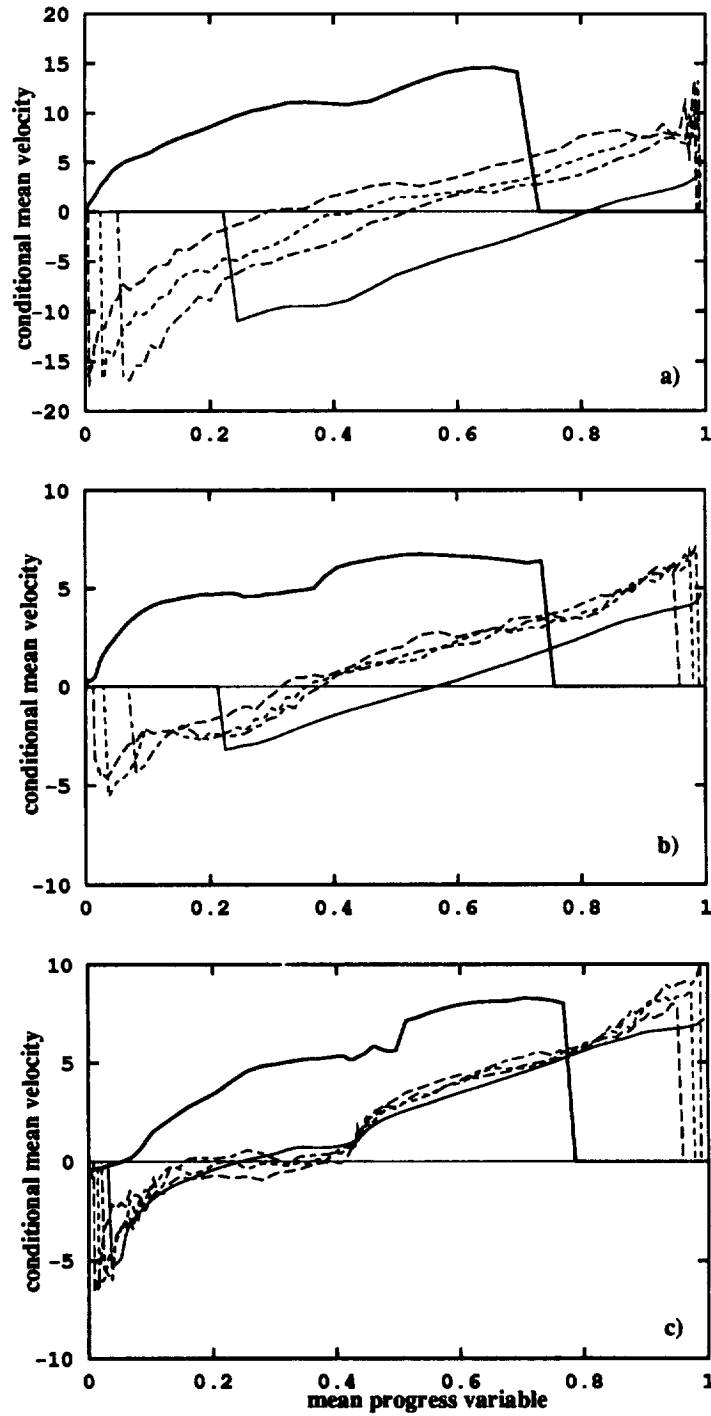


FIGURE 11. Profiles of $\langle U_1 | \zeta \rangle$ versus \tilde{c} . a) $Le = 1.0 - t/\tau_0 = 1.4$ b) $Le = 1.0 - t/\tau_0 = 4.5$ c) $Le = 0.8 - t/\tau_0 = 4.5$. $\zeta = 0.0$: — ; $\zeta = 0.25$: - - - ; $\zeta = 0.5$: ···· ; $\zeta = 0.75$: - · - · ; $\zeta = 1.0$: ———

with the velocity fluctuations in the unburnt gas. Thus, on most part of the flame front, the burnt gases are animated with negative velocities (toward the fresh gases) whereas the fresh gases move with positive velocities (toward the burnt gases). In the turbulent flame front, fingers of fresh gases appear in the burnt gases (and conversely).

We can also notice only a slight acceleration of the gases through the laminar flame front. All the isopleth contours are moved with the same displacement velocity. This is probably due to the fact that the pressure difference across the instantaneous flame front is insufficient to produce significant acceleration of the fluid through the instantaneous flame front in the x direction. Acceleration of the burnt gas occurs in the mean pressure gradient across the turbulent flame brush as a whole rather than in the instantaneous flame fronts. It seems that the instantaneous flame fronts adjust themselves to provide dilatation without acceleration. If this finding is sustained in other studies, it could be an important hypothesis on which to base a new approach to the theory of turbulent premixed flame propagation. It is evident that the variation of $\langle U_1 | \zeta \rangle$ through the flame brush will be significant in CMC modeling.

2.4.3 Turbulent diffusion fluxes

In turbulent combustion modeling, the turbulent fluxes of the mean progress variable are classically closed using a gradient transport approximation:

$$-\overline{u_k'' c''} = \frac{\nu_t}{Sc_t} \frac{\partial \tilde{c}}{\partial x_k} \quad (24)$$

where ν_t is the eddy viscosity and Sc_t a Schmidt number. From previous studies, it is known that such modeling is not always sound for turbulent premixed flames (Borghi & Dutoya 1978, Libby & Bray 1981, Mantel & Borghi 1994, Moss 1980). Both Dutoya & Borghi (1978) and Mantel *et al.* (1993) found that the Schmidt number Sc_t is not constant and varies significantly across the turbulent flame front. Moreover, the modeling of the turbulent flux strongly affects the structure of the turbulent flame brush. In their study, Mantel *et al.* (1993) show that the turbulent flame thickness is over-estimated by about 50% by the gradient transport approximation. Libby & Bray (1981) have even formulated a model for counter-gradient diffusion due to the large variation of density occurring in reactive flows in accordance with the experimental results of Moss (1980). With a sufficiently high heat release ($\tau = T_b/T_u - 1 > 3$), the authors show that a pressure gradient present in the flow can preferentially accelerate the low density gases and then create counter-gradient diffusion processes. However, the pressure gradient is not the only candidate able to provoke counter-gradient diffusion. In a recent study, Trouvé *et al.* (1994) show that while counter-gradient diffusion is present at low turbulence, in the presence of strong turbulence the flame brush tends to become more and more wrinkled and thickened, leading to classical gradient diffusion transport. The authors also show that the wrinkling of the turbulent flame brush is a crucial parameter controlling gradient and counter-gradient diffusion.

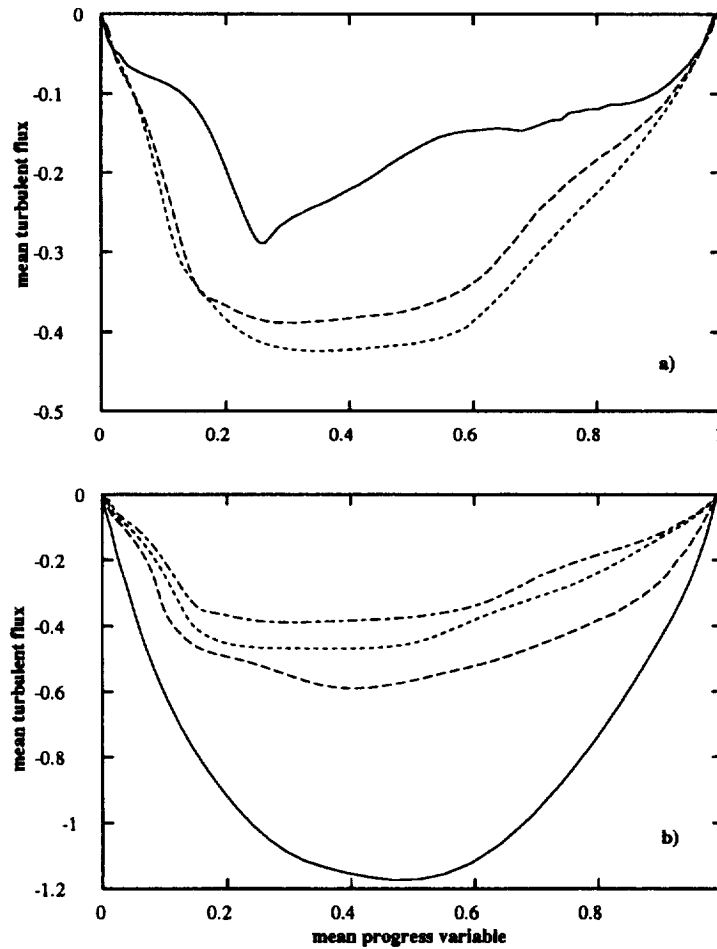


FIGURE 12. Profiles of $\widetilde{u''c''}$ versus \tilde{c} . Same legend as in Fig. 2.

From the DNS, we have computed the turbulent fluxes $\widetilde{u''c''}$ and $\widetilde{u''c''^2}$ across the flame brush at different times of the interaction and Lewis number (see Figs. 12 and 13). For the same heat release as in Libby & Bray (1981), no counter-gradient diffusion is observed for $\widetilde{u''c''}$ from the DNS. Similarly, no counter-gradient diffusion is observed for the turbulent flux $\widetilde{u''c''^2}$.

3. Conclusion

Conditional statistics for the scalar dissipation N_ζ and the mean velocity $\langle U_1 | \zeta \rangle$ have been extracted from direct numerical simulation. The simulations used in this study have been performed by Trouvé & Poinso (1994) and describe the interaction between a premixed flame with realistic heat release and an isotropic decaying turbulent flow field. The turbulence intensity is at the high end of the range of interest and the Damköhler numbers at the low end.

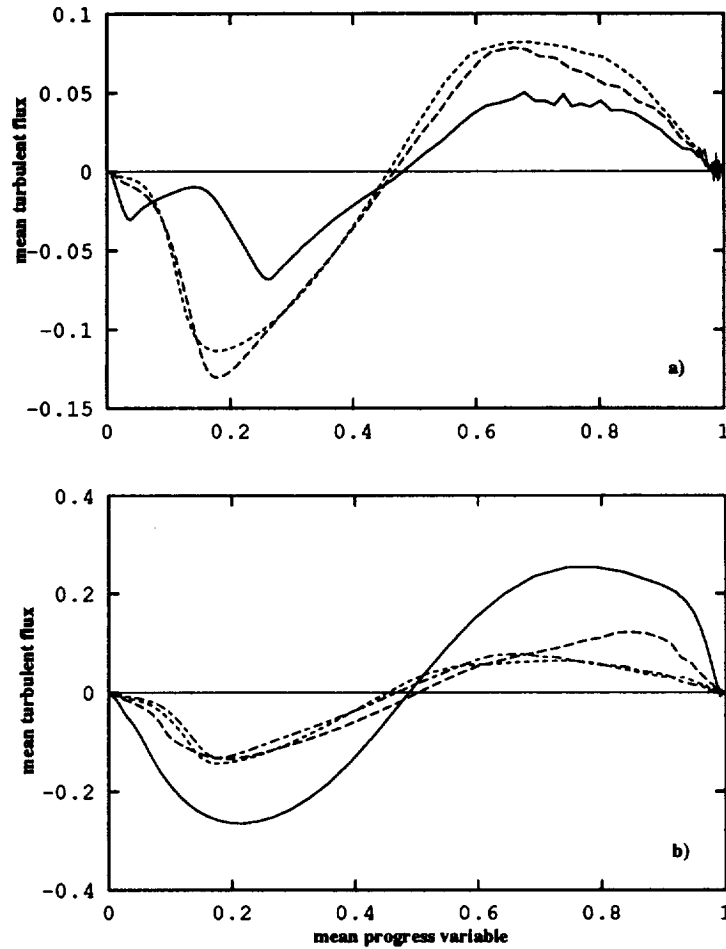


FIGURE 13. Profiles of $\widetilde{u''c''}$ versus \tilde{c} . Same legend as in Fig. 2.

The conditional scalar dissipation N_ζ behaves differently in different parts of the instantaneous flame fronts. In the reaction zone, N_ζ is weakly affected by the turbulent mixing whereas in the preheat zone, the local gradients of the progress variable ζ are steeper due to the stretch effects which tend to increase N_ζ . This is particularly notable when the Damköhler number is low. As the time goes on, Da increases (due to the decay of the turbulence in the simulations), and locally, the instantaneous flame fronts resemble more the laminar flamelet.

As expected from the heat release, the conditional mean velocity (x -component) $\langle U_1 | \zeta \rangle$ evolves almost linearly through the turbulent flame brush. We also notice a negative slip velocity, which characterizes the wrinkling of the turbulent flame. We found that in this simulation, burnt gases are moved towards the fresh gases and vice versa, producing a highly wrinkled flame as can be observed in Trouvé & Poinot (1994). Due to a weak local pressure gradient, only a slight acceleration of the gases across the instantaneous flame fronts is observed.

The weighted pdf $\tilde{P}(\zeta)$ derived from the DNS shows a strongly bimodal shape (for $\zeta = 0$ and $\zeta = 1$). Between these two peaks, non-negligible values for $\tilde{P}(\zeta)$ are observed (typically 0.2) which characterize intermediate states. A satisfying agreement is observed between $\tilde{P}(\zeta)$ estimated from a β function and $\tilde{P}(\zeta)$ extracted from the DNS.

The turbulent fluxes $\widetilde{u_1'' c''}$ and $\widetilde{u_1'' c''^2}$ across the flame brush are derived from the DNS. Contrary to previous studies (Libby & Bray 1981, Moss 1980), no counter-gradients have been found in these simulations. According to the recent study of Trouvé *et al.* (1994), the presence of a strong wrinkling of the turbulent flame brush is more favorable to gradient diffusion.

The present study constitutes a first analysis of conditional statistics in premixed turbulent flames. Further experimental and numerical studies have to be done in order to provide new information, notably at higher Reynolds and Damköhler numbers.

Acknowledgements

The authors would like to gratefully acknowledge Drs. A. Trouvé and T. Poinso, who performed the direct numerical simulations at the Center for Turbulence Research of Stanford University and NASA Ames Research Center.

REFERENCES

- ABRAHAM, J., WILLIAMS, F. A. & BRACCO, F. V. 1985 A Discussion of Turbulent Flame Structure in Premixed Charge Engine. *SAE Paper 850345*.
- BÉGUIER, C., DEKEYSER, J. & LAUNDER, B. E. 1978 Ratio of the Scalar and Velocity Dissipation Time Scales in Shear Flow Turbulence. *Phys. Fluids*. **21-3**, 307-310.
- BIDEAUX, E., VERVISCH, L. & BRAY, K. N. C. 1994 Study of the Transport Equation for a Surface Density Function and Some Implications for Turbulent Combustion Modelling. *Submitted to Phys. Fluids*.
- BILGER, R. W. 1993-a Conditional Moment Closure for Turbulent Reacting Flows. *Phys. Fluids*. **A5-2**, 436-444.
- BILGER, R. W. 1993-b Conditional Moment Closure Modelling and Advanced Laser Measurements. In *Turbulence and Molecular Processes in Combustion*, T. Takeno (Editor), pp 267-285, Elsevier Science Publishers.
- BILGER, R. W. 1993-c Scalars and their Dissipation in Turbulent Reactive Flows: An Overview of Measurements Needs and Capabilities. *Western States Section of The Combustion Institute*, Paper 93-059.
- BORGHI, R. 1985 On the Structure and Morphology of Turbulent Premixed Flames. *Recent Advances in Aerospace Science* (ed. C. Bruno and C. Casci).
- BORGHI, R. 1988 Turbulent Combustion Modelling. *Progress in Energy and Combustion Science*. **14**, 245-292.

- BORGHI, R. 1990 Turbulent Premixed Combustion: Further Discussions on the Scales of Fluctuations. *Combustion and Flame*. **80**, 304-312.
- BORGHI, R. & DUTOYA, D. 1978 On the Scale of the Fluctuations in Turbulent Combustion. *Seventeenth Symposium (International) on Combustion, The Combustion Institute, Pittsburgh*. 235-244.
- BRAY, K. N. C. 1980 Turbulent Reacting Flows with Premixed Reactants. *Topics in Applied Physics*. **44**, 115-183, Springer Verlag.
- BRAY, K. N. C. & LIBBY, P. A. 1986 Passage Times and Flamelet Crossing Frequencies in Premixed Turbulent Combustion. *Combustion, Science and Technology*. **47**, 253-274.
- CANDEL, S. M. & POINSOT, T. J. 1990 Flame Stretch and the Balance Equation for the Flame Area. *Combustion, Science and Technology*. **70**, 1-15.
- DOPAZO, C. 1977 On Conditional Averages for Intermittent Turbulent Flows. *J. Fluid Mech.* **81**, 433-438.
- JANICKA, J. & KOLLMANN, W. 1978 A Two-Variables Formalism for the Treatment of Chemical Reactions in Turbulent H₂-Air Diffusion Flames. *Seventeen Symposium (International) on Combustion, The Combustion Institute, Pittsburgh*. 421-430.
- JAYESH & WARHAFT, Z. 1992 Probability Distribution, Conditional Dissipation, and Transport of Passive Temperature Fluctuations in Grid-Generated Turbulence. *Phys. Fluids*. **A4-10**, 2292-2307.
- KERSTEIN, A., ASHURST, W. T. & WILLIAMS, F. A. 1988 Field Equation for Interface Propagation in an Unsteady Homogeneous Flow Field. *Phys. Review*. **A-37-7**, 2728-2731.
- KLIMENKO, A. Y. 1990 Multicomponent Diffusion of Various Admixtures in Turbulent Flows. *Fluid Dynamics*. **25**, 327-334.
- LELE, S. K. 1992 Compact Finite Difference Schemes with Spectral-like Resolution. *J. Comp. Phys.* **103**, 16-42.
- LI, J. D. & BILGER, R. W. 1993 Measurement and Prediction of the Conditional Variance in a Turbulent Reactive-Scalar Mixing Layer. *Phys. Fluids*. **A5-12**, 3255-3264.
- LIBBY, P. A. 1975 On the Prediction of Intermittent Turbulent Flows. *J. Fluid Mech.* **68**, 273-295.
- LIBBY, P. A. & BRAY, K. N. C. 1981 Countergradient Diffusion in Premixed Turbulent Flames. *AIAA Journal*. **19-2**, 205-213.
- MANTEL, T. & BORGHI, R. 1994 A New Model of Premixed Wrinkled Flame Based on a Scalar Dissipation Equation. *Combustion and Flame*. **96**, 443-457.
- MANTEL, T., BORGHI, R. & PICART, A. 1993 Turbulent Premixed Flame Propagation Revisited with a New Model. *Ninth Symposium on Turbulent Shear Flows*.

- MELL, W. E., NILSEN, V., KOSALY, G. & RILEY, J. J. 1994 Investigation of Closure Models for Non-Premixed Turbulent Reacting Flows. *Phys. Fluids*. **6-3**, 1331-1356.
- MOSS, J. B. 1980 Simultaneous Measurements of Concentration and Velocity in an Open Premixed Turbulent Flame. *Combustion, Science and Technology*. **22**, 119-129.
- O'BRIEN, E. E. 1985 The Probability Density Function (Pdf) Approach to Reacting Turbulent Flows. *Topics in Applied Physics, Springer Verlag*. **44**, 185-218.
- PETERS, N. 1986 Laminar Flamelet Concepts in Turbulent Combustion. *Twenty-First Symposium (International) on Combustion, The Combustion Institute, Pittsburgh*. 1231-1250.
- PETERS, N. 1992 A Spectral Closure for Premixed Turbulent Combustion in the Flamelet Regime. *J. Fluid Mech.* **242**, 611-629.
- POINSOT, T. J. & LELE, S. K. 1992 Boundary Conditions for Direct Simulations of Compressible Viscous Flows. *J. Comp. Phys.* **101**, 104-129.
- POPE, S. B. 1981 Transport Equation for the Joint Probability Density Function of Velocity and Scalars in Turbulent Flows. *Phys. Fluids*. **24-4**, 588-596.
- POPE, S. B. 1985-a Evolution of Surface in Turbulence. *Int. Journal of Ing. Sci.* **26**, 445-469.
- POPE, S. B. 1985-b Pdf Methods for Turbulent Reactive Flows. *Progress in Energy and Combustion Science*. **11**, 119-192.
- SAID, R. & BORGHINI, R. 1988 A Simulation with a Cellular Automaton for Turbulent Combustion Modeling. *Twenty-Second Symposium (International) on Combustion, The Combustion Institute, Pittsburgh*. 569-577.
- SMITH, N. S. A., BILGER, R. W. & CHEN, J. Y. 1992 Modelling of Non-Premixed Hydrogen Jet Flames Using a Conditional Moment Closure. *Twenty-fourth Symposium (International) on Combustion, The Combustion Institute, Pittsburgh*. 263-269.
- SMITH, N. S. A., BILGER, R. W., CARTER, C. D., BARLOW, R. S., & CHEN, J. Y. 1993 Comparison of CMC and PDF Modelling Predictions with Experimental Nitric Oxide LIF/Raman Measurements in a Turbulent H₂ Jet Flame. *Fourteenth ICDERS*.
- SPALDING, D. B. 1971 Mixing and Chemical Reaction in Steady Confined Turbulent Flames. *Thirteenth Symposium (International) on Combustion, The Combustion Institute, Pittsburgh*. 649-657.
- TROUVÉ, A. & POINSOT, T. J. 1994 The Evolution Equation for the Flame Surface Density in Turbulent Premixed Combustion. *J. Fluid Mech.* **278**, 1-31.

- TROUVÉ, A., VEYNANTE, D., BRAY, K. N. C. & MANTEL, T. 1994 Flame Surface Dynamics and Counter-Gradient Diffusion in Premixed Turbulent Combustion. *Proceedings of the Summer Program*. Center for Turbulence Research, NASA Ames/Stanford Univ.
- VERVISCH, L. 1991 Prise en compte d'Effets de Cinétique Chimique dans les Flamme de Diffusion Turbulentes par l'Approche Fonction Densité de Probabilité. *Thèse de Doctorat, Université de Rouen*.
- WILLIAMS, F. A. 1985-a *Combustion Theory* second Ed., Benjamin-Cummings.
- WILLIAMS, F. A. 1985-b In *The Mathematics of Combustion*, SIAM Philadelphia. 97-131.
- WRAY, A. A. 1992 Minimal Storage Time-Advancement Schemes for Spectral Methods. Private Communication.

Lewis number and Damköhler number effects in vortex-flame interactions

By J.-M. Samaniego

1. Motivation and objectives

Premixed flames are encountered in numerous practical configurations, and a better knowledge of the fundamental mechanisms controlling their propagation is needed to help model their behavior. In practical devices, premixed flames generally propagate into a turbulent stream of reactants, and their structure and local flame speed are modified. Although some recent studies demonstrate the persistence of laminar flame structures under highly turbulent conditions (Poinsot *et al.* 1991, Furukawa *et al.* 1993), the structure of turbulent premixed flames, either as a flamelet or thickened flame, is still a matter of debate. Hence, the development of turbulent combustion diagrams is an ongoing effort (Borghi 1988, Poinsot *et al.* 1991). However, despite uncertainties concerning the actual structure of premixed flames in real combustion devices, studies of the propagation properties of a laminar flame in turbulent flow conditions contribute to a better understanding of turbulent premixed flames. In such flows, premixed flames experience stretch, strain, curvature, and unsteadiness, and are subject to various effects depending on the thermodiffusive properties of the mixture (Lewis number), adiabaticity (heat losses), and detailed kinetics (Clavin 1985, Borghi 1988, Law 1988, Clavin 1994).

In order to study these effects in detail, a combined experimental-numerical study of the interaction of a two-dimensional vortex pair with a plane premixed laminar flame has been carried out. The selected geometry is two-dimensional in order to allow for the use of quantitative line-of-sight measurement techniques and for comparisons with two-dimensional direct numerical simulations. The experiment is used to identify possible effects of the Lewis number and of radiative heat losses, and direct numerical simulations reproducing the experimental conditions are used to investigate the role of the Lewis number, of heat losses, and of multi-step kinetics. The heat losses considered in this study are essentially radiative losses from the burnt gases and do not include conductive losses to the walls.

This report presents the final results of this study of vortex-flame interactions. The main result is the creation of experimental data sets of vortex-flame interactions, which demonstrate the importance of the Lewis and Damköhler numbers to the flame and which allow for comparison with direct numerical simulations. In turn, the comparison between experimental and numerical results, presented in Mantel 1994, shows that the Lewis number effects and complex chemistry play significant roles, which can be reproduced using a two-step reaction mechanism.

PREVIOUS PAGE BLANK NOT FILMED

PAGE 28 INTENTIONALLY BLANK¹

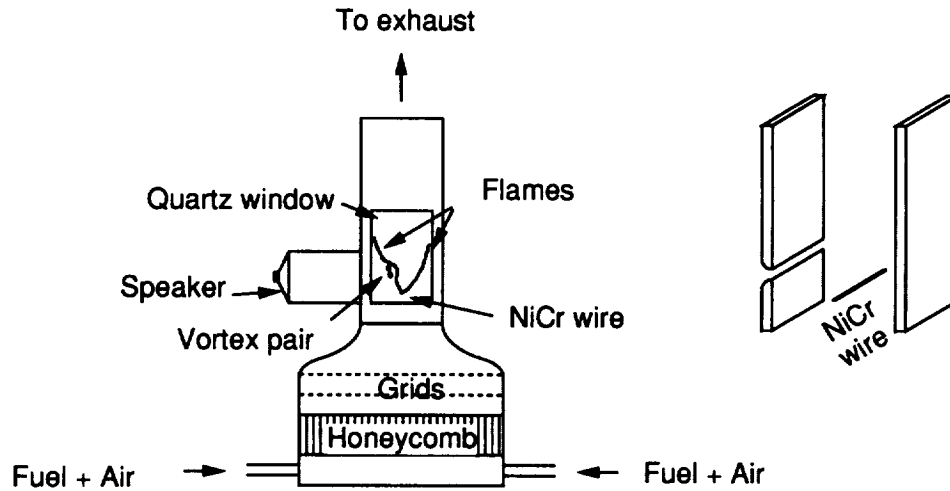


FIGURE 1. Schematic view of the facility

2. Accomplishments

2.1 Experimental details

An experimental facility with a two-dimensional flow has been developed and has been described in the last issue of the Annual Research Briefs, where details about the vortex generation and flame stabilization are reported (Samaniego 1993). The two-dimensionality of the flow field is an important feature of this study since it allows for comparison with two-dimensional direct numerical simulations of vortex-flame interactions. The choice of a two-dimensional flow field is dictated by the necessity of providing numerous quantitative experimental and numerical data in the simplest though relevant flow configuration by the use of line-of-sight CO_2^* emission imaging as a quantitative measurement of the heat release rate, and by limitations of current computer capabilities that would render three-dimensional calculations with multi-step kinetics too expensive.

The test section comprises a vertical duct, with a square cross-section of 63.5×63.5 mm, equipped with quartz windows for optical access (see Fig. 1). Mixtures of fuel and oxidizer are fed into the test section through a contoured converging nozzle. Different fuel and oxidizer mixtures are used to investigate the effect of the Lewis number. The Lewis number is determined using mixture-averaged properties (Strehlow 1979, Williams 1985). Five fuel-lean mixtures were investigated: $\phi = 0.55$ CH_4/Air ($Le = 0.96$), $\phi = 0.46$ C_2H_4/Air ($Le = 1.24$), $\phi = 0.51$ C_3H_8/Air ($Le = 1.60$), $\phi = 0.61$ $CH_4/O_2/CO_2/Ar$ ($Le = 0.80$), and $\phi = 0.61$ $CH_4/O_2/CO_2/He$ ($Le = 1.54$). The flame is stabilized on a heated Nichrome wire of 0.5 mm diameter, resulting in a V-shaped flame.

Several parameters describing the vortex pair and the flame control the interaction between the vortex and the flame. The vortex parameters, determined from smoke

Table 1. Vortex parameters

<i>type of vortex</i>	<i>s (cm)</i>	<i>V_D (cm/s)</i>	<i>R (cm)</i>	<i>τ_r (ms)</i>
Slow	0.85	135.	10.0	4.15
Medium	0.60	350.	4.0	2.07
Fast	0.60	600.	7.4	1.09

Table 2. Flame parameters

<i>Mixture</i>	<i>φ</i>	<i>T_{ad}</i> (K)	<i>α_m</i> (deg)	<i>S_L</i> (cm/s)	<i>δ_L</i> (cm)	<i>Le</i>	<i>HL</i> ×10 ⁻³
<i>CH₄/Air</i>	0.55	1567	13	9.5	0.022	0.94	0.55
<i>C₂H₄/Air</i>	0.46	1515		9	0.022	1.25	
<i>C₃H₈/Air</i>	0.51	1530	15	9	0.020	1.60	0.40
<i>CH₄/O₂/CO₂/He</i>	0.61	1643		13.8	0.033	1.54	1.10
<i>CH₄/O₂/CO₂/Ar</i>	0.61	1615		6.7	0.024	0.82	2.50

visualization experiments, are: the distance between the vortex centers, s , the vortex pair self-induced velocity, V_D , and the radius of curvature of the trajectory, R . The flame parameters are: the mean flame angle, α_m , the flame speed, S_L , the flame thickness, δ_L , the Lewis number, Le , and a heat loss coefficient, HL , which is defined as the ratio of the radiative loss in the reaction zone to the chemical energy release. They depend on the mixture composition (fuel, diluent) and on the bulk flow velocity, V_0 . In the present study, $V_0 = 0.35$ m/s. The vortex and flame parameters are reported in Tables 1 and 2. Details on the determination of these parameters can be found in Samaniego *et al.* 1994a.

Line-of-sight CO_2^* emission imaging, using an intensified CCD camera, is performed to obtain heat release rate fields. Each image is digitized in a 184×240 8-bits pixel array (a pixel corresponds to a field of view of 0.364×0.364 mm). The light intensifier is used as a fast shutter in order to freeze the flow field. The exposure time is $250 \mu s$, resulting in a spatial resolution of 1.5 mm in the worst case. A timing circuit allows the triggering of the intensifier at selected instants during the interaction. For each value of the time delay, ten to fifty realizations are averaged in order to improve the signal-to-noise ratio. Images are corrected for background noise and pixel-to-pixel variations. After correction, the uncertainty on the pixel

value is $\pm 2\%$ of the maximum value in the worst case.

2.2 Determination of the heat release rate

The rate of heat release is an important flame quantity which controls its propagation, and its monitoring provides insight into the respective effects of the Lewis number, radiative losses, and complex chemistry. The choice for studying this quantity is made for two reasons: first, it can be determined experimentally by measuring the flame chemiluminescence; second, this quantity is predicted by most combustion models and can therefore be used for their validation by comparison with experimental data.

Chemiluminescence refers to light spontaneously emitted by electronically excited molecules as they decay to their ground state. In hydrocarbon flames such as those investigated here, flame chemiluminescence occurs in the UV and visible range of the spectrum and is due principally to four emitters: CH^* , C_2^* , OH^* , and CO_2^* . These electronically-excited molecules have different emission spectra. The first three emitters have band-structured emission spectra which correspond to specific electronic transitions (CH^* peak at 431.5 nm corresponding to the $A^2\Delta \rightarrow X^2\Pi$ transition, C_2^* peak at 516.6 nm corresponding to the $A^3\Pi - X^3\Pi$ transition, OH^* peak at 306.4 nm corresponding to the $^2\Sigma^+ \rightarrow ^2\Pi$ transition Gaydon 1974), while CO_2^* has a broadband emission spectrum extending from 250 to 800 nm (Myers & Bartle 1967).

Recently, Samaniego *et al.* 1994b, after showing that CO_2^* is the main emitter in fuel-lean flames, have successfully correlated the CO_2^* emission intensity and the rate of heat release for a $\phi = 0.55$ CH_4/Air flame based on complex chemistry calculations of strained flames. The resulting correlation takes the form:

$$\frac{Q}{Q_0} = \left(\frac{I}{I_0} \right)^{0.37} \quad (1)$$

where Q is the integral of the heat release rate, Q , across the flame front, i.e.:

$$Q = \int_{-\infty}^{+\infty} Q dx \quad ,$$

I is the CO_2^* emission intensity integrated across the flame front, i.e.:

$$I = \int_{-\infty}^{+\infty} I dx \quad ,$$

and the subscript 0 refers to the unstrained premixed laminar CH_4/Air flame ($\phi = 0.55$).

It was shown that expression (1) is not affected by unsteadiness and can be used to determine the heat release rate in situations where strain-rate is the only significant parameter controlling the flame evolution. As is discussed later, it is the case in the present study of vortex-flame interactions since the effect of curvature, which is not accounted for in Eq. (1), can be neglected.



FIGURE 2. Dithered images of CO_2^* emission of a $\phi = 0.51$ propane-air flame. *left:* $t = 0$, *center:* $t = 17$ ms, *right:* $t = 19$ ms.

However, Eq. (1) is only strictly valid for the $\phi = 0.55$ CH_4 /Air flame, and new correlations should be sought for other mixture compositions (i.e. different fuel, different diluent).

2.3 CO_2^* emission imaging

Instantaneous images of CO_2^* emission from the flame were obtained using an intensified Amperex CCD camera equipped with a NIKON glass lens ($f = 105$ mm, $f/1.2$) and a band-pass filter BG39 with cut-off wavelengths at 340 and 700 nm. This filter is used to reject near-infrared emission (700-1200 nm) from the burnt gases originating from H_2O excited molecules (Gaydon 1974).

Fig. 2 shows a sequence of three flame emission images of a C_3H_8 /Air flame at $\phi = 0.51$ taken during a vortex-flame interaction. The parameters of this interaction are: $s = 6.0$ mm, $V_D = 3.5$ m/s, $R = 40$ mm, $S_L \simeq 0.10$ m/s, $\delta_L \simeq 1.0$ mm, $Le = 1.60$, $\alpha \simeq 15$ degrees.

The first image shows the unperturbed flame fronts. The next two images in Fig. 2 are taken respectively at $t = 17$ ms and $t = 19$ ms. Three regions in the distorted portion of the flame can be identified: 1) a region of extensive strain-rate and negative curvature, located just ahead of the vortex pair. In this region, strain-rate effects are predominant, and Eq. (1) can be confidently used to infer the heat release rate; 2) & 3) regions of high positive curvature, located above and under region 1. In these regions, curvature may play a significant role, and the validity of Eq. (1) remains to be evaluated. Therefore, quantitative comparisons between experimental and numerical data should be restricted to the regions of high strain.

For this purpose, \mathcal{I}_{min} is defined as the minimum value of $\mathcal{I}(\sigma)$, where $\mathcal{I}(\sigma)$ is defined as the integral of the CO_2^* emission, I , across the reaction zone, at the

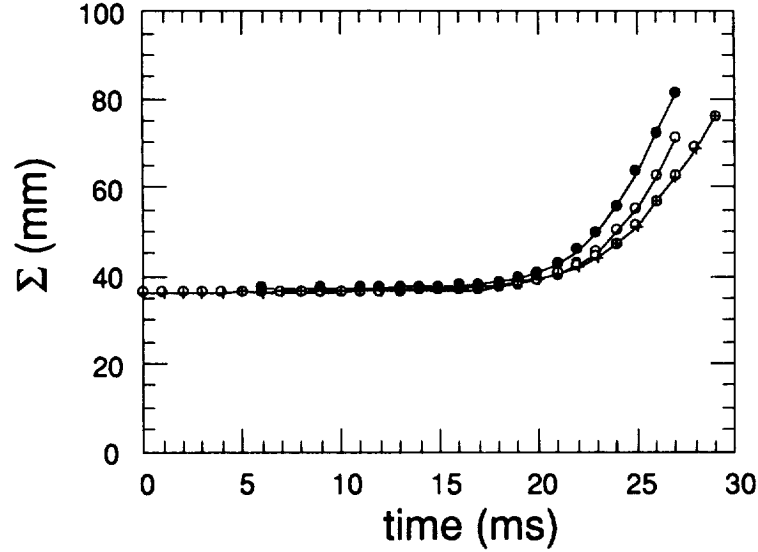


FIGURE 3. Slow vortex. Evolution of Σ . \circ : $Le = 0.94$, \square : $Le = 1.25$, \bullet : $Le = 1.60$ (see Table 2).

location σ along the flame front, i.e.:

$$\mathcal{I}(\sigma) = \int_{\sigma^\perp} I d\sigma^\perp,$$

where \perp indicates that integration is performed along a normal-to-the-flame front, and

$$\mathcal{I}_{min} = \min_{\sigma} \mathcal{I}(\sigma)$$

In all cases, \mathcal{I}_{min} occurs in front of the vortex pair in the region of high extensive strain. The corresponding minimum heat release rate, Q_{min} is obtained from \mathcal{I}_{min} using expression (1).

2.4 Effect of the Lewis number

The theory of stretched flames predicts that the behavior of strained flames is controlled by the Lewis number, Le (Clavin 1985, Law 1988). For positively stretched flames such as in vortex-flame interactions, the burning rate should increase for $Le < 1$ flames while it should decrease for $Le > 1$ flames. This prediction is checked by monitoring the evolution of \mathcal{I}_{min} , during vortex-flame interactions, between the slow vortex and all flames (each flame corresponds to a different Lewis number - see Tables 1 and 2).

It is first verified that all flames undergo the same stretch history. Fig. 3 shows the evolution of the flame surface area, Σ , during vortex-flame interactions with the

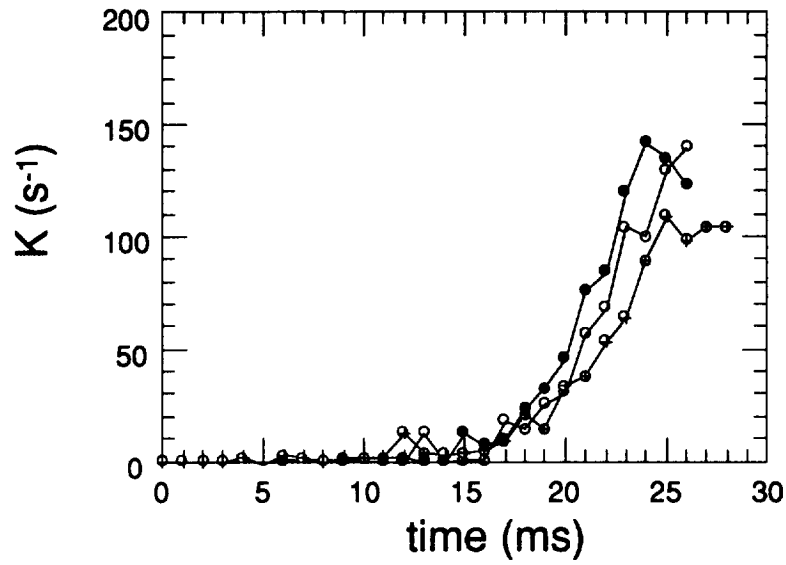


FIGURE 4. Slow vortex. Evolution of K_{mean} . \circ : $Le = 0.94$, \bullet : $Le = 1.25$, \bullet : $Le = 1.60$ (see Table 2).

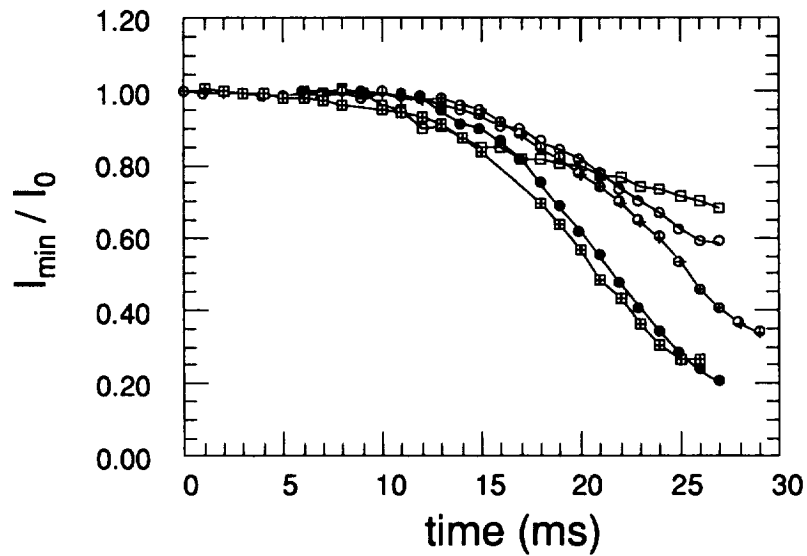


FIGURE 5. Slow vortex. Evolution of l_{min} for all investigated flames (see Table 2). \square : $Le = 0.82$, \circ : $Le = 0.94$, \bullet : $Le = 1.25$, \blacksquare : $Le = 1.54$, \bullet : $Le = 1.60$.

slow vortex pair for all flames. The flame surface area, Σ , starts increasing after $t = 15$ ms. A mean stretch-rate, K_{mean} , can be derived:

$$K_{mean} = \frac{1}{\Sigma} \frac{d\Sigma}{dt}$$

K_{mean} also starts increasing after $t = 15 \text{ ms}$ and reaches about 100 to 150 s^{-1} at $t = 25 \text{ ms}$ (see Fig. 4). All flames experience the same overall stretch history which allows us to interpret possible differences between these flames in terms of a Lewis number effect.

The effect of the Lewis number on the evolution of \mathcal{I}_{min} for all flames is shown in Fig. 5. In all cases, \mathcal{I}_{min} starts at the value of the unperturbed laminar flame and then decreases under the action of the vortex pair. It can be noticed that the decrease is more pronounced for higher Lewis number flames. This is better demonstrated in Fig. 6 where the maximum slope of the evolution of \mathcal{I}_{min} , b , is plotted as a function of the Lewis number, where the slope b decreases with increasing Lewis number.

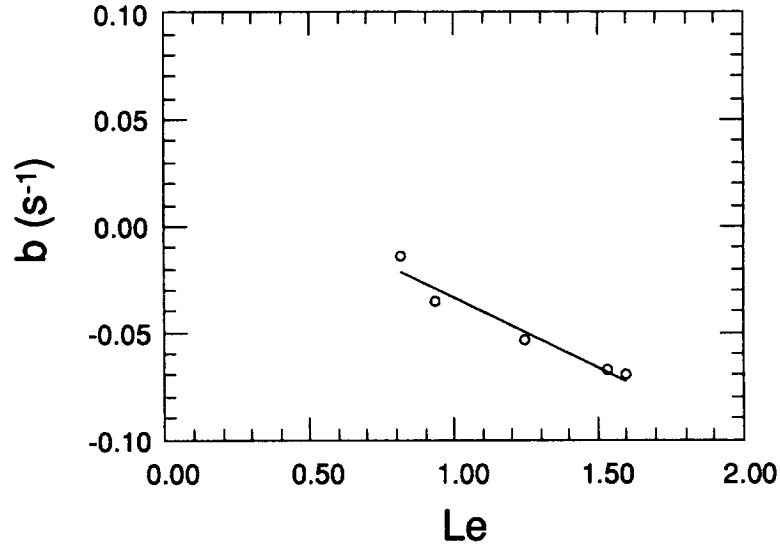


FIGURE 6. Slow vortex. Correlation between the rate of variation of \mathcal{I}_{min} (b), with the Lewis number (Le).

These results are only in partial agreement with the asymptotic theory: higher Lewis numbers lead to flames that are weaker when strained. However, the theory predicts that the burning rate of $Le < 1$ flames increases with strain, but we observe a decrease of \mathcal{I}_{min} for all flames, including the $Le = 0.8$ flame. This may be attributed to various causes: unsteady effects (see section 2.5, theory limited to low stretch-rates, complex chemistry effects (see DNS).

2.5 Effect of the Damköhler number

Unsteadiness is an important factor in these vortex-flame interactions which is not accounted for in the theory of stretched flames. Unsteadiness is quantified by the

Damköhler number, defined as the ratio of a mechanical time, τ_m , over a chemical time, τ_c , i.e.

$$Da = \frac{\tau_m}{\tau_c}$$

In this study, τ_m is the characteristic time of evolution of the flame surface area and τ_c is the residence time through the flame, i.e. $\tau_c = \delta_L/S_L$. τ_m is defined by the time for Σ to increase from $1.25 \times \Sigma_0$ to $2.00 \times \Sigma_0$ where Σ_0 is the unperturbed value.

2.5.1 Observations

The effect of the Damköhler number is determined by investigating the evolution of the overall heat release rate Q_{tot} , and the minimum heat release rate Q_{min} . Q_{tot} is defined as the total heat released by the flame of surface area Σ and is computed as:

$$Q_{tot} = \int_{\Sigma} Q(\sigma) d\sigma \quad (2)$$

Fig. 7 shows the evolution of Σ , Q_{tot} , and Q_{min} for the $\phi = 0.55$ CH_4/Air flame during its interaction with the slow, medium, and fast vortex pairs (see Tables 1 and 2). These interactions are characterized by $Da = 1.80, 0.90,$ and 0.47 , respectively. Lower values of Da can be interpreted as higher stretch rates. Each set of curves corresponds to a different Damköhler number. In all cases Q_{tot} lags Σ . This is consistent with the fact that Q_{min} decreases due to flame stretch. Indeed, if $Q(\sigma)$ were constant along the flame front during vortex-flame interactions, Q_{tot} would be proportional to Σ (see expression (2)). Hence, the non-linearity of the relationship between Q_{tot} and Σ is a consequence of stretching due to the vortex pair.

In order to stress the effect of Da , Σ and Q_{tot} are plotted in a non-dimensional time-frame, t^+ , where time is non-dimensionalized by τ_m , and the origin corresponds to the time at which $\Sigma = 1.25 \times \Sigma_0$ (Fig. 8). The evolution of Σ is independent of the Damköhler number. This follows mainly from the non-dimensionalization procedure which imposes $\Sigma(t^+ = 0) = 1.25 \times \Sigma_0$ and $\Sigma(t^+ = 1) = 2.00 \times \Sigma_0$. The evolution of Q_{tot} shows a certain similarity in all three cases: Q_{tot} starts decreasing, reaches a minimum value, and finally increases at a pace comparable with the evolution of Σ . One can notice that the minimum value reached by Q_{tot} decreases with decreasing Da and that higher values of Da lead to less non-linearity between Q_{tot} and Σ . Third, the decrease Q_{min} is less pronounced for higher values of Da . These observations display trends that are in agreement with the idealized infinitely fast chemistry limit, or $Da \rightarrow \infty$, where the internal structure of the flame is not affected by the flow. In this case, $Q(\sigma)$ would be constant, and Q_{tot} would be proportional to Σ . Indeed, as shown in Fig. 8, Q_{tot} converges towards Σ as Da increases.

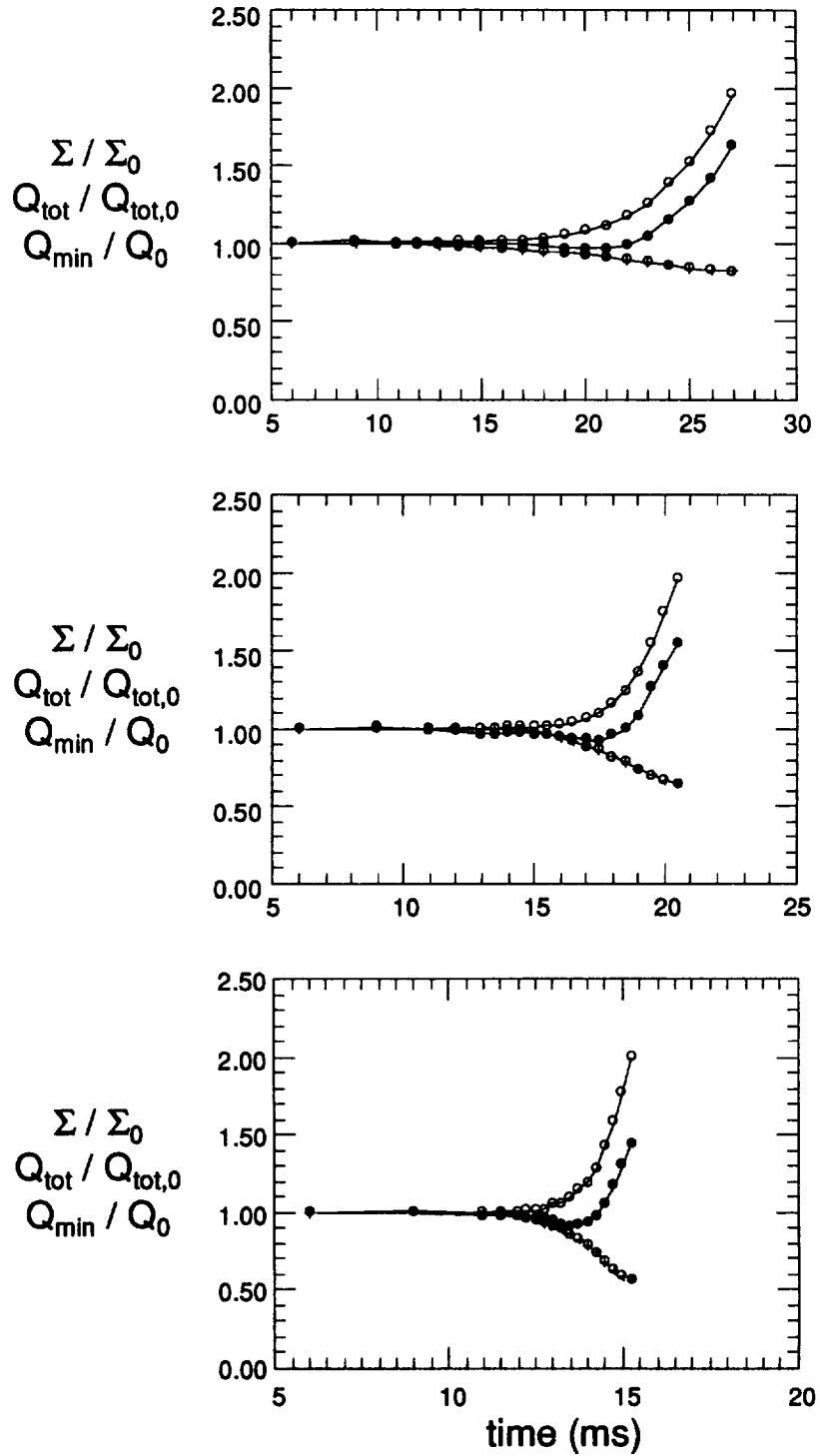


FIGURE 7. CH_4/Air flame ($\phi = 0.55$). Evolution of Σ/Σ_0 (\circ), $Q_{tot}/Q_{tot,0}$ (\bullet), and Q_{min}/Q_0 (\circ). *Top*: slow vortex ($Da = 1.80$), *center*: medium vortex ($Da = 0.90$), *bottom*: fast vortex ($Da = 0.47$).

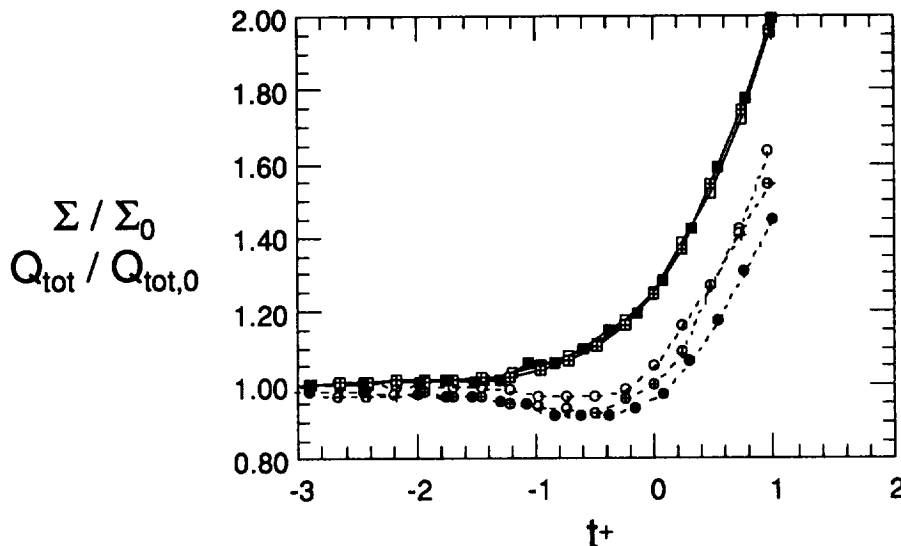


FIGURE 8. CH_4/Air flame ($\phi = 0.55$). Effect of Da on the relationship between Σ/Σ_0 and $Q_{tot}/Q_{tot,0}$. $Q_{tot}/Q_{tot,0} \rightarrow \circ$: $Da = 1.80$, \bullet : $Da = 0.90$, \blacksquare : $Da = 0.47$. $\Sigma/\Sigma_0 \rightarrow \square$: $Da = 1.80$, \blacksquare : $Da = 0.90$, \blacksquare : $Da = 0.47$.

2.5.2 Stretching-relaxation mechanism

For finite values of Da , unsteadiness, in addition to stretch, plays an important role. This can be seen in recent studies of unsteady strained laminar flames (see for example Darabiha 1992, Egolfopoulos 1994). A simple stretching-relaxation model accounting for unsteadiness may be derived. The main assumption is that two mechanisms are important: unsteady strain which tends to thin the flame without modifying the internal flame structure, and the diffusion-reaction process which relaxes the flame back to an unstrained laminar structure. Effects of curvature are neglected. Both mechanisms contribute to dQ/dt . They can be modeled by two additive effects: a term of the form $-KQ$ due to stretch, and a relaxation term of the form $(Q_0 - Q)/\tau_r$, where τ_r is a relaxation time. The term due to strain-rate can be justified by two arguments: 1) curvature being neglected, stretch is equal to the strain-rate tangential to the flame front, and we have $K = a_T$; 2) the flame front undergoes a compression $-a_T$ along its normal. Therefore the flame front is compressed at a rate $-K$ along its normal, and the rate of change of Q due to stretch is equal to $-KQ$. The second term is an *ad-hoc* representation of the diffusion-reaction process using a linear relaxation model and is justified by the fact that the Q must relax to Q_0 in the absence of stretch (actually, different forms for the relaxation term could be used since there is no real justification for a linear relaxation process). Therefore, an evolution equation for Q may be derived:

$$\frac{dQ}{dt} = -KQ + \frac{Q_0 - Q}{\tau_r} \quad (3)$$

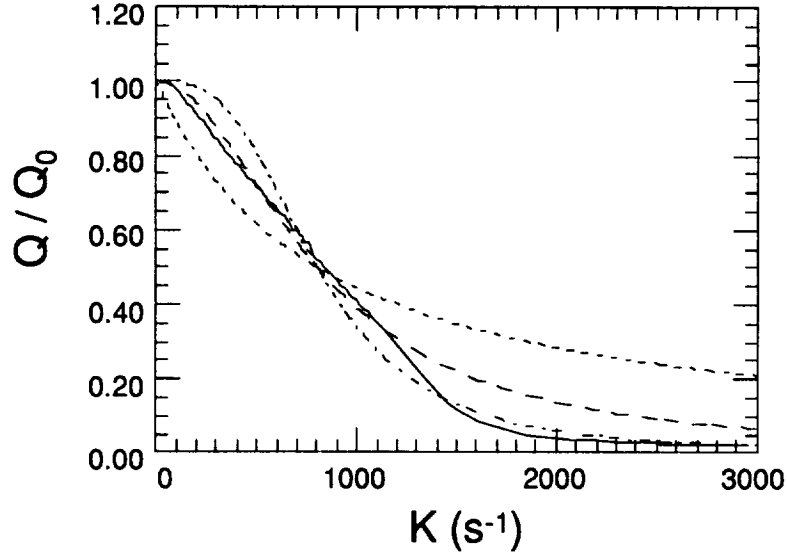


FIGURE 9. Evolution of Q/Q_0 with strain-rate for a steady strained CH_4/Air flame ($\phi = 0.55$). Comparison between model predictions (with $\tau_r = 1.25$ ms) and complex chemistry calculations. — : complex chemistry, ---- : linear relaxation model, -.- : quadratic relaxation model, - - - : cubic relaxation model.

Interestingly enough, in the steady case (i.e. $\frac{dQ}{dt} = 0$), this model yields:

$$\frac{Q}{Q_0} = \frac{1}{1 + K\tau_r}$$

This prediction is compared to the evolution of the relative heat release rate for a strained $\phi = 0.55$ CH_4/Air flame, computed from complex chemistry calculations (Samaniego *et al.* 1994b) (Fig. 9). Other predictions using non-linear relaxation terms are also plotted for comparison (quadratic: $\frac{Q_0}{\tau_r}(1 - Q/Q_0)^{1/2}$, and cubic: $\frac{Q_0}{\tau_r}(1 - Q/Q_0)^{1/3}$). In this case, $\tau_r = 1.25$ ms is the same for all three relaxation models and is chosen to best reproduce the evolution of Q/Q_0 predicted by the complex chemistry calculations. It appears that all relaxation models predict correctly the qualitative behavior of Q/Q_0 and that quadratic relaxation provides the best quantitative agreement. In the following, the linear relaxation model, although imperfect, is used to further investigate the relationship between Q_{tot} and Σ .

Eq. (3) may be integrated over Σ using a transport theorem which accounts for the fact that Σ also changes in time (see Candel & Poinso 1990). One obtains, after proper non-dimensionalization:

$$\frac{C}{Da} \frac{dQ_{tot}^+}{dt^+} + Q_{tot}^+ = \Sigma^+ \quad (4)$$

where $t^+ = t/\tau_m$, $C = \tau_r/\tau_c$ is a constant, $Q_{tot}^+ = Q_{tot}/Q_{tot_0}$, and $\Sigma^+ = \Sigma/\Sigma_0$.

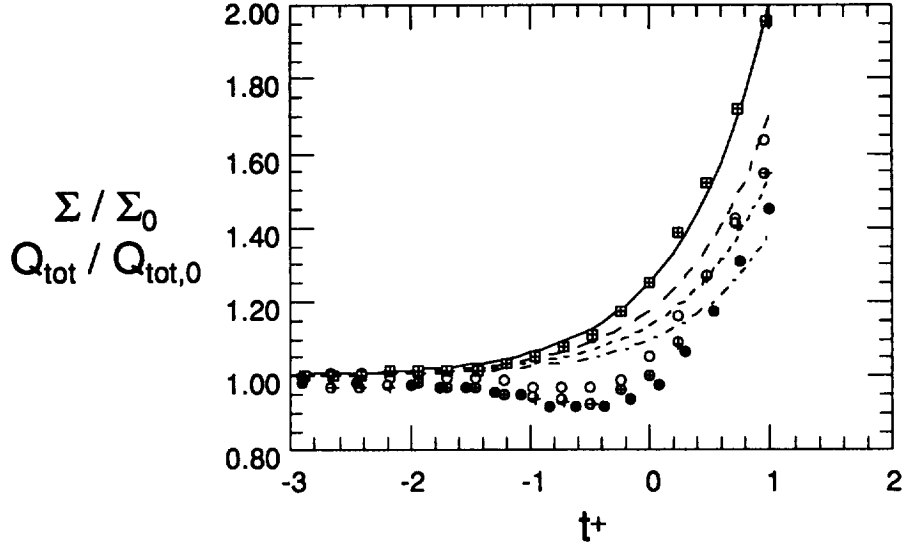


FIGURE 10. Evolution of $Q_{tot}/Q_{tot,0}$ during vortex-flame interactions. Comparison between the linear model ($\tau_r = 1.25$ ms) and measurements. Model (Eqs. 5 and 6) \rightarrow — : Σ^+ , --- : Q_{tot}^+ for $Da = 1.80$, - - - : Q_{tot}^+ for $Da = 0.90$, ··· : Q_{tot}^+ for $Da = 0.47$. Experiment \rightarrow \boxplus : Σ^+ , \circ : Q_{tot}^+ for $Da = 1.80$, \diamond : Q_{tot}^+ for $Da = 0.90$, \bullet : Q_{tot}^+ for $Da = 0.47$.

From this expression it can be seen that, in the limit $Da \rightarrow \infty$, $Q_{tot}^+ = \Sigma^+$ and the total heat release rate is proportional to the flame surface area, and, in the limit $Da \rightarrow 0$, $Q_{tot}^+ = 1$ and the total heat release rate is constant.

In turn, Eq. (4) can be integrated once the evolution of Σ is known. A convenient analytic expression for Σ^+ is provided by:

$$\Sigma^+ = 1 + 4^{t-1} \quad (5)$$

This formulation mimics the exponential-like growth of Σ^+ in Fig. 8, and satisfies $\Sigma^+(0) = 1.25$ and $\Sigma^+(1) = 2$. Integrating (4) yields:

$$Q_{tot}^+ = 1 + \frac{Da}{(Da + C \ln 4)} 4^{t-1} \quad (6)$$

Fig. 10 shows a prediction of the effect of the Damköhler number using these analytic expressions for Σ and Q_{tot} , with $C = 0.25$. Despite some discrepancies, in particular, the inability of the model to reproduce the initial decrease of Q_{tot} , the effect of Da on Q_{tot} is qualitatively well reproduced.

3. Conclusion

This experimental study of vortex-flame interactions has been successfully conducted, and the initial goals of this study have been achieved. The results have

demonstrated the importance of the thermodiffusive diffusive properties (Lewis number) and of unsteadiness (Damköhler number) on the response of the flame. Quantitative comparisons with direct numerical simulations have demonstrated the importance of complex chemistry effects which could be reproduced using a two-step mechanism.

Further experimental studies of vortex-flame interactions could be carried out to elucidate the effect of the flame (heat release) on the vorticity field. Preliminary results show that the vortex pair is significantly altered in the presence of a flame, and this might be due to the baroclinic torque as well as to buoyancy. This study would shed new light upon the interaction between turbulence and heat release, such as possible jump conditions for turbulence statistics through the flame.

Acknowledgements

This study was made in collaboration with Prof. C. T. Bowman of the High Temperature Gasdynamics Laboratory, Stanford, and in conjunction with a numerical study carried out by Dr. T. Mantel (CTR). I would like to express my gratitude to Dr. T. Poinso (CERFACS, France), instigator of this study, for his encouragements and fruitful conversations. I would also like to thank F. Levy for his invaluable help during the construction of the facility.

Erratum

The author would like to point out two errors that were made in the previous issue of the Annual Research Briefs (Samaniego 1993). First, what he mistakenly referred to as CH^* emission is actually CO_2^* emission. Second, the presumed linear relationship between the so-denominated CH^* emission and reaction rate does not apply. Both these errors were made before the study on CO_2^* emission, which identified CO_2^* as the main emitter in these flames and led to a quantitative (non-linear) relationship between CO_2^* emission and heat release rate (Samaniego *et al.* 1994b).

REFERENCES

- BORGHI, R. 1988 Turbulent Combustion Modeling. *Prog. Energy Combust. Sci.* **14**, 245-292.
- CANDEL, S. & POINSOT, T. 1990 Flame stretch and the balance equation for the flame area. *Combust. Sci. Tech.* **70**, 1-15.
- CLAVIN, P. 1985 Dynamic behavior of premixed flame fronts in laminar and turbulent flows. *Prog. Energy Comb. Sci.* **11**, 1-59.
- CLAVIN, P. 1994 Premixed Combustion and Gasdynamics. *Ann. Rev. Fluid Mech.* **26**, 321-352.
- DARABIHA, N. 1992 Transient Behavior of Laminar Counterflow Hydrogen-Air Diffusion Flames With Complex Chemistry. *Combust. Sci. Tech.* **86**, 163-181.

- EGOLFOPOULOS, F. N. 1994 Dynamics and Structure of Unsteady, Strained, Laminar Premixed Flames. *to appear in the proceedings of the Twenty Fifth Symposium (International) on Combustion*, The Combustion Institute, Pittsburg.
- FURUKAWA, J., MARUTA, K., NAKAMURA, T. & HIRANO, T. 1993 Local Reaction Zone Configuration of High intensity Turbulent Premixed Flames. *Combust. Sci. Tech.* **90**, 267-280.
- GAYDON, A. G. 1974 *The Spectroscopy of Flames*. Chapman & Hall, London.
- LAW, C. K. 1988 Dynamics of Stretched Flames. *Twenty-Second Symposium (International) on Combustion* The Combustion Institute, Pittsburg, 1381-1402.
- MANTEL, T. 1994 Fundamental mechanisms in premixed flame propagation via vortex-flame interactions - numerical simulations. *Annual Research Briefs 1994*. Center for Turbulence Research, NASA Ames Research Center and Stanford University.
- MYERS, B. F. & BARTLE, E. R. 1967 Shock-Tube Study of the Radiative Processes in Systems Containing Atomic Oxygen and Carbon Monoxide at High Temperature. *J. Chem. Phys.* **47**, 1783-1792.
- POINSOT, T., VEYNANTE, D. & CANDEL, S. 1991 Quenching processes and premixed turbulent combustion diagrams. *J. Fluid Mech.* **228**, 561-605.
- SAMANIEGO, J.-M. 1993 Stretch-Induced Quenching in Flame-Vortex Interactions. *Annual Research Briefs 1993*. Center for Turbulence Research, NASA Ames/Stanford University.
- SAMANIEGO, J.-M., MANTEL, T. & BOWMAN, C. T. 1994a Fundamental Mechanisms of Premixed Flame Propagation Via Vortex-Flame Interactions. Part 1: Experiment. *In preparation*.
- SAMANIEGO, J.-M., EGOLFOPOULOS, F. N. & BOWMAN, C. T. 1994b CO_2^* Chemiluminescence in Premixed Flames. *In preparation*.
- STREHLOW, R. A. 1979 *Fundamentals of Combustion*. Robert E. Kreiger Publishing Company, Huntington, New York.
- WILLIAMS, F. A. 1985 *Combustion Theory*. The Benjamin/Cummings Publishing Company, Inc., Menlo Park.

Fundamental mechanisms in premixed flame propagation via vortex-flame interactions - numerical simulations

By T. Mantel

1. Motivation and objectives

During the past few years, direct numerical simulations (DNS) have been extensively used to study turbulent reacting flows in order to obtain a better understanding of the interaction between a turbulent flow field and a flame front, mainly for modeling purposes. We can cite different studies with increasing degree of complexity. Three-dimensional DNS of a decaying isotropic turbulence with chemical reactions (no heat release and constant density) have been carried out by Picart *et al.* (1988), Rutland *et al.* (1990), El Tahry *et al.* (1991). More recently, heat release and variable density have been taken into account by Poinso *et al.* (1991), who have analyzed the interaction between a two-dimensional vortex pair and a premixed laminar flame. Haworth & Poinso (1992) and Trouvé & Poinso (1994) focused their attention on the effects of the Lewis number by studying the interaction between (respectively) a two- and three-dimensional decaying homogeneous turbulence and a premixed flame front. We can also note the work of Poinso *et al.* (1994), who performed a two-dimensional interaction between a turbulent flame front and a cold wall.

Due to the limitations of the available computers, all the studies cited above have been performed using a one-step irreversible reaction (Reactants \rightarrow Products) to describe the chemistry occurring in a flame. Consequently, some conclusions of these studies remain questionable due to complex chemistry effects. This last remark is supported by the work of Baum *et al.* (1992), who have studied the interaction between a two-dimensional decaying isotropic turbulence and a stoichiometric hydrogen-air premixed flame using the 9 species, 19 reactions scheme of Miller *et al.* (1982). Despite the Lewis number (based on H_2) of their simulation being definitely less than unity, the local flamelet speed S_n decreases with increasing tangential strain rate, which corresponds to the behavior of a flame having a Lewis number greater than unity (Clavin 1985, Law 1988). The Lewis number is defined as the ratio of the thermal diffusivity (in the fresh gases) α_u and of the molecular diffusivity of the limiting species \mathcal{D} : $Le = \alpha_u / \mathcal{D}$. Moreover, they find a better correlation between the tangential strain rate and S_n rather than the local curvature and S_n .

This contradicts partially the previous work of Haworth & Poinso (1992), who studied the same configuration using a one-step Arrhenius chemistry. In that study, they observe that the curvature seems to be the determinant parameter controlling the local flame structure. They notice a strong correlation between the curvature and the local flame velocity S_n for all the Lewis numbers investigated ($Le = 0.8$,

PRECEDING PAGE BLANK NOT FILMED

PAGE 44 INTENTIONALLY BLANK[†]

1.0, and 1.2). For the tangential strain rate, they found a significant correlation (with S_n) for $Le = 1.0$.

This short discussion points out the need to verify the limit of validity of simple mechanisms able to be implemented in DNS codes. Because reduced chemical mechanisms are available and represent a good compromise between (too) simple mechanisms and (unreachable) full chemical schemes, it is of primary interest to investigate the behaviors of some of these models on a configuration which exhibits the fundamental mechanisms occurring in premixed turbulent flames and for which experimental results are available.

The interaction between vortex pairs or ring vortices and a premixed planar flame possesses the major features encountered in turbulent premixed combustion such as unsteadiness, stretch, curvature, Lewis number, radiative heat losses, and complex chemistry effects. This simplistic configuration has been previously studied both experimentally and numerically for different purposes by several authors (Poinsot *et al.* 1991, Rutland & Ferziger 1991, Lee *et al.* 1993, Roberts *et al.* 1992-1993, Samaniego *et al.* 1994-b, Driscoll *et al.* 1994). Some of these works have focused their attention on the effects of radiative heat losses and of the strain on the quenching of a premixed flame. The motivation of these studies was to propose an update of the premixed turbulent combustion diagrams to clarify the limit between the flamelet and non-flamelet combustion regimes (Poinsot *et al.* 1991, Roberts *et al.* 1993). Other studies have extracted different statistics of curvature and orientation factors of turbulent premixed flame fronts (Lee *et al.* 1993).

The goal of the present study is to assess numerically the ability of single-step and two-step chemical models to describe the main features encountered during the interaction between a two-dimensional vortex pair and a premixed laminar flame.

This paper represents the second part of a joint experimental and numerical project concerning vortex flame interactions performed at the Center for Turbulence Research. This first part investigated by Samaniego *et al.* (1994-b) concerns the experimental aspect of this project. Thus, the configuration retained in our study corresponds to the experimental one of Samaniego *et al.* (1994-b). Briefly, it concerns the interaction between a two-dimensional vortex pair generated by acoustic excitation and a V-shaped flame stabilized on a heated wire. In the experiment, imaging of the light emitted by the flame and smoke visualization of the flow field have been carried out to provide initial conditions to the simulation and eventually data to perform quantitative comparisons between the experiment and the simulation. Light emission imaging allows determination of the time history of the flame surface area, of the global heat release, and of the distribution of the heat release along the flame front. The characteristics of the vortex pair (circulation, position of the vortices with respect to the flame, distance between the center of the vortices) are obtained from smoke visualization.

In the two-step mechanism, the reaction kinetics are represented by a first chain branching reaction $A + X \rightarrow 2X$ and a second chain termination reaction $X + X \rightarrow P$ (Zel'dovich 1948). This mechanism has been successfully used to analyze different features of premixed laminar flames (Liñán 1971, Hocks *et al.* 1981, Seshadry and

Peters 1983). In particular, Seshadry and Peters (1983) investigated the response of a premixed laminar flame to an external strain. They pointed out the relative role of the Lewis number for the reactant A and the intermediate species X. In the case of a positive stretch, they show that the high diffusivity of the intermediate species contributes to a decrease of the reaction rate independently of the Lewis number of the reactant species.

This paper presents the fundamental mechanisms occurring during vortex-flame interactions and the relative impact of the major parameters encountered in turbulent premixed flames and suspected of playing a role in quenching mechanism:

- Influence of stretch is investigated by analyzing the contribution of curvature and tangential strain on the local structure of the flame. The effect of Lewis number on the flame response to a strained field is analyzed.
- Radiative heat losses which are suspected to be partially or totally responsible for quenching (Poinsot *et al.* 1991, Roberts *et al.* 1993) are also investigated.
- The effect of the diffusion of radicals is studied using a two-step mechanism in which an intermediate species is present. The parameters of the two-step mechanism are entirely determined from physical arguments.
- Precise quantitative comparisons between the DNS and the experimental results of Samaniégo *et al.* (1994-b) are performed. These comparisons concern the evolution of the minimum heat release rate found along the flame front during the interaction and the distribution of the heat release rate along the flame front.

2. Accomplishments

2.1 The mathematical model

2.1.1 The conservation equations

The DNS code has been developed at the Center for Turbulence Research following the methodology of Lele (1992) and Poinsot & Lele (1992). The code fully resolves the compressible Navier-Stokes equations using a sixth order spatial scheme (Lele 1992) and a third order temporal scheme (Wray 1990). Due to the heat release and the resulting gas expansion, the boundary conditions of the computational domain are inflow/outflow (Poinsot & Lele 1992). The transport equations solved in the DNS code can be written

$$\frac{\partial \rho}{\partial t} + \frac{\partial}{\partial x_j}(\rho u_j) = 0 \quad (2.1)$$

$$\frac{\partial \rho u_i}{\partial t} + \frac{\partial}{\partial x_j}(\rho u_i u_j) = -\frac{\partial p}{\partial x_i} + \frac{\partial \tau_{ij}}{\partial x_j} \quad (2.2)$$

$$\frac{\partial \rho E}{\partial t} + \frac{\partial}{\partial x_j}[(\rho E + p)u_j] = \frac{\partial}{\partial x_j}(u_i \tau_{ij}) + \frac{\partial}{\partial x_j} \left(\lambda \frac{\partial T}{\partial x_j} \right) + \dot{Q} - h(T - T_u) \quad (2.3)$$

where

$$\tau_{ij} = \mu \left(\frac{\partial u_i}{\partial x_j} + \frac{\partial u_j}{\partial x_i} \right) - \frac{2}{3} \mu \frac{\partial u_k}{\partial x_k} \delta_{ij} \quad (2.4)$$

$$\rho E = \frac{1}{2} \rho u_i^2 + \frac{p}{\gamma - 1} \quad (2.5)$$

The transport equation for the species α is classically written:

$$\frac{\partial \rho Y_\alpha}{\partial t} + \frac{\partial}{\partial x_j} (\rho u_j Y_\alpha) = - \frac{\partial \mathcal{J}_j^\alpha}{\partial x_j} + \dot{w}_\alpha \quad (2.6)$$

where \mathcal{J}_j^α is the diffusion of the species α flux modeled using a Fickian approximation and \dot{w}_α the sink term due to chemical reaction.

Here ρE represents the total energy, \dot{Q} is the heat released by chemical reaction per unit mass of fresh gas, the subscript u corresponds to the unburnt gases. (\dot{Q} and \dot{w}_α will be defined in detail later in this section for the one-step and two-step chemical models.) In the energy equation, the heat losses are represented by a term linear in temperature and a heat loss parameter h which will be described later.

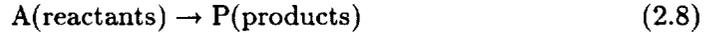
The transport properties of the fluid are temperature dependent following a power law:

$$\frac{\mu}{\mu_u} = \left(\frac{T}{T_u} \right)^b \quad (2.7)$$

where μ represents the dynamic viscosity and b is a constant (here $b = 0.76$). The thermal conductivity λ and the molecular diffusivities \mathcal{D}_α for the species are determined by assuming constant Prandtl and Schmidt numbers.

2.1.2 The one-step chemical model

In this model, the chemistry is described by a single step irreversible reaction:



The reaction rate of this reaction is expressed using a classical Arrhenius law. Following the notations of Williams (1985) the reaction rate for the deficient species (subscript A) can be written

$$\dot{w}_A = \Lambda \rho Y_A \exp \left(- \frac{\beta(1 - \Theta)}{1 - \alpha(1 - \Theta)} \right) \quad (2.9)$$

where

$$\begin{aligned} \Theta &= (T - T_u)/(T_b - T_u) \text{ is the reduced temperature;} \\ \alpha &= (T_b - T_u)/T_b \text{ represents the heat release parameter;} \\ \beta &= \alpha E_a/R^0 T_b \text{ is the Zel'dovich number;} \\ \Lambda &= B \exp(-\beta/\alpha) \text{ is the pre-exponential factor.} \end{aligned}$$

T_b and E_a represent respectively the temperature in the burnt gases and the activation energy of the reaction, R^0 being the universal gas constant.

The source term \dot{Q} appearing in Eq. 2.3 is

$$\dot{Q} = (-\Delta_f^0)\dot{w}_A \quad (2.10)$$

where $(-\Delta_f^0)$ is the heat of reaction per unit mass of reactant.

2.1.3 The two-step chemical model

The two-step mechanism initially proposed by Zel'dovich (1948) consists of a first order chain branching reaction and a second-order termination reaction:



In the first reaction, two radicals X are created while one radical is consumed during the transformation of the reactant A into X . This initiation step is essential because it provides radicals to initiate chain reactions. This type of reaction is considered as thermo-neutral and has a high activation energy. Then, two radicals recombine to form the product P during the termination step (or chain breaking). This recombination step is highly exothermic and all the energy is released during this step. These approximations are consistent with the simplistic description that the more exothermic a reaction is, the smaller the activation energy.

Thus, using this description and considering equal molecular weight ($W = W_A = W_X$), the reaction rates for the two reactions are

$$RR_1 = \frac{\Lambda_1}{W} \rho^2 Y_A Y_X \exp\left(-\frac{\beta_1(1-\Theta)}{1-\alpha(1-\Theta)}\right) \quad (2.13)$$

$$RR_2 = \frac{\Lambda_2}{W} \rho^2 Y_X^2 \quad (2.14)$$

and for the two species,

$$\dot{w}_A = -\Lambda_1 \rho^2 Y_A Y_X \exp\left(-\frac{\beta_1(1-\Theta)}{1-\alpha(1-\Theta)}\right) \quad (2.15)$$

$$\dot{w}_X = \Lambda_1 \rho^2 Y_A Y_X \exp\left(-\frac{\beta_1(1-\Theta)}{1-\alpha(1-\Theta)}\right) - 2\Lambda_2 \rho^2 Y_X^2 \quad (2.16)$$

where

$$\Lambda_1 = \frac{B_1}{W} \exp\left(-\frac{\beta_1}{\alpha}\right) ; \quad \Lambda_2 = \frac{B_2}{W}$$

In the energy equation, the source term due to chemical reactions is

$$\dot{Q} = \sum_{k=1}^R (-\Delta H_k^0) RR_k \quad (2.17)$$

where ΔH_k^0 is the heat released by the k^{th} reaction. In the present case, we consider that the first reaction is thermo-neutral and all the heat is liberated during the second reaction. Thus \dot{Q} becomes

$$\dot{Q} = (-\Delta H_2^0) \frac{\Lambda_2}{W} \rho^2 Y_X^2. \quad (2.18)$$

This mechanism has been utilized in various studies concerning premixed laminar flames. Liñán (1971) proposed to represent a premixed laminar flame as a succession of layers in which different transformations occur. On the unburnt gas side, a thick preheat zone (relative to the laminar flame itself) is present. In this layer, only diffusion and convection phenomena take place and chemical reactions do not exist. Then, the chemistry of the hydrocarbons takes place in a thin layer in which radicals are produced. These radicals are transported (by diffusion and convection towards the burnt gases and by diffusion towards the fresh gases) and recombine into products in a broader layer including the hydrocarbon consumption layer. Different regimes were encountered by Liñán depending on the ratio of the frequency factors of the two reactions Λ_2/Λ_1 .

Hocks *et al.* (1981) investigated the quenching processes related to the interaction between a premixed laminar flame and a cold wall. The authors conclude that the two-step mechanism is able to describe the mechanism leading to flame quenching. It appears that the behavior of the flame close to the wall is strongly dependent on the maximum concentration of the intermediate species, which is essentially determined by the ratio Λ_2/Λ_1 .

Later, Seshadry & Peters (1983) studied the structure of a planar premixed laminar flame submitted to stretch. Considering a high activation energy for the first reaction, the authors derived an asymptotic expansion for the temperature. They found that the first order temperature can be expressed as a function of the stretch and the Lewis numbers for the reactant and the intermediate species:

$$T_0^1 = -K^* \left\{ \frac{Le_A - 1}{Le_A} + (-\Delta H_2^*) \left[\frac{1 - Le_X}{Le_X} I_0 \right] \right\}. \quad (2.19)$$

The subscript 0 refers to the axial coordinate where Y_X is maximum, I is a function always positive, K^* is a non-dimensionalized stretch and $(-\Delta H_2^*)$ is the non-dimensionalized heat of reaction of the recombination step. The relation (2.19) points out the respective roles of the diffusivities of the reactant and of the intermediate species. Considering only the first term on the RHS of Eq. 2.19, for positive stretch the temperature decreases (increases) for $Le_A > 1$ ($Le_A < 1$). For $Le_A = 1$, the temperature remains constant equal to the zero order temperature, regardless of the value of the stretch. This recovers the classical conclusions of the role played by the Lewis number of the reactant on stretched flames (Clavin 1985, Law 1988).

The second term on the RHS of (2.19) enhances the effects of diffusivity of the intermediate species on the dynamics of stretched flames. Since radicals are mostly very light species, they have high diffusivities leading to Lewis numbers significantly less than unity. Thus, in case of positive (negative) stretch, the diffusivity of the

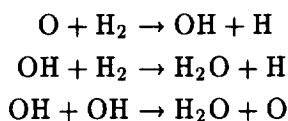
intermediate species tends to decrease (increase) the temperature and then the local laminar flame speed. This result points out that even for $Le_A = 1$, the flame can be sensitive to the effect of stretch and exhibits locally a variation of the laminar flame speed.

This brief description shows the ability of the two-step mechanism to describe fundamental phenomena occurring in premixed flames in different configurations. However, it also points out the appearance of new parameters such as the ratio of the frequency factors Λ_2/Λ_1 , the Lewis number for the intermediate species, the activation energy and the heat released by each of the two-step mechanism. This represents an infinity of combinations between these parameters. The challenge, then, is to provide this model with a realistic set of parameters representative of the fundamental mechanisms encountered in the kinetics of hydrocarbons.

To do so, we will focus our attention on the hydrogen-oxygen submechanism which is hierarchically the first submechanism (followed by the oxidation of carbon monoxide) occurring in the chemistry of hydrocarbons (Glassman 1987, Westbrook and Dryer 1984). In this submechanism, the H atoms play a determining role because they provide a major source of radicals in the branching reactions of the oxidation of H_2 . Furthermore, the concentration of H radical directly affects the overall heat release and, consequently, the reaction rate (Westbrook and Dryer 1984). In the $H_2 - O_2$ submechanism, one of the most important chain branchings is

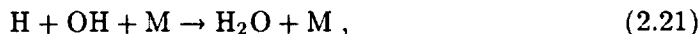


In the chain branching reaction (2.20), one H atom is consumed whereas radicals O and hydroxyl OH are produced and contribute to further branching reactions in which H radicals are created such as



The reaction 2.20 is endothermic of 17 kcal/mol and has an activation energy of 14.4 kcal/mol (Yu *et al.* 1994).

Then, radicals are transformed to form product and liberate energy in chain breaking reaction. In the high temperature regime, a principal termination reaction is



where M is a third body. During this step, radicals H and OH recombine to form products of combustion (here water). This reaction is highly exothermic (120 kcal/mol) and has a zero activation energy.

The rate coefficients for these two reactions are reported in Table 1.

From these considerations, all the parameters appearing in the two-step mechanism 2.11 and 2.12 can be estimated from the rate coefficients reported in Table 1. The ratio of the frequency factors Λ_2/Λ_1 of reactions 2.11 and 2.12 can be determined from the values of B_1 and B_2 and from the temperature of the burnt gases.

$k = BT^n e^{-E_A/R^0T}$				
reaction	B ($\text{cm}^3 \text{mol}^{-1} \text{s}^{-1}$)	n	E_A (kJ/mol)	ref
$\text{HO}_2 \rightarrow \text{OH} + \text{O}$	$8.3 \cdot 10^{13}$	0	60.3	Yu <i>et al.</i> 1994
$\text{H} + \text{OH} + \text{M} \rightarrow \text{H}_2\text{O} + \text{M}$	$1.6 \cdot 10^{22}$	-2	0	Miller and Bowman 1984

Table 1. Reacting mechanism, rate coefficients

As we mentioned previously, the H atoms play a determinant role in the chemistry of hydrocarbons. Thus, we will identify the intermediate species X of the two-step mechanism to the H atom which leads to a Lewis number for X, $Le_X = 0.15$. The activation energies of the two-step mechanism are those of the reactions 2.10 and 2.11 reported in Table 1.

2.1.4 Initialization of the two-step mechanism

To initialize the one-dimensional laminar flame using the two-step mechanism, the assumption of quasisteady state for the intermediate species is considered. Thus from Eq. 2.16, the concentration of the radical is directly related to the concentration of the species A and to the temperature:

$$Y_X = \frac{1}{2} \frac{\Lambda_1}{\Lambda_2} Y_A \exp\left(-\frac{\beta_1(1-\Theta)}{1-\alpha(1-\Theta)}\right) \quad (2.22)$$

We note that using Eq. 2.22 in Eq. 2.15 makes the two-step mechanism (under the assumption of quasi steady state for the intermediate species) reduce to the one-step second-order mechanism,



2.1.5 The radiative heat loss model

The radiative heat losses are taken into account in the energy equation by a linear term in temperature. The heat loss parameter h appearing in Eq. 2.3 comes from the asymptotic analysis of Williams (1985-pp 271-276). He considers the asymptotic structure of a one-dimensional premixed laminar flame submitted to radiation or conduction to a wall. Considering constant properties for the fluid, Williams proposes

$$h = \frac{l}{2\beta} Pr^2 \lambda \left(\frac{S_L^{ad}}{\nu_u}\right)^2, \quad (2.24)$$

where l is a constant and Pr a Prandtl number, ν_u represents the molecular viscosity in the fresh gases and S_L^{ad} the adiabatic laminar flame speed.

2.1.6 Configuration

The configuration retained in this study concerns the interaction between a two-dimensional vortex pair and a planar premixed laminar flame. This geometry corresponds to the experimental device of Samaniego *et al.* (1994). In the experiment, a mixture of methane or propane and air is introduced in a vertical channel of square cross section. The flame is stabilized on a heated wire and exhibits a two-dimensional V-shape. On the left side of the duct, a vortex pair is generated by acoustic excitation and interacts with the flame (see Fig. 1). Then, during the main duration of the interaction, the flow keeps its two-dimensionality. The DNS of all the experimental domain cannot be considered because of the high computational time and memory requirement. Nevertheless, the second flame (on the right of Fig. 1) does not play any significant role during the early stages of the interaction and allows us to consider only the left side of the domain where the interaction occurs (Samaniego *et al.* 1994). Moreover, one can demonstrate that due to the Galilean invariance of the Navier-Stokes equations, the problem is equivalent to considering a sub-domain related to the frame of reference of the flame and convected by the mean flow field.

The characteristics of the vortices (circulation, size, distance with respect to the flame, angle of impingement) are obtained from the experiment and are reported in Table 2. Here, the Damköhler is defined by $Da = sS_L^0^2 / V_D \alpha_u$ and the laminar flame thickness by $\delta_f = \alpha_u / S_L^0$. Three vortex pairs having different circulations and sizes are studied. For each interaction, a methane-air flame and a propane-air flame are investigated in order to study the effects of the Lewis number. The methane-air flame with an equivalence ratio of 0.55 exhibits a Lewis number equal to unity whereas the propane-air flame with an equivalence ratio of 0.50 has a Lewis number of 1.8. The parameters of the different cases analyzed in this study are reported in Table 2.

Since the structure of the vortex has not been precisely determined in the experiment, it is difficult to locate our study in the diagram of flame-vortex interactions proposed by Poinsot *et al.* (1991). Nevertheless, from the PIV measurements of Driscoll *et al.* (1994), the maximum tangential velocity of the vortices u_θ^{max} and the radius of the vortex core σ can be estimated. Driscoll *et al.* determined that $2 \leq u_\theta^{max} / V_D \leq 6$ and $1/2 \leq \sigma / s \leq 1/6$, where V_D is the displacement velocity of the vortex pair and s the distance separating the center of the vortices. Thus, we can roughly locate our study in the quenching region of the diagram represented in Fig. 2.

The temperature jump across the flame front is set exactly equal to 5, leading to the heat release parameter $\alpha = 0.8$.

Vortex pairs can be easily generated numerically, and several authors have proposed analytical solutions that satisfy the Navier-Stokes equations. Among these solutions, one of the most used in numerical simulations are the Oseen vortex (Oseen 1911) and the vortex “hat” used by Rutland (1989). The expression for the circulation Γ , the vorticity ω_z , and the tangential velocity u_θ are expressed in Table 3 in function of the radial coordinate r , the vortex strength Ψ , and the core radius

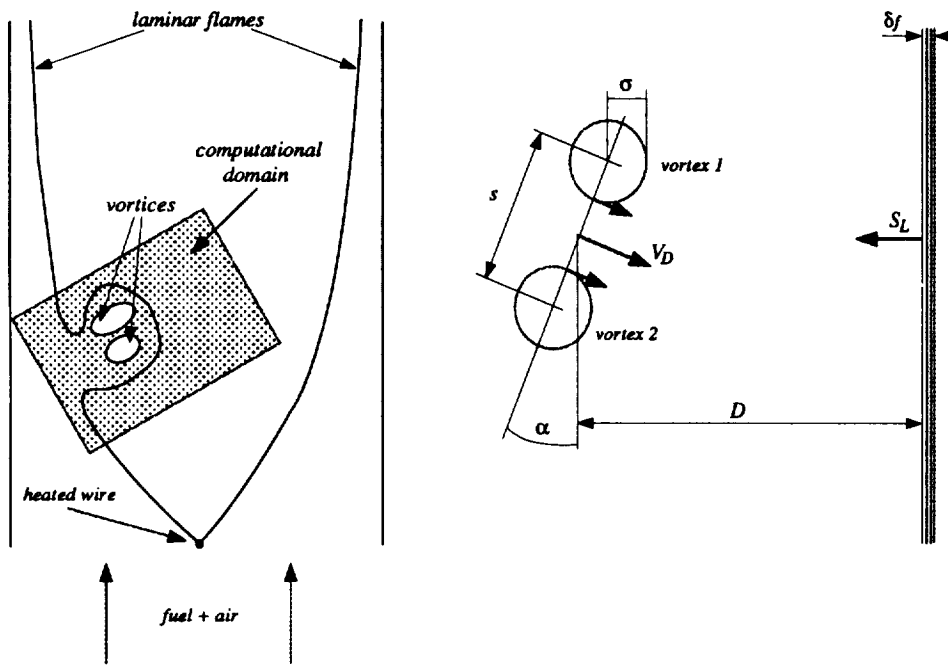


FIGURE 1. Schematic description of the configuration

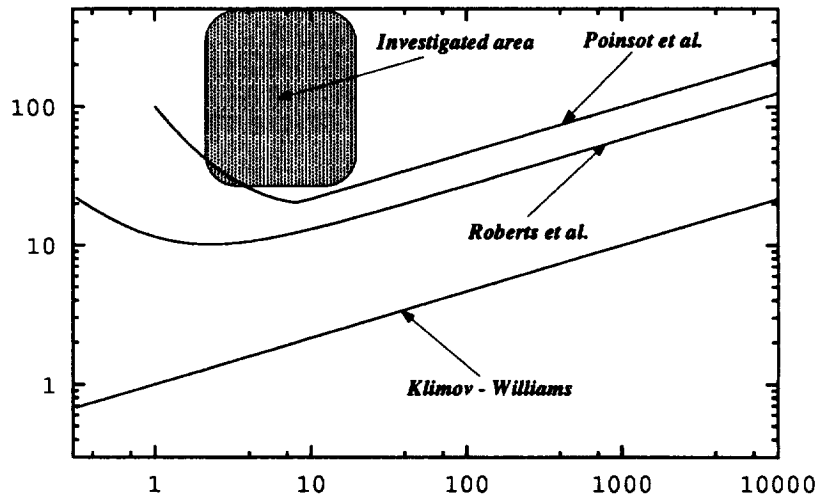


FIGURE 2. Diagram of vortex-flame interactions

		vortex 1		vortex 2					
Le	case	$\Gamma_1/S_L^0 \delta_f$	Re_1	$\Gamma_2/S_L^0 \delta_f$	Re_2	s/δ_f	D/δ_f	V_D/S_L	Da
1.0	1	3286	4600	3569	5000	36.5	104.8	14.9	1.9
	2	5657	8000	6686	9333	25.7	104.8	38.1	0.53
	3	10286	14667	11314	16000	25.7	104.8	66.8	0.3
1.8	1	3286	4600	3571	5000	40.5	104.8	13.5	2.91
	2	5714	8000	6667	9333	28.6	104.8	34.5	0.81
	3	10476	14667	11428	16000	28.6	104.8	61.0	0.45

Table 2. Dimensionless parameters for each configuration

vortex "hat"	Oseen vortex
$\Gamma = 2\pi\Psi \frac{r^2}{\sigma^2} \exp\left(-\frac{r^2}{\sigma^2}\right)$	$\Gamma = \Psi \left(1 - \exp\left(-\frac{r^2}{\sigma^2}\right)\right)$
$\omega_z = \frac{\Psi}{\sigma^2} \left(2 - \frac{r^2}{\sigma^2}\right) \exp\left(-\frac{r^2}{2\sigma^2}\right)$	$\omega_z = \frac{\Psi}{\pi\sigma^2} \exp\left(-\frac{r^2}{\sigma^2}\right)$
$u_\theta = \frac{\Psi r}{\sigma^2} \exp\left(-\frac{r^2}{2\sigma^2}\right)$	$u_\theta = \frac{\Psi}{2\pi r} \left(1 - \exp\left(-\frac{r^2}{\sigma^2}\right)\right)$

Table 3. Circulation Γ , vorticity ω_z , and tangential velocity u_θ for the vortex "hat" and the Oseen vortex

σ . The distribution of these quantities for the Oseen vortex and for the vortex "hat" are schematically represented in Fig. 3.

Because its compact structure allows us to avoid numerical difficulties related to the boundaries of the domain (and then to reduce the size of the computational box), the vortex "hat" has been utilized in several studies (Rutland & Ferziger 1991, Poinso *et al.* 1991). However, the vortex "hat" exhibits a rapid decrease of the tangential velocity and an inversion of the sign of the vorticity for $r = \sqrt{2}\sigma$, which is not representative of real vortices. During the interaction with the flame, this opposite vorticity generates undesirable stretch, leading to an artificial increase of the flame length. To avoid these problems and to perform future quantitative comparison with the experimental results of Samaniégo *et al.* (1994), the Oseen

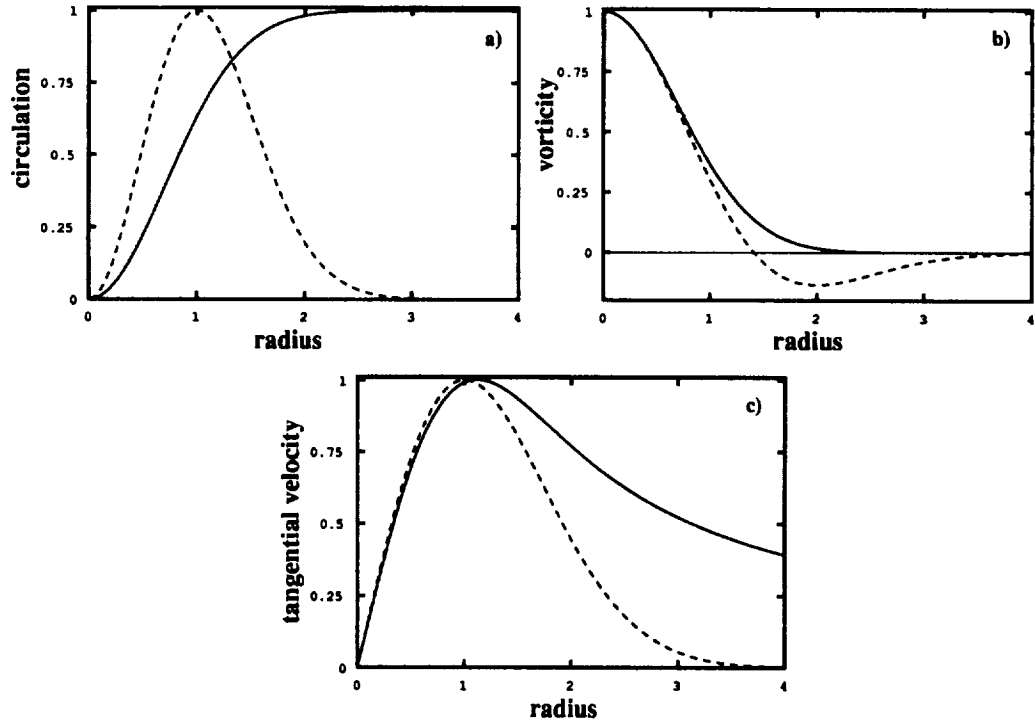


FIGURE 3. Characteristics of the vortices a) circulation Γ , b) vorticity ω_z , c) tangential velocity u_θ ; — : Oseen vortex; : "hat vortex".

vortex is utilized in all our simulations.

For these two-dimensional simulations, the computational domain is typically composed by 300000 grid points (750×400).

2.1.7 Remarks

In the simulations, some parameters have to be treated carefully in order to perform quantitative comparisons with the experiment. The interaction between the vortex pair and the flame can be entirely defined by the following set of parameters:

- the ratio between the displacement velocity of the vortex pair and the laminar flame speed V_D/S_L ;
- the ratio between the distance separating the center of the vortices and the laminar flame thickness s/δ_f ;
- the distance D separating the vortex pair and the flame;
- the temperature jump across the flame front represented by the heat release parameter α ;
- the activation energy of the chemical reaction(s) represented by the Zel'dovich number(s) $\beta_{(k)}$;
- the ratio between the frequency factors Λ_2/Λ_1 for the two-step mechanism.

Although it sets the laminar flame velocity, the frequency factor Λ for the one-step chemical model (and Λ_1 for the two-step mechanism) is not a determining parameter in this study. Indeed, the laminar flame velocity can be chosen arbitrarily as long as the ratio V_D/S_L is appropriate and the effects related to the compressibility of the flow are avoided. The only restriction is to limit the Mach number, based on the maximum velocity present in the flow field, to be below a critical value (i.e. 0.2). This restriction has an important practical impact, because it considerably reduces the computational time of the simulations.

As we have already mentioned, the experiment allows us to determine the individual circulation of the vortices and the distance separating the center of the vortices, the radius of the viscous core σ and the exact distribution of the tangential velocity being unknown. However, the information provided by the experiment is enough to give a good representation of the interaction. Vortex pairs propagate by mutual induction, and, for point vortices, the displacement velocity of the ensemble is defined by the circulation of the vortices Γ and the distance separating the vortices s (Prandtl & Tietjens 1934):

$$V_D = \frac{\Gamma}{2\pi s} \quad (2.25)$$

Although in the experiment the vortex cores definitely have a finite radius, some simulations performed on simple cases show that as long as the circulation of each of the vortices is conserved and the radius of the viscous cores is restricted to $0 < \sigma/s < 1/2$, the dynamics of the interaction and the strain field applied to the flame are the same. Thus, in all the simulations presented here, the ratio σ/s is set to $1/3$.

In other words, for given circulation Γ and distance s , vortex flame interactions can be represented either by point vortices or by finite viscous core radius and lead to the same conclusions. This last point has a very important impact on the elaboration of combustion diagrams for vortex flame interactions proposed by Poinso *et al.* (1991) usually defined by u_θ^{max}/S_L and σ/δ_f . Thus, using the characteristics of the Oseen vortex reported on Table 3, a vortex flame interaction can be represented in the diagram by an infinity of points related by the relation:

$$\frac{u_\theta^{max}}{S_L} = \frac{Re_v}{2\pi} Pr \left(\frac{\sigma}{\delta_f} \right)^{-1} \quad (2.26)$$

where $Re_v = \Gamma/\nu$ is the Reynolds number of the vortex. Here, we propose to use the parameters V_D/S_L and s/δ_f to classify vortex flame interactions in the diagram of Poinso *et al.* (1991). Note that, since the ratios u_θ^{max}/V_D and σ/s in Poinso *et al.* (1991) and Roberts *et al.* (1993) are not far from unity, the conclusions of their study are still valid and are not contradicted by our comments.

2.1.8 Post processing

The experimental results obtained by Samaniego *et al.* (1994) concern essentially the CH emission of the flame during the interaction. The CH emission of the flame is directly related to the heat release rate of the flame, as shown by the numerical

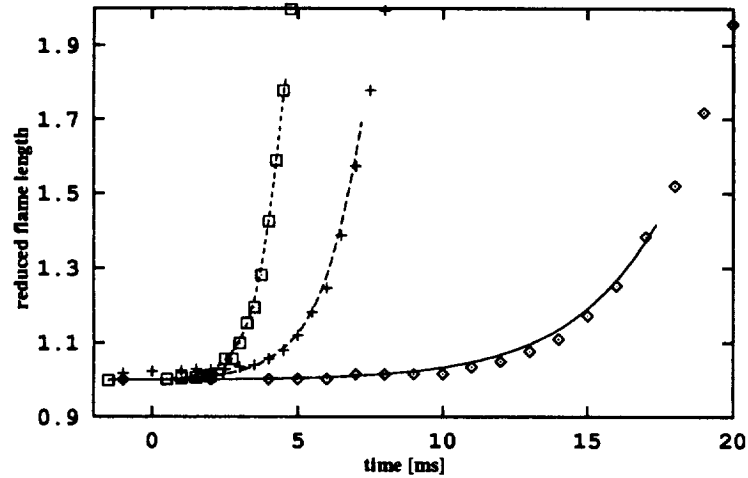


FIGURE 4. Evolution in time of the reduced flame length Σ^* ; Case 1: — : DNS, \diamond : exp; Case 2: ---- : DNS, + : exp; Case 3: : DNS, \square : exp

analysis of Samaniégo (1994). Samaniego *et al.* relate the light emission of a strained laminar methane-air flame I_{CH_4} and the light emission of a strained laminar propane-air flame $I_{\text{C}_3\text{H}_8}$ to the heat release rate RR according to the following power laws:

$$RR = I_{\text{CH}_4}^{0.37} \quad (2.27)$$

$$RR = I_{\text{C}_3\text{H}_8}^{0.63} \quad (2.28)$$

Thus, quantitative comparisons will be performed accurately both for methane-air and propane-air flames.

In this section, local characteristics of the flame such as the tangential strain, the curvature, the normal towards the fresh gases, and the flame length Σ are obtained at the flame front location $Y_A/Y_{A_u} = 0.2$ where Y_A represents the mass fraction of the reactant A .

2.2 Results

In the first part of this section, the results are presented for simulations performed with the one-step chemical model. In this model, the heat release parameter α is set to 0.8 and the Zel'dovich number β to 8.0, corresponding to an activation energy of 30 kcal/mol.

Before discussing in more detail the physical effects affecting the local structure of the flame during the interaction, the evolution in time of the reduced flame length $\Sigma^* = \Sigma/\Sigma_0$ for $Le = 1.0$ and the three interactions shown in Table 2 are presented in Fig. 4.

The comparison with the experimental results of Samaniego *et al.* (1994) points out that the dynamics of the interactions is very well reproduced by the simulation. This enhances the reasonable approximations made concerning the internal structure of the vortices and their initialization.

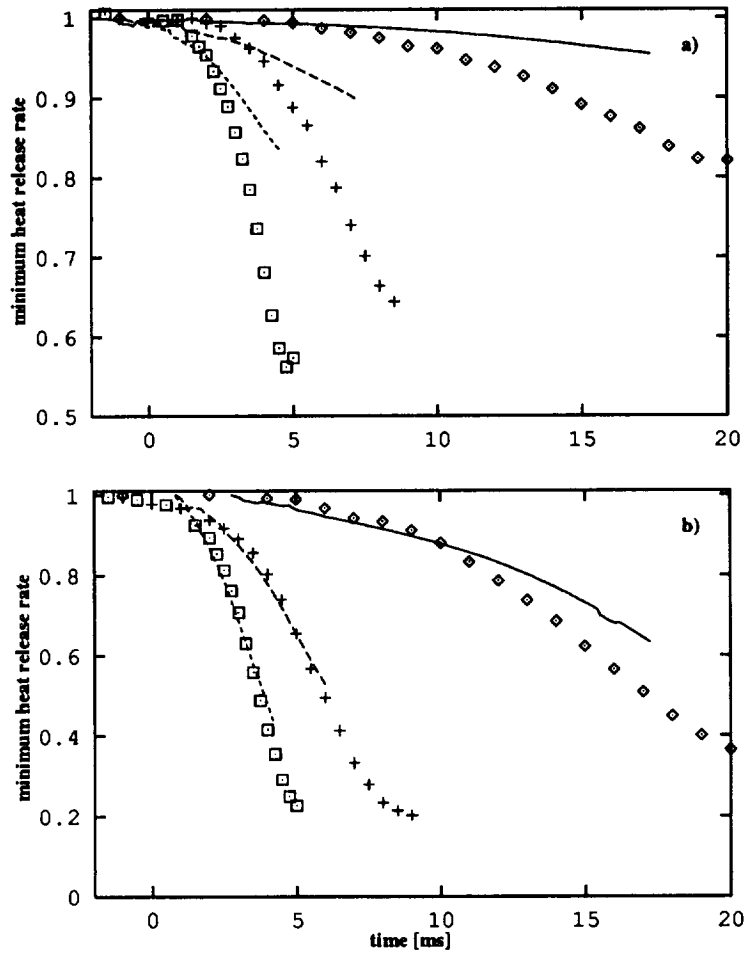


FIGURE 5. Evolution in time of the minimum heat release rate. a) $Le = 1.0$; b) $Le = 1.8$ Case 1: — : DNS, \diamond : exp; Case 2: - - - : DNS, + : exp; Case 3: ····· : DNS, \square : exp

Fig. 5 describes the time evolution of the minimum of the heat release rate along the flame front for the different interactions presented in Table 2. For $Le = 1.0$ (Fig. 5-a), the agreement is poor between the simulations and the experiment even if the sensitivity to the Damköhler number is qualitatively represented by the DNS. For $Le = 1.8$ (corresponding to the propane-air flame), the simulations seem to well reproduce the decrease of the minimum heat release rate for the three interactions, especially those corresponding to low Damköhler numbers.

The same comments can be made concerning the distribution of the heat release rate along the flame front where the simulations greatly overestimate the heat release for $Le = 1.0$ (see Fig. 6), whereas the agreement is notably better for $Le = 1.8$ (see Fig. 7).

For $Le = 1.8$, the Lewis number effect alone can explain the decrease of the heat

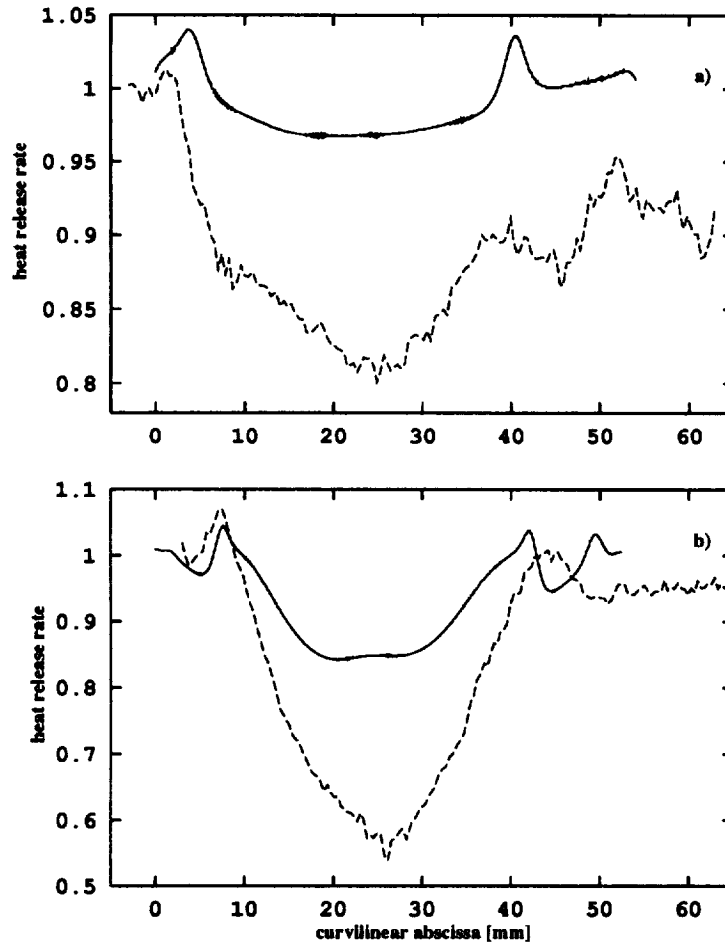


FIGURE 6. Distribution of the heat release rate along the flame front. $Le = 1.0$; a): case 1, b): case 3 ; — : DNS, ---- : exp

release rate during the interaction and seems to be the parameter controlling the local structure of the flame. However, the simulations presented here are performed for an adiabatic flame using a one-step chemical model. Thus, phenomena such as radiative heat losses and complex chemistry effects are not taken into account and could have a significant impact on the interaction, which could explain the discrepancies found between the DNS and the experiment, especially for $Le = 1.0$.

In the following sections, the contributions of the major physical effects suspected of playing a role in the mechanism of extinction (stretch, heat losses, complex chemistry) and responsible for the decrease of the heat release rate observed during the interaction will be analyzed in detail.

2.2.1 Analysis of the stretch

In the configuration studied here, the flame is subjected to curvature and straining

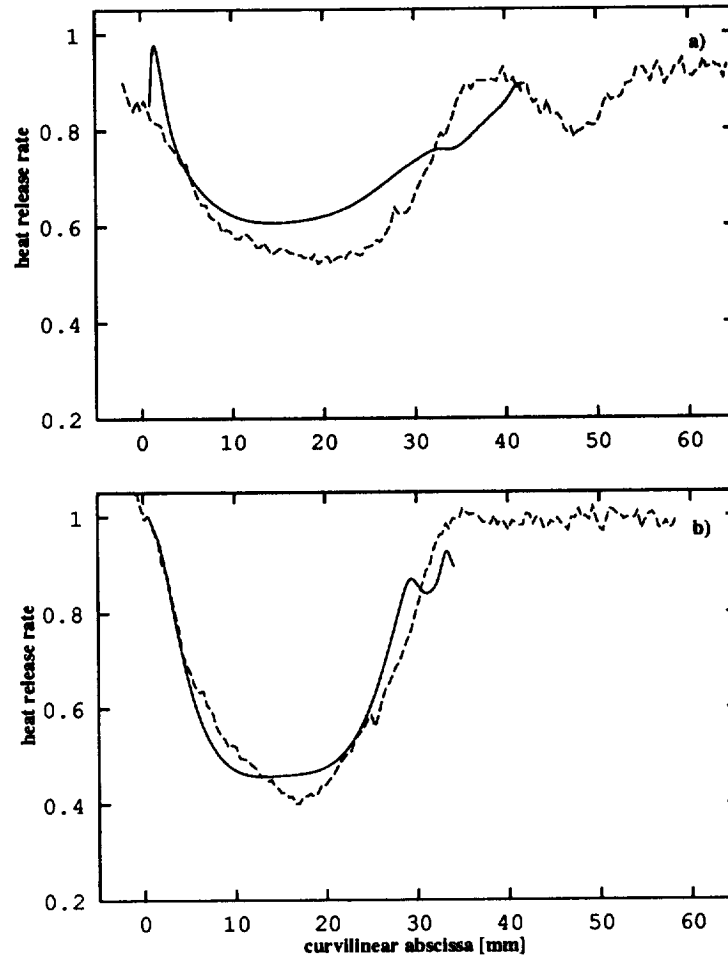


FIGURE 7. Distribution of the heat release rate along the flame front $Le = 1.8$; a): case 1, b): case 3; — : DNS, ---- : exp

effects, causing a modification of the flame length. These changes imposed on the flame can be estimated from the flame stretch κ . From Williams (1985), κ is defined by the rate of change of a Lagrangian flame surface element A :

$$\kappa = \frac{1}{A} \frac{dA}{dt} \quad (2.29)$$

This expression can be rewritten in terms of flame stretch and flame curvature (Matalon 1983, Candel & Poinsot 1990):

$$\kappa = \mathbf{nn} : \nabla \mathbf{w} + \nabla \cdot \mathbf{w} \quad (2.30)$$

where \mathbf{n} is the unit vector normal to the flame surface pointing towards the fresh gases:

$$\mathbf{n} = - \frac{\nabla \mathbf{c}}{|\nabla \mathbf{c}|} \quad (2.31)$$

and \mathbf{w} is the local velocity of the flame surface. In indicial notation, $\mathbf{nn} : \nabla \mathbf{w} = n_i n_j \partial w_i / \partial x_j$. The local flame front velocity can be decomposed in a convective velocity in the fresh gases \mathbf{u} and a displacement speed S_d (see Poinso *et al.* 1992). Thus, expression 2.30 becomes:

$$\kappa = \nabla_t \cdot \mathbf{u} - \frac{S_d}{\mathcal{R}} \quad (2.32)$$

where $\nabla_t \cdot \mathbf{u}$ represents the strain contribution and S_d/\mathcal{R} the curvature term (\mathcal{R} is the local radius of curvature of the flame front).

As it has been shown by Poinso *et al.* (1992), the displacement speed S_d is not equal to the laminar flame speed S_L and can be significantly different. The displacement speed can be exactly determined by solving the equation for an iso-contour $c = c_0$ (which is nothing but the G-equation described in Kerstein *et al.* 1988) as it has been proposed by Trouvé & Poinso (1994). The equation for an iso-scalar surface $c = c_0$ is written:

$$\frac{\partial c}{\partial t} + \mathbf{w} \cdot \nabla c = 0 \quad (2.33)$$

Utilizing Eq. 2.30 in Eq. 2.32 and noting that $S_d = \mathbf{w} \cdot \mathbf{n} - \mathbf{u} \cdot \mathbf{n}$, an expression for S_d can be derived:

$$S_d = \frac{1}{|\nabla c|} \left(\frac{\partial c}{\partial t} + \mathbf{u} \cdot \nabla c \right) \quad (2.34)$$

Fig. 8 represents the relative contribution of strain and curvature on the stretch along the flame front for case 3 of Table 2 at the end of the interaction ($t = 3.3\text{ms}$).

One sees that the maximum stretch does not appear on the trajectory described by the ensemble as it could be expected. The maximum of stretch occurs on both sides of this trajectory corresponding to each of the vortices. This feature was also observed by Driscoll *et al.* (1994) in their PIV measurements.

As expected due to the size of the vortex pair compared to the flame thickness, the contribution of the curvature on the global stretch is very weak (about a few percent) compared to the contribution of the tangential strain, especially in regions where a significant decrease of the heat release rate is observed. This corroborates the conclusions of Driscoll *et al.* (1994), who performed a measurement of the velocity field during vortex-flame interaction using a PIV technique. We can also see that the levels of strain rate reached during the interaction are extremely high compared to the extinction strain rate measured for steady counterflowing premixed flames (Law *et al.* 1986, Tsuji & Yamaoka 1982) and for the vortex-flame interaction of Driscoll *et al.* (1994). In Tsuji & Yamaoka (1982), the extinction strain rate of a methane-air flame with an equivalence ratio of 0.52 is only 42s^{-1} . During the interaction of ring vortices and a premixed methane-air flame with an equivalence ratio of 0.55, the extinction strain rate measured by Driscoll *et al.* (1994) is 35s^{-1} and corresponds to a Karlovitz number of 0.12. In the present interactions, the Karlovitz number reaches higher values up to 3.0 (see Fig. 9).

Apparently, the configuration retained in our study exhibits a very resistant flame compared to the steady situations of Tsuji & Yamaoka (1982) and particularly compared to the ring vortices-flame interaction of Driscoll *et al.* (1994). In this last study, local quenching is clearly observed during the interaction. On the contrary in our study (both in the experiment and in the simulations), all the cases investigated here are far from the quenching limit encountered by Roberts *et al.* (1993) and by Driscoll *et al.* (1994). In all our simulations, the minimum heat release rate never decreases under 30% of the heat release rate corresponding to an unstrained laminar flame (see Fig. 5). Moreover, we observe that it is more difficult to quench a methane-air flame having a Lewis number of unity rather than a propane-air flame with $Le = 1.8$. These conclusions are in accordance with the classical analytical results concerning the theory of stretched flames (Clavin & Williams 1982, Clavin 1985, Law 1988) and also with the experimental results of Law *et al.* (1986), but are in contradiction with the observations of Roberts *et al.* (1993).

For $Le = 1.0$, we observe a good correlation between the strain rate and the local flame speed with a slight negative slope¹ (see Fig. 10-a). This is due to the compression of the reaction zone by the local extensive strain. This observation is consistent with the results of Haworth & Poinso (1992) and is illustrated in Fig. 11, which shows the scatter plot of the thermal flame thickness $\delta_T^* = \delta_T / \delta_T^{uns}$ (based on the maximum temperature gradient) versus the local flame speed. A very good correlation is found between δ_T^* and S_L^* and clearly shows a compression of the flame (down to 70% for the higher strain rates) corresponding to low values of S_L^* . Conversely, a thickening of the flame (up to 10%) corresponds to higher flame velocities and regions of compression of the flame.

For $Le = 1.8$ (see Fig.10-b), the correlation between S_L^* and Ka is less obvious even if we observe a clear decrease of the local flamelet velocity for positive stretch as it can be expected for strained laminar flame having a Lewis number greater than unity.

2.2.2 Effect of the radiative heat losses

Radiative heat losses occurring in the burnt gases of a premixed laminar flame produce a natural decay of the temperature and have been suspected of being partially or totally responsible for quenching during vortex-flame interaction (Poinso *et al.* 1991, Roberts *et al.* 1993). In their numerical study (and using a one-step mechanism for the chemistry), Poinso *et al.* (1991) concluded that stretch alone cannot be responsible for quenching. Local extinction occurs only when stretch and radiative heat losses present in the burnt gases are combined. The authors observed that during the quenching process, pockets of fresh gases can be present in the burnt gases and cannot reignite due to a too low temperature. However, in order to obtain such behavior, very high (and unrealistic) heat losses have been imposed to the flame. In comparison, we will see that the heat losses measured by Roberts *et al.* (1993) and by Samaniego *et al.* (1994) are lower by an order of magnitude than in

¹ The local flame speed is calculated by integrating the reaction rate in a direction normal to the flame front: $S_L = \frac{1}{\rho_u Y_{A_u}} \int_{-\infty}^{\infty} \dot{w} dn$

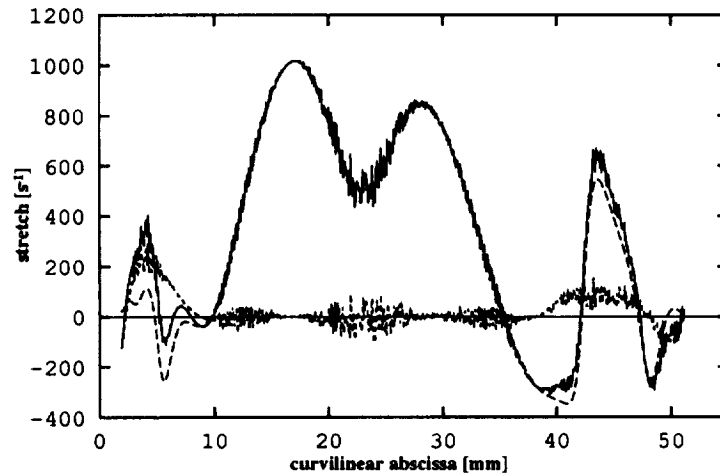


FIGURE 8. Contribution of tangential strain and curvature on stretch, Case 3 $Le = 1.0$; — : total stretch, ---- : curvature, - · - · : tangential strain

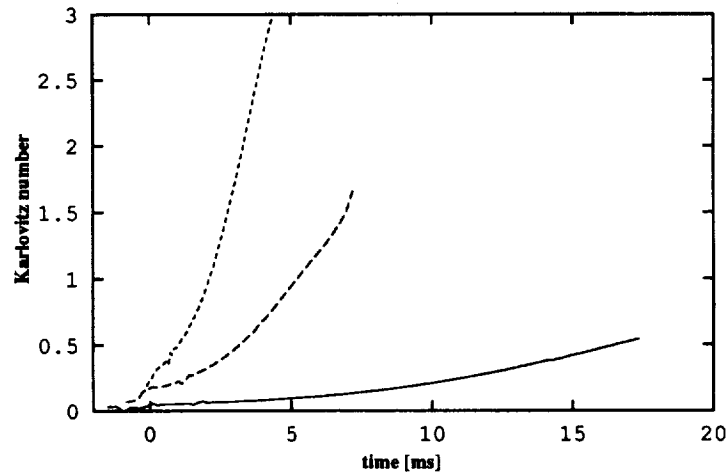


FIGURE 9. Evolution in time of the Karlovitz number for $Le = 1.0$
 — : case 1, ---- : case 2, - · - · : case 3

Poinsot *et al.* (1991). Since in their simulations a single-step mechanism has been used, it is still not clear if quenching in real flames is due to combined stretch and heat loss effects, or to combined stretch and complex chemistry effects.

Here, in order to quantify the impact of realistic heat losses on the distribution of the reaction rate along the flame front, a simulation corresponding to the interaction 2 of Table 2 for $Le = 1.0$ is performed. Different levels of heat loss corresponding to the experiments of Roberts *et al.* (1993) and Samaniego *et al.* (1994) and to the numerical study of Poinsot *et al.* (1991) are investigated. Before discussing the results of these simulations, the quenching limit of a one-dimensional non-adiabatic

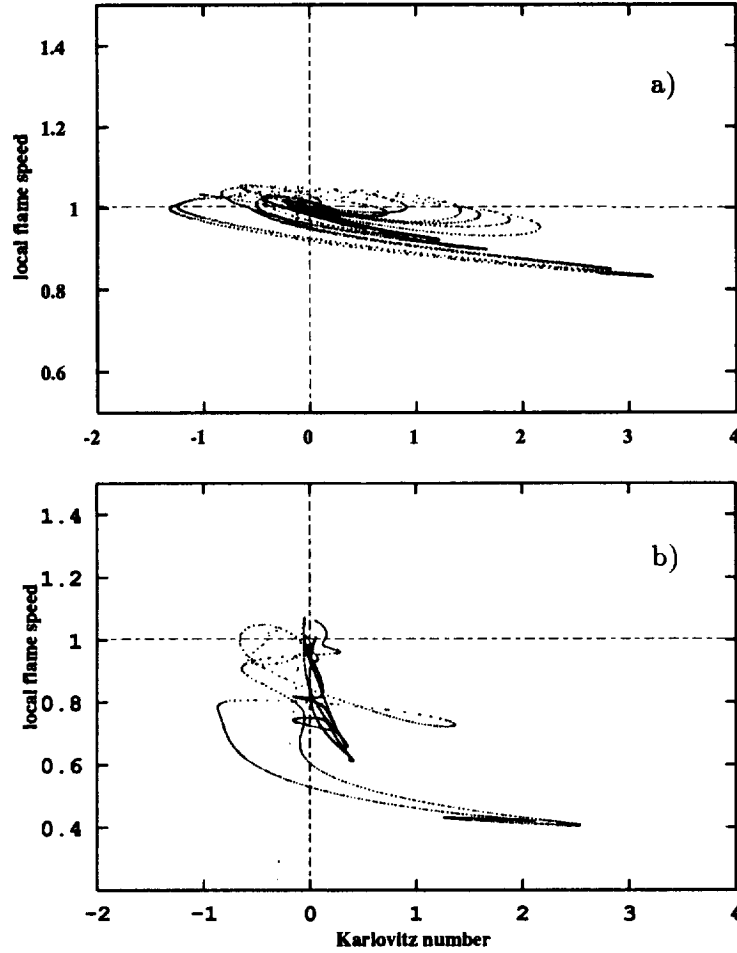


FIGURE 10. Scatter plot of local flame speed versus Karlovitz number, a): $Le = 1.0$; b): $Le = 1.8$

flame is investigated. This analysis should allow us to recover the asymptotic solution of Williams (1985), who proposes an analytical relation between the laminar flame velocity and the heat loss parameter. This relation is expressed (Williams 1985 p. 275):

$$\xi^2 = \exp\left(-\frac{l}{\xi^2}\right) \quad (2.34)$$

where $\xi = S_L/S_L^{ad}$. From this relation, the quenching limit corresponds to $l = 1/e$ leading to a reduced laminar burning velocity $\xi = 1/\sqrt{e}$.

Fig. 12 shows the evolution of the burning velocity ratio ξ versus the heat loss parameter l given by the simulation and by the relation 2.34 for two different Zel'dovich numbers ($\beta = 8$ and $\beta = 16$). A very good agreement is found between the simulations and the asymptotic theory of Williams, especially for very large activation

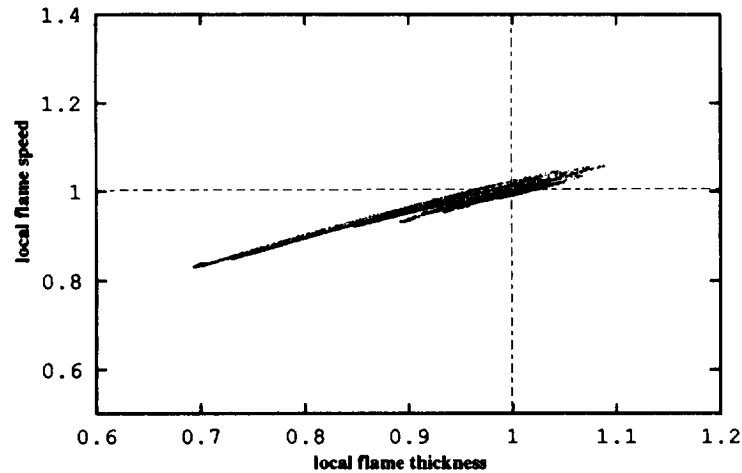


FIGURE 11. Scatter plot of local flame speed versus the reduced local flame thickness

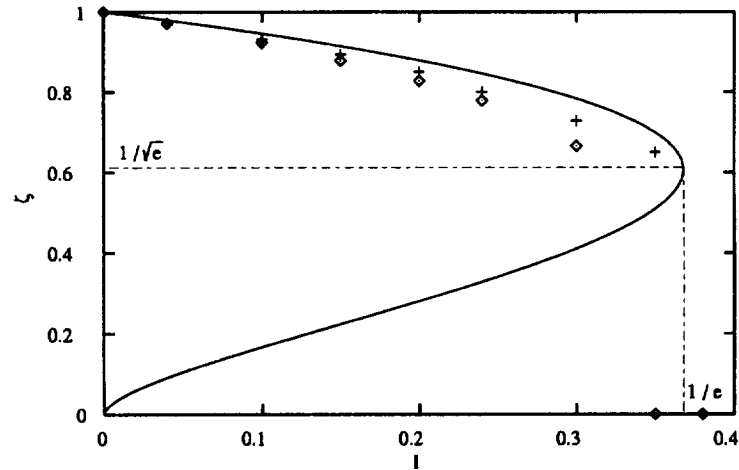


FIGURE 12. Burning velocity ratio versus heat loss parameter ; — asymptotic theory, \diamond : $\beta = 8.0$, $+$: $\beta = 16.0$

energy.

In the simulation corresponding to the case 2 for $Le = 1.0$, various values for the heat loss parameter l are investigated. The case $l = 0$ corresponds to the adiabatic case, $l = 0.008$ and $l = 0.027$ to the heat losses estimated from the experiment of Samaniégo *et al.* (1994) and from Roberts *et al.* (1993). The case $l = 0.3$ represents the heat losses used by Poinso *et al.* (1991). According to Fig. 12, only a negligible effect of radiative heat losses is expected to be found in Samaniégo *et al.* (1994) and in Roberts *et al.* (1992). Nevertheless, the effect should be much more pronounced for the heat losses of Poinso *et al.* (1991) which are close to the

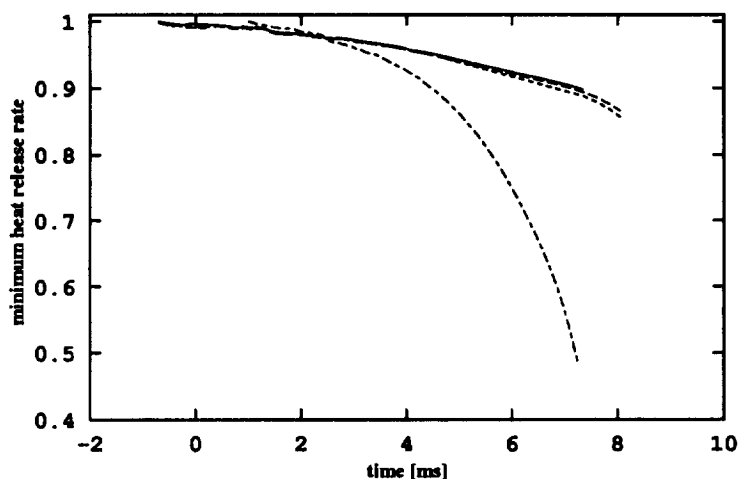


FIGURE 13. Evolution in time of the minimum heat release rate, case 2 $Le = 1.0$; ——— adiabatic, - - - - : $l = 0.008$, ····· : $l = 0.027$, - · - · : $l = 0.3$.

quenching limit observed for a one-dimensional unstrained non-adiabatic laminar flame. Fig. 13 represents the time history of the minimum heat release encountered along the flame front. As expected, the heat losses found in the two experiments have a negligible effect on the evolution of the heat release rate. On the other hand, very intense heat losses (more representative of conductive heat losses to a wall) can lead to a dramatic decrease of the heat release and to probable local quenching even if the computation does not go sufficiently far in the interaction to clearly show it.

These simulations are performed using a one-step chemical model and do not take into account combined effects of radiative heat losses and complex chemistry. These combined effects can have a significant influence on the flame structure when the flame is close to its flammability limits, as illustrated by the numerical study of Egolfopoulos (1994). The author investigates the response of a lean methane-air flame submitted to stretch and radiative heat losses using the GRI (Gaz Research Institute) mechanism. For a laminar methane-air flame with an equivalence ratio of 0.55, Fig. 14 shows the evolution of the reduced heat release \dot{Q}/\dot{Q}_0^{ad} as a function of the tangential strain. Results for the adiabatic and non-adiabatic cases are presented. We can observe that the heat release rate is strongly influenced by the heat losses for the unstrained laminar flame and decreases down to 0.83. For high values of the strain (typically those encountered in our configuration), the effect of the radiative heat losses compared to the effect of the strain on the decrease of \dot{Q}/\dot{Q}_0^{ad} is much weaker.

2.2.3 Role of an intermediate species in strained laminar flames

The chemistry of simple hydrocarbons such as methane can be described by full mechanisms available in the literature (Westbrook & Dryer 1984, Miller & Bowman 1989). The coupling of these mechanisms with a DNS code has been performed by Baum *et al.* (1992) but leads to extremely high computational time. As an

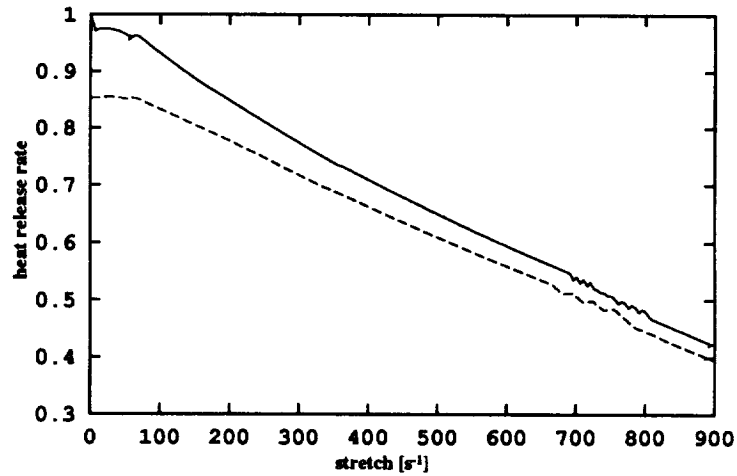


FIGURE 14. variation of the heat release rate versus stretch for a one-dimensional premixed strained flame (from Egolfopoulos 1994) — : adiabatic , ---- : non-adiabatic

alternate possibility, reduced chemical schemes for the combustion of methane-air flames (Peters & Williams 1987) and for propane-air flames as well (Kennel *et al.* 1990) exist and can be used in DNS codes.

Here, a two-step mechanism described by a first chain branching step $A + X \rightarrow 2X$ and a second chain terminating step $X + X \rightarrow P$ is utilized to analyze the structure of the flame during its interaction with a vortex pair.

In the asymptotic analysis of a premixed laminar flame submitted to stretch, Seshadry & Peters 1983 have put into evidence the role played by the radical species on the flame structure (see §2.1.3).

Since the Lewis number for the intermediate species is less than unity (due to the high diffusivity of the radicals), positive stretch will generate a high diffusion of radicals out of the reaction zone. Thus, the concentration of radicals in the reaction zone will decrease, leading to a lower heat release rate (because of the quadratic dependence on Y_X of the heat release rate, see Eq. 2.14). This behavior is well reproduced by the asymptotic expression for the temperature given by Eq. 2.19.

From the discussion presented in §2.1.3, the set of parameters for the two-step mechanism can entirely be determined by considering the data presented in Table 1 and the temperature of the burnt gases (in the experiment $T_b = 1500K$). This leads to $\Lambda_2/\Lambda_1 = 0.53$, $\beta_1 = 4.83$, $\beta_2 = 0$, and $Le_X = 0.15$ (here using the Lewis number for the H atom).

Fig.15 shows the evolution in time of the minimum heat release rate during the interactions for $Le = 1.0$ and $Le = 1.8$ for the cases 1 and 3 of Table 2. Here, the decrease of \dot{Q} is very well reproduced by the two-step mechanism, regardless of the Damköhler number. This is particularly interesting for the methane-air flame cases for which the one-step mechanism poorly describes the decrease of \dot{Q} (see Fig. 5-a).

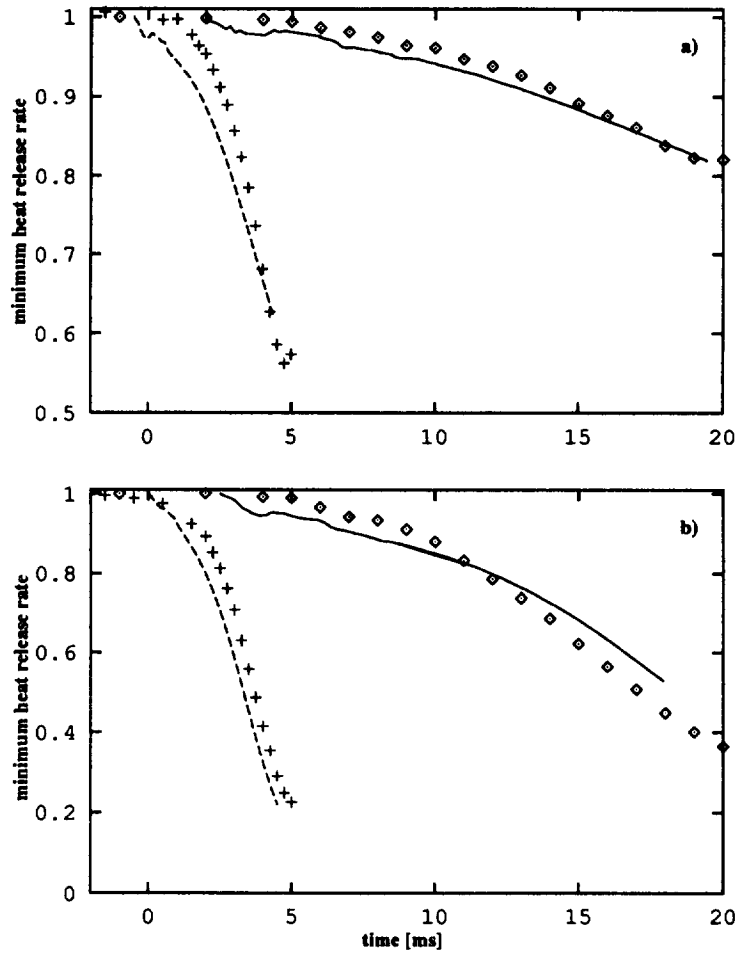


FIGURE 15. Evolution in time of the minimum heat release rate. a) $Le = 1.0$ b) $Le = 1.8$ Case 1: — : DNS, \diamond : exp; Case 2: ---- : DNS, + : exp; Case 3: : DNS, \square : exp.

The coherent behavior of the two-step mechanism is confirmed by the distribution of \dot{Q} along the flame front (see Figs. 16 and 17). For $Le = 1.0$, the agreement between the DNS and the experiment is excellent and is greatly improved compared to the results obtained with the one-step mechanism (see Fig. 6). A minor quantitative discrepancy exists in regions of the flame where curvature effects are non-negligible although the tendencies are well reproduced.

The same comment can be made for $Le = 1.8$, where a good agreement is observed for the two Damköhler numbers studied here (Figs. 15-b and 17). However, the two-step mechanism does not significantly improve the results, which are already satisfactory using the one-step model (see Fig. 7).

Fig. 18 shows the scatter plot of the local flame speed versus the Karlovitz number. Regions of the flame submitted to positive stretch exhibits a decrease of the local

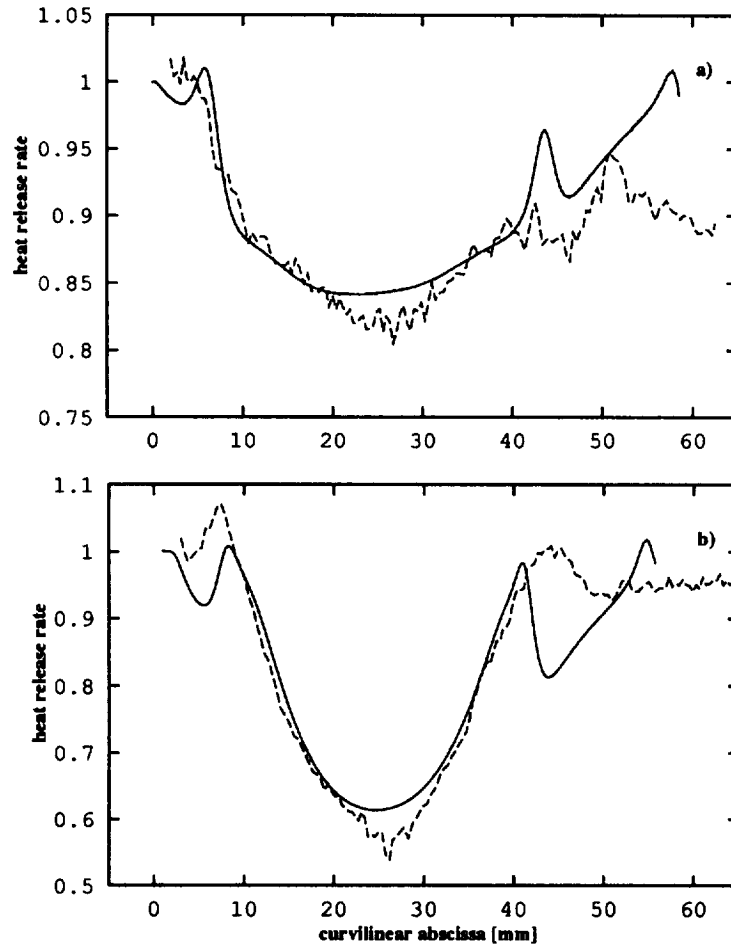


FIGURE 16. Distribution of the heat release rate along the flame front. $Le = 1.0$; a): case 1, b): case 3; — : DNS, ---- : exp.

flame speed as it is observed for stretched flames having a Lewis number greater than unity. As a consequence, a flame having a Lewis number of unity described with a two-step mechanism behaves like a laminar flame having an apparent Lewis number greater than unity. This particular point provides evidence for the existence of a critical Lewis number Le_c smaller than unity for which moderate stretch does not affect the flame structure.

According to these observations, the concentration of radicals seems to be the key parameter which controls the local flame structure and quenching mechanism. This has been shown by the asymptotic analysis on the structure of strained premixed flames by Seshadry & Peters (1983) and is confirmed in the present study. Moreover, the quenching of a premixed laminar flame propagating toward a cold wall is also strongly dependent on the concentration of radicals (Hocks *et al.* 1981).

However, it is difficult to separate which parameter of the two-step mechanism

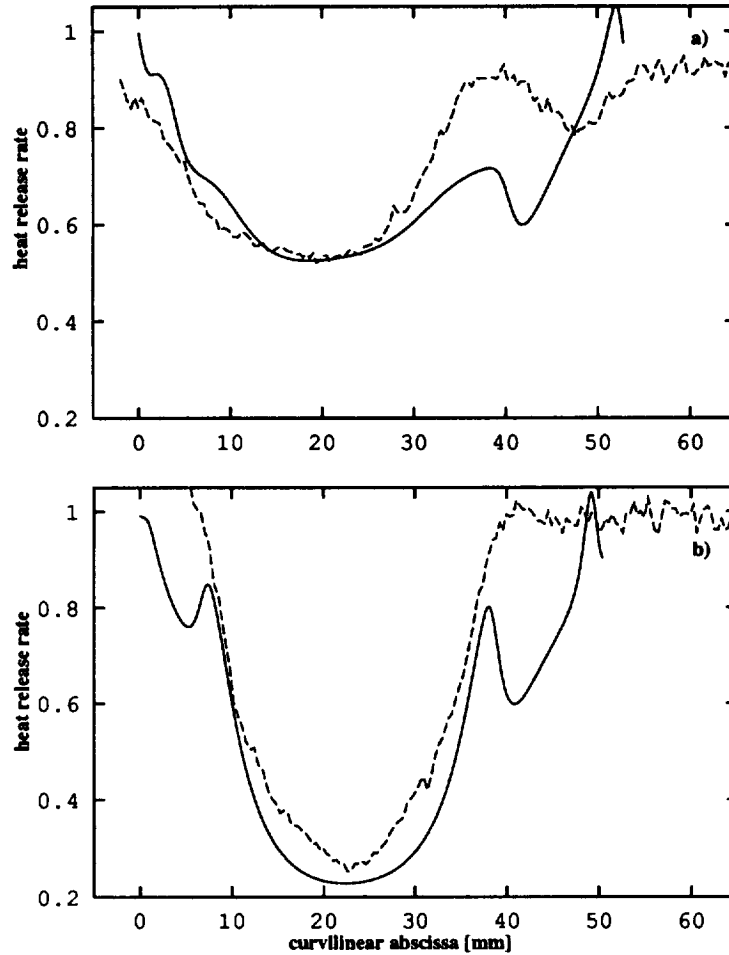


FIGURE 17. Distribution of the heat release rate along the flame front. $Le = 1.8$; a): case 1, b): case 3; — : DNS, ---- : exp.

is predominant (ratio Λ_2/Λ_1 , Lewis number for the intermediate species, activation energy for the first and second step). For instance, to describe the flame quenching at a wall, Hocks *et al.* (1981) have considered a low recombination regime, a high activation energy for the first reaction, and equal diffusivities of heat and mass ($\Lambda_2/\Lambda_1 = 5 \cdot 10^{-4}$, $\beta_1 = 8.5$, $\beta_2 = 0$, $Le_X = 1.0$). This choice has been made arbitrarily by the authors and justified by comparing the concentration of radicals given by the two-step mechanism to the concentration of intermediate species such as OH, H, and O given by complex chemistry calculations of the same configuration. Here, the choice of the set of parameters is based on physical arguments (justified in §2.1.3), which seems to be reasonable if we consider the agreement between the DNS and the experiment for all the cases studied here. The two-step mechanism shows its ability to describe vortex-flame interactions on a large range of Damköhler number (0.3 to 2.9).

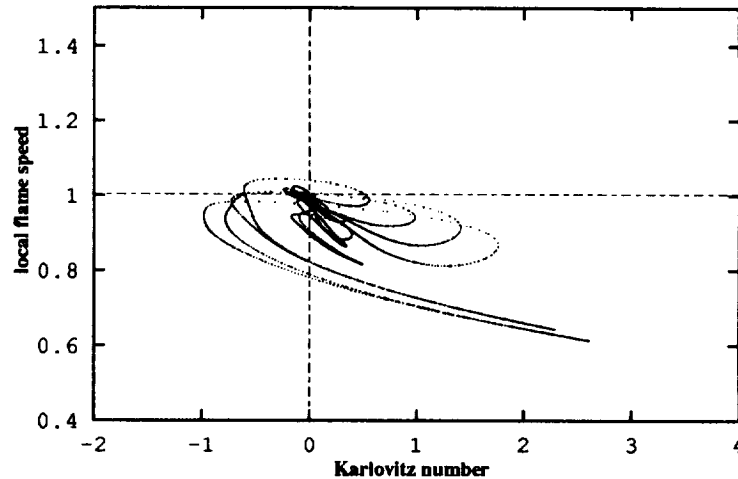


FIGURE 18. Scatter plot of local flame speed versus the Karlovitz number.

Conclusion

Direct numerical simulations of flame vortex interactions are performed using one-step and two-step chemical models.

Simulations performed with the one-step mechanism exhibit a strong disagreement between the DNS and the experiment for all the interactions with $Le = 1.0$. The simulations greatly overestimate the distribution of the heat release rate along the flame front during the interaction. On the contrary, for $Le = 1.8$, the agreement between the simulations and the experimental results is satisfactory for all the interactions corresponding to large range of Damköhler numbers (0.3 to 2.9).

- The analysis of the stretch shows a negligible contribution of the curvature due to the large size of the vortex pair compared to the laminar flame thickness. The tangential strain generated by the vortices is responsible for the stretch felt by the flame.
- Radiative heat losses representative of those encountered in the experiment have no effect on the local flame structure. However, tremendous heat losses (more representative of heat losses by conduction to a cold wall) have a dramatic effect on the heat release and lead to local quenching.
- For the two-step mechanism, the set of parameters is entirely determined by considering the rate coefficients of the chain branching reaction $H + O_2 \rightarrow OH + O$ and the terminating reaction $H + OH + M \rightarrow H_2O + M$, which are the most important chain branching and chain breaking reactions of the $H_2 - O_2$ submechanism occurring in the chemistry of hydrocarbons. All the simulations performed with this model (for both $Le = 1.0$ and $Le = 1.8$) lead to very good agreement with the experimental results. During the interaction between the flame and the vortex pair, the concentration of radicals seems to be the key parameter controlling the local structure and the quenching mechanism.

As a consequence, it appears that the two-step mechanism with the set of parameters chosen here is sufficient to describe all the interactions performed experimentally by Samaniégo *et al.* (1994-b).

Since most of the phenomena encountered in these interactions are also present in turbulent premixed flames, it is tempting to extrapolate these conclusions to a general description of turbulent premixed flames.

Acknowledgements

The author would like to thank Professor C. T. Bowman from the Stanford High Temperature Gasdynamic Laboratory for his helpful suggestions concerning the two-step mechanism and Dr. T. Poinsot from CERFACS (France) for his support and his numerous comments. I would specially thank Dr. G. Ruetsch for his valuable help in the implementation of the two-step mechanism and for his constant support and Dr. J.-M. Samaniégo for his perspicacious suggestions and for the innumerable discussions we had during the course of this study.

REFERENCES

- BAUM, M., POINSOT, T. J. & HAWORTH, D. C. 1992 Numerical Simulations of Turbulent Premixed $H_2/O_2/N_2$ Flames with Complex Chemistry. *Proc. of the 1992 Summer Program*. CTR, NASA Ames/Stanford Univ. 345-366.
- CANDEL, S. M. & POINSOT, T. J. 1990 Flame Stretch and the Balance Equation for the Flame Area. *Combust. Sci. and Tech.* **70**, 1-15.
- CLAVIN, P. 1985 Dynamic Behaviour of Premixed Flame Fronts in Laminar and Turbulent Flows. *Prog. Energy Combust. Sci.* **11**, 1-59.
- CLAVIN, P. & WILLIAMS, F. A. 1982 Effects of Molecular Diffusion and of Thermal expansion on the Structure and Dynamics of Premixed Flames in Turbulent Flows of Large Scales and Low Intensities. *J. Fluid Mech.* **116**, 251-282.
- DRISCOLL, J. F., SUTKUS, D. J., ROBERTS, W. L., POST, M. E. & GOSS, L. P. 1994 The Strain Exerted by a Vortex on a Flame Determined from Velocity Fields Images. *Combust. Sci. and Tech.* **96**, 213-229.
- EGOLFOPOULOS, F. N. 1994 Geometric and Radiation Effects on Steady and Unsteady Strained Laminar Flames. *Twenty-Fifth Symposium (International) on Combustion*.
- EL TAHRY, S. H., RUTLAND, C. J. & FERZIGER, J. H. 1991 Structure and Propagation Speeds of Turbulent Premixed Flames - A Numerical Study. *Combust. and Flame*. **83**, 155-173.
- GLASSMAN, I. 1987 *Combustion*. Academic Press 2nd Ed.
- HAWORTH, D. C & POINSOT, T. J. 1992 Numerical Simulations of Lewis Number Effects in Turbulent Premixed Flames. *244*. **405-436**.
- HOCKS, W., PETERS, N. & ADOMEIT, G. 1981 Flame Quenching in Front of a Cold Wall Under Two-Step Kinetics. *Combust. and Flame*. **41**, 157-170.

- KEE, R. J., RUPLEY, F. M. & MILLER, J. A. 1989 Chemkin-II: A Fortran Chemical Kinetics Package for the Analysis of Gas Phase Chemical Kinetics. *Report SAND89-8009B* Sandia National Laboratories.
- KERSTEIN, A. R., ASHURST, W. T. & WILLIAMS, F. A. 1988 Field Equation for Interface Propagation in an Unsteady Homogeneous Flow Field. *Physical Review. A* **37-7**, 2728-2731.
- LAW, C. K. 1988 Dynamics of Stretched Flames. *Twenty-Second Symposium (International) on Combustion*. 1419-1426.
- LAW, C. K. & EGOLFOPOULOS, F. N. 1992 *Twenty-Fourth Symposium (International) on Combustion*. 137-144.
- LAW, C. K., ZHU, D. L. & YU, G. 1986 Propagation and Extinction of Stretched Premixed FLames. *Twenty-First Symposium (International) on Combustion*. 1419-1426.
- LEE, T. W., LEE, J. G., NYE, D. A. & SANTAVICCA, D. A. 1993 Local Response and Surface Properties of Premixed Flames During Interactions with Karman Vortex Streets. *Combust and Flame*. **94**, 146-160.
- LELE, S. K. 1992 Compact Finite Difference Schemes with Spectral-like Resolution. *J. Comp. Phys.* **103**, 16-42.
- MATALON, M. 1983 On Flame Stretch. *Combust. Sci. and Tech.* **31**, 169-18.1
- MILLER, J. A. & BOWMAN, C. T. 1989 Mechanism and Modelling of Nitrogen Chemistry in Combustion. *Prog. Energy Combust. Sci.* **15**, 287-338.
- MILLER, J. A., MITCHELL, R. E. SMOOKE, M. D. & KEE, R. J. 1982 Toward a Comprehensive Chemical Kinetic Mechanism for the Oxydation of Acetylene: Comparison of Model Predictions with Results from Flame and Shock Tube Experiments. *Nineteenth Symposium (International) on Combustion*. 181-196.
- OSEEN, C. W. 1911 *Arkiv. Mat. Astron. Fys.* **7**, 1.
- PICART, A., BORCHI, R. & CHOLLET, J. P. 1988 Numerical Simulation of Turbulent Reacting Flows. *Comput. and Fluids*. **16-4**, 474-484.
- POINSOT, T., ECHEKKI, T. & MUNGAL, M. G. 1992 A Study of Laminar Flame Tip and Implications for Premixed Turbulent Combustion. *Combust. Sci. and Tech.* **81**, 45-73.
- POINSOT, T. J., HAWORTH, D. C. & BRUNEAUX, G. 1993 Direct Simulations and Modelling of Flame-Wall Interactions for Premixed Turbulent Combustion. *Combust. and Flame*. **95**, 118-132.
- POINSOT, T. J. & LELE, S. K. 1992 Boundary Conditions for Direct Numerical Simulations of Compressible Viscous Flows. *J. Comp. Phys.* **101**, 104-129.
- POINSOT, T. J., VEYNANTE, D. & CANDEL, S. M. 1991 Quenching Processes and Premixed Turbulent Combustion Diagrams. *J. Fluid Mech.* **228**, 581-606.
- PRANDTL, L. & TIETJENS, O. G. 1934 *Fundamentals of Hydro and Aeromechanics*. Dover.

- ROBERTS, W. L., DRISCOLL, J. F., DRAKE, M. C. & GOSS, L. P. 1993 Images of the Quenching of a Flame by a Vortex to Quantify Regimes of Turbulent Combustion. *Combust. and Flame*. **94**, 58-69.
- ROBERTS, W. L., DRISCOLL, J. F., DRAKE, M. C. & RATCLIFFE, J. W. 1992 OH Fluorescence Images of the Quenching of a Premixed Flame during an Interaction with a Vortex. *Twenty-Fourth Symposium (International) on Combustion*. 169-176.
- RUTLAND, C. J. 1989 Effects of Strain, Vorticity and Turbulence on Premixed Flames. *PhD Thesis* Stanford University, Thermosciences Div.
- RUTLAND, C. J. & FERZIGER, J. H. 1991 Simulation of Flame-Vortex Interactions. *Combust and Flame*. **83**, 343-360.
- RUTLAND, C. J., FERZIGER, J. H. & EL TAHRY, S. H. 1990 Full Numerical Simulation and Modelling of Turbulent Premixed Flames. *Twenty-Third Symposium (International) on Combustion*. 621-627.
- SAMANIÉGO, J.-M. 1994 Lewis number and Damköhler number effects in vortex-flame interactions. *CTR Research Briefs - 1994*, NASA Ames/Stanford Univ.
- SAMANIÉGO, J.-M., MANTEL, T. & BOWMAN, C. T. 1994 Fundamental Mechanisms in Premixed Flame Propagation Via Vortex Flame Interactions - Part I: Experiment. Submitted to *J. Fluid Mech*.
- SESHADRY, K. & PETERS, N. 1983 The influence of stretch on a premixed flame with two-step kinetics.
- TSUJI, H. & YAMAOKA, I. 1982 *Nineteenth Symposium (International) on Combustion*. 1533.
- TROUVÉ, A. & POINSOT, T. 1994 The Evolution Equation for the Flame Surface Density in Turbulent Premixed Combustion. *J. Fluid Mech*. **278**, 1-31.
- WESTBROOK, C. K. & DRYER, F. L. 1984 Chemical Kinetic Modeling of Hydrocarbon Combustion. *Prog. Energy Combust. Sci*. **10**, 1-57.
- WILLIAMS, F. A. 1985 *Combustion Theory*. Addison-Wesley 2nd Ed.
- WRAY, A. A. 1990 Minimal Storage Time-Advancement Schemes for Spectral Methods. Private communication.
- YU, C. L., FRENKLACH, M., MASTEN, D. A., HANSON, R. K. & BOWMAN, C. T. 1994 Reexamination of Shock-Tube Measurements of the Rate Coefficient of $\text{H} + \text{O}_2 \rightarrow \text{OH} + \text{O}$. *Journal of Physical Chemistry*. **98**, 4770-4771.
- ZEL'DOVICH, Y. B. 1948 Theory of Flame Propagation. *Zhur. Fizi. Khi. (USSR)*. **22**, 27-49.

Triple flames and flame stabilization

By J. E. Broadwell

1. Motivation and objectives

It is now well established that when turbulent jet flames are lifted, combustion begins, i.e., the flame is stabilized, at an axial station where the fuel and air are partially pre-mixed. One might expect, therefore, that the beginning of the combustion zone would be a triple flame. Such flames are described by G. R. Ruetsch, 1994. However, the recent experiments of Schefer *et al.* 1994a,b, together with the earlier work of Seitzman *et al.* 1990, provide data that are, so far, difficult to reconcile with the presence of triple flames. In particular, laser images of CH and OH, marking combustion zones, do not exhibit shapes typical of triple flames, and, more significantly, the lifted flame appears to have a propagation speed that is an order of magnitude higher than the laminar flame speed. The speed of triple flames studied thus far exceeds the laminar value by a factor less than two. The objective of the present task is the resolution of this apparent conflict between the experiments and the triple flame characteristics, and the clarification of the mechanisms controlling flame stability.

2. Accomplishments

So far, several possible explanations of the difficulty have been identified and are being investigated. These include:

- (1) The resolution achieved in the experiments: is it sufficient to exhibit the structure of a triple flame?
- (2) Is the flow field in the neighborhood of the stabilization point sufficiently close to that for which triple flames are known to exist?
- (3) Can triple flames be generated that have higher propagation speeds?
- (4) Does the unsteadiness of the laboratory flames introduce an essential new element into the problem?
- (5) Are flame ignition limits essential in the calculation of triple flames that more closely resemble lifted flames?

Investigation of these points is underway.

3. Future work

The work on this project is in collaboration with G. R. Ruetsch, who is investigating structure of triple flames by direct numerical solution of the appropriate equations. Dr. Robert Schefer of the Combustion Research Facility, Sandia National Laboratories, Livermore, has generously agreed to provide more detailed data concerning his lifted flames and to discuss his plans for further experiments in this area.

Analysis of the results from these two projects should lead to a conclusion concerning the relevance of triple flames to the subject of flame stabilization.

REFERENCES

- RUETSCH, G. R. 1994 Flame propagation under partially-premixed conditions. *Annual Research Briefs - 1994*. CTR, NASA Ames/Stanford Univ.
- SCHEFER, R. W., NAMAZIAN, M. & KELLY, J. 1994a Stabilization of lifted turbulent-jet diffusion flames. *Combust. & Flame*, to appear.
- SCHEFER, R. W., NAMAZIAN, M., FILTOPOULOS, E. E. J. & KELLY, J. 1994b Temporal evolution of turbulence/chemistry interactions in lifted, turbulent-jet flames. *Twenty-Fifth Symposium (International) on Combustion* (to appear). The Combustion Institute.
- SEITZMAN, J. M., UNGUT, A., PAUL, P. H. & HANSON, R. K. 1990 Imaging and characterization of OH structures in a turbulent nonpremixed flame. *Twenty-Third Symposium (International) on Combustion*. The Combustion Institute, 637-644.

Flame propagation under partially-premixed conditions

By G. R. Ruetsch

1. Motivation and objectives

In combustion, flames are generally categorized according to the distribution of reactants in the flow. For homogeneous mixtures of fuel and oxidizer, flames are designated as premixed, and when the fuel and oxidizer are initially separated, non-premixed or diffusion flames arise. There are many instances when flames clearly fall in one of these two categories, such as premixed flames in internal combustion engines and diffusion flames during later stages of combustion in diesel engines.

There are, however, many practical situations where flames cannot be considered as purely premixed or non-premixed. One important phenomenon that occurs in such partially-premixed conditions concerns how diffusion flames are stabilized in mixing layers. Through the imbalance between chemical source and diffusion, premixed flames can propagate into unburned regions, whereas diffusion flames by themselves have no such propagation mechanism. Therefore, some degree of pre-mixing is necessary for diffusion flame stabilization. Liñán 1994 shows that there are two possibilities for stabilization of diffusion flames in laminar mixing layers. The flame can either be stabilized near the splitter plate or stabilized farther downstream, as a lifted flame. In the former case the flame is anchored in the wake of the splitter plate, and the velocity deficit of the wake and heat conduction to the plate play important roles in stabilization and must be taken into account. These anchored flames have been examined by Veynante *et al.* 1994. In the case of the lifted flame these mechanisms are absent, and laminar flame stabilization is achieved through "triple flames," i.e. a flame composed of two premixed flames, one fuel rich and the other lean, and a trailing diffusion flame. The two premixed wings provide the ability to propagate, and the diffusion wing provides an anchor for the trailing diffusion flame.

In addition to regions where diffusion flame stabilization takes place, partially-premixed conditions also exist during the ignition process in nonpremixed systems. Numerical simulations by Réveillon *et al.* 1994 of the ignition process in a weakly stirred mixture of fuel and oxidizer show that triple flames propagate along lines of stoichiometric mixture fraction throughout the fluid. In addition, Peters 1994 notes that NO_x emissions are likely to be large in such transient cases, and therefore an understanding of triple flames can provide beneficial information concerning pollutant formation.

One of the first observations of triple flames was made by Phillips 1965, where he investigated a triple flame propagating in a methane mixing layer. More recently, Kioni *et al.* 1993 have analyzed triple flames both experimentally and numerically. In their numerical approach, they first develop a model for triple flames in a counterflow geometry under the assumption of zero heat release and then solve these

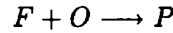
equations numerically to analyze the structure and propagation of these flames. There have also been numerous analytical studies of triple flames under various assumptions by Dold 1989, Dold *et al.* 1991, and Hartley and Dold 1991.

This study concentrates on developing a better understanding of triple flames. More precisely, we relax the assumption of zero heat release which has been used in many of the previously mentioned analytical studies. The effects of heat release in turbulent mixing layers have been previously studied by McMurtry *et al.* 1989, where the influence of heat release on the large-scale structures, entrainment, and other properties of shear layers has been analyzed. However, such simulations are temporal and do not address the issues of stabilization and flame propagation. In order to investigate the role heat release plays in flame propagation in partially-premixed combustion, we return to a simple flow field and investigate the behavior of flames in a laminar environment.

1.1 Numerical simulation and flow configuration

We use direct numerical simulations to solve the fully-compressible Navier-Stokes equations in this investigation. The simulation used is a two-dimensional version of the code previously developed by Trounev 1991. This code uses the high-order compact finite difference scheme of Lele 1992 for spatial differentiation, the third order Runge-Kutta scheme of Wray for time advancement, and the Navier-Stokes characteristic boundary conditions method of Poinso and Lele 1992. Below we summarize some of the important features and assumptions of the code relevant to this work; for further details on the numerical method readers are referred to Lele 1992 and Poinso and Lele 1992.

The chemical scheme we consider is represented by a one-step global reaction between a fuel and oxidizer:



where we have assumed unity stoichiometric coefficients for simplicity. The reaction rate behaves according to the Arrhenius form:

$$\dot{\omega} = K \rho Y_F \rho Y_O \exp\left(-\frac{T_{ac}}{T}\right)$$

where ρ is the density, T_{ac} is the activation temperature, K is the pre-exponential factor, and Y_F and Y_O are the fuel and oxidizer mass fractions. Following Williams 1986, we can write this reaction rate as

$$\dot{\omega} = \Lambda \rho Y_F \rho Y_O \exp\left(-\frac{\beta(1-\theta)}{1-\alpha(1-\theta)}\right)$$

where the reduced pre-exponential factor(Λ), heat release parameter(α), Zel'dovich number(β), and reduced temperature(θ) are defined by:

$$\Lambda = K \exp(-\beta/\alpha); \quad \alpha = \frac{T_f - T_0}{T_f}; \quad \beta = \frac{\alpha T_{ac}}{T_f}; \quad \theta = \frac{T - T_0}{T_f - T_0}$$

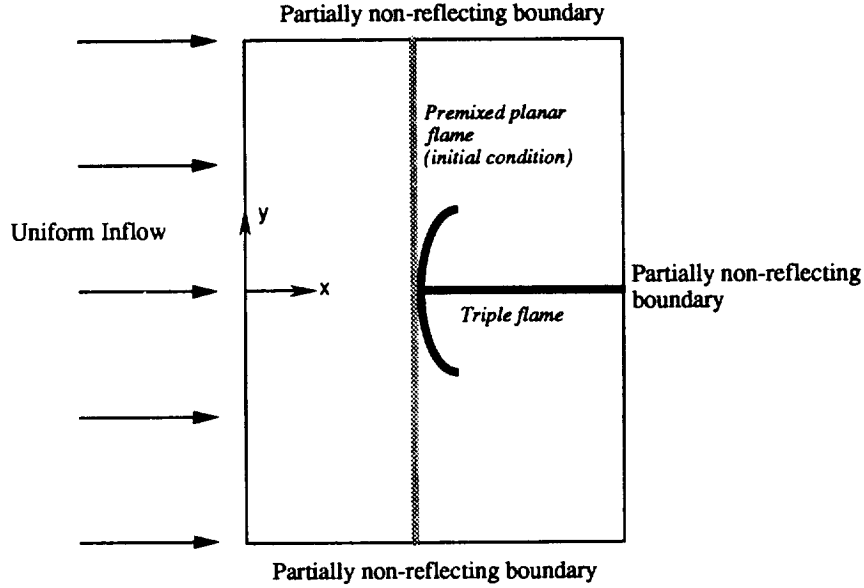


FIGURE 1. Computational domain used in the simulations.

with T_f being the adiabatic flame temperature and T_0 taken in the ambient flow. In this study we hold the Zel'dovich number constant at $\beta = 8$ and use heat release parameters of $\alpha = 0.5, 2/3, 0.75,$ and 0.8 .

The transport coefficients in the simulations are temperature dependent. This temperature dependence is expressed through the molecular viscosity, μ , given by:

$$\mu = \mu_0 \left(\frac{T}{T_0} \right)^a$$

with $a = 0.76$. The temperature dependence of the thermal conductivity, λ , and the mass diffusivities, \mathcal{D}_k , is obtained by requiring the Lewis and Prandtl numbers to be constant:

$$Le_k = \frac{\lambda}{\rho \mathcal{D}_k c_p}; \quad Pr = \frac{\mu c_p}{\lambda},$$

where $k = F, O$ refers to either the fuel or oxidizer species. We assume unity Lewis numbers throughout this study.

We solve the compressible Navier-Stokes equations in a two-dimensional domain depicted in Fig. 1. At the boundaries we use an inflow boundary condition on the left and nearly-perfect reflective boundary conditions, required to avoid pressure drift, at the outflow and sides. Although the inflow conditions are prescribed, values can

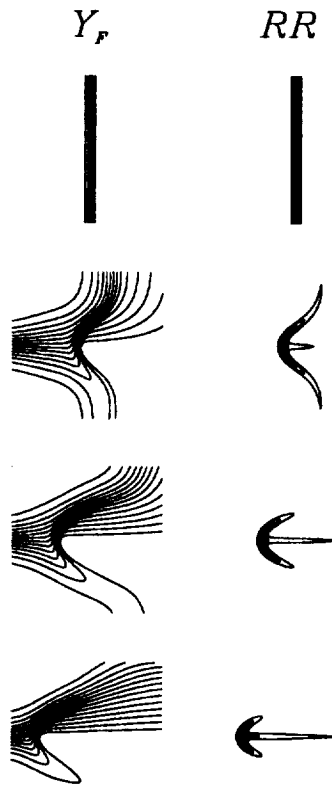


FIGURE 2. Response of a planar premixed flame to a mixture fraction gradient. The first row in the time sequence shows the premixed flame in a steady-state situation. As the mixture fraction gradient reaches the flame, the structure and velocity of the flame change.

be changed during the simulation. Within this domain we initialize the flow with a planar premixed flame where the mixture fraction, defined as

$$Z = \frac{1 + Y_F - Y_O}{2},$$

is everywhere equal to its stoichiometric value, $Z_s = 0.5$. The incoming flow is uniform and set equal to the premixed laminar flame speed, S_L^0 . Also associated with the flame is the premixed flame thickness, δ_L^0 .

After the flow and flame are initialized, the mixture fraction is varied at the inlet from its uniform stoichiometric value to a tanh profile varying from zero to one. We characterize the thickness of this mixing layer by the slope of the profile at

stoichiometric conditions and the overall change in mixture fraction, which gives:

$$\delta_M(x) = \Delta Z \left(\frac{\partial Z}{\partial y} \Big|_{y=0} \right)^{-1} = \left(\frac{\partial Z}{\partial y} \Big|_{y=0} \right)^{-1}$$

It is important to realize that this measure does not remain constant along the stoichiometric line and is a function of x . We can form a Damköhler number using the mixing thickness and the planar flame thickness. Since the characteristic velocity for both chemical and physical processes is the same, we can simply define the Damköhler number as:

$$D = \frac{\tau_p}{\tau_c} = \frac{\delta_M}{\delta_L^0},$$

which can be thought of as a dimensionless mixing thickness. The mixing thickness used in this expression is evaluated at the location of the maximum reaction rate.

An example of a flame's response to a variable mixture fraction is shown in Fig. 2. With the uniform flow approaching from the left, as the mixture fraction gradient reaches the flame surface only the centerline is exposed to the stoichiometric mixture fraction and locally maintains the planar flame speed and reaction rate. Above this point the mixture is fuel rich, and below fuel lean. As a result, these regions of non-unity equivalence ratio burn less, the reaction rate drops, and the local flame speed is reduced. The excess fuel and oxidizer then combine behind the premixed flame along the stoichiometric surface and burn in a trailing diffusion flame. Thus the "triple" flame refers to the fuel-rich premixed flame, the fuel-lean premixed flame, and the trailing diffusion flame.

In addition to the change in structure that occurs when the planar premixed flame is subjected to a mixture fraction gradient, the propagation velocity of the flame increases as observed in Fig. 2. In order to study the triple flame in further detail, a method of stabilizing the flame in the computational domain is needed. We accomplish this by calculating the relative progression velocity of iso-scalar surfaces. This method results from equating the transport equation for a scalar variable Y :

$$\rho \frac{DY}{Dt} = \frac{\partial}{\partial x_i} \left(\rho \mathcal{D} \frac{\partial Y}{\partial x_i} \right) + \dot{w}_Y$$

with the Hamilton-Jacobi equation for the scalar field (Kerstein *et al.* 1989):

$$\rho \frac{DY}{Dt} = \rho V |\nabla Y|.$$

Solving for the relative progression velocity of the iso-concentration surface, V , we obtain:

$$V = \frac{1}{\rho |\nabla Y|} \frac{\partial}{\partial x_i} \left(\rho \mathcal{D} \frac{\partial Y}{\partial x_i} \right) + \frac{1}{\rho |\nabla Y|} \dot{w}_Y$$

This relation is evaluated on the centerline in the preheat zone and subtracted from the local fluid velocity, giving the correction to be applied at the inlet. If one were

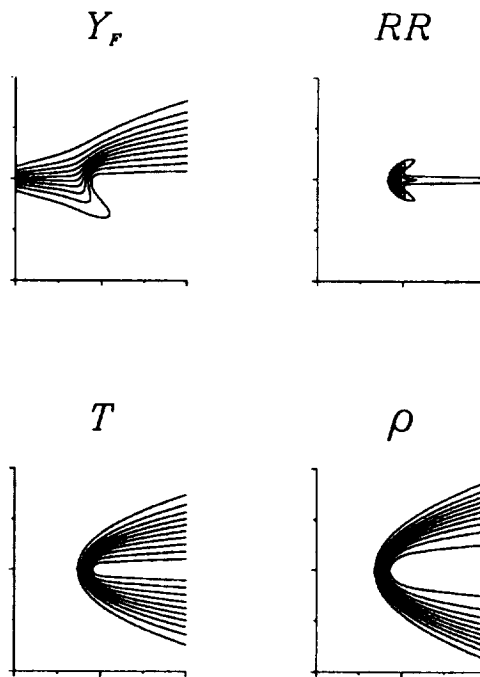


FIGURE 3. Contours of mass fraction, reaction rate, temperature, and density for a stabilized triple flame.

to apply this correction at the inlet alone, then changes to the flame would only occur after the convective time required to reach the flame, which is both time consuming and can also introduce stability problems. A more efficient method is to apply the correction to all points in the flow as a Galilean transformation, such that the steady-state situation is quickly reached.

Some care must be taken in choosing the size of the computational domain. Because the triple flame redirects the flow laterally, the top and bottom boundaries must be moved far enough from the stoichiometric conditions so that the viscous boundary conditions do not affect the flame speed. To avoid this problem, an unevenly spaced grid is used in the lateral direction where points are clustered about the stoichiometric line so that the lateral boundaries can be moved far away from the flame. In addition, all results presented here were run on different sized domains to check that the size of the computational domain does not play a role in the flame speed.

2. Accomplishments

To begin the investigation of heat release effects on triple flames, we first describe some general characteristics of triple flames. We have briefly described the structure of triple flames in the time sequence of Fig. 2, where the flame propagates relative to the inflow. Fig. 3 shows similar contours, in addition to the temperature and density fields, for a triple flame stabilized in the computational domain. The effects of heat release are clearly seen in the temperature and density plots, where the temperature rises and density decreases behind the premixed wings of the flame, along with the effects of the nonuniform mixture fraction gradient, where the temperature and density fields display lateral variations.

Lateral diffusion of temperature and species plays an important role in triple flames. Behind the premixed wings of the flame, heat is conducted away from the stoichiometric line. This conduction is important because, unlike one-dimensional flames with an infinite heat reservoir in the burned regions, heat from the triple flame is convected to regions which do not contribute to flame propagation. Thus, quenching is more likely to occur if enough heat is conducted laterally away from the flame. Lateral diffusion of species is also important and is responsible for the diffusion wing of the flame.

Another way to determine the role of lateral diffusion is to compare one-dimensional profiles of different quantities along the stoichiometric line of the triple flame with those of the one-dimensional flame used to initialize the simulations. These plots are presented in Fig. 4 where the quantities are scaled by their minimum and maximum values of the one-dimensional flame. The behavior of all quantities is similar up to, and somewhat behind, the maximum reaction rate. Behind the premixed reaction zone, we observe that only the density profile is roughly equal in both cases. We observe a drop in temperature and an increase in fuel (and also oxidizer) mass fraction relative to the one-dimensional case. The change in reaction rate is dominated by the increased mass fractions of the reactants, and consequently an increase in the reaction rate is observed behind the flame. This reaction rate corresponds to the burning in the trailing diffusion flame and is a sizable percentage of the maximum reaction rate. These differences between the one-dimensional profiles and profiles through the stoichiometric line in the triple flame become larger as we increase the mixture fraction gradient.

Up to this point we have not included the velocity in our analysis. We have postponed this until the next section since the velocity field in the triple flame is quite different than in the planar flame and requires a detailed investigation.

2.1 *Effects of heat release on flame propagation*

We now turn our attention to studying the effect of heat release on the triple flame and, in particular, how this affects the propagation velocity. The analytical work of Dold 1989 and Hartley and Dold 1991 provide estimates of the triple-flame speed for weak ($\beta\partial Z/\partial y \rightarrow 0$) and moderate ($\beta\partial Z/\partial y \sim O(1)$) values of the mixture fraction gradient under the assumption of zero heat release. They find that the flame speed is greatest for zero mixture fraction gradient, corresponding to a planar flame, and then decreases as the mixture fraction gradient increases. This is in

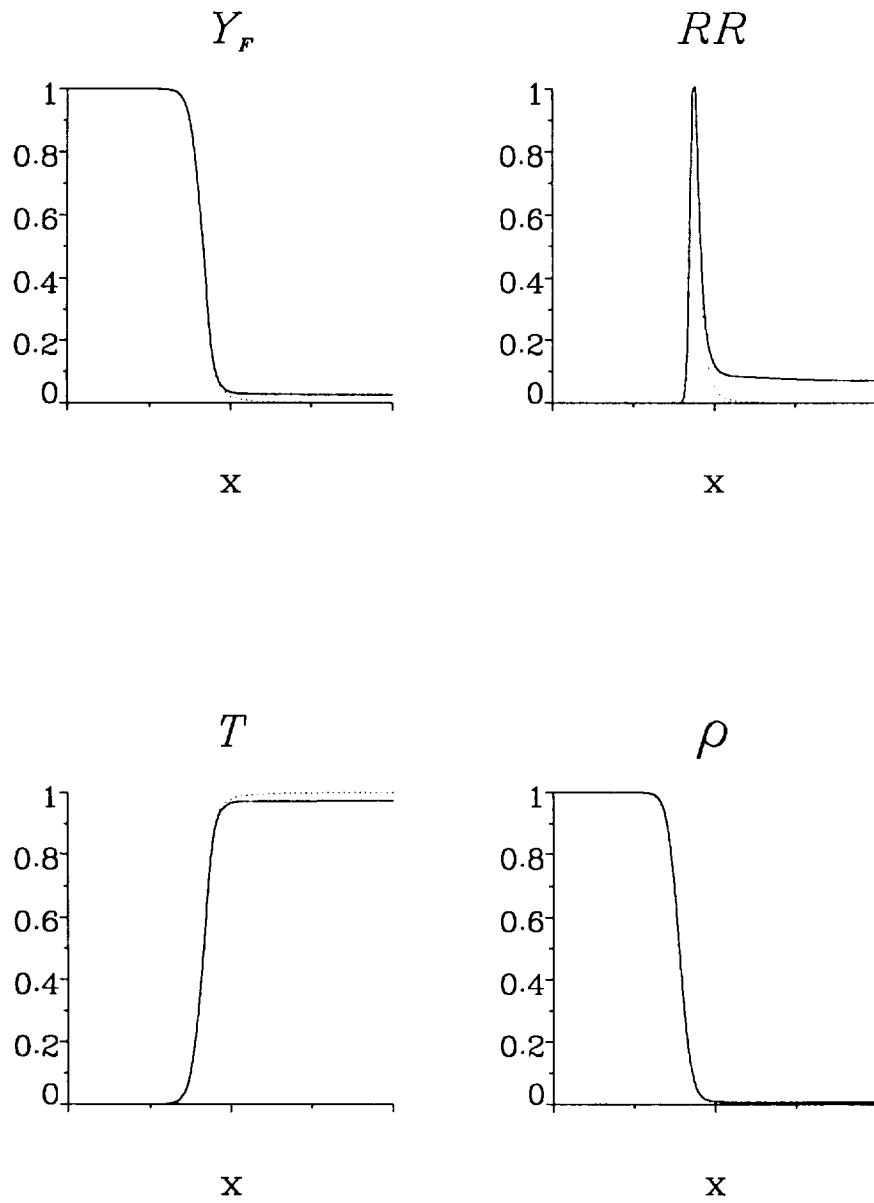


FIGURE 4. Profiles of various quantities in a one-dimensional flame (----) and along the centerline of the triple flame (—). Lateral heat conduction reduces the temperature of the triple flame, and diffusion of fuel and oxidizer increase the reaction rate behind the premixed flame.

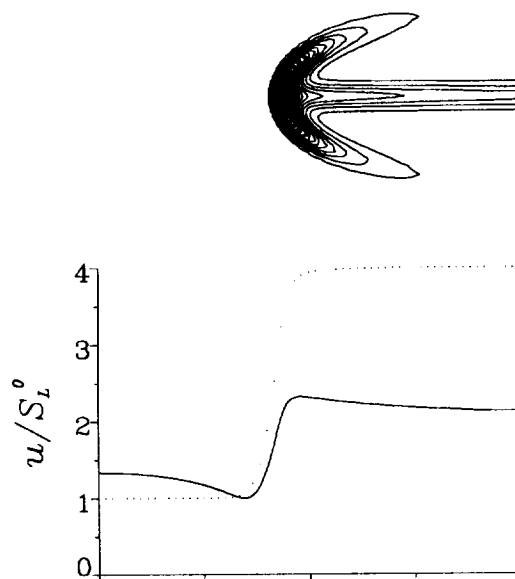


FIGURE 5. Contour lines of the reaction rate along with the horizontal velocity component along the stoichiometric or symmetry line for a stabilized triple flame (—) and planar premixed flame (----). For the triple flame the velocity reaches a minimum just in front of the flame which is close to the planar flame velocity. Upstream of the flame, however, the velocity is larger.

contrast to the change in flame speed we observe from the time sequence in Fig. 2. The discrepancy lies in the assumptions concerning heat release. To investigate this further, we examine the velocity field along the centerline of the triple flame in Fig. 5. Here we observe that, in addition to the rise in velocity through the flame, the horizontal velocity component reaches a minimum before the flame. The velocity at this minimum is close to the planar laminar flame speed, and far upstream the velocity is larger. Therefore it is necessary to distinguish these two velocities. The local flame speed is important in terms of chemical reaction, whereas the upstream or far-field flame speed is identified with the propagation of the entire structure, U_F .

The mechanism responsible for this velocity difference can be seen in the sketch of Fig. 6. Here we examine the velocity vectors before and after they pass through the flame surface. In cases with heat release, the component of the velocity perpendicular to the flame increases across the surface, whereas the tangential component remains unchanged. The jump in the perpendicular velocity component results in a bending of the velocity vector towards the centerline. This redirection of the flow is accommodated by the divergence of the streamlines ahead of the flame, resulting in

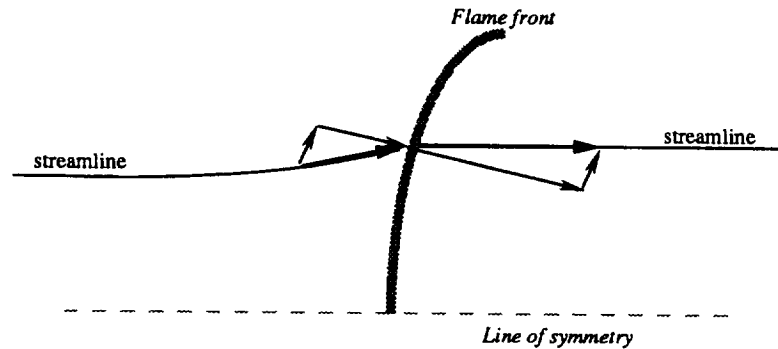


FIGURE 6. Mechanism responsible for increased flame speeds. Due to heat release the normal velocity across the flame is increased, whereas the tangential component remains unchanged. This redirection of flow towards the centerline causes the streamlines to diverge in front of the flame, resulting in a decrease in the flow velocity in front of the flame.

the decrease of the velocity observed in Fig. 5. Since the local flame speed along the stoichiometric line is near S_L^0 , the flame can be stabilized only if the flow speed at this point remains at this value, which requires an increase in the upstream velocity. Note that in absence of heat release, there is no flow redirection across the flame, and therefore the far-field and local flame speeds are equal.

2.2 Effect of mixture fraction gradients

In their previous analytical work, Dold 1989 and Hartley and Dold 1991 observed a large effect of the mixture fraction gradient on the triple-flame propagation. Due to the effects of flame curvature, they observed a decrease in the flame speed as the mixture fraction gradient increases or equivalently the mixing thickness decreases. Thus for zero heat release cases the planar premixed flame represents an upper limit for the flame speed.

For cases with heat release, locally these same arguments still apply, however the far-field flame speed is much more affected by heat release than by flame curvature. This is depicted in Fig. 7, where the far-field flame speed, U_F/S_L^0 , and the local flame speeds are plotted versus the nondimensional mixing thickness or Damköhler number. Here we see that, in agreement with the zero heat release analysis, the local flame speeds remain of the order of S_L^0 , decreasing slightly below this value for small values of the mixing thickness. Also plotted in this figure is the difference between the local and far-field velocities. This difference eliminates the change in local conditions, and is therefore a true measure of the effect of heat release. As one can see from Fig. 7, this difference increases as the mixing thickness becomes

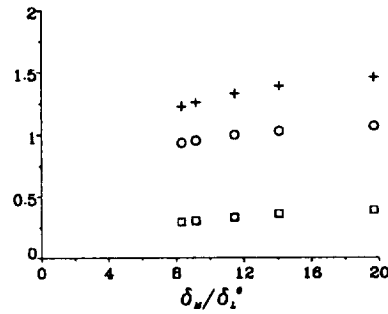


FIGURE 7. Far-field flame speed(+), local flame speed(o), and their differences(□) as a function of the local mixing thickness. All flame speeds are normalized by S_L^0 , and for all cases $\alpha = 0.75$.

larger.

The reason for the increased effect of heat release as the mixing thickness becomes larger can be explained by Fig. 8. In Fig. 8 we plot the streamfunction through two flames with different mixing thicknesses. Since the maximum reaction rate is at the same streamwise location, we can superpose the two streamline patterns to determine how the flow redirection differs in these two cases. At streamwise locations near the maximum reaction rate and close to the stoichiometric line the two cases are similar. As we progress farther downstream, the case with the smaller mixing thickness spreads more laterally due to the greater burning in the diffusion flame. As we move laterally to regions further from stoichiometric conditions, the deflections of the streamlines away from the stoichiometric line become greater for the larger mixing thickness case. Recall that the mechanism for increased far-field flame speed relies on the acceleration of the normal velocity component through the flame. The local velocity jump across the flame is strongly related to the local reaction rate, which is in turn affected by the local mixture fraction. Thus, the distribution of the reaction rate along the premixed wings becomes an important characteristic and is the reason for the different streamline pattern farther from stoichiometric conditions. For small mixing thicknesses, the reaction rate drops off quickly as one moves away from stoichiometric conditions. For larger mixing thicknesses the reaction rate remains stronger as one moves along the premixed wings, and thus the redirection in the flow is more pronounced.

2.2.1 Small mixing thicknesses and resistance to quenching

For small values of the mixing thickness one might expect quenching to occur. Quenching would result from the lateral conduction of heat away from the flame. In previous analytical work (*cf.* Hartley and Dold 1991), however, quenching was not observed. Under the assumption of zero heat release, quenching was present

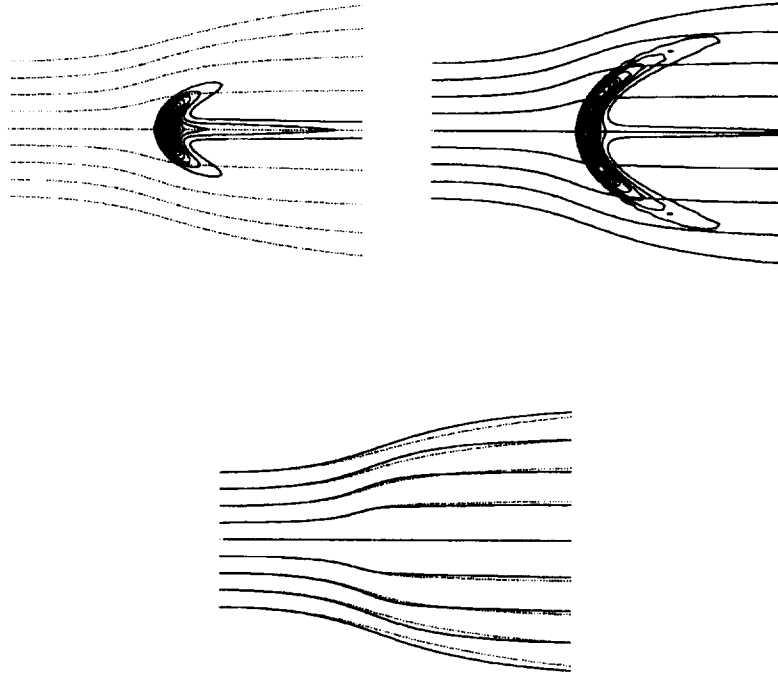


FIGURE 8. Streamlines for flames with small (left, - - - -) and large (right, ———) mixing thicknesses. The streamlines are superposed beneath.

only when the flame was subjected to an external strain field (Dold *et al.* 1991). Kioni *et al.* 1993 have simulated triple flames under external strain and have found negative propagation velocities, or an extinction front, to occur when the mixing thickness is small enough, once again under the assumption of zero heat release. In our present study, therefore, we do not expect quenching to occur since no *external* strain is present. Furthermore, in cases with heat release the resistance to quenching is enhanced. This added resistance to quenching occurs as the flame-generated straining motion which creates the reduction in the horizontal velocity also decreases the effective mixture fraction gradient in front of the flame and, therefore, limits how small the effective Damköhler number can become in Fig. 7. This reduction in the local mixture fraction gradient is observed in Fig. 9. Here the mixture fraction gradient along vertical slices is taken at the inlet and on a slice through the maximum reaction rate. The mixture fraction gradient is everywhere reduced by diffusion, but near stoichiometric conditions the effect of the heat release-induced strain on the mixture fraction gradient is dominant.

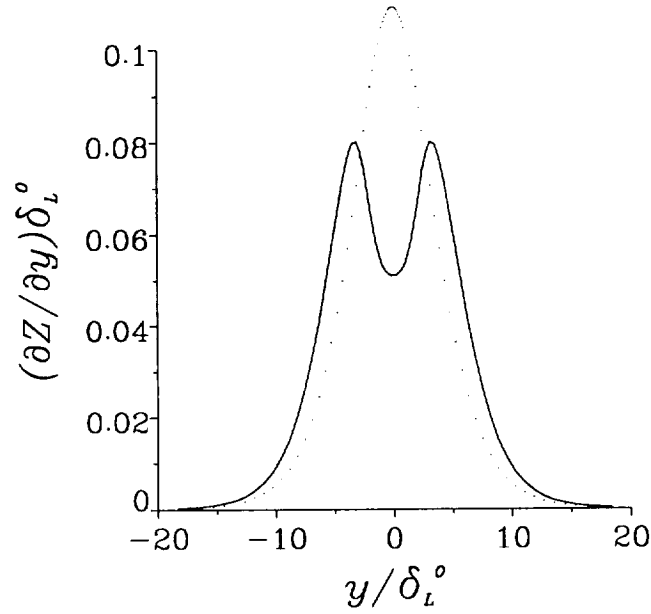


FIGURE 9. Vertical mixture fraction gradient profile at the inlet (.....) and on the vertical line passing through the maximum reaction rate (—).

2.2.2 Large mixing thicknesses and scaling laws

We have seen that for the range of mixing thicknesses considered in this study, as we increase the mixing thickness the propagation speed increases. We expect that for very large mixing thicknesses, where $\delta_M/\delta_L^0 \gg 1$, the flame speed reaches some asymptotic value.

We can derive an estimate of the flame speed by considering conservation relations applied to several locations along the stoichiometric line, shown in Fig. 10. These locations are: (1) far upstream, (2) immediately preceding the flame, (3) immediately following the flame, and (4) far downstream. For large mixing thicknesses, the flow in the immediate vicinity of the flame is nearly one-dimensional. Thus between stations (2) and (3) we can apply the Rankine-Hugoniot relations:

$$\rho_2 u_2 = \rho_3 u_3 \quad (1)$$

$$P_2 + \rho_2 u_2^2 = P_3 + \rho_3 u_3^2 \quad (2)$$

On either side of the flame the density can be taken as constant,

$$\rho_1 = \rho_2; \quad \rho_3 = \rho_4$$

so along the stoichiometric streamline we have

$$P_1 + \frac{1}{2}\rho_1 u_1^2 = P_2 + \frac{1}{2}\rho_2 u_2^2 \quad (3)$$

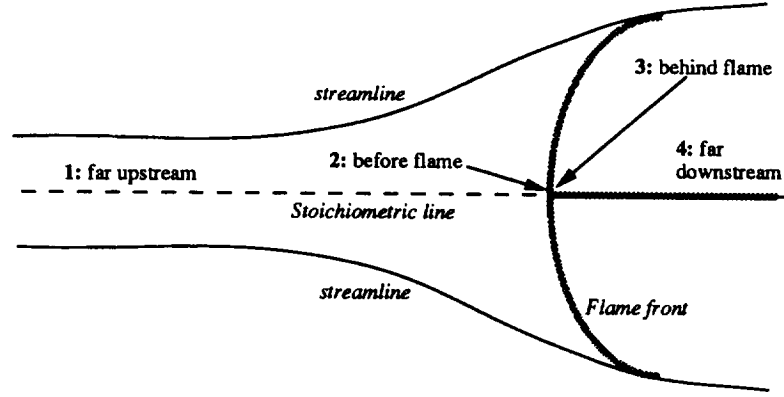


FIGURE 10. Triple flame for large mixing thicknesses. Propagation speed can be determined using conservation relations along the stoichiometric (dashed) line at stations 1-4, and also in the streamtube traced by the thin solid lines.

$$P_3 + \frac{1}{2}\rho_3 u_3^2 = P_4 + \frac{1}{2}\rho_4 u_4^2 \quad (4)$$

We identify the flow velocity in front of the triple-flame along the stoichiometric surface as the planar premixed flame speed:

$$u_2 = S_L^0$$

thus we are interested in determining u_1/u_2 . In addition to the above relations we need to apply integral conservation laws. We choose a control volume which connects the upstream and downstream locations by streamlines which "touch" the edges of the premixed flames. If we denote the thickness of the control volume at any location by δ , then for mass conservation we have:

$$\rho_1 u_1 \delta_1 \sim \rho_4 u_4 \delta_4 \quad (5)$$

where as a first approximation we have assumed u_4 is constant behind the flame far downstream.

Combining these conservation relations and solving for u_1/u_2 we have:

$$\left(\frac{u_1}{u_2}\right)^2 = \frac{\left(\frac{\rho_1}{\rho_4} - 1\right)}{\frac{P_1 - P_4}{\frac{1}{2}\rho_1 u_1^2} + 1 - \frac{\rho_1}{\rho_4} \left(\frac{\delta_1}{\delta_4}\right)^2} \quad (6)$$

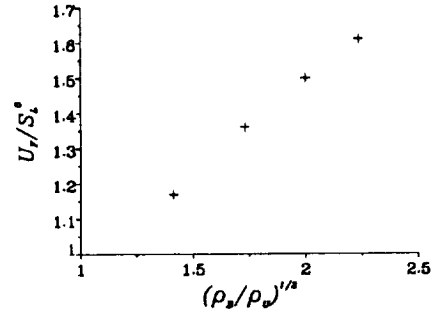


FIGURE 11. Flames speed ratio versus density ratio in simulation.

Equation 6 thus provides us with the propagation speed relative to the planar flame speed as a function of the density, pressures, and thicknesses at stations (1) and (4). However, we would like to have this expression in terms of the densities alone. So, we need an integral form for momentum conservation over the control volume. If we denote the average pressure along the control volume streamlines as P_s , then the global momentum relation is:

$$P_1 \delta_1 + \rho_1 u_1^2 \delta_1 + P_s (\delta_4 - \delta_1) = P_4 \delta_4 + \rho_4 u_4^2 \delta_4 \quad (7)$$

If we further make assumption that $P_1 = P_4 = P_s$, then Eq. 7 gives:

$$\rho_1 u_1^2 \delta_1 = \rho_4 u_4^2 \delta_4$$

which after using the overall mass conservation equation, we obtain:

$$u_1 = u_4; \quad \frac{\delta_1}{\delta_4} = \frac{\rho_4}{\rho_1}$$

Substituting this into Eq. 6 along with the equal pressure assumption gives:

$$\frac{U_F}{S_L^0} = \frac{u_1}{u_2} \sim \left(\frac{\rho_1}{\rho_4} \right)^{1/2} \quad (8)$$

Numerically we cannot simulate flames with the length-scale ratios required in the above formulation; however, we do observe the scaling behavior in Eq. 8 for our simulations with large mixing thicknesses, shown in Fig. 11.

3. Future work

In this study we have investigated one possible flame structure that can occur in partially-premixed conditions. We have established the role that heat release plays

on this flame and its propagation assuming rather benign conditions for the flow and chemistry. Just as we have relaxed the assumption of zero heat release used in previous studies, in the future we must also relax the assumptions presently made concerning the flow field and chemical reaction mechanism.

The assumption of uniform parallel flow has enabled us to determine how the flow is modified by heat release, but is too simple a model to describe the behavior of flames in turbulent combustion. As a first step towards understanding flame stabilization in turbulent combustion, the response of triple flames to vortices was examined in Veynante *et al.* 1994, where triple flames were found to be more robust than nonpremixed flames under similar circumstances. However, even before we consider turbulent or vortical flows, there are several questions one can ask about flame behavior in simpler flows.

In many practical applications reactants are mixed in jet flows, where the fuel and oxidizer streams have different velocities. In such cases the lateral position of the flame, i.e. whether it lies in the fuel or oxidizer stream, can greatly affect stabilization. There are several parameters that can change the flame position. Stoichiometry clearly has a large affect on flame positioning. The effects of stoichiometry on triple-flame structure has been investigated for zero heat release flames by Dold 1989, but how this is coupled with heat release has yet to be determined. Non-unity Lewis numbers can also modify flame positioning. A method for simulating non-unity Lewis numbers in diffusion flames has been developed by Liñán *et al.* 1994, where the position of the diffusion flame in a shear layer was found to play a large role in the overall dynamics. Non-unity Lewis numbers modify more than the flame position, however. Buckmaster and Matalon 1988 showed for zero heat-release flames that the triple-flame structure can be altered dramatically where one of the premixed wings can point into the oncoming flow. Lewis number effects can also modify the flame propagation, and this is expected to have a very pronounced effect due to the large curvature inherent to the triple-flame structure.

Aside from including more complicated flow, stoichiometry, and Lewis number effects in studies of partially-premixed combustion, there are other modifications that can be implemented. We have shown in this study that the distribution of the reaction rate along the premixed wings of triple flames greatly affects the flame propagation. Because of this, flammability limits included in the chemical mechanism can be introduced. Extending the chemical model to include multiple steps is also desirable in certain cases. This is especially true if one is interested in NO_x formation during ignition. Because NO_x formation occurs during non-equilibrium combustion, multi-step chemistry is necessary for investigating pollutant formation.

Acknowledgments

The author would like to thank T. Mantel, J.-M. Samaniego, and L. Vervisch for their helpful suggestions throughout this study. A. Liñán, T. Poinso, and D. Veynante also provided helpful information and discussions during the CTR summer program.

REFERENCES

- BUCKMASTER, J. & MATALON, M. 1988 Anomalous Lewis number effects in tribrachial flames. *Twenty-second Symposium (International) on Combustion*, The Combustion Institute, p. 1527.
- DOLD, J. W. 1989 Flame propagation in a nonuniform mixture: analysis of a slowly varying triple flame. *Combust. & Flame*. **76**, 71.
- DOLD, J. W., HARTLEY, L. J. & GREEN, D. 1991 Dynamics of laminar triple-flamelet structures in non-premixed turbulent combustion. *Dynamical Issues in Combustion Theory*. Springer-Verlag, 83.
- HARTLEY, L. J. & DOLD, W. 1991 Flame propagation in a nonuniform mixture: analysis of a propagating triple-flame. *Comb. Sci. & Tech.* **80**, 23.
- KERSTEIN, A. K., ASHURST, WM. T., & WILLIAMS, F. A. 1988 Field equation for interface propagation in an unsteady homogeneous flow field. *Phys. Rev. A*. **37**, 2728.
- KIONI, P. N., ROGG, B., BRAY, K. N. C. & LIÑÁN, A. 1993 Flame spread in laminar mixing layers: the triple flame. *Combust. & Flame*. **95**, 276.
- LELE, S. 1992 Compact finite difference schemes with spectral-like resolution. *J. Comp. Phys.* **103**, 16.
- LIÑÁN, A. 1994 Ignition and flame spread in laminar mixing layers. *Combustion in high speed flows*. ed. Buckmaster, Jackson, and Kumar, Kluwer Acad. Pub., 461.
- LIÑÁN, A., ORLANDI, P., VERZICCO, R., & HIGUERA, F. J. 1994 Effects of non-unity Lewis numbers in diffusion flames. *Proceedings of the 1994 Summer Program*. Center for Turbulence Research, NASA Ames/Stanford University.
- MCMURTRY, P. A., RILEY, J. J., & METCALFE, R. W. 1989 Effects of heat release on the large-scale structure in turbulent mixing layers. *J. Fluid Mech.* **199**, 297.
- PETERS, N. 1983 Local quenching due to flame stretch and non-premixed turbulent combustion. *Comb. Sci. & Tech.* **30**, 1.
- PETERS, N. 1994 The modeling of combustion and pollutant formation in engine flows. *Proceedings from a small conference*.
- PHILLIPS, H. 1965 Flame in a buoyant methane layer. *10th International Symposium on Combustion*. p. 1277.
- POINSOT, T. & LELE, S. 1992 Boundary conditions for direct simulations of compressible viscous flows. *J. Comp. Phys.* **101**, 104.
- RÉVEILLON, J., DOMINGO, P., & VERVISCH, L. 1994 Autoignition in non-uniform mixture. To be published.
- TROUVE, A. 1991 Simulation of flame-turbulence interaction in premixed combustion. *Annual Research Briefs 1991*. CTR, Stanford University/Nasa Ames.

- VERVISCH, L., KOLLMANN, W., & BRAY K. N. C. 1994 Pdf modeling for premixed turbulent combustion based on the properties of iso-concentration surfaces. *Proceedings of the 1994 Summer Program*. CTR, NASA Ames/Stanford University.
- VEYNANTE, D., VERVISCH, L., POINSOT, T., LIÑÁN, A. & RUETSCH, G. 1994 Triple flame structure and diffusion flame stabilization. *Proceedings of the 1994 Summer Program*. CTR, NASA Ames/Stanford University.
- WILLIAMS, F. A. *Combustion Theory* Addison-Wesley, NY, 1986.
- WRAY, A. A. Private communication.

Turbulence modeling for separated flow

By P. A. Durbin

1. Motivation and objectives

Two projects are described in this report. The first involves assessing turbulence models in separated flow. The second addresses the anomalous behavior of certain turbulence models, such as $k - \varepsilon$, in stagnation point flow.

The primary motivation for developing turbulent transport models is to provide tools for computing non-equilibrium, or complex, turbulent flows. Simple flows can be analyzed using data correlations or algebraic eddy viscosities, but in more complicated flows such as a massively separated boundary layer, a more elaborate level of modeling is required. It is widely believed that at least a two-equation transport model is required in such cases. The transport equations determine the evolution of suitable velocity and time-scales of the turbulence. The appropriate velocity scale for turbulent transport toward a wall is the normal component, $\overline{v^2}$, not the turbulent intensity, k . This and other considerations motivated the $k - \varepsilon - v^2$ model, which can be used in wall-bounded flows. Applications to complex geometry require a generalized interpretation of the velocity scale $\overline{v^2}$. The model originally was developed for attached or mildly separated boundary layers. Rather promising results were obtained in tests of the formulation. Here the model is assessed in strongly separated flows. Doing so requires that $\overline{v^2}$ be regarded simply as a velocity scale that satisfies boundary conditions suitable for the normal component of turbulent intensity; it cannot be regarded as the 'y-component' because that would be inappropriate in general geometries that can have surfaces aligned in any direction. This loosened understanding of $\overline{v^2}$ presents no operational difficulties.

Two equation models as well as the $k - \varepsilon - v^2$ model predict an anomalously large growth of turbulent kinetic energy in stagnation point flows. Even when the stagnation point region is not of interest *per se*, this spurious behavior can upset the rest of the flow computation. A formal upper limit to the turbulent time-scale in such models alleviates their stagnation point anomaly. This bound is derived in §2.4 and is illustrated with the stagnation point flow at the leading edge of an airfoil.

2. Accomplishments

The governing equations of the $k - \varepsilon - v^2$ model will not be presented here. Their initial development is described in Durbin (1991), and a more complete description of the present work will appear in Durbin (1994). The mean flow satisfies the incompressible Navier-Stokes equations with an eddy viscosity. The turbulence model uses the standard $k - \varepsilon$ equations, a $\overline{v^2}$ transport equation and an elliptic relaxation equation for the source term f_{22} in the $\overline{v^2}$ -equation.

The computations were done with an extended version of the INS2D code of Rogers and Kwak (1990). The extensions required for the present computations

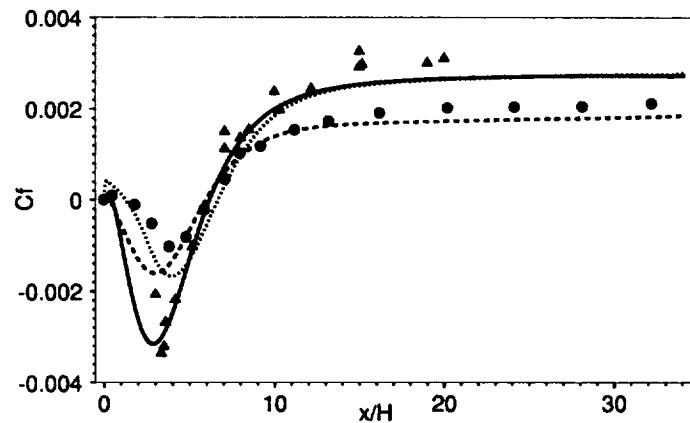


FIGURE 1. Skin friction coefficient on wall downstream of the backstep compared to experiments of Jovic and Driver (—, \blacktriangle) and Driver and Seegmiller (----, \bullet). line is solution to SSG model for Jovic and Driver flow.

consist of providing subroutines to solve the transport and elliptic relaxation equations of the $k - \varepsilon - v^2$ model. This code development will not be described here. The numerics are discussed in Durbin (1994). The program can solve full second moment closure models as well as eddy viscosity models.

The present study included assessment of second-moment closures in separated flow. The results were generally less satisfactory than $k - \varepsilon - v^2$. These second-moment computations will not be presented.

Sections 2.1–2.3 present three separated flows: these illustrate sharp edge separation; smooth wall, pressure driven separation; and unsteady vortex shedding. This last case was studied at the suggestion of colleagues at Pratt & Whitney.

2.1 Flow over backward facing steps

The backstep flow configurations studied experimentally by Jovic and Driver (1993) and by Driver and Seegmiller (1985) were computed with the $k - \varepsilon - v^2$ model and with second-moment closure models. The JD experiment had a step height Reynolds number of 5,000; the DS case had $Re = 37,500$. Both the IP and SSG second-moment closures as incorporated into the elliptic relaxation procedure were tried. Computations showed that they significantly under-predict the magnitude of the reversed flow downstream of the step, as suggested by the dotted skin friction curve in Fig. 1: this should be compared to the solid line and triangles.

Computed and experimental skin friction coefficients on the wall downstream of the step are compared in Fig. 1. The computed reattachment point at $x = 6.2$ step heights is in agreement with the data. The relatively large negative skin friction in the JD experiment is due to low Reynolds number. The $k - \varepsilon - v^2$ model correctly shows this sensitivity to Reynolds number. Overall, the agreement with experiment is better than has been found using the standard $k - \varepsilon$ model with wall functions (Driver and Seegmiller, 1985); numerous independent computations have shown

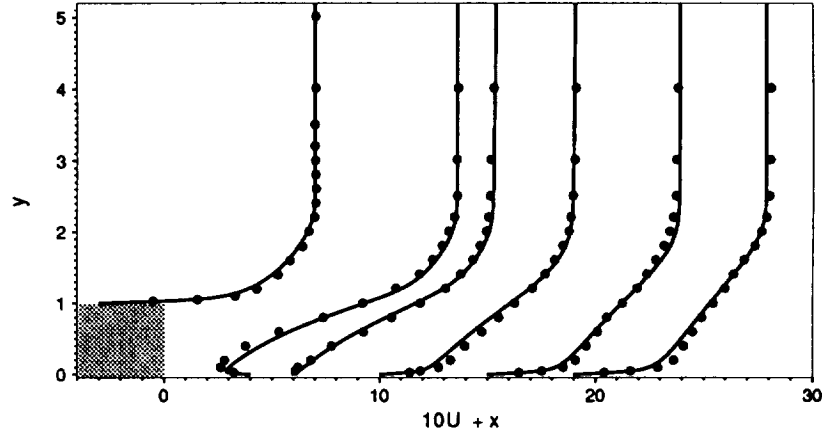


FIGURE 2. Mean velocity profiles for the Jovic and Driver experiment.

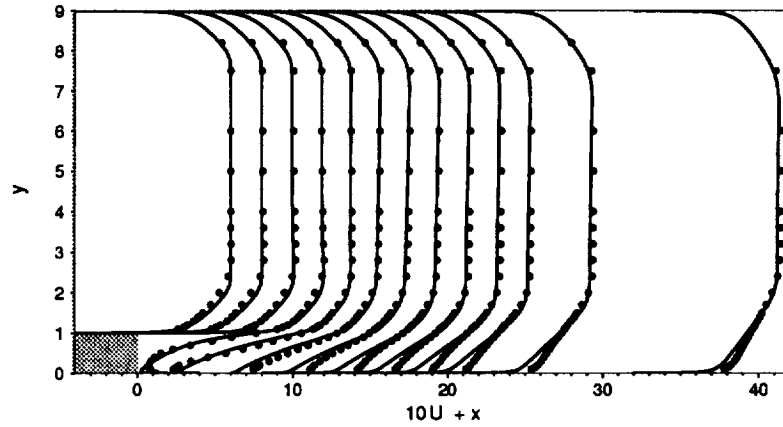


FIGURE 3. Mean velocity profiles for the Driver and Seegmiller experiment.

that model under-predicts the reattachment length.

Figs. 2 and 3 show profiles of the U -component of velocity. These profiles are plotted in the form $10U + x$ to display their evolution down the duct. The agreement between model and experiment in the JD case is quite good. In the higher Reynolds number DS case, the agreement is good for $x < 8$, but the model solution for the boundary layer downstream of reattachment recovers more slowly than the data. This slow recovery downstream of reattachment is a universal problem of turbulence models shown by Reynolds stress as well as $k - \epsilon$ models.

2.2 A separated diffuser

Obi *et al.* (1993) measured the flow in a one-sided, 10° plane diffuser. The expansion ratio of 4.7 was sufficient to produce a separation bubble on the sloping wall; hence, this provides a test case for smooth, adverse pressure driven separation. The entrance to the diffuser consisted of a long plane channel (aspect ratio 35) in

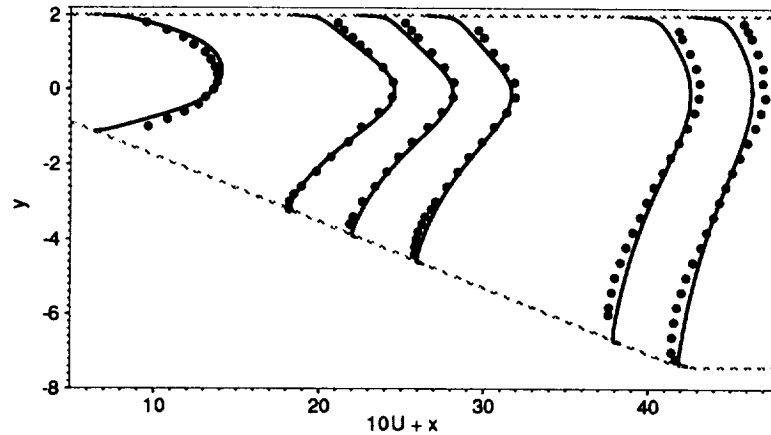


FIGURE 4. Mean velocity profiles in the Obi, *et al.* diffuser. Both Eq. (9) (—) and a constant value of 1.55 (- - - -) were used for $C_{\epsilon_1}^z$. The light dashed lines show the diffuser surface.

order to produce fully developed flow. The Reynolds number based on the half-height of this channel was 10,000. The computational inflow profiles were obtained by solving fully developed channel flow with a parabolic code. Fig. 4 shows profiles of $10U + x$. The boundary of the diffuser is indicated in the figure—note, however, that the aspect ratio of this figure is not unity: the actual duct is more elongated. The profiles on the ramp are in good agreement with the data, showing the smooth separation; further downstream, the predicted backflow is less strong than the data. Note that the mass flux is constant, so less backflow near the lower wall is necessarily accompanied by less forward flow in the upper part of the channel. Second moment closure computations of this flow failed to predict the separation in this flow. Both SSG and IP second-moment closure models gave only a tiny region of reversed flow at the foot of the ramp.

2.3 Vortex shedding behind a triangular cylinder

The flow around a triangular cylinder in a duct was measured by Sjunnesson (presented in Johansson *et al.* 1993). This geometry provides an example of bluff body flow with fixed separation points. The study by Sjunnesson was motivated by the application to flame holders. The geometry consists of a 6:1 aspect ratio equilateral triangular cylinder centered symmetrically in a duct three cylinder sides high. The Reynolds number based on the cylinder side and inlet velocity was about 42,500.

Both steady state and (statistically) unsteady solutions were computed. By taking a large artificial time-step on the order of the shedding period in length, we obtained symmetric, steady solutions. Upon introducing an asymmetric disturbance and taking a smaller step, an oscillatory solution was obtained. Fig. 5 is a composite showing the time-averaged U-contours of the unsteady computation in the upper half and the steady state solution in the lower. It shows that the steady-state

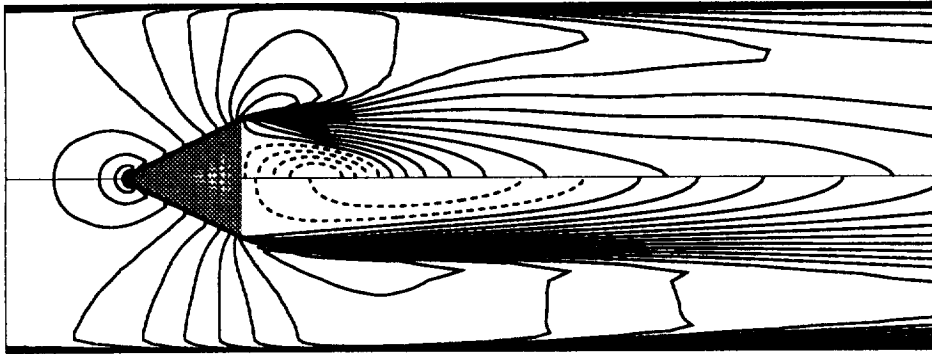


FIGURE 5. U-contours for a steady calculation (lower half) and time-average of an unsteady computation with vortex shedding (upper half).

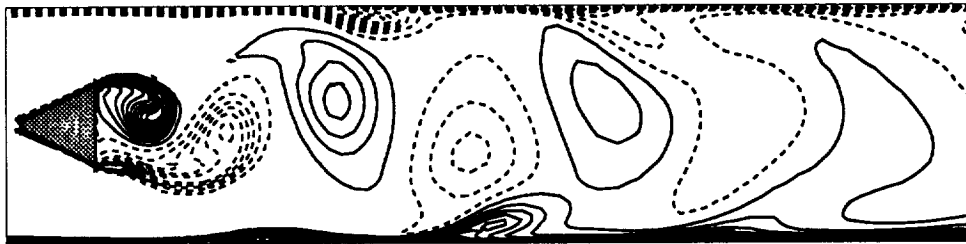


FIGURE 6. Instantaneous vorticity contours showing shedding in the time accurate computation.

separation bubble is over twice as long as the averaged, unsteady bubble.

Instantaneous vorticity contours, in Fig. 6, show the asymmetric flow in the time accurate computation. The interaction between the vortex street and the boundary layers in the side walls results in eruption of secondary vorticity. The complexity of such interactions underscores the need to resolve the coherent vortices in this type of flow.

Fig. 7 shows profiles of the time-averaged U-velocity component in the wake. The computational results were obtained by averaging the numerical solution over one period of the vortex shedding. The profiles are displayed evenly spaced, but the actual locations were $x = 0.375, 0.95, 1.525, 3.75,$ and 9.4 heights downstream of the rear face of the cylinder. The agreement between experiment and model is excellent. The first profile at $x = 0.375$ shows the sharp boundary and large velocity deficit of the near wake. By $x = 0.95$ the wake profile has altered substantially and is undergoing transition to a Gaussian form. The different curves show the convergence of the solution with grid refinement. It can be concluded that the

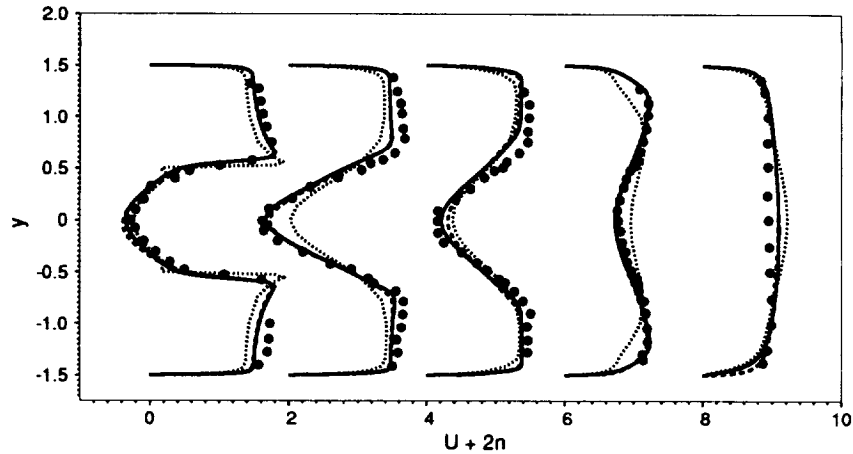


FIGURE 7. Time-averaged velocity profiles in the wake of a triangular cylinder. The calculations are shown for three grids: 141×101 (—), 121×91 (----); 71×51 (.....)

statistical unsteadiness produced by vortex shedding must be resolved in order to compute this flow. The steady state computation of this flow is as dubious as a homogeneous computation of a spatially homogeneous flow; it leads to quite erroneous predictions.

2.4 On the $k - \epsilon$ stagnation point anomaly

Two equation models as well as $k - \epsilon - v^2$ predict an anomalously large growth of turbulent kinetic energy near to stagnation points (Launder and Kato, 1993; Menter, 1992). This can cause difficulties in aerodynamic flows with a free-stream impinging on a blunt leading edge. Even when the stagnation point region is not of interest *per se*, this spurious behavior can upset the rest of the flow computation. The usual explanation for the stagnation point anomaly is that the eddy viscosity formula

$$\overline{u_i u_j} = -2\nu_t S_{ij} + \frac{2}{3} k \delta_{ij} \quad (1)$$

gives an erroneous normal stress difference (Launder and Kato 1993). In (1), $S_{ij} = (\partial_i U_j + \partial_j U_i)/2$ is the rate of strain and

$$\nu_t = C_\mu k T \quad (2)$$

is the eddy viscosity. T is the turbulent time-scale (e.g., k/ϵ).

Some of our computations suggest an alternative understanding of the anomaly: as the stagnation point is approached, T becomes very large. The ϵ -equation is of the form

$$\partial_t \epsilon + U \cdot \nabla \epsilon = \frac{C_{\epsilon_1} \mathcal{P} - C_{\epsilon_2} \epsilon}{T} + \nabla \cdot \left(\left(\nu + \frac{\nu_t}{\sigma_\epsilon} \right) \nabla \epsilon \right), \quad (3)$$

where the rate of turbulent energy production is $\mathcal{P} = 2\nu_t S_{ij} S_{ji}$. A large value of T in Eq. (3) causes the production of ε to be too small, allowing spuriously high turbulent kinetic energy. The stagnation point anomaly can be ameliorated by imposing a bound on the time-scale. In the following we will derive the constraint

$$T = \min \left(\frac{k}{\varepsilon}, \frac{2}{3C_\mu} \sqrt{\frac{3}{8|\mathbf{S}|^2}} \right). \quad (4)$$

where $S_{ij} S_{ji} \equiv |\mathbf{S}|^2$. In most situations this reduces to $T = k/\varepsilon$; in highly strained flow the upper bound comes into play.

The constraint will be derived by requiring that (1) satisfy $2k \geq \overline{u^2} \geq 0$, which can be called a ‘realizability condition’. The rate of strain tensor S_{ij} is symmetric and becomes purely diagonal in principal-axes coordinates. The diagonal elements, λ_α , $\alpha = 1 \dots 3$, are its eigenvalues and satisfy

$$\lambda_1^2 + \lambda_2^2 + \lambda_3^2 = |\mathbf{S}|^2. \quad (5)$$

In incompressible flow

$$\lambda_1 + \lambda_2 + \lambda_3 = 0 \quad (6)$$

It follows from (5) and (6) that

$$|\lambda_\alpha| = \sqrt{|\mathbf{S}|^2/2} \quad (7)$$

in two dimensions (i.e., when $\lambda_3 = 0$), and

$$|\lambda_\alpha| \leq \sqrt{2|\mathbf{S}|^2/3} \quad (8)$$

in three dimensions.

If (1) is written in the principal axes of S_{ij} , it becomes

$$\overline{u_\alpha^2} = -2\nu_t \lambda_\alpha + \frac{2}{3}k. \quad (9)$$

Of the constrains $\overline{u_\alpha^2} \geq 0$ and $2k \geq \overline{u_\alpha^2}$, $\forall \alpha$, the former is more stringent; this constraint is

$$2\nu_t \max_\alpha \lambda_\alpha \leq \frac{2}{3}k. \quad (10)$$

Substituting (2) into (11) results in the time-scale bound

$$T \leq \frac{1}{3C_\mu} \frac{1}{\max \lambda_\alpha} \quad (11)$$

which gives

$$T \leq \frac{2}{3C_\mu} \frac{1}{\sqrt{2|\mathbf{S}|^2}} \quad (12)$$

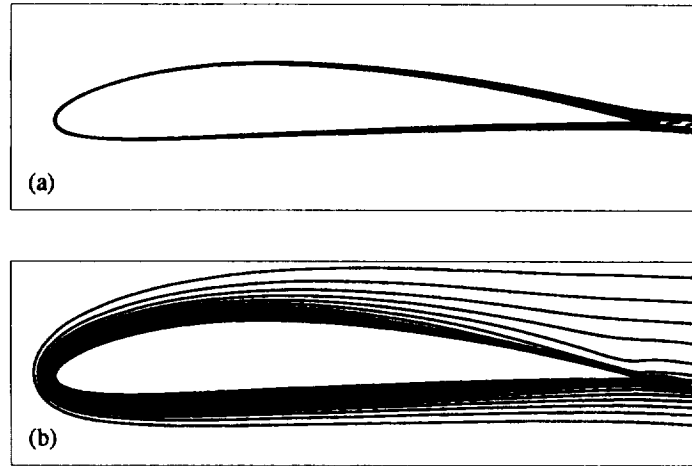


FIGURE 8. Contours of constant k/U_∞^2 : (a), with (6) imposed; (b), without constraint. Contour intervals of 1.5×10^{-3} .

in two dimensions, and

$$T \leq \frac{2}{3C_\mu} \sqrt{\frac{3}{8|S|^2}} \quad (13)$$

in three dimensions. These bounds might be imposed computationally by Eq. 4.

Fig. 8 shows k contours for the flow over a NACA4412 airfoil at zero angle of attack and with $k = 4 \times 10^{-4} U_\infty^2$ in the approach flow, with and without the constraint on T . This computation was done with the $k - \varepsilon - v^2$ model. The constraint prevents the spurious growth of k although some amplification still occurs.

3. Future plans

Flows with mean swirl are of interest for their role in enhancing mixing both by turbulent and mean motion. The swirl can have a stabilizing as well as a destabilizing effect on the turbulence. I have written an axi-symmetric extension to the INS-2D computer program and added the capability to compute swirling flow. This is in order to study confined coaxial jets with or without swirl. High swirl can produce vortex breakdown on the centerline of the jet. This type of flow occurs in various combustors.

The present vortex shedding calculations suggest that the application of turbulence models to separation control by external periodic excitation should be explored. This is a problem that Hans Kaltenbach has been investigating by LES.

REFERENCES

- DRIVER, D. & SEEGMILLER, H. L. 1985 Features of a reattaching turbulent shear layer in divergent channel flow. *AIAA Journal*. **23**, 163-171.

- DURBIN, P. A. 1991 Near-wall turbulence closure modeling without 'damping functions'. *Theoret. Comput. Fluid Dynamics*. **3**, 1–13.
- DURBIN, P. A. 1994 Separated flow computations with the $k-\varepsilon-v^2$ model. *AIAA Journal*. To appear.
- JOHANSSON, S., DAVIDSON, L. & OLSSON, E. 1993 Numerical simulation of the vortex shedding past triangular cylinders at high Reynolds number using a $k-\varepsilon$ turbulence model. *Int. J. Num. Meth. Fluids*. **16**, 859–878.
- JOVIC, S. & DRIVER, D. 1993 Backward-facing step measurements at low Reynolds number, private communication.
- LAUNDER, B. E. & KATO, M. 1993 Modelling flow-induced oscillations in turbulent flow around a square cylinder. *ASME-FED*. **157**, 189–199
- MENTER, F. R. 1992 Improved two-equation $k-\omega$ models for aerodynamic flows. *NASA TM*. **103975**.
- OBI, S., OHIMUZI, H., AOKI, K. & MASUDA, S. 1993 Experimental and computational study of turbulent separating flow in an asymmetric plane diffuser, 9th *Symp. on Turbulent Shear Flows*, Kyoto, Japan.
- ROGERS, S. E. & KWAK, D. 1990 Upwind differencing scheme for the time-accurate incompressible Navier-Stokes equations. *AIAA Journal*. **28**, 253–262.

Notes on rotating turbulence

By O. Zeman

1. Motivations and objectives

The purpose of this work was to investigate the turbulent constitutive relation when turbulence is subjected to solid body rotation. Rotating turbulent flows exist in many industrial and geo- and astrophysical applications.

2. Accomplishments

2.1 Note on spectra and decay of rotating homogeneous turbulence

Recently, Squires, Chasnov, Mansour, & Cambon (1993) (hereon SCMC) addressed the problem of asymptotic behavior of homogeneous turbulence. Briefly, to summarize their results and findings, they applied a spectral LES method to achieve an asymptotic, equilibrium evolution of initially isotropic turbulence subjected to solid body rotation of angular speed Ω . The computations, which were run for times of order $O(10^3)$ of initial turbulence time scales, confirmed the prediction of the asymptotic decay laws. The authors used two different (initial) spectral forms of the energy spectrum $E(k)$ at low wavenumber k :

$$E(k) = 2\pi k^2 A_0 + \dots \quad \text{and} \quad E(k) = 2\pi k^4 A_2 + \dots$$

In nonrotating turbulence the two spectral forms are known to produce different time decay exponents (n) of the turbulent kinetic energy $\frac{1}{2}q^2 = \int_0^\infty E(k)dk \propto t^{-n}$. For the k^2 spectrum, $n = 6/5$, and for the k^4 spectrum, $n = 10/7$. In the presence of rotation the following asymptotic decay laws were proposed in SCMC:

$$q^2 \propto A_0^{2/5} t^{-3/5} \Omega^{3/5} \quad (k^2 \text{ spectrum}) \quad (1)$$

$$q^2 \propto A_2^{2/7} t^{-5/7} \Omega^{5/7} \quad (k^4 \text{ spectrum}) \quad (2)$$

The above laws were confirmed by the LES computations within a few percent. Computations also indicated that the rotating turbulence has a tendency toward a two-dimensional state in the sense that the spectral energy tends to concentrate at wavenumbers normal to the rotation axis, i.e. the gradients with respect to the wavenumber parallel to Ω become relatively small. At the same time the turbulence remained remarkably close to isotropy if measured by departure from the isotropy tensor $b_{ij} = \langle u_i u_j \rangle / q^2 - 1/3 \delta_{ij}$. This suggests a turbulence structure consisting of vortices aligned with the rotation axis and of jet-like (fluctuating) flow parallel to the rotation axis.

The purpose of this note is to explain the behavior of the rotating turbulence on the basis of a model for the spectral energy transfer, and to propose modification

of the turbulence spectrum when the rotation is much more rapid than the eddy turnover time scale. We start with a simplified Lagrangian description of the relation between stress and mean strain in rotating turbulence. The resulting relationship is then used to describe the energy transfer from larger to smaller scales in the spirit of the analysis described in Tennekes & Lumley (1972) for nonrotating turbulence.

Denoting Lagrangian fluctuating velocity components by v_i and taking the rotation vector to be $\Omega = (0, 0, \Omega)$, one can write equations for the motion of fluid particles originating at some point in space and time (\mathbf{a}_o, t_o) as follows:

$$\frac{dv_i}{dt} = -v_j U_{i,j} + 2\epsilon_{ij3}\Omega v_j + \Pi_i \quad (3)$$

Here, U_i represents a background mean velocity field which is considered as slow varying with respect to the characteristic Lagrangian (turbulence) time scale τ_L and length scale ($\propto q\tau_L$). Π_i 's are random forcing terms comprising the effect of the fluctuating pressure and higher order correlations. The viscous terms are taken to be negligible on account of the high turbulence Reynolds number assumption ($Re_T \propto q^2\tau_L/\nu \gg 1$). The velocities v_i are functions of position and time $v_i(\mathbf{X}, t)$ of the fluid particle, with the initial position $\mathbf{X}(t_o) = \mathbf{a}_o$. Because turbulence is statistically homogeneous, we shall suppress the space dependence and utilize the ensemble-average identity $\langle v_i v_j \rangle(t) = \langle u_i u_j \rangle(t)$, i.e., the one-point Lagrangian averages (over all initial locations) are equal to the Eulerian averages (over the flow volume). A useful reference for Lagrangian description of turbulence is Monin & Yaglom (1971).

Now, neglecting the effect of Π_i and assuming that the gradients $U_{i,3}$ of the slow-varying velocity field (in the rotation direction) are negligible, it is possible to formulate a stress-strain relation $\langle v_1 v_2 \rangle \propto -S_{12}$ ($S_{ij} = \frac{1}{2}(U_{i,j} + U_{j,i})$ is the slow strain tensor). This is achieved first by integrating (3) to obtain expressions for v_1, v_2 :

$$v_1(t) = v_{1o}(t_o) - U_{1,j} \int_{t_o}^t v_j(t') dt' + 2\Omega \int_{t_o}^t v_2(t') dt'$$

$$v_2(t) = v_{2o}(t_o) - U_{2,j} \int_{t_o}^t v_j(t') dt' - 2\Omega \int_{t_o}^t v_1(t') dt'$$

Further manipulations yield an expression

$$\langle v_1 v_2 \rangle = \langle u_1 u_2 \rangle = -\left[c_1 \frac{\frac{1}{3} q^2 \tau_L}{1 + 4c_2 \tau_L^2 \Omega (2\Omega - R_{12})} \right] 2S_{12} = -2\nu_T S_{12}. \quad (4)$$

Here, all the required Lagrangian time scales such as $T_{L\alpha} = \langle v_\alpha^2 \rangle^{-1} \int_0^\infty \langle v_\alpha(t') v_\alpha(t_o) \rangle dt'$ were written for simplicity as a single time scale τ_L , which is in turn proportional to the turbulence time scale ℓ/u' (ℓ and u' being characteristic length and velocity scales); R_{ij} is the asymmetric complement to S_{ij} . The presumed differences in timescale magnitudes are absorbed in the free constants c_i . Clearly, (4) expresses a turbulent constitutive relation in the presence of rotation; the effective

eddy viscosity ν_T is evidently diminished by a factor depending on $(\tau_L \Omega)^2$. Although in the following analysis the flow field represented by S_{ij} and R_{ij} is taken as random, it is of interest to interpret (4) considering a homogeneous rotating shear flow with $S_{12} = R_{12} = \frac{1}{2}U_{1,2} = \frac{1}{2}S$. Then we note that the nature of the constitutive relation (4) is such that ν_T is maximized for $(\Omega/S)_{max} = 0.125$. On the other hand, the LES results of Bardina *et al.* (1985) and linear stability analysis (see e.g. Speziale, 1991) indicate the maximum turbulence amplification at $(\Omega/S)_{max} = 0.25$. Since in the following analysis R_{12} is neglected, the exact value of $(\Omega/S)_{max}$ is irrelevant to our problem. A stress-strain relation analogous to (4) has also been derived in cylindrical coordinates for a turbulent line vortex by Zeman (1994a) (comparable when the vortex flow is in solid body rotation i.e. when $U_{azimuth} = r\Omega$).

Now we shall relax the relation in (4) so that $S_{12} = S(k')$ represents the strain of eddies (of size $\propto 1/k'$) larger than the wavenumber k of the stress $\langle u_1 u_2 \rangle(k)$. Following the line of reasoning in Tennekes & Lumley (Section 8.4) concerning the spectral transfer in nearly isotropic turbulence, the spectral energy flux $T(k)$ across the wavenumber k in the inertial subrange is effected mainly by local interaction so that $T(k) \propto -S_{ij}(k') \langle u_i u_j(k'') \rangle \propto \nu_T(k'') S^2(k')$ where, approximately, $k/3 < k' \leq k$ and $k'' = 3k'$. As shown in Tennekes & Lumley, the quantities at k' or k'' are directly related to the same quantities at k , thus e.g., $S(k') \propto (E(k)k^3)^{1/2} \propto \tau_L^{-1}(k'')$. Utilizing (4) to express $T(k)$ in terms of quantities (depending now on $E(k)$, k , Ω) and neglecting the contribution ΩR_{12} in (4) ($R_{12}(k)$ is a random quantity with zero mean and $|R_{12}| \ll \Omega$), we obtain a relationship

$$T(k) \propto \nu_T(k'') S^2(k') \propto \frac{(Ek)^{3/2} k}{1 + c_3 \frac{\Omega^2}{Ek^3}}.$$

In the inertial subrange the spectral energy flux $T(k)$ across each wavenumber is constant and equal to the dissipation ϵ , and the above equation can be written as

$$\epsilon = \alpha^{-3/2} \frac{(Ek)^{3/2} k}{1 + c_3 \frac{\Omega^2}{Ek^3}}, \quad (5)$$

where α is the Kolmogorov constant and c_3 is another free coefficient. Evidently, (5) represents an implicit relation for the energy spectrum $E(k, \epsilon, \Omega) = 0$ in the presence of rotation. For more insight into the meaning of (5), it is useful to define a rotation (cut-off) wavenumber k_Ω

$$k_\Omega = \left(\frac{\Omega^3}{\epsilon}\right)^{1/2}, \quad (6)$$

which delimits the region of the spectrum where the rotation effects are important, i.e., $k < k_\Omega$; (note that k_Ω^{-1} is analogous to the Ozmidov length in stratified turbulence). In the region where $k \ll k_\Omega$, (5) results in an explicit expression

$$E(k) \propto \epsilon^{2/5} \Omega^{4/5} k^{-11/5}, \quad (7)$$

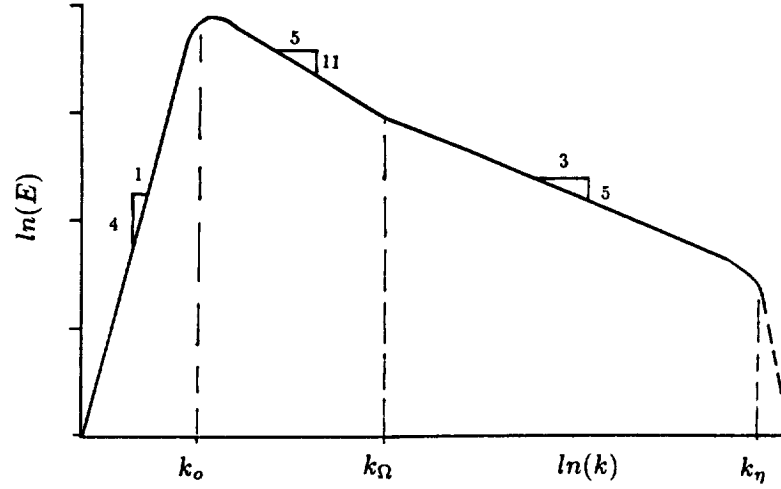


FIGURE 1. Sketch of the turbulence energy spectrum subjected to rotation; k_o and k_η are, respectively, the large-eddy and Kolmogorov scale wavenumbers, k_Ω is defined in (6).

while for $k \gg k_\Omega$ the Kolmogorov inertial subrange $E(k) = \alpha \epsilon^{2/3} k^{-5/3}$ is recovered. The sketch of the spectrum (with exaggerated slope change) is depicted in Fig. 1. A general solution of (5) (with $c_3 = 1$) is obtained in the form

$$x = \left(\frac{y^5}{1 + 2y + y^2} \right)^{1/4}, \quad (8)$$

where $x = k/k_\Omega$ and $y = Ek^3/\Omega^2$. Fig. 2 shows the solutions of the above equation emphasizing the rotation-affected range by plotting $Ek^{11/5}$ and $Ek^{5/3}$. It is seen that the spectrum of the form (7) is approximately valid for $k/k_\Omega \leq 10^{-1}$. It should be noted that expressing the eddy viscosity (in square brackets) in (4) in terms of spectral quantities at a given k , one obtains

$$\nu_T(k) = \frac{(E/k)^{1/2}}{1 + c_4/y(k)}, \quad (9)$$

hence the parameter Ω^2/Ek^3 is the measure of the damping effect of rotation on the local eddy viscosity. It is of interest that the same parameter appears in the expression for the subgrid-scale eddy viscosity in the LES of SCMC. Although the functional dependence of $\nu_T(k)$ on y is far more complicated, both CSMC and expression (9) give the same asymptotic dependence $\nu_T(k) \propto y$ if $y \ll 1$.

If there exists a self-similar spectrum as sketched in Fig. 1 (with $k_o < k_\Omega \ll k_\eta$), then (7) also contains information concerning the turbulence energy decay.

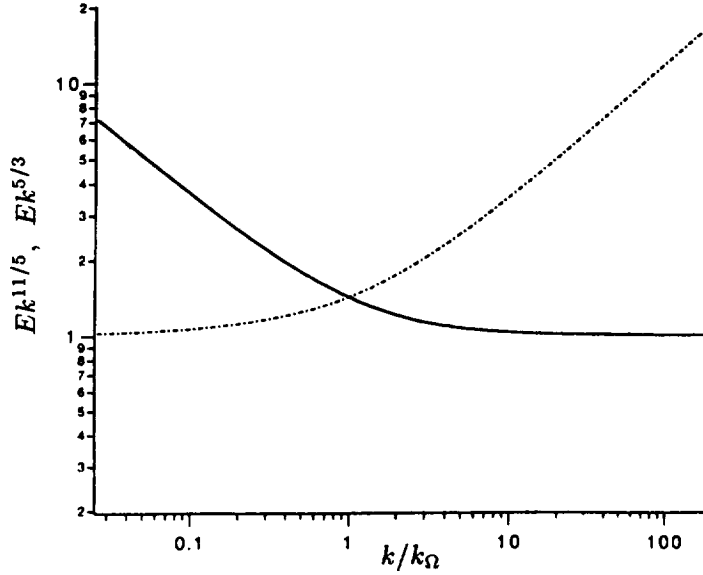


FIGURE 2. Spectral energy quantities $Ek^{11/5}$ (---) and $Ek^{5/3}$ (—) vs. k/k_{Ω} , based on the solution to (8). par

Assuming a k^4 spectrum for $k \leq k_o$, then $\frac{1}{2}q_{,t}^2 \propto A_2(k_o^5)_{,t} \propto -\epsilon$, and using (7) one obtains

$$q^2 \propto t^{-10/21} \Omega^{20/21} A_2^{2/7}. \quad (10)$$

The exponent $n = 10/21$ is lower than $n = 5/7$ in (2) derived from the dimensional analysis in SCMC. If, however, the rotation damping factor in (5) can be generalized to $1 + c_4 y^{-1} \propto y^{-m}$, one obtains the relation $n = 10/(7 + 14m)$. Hence, to satisfy the decay exponent $n = 5/7$ proposed in (2), m must take on the value $m = 1/2$. This leads to a spectral form

$$E(k) \propto (\epsilon \Omega)^{1/2} k^{-2},$$

different from (7). Analogous relations can be obtained for the k^2 spectrum to satisfy (1).

In summary, from Lagrangian analysis a relation between turbulent stress and strain in rotating homogeneous turbulence was inferred. This relation was utilized to derive the spectral energy flux and, ultimately, the energy spectrum form. If the rotation wavenumber k_{Ω} lies in the inertial subrange, then for wavenumbers less than k_{Ω} the turbulence motions are affected by rotation and the energy spectrum slope is modified. The present findings provide a new insight into the nature of the rotation effects on turbulence and, needless to say, their confirmation by (numerical) experiments would be desirable. It may, however, be difficult to experimentally distinguish the change in the spectral slope around the rotation wavenumber. The energy decay laws inferred in CSMC and the present results suggest a modification of the ϵ model equation and eddy viscosity in $k - \epsilon$ models. This is a subject of the following note.

2.2 A note on the eddy viscosity in rotating turbulence

A suggested generalization of the expression for the eddy viscosity (in the constitutive relation $\overline{u_i u_j} = -2\nu_T S_{ij} + \frac{1}{3}q^2 \delta_{ij}$) in rotating turbulence derived by Zeman (1994b) (Eq. (4) in preceding Section 2.1) is

$$\nu_T = \frac{\nu_{T_o}}{1 + c_5 \Omega_k (\Omega_k - \epsilon_{ijk} R_{ij}) \tau^2}. \quad (11)$$

Here, ν_{T_o} is the appropriate eddy viscosity for nonrotating flow; otherwise the notation is as in Section 2.1, i.e., $q^2 = \overline{u_j u_j}$ is twice turbulent kinetic energy (TKE), $\tau = q^2/\epsilon$, and $R_{ij} = \frac{1}{2}(U_{i,j} - U_{j,i})$ is the rotation tensor. The optimal value of the numerical constant c_5 was found to be $c_5 \approx 0.1$.

In homogenous rotating turbulence with shear $S = \partial U_1/\partial x_2 = 2R_{12}$ and with the reference frame rotation $\Omega_j = \Omega_3$, (11) reduces to

$$\nu_T = \frac{\nu_{T_o}}{1 + c_5 \Omega (\Omega - S/2) \tau^2}. \quad (12)$$

For a given value of the rotation-free viscosity ν_{T_o} and assumed constant value of the normalized shear $S\tau = Sq^2/\epsilon$, the eddy viscosity ν_T is solely a function of the ratio Ω/S and reaches maximum when $\Omega/S = 0.25$ in agreement with linear stability analysis. The function $\nu_T(\Omega/S)$ is symmetric about $\Omega/S = 0.25$ and falls off rapidly with increasing departure from 0.25. With the (tested) value of $S\tau = 12$, ν_T decreases by a factor of 14 as Ω/S changes from 0.25 to 0.25 ± 0.75 .

Apart from the eddy viscosity, the rotation also affects the Kolmogorov energy cascade and therefore the rate of dissipation. The author proposed a correction to the ϵ equation to represent this effect (reported also in Hadid, Mansour & Zeman 1994). In the case of purely decaying turbulence subjected to rotation, the modified ϵ equation is

$$\frac{\partial \epsilon}{\partial t} = -\beta \frac{\epsilon^2}{q^2}, \quad (13)$$

where β is now a function of the rotation parameter $\omega = |\mathbf{\Omega}|\tau$, in the following way

$$\beta = 3.7 + \frac{5}{3} \frac{\omega^2}{1 + \omega^2}. \quad (14)$$

In this formulation, (13) satisfies the decay law $\partial q^2/\partial t \propto t^{-n}$ so that the energy decay exponent n is 1.2 when $\omega = 0$ and $n = 0.6$ when $\omega \gg 1$. The latter value is based on the asymptotic decay of rotating turbulence inferred from the scaling analysis and LES results of Squires *et al.* (1993) (when the energy spectrum $E(k)$ at the large scale end behaves as $E \propto k^4$). The form of the function (14) has been based on the analysis of Zeman (1994b). The model-experiment comparison for rotating decaying turbulence using (13) and (14) is shown in Fig. 3. The data are from the experiment of Wigeland & Nagib (1978).

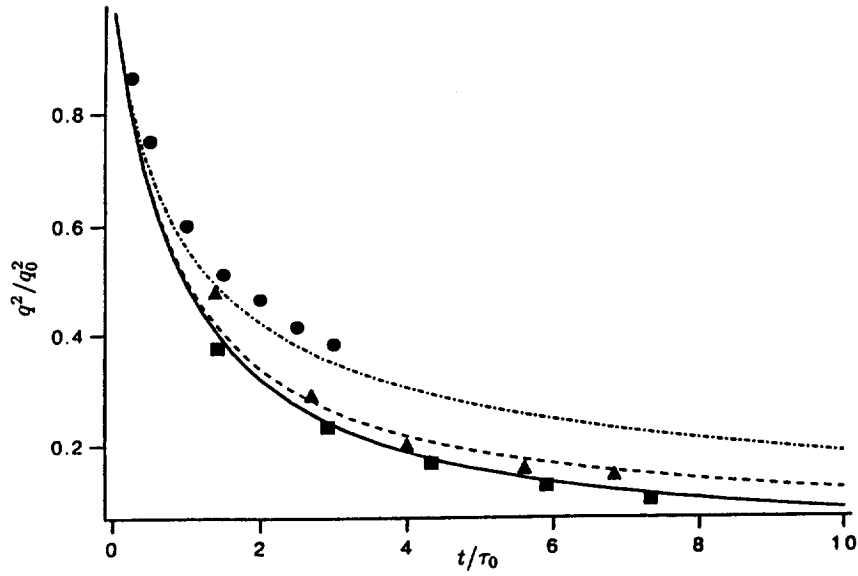


FIGURE 3. Decay of rotating turbulence; model-experiment comparison. Data points are from Wigeland & Nagib (1978). $\Omega\tau_0 = 0.12$ (—), 0.47 (----), 70.0 (-·-·-); $\Omega\tau_0 = 0.12$ (■), 0.47 (▲), and 70.0 (●).

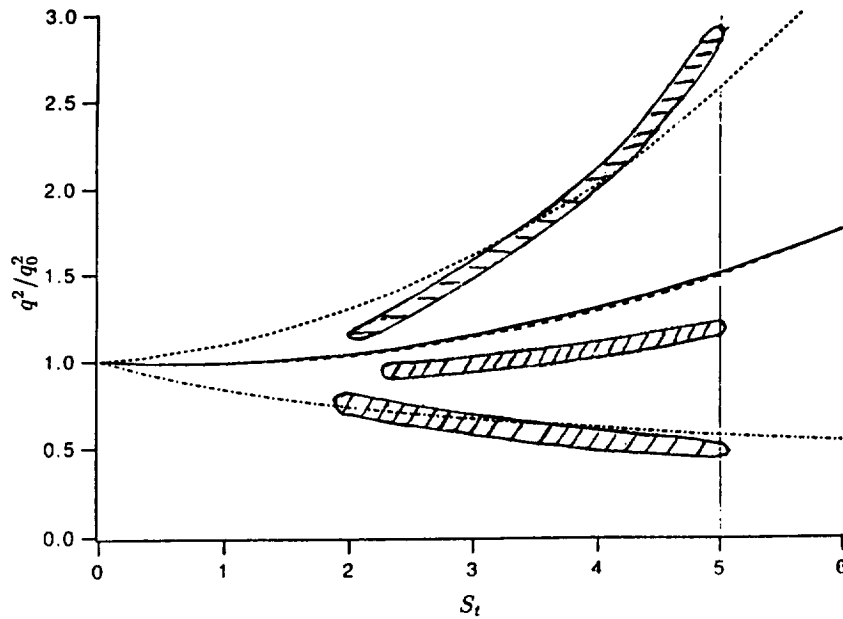


FIGURE 4. Shear-driven turbulence with rotation: $k-\epsilon$ model prediction (with modified viscosity in (12)); cross-hatched areas represent roughly the DNS results of Bardina *et al.* (1985). $\Omega/S = 0.0$ (—), 0.25 (----), 0.5 (-·-·-), and -0.5 (— — —).

In the presence of shear $S = \partial U_1 / \partial x_2$, the relevant $k - \epsilon$ model equations are

$$\frac{1}{2} \frac{\partial q^2}{\partial t} = P - \epsilon, \quad (15)$$

and (13) changes to

$$\frac{\partial \epsilon}{\partial t} = -\beta(\epsilon - 0.75P) \frac{\epsilon}{q^2}. \quad (13')$$

The TKE production rate $P = 4\nu_T S_{ij} S_{ij} = \nu_T S^2$ is determined with the aid of the modified eddy viscosity in (12); the rotation parameter ω in (14) now has to include the contribution due to the presence of shear, i.e. $\omega^2 = (\Omega_k - \epsilon_{ijk} R_{ij})^2 \tau^2 = (\Omega - S/2)^2 \tau^2$. The results of comparison between the model represented by (13') and (15) and the DNS results of Bardina *et al.* (1985) are presented in Fig. 4. The trend in the turbulence evolution with varying Ω/S is apparently predicted although the $k - \epsilon$ model is incapable of predicting the rapid distortion regime during the initial development when $St < 1$. It is noted, however, that the majority of the Reynolds stress closure models are incapable of reproducing the Ω effect on shear turbulence, particularly for the case of maximum amplification when $\Omega/S = 0.25$.

REFERENCES

- BARDINA, J., FERZIGER, J. H., & ROGALLO, R. S. 1985 Effect of rotation on isotropic turbulence: computation and modeling. *J. Fluid Mech.* **154**, 321.
- HADID, A. H., MANSOUR, N. N., & ZEMAN, O. 1994 Single point modeling of rotating turbulent flows. *Proceedings of the Summer Program*. Center for Turbulence Research, NASA Ames-Stanford University.
- MONIN, A. S. & YAGLOM, A. M. 1971 *Statistical Fluid Mechanics: Mechanics of turbulence*, Vol. 1, The MIT Press, 1971.
- SQUIRES, K. D., CHASNOV, J. R., MANSOUR, N. N., & CAMBON, C. 1993 Investigation of the asymptotic state of rotating turbulence using LES. *Annual Research Briefs - 1993*. Center for Turbulence Research, NASA Ames-Stanford University.
- SPEZIALE, C. G. 1991 Analytical methods for Reynolds-stress closures in turbulence. *Ann. Rev. Fluid Mech.* **23**, 107.
- TENNEKES, H. & LUMLEY J. L. 1972 *A First Course in Turbulence*. The MIT Press, 1972.
- WIGELAND, R. A. & NAGIB, H. M. 1978 Grid-generated turbulence with and without rotation. *IIT Fluids and Heat Transfer Rep. R78-1*. IIT, Chicago, IL.
- ZEMAN O. 1994a The persistence of trailing vortices: a modeling study. *Phys. Fluids*. To appear.
- ZEMAN O. 1994b A note on the spectra and decay of rotating turbulence. *Phys. Fluids*. **6**, 3221-3223.

A dynamic localization model with stochastic backscatter

By D. Carati & S. Ghosal

1. Motivation and objectives

1.1 The dynamic localization procedure

The modeling of subgrid scales in large-eddy simulation (LES) has been rationalized by the introduction of the dynamic localization procedure (Ghosal *et al.* 1993, 1994). This method allows one to compute rather than prescribe the unknown coefficients in the subgrid-scale model. Formally, the LES equations are supposed to be obtained by applying to the Navier-Stokes equations a “grid filter” operation defined as:

$$\bar{\psi}(\mathbf{x}) = \int_V d\mathbf{y} G\left(\frac{\mathbf{x}-\mathbf{y}}{\Delta}\right) \psi(\mathbf{y}), \quad (1)$$

where G is a kernel damping the fluctuations with a characteristic length shorter than Δ . The resulting equations (here we only consider incompressible flows)

$$\partial_t \bar{u}_i + \partial_j (\bar{u}_j \bar{u}_i) = \nu_0 \nabla^2 \bar{u}_i - \partial_i \bar{p} - \partial_j \tau_{ij}, \quad (2)$$

contain an unknown “subgrid stress” tensor τ_{ij} that needs to be modeled:

$$\tau_{ij} = \overline{u_i u_j} - \bar{u}_i \bar{u}_j. \quad (3)$$

Though the subgrid stress itself is unknown, an identity between subgrid stresses generated by different filters has been derived (Germano *et al.* 1991) and is the basic ingredient of the dynamic procedure:

$$L_{ij} = T_{ij} - \widehat{\tau}_{ij}, \quad (4)$$

where $L_{ij} = \widehat{\overline{u_i u_j}} - \widehat{\bar{u}_i} \widehat{\bar{u}_j}$ is the Leonard tensor and $T_{ij} = \overline{\widehat{u_i u_j}} - \widehat{\bar{u}_i} \widehat{\bar{u}_j}$ is the subgrid stress tensor generated by a second filter defined by:

$$\widehat{\psi}(\mathbf{x}) = \int_V d\mathbf{y} \widehat{G}\left(\frac{\mathbf{x}-\mathbf{y}}{\widehat{\Delta}}\right) \psi(\mathbf{y}). \quad (5)$$

Here \widehat{G} is a kernel damping the fluctuations with a characteristic length shorter than $\widehat{\Delta}$. It will be referred to as the “test filter”. If models τ_{ij}^M , T_{ij}^M are used for these quantities, the difference between the right- and the left-hand sides of relation (4),

$$E_{ij} \equiv L_{ij} + \widehat{\tau}_{ij}^M - T_{ij}^M \neq 0, \quad (6)$$

may be used as “quality indicators” for the subgrid-scale models. In practice, if the models contain a small number of unknown parameters (like in the Smagorinsky (1963) model $\tau_{ij} - \frac{1}{3}\delta_{ij}\tau_{kk} = -2C\Delta^2|\bar{S}|\bar{S}_{ij}$), the dynamic procedure proposes to determine these parameters by minimizing the quantity:

$$\mathcal{F}[C] = \int_V d\mathbf{y} E_{ij}[\mathbf{y}; C] E_{ij}[\mathbf{y}; C]. \quad (7)$$

This procedure partially removes the arbitrariness inherent to modeling in LES. However, the success of the dynamic procedure still strongly depends on the quality of the model for which it is implemented.

1.2 Dynamic localization model with k -equation

This model is motivated by the following considerations. When no constraint is imposed on the Smagorinsky coefficient C , the minimum of the functional $\mathcal{F}[C]$ is achieved for a field C , which can be locally negative. In this case, the model exhibits local reverse energy transfer. This is one of the simplest adaptations of the standard Smagorinsky expression to allow for a variable C and backscatter (Piomelli *et al.* 1991). However, it leads to some difficulties. A negative eddy viscosity generates an exponential amplification of local disturbances instead of the traditional exponential damping. The resulting backscatter is an “auto-catalytic” phenomenon which does not correspond to the real physics of reverse energy transfer in turbulent flows. As a consequence, unphysical instabilities in the LES equations have been observed when the coefficient C in the Smagorinsky model is determined by an unconstrained (no positivity required) variational procedure. The backscatter appears to be unsaturated and the model is unusable. However, Ghosal *et al.* (1993, 1994) have stressed that the reverse flow of energy must be quenched at the latest when all the subgrid-scale energy has been removed, and they have proposed to use the alternate representation

$$\nu_t = 2 C' \bar{\Delta} k^{1/2} \quad (8)$$

instead of the Smagorinsky scaling. Here, k represents the subgrid-scale energy for which a separate transport equation is needed. The basic DLM(k) equations are given in (Ghosal *et al.* 1993, 1994). It can be shown that this model is stable. This approach involving the subgrid-scale kinetic energy is the first self-consistent model in which backscatter is accounted for in the framework of the dynamic procedure.

The combination of a locally negative transport coefficient and a saturation process is reminiscent of some instabilities in complex fluids. For example, phase separation in multicomponent mixtures can be described by instabilities created by a negative diffusion coefficient and saturated by surface tension effects (which are usually modeled by “hyperdiffusivity” terms). Roughly speaking, the DLM(k) picture for backscatter is similar. At some locations in the fluid, the eddy viscosity becomes negative. In a first stage, this generates an instability characterized by an exponential amplification of the local disturbances. In a second stage, a saturation process arrests the further growth of the instability. Later, the rapid changes in

the turbulent velocity are likely to modify the local conditions, and the viscosity is expected to go back to positive values. This process does not explicitly take into account the possible stochastic nature of backscatter, but is not incompatible with a “molecular representation” of the small eddies. Indeed, the large diversity of small-scale eddies suggests that the turbulent fluid should behave more like a very complex (in a rheological sense) medium, and one should not expect the eddy viscosity to remain positive at every space time point.

Although preliminary tests of this model have been satisfactory, the use of a negative eddy viscosity to describe backscatter is probably a crude representation of the physics of reverse transfer of energy. Indeed, the model is fully deterministic. Knowing the filtered velocity field and the subgrid-scale energy, the subgrid stress is automatically determined. Obviously, this is only an approximation. It is very unlikely that the small scales influence the large scale evolution only through k . This is nevertheless an improvement when compared to the traditional Smagorinsky model in which no information from the small scales is included. However, we know that the LES equations cannot be fully deterministic since the small scales are not resolved. This stems from an important distinction between equilibrium hydrodynamics and turbulence. In equilibrium hydrodynamics, the molecular motions are also not resolved. However, there is a clear separation of scale between these unresolved motions and the relevant hydrodynamic scales. The result of molecular motions can then be separated into an average effect (the molecular viscosity) and some fluctuations. Due to the large number of molecules present in a box with size of the order of the hydrodynamic scale, the ratio between fluctuations and the average effect should be very small (as a result of the “law of large numbers”). For that reason, the hydrodynamic balance equations are usually purely deterministic. In turbulence however, there is no clear separation of scale between small and large eddies. In that case, the fluctuations around a deterministic eddy viscosity term could be significant. An eddy noise would then appear through a stochastic term in the subgrid-scale model and could be the source of backscatter. Some existing models have already represented reverse energy transfers by random terms. For example, a random eddy force derived from the eddy damped quasi-normal Markovian approximation has been used with some success in LES of isotropic turbulence by Chasnov (1991). This idea has been extended to boundary layers by Mason & Thomson (1992) and a similar approach has also been used by Leith (1990) to study LES of mixing layers. However, all these stochastic models contain an arbitrary parameter that must be tuned to obtain satisfactory results. Here we present an alternative subgrid-scale model in which the dynamic procedure is combined with a stochastic representation of backscatter. Following the dynamic procedure, no arbitrary parameter will be introduced in the model. Such a model represents a more traditional picture (Kraichnan, 1976; Leslie & Quarini, 1979) of backscatter than a negative eddy viscosity based model. However, it must be stressed that the true energy transfers between small and large scales are probably much more complex than that described by either an eddy viscosity or an eddy noise formalism. Both these models probably remain rather crude approximations to the real

physical process.

2. Accomplishments

2.1 Stochastic dynamic localization model

The DLM(k) proposed by Ghosal *et al.* (1993, 1994) accounts for backscatter through a purely deterministic eddy viscosity. Let us now adopt a different point of view and assume that backscatter may be represented by a stochastic forcing term. At grid level, the proposed model is:

$$\partial_j \tau_{ij} = \partial_j (C \beta_{ij}) + f_i, \quad (9)$$

where $\beta_{ij} = -2 \Delta^2 |\bar{S}| \bar{S}_{ij}$ corresponds to the standard Smagorinsky model and f_i is an eddy force. For the sake of simplicity we will choose the simplest temporal behavior for \mathbf{f} by assuming that the eddy force is a white noise process. The general form of its two-point, two-time correlation is then given by:

$$\langle f_i(\mathbf{r}, t) f_j(\mathbf{r}', t') \rangle = A^2(\mathbf{r}, t) H_{ij}(\mathbf{r} - \mathbf{r}') \delta(t - t'), \quad (10)$$

where (\mathbf{r}, t) and (\mathbf{r}', t') are two space-time points. The operator $\langle \dots \rangle$ will denote the averaging over all possible realizations of the random force conditioned on a given velocity field $\mathbf{u}(\mathbf{r}, t)$. The functions H_{ij} characterizing the forcing correlation will be discussed later. We only assume that the prefactor A^2 is chosen so that $H_{ii}(0) = 1$. In what follows, f_i is supposed to be divergence free (this can always be ensured by suitably modifying the pressure term). The choice of a solenoidal force is not essential but it simplifies the following discussion because the pressure then does not involve the random fields used to model the stochastic force. In some sense, the white noise process can be seen as the “most stochastic” choice. Thus, comparison between the stochastic dynamic localization model, DLM(S) defined by (9), and the DLM(k) should show what are the respective advantages (if any) of stochastic and deterministic models for backscatter.

It should be noted that the DLM(S) only models the divergence of the subgrid-scale stress. This is justified because the divergence is the only quantity needed in the LES equations. Also, the introduction of a stochastic force is much easier in the formulation (9). Thus, the quantity $\partial_j E_{ij}$ should be used in the dynamic procedure instead of E_{ij} . However, this would lead to major difficulties: The unknown quantities A and C would be determined by stochastic, integro-differential equations. The resolution of such equations would dramatically reduce the performances of the model. To avoid these problems, we propose to base the minimization procedure on the quantity $\langle E_{ij} \rangle$ instead of $\partial_j E_{ij}$ where the average is performed over all the possible realizations of the random noise f_i *conditioned on a fixed velocity field* $\mathbf{u}(\mathbf{r}, t)$. This is a convenient approximation which results in the following simplifications. First, the error tensor $\langle E_{ij} \rangle$ is deterministic and totally independent of the random forces:

$$\langle E_{ij} \rangle = L_{ij} + C \widehat{\beta}_{ij} - C \alpha_{ij}, \quad (11)$$

where $\alpha_{ij} = -2 \widehat{\Delta}^2 |\widehat{S}| \widehat{S}_{ij}$. Also, C is now determined by minimizing $\int_V dy \langle E_{ij} \rangle \langle E_{ij} \rangle$ which is exactly the same variational problem as in the deterministic models. Finally, since the DLM(S) is supposed to model backscatter by the eddy force, it is natural to assume that the Smagorinsky term is purely dissipative. The parameter C has then to be determined by the constrained dynamic localization model, DLM(+), (see Ghosal *et al.* 1993, 1994).

Since the force disappears from this first part of the dynamic procedure due to the conditional averaging over all realizations of the random force, we need an extra-relation for determining its amplitude. It can be obtained by noting that, even though the average effect of the force vanishes in the equations for the mean momentum, it will lead to a finite effect in the energy balance equation. Two equivalent energy equations may be obtained for the quantity $\widehat{E} = \widehat{u}_i \widehat{u}_i / 2$:

$$\partial_t \widehat{E} = \dots - \widehat{u}_i \partial_j (C \alpha_{ij} + P \delta_{ij}) + \mathcal{E}_F, \quad (12a)$$

$$\partial_t \widehat{E} = \dots - \widehat{u}_i \partial_j (\widehat{C} \beta_{ij} + L_{ij} + \widehat{p} \delta_{ij}) + \mathcal{E}_f, \quad (12b)$$

where ... stands for the viscous and inertial terms that are identical in both these equations. The pressure terms P and p are determined to keep the velocity divergence free at grid and test level. The quantities \mathcal{E}_F and \mathcal{E}_f represent the energy input in the system respectively by F_i (the test level eddy force) and \widehat{f}_i (the filtered grid level eddy force). The difference between the right-hand sides of Eqs. (12a) and (12b)

$$Z \equiv \mathcal{E}_F - \mathcal{E}_f - g \neq 0 \quad (13)$$

plays exactly the same role for the energy transfer as the quantities E_{ij} for the subgrid-scale stress. Here g is a known quantity (C has been determined by the DLM(+)) given by

$$g = \widehat{u}_i \partial_j \left(C \alpha_{ij} + P \delta_{ij} - \widehat{C} \beta_{ij} - L_{ij} - \widehat{p} \delta_{ij} \right). \quad (14)$$

The minimization of the quantity $\mathcal{Z} = \int_V dr \langle Z \rangle^2$ can now be used as a variational determination of the parameters that enter the model for the eddy force. At this point, little has been said about the statistical characteristics of the stochastic force itself. The variational problem presented here could be used together with a wide variety of choices for the eddy force.

Let us now discuss some additional assumptions that will greatly simplify the DLM(S) equations. From a computational point of view, it will be very convenient to consider the limiting case for which f_i at different grid points may be assumed to be completely uncorrelated. This avoids the non-trivial problem of generating random numbers with complex spatial correlations. This is also physically plausible since the eddy force is assumed to model random phenomena due to structures smaller than the mesh grid. Thus, the function H_{ij} will be assumed to be negligible

for distances $|\mathbf{r} - \mathbf{r}'|$ larger than the mesh grid. Here we also assume that the probability distribution function of f_i corresponds to a Gaussian process. In that case, a force characterized by the correlations (10) leads to an average energy input

$$\mathcal{E}_f = \frac{1}{2} A^2(\mathbf{r}, t) H_{ii}(0) = \frac{1}{2} A^2(\mathbf{r}, t). \quad (15)$$

Let us now show how the dynamic procedure can be used to determine this energy input. The variational formulation presented above does not directly involve \mathcal{E}_f . However, we can easily relate it to \mathcal{E}_f using Kolmogorov type ideas about energy transfer in the inertial range. Indeed, all the models used in LES - and model (9) is not an exception - are based on such arguments. Thus, the transfer rate is supposed to be independent of the filter width (in the inertial range), and we may assume that the backscatter rate has the same property $\langle \mathcal{E}_f \rangle = \langle \mathcal{E}_F \rangle$. Moreover, the test-filter acts like a local averaging of the random numbers f 's which are almost uncorrelated (the two-point correlation is assumed to decay rapidly) and which vanish on the average. Thus, \hat{f} is much smaller than f , and $\langle \mathcal{E}_{\hat{f}} \rangle$ can be neglected when compared to $\langle \mathcal{E}_f \rangle$. It can then be assumed that $\langle \mathcal{E}_{\hat{f}} \rangle \ll \langle \mathcal{E}_f \rangle = \langle \mathcal{E}_F \rangle$. Thus, relation (13) gives

$$\langle Z \rangle = \langle \mathcal{E}_f \rangle - g. \quad (16)$$

Let us now consider a simple model for the stochastic force:

$$f_i = P_{ij}(\mathcal{A} e_j) \quad (17)$$

where \mathcal{A} is a (dimensional) coefficient which plays a role similar to the Smagorinsky coefficient C . The operator $P_{ij} = \delta_{ij} - \nabla^{-2} \nabla_i \nabla_j$ takes out the divergence of the vector $\mathcal{A} e_j$. Here e_i are random numbers for which the probability distribution function is supposed to be Gaussian and isotropic:

$$\langle e_i(\mathbf{r}, t) \rangle = 0, \quad (18a)$$

$$\langle e_i(\mathbf{r}, t) e_j(\mathbf{r}', t') \rangle = \frac{1}{3} \delta_{ij} \delta(t - t') \delta_{\mathbf{r}, \mathbf{r}'}, \quad (18b)$$

Here, we focus on the discrete equations and consequently we have used the Kronecker symbol. In agreement with the arguments leading to relation (16), the two-point correlation vanishes for $\mathbf{r} \neq \mathbf{r}'$. Comparison of (17) and (18) with (10) shows that $H_{ij}(\mathbf{r}, \mathbf{r}') = P_{ik} P_{jk} \delta_{\mathbf{r}, \mathbf{r}'}/2$ and $A^2 = 2\mathcal{A}^2/3$. Thus, the energy input is:

$$\langle \mathcal{E}_f \rangle = \frac{1}{2} A^2 = \frac{1}{3} \mathcal{A}^2. \quad (19)$$

The variational problem can then be used to determine \mathcal{A} by minimizing

$$\mathcal{Z}[\mathcal{A}] = \int_V dy \left(\frac{\mathcal{A}^2}{3} - g \right)^2. \quad (20)$$

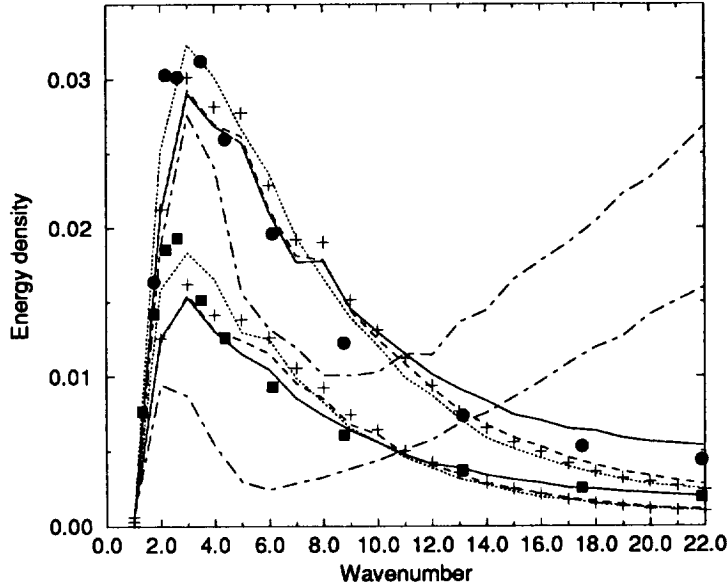


FIGURE 1. Time evolution of spectra in decaying isotropic turbulence — : DLM(k); +: DLM(+); ---- : DM; : DLM(S); -·-· : no model; ●: experiment (t=1.55); ■ : experiment (t=2.70).

Following the method used by Ghosal *et al.* (1993, 1994) this leads to

$$\mathcal{A}^2 = 3 [g]_+, \tag{21}$$

where $[x]_+ = (x + |x|)/2$. Thus, if we consider that the random numbers e_i are uncorrelated for different grid points, the DLM(S) is defined by (9) and (17) in which C has to be determined by the DLM(+), and the forcing amplitude \mathcal{A} is given by the explicit relation (21).

2.2 Results

The model described in the previous section has been extensively tested and compared to other models (the original dynamic model: DM; the constrained dynamic localization model: DLM(+), and the DLM(k)) for forced and decaying isotropic flows. We will not discuss in detail the conditions of these simulations which are the same as those presented in previous reports (Ghosal *et al.* 1993 and Ghosal 1993).

Fig. 1 shows the result of a simulation performed using 48 grid points in each direction. This seems to be the smallest simulation that would be consistent with the condition implicit in the idea of LES, viz., that the subgrid scales should carry significantly less energy than the resolved scales.

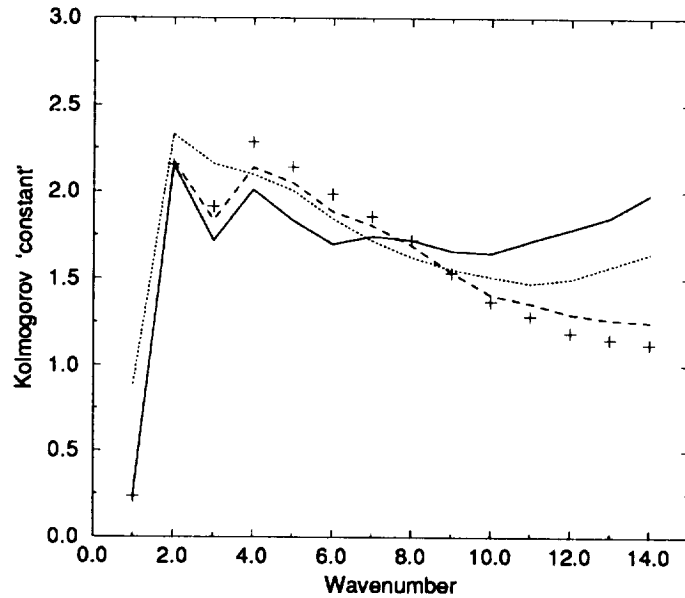


FIGURE 2. Prediction of Kolmogorov's 5/3 law and the Kolmogorov constant in forced isotropic turbulence at steady state — : DLM(k); +: DLM(+); ---- : DM; : DLM(S).

All four models predict decays in the resolved energy that are in good agreement with the experiment (Comte-Bellot and Corrsin 1971).

In the asymptotic self-similar regime the energy decays as a power law $E \sim t^{-\alpha}$. It is not clear that such a self similar regime is reached in the present experiment since only three experimental points are available. However, the three experimental points almost lie on a straight line on a log-log plot. The decay exponent is thus estimated to be $\alpha \approx 1.20$. A least-square fit to the LES data yields the values $\alpha = 1.27$, DM; $\alpha = 1.21$, DLM(+); $\alpha = 1.28$, DLM(k); $\alpha = 1.17$, DLM(S). The predictions of LES are in good agreement with the value estimated from the experiment. These values are slightly lower than those obtained in the higher resolution LES with spectral eddy viscosity by Métais & Lesieur (1992). Results of running the simulation with no subgrid-scale model are also presented.

The average energy spectrum $E(\kappa)$ is obtained in forced turbulence. Fig. 2 shows $C_\kappa = \epsilon^{-2/3} \kappa^{5/3} E(\kappa)$ plotted against the wavenumber κ . According to Kolmogorov's 5/3 law (Kolmogorov, 1941), C_κ should be a constant in the inertial range. It is seen that the dynamic models with backscatter agree better with the 5/3 law than the purely dissipative models. Our best estimates for the Kolmogorov constant based on DLM(k) and DLM(S) are $C_\kappa \approx 1.8$ and $C_\kappa \approx 1.6$ respectively. The experimentally measured values of C_κ are in the range 1.3 – 2.1 (Chasnov, 1991), though 1.5 is the

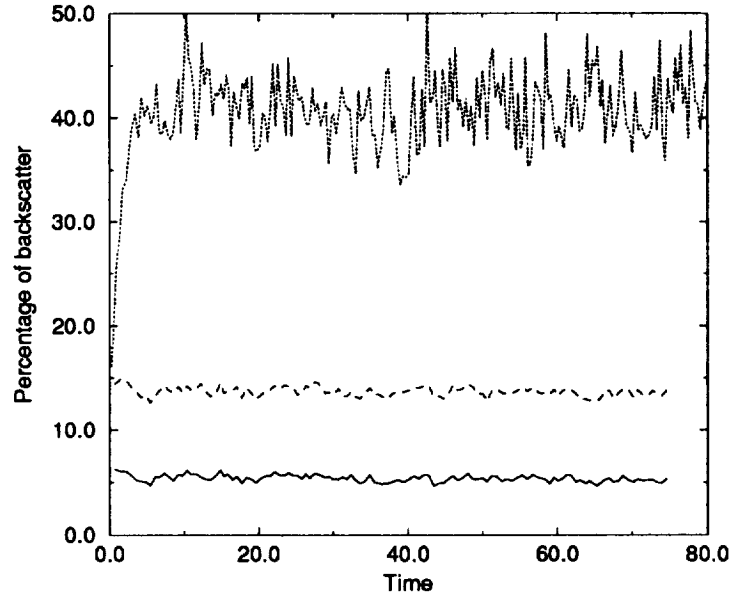


FIGURE 3. The level of backscatter as measured by energy transfer in forced isotropic turbulence at steady state — : DLM(k); : DLM(S) and ---- : as measured by fraction of points that have negative eddy-viscosity in DLM(k).

commonly accepted value (Saddoughi & Veeravalli, 1994). The spectra predicted by the DM and DLM(+) are almost identical to each other, and they seem to decay somewhat faster than the 5/3 law. As expected these models without backscatter seem to be too dissipative.

Fig. 3 shows the level of backscatter measured in two different ways. The solid line is the amount of energy being transferred from the subgrid to the large scales as a fraction of the net transfer as measured by

$$\frac{\int [\tau_{ij} \overline{S_{ij}}]_+ d^3 \mathbf{x}}{|\int \tau_{ij} \overline{S_{ij}} d^3 \mathbf{x}|} \quad \text{for the DLM(k)}$$

$$\frac{\mathcal{E}_f}{\mathcal{E}_{sgs} - \mathcal{E}_f} \quad \text{for the DLM(S)}$$

The dotted line is simply the fraction of grid points at which the Smagorinsky coefficient is positive (only for the DLM(k); in the DLM(S) C is constrained to be positive). Here, we notice a substantial difference between the two models accounting for backscatter. The deterministic DLM(k) predicts a much smaller amounts of backscatter than the stochastic DLM(S).

3. Future plans

The first test of the DLM(S) has shown that this model is able to reproduce most of the feature of isotropic turbulence. However, the way backscatter is accounted for does not seem to play a major role in the present simulations. The main difference in the predictions obtained by these models concerns the rate of backscatter which is significantly higher in the DLM(S) than in the DLM(k). However, it may be unsafe to conclude that one of the models performs better from this difference. Indeed, there is not a lot of measurement of backscatter rate, and in addition, this rate has been shown to be filter-dependent in DNS (Piomelli *et al.* 1991). Other performances of these two model are similar.

DLM(S) is cheaper to implement, but the DLM(k) provides more information since it predicts the subgrid-scale energy as well as the pressure. Complex flows could differentiate further between these models, and the next step in the validation of the stochastic model will be to implement it for more complex geometries. Preliminary work in the channel flow (Cabot, 1994) has shown that a slightly modified version of the DLM(S) from which the pressure totally disappears could be implemented more easily than the formulation presented here. The advantage of developing a model without explicit need of the pressure is obvious in complex geometries in which the pressure has to be obtained by a "Poisson solver". We thus plan to further develop this modified version of the DLM(S). Further tests in channel flows and mixing layer should follow.

Acknowledgments

The computer code used to perform these tests was developed by modifying a basic Navier-Stokes solver given to us by Dr. Nagi Mansour. We would also like to thank Dr. Thomas Lund for his help with certain aspects of the software and for many useful discussions.

REFERENCES

- CABOT, W. 1994 private communication.
- CHASNOV, J. 1991 Simulation of the Kolmogorov inertial subrange using an improved subgrid model. *Phys. Fluids A*, **3**, 188.
- COMTE-BELLOT, G. & CORRISIN, S. 1971 Simple Eulerian time correlations of full and narrow band velocity signals in grid generated 'isotropic' turbulence. *J. Fluid Mech.* **48**, 273.
- GERMANO, M., PIOMELLI, U., MOIN, P., & CABOT, W. 1991 A dynamic subgrid-scale eddy-viscosity model. *Phys. Fluids A*, **3**, 1760.
- GHOSAL, S. 1993 On the large-eddy simulation of turbulent flows in complex geometries. In *Annual Research Briefs-1993*, Center for Turbulence Research, NASA Ames/Stanford Univ.
- GHOSAL, S., LUND, T., & MOIN, P. 1993 A local dynamic model for LES. In *Annual Research Briefs-1992*, Center for Turbulence Research, NASA Ames/Stanford Univ.

- GHOSAL, G., LUND, T., MOIN, P., & AKSELVOLL, K. 1994 The Dynamic Localization Model for large-eddy simulation of turbulent flows. *J. Fluid Mech.* To appear.
- KOLMOGOROV, A. 1941 Local Structure of Turbulence in an Incompressible Fluid at Very High Reynolds Numbers. *Dokl. AN SSSR.* **30**, 299.
- KRAICHNAN, R. 1976 Eddy Viscosity in Two and Three Dimensions. *J. Atmos. Sci.* **33**, 1521.
- LEITH, C. 1990 Stochastic backscatter in a subgrid-scale model: Plane shear mixing layer. *Phys. Fluids A.* **2**, 297.
- LESLIE, D. & QUARINI, G. 1979 The Application of Turbulence Theory to the Formulation of Subgrid Modeling Procedures. *J. Fluid Mech.* **91**, 65.
- MASON, P. & THOMSON, D. 1992 Stochastic backscatter in large-eddy simulations of boundary layers. *J. Fluid Mech.* **242**, 51.
- MÉTAIS, O. & LESIEUR, M. 1992 Spectral large-eddy simulation of isotropic and stably stratified turbulence. *J. Fluid Mech.* **239**, 157.
- PIOMELLI, U., CABOT, C., MOIN, P., & LEE, S. 1991 Subgrid-scale back-scatter in turbulent and transitional flows. *Phys. Fluids A.* **3**, 1766.
- SADDOUGHI, S. & VEERAVALLI, S. 1994 Local isotropy in turbulent boundary layers at high Reynolds number. *J. Fluid Mech.* **268**, 333.
- SMAGORINSKY, J. 1963 General circulation experiments with the primitive equations. *Mon. Weather Rev.* **91**, 99.

Large-eddy simulation of a plane wake

By S. Ghosal AND M. Rogers¹

1. Motivation and objectives

In a previous report (Ghosal *et al.*, 1992, 1994) the theoretical development leading to the dynamic localization model (DLM) for large-eddy simulation (LES) was presented. The method has been successfully applied to isotropic turbulence (Ghosal *et al.*, 1992, 1993, 1994, Carati *et al.*, 1994 - see also the report in this volume), channel flow (Cabot, 1993 - see also the report in this volume) and the flow over a backward-facing step (Akselvoll & Moin, 1993a & b). Here we apply the model to the computation of the temporally developing plane wake. The two main objectives of this project are:

(A) Use the model to perform an LES of a time developing plane wake and compare the results with direct numerical simulation (DNS) data to see if important statistical measures can be reliably predicted. Also, to provide a relative evaluation of the several versions of the model in terms of predictive capability and cost.

(B) If the tests in (A) show that the model generates reliable predictions, then use the LES to study various aspects of the physics of turbulent wakes and mixing layers.

According to the notation introduced earlier (see the references above), we recognize four versions of DLM:

(1) Dynamic model (DM): Special case of the DLM applicable only to flows with homogeneous directions.

(2) Dynamic localization model (constrained) [DLM(+)]: A limited version of the more general DLM, explicitly prevents backscatter by enforcing a positivity requirement on the Smagorinsky coefficient.

(3) Dynamic localization model (k-equation) [DLM(k)]: Extended version of DLM that incorporates backscatter by introducing a budget equation for the sub-grid kinetic energy.

(4) Dynamic localization model (stochastic) [DLM(S)]: Alternate extension of DLM that incorporates backscatter by a stochastic term.

Tests of the DM and DLM(+) will be presented in this report. The more elaborate models DLM(k) and DLM(S) that incorporate backscatter have not yet been tested for this flow. In the next section we briefly review the two versions of the model tested. No derivations are presented here; the reader is referred to the appropriate references (Ghosal *et al.*, 1992, 1994, and references therein) for the underlying theory.

¹ NASA Ames Research Center

2. Accomplishments

2.1 Background

2.1.1 The dynamic model (DM)

In its present form, the dynamic model can be written in the following way. For homogeneous turbulence the coefficient C is constant in space (but it may be time dependent) and is given by

$$C(t) = \frac{\langle m_{ij} L_{ij} \rangle}{\langle m_{kl} m_{kl} \rangle}. \quad (1)$$

Here $L_{ij} = \widehat{u_i u_j} - \widehat{u_i} \widehat{u_j}$ is the Leonard term and $m_{ij} = \Delta^2 \widehat{|\widehat{S}}| \widehat{S}_{ij} - \widehat{\Delta}^2 \widehat{|\widehat{S}}| \widehat{S}_{ij}$, where $\widehat{u_i}$ and \widehat{S}_{ij} are the filtered velocity and strain rates and the ‘hat’ denotes the “test filtering” operation:

$$\widehat{f}(\mathbf{x}) = \int G(\mathbf{x}, \mathbf{y}) f(\mathbf{y}) d\mathbf{y}. \quad (2)$$

The ‘grid-level’ filter-width is Δ (usually taken to be of the order of the grid spacing) and $\widehat{\Delta}$ ($\widehat{\Delta} > \Delta$) is the ‘test-level’ filter-width. The angular brackets denote averaging over the volume of the domain.

For flows that are not completely homogeneous but have one or two homogeneous direction(s) the DM can still be applied *provided one assumes that the “test filtering” operation is performed only in the homogeneous direction(s)*. Such an assumption can be justified if the grid in the inhomogeneous direction(s) is so fine that the flow is fully resolved in that direction, but in general it is not strictly valid. If one considers a flow (such as the plane wake considered in this report) that is homogeneous in the $x - z$ plane but inhomogeneous in y , then the DM can be written as

$$C(y, t) = \frac{\langle m_{ij} L_{ij} \rangle_{xz}}{\langle m_{kl} m_{kl} \rangle_{xz}}. \quad (3)$$

where the angular brackets now denote averaging over the homogeneous $x - z$ planes.

A serious problem with the DM is that it can be applied only to homogeneous flows or (under additional assumptions) to flows with at least one homogeneous direction. This deficiency is removed by the DLM described next.

2.1.2 The dynamic localization model: constrained [DLM(+)]

In DLM(+) one obtains $C(\mathbf{x})$ as a function of position at each time-step by solving an integral equation

$$C(\mathbf{x}) = \left[f(\mathbf{x}) + \int \mathcal{K}(\mathbf{x}, \mathbf{y}) C(\mathbf{y}) d\mathbf{y} \right]_+ \quad (4)$$

where the suffix “+” indicates the positive part and

$$f(\mathbf{x}) = \frac{1}{\alpha_{kl}(\mathbf{x}) \alpha_{kl}(\mathbf{x})} \left[\alpha_{ij}(\mathbf{x}) L_{ij}(\mathbf{x}) - \beta_{ij}(\mathbf{x}) \int L_{ij}(\mathbf{y}) G(\mathbf{y}, \mathbf{x}) d\mathbf{y} \right], \quad (5)$$

$$\mathcal{K}(\mathbf{x}, \mathbf{y}) = \frac{\mathcal{K}_A(\mathbf{x}, \mathbf{y}) + \mathcal{K}_A(\mathbf{y}, \mathbf{x}) - \mathcal{K}_S(\mathbf{x}, \mathbf{y})}{\alpha_{kl}(\mathbf{x})\alpha_{kl}(\mathbf{x})}, \quad (6)$$

$$\mathcal{K}_A(\mathbf{x}, \mathbf{y}) = \alpha_{ij}(\mathbf{x})\beta_{ij}(\mathbf{y})G(\mathbf{x}, \mathbf{y}) \quad (7)$$

and

$$\mathcal{K}_S(\mathbf{x}, \mathbf{y}) = \beta_{ij}(\mathbf{x})\beta_{ij}(\mathbf{y}) \int G(\mathbf{z}, \mathbf{x})G(\mathbf{z}, \mathbf{y}) d\mathbf{z}. \quad (8)$$

In these expressions $G(\mathbf{x}, \mathbf{y})$ is the “test filter” $\alpha_{ij} = -2\widehat{\Delta}^2|\widehat{S}|\widehat{S}_{ij}$, $\beta_{ij} = -2\Delta^2|\overline{S}|\overline{S}_{ij}$ and L_{ij} is the Leonard term.

The principal weakness of DLM(+) (as well as the DM) is that the restriction of C to only positive values is somewhat contrived because it does not account for backscatter. However, unlike the DM, the DLM(+) is completely general and can be applied to arbitrary inhomogeneous flows.

2.1.3 The problem of the temporally developing wake

In a temporally developing wake the flow is statistically homogeneous in the streamwise (x) and spanwise (z) directions and inhomogeneous in the normal (y) direction. The governing equations are the incompressible Navier-Stokes equations with periodic boundary conditions in x and z . In the y -direction the domain is infinite and the velocity field is assumed to asymptotically approach the free-stream velocity, which can be taken as zero in a suitably chosen reference frame. This system can be considered to be an approximation to the physically more interesting spatially developing wake. If one imagines a ‘box’ being advected downstream at the ‘free-stream’ velocity, then the motion of the fluid in the imaginary box approximates a temporally developing wake. The integrated mass flux deficit

$$\mu = - \int_{-\infty}^{+\infty} \delta U(y) dy \quad (9)$$

is conserved in a temporally developing wake, as opposed to the momentum flux deficit

$$\mu_* = - \int_{-\infty}^{+\infty} (U_\infty + \delta U(y))\delta U(y) dy, \quad (10)$$

which is conserved for a spatially developing wake. Clearly, if the mean velocity deficit δU is small compared to the free stream velocity U_∞ , then $\mu_* \approx U_\infty\mu$. A suitable scale for the velocity is the initial centerplane velocity deficit $\delta U_0 = -(\delta U(0))_{t=0}$ and a suitable length scale is then $\mu/\delta U_0$. The corresponding time scale is $\mu/(\delta U_0)^2$. We will quote most of our results in these units.

2.2 Computational methods

The numerical method used is a spectral method in vorticity variables. Both the velocity and vorticity are periodic in the x and z directions and can therefore be expanded in a basis of trigonometric functions for these variables. The y -direction is somewhat more difficult to deal with since the domain is infinite in y . One

method is to choose a basis of functions that have an infinite support (such as the Jacobi polynomials coupled with a mapping to the infinite interval) for the y -direction (Spalart *et al.*, 1991). However, here we use a trick that leads to a simpler code. We take advantage of the fact that in a wake the vorticity field is much more confined in the y direction than the velocity field. One then expands the vorticity in a trigonometric series in y defined over (y_{min}, y_{max}) with periodic boundary conditions. This is permissible provided that the vorticity is narrowly confined around $y = 0$ and effectively decays to zero at the boundaries y_{min} and y_{max} . The velocity field is not so confined and cannot be represented in terms of these trigonometric functions. But once the vorticity field is determined, the correct velocity field may be obtained by adding a potential “correction” to the periodic velocity field associated with the vorticity field so as to match the boundary conditions at $y = \pm\infty$. Further details of the computational method may be found in Corral and Jimenez (1993). The method of solving the integral equation to determine the coefficient C has been described elsewhere (Ghosal *et al.*, 1992, 1994). The test filter width in these computations was taken to be twice the grid-filter width, $\hat{\Delta} = 2\Delta$, and a ‘top-hat’ filter was used with a Simpson’s rule quadrature.

For initial conditions we take two realizations of ‘turbulence over a flat plate’ from DNS data generated by Spalart (1988) and ‘sandwich’ them to produce a wake. Physically this corresponds to a situation where two independent boundary layers exist on either side of a rigid plate and the plate is instantaneously “dissolved” without disturbing the surrounding fluid. All the parameters in the LES are chosen so as to correspond to the “unforced wake” case of Moser and Rogers (1994) mentioned above.

The LES reported here was performed on a grid of size $N_x = 64$, $N_y = 48$, and $N_z = 16$. Therefore, all DNS data must first be ‘filtered’ to the same resolution as the LES. This is done by truncating the DNS data in Fourier space to the same number of modes retained in the LES. This filtering procedure is applied to the initial conditions as well as to all DNS data with which we wish to compare our LES results. The ‘filtered DNS’ represents the theoretical best that can be achieved by any LES. The LES with DM took about 11 minutes of CPU time. For the DLM(+) the CPU time depended on the level of convergence required for the solution of the integral equation. We measured the degree of convergence by the rms error in satisfying the integral equation normalized by the maximum value of $\langle C \rangle_{zz}$. When it was required that the error as defined above should not exceed 10^{-4} , the DLM(+) used about 18 minutes of CPU time. To test if this level of convergence was adequate, the simulation was rerun with the convergence criterion set at 10^{-9} . There were no observable differences in any of the computed statistical measures. For comparison, the high resolution DNS of Moser and Rogers of the same flow over the same time interval cost about 200 CPU hours. All computations were performed on a CRAY C90.

2.3 Results

The gross features of the wake are characterized by the maximum wake deficit δU_m of the mean velocity profile and the ‘half-width’ b of the wake. The half-width

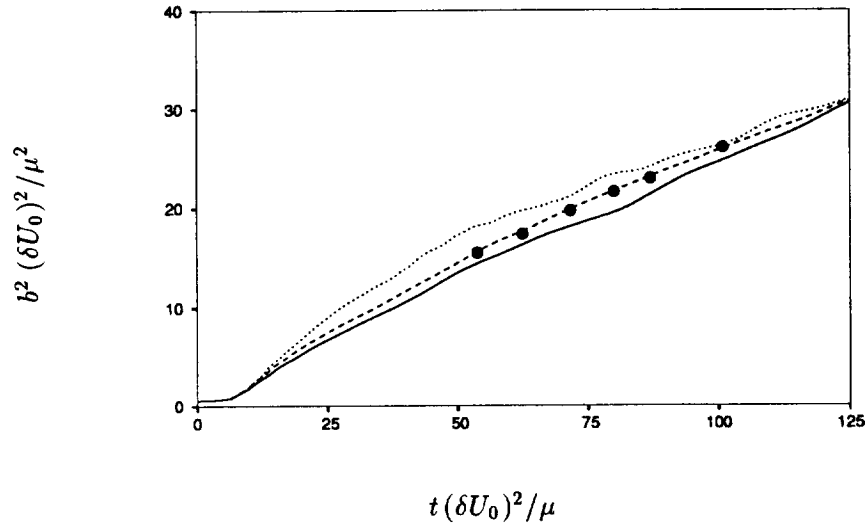


FIGURE 1. The square of the wake-width as a function of time using DLM(+) —; DM - - -; No model ·····; filtered DNS ●

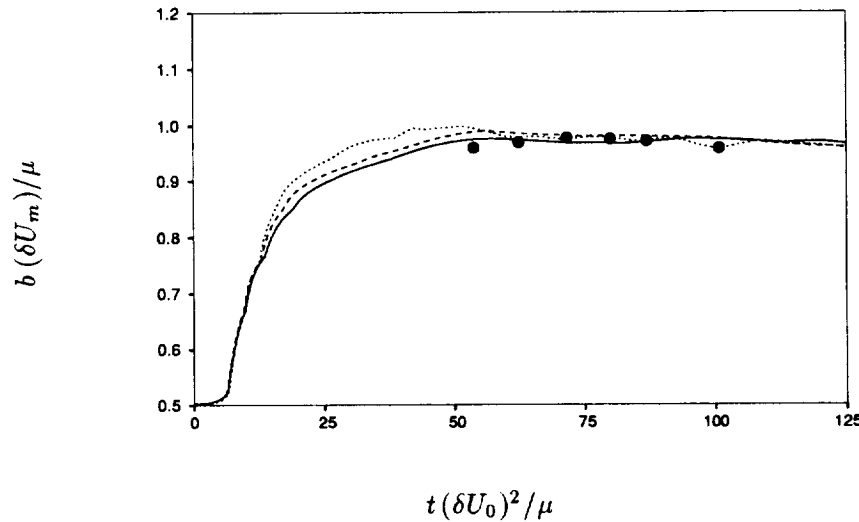


FIGURE 2. The product of the wake-width and the maximum velocity deficit as a function of time using DLM(+) —; DM - - -; No model ·····; filtered DNS ●

is defined here as the distance between the two points at which the mean velocity deficit is half its maximum value. Fig. 1 shows b^2 plotted as a function of the time t for the LES, filtered DNS, and LES with the subgrid model turned off. The prediction of the DM is closest to the filtered DNS. The width grows as $b \sim \sqrt{t}$

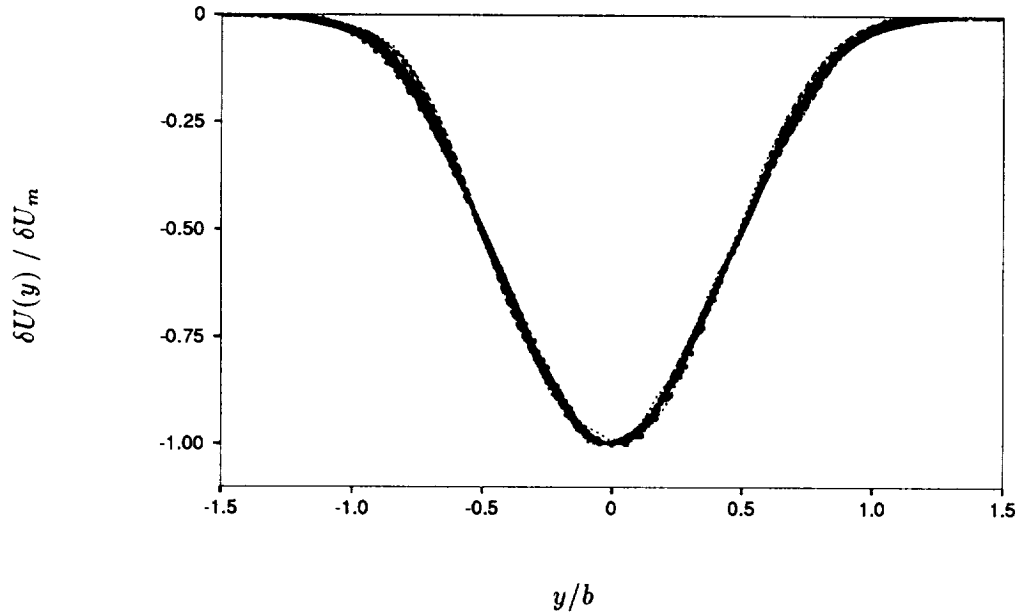


FIGURE 3. The mean wake velocity deficit in self-similar coordinates using DLM(+) —+—; DM — — —; No model ·····; filtered DNS ●

in the self-similar region ($t(\delta U_0)^2/\mu \approx 50 - 100$) as expected. Fig. 2 shows the product $b(\delta U_m)$ as a function of t . In all cases this quantity exhibits a plateau during the self-similar period. Note that the Reynolds number $Re_b = b\delta U_m/\nu = 2000b\delta U_m/\mu \approx 2000$ in the self-similar period.

Fig. 3 shows the mean velocity profile plotted in self-similar coordinates $\delta U_* = \delta U/\delta U_m$ and $y_* = y/b$ for $t(\delta U_0)^2/\mu \approx 50 - 100$. In all cases very good self-similar collapse is observed (even with the subgrid model turned off!). Thus, the mean velocity profile is quite insensitive to the subgrid model.

Figs. 4 (A), (B), (C), and (D) show the second-order velocity statistics $\langle u^2 \rangle$, $\langle v^2 \rangle$, $\langle w^2 \rangle$, and $\langle uv \rangle$ respectively. Here u , v , and w are the velocities in the x , y , and z directions, respectively, with the mean velocity subtracted out. The angular brackets denote averaging over $x - z$ planes. In all cases it is observed that both the DM and DLM(+) predict the second-order statistics very well. The quality of the predictions deteriorates significantly if the model is turned off (except for $\langle uv \rangle$). The better agreement for the $\langle uv \rangle$ profile is to be expected since it is directly related to the mean velocity profile $\delta U(y)$ through the x -component of the momentum equation and we have already seen that $\delta U(y)$ is insensitive to the subgrid model.

Figs. 5 (A), (B), (C), and (D) show the second-order vorticity statistics $\langle \omega_x^2 \rangle$, $\langle \omega_y^2 \rangle$, $\langle \omega_z^2 \rangle$, and $\langle \omega_x \omega_y \rangle$ respectively. Here ω_x , ω_y , and ω_z are the vorticities in the x , y , and z directions, respectively, with the mean vorticity subtracted out. The angular brackets denote averaging over $x - z$ planes. The agreement of the DM as well as the DLM(+) predictions with the filtered DNS is seen to be very good. When the

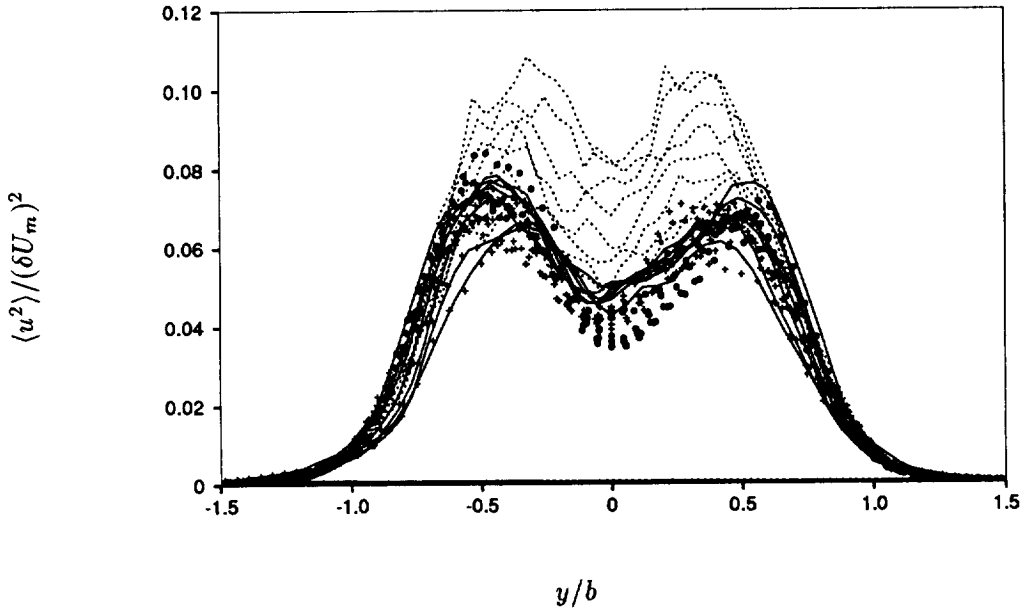


FIGURE 4A. The mean streamwise intensity of turbulence in self-similar coordinates using DLM(+) +; DM —; No model ·····; filtered DNS •

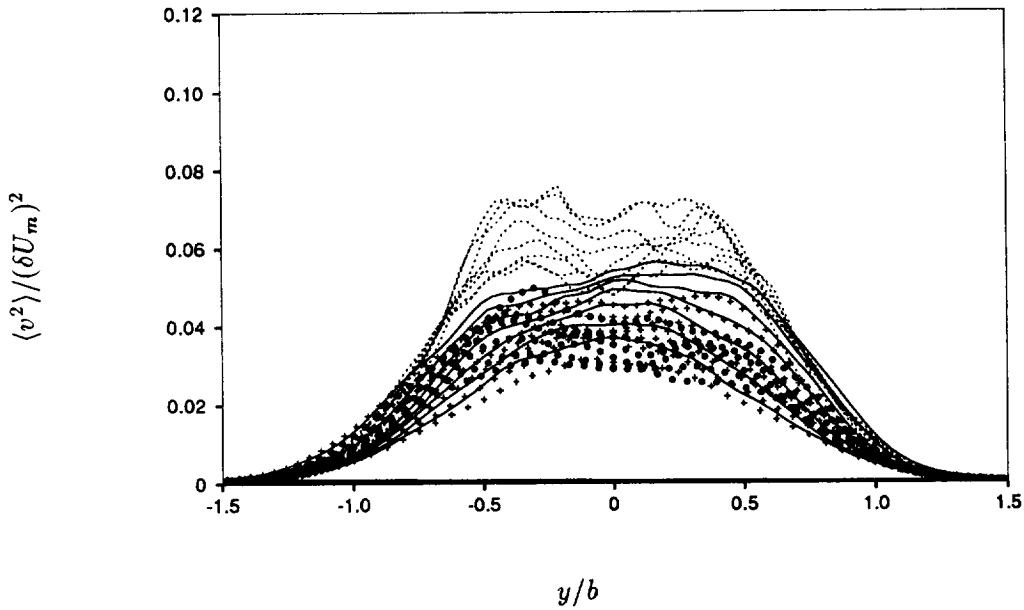


FIGURE 4B. The mean cross-stream intensity of turbulence in self-similar coordinates using DLM(+) +; DM —; No model ·····; filtered DNS •

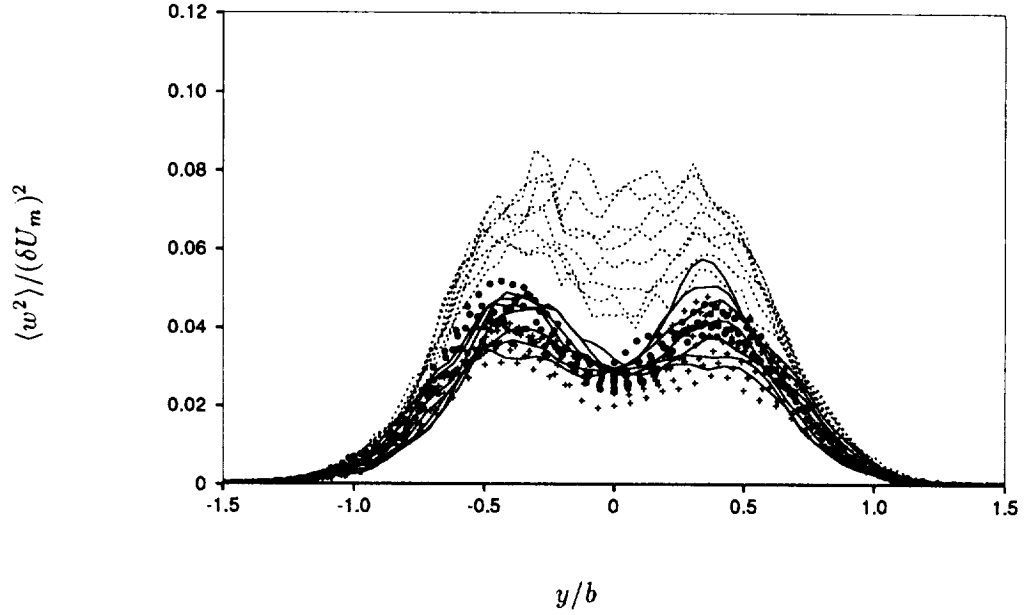


FIGURE 4C. The mean spanwise intensity of turbulence in self-similar coordinates using DLM(+) +; DM —; No model ·····; filtered DNS •

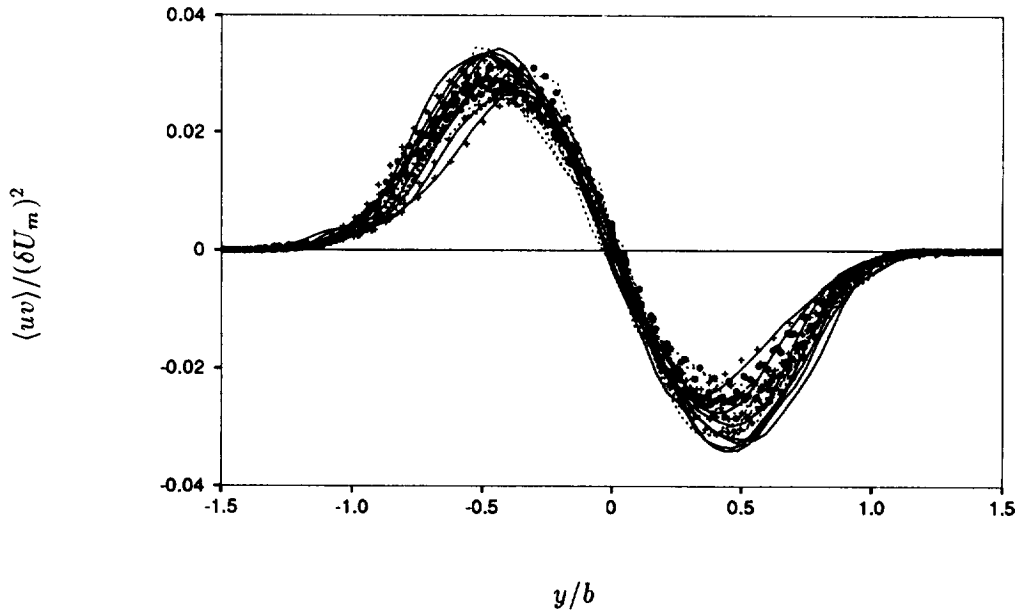


FIGURE 4D. The mean turbulent stress uv in self-similar coordinates using DLM(+) +; DM —; No model ·····; filtered DNS •

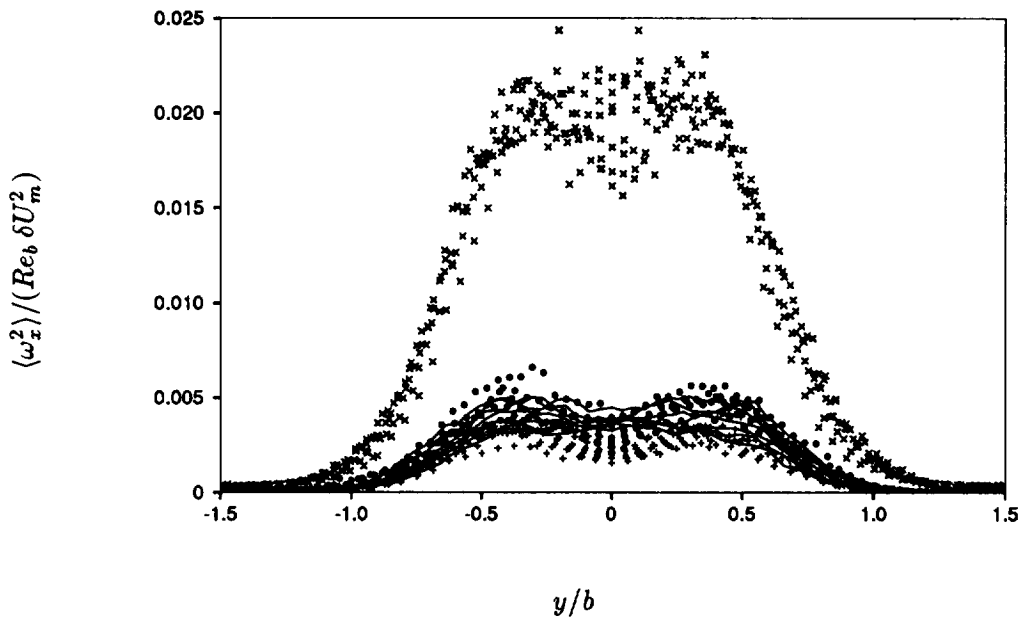


FIGURE 5A. The mean intensity of streamwise vorticity in self-similar coordinates using DLM(+) +; DM —; No model x; filtered DNS •

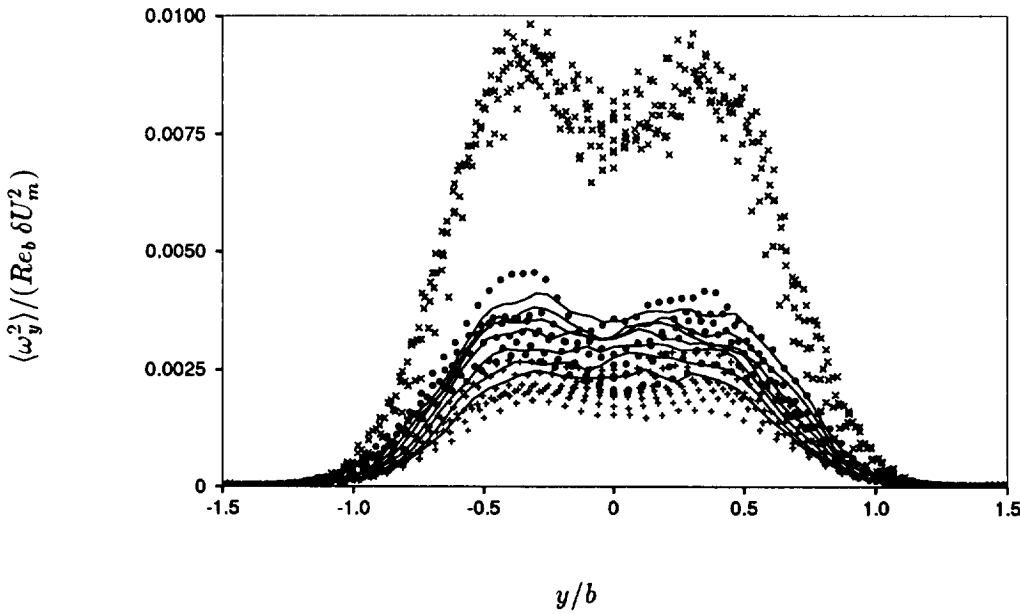


FIGURE 5B. The mean cross-stream intensity of vorticity in self-similar coordinates using DLM(+) +; DM —; No model x; filtered DNS •

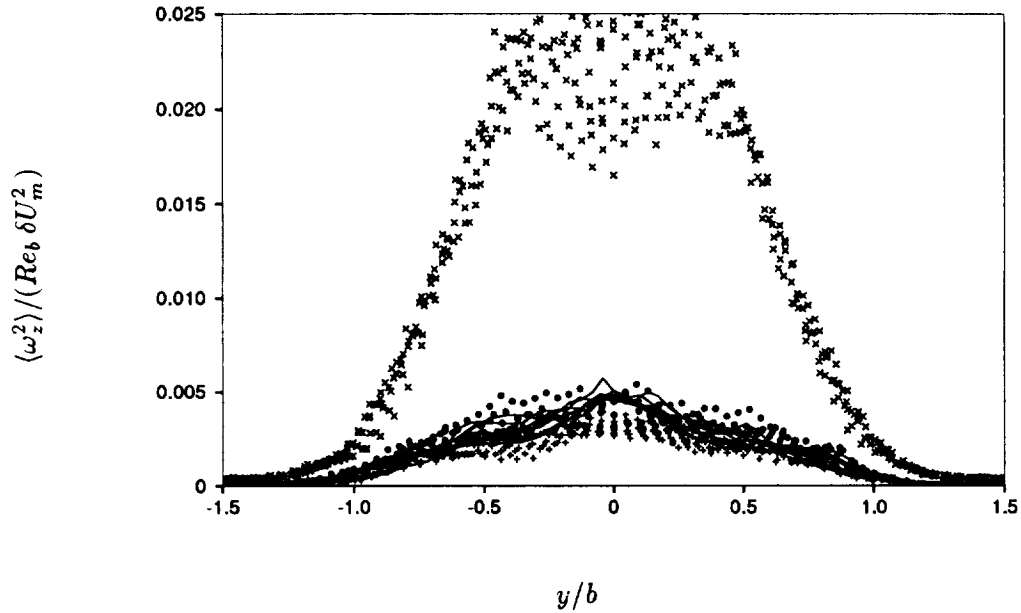


FIGURE 5C. The mean spanwise intensity of vorticity in self-similar coordinates using DLM(+) +; DM —; No model x; filtered DNS •

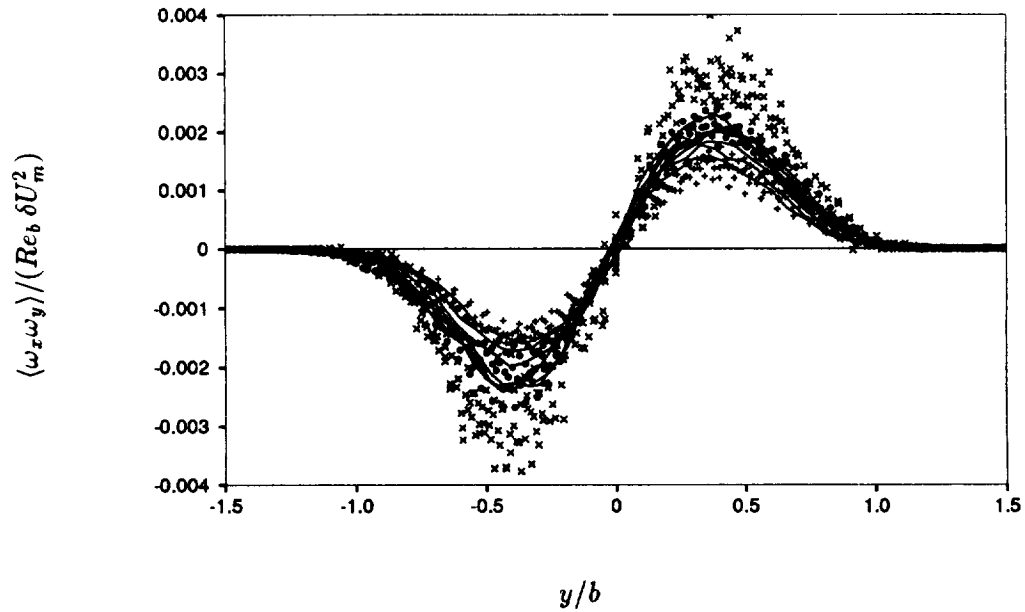


FIGURE 5D. The mean vorticity product $\omega_x \omega_y$ in self-similar coordinates using DLM(+) +; DM —; No model x; filtered DNS •

model is turned off the agreement with the filtered DNS is seen to be very poor. The magnitudes of the enstrophy components are about four times the corresponding filtered DNS levels. Here one might ask if it is reasonable or useful to use an LES to predict vorticity statistics since it is known that small scales not resolved by LES are the primary contributors to enstrophy. Indeed, $\langle \omega_x^2 \rangle$, $\langle \omega_y^2 \rangle$, and $\langle \omega_z^2 \rangle$ for the filtered DNS are about a fifth of their levels in the unfiltered DNS. However, good prediction of vorticity statistics is important because these statistics are a sensitive measure of the scales close to the threshold of resolution of the LES. The fact that even vorticity statistics are captured by the LES suggests that all of the resolved scales and not just the lowest wavenumber modes are faithfully represented in the simulation. Thus, we use vorticity statistics as a “quality indicator” of the LES rather than as a quantity of practical importance to the user.

In Figs. 4 and 5 it is apparent that the self-similar collapse is not perfect but that there is a systematic variation between the curves at different times in the simulation, even when scaled in self-similar variables. This is the case not only for the LES, but also for the filtered DNS. This is an artifact of the filtering procedure itself and can be understood in the following way. The flow evolves self-similarly at constant Reynolds number $Re_b = b(\delta U_m)/\nu$ (see Fig. 2) in the self-similar region but the length scales increase in time. Thus, as the flow evolves, the energy spectrum shifts to the left without changing form. Since the grid size is held fixed, this implies that more and more of the energy becomes ‘resolved’ as the spectrum shifts to lower wavenumbers past $\bar{k} = 2\pi/\Delta$. Therefore the resolved part of the second-order statistics increases with time. This is precisely what is observed in the filtered DNS and LES data and is responsible for the systematic increasing trend during the self-similar period.

In addition to obtaining quantitative predictions, one also hopes to gain some qualitative understanding of the large-scale flow structures from an LES. Thus, it is of interest to see if the model is able to generate structures that look realistic. As an example a typical contour plot of the v -velocity is presented in Fig. 6 over an $x-y$ plane. It is seen that Fig. 6(C) (LES with model) bears an overall resemblance to Fig. 6(B) (filtered DNS) in the sense that it has a similar number of ‘eddies’ of approximately similar size and shape. However, Fig. 6(D) (LES without model) looks qualitatively different from Fig. 6(B) in the sense that it has a profusion of poorly resolved small-scale structures. A similar statement can be made about the other flow variables. The times at which the contours are shown in Fig. 6 for the DNS and LES do not correspond exactly, but they are close, varying from $t(\delta U_0)^2/\mu \approx 62.4$ to 66.3, and are in the developed region (see Fig. 1).

It may appear that even though the no-model case (Fig. 6(D)) has far too many small-scale fluctuations compared to the filtered DNS (Fig. 6(B)), it does resemble somewhat the full DNS of Fig. 6(A). That this is not the case becomes clear on examination of the energy spectrum. Fig. 7 shows the one-dimensional spectrum

$$q^2(k_x) = \sum_{k_z} (|\tilde{u}(k_x, k_z)|^2 + |\tilde{v}(k_x, k_z)|^2 + |\tilde{w}(k_x, k_z)|^2) \quad (11)$$

at the plane $y = 0$ for the same fields whose v -contour plots are shown in Fig. 6.

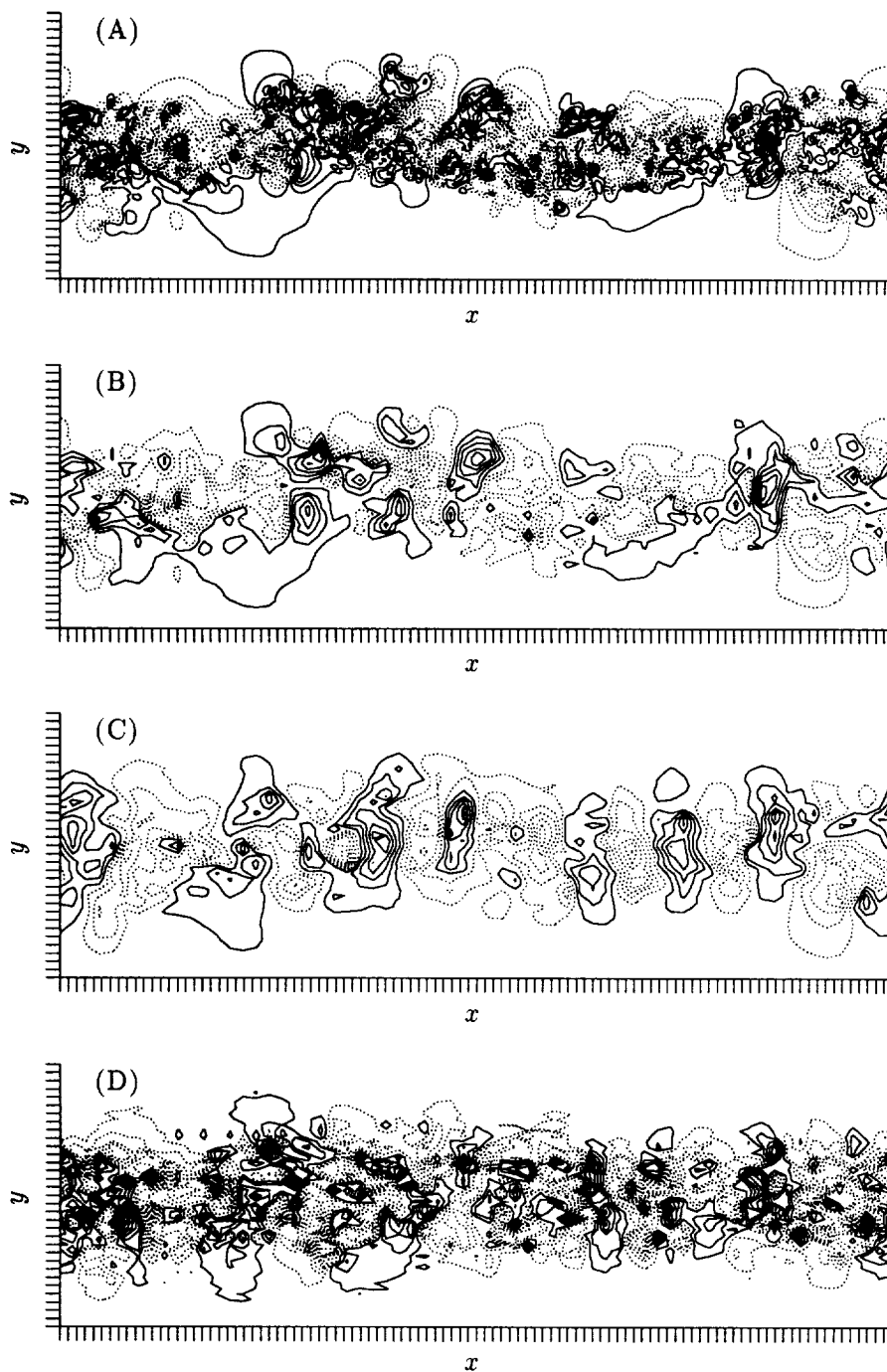


FIGURE 6. A typical iso-velocity contour plot for component v in the $x - y$ plane for (A) DNS (B) Filtered DNS (C), DLM(+) and (D) No model.

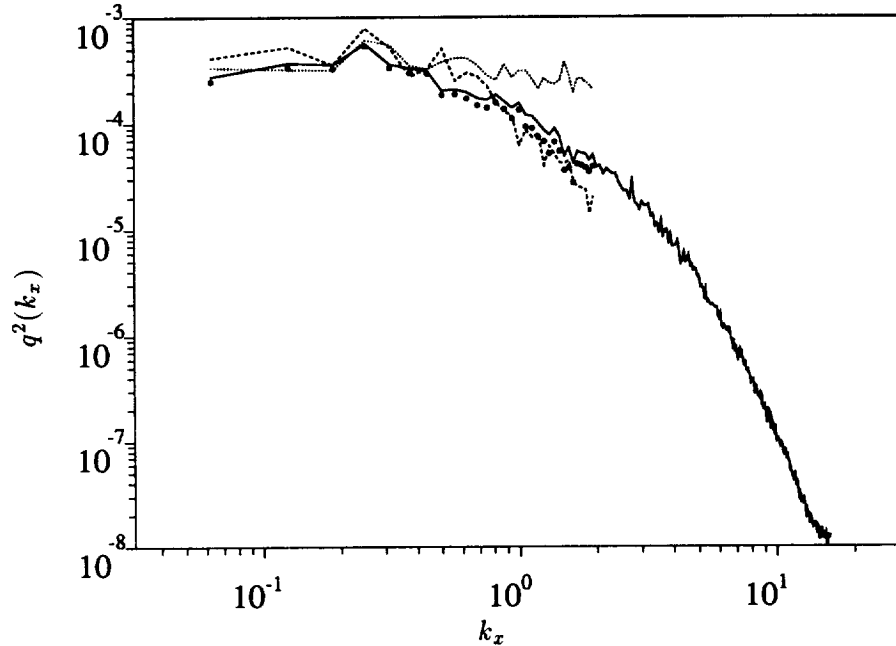


FIGURE 7. The ' q^2 -spectrum' (see text) for LES using DLM(+) - - -; using no model ·····; filtered DNS •; DNS —.

Here ' \sim ' denotes Fourier-transform in the $x-z$ plane. The filtered DNS is very close to, but slightly below (on account of filtering in the y -direction), the full DNS, up to the maximum k_x represented in the LES. The LES matches the filtered DNS closely. However, for the no-model case, energy piles up at the high wavenumbers because of the lack of a dissipation mechanism, and this results in a 'flat' rather than decaying energy spectrum. The small-scale fluctuations seen in Fig. 6(D) are a manifestation of this unphysical 'pile-up' of energy and have no relation to the true fine structure seen in the highly resolved DNS of Fig. 6(A). Indeed, it is quite impossible to reproduce the fine structure of the DNS with the vastly reduced number of modes in an LES, and the 'filtered' DNS is the ideal limit one can hope to achieve.

In summary, mean velocity profiles plotted in self-similar coordinates are very insensitive to the choice of subgrid models. The prediction of the self-similar growth of the wake width is improved by the subgrid model, but the results with no model are nevertheless tolerable. Second-order velocity and vorticity statistics are predicted very well by both the DM and DLM(+), but the predictions of these statistics without the model are very poor. The flow structures in the LES have a strong visual resemblance to those of the corresponding filtered DNS, but this is not the case if the LES is performed with no subgrid model. The LES represents a very significant saving in CPU time over the corresponding DNS. The results presented here suggest that LES can provide accurate predictions when information related to small-scale structures is not required.

3. Future plans

In generating the results presented in this report, the “test filter” was implemented only in the x and z directions. This was done as a first step because filtering only in the homogeneous directions is easiest to implement in the code. However, there are some serious difficulties associated with this. In situations where the grid spacings in all three directions are not the same, there is no unique way of defining the “grid-filter width” Δ . Some possible choices are

- (A) $\Delta = (\Delta_x \Delta_y \Delta_z)^{1/3}$
- (B) $\Delta = (\Delta_x^2 + \Delta_y^2 + \Delta_z^2)^{1/2}$
- (C) $\Delta = \max[\Delta_x, \Delta_y, \Delta_z]$
- (D) $\Delta = (\Delta_x \Delta_z)^{1/2}$.

The choice (D) may be thought of as a natural modification of (A) when $\Delta_y \ll \Delta_x, \Delta_z$. In this case (A) would give an unreasonably small length scale.

Now, if the filtering is done in all three directions, then $\hat{\Delta}_x = 2\Delta_x$, $\hat{\Delta}_y = 2\Delta_y$, and $\hat{\Delta}_z = 2\Delta_z$ so that all the possible choices (A), (B), (C), and (D) give the same value for the filter-width ratio $\hat{\Delta}/\Delta = 2$. It is easily shown that only the combination $C\Delta^2$ is computed in the dynamic model and that the grid and test filter-widths enter only as the ratio $\hat{\Delta}/\Delta$. Thus when the model is properly implemented with a 3D-filter, it is unaffected by the choice of filter-width definition. In fact, any filter width $\Delta = f(\Delta_x, \Delta_y, \Delta_z)$ where f is a homogeneous function (i.e. $f(a\Delta_x, b\Delta_y, c\Delta_z) = abc f(\Delta_x, \Delta_y, \Delta_z)$) will yield the same filter-width ratio. This is no longer true if the filtering is only done in $x - z$ planes as in the current simulations. In this case $\hat{\Delta}_x = 2\Delta_x$, $\hat{\Delta}_y = \Delta_y$, and $\hat{\Delta}_z = 2\Delta_z$, so that (C) and (D) give $\hat{\Delta}/\Delta = 2$. (A) gives $\hat{\Delta}/\Delta = 2^{2/3}$, and (B) gives a result that depends on the aspect ratio of the grid. In the simulations presented here we have chosen $\hat{\Delta}/\Delta = 2$, but the results change significantly if an alternate value for this ratio is used. These results should therefore be regarded as preliminary, and more careful tests using full 3D filtering need to be done before they can be considered reliable.

We would like to test two other versions of the dynamic localization model viz. DLM(k) and DLM(S). The first one accounts for backscatter by means of a budget equation for the subgrid kinetic energy (Ghosal *et al.*, 1992, 1994) while the second regards backscatter as a stochastic forcing. Apart from being able to represent backscatter (which may or may not be a significant effect), the DLM(k) has the additional advantage that it allows one to compute the full subgrid-stress tensor instead of simply the deviatoric part. This makes it possible to determine the resolved pressure, a quantity that cannot be determined if only the deviatoric part of the stress is known.

Both DNS and experiments on plane wakes show a range of growth rates that seem to be sensitive to initial conditions (Moser and Rogers, 1994). It has been proposed that this could be due to the existence of non-unique self-similar states, any one of which can be selected in a given realization depending on the initial conditions (George, 1989). In order to investigate such possible dependence on initial conditions, Moser and Rogers (1994) amplified the 2D components of the initial velocity field in their simulation. It has been found that it is possible to

significantly alter the growth rate by such “2D forcing”. We would like to check if LES is able to predict correctly the growth rates in such forced wakes. If it does, then LES can be used as a research tool to test whether alternate self-similar states are indeed sustained. This requires long-time simulations that are prohibitively expensive using current DNS.

We would like to thank Dr. Parviz Moin for his critical comments on an earlier version of this manuscript.

REFERENCES

- AKSELVOLL, K. & MOIN, P. 1993a Large-eddy simulation of a backward facing step flow. *2nd international symposium on engineering turbulence modeling and measurements*, Florence, Italy.
- AKSELVOLL, K. & MOIN, P. 1993b Application of the dynamic localization model to large-eddy simulation of turbulent flow over a backward facing step. *ASME Fluids engineering conference*, Washington D. C.
- CABOT, W. 1993 Dynamic localization and second-order subgrid-scale models in large-eddy simulations of channel flow. *Annual Research Briefs-1993* Center for Turbulence Research, Stanford Univ./NASA Ames, 129-144.
- CARATI, D., GHOSAL, S. & MOIN, P. 1994 On the representation of backscatter in dynamic localization models. *Phys. of Fluids* (submitted).
- CORRAL, R. & JIMENEZ, J. 1993 Fourier/Chebyshev methods for the incompressible Navier-Stokes equations in infinite domains. *J. Comp. Phys.* (to appear).
- GEORGE W. K. 1989 The self preservation of turbulent flows and its relation to initial conditions and coherent structure. *Advances in Turbulence*, Ed. W. K. George & R. Arndt (Hemisphere, New York).
- GHOSAL, S., LUND, T. S. & MOIN, P. 1992 A local dynamic model for large-eddy simulation. *Annual Research Briefs-1992* Center for Turbulence Research, Stanford Univ./NASA Ames, 3-25.
- GHOSAL S. 1993 On the large-eddy simulation of turbulent flows in complex geometry. *Annual Research Briefs-1992* Center for Turbulence Research, Stanford Univ./NASA Ames, 111-128.
- GHOSAL, S., LUND, T. S., MOIN, P. & AKSELVOLL, K. 1994 A dynamic localization model for large-eddy simulation of turbulent flows. *J. Fluid Mech.* (to appear).
- MOSER, R. D. & ROGERS, M. M. 1994 Direct simulation of a self-similar plane wake. *NASA Tech. Mem.* 108815.
- SPALART, P. R., MOSER, R. D. & ROGERS, M. M. 1991 Spectral methods for the Navier-Stokes equations with one infinite and two periodic directions. *J. Comp. Phys.* **96**, 297-324.
- SPALART, P. R. 1988 Direct simulation of a turbulent boundary layer up to $Re_\theta = 1410$. *J. Fluid Mech.* **187**, 61-98.

Local dynamic subgrid-scale models in channel flow

By W. Cabot

1. Motivation & objectives

The dynamic subgrid-scale (SGS) model (Germano *et al.*, 1991) has given good results in the large-eddy simulation (LES) of homogeneous isotropic or shear flow, and in the LES of channel flow, using averaging in two or three homogeneous directions (the DA model). In order to simulate flows in general, complex geometries (with few or no homogeneous directions), the dynamic SGS model needs to be applied at a local level in a numerically stable way. Channel flow, which is inhomogeneous and wall-bounded flow in only one direction, provides a good initial test for local SGS models. Tests of the dynamic localization model (Ghosal *et al.*, 1993) were performed previously in channel flow (Cabot, 1993) using a pseudospectral code (Kim *et al.*, 1987), and good results were obtained. Numerical instability due to persistently negative eddy viscosity was avoided by either constraining the eddy viscosity to be positive or by limiting the time that eddy viscosities could remain negative by co-evolving the SGS kinetic energy (the DLk model). The DLk model, however, was too expensive to run in the pseudospectral code due to a large near-wall term in the auxiliary SGS kinetic energy (k) equation. One objective was then to implement the DLk model in a second-order central finite difference channel code, in which the auxiliary k equation could be integrated implicitly in time at great reduction in cost, and to assess its performance in comparison with the plane-averaged dynamic model or with no model at all, and with direct numerical simulation (DNS) and/or experimental data.

Other local dynamic SGS models have been proposed recently, e.g., constrained dynamic models with random backscatter (Carati & Ghosal, in this volume), and with eddy viscosity terms that are averaged in time over material path lines rather than in space (Meneveau *et al.*, 1994). Another objective was to incorporate and test these models in channel flow.

2. Accomplishments

2.1 Dynamic localization models in a finite-difference channel code

2.1.1 Implementation & cases

Dynamic localization (DL) models (Ghosal *et al.*, 1993) were implemented in a finite-difference code with second-order central differencing on a staggered mesh and a third-order Runge-Kutta time integration and were used to simulate channel flow for different friction Reynolds numbers, $Re_\tau = u_\tau \delta / \nu$, where ν is the molecular viscosity, δ is the channel half-width, and the friction speed u_τ is the square root of

the wall stress. Simulations were also performed using the plane-averaged dynamic (DA) model and no model at all.

In the standard dynamic model, the residual Reynolds stress that appears in the Navier-Stokes equation,

$$\tau_{ij} = \overline{u_i u_j} - \bar{u}_i \bar{u}_j \quad (1)$$

(where the overbar denotes the grid filter) is modeled with a Smagorinsky base model ($-2C\Delta^2|\overline{\mathbf{S}}|\overline{\mathbf{S}}_{ij}$, where \mathbf{S} is the strain tensor and Δ the grid filter width). The dynamic coefficient C is found by minimizing the error between the ‘‘Germano identity’’,

$$L_{ij} = \widehat{\overline{u_i u_j}} - \widehat{\bar{u}_i \bar{u}_j} \quad (2)$$

and its model terms (the caret denoting a test filter at a coarser scale than the grid filter). The error is thus

$$E_{ij} = L_{ij} + 2C\Delta^2|\widehat{\overline{\mathbf{S}}}| \widehat{\overline{\mathbf{S}}}_{ij} - 2C\widehat{\Delta}^2|\widehat{\overline{\mathbf{S}}}| \widehat{\overline{\mathbf{S}}}_{ij}, \quad (3)$$

where, in practice, $\widehat{\Delta} = 2\Delta$ is chosen. In the DA model, C is a global coefficient (independent of the homogeneous directions) that is found algebraically by a simple least-squares minimization of error (Lilly, 1992). In the DL model, local values of C are found by a global minimization using an iterative procedure. In the constrained dynamic localization (DL+) model, the minimization is subject to the constraint that the dynamic coefficient not be negative. Except for one simulation case, no explicit filtering was performed in the inhomogeneous wall-normal direction, and the error minimization to determine the dynamic coefficient is always performed independently in individual horizontal planes. Tophat filters were used in all the cases discussed here.

In the unconstrained (DLk) model, an auxiliary equation for the SGS residual kinetic energy is evolved, which itself contains additional dynamic coefficients for diffusion and dissipation terms. In the finite difference code, the dissipation term in the k equation, $-C_k(\mathbf{x})k^{3/2}/\Delta$, was integrated implicitly from fractional time step j to $j+1$ by time-splitting only a linear factor of k in the expression with the remainder evaluated at the prior time step n , viz., $-1/2(k^{[j+1]} + k^{[j]})(C_k k^{1/2}/\Delta)^{[n]}$. Since $C_k \geq 0$, the latter term acts like a positive diffusion rate, making the implicit integration stable even for large time steps. As one expects physically, C_k varies roughly as y_w^{-3} near the walls; and, as found in the pseudospectral code, k varies roughly as y_w^2 even though the numerical boundary conditions only enforce a linear wall behavior (cf. Cabot, 1993).

2.1.2 Computational costs

With the DLk model, time steps approaching the convective CFL limit would now be possible with the partial implicit method were it not for large negative eddy viscosities that now arise and that must be integrated explicitly. This limits the time step, becoming a much more severe problem at higher Re_τ . For the DA and DL+ model, the (mostly) positive eddy viscosity is integrated implicitly and does

not affect the time step. The cost per time step using the DLk model (when the dynamic coefficients are computed at each time step) is about *twice* that for the DA model. At $Re_\tau = 400$, the time step also had to be 2.0 to 2.5 times smaller for the DLk model. At $Re_\tau = 1030$, the time step had to be reduced five-fold. Some expense was saved in this case by computing the dynamic coefficients every other time step. Also, fewer iterations were needed since the solution changed little from the prior time step. This resulted in the DLk simulations costing only 40% more per time step than with the DA model, hence making it seven times more expensive overall. At larger Re_τ , one can further reduce costs per step by computing dynamic coefficients at larger intervals, but the time step must still be taken increasingly smaller, which may more than offset any such savings. It appears, then, that the DLk model will generally be several times more expensive to run than simpler SGS models in this type of code.

2.1.3 LES results

Channel flow cases were examined using $Re_\tau = 180$ in a $4\pi \times 2 \times 4\pi/3$ domain (in units of δ) on $32 \times 65 \times 32$ and $64 \times 65 \times 64$ meshes (giving a spanwise resolution, in wall units, of $\Delta z^+ = Re_\tau \Delta z / \delta = 24$ and 12, respectively), and for $Re_\tau = 400$, 650, and 1030 in a $2\pi \times 2 \times 2\pi/3$ domain, on a $64 \times 65 \times 64$ mesh ($\Delta z^+ = 13$, 21, and 34, respectively).

All LES cases for $Re_\tau = 180$ on the coarse mesh ($32 \times 65 \times 32$) give mean streamwise velocities in wall units ($U^+ = U/u_\tau$) and streamwise fluctuation intensities (u_{rms}/u_τ) well in excess of the DNS results (Kim *et al.*, 1987), as seen in Fig. 1. (The DNS velocity fields were filtered by a tophat filter of the same width as the LES cases.) *Even with no model*, U^+ is slightly larger than that for DNS. Also note that no finite difference simulation at $Re_\tau = 180$ appears to give a flat log region. The DA model gives the worst overall results while the DLk model gives somewhat better results (DL+ results being intermediate). On a finer mesh ($64 \times 65 \times 64$) at $Re_\tau = 180$, it was found that SGS models have a much smaller effect (Fig. 2). Values of U^+ with no model and the DA model differ by about 6% in the log region, the latter agreeing quite well with DNS results, and the velocity intensities are also in good agreement with (filtered) DNS results. In contrast, the pseudospectral code for the same parameters and domain size on a $32 \times 65 \times 32$ mesh gives U^+ 15% below DNS results in the log region with no model and gives good agreement with the DNS results with any dynamic SGS model (Cabot, 1993). Conventional wisdom has it that spectral resolution is about twice that of finite differences on the same mesh, so the horizontal resolution for pseudospectral case should be comparable to that of the finite difference cases on the finer mesh shown in Fig. 2. (However, the wall-normal resolution for the Chebyshev expansion in the pseudospectral code and that for the second-order finite difference are probably different. Dealiasing is also usually employed in the homogeneous directions in the spectral codes.)

For $Re_\tau = 400$ (Fig. 3), the LES with no SGS model again gives U^+ about 6% below DNS (J. Kim, private communication) and the log law ($U^+ = 5.0 + 2.5 \ln y^+$); including the SGS models causes U^+ to rise close to the log law and DNS. Values of resolved velocity fluctuation intensities, with or without SGS models,

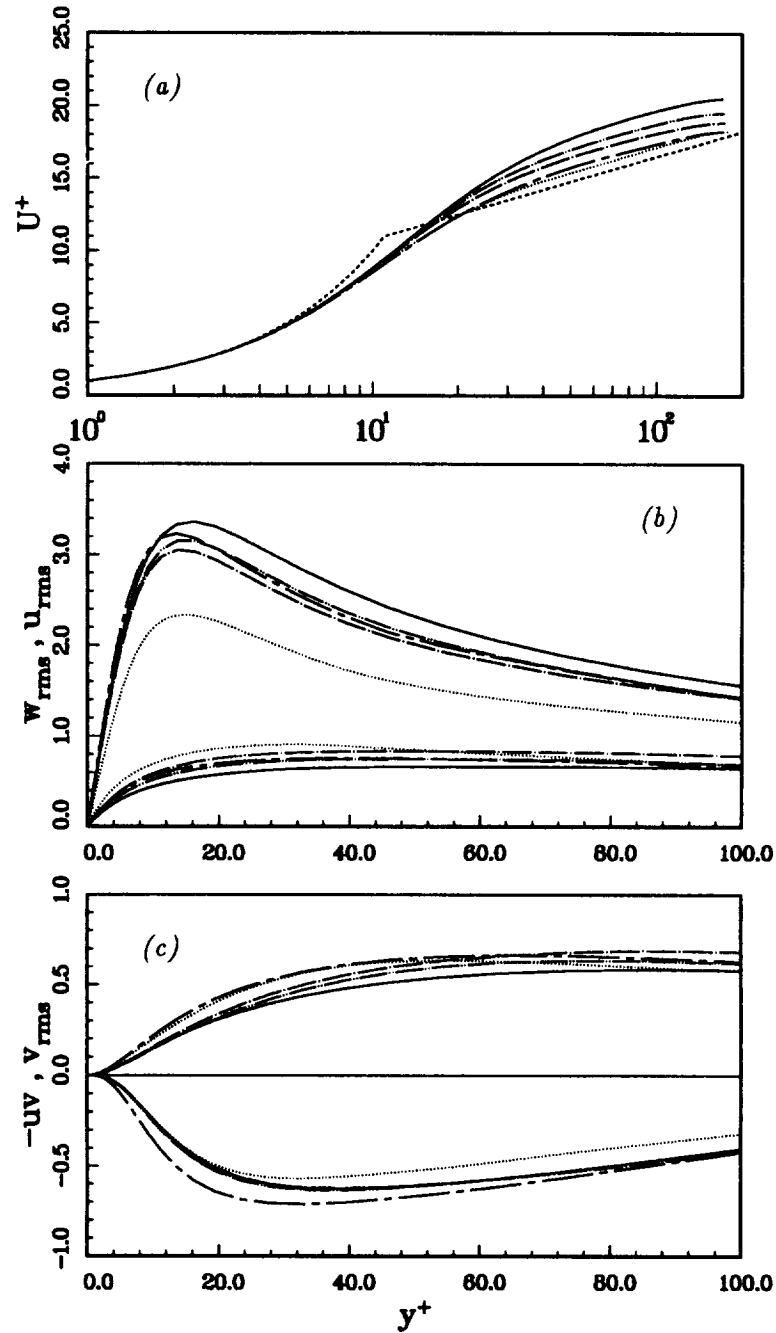


FIGURE 1. Mean streamwise velocity (a), resolved velocity intensities (b,c), and resolved Reynolds stress (c) for the LES of $Re_\tau = 180$ channel flow with the second-order finite difference code on a coarse mesh as functions of distance from the wall (all in wall units): ---- Log law, $U^+ = 5 + 2.5 \ln y^+$; DNS (filtered); and LES with ---- no SGS model, — DA model, -·-·- DL+ model, and -·-·- DLk model.

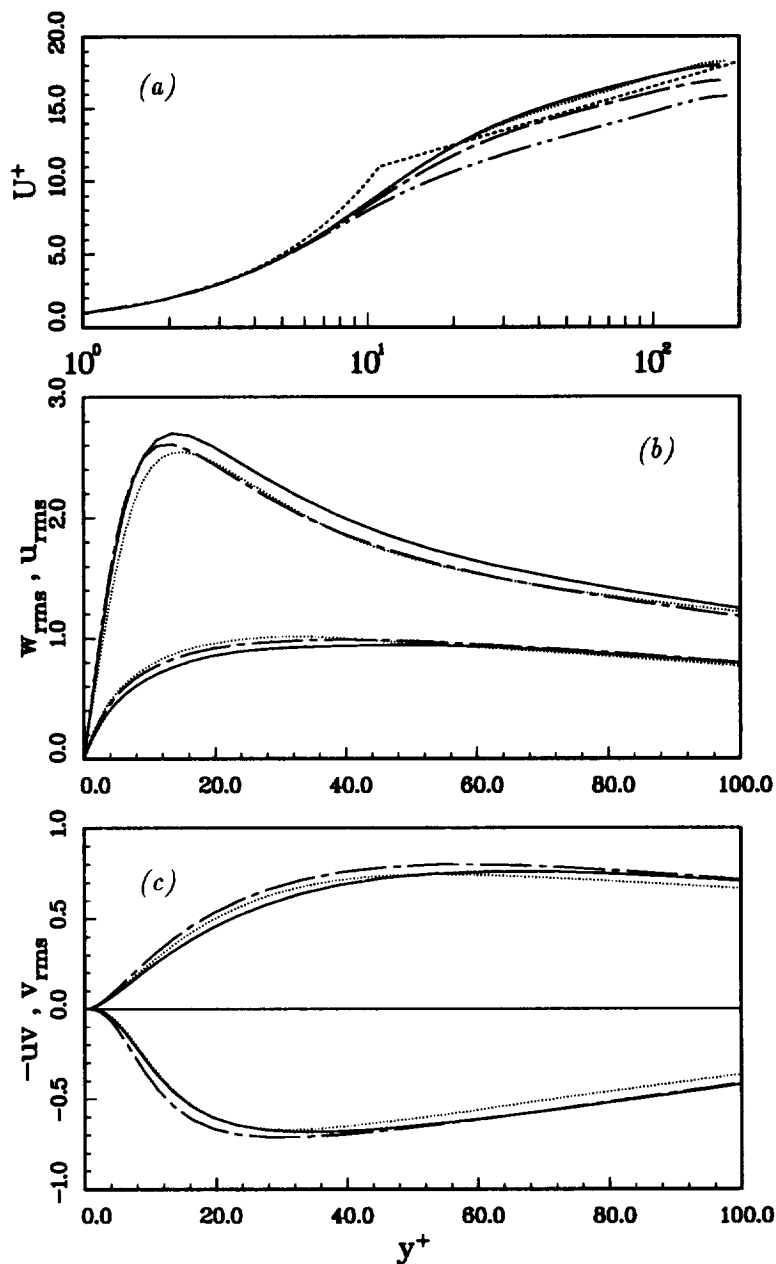


FIGURE 2. Mean streamwise velocity (a), resolved velocity intensities (b,c), and resolved Reynolds stress (c) for the LES of $Re_\tau = 180$ channel flow with the second-order finite difference code on a fine mesh as functions of distance from the wall (all in wall units): ---- Log law, $U^+ = 5 + 2.5 \ln y^+$; DNS (filtered); and LES with --- no SGS model and — DA model. In (a), LES results from the pseudospectral code with no SGS model with comparable resolution (- - - -) are shown; with the DA model, U^+ lies on top of the DNS results for this case.

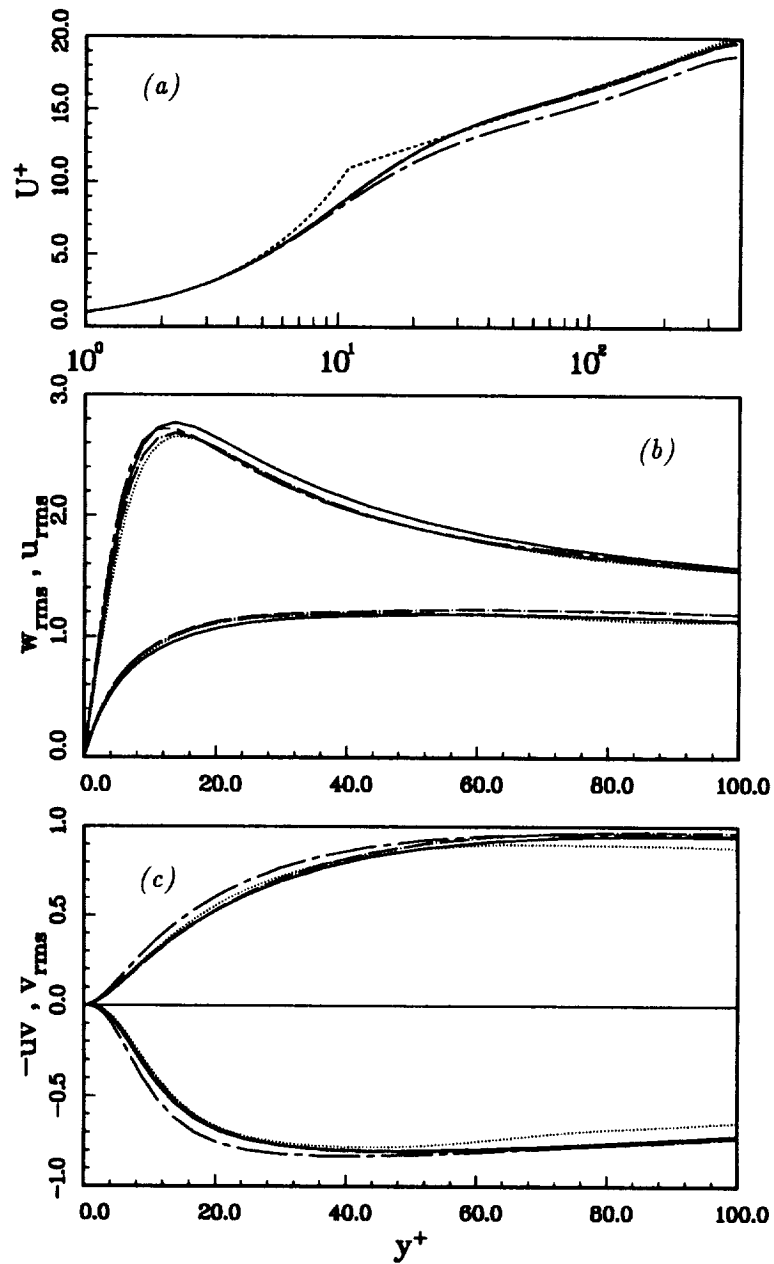


FIGURE 3. Mean streamwise velocity (a), resolved velocity intensities (b,c), and resolved Reynolds stress (c) for the LES of $Re_\tau = 400$ channel flow with the second-order finite difference code as functions of distance from the wall (all in wall units): ----- Log law, $U^+ = 5 + 2.5 \ln y^+$; DNS (filtered); and LES with --- no SGS model, — DA model, and - - - DLk model.

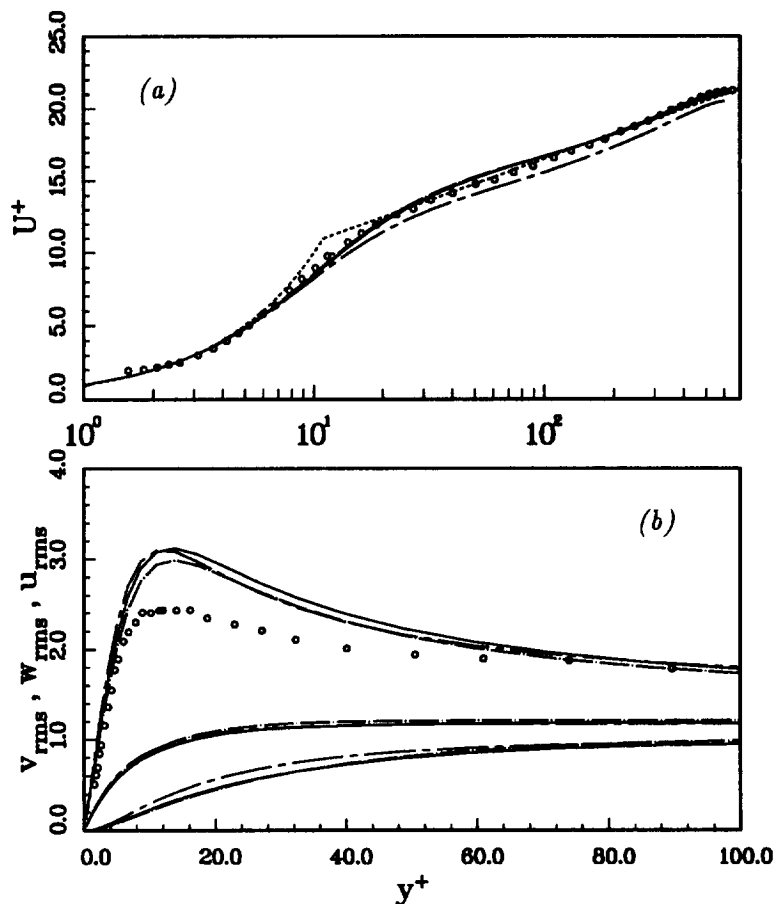


FIGURE 4. Mean streamwise velocity (a) and resolved velocity intensities (b) for the LES of $Re_\tau = 650$ channel flow with the second-order finite difference code as functions of distance from the wall (all in wall units): ---- Log law, $U^+ = 5 + 2.5 \ln y^+$; $\circ \circ \circ$ experimental data; and LES with ---- no SGS model, — DA model, and — DLk model.

agree fairly well with filtered DNS data. DA and DLk model results are almost indistinguishable. At the higher values of Re_τ , with increasingly poorer resolution, the quality of u_{rms} results degenerates considerably in comparison with experimental data by Hussain & Reynolds (1970) (Figs. 4 & 5). The presence of SGS models makes little difference to levels of velocity fluctuation intensities, with u_{rms} becoming progressively higher than experimental results in the buffer region (peaking at 3.1 and 3.6 for $Re_\tau = 650$ and 1030 simulations with the DA model and 3.0 and 3.4 with the DLk model, compared with 2.5 in the Hussain & Reynolds experiment). For $Re_\tau = 650$ (Fig. 4), U^+ is about 5% below experiment and log law with no SGS model; with SGS models it rises to the proper level in the core of the flow but develops a bump just above the buffer region. At $Re_\tau = 1030$ (Fig. 5), U^+ with no SGS model is actually on the experimental and log-law curve; additional viscosity

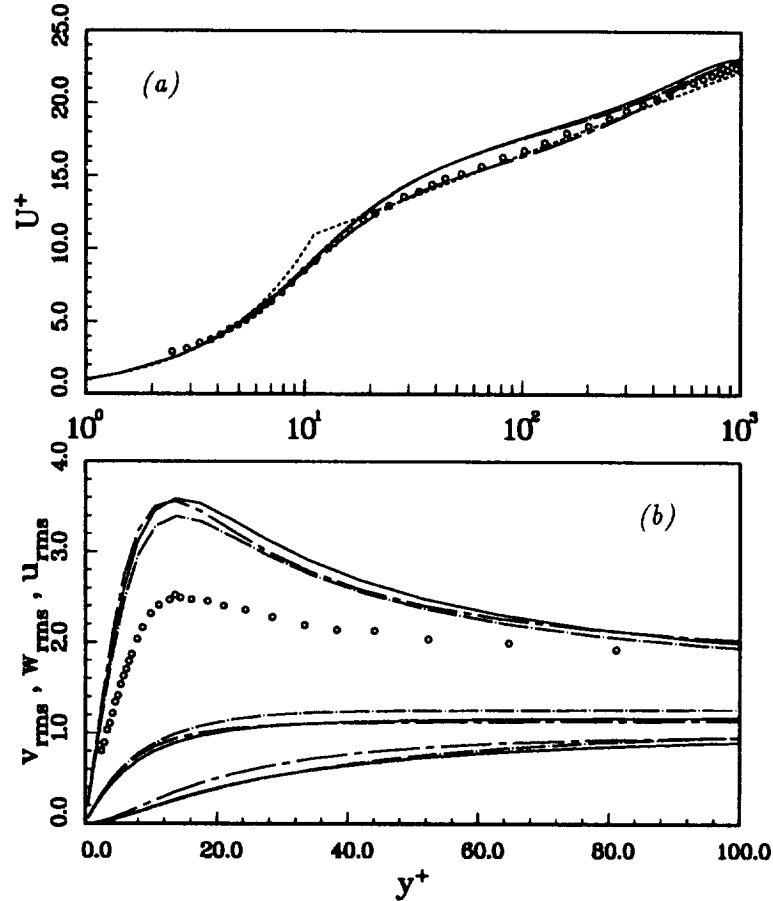


FIGURE 5. The same as Fig. 4, but for $Re_\tau = 1030$.

from the SGS models raises U^+ about 5% above this.

Note that prior LES with a DA model at $Re_\tau \approx 1400$ (using a code that was spectral in horizontal directions and used unstaggered finite differences in the wall-normal direction) gave fair agreement between U^+ and the log law (Cabot & Moin, 1993); it not only exhibited the bump beyond the buffer region, but it also gave much too large values of u_{rms} , peaking at 3.7. This LES was performed on the same domain size with a $32 \times 125 \times 64$ mesh ($\Delta z^+ = 46$). Piomelli (1993), using a pseudospectral code, found peak values of u_{rms} of 2.8 and 3.0 for $Re_\tau = 1050$ and 2000 with $\Delta z^+ = 26$ and 40, respectively, with U^+ in good agreement with the log law and experimental data.

2.1.4 Overall assessment

At coarse resolution, the second-order finite-difference scheme appears to have errors associated with it that act like extra dissipation; this causes the values of U^+ in some simulations with no SGS model to give *coincidentally* good results compared with DNS results. (The second-order statistics are less impressive.) When a SGS model is used, its (real) dissipation causes the U^+ to rise and appear to give worse

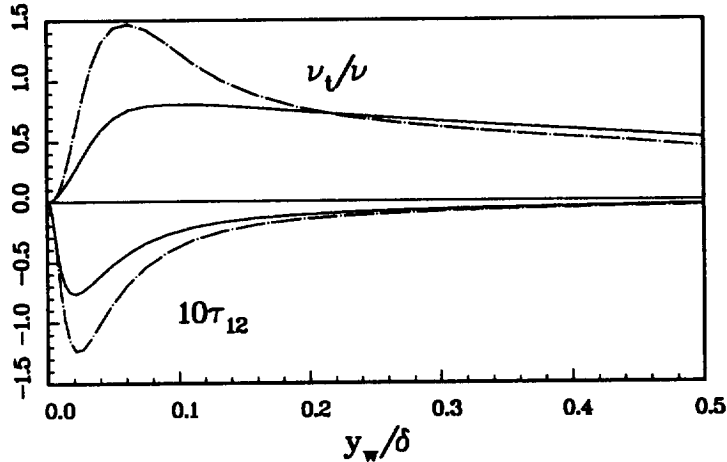


FIGURE 6. Mean eddy viscosity (scaled by the molecular value) and the mean SGS Reynolds stress (in wall units) from the wall halfway to mid-channel for $Re_\tau = 1030$ using the DA model (—) and DLk model (---).

results. There is some preliminary evidence suggesting that aliasing error in the second-order finite difference code may at least be partially responsible for these differences (A. Kravchenko, private communication). This trend persists at finer resolutions, but there the SGS model makes little difference. Indeed, the mean eddy viscosity (ν_t) predicted by dynamic SGS models in the second-order finite-difference code remains approximately equal to or less than the molecular viscosity even at the highest Reynolds numbers simulated, whereas the ν_t/ν climbs steadily with increasing Re_τ in the pseudospectral code, with peak mean values of about 5 found at $Re_\tau = 1400$. This may be caused by the removal of high-wavenumber information by the second-order finite differencing, just where the dynamic procedure samples to predict the eddy viscosity.

Mean velocity fluctuation intensities, especially the streamwise component, are more sensitive to spanwise resolution measured in wall units (Δz^+), with good results in the second-order finite-difference code for $\Delta z^+ \approx 12$, and progressively worse results for higher values. Pseudospectral codes appear to get comparable results at roughly half the horizontal resolution. Large excesses in u_{rms} (and deficits in w_{rms}) are always associated with a bump in U^+ outside of the buffer region.

In the low- Re , coarse-resolution LES, the DLk model gives somewhat better results than the DA model. But at finer resolutions and higher Reynolds numbers, there is little discernible difference in first- or second-order statistics between them, even though *mean* eddy viscosity and Reynolds stresses from the DLk model are 50–100% greater in the buffer region than those from the DA model (Fig. 6).

2.1.5 Wall-normal filtering

Tophat filtering in the wall-normal (y) direction, in addition to plane filtering, was implemented in the DA model in both finite-difference and pseudospectral codes.

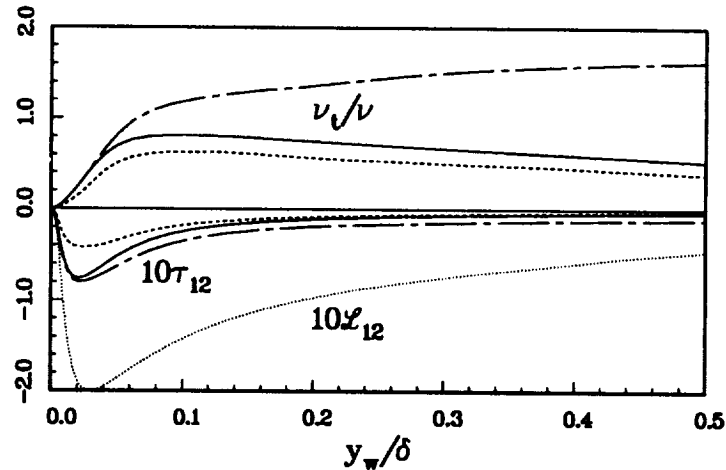


FIGURE 7. Mean eddy viscosity (scaled by the molecular value) and the mean SGS Reynolds stress (in wall units) from the wall halfway to mid-channel for $Re_\tau = 1030$ using the DA model with $\Delta = h$ and plane-filtering (—) or volume-filtering (---). Also shown are results from the mixed plane-filtered DA model with $\Delta = 3h/2$ (- - - -); the Reynolds stress contribution from the (resolved-scale) Leonard term \mathcal{L}_{12} is also shown (.....) for this case.

This volume filtering causes second-order errors due to non-commutivity with spatial derivatives (cf. Ghosal & Moin, 1993). No higher-order corrections were used, which in principle are needed for the pseudospectral code but not for the second-order finite-difference code. In both codes the y -dependent dynamic coefficient $C(y)$ was removed inconsistently from the filter in the model part of Germano identity (cf. eq.[3]). In one case for the finite-difference code, C was kept consistently in the filtered expression (requiring the solution of a tridiagonal matrix for C), but this resulted in only a small ($\sim 5\%$) correction.

For the pseudospectral code at low Re_τ , the volume filtering gives eddy viscosities larger than plane filtering by only about 20% near mid-channel, the two values approaching near the walls. Results for the consistent version of the volume-filtered SGS model in the finite difference code are shown in Figs. 7 & 8 for $Re_\tau = 1030$. The eddy viscosity is seen to be increased three-fold in the interior of the channel (Fig. 7), but it approaches the plane-filtered case near the walls where the strain is greatest. For $y/\delta < 0.1$ ($y^+ < 100$), the residual stress with volume filtering is greater by less than 10% compared with plane filtering. The enhanced eddy viscosity from y -filtering has the overall effect of increasing U by a few percent (making it even worse in comparison with experimental data and the log law; see Fig. 8), with very little effect on values of velocity fluctuation intensities.

2.1.6 Explicit grid filtering

Greater numerical accuracy should be obtained in the LES when the grid filter Δ applied to the Navier-Stokes equations is much greater than the actual mesh size h (see Rogallo & Moin, 1984, and references therein). In the previous applications,

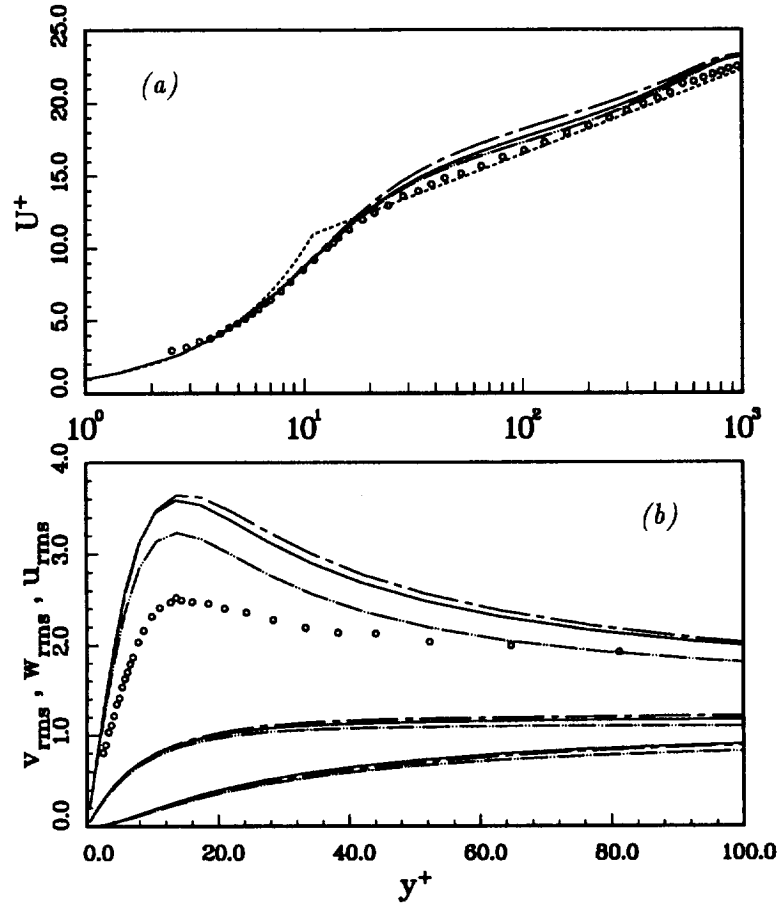


FIGURE 8. Mean streamwise velocity (a) and resolved velocity intensities (b) for the LES of $Re_\tau = 1030$ channel flow with the second-order finite difference code as functions of distance from the wall (all in wall units): ---- Log law, $U^+ = 5 + 2.5 \ln y^+$; $\circ \circ \circ$ experimental data; and LES using the DA model with $\Delta = h$ and plane-filtering (—) or volume-filtering (---), and using the mixed DA model with $\Delta = 3h/2$ and plane-filtering (-·-·-).

however, we have chosen $\Delta = h$ in order to minimize computation time, albeit inaccurate. A simulation with the finite difference code using the DA model was performed using $\Delta = 3h/2$ and, now, a test filter $\hat{\Delta} = 2\Delta = 3h$. (Filtering and averaging was performed only in horizontal planes with a tophat filter, and no dealiasing was used.) Information about the grid filter is communicated to the filtered linear terms in the Navier-Stokes equation only through the nonlinear Reynolds stress terms. The resolved Reynolds stress terms are influenced to some extent by the mesh on which the flow is represented, which effectively cuts off information at wavelengths shorter than the mesh size. In the standard dynamic model, the residual Reynolds stress depends only on relative differences between the test and grid filters, with no *explicit* dependence on the grid filter. Here a “mixed” dynamic SGS

model was used in which there is explicit dependence on the grid filter.

When the velocity components u_i are decomposed into filtered and residual (mostly small-scale) components, $\bar{u}_i + u'_i$, the residual stress can be written

$$\tau_{ij} = \mathcal{L}_{ij} + \mathcal{C}_{ij} + \mathcal{R}_{ij} , \quad (4)$$

where

$$\begin{aligned} \mathcal{L}_{ij} &= \overline{\bar{u}_i \bar{u}_j} - \bar{\bar{u}_i} \bar{\bar{u}_j} , \\ \mathcal{C}_{ij} &= \overline{\bar{u}_i u'_j + u'_i \bar{u}_j} - \bar{\bar{u}_i} \bar{u}'_j - \bar{u}'_i \bar{\bar{u}_j} , \\ \mathcal{R}_{ij} &= \overline{u'_i u'_j} - \bar{u}'_i \bar{u}'_j \end{aligned}$$

are the Galilean invariant Leonard, cross, and stress terms (Germano, 1986). In the mixed dynamic model, \mathcal{L}_{ij} is computed from the resolved field, and the unknown $\mathcal{C}_{ij} + \mathcal{R}_{ij}$ is fitted with a Smagorinsky model using the standard the dynamic model technique. This model has been used successfully by Zang *et al.* (1993) for flow over a cavity (although the grid filter was chosen in their case to be the same as the mesh size).

The LES of channel flow for the $Re_\tau = 1030$ case was repeated using this mixed model with $\Delta = 3h/2$. It was found that the residual stress contribution from the Leonard term is much greater than that from the dynamically modeled terms (Fig. 7). The mean streamwise velocity and the streamwise fluctuation intensity are seen in Fig. 8 to be in somewhat better agreement with experimental data using the mixed model than with the standard DA model with $\Delta = h$, but the streamwise fluctuation intensity is still too high in the buffer region.

2.2 Other local SGS models

2.2.1 Local Lagrangian model

An alternative to spatial averaging in complex flows is to use some sort of temporal averaging. Meneveau *et al.* (1994) as part of the 1994 CTR Summer Program proposed effectively to average expressions in the dynamic model in time over Lagrangian material trajectories. The local dynamic Smagorinsky coefficient C for the residual stress is estimated, neglecting (inconsistently) the filtering of C in Eq. (3), by

$$L_{ij} \sim CM_{ij} , \quad M_{ij} \equiv 2\hat{\Delta}^2 |\widehat{\mathbf{S}}| \widehat{S}_{ij} - 2\Delta^2 |\widehat{\mathbf{S}}| \widehat{S}_{ij} , \quad (5)$$

and, by least-squares fitting over components,

$$C \sim \mathbf{L} : \mathbf{M} / \mathbf{M} : \mathbf{M} . \quad (6)$$

In the ‘‘local Lagrangian’’ model, Meneveau *et al.* replaced this with

$$C \sim I_{LM} / I_{MM} , \quad (7)$$

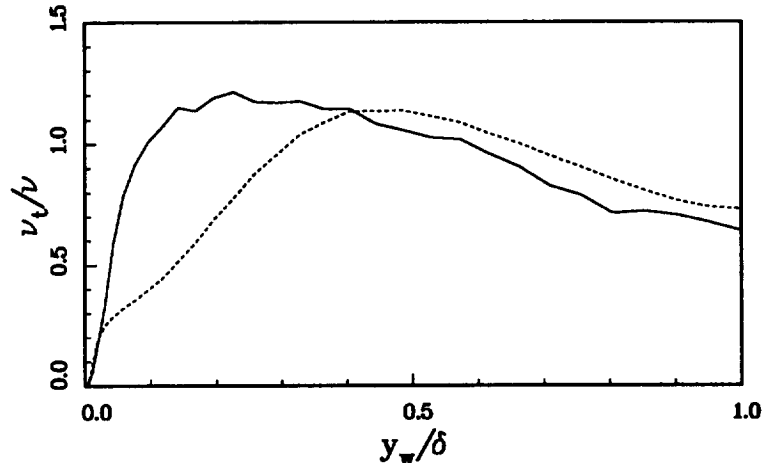


FIGURE 9. Mean eddy viscosity (scaled by the molecular value) from the wall to mid-channel for $Re_\tau = 650$ using the DA model (—) and LL model (- - -).

where I_{LM} and I_{MM} are values of $L : M$ and $M : M$ averaged over estimated Lagrangian trajectories. Note that the averaging carries full three-dimensional information, unlike the DA model in channel flow. I_{LM} was constrained to be positive to ensure numerical stability, and the time scale was chosen (somewhat arbitrarily) to be comparable to $(I_{LM})^{-1/4} \Delta$. The sensitivity of results to different Lagrangian time scales needs to be explored further.

This model was tested in homogeneous flows, and it was also implemented in a pseudospectral channel code. Simulations of fully developed turbulent channel flow with $Re_\tau = 650$ were performed with the local Lagrangian (LL) model and the standard plane-averaged (DA) model. It was found that the LL model gave significantly lower eddy viscosities above the buffer region to about $y^+ = 200$ (Fig. 9), perhaps due to ejection events from the walls, the memory of which is retained by the LL model. Wall-normal mixing in C is also evident in its near-wall behavior, varying as $y^{+2.5}$ rather than the expected y^{+3} . The lower eddy viscosities in the LL model resulted in values of U^+ lower by about 10% in the log layer than those from the DA model; the streamwise velocity intensity was also slightly lower with the LL model, peaking at 2.8 compared with 3.0 with the DA model.

A transition case was performed with an initial centerline Reynolds number of 8000 (like the LES by Germano *et al.*, 1991 and prior DNS and LES referenced therein) using both the LL and DA models. The numerical mesh was refined at several times, which also required I_{LM} and I_{MM} to be interpolated on finer grids. The test-to-filter width ratio was held constant, but $\Delta = h$ changed on remeshing, causing the values of $L : M$ and $M : M$ to shift as well. In order to reduce transients, I_{LM} and I_{MM} were also rescaled using the plane-averaged values of the revised $L : M$ and $M : M$; however, a more general technique is required for more complex flows. The LL model was generally (but not always) slightly less dissipative in the transition calculation than the DA model (Fig. 10); the exceptions appear to be a result of the LL model lagging behind the DA model in responding to higher

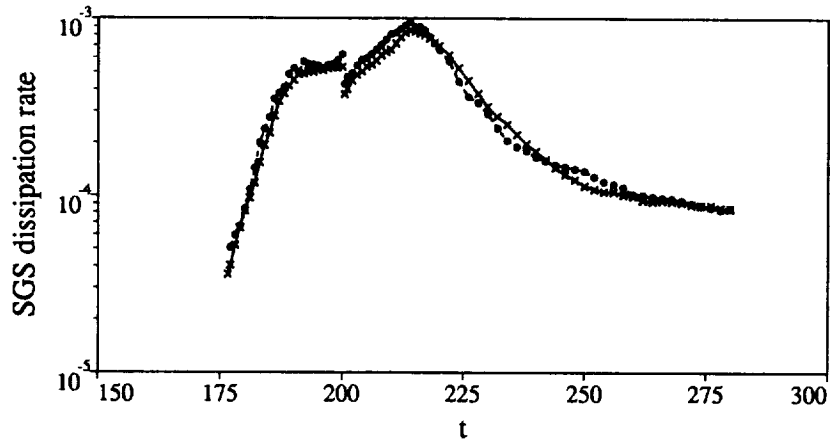


FIGURE 10. SGS dissipation rate of kinetic energy during transition in channel flow with $Re_c = 8000$: $\bullet \bullet \bullet$ DA model, $\times \times \times$ LL model. The mesh was refined at time $t = 200$ from $32 \times 65 \times 48$ to $48 \times 65 \times 64$. (All quantities are in units constructed from the initial mid-channel streamwise velocity and the channel half-width.)

turbulence levels. The LL model also gave a much more pronounced plateau in the time history of the wall stress in the peak region, which may also be due to the inherent lag of SGS stresses in the LL model. Both models gave similarly good results compared with prior LES and DNS (see Meneveau *et al.*, 1994).

2.2.2 Random backscatter model

In order to retain the realistic characteristic of backscatter of energy from the small, unresolved scales to the large, resolved scales in a local SGS model and still maintain numerical stability, Carati & Ghosal (in this volume) proposed to represent the backscatter as a random process while constraining the local eddy viscosity from the dynamic model to be non-negative (i.e., using the DL+ model). The amplitude of random forcing is related to the error in determining C locally from Eq. (3), which will be largest with the DL+ model in regions where negative values of C would arise in the unconstrained case. In Carati & Ghosal's original formulation, the amplitude of random forcing A for each component in the Navier-Stokes equation is given by

$$A^2 = [-3\hat{\mathbf{u}} \cdot (\nabla \cdot \mathbf{E})^* / \Delta t]_+, \quad (8)$$

where $(\nabla \cdot \mathbf{E})^*$ is the divergence-free derivative of the error in Eq. (3), and Δt is the time step, corresponding to an energy injection rate by the random forcing of $-\hat{\mathbf{u}} \cdot (\nabla \cdot \mathbf{E})^*$. Note that only the positive part of (8) is used so that A is defined. To make $\nabla \cdot \mathbf{E}$ divergence-free generally requires the auxiliary solution of a Helmholtz equation for a quantity related to the residual pressure; it results in a globally energy-neutral redistribution of the energy injection. The computation is cheaper (and, in most cases, not greater affected) if the divergence of $\nabla \cdot \mathbf{E}$ is retained, in

which case (8) is replaced by

$$A^2 = [-2\widehat{\mathbf{u}} \cdot (\nabla \cdot \mathbf{E})/\Delta t]_+ . \quad (9)$$

While either formulation works well in homogeneous flow, it is found in channel flow that they generate large enough amplitudes to destabilize the numerical integration. This is because $\widehat{\mathbf{u}}$ contains a large mean flow component, and, when only positive values of A^2 are retained in (8) or (9), it gives spuriously large values (since large, offsetting negative values are discarded). One can recast $-\widehat{\mathbf{u}} \cdot (\nabla \cdot \mathbf{E})$ as $\mathbf{E} : \widehat{\mathbf{S}}$ plus diffusion terms with zero volume average. Neglecting these diffusion terms, one can recast (9) as

$$A^2 = [2\mathbf{E} : \widehat{\mathbf{S}}/\Delta t]_+ , \quad (10)$$

which gives much lower amplitudes and appears to be numerically stable in the channel flow code. Equilibrium statistics have not yet been accumulated to determine the performance of the random backscatter model.

3. Future plans

3.1 LES with random backscatter

Several channel flow simulations will be performed using the constrained dynamic localization SGS model with random backscatter (§2.3); the resulting statistics will be compared with those using other SGS models and with DNS and/or experimental data. The validity of using expression (10) instead of (8) in the framework of the formulation by Carati & Ghosal (in this volume) will be explored. The present formulation also assumes isotropy in the random forcing term, which is clearly not valid near the walls in the channel; a more general formulation will be explored to address this shortcoming, and, more pragmatically, it will be determined if in fact the channel flow is sensitive to such details in the forcing.

3.2 Second-order commutation error corrections

The correct governing equations for LES with non-uniform grids should generally include additional terms due to the non-commutation of spatial derivatives and the grid filter. Correction terms determined by Ghosal & Moin (1993) will be incorporated in a pseudospectral channel code and their effects will be determined in LES of channel flow with explicit volume filtering. The second-order commutation errors are expected to be the same order as the differencing errors in a second-order finite difference code, making it unnecessary to include them. However, the commutation terms will be included in fourth-order finite difference schemes that are being developed for LES.

3.3 Dealiased finite difference simulations

There is some evidence that aliasing errors in the second-order finite difference simulations are responsible for some discrepancies with pseudospectral results. Also, since the high-wavenumber information in second-order finite differences is known to be inaccurate, and this directly affects the results from the dynamic procedure,

simulations need to be crafted in ways that reduce this inaccuracy. Channel flow simulations will be performed with a second-order finite difference code that uses dealiasing of nonlinear products; in homogeneous directions this could be done with spectral methods, but more general procedures are required for more complex geometries. Most future simulations will be performed with grid filters that are at least twice the actual grid spacing to improve numerical accuracy of the LES, and this additional "padding" can in principle be used in the general dealiasing procedure. It will also be determined if mixed dynamic SGS models with explicit dependence on the grid filter (§2.1.6) give better results in general than the standard dynamic model for these cases.

REFERENCES

- CABOT, W. 1993 Dynamic localization and second-order subgrid-scale models in large eddy simulations of channel flow. In *Annual Research Briefs 1993*, Center for Turbulence Research, Stanford Univ./NASA Ames Research Center, 129–144.
- CABOT, W., & MOIN, P. 1993 Large-eddy simulation of scalar transport with the dynamic subgrid-scale model. In *Large Eddy Simulation of Complex Engineering and Geophysical Flows*, ed. B. Galperin & S. A. Orszag (Camb. Univ. Press).
- GERMANO, M. 1986 A proposal for a redefinition of the turbulent stresses in the filtered Navier-Stokes equations. *Phys. Fluids*. **29**, 2323–2324.
- GERMANO, M., PIOMELLI, U., MOIN, P., & CABOT, W. H. 1991 A dynamic subgrid-scale eddy viscosity model. *Phys. Fluids A*. **3**, 1760–1765.
- GHOSAL, S., LUND, T. S., MOIN, P., & AKSELVOLL, K. 1994 A dynamic localization model for large-eddy simulation of turbulent flows, *J. Fluid Mech.*, in press.
- GHOSAL, S., & MOIN, P. 1993 The basic equations for the large-eddy simulation of turbulent flows in complex geometry. *Manuscript 143*, Center for Turbulence Research, Stanford Univ./NASA Ames Research Center.
- HUSSAIN, A. K. M. F., & REYNOLDS, W. C. 1970 The mechanics of a perturbation wave in turbulent shear flow. Stanford Univ. Dept. of Mech. Eng. Rep. FM-6.
- KIM, J., MOIN, P., & MOSER, R. 1987 Turbulence statistics in fully developed channel flow at low Reynolds number. *J. Fluid Mech.* **177**, 133–166.
- LILLY, D. 1992 A proposed modification of the Germano subgrid-scale closure method. *Phys. Fluids A*. **4**, 633–635.
- MENEVEAU, C., LUND, T. S., & CABOT, W. 1994 A Lagrangian dynamic subgrid-scale model of turbulence. In *Proceedings of the Summer Program 1994*, Center for Turbulence Research, Stanford Univ./NASA Ames Research Center.

- PIOMELLI, U. 1993 High Reynolds number calculations using the dynamic subgrid-scale stress model. *Phys. Fluids A*. **5**, 1484–1490.
- ROGALLO, R. S., & MOIN, P. 1984 Numerical simulation of turbulent flows. *Ann. Rev. Fluid Mech.* **16**, 99–137.
- ZANG, Y., STREET, R. L., & KOSEFF, J. R. 1993 A dynamic mixed model and its application to turbulent recirculating flows. *Phys. Fluids A*. **5**, 3186–3196.

511-02
40691

12 161
N95-22448

Unstructured-grid large-eddy simulation of flow over an airfoil

By Kenneth Jansen

1. Motivation and objectives

Historically, large-eddy simulations (LES) have been restricted to simple geometries where spectral or finite difference methods have dominated due to their efficient use of structured grids. Structured grids, however, not only have difficulty representing complex domains and adapting to complicated flow features, but also are rather inefficient for simulating flows at high Reynolds numbers. The lack of efficiency stems from the need to resolve the viscous sublayer, which requires very fine resolution in all three directions near the wall. Structured grids make use of a stretching to reduce the normal grid spacing but must carry the fine resolution in the streamwise and spanwise directions throughout the domain. The unnecessarily fine grid for much of the domain leads to disturbingly high grid estimates. Chapman (1979), and later Moin & Jimenez (1993), pointed out that, in order to advance the technology to airfoils at flight Reynolds numbers, structured grids must be abandoned in lieu of what are known as nested or unstructured grids. Fig. 1 illustrates the ability of an unstructured mesh to refine only the near-wall region. Note the large number of points near the wall (where the fine vortical features need better resolution) and the coarseness in all directions away from the wall (where the scales are much larger). The important difference between this approach and the usual structured grid stretching is that the number of elements used to discretize the spanwise and streamwise features of the flow is reduced in each successive layer coming off the wall. This is due to the fact that the elements not only grow in the normal direction but in the other directions as well. This greatly reduces the total number of points or elements required for a given Reynolds number flow.

The finite element method can efficiently solve the Navier-Stokes equations on unstructured grids. Although the CPU cost per time step per element is somewhat higher than structured grid methods, this effect is more than offset by the reduction in the number of elements. The use of unstructured grids, coupled with the advances in dynamic subgrid-scale modeling such as those made by Germano *et al.* (1991) and Ghosal *et al.* (1994), make LES of an airfoil tractable. We have chosen the NACA 4412 airfoil at maximum lift as the first simulation since this flow has not been successfully simulated with the Reynolds-averaged Navier-Stokes equations. Coles and Wadcock (1979) performed a detailed experimental study of this flow. Subsequently, Hasting and Williams (1987) also performed an experimental study. Finally, Wadcock (1987) re-examined the Coles and Wadcock data and the Hastings and Williams data. He synthesized the existing data with some recent measurements and concluded that the maximum lift configuration for the NACA 4412 airfoil at Reynolds number based on chord $Re_c = u_\infty c / \nu = 1.64 \times 10^6$ is 12° angle of attack.

PRECEDING PAGE BLANK NOT FILMED

PAGE 160 INTENTIONALLY BLANK

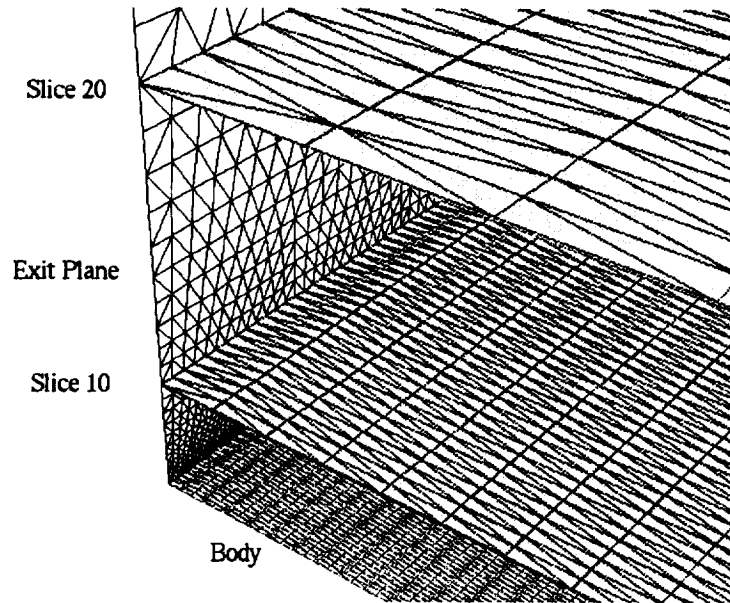


FIGURE 1. A portion of an unstructured grid that illustrates the varying resolution in the streamwise and spanwise directions in layers coming off the wall. Note that the y direction has been scaled to allow visualization of each layer.

2. Accomplishments

2.1 Mesh generation

A mesh generator has been developed which achieves special requirements of large-eddy simulation. These requirements arise from the need to resolve the near-wall structures. In this region the elements should have a streamwise spacing of 200 wall units ($\Delta_x^+ = 200$), a spanwise spacing of 50 wall units ($\Delta_z^+ = 50$), and a normal direction spacing of 1 wall unit ($\Delta_y^+ = 1$). A wall unit is a function of the friction velocity (u_τ) and, therefore, is also a function of position on the airfoil. The experimental friction velocity was used to determine the appropriate spacing in each direction at each point on the airfoil. This fine near-wall spacing is continued in the normal direction for approximately 30 wall units. Only the normal direction spacing is allowed to grow in this interval. Once outside of the near-wall region ($y^+ = 30$), the turbulent scales that need to be resolved become larger and the grid is smoothly coarsened in all directions. Great care is taken to ensure a smooth transition as preliminary studies have shown that non-smooth coarsening in the presence of gradients can greatly reduce accuracy. The domain can be made reasonably short in the spanwise direction by employing periodicity. Moin & Jimenéz predicted unstructured or zonal grids of the type described above would lead to meshes with 1.2×10^6 points for airfoils with a chord Reynolds number of $Re_c = 1.0 \times 10^6$, assuming a span of one-fifth of the chord. The mesh generated

for this span contains 1.0×10^6 points, which is 20 percent less than the prediction even though the Reynolds number is 64 percent higher. The additional savings are the result of the use of the local wall units to determine spacing rather than a global wall unit assumption as was done in the past (Chapman, Moin & Jimenéz, and Jansen (1993a)). A structured grid mesh with the same near-wall resolution would require over 2.6×10^7 points. The difference becomes even more dramatic at flight Reynolds numbers.

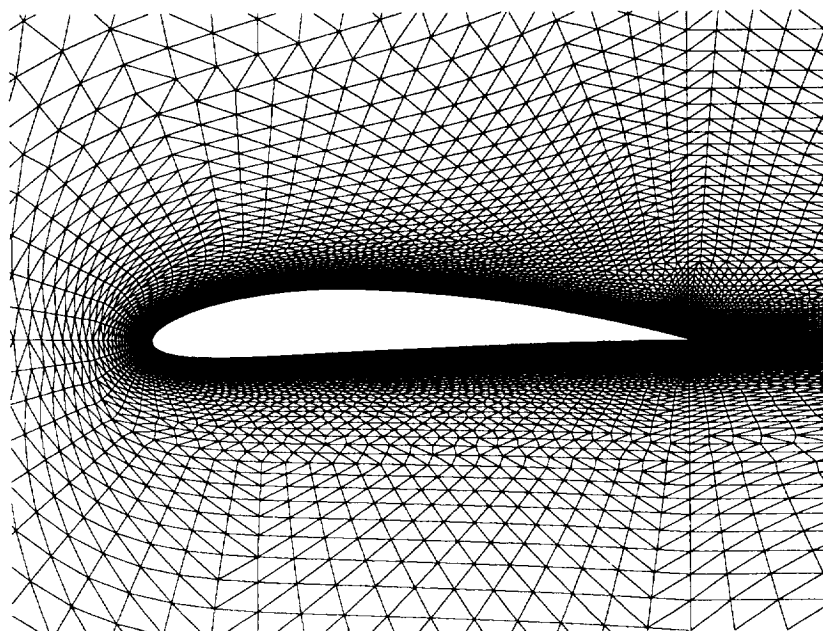


FIGURE 2. The periodic plane of the three-dimensional airfoil mesh (the mesh has been magnified to show the resolution near the airfoil).

The periodic plane of the three-dimensional airfoil mesh generated for this flow can be seen in Fig. 2. Note the smooth variation in element size. Note also the rapid growth in Δ_y in the wake. This not only reduces the number of points required, but also reduces stiffness associated with fine spacing in a region of fairly large vertical flow (large vortical motions shedding off of the tail). Fig. 3 is a plan view of the grid at approximately 30 wall units off of the upper surface. Note the variation in spanwise and streamwise spacing as a function of chord position. The figure has been broken in three pieces to afford a closer look at the very narrow domain. The spanwise domain has been reduced by a factor of four to allow more rapid computation of preliminary results presented in section 2.4. This grid contains only 0.25×10^6 points.

2.2 Computer code

The finite element formulation being used in this work is based upon the work

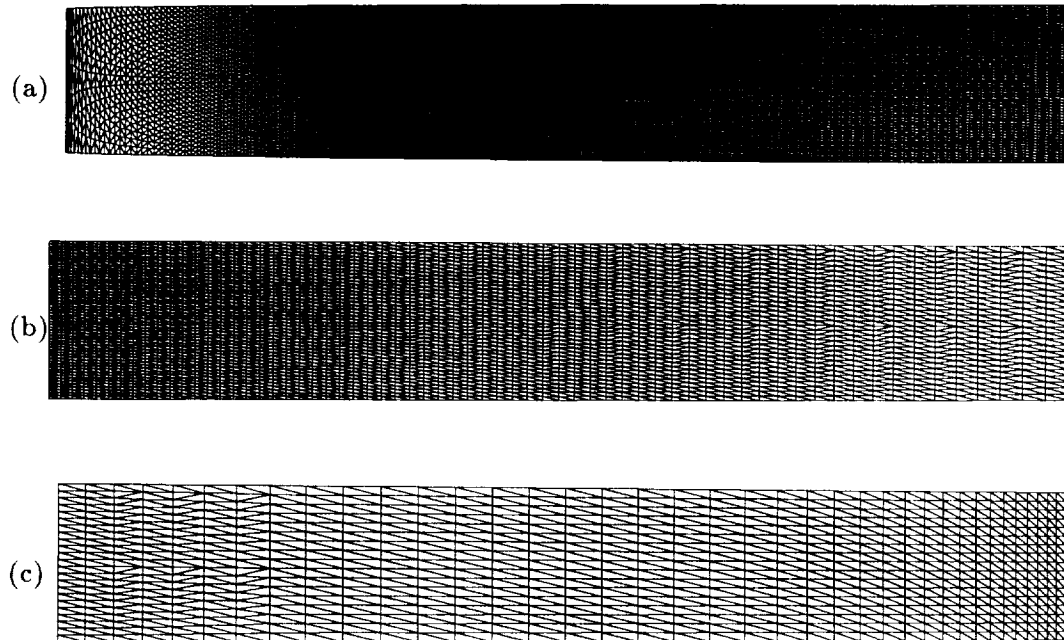


FIGURE 3. Plan view of a slice through a three-dimensional airfoil grid at $y^+ = 30$ from the upper surface. (a) displays the first third of the chord ($0.0 < x/c < 0.33$), (b) the second third ($0.33 < x/c < 0.67$) and (c) the final third ($0.67 < x/c < 1.0$). Note that the large variation in spanwise and streamwise spacing match the resolution requirements of the flow locally.

of Jansen *et al.* (1993b) and Johan *et al.* (1993). The code was extended to time-accurate calculations in the past year and was validated by solving the problem of vortex shedding behind a cylinder. Implicit time integration is required due to the very high acoustic CFL numbers encountered in flows of this type. Different integration schemes were studied and the trapezoidal rule was found to be the most efficient for external flow problems. It should be noted that this time-integration scheme was observed to be a poor choice for internal flows such as channel flows due to undamped acoustic waves in a bounded domain. To perform this type of simulation properly would require development of a new time integration scheme that would damp temporally unresolved acoustic waves. The computational domain of the airfoil has open boundaries far from the airfoil surface, and no such difficulties arise in this case.

The code has proven to be very efficient on parallel architectures such as the CM5. For large problems, such as the one we consider here, very high flop rates can be achieved (25 MFLOPS per processor). The CM5 has also been a far more available resource than the Cray C90 in the past year.

2.3 Filtering operators for the finite element method

The dynamic model requires a “test filtering” operation defined as

$$\hat{f}(\mathbf{x}) = \int f(\mathbf{x}')G(\mathbf{x}, \mathbf{x}')d\mathbf{x}'$$

as part of the procedure to determine the model coefficient (Germano *et al.* and Ghosal *et al.*). If G is a “top-hat” filter and the above equation is integrated with Simpson’s rule, the filtering operation leads to the following formula for each internal node A ($A = 1, \dots, n_p$) in the mesh with n_p such internal nodes

$$\hat{f}^A = \frac{1}{6}(4f^A + f_E^A + f_W^A)$$

where the subscripts E and W denote the point due East and West for node A . In multi-dimensions the process is simply repeated in each direction. On an unstructured grid there often is not a point due East or West. Furthermore, the location of the points that might approximate the due East or West neighbor is not simply determined through a recursive formula as is the case in a structured grid. One could pre-process these approximate neighbors and store a pointer list for each point in the grid. This would require additional memory which is unattractive. Also, for parallel machines this approach is very inefficient. The inefficiency stems from the fact that the nodal data is scattered among the processors and retrieval of that data requires substantial communication. The time required to perform these communication operations is often much larger than the time required to perform the actual calculations on parallel machines. For this reason it is attractive to explore element-based filtering procedures which minimize the amount of communication required. Four alternative filtering operators have been developed and are described next.

Method 1.) Start by obtaining the function at the element centroids, f^e , where the superscript e corresponds to the e^{th} element. Then define the following filter operation,

$$\hat{f}^e = w_0 f^e + \sum_{i=1}^{n_f} w_i f_i^e$$

where f_i^e is the function value at the centroid of the element on the other side of the i^{th} face (there are n_f such faces for each element), and w_i are filter weights. For example, triangles have three faces, therefore, the filtering operation of a given function for a particular triangle involves the function value within the triangle and the function values within the three other triangles which surround it as illustrated in Fig. 4.

The problem with this method is that it requires an additional data structure to determine the elements which lie on the other side of each face of a given element. This data structure is not immediately available from existing finite element data structures. It could be pre-processed and stored, but this is unattractive. This

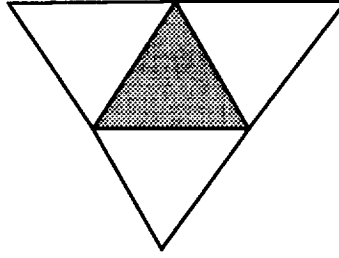


FIGURE 4. In method 1 the dynamic model filter for the function in the shaded triangle is determined through a weighted combination of the function value within the shaded triangle and the function values within the triangles which share a face with it (the 3 white triangles).

method may prove effective for finite volume schemes using an edge-based data structure.

Method 2.) An alternative approach is to approximate the the filtering operator by

$$\hat{f}(\mathbf{x}) = f(\mathbf{x}) + \frac{1}{m} \tilde{\nabla}^2 f(\mathbf{x}) + O(\delta^4)$$

which extends the work of Carati (1994) to non-isotropic grids. Here $\tilde{\nabla}$ is a non-dimensional gradient (i.e. the gradient in a particular direction multiplied by the discretization width in that direction).

$$\tilde{\nabla} = \Delta_x \frac{\partial}{\partial x} \mathbf{i} + \Delta_y \frac{\partial}{\partial y} \mathbf{j} + \Delta_z \frac{\partial}{\partial z} \mathbf{k}$$

It is easily verified that this procedure gives the same result as a one-dimensional top-hat filter integrated with Simpson's rule ($m = 3$). In general $m = d + 2$ where d is the number of space dimensions.

This filter can be evaluated quite rapidly with the finite element method

$$\hat{f}^A = f^A - \frac{1}{d+2} \{M^{BA}\}^{-1} \left(\int_{\Omega} N_{,i_n}^B f_{,i_n} d\Omega - \int_{\Gamma} N^B f_{,i_n} n_{i_n} d\Gamma \right)$$

where N^A is the basis function for node A (likewise B can be any node ($B = 1, \dots, n_p$)), $\{M^{BA}\}$ is the finite element "mass matrix", Ω is the spatial domain, Γ is the boundary of the domain, and the subscript $,i_n$ denotes differentiation in the i^{th} direction multiplied by the length of the element in this direction. Note that we have included the boundary terms (there will be contributions when f is the strain-rate tensor due the non-zero strain-rates at the boundaries).

While this method requires more floating point operations than method 1, it requires no additional data structures (it uses existing finite element data structures) and very little communication. Algorithms of this type are already coded for the viscous terms; consequently these operations were easily parallelized.

The filtering operation defined above requires that all quantities that need to be filtered must be defined at the nodes. The most commonly used basis functions in finite element methods are C^0 continuous piece-wise polynomials. Function spaces of this type yield gradient quantities (such as the strain-rates) that are discontinuous at element boundaries. Before the filtering operator can be applied, it is necessary to project the strain-rates from the elements to the nodes. This is accomplished by a consistent finite element projection operator

$$S_{ij}^A = \{M^{BA}\}^{-1} \sum_{e=1}^{n_{el}} \int_{\Omega_e} N^B S_{ij}^e d\Omega_e$$

here S_{ij}^A is the strain-rate tensor at node A and S_{ij}^e is the strain-rate tensor as defined in element e . Note that the sum is over all the element domains Ω_e (there are n_{el} such domains).

With the strain-rate tensor globally projected to the nodes, we next interpolate $S_{ij}(\mathbf{x})$ with the basis functions,

$$S_{ij}(\mathbf{x}) = \sum_{A=1}^{n_p} N^A(\mathbf{x}) S_{ij}^A$$

The above procedure has been implemented in the parallel code. The tests thus far have used a “lumped mass” for $\{M^{BA}\}$, making inversion trivial. The cost of the dynamic model calculation of the eddy viscosity is less than one-fifth of a non-linear iteration. Therefore, even when only performing two non-linear iterations, the cost of the dynamic model is less than 10 percent of the total cost. This is as cheap or cheaper than many three-dimensional structured grid filtering operators. As mentioned before it also requires no additional memory.

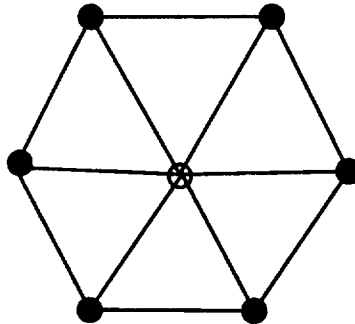


FIGURE 5. Generalized box filter for node A is defined as $G(\mathbf{x}^A) = 1$ for all the triangles surrounding node A .

Method 3.) The third method generalizes the notion of a top-hat or box filter to unstructured grids. Since the element domains do not necessarily form boxes,

it is more practical to define the filter function for node A as $G(\mathbf{x}^A) = 1$ for all the triangles which have node A as a vertex (see Fig. 5). In three dimensions this generalized box filter is an approximation to an ellipsoid (for isotropic grids it is approximately a sphere). This filter function is easily integrated against the function we desire to filter with the rectangle integration rule (equivalent to trapezoidal rule if the function is linear). This method has been implemented and is slightly cheaper than method 2 but may be less accurate since rectangle rule is less accurate than Simpson's rule. The new generalized box filter is not formed by structured grid lines, making Simpson's rule integration impossible. Studies are underway to quantify the differences between methods 2 and 3.

Method 4.) The fourth method is only appropriate when using a higher-order function space. Consider for example a one-dimensional quadratic element as shown in Fig. 6. It is possible to construct a filter from a combination of two interpolations. In our one-dimensional example the filtered value of a function f at the center of the element can be a weighted combination of the quadratic interpolation (which involves all three points) and linear interpolation of the endpoints viz.

$$\hat{f} = \beta(f_{lin} + \alpha f_{quadr})$$

α and β can be determined to represent the filter of choice. For example $\alpha = \frac{1}{4}$, $\beta = \frac{2}{3}$ is equivalent to a top-hat filter integrated with Simpson's rule. Quadrilaterals (in two-dimensions) and hexahedra (in three-dimensions) pose no additional difficulty as they are constructed from tensor products of these one-dimensional functions. Triangles and tetrahedra are not quite so trivial but can none the less be constructed (see Fig. 7). The only difference here is that there is not a node at the center of the element.

Implicit in this method is the assumption that it is sufficient to calculate the dynamic model coefficient once in each element. This filtering method is only meaningful on the interior of the element since at the endpoints (or corners in multi-dimensions) the different functional representations yield the same value. At these positions no filtering would be accomplished. This is of little concern for tetrahedral meshes since in this case there are roughly the same number of quadratic tetrahedra as there are nodal points. Therefore, the number of points where the dynamic model coefficient is evaluated is roughly the same. What has changed is the point in space where the dynamic model coefficient is calculated. We have simply moved the position where we evaluate the dynamic model coefficient from the nodes to the element centroids. The reason for doing this is that no communication is required to determine the dynamic model coefficient at the centroid using this method. This approach promises to be far less costly than methods 2 and 3.

2.4 Preliminary simulations

To obtain a reasonable initial condition, the two-dimensional Reynolds-averaged Navier-Stokes equations were solved with a one-equation eddy-viscosity model. Three-dimensional turbulence fluctuations from Choi's (1994) structured grid simulation were then added to this two-dimensional Reynolds-averaged solution to obtain a reasonable three-dimensional starting field.

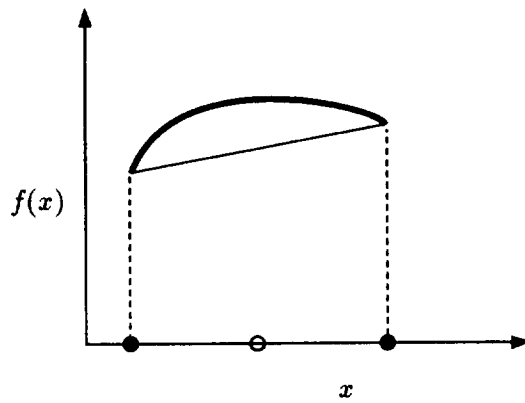


FIGURE 6. One-dimensional quadratic element is comprised of three nodes which quadratically interpolate (bold line) the nodal values of the function $f(x)$. By eliminating the center node (unfilled circle), a linear interpolant can be constructed (thin line) from the end nodes (filled circles).

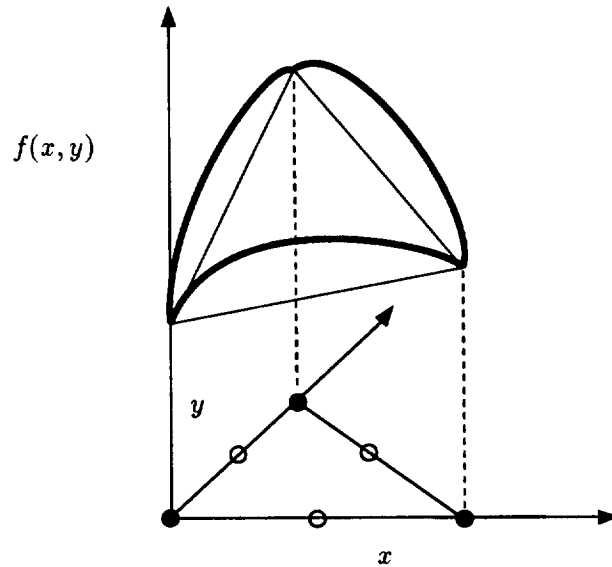


FIGURE 7. Quadratic triangle element is comprised of six nodes which quadratically interpolate the nodal values of the function $f(x, y)$. By eliminating the center node on each edge (unfilled circles), a linear interpolant can be constructed from the end nodes (filled circles).

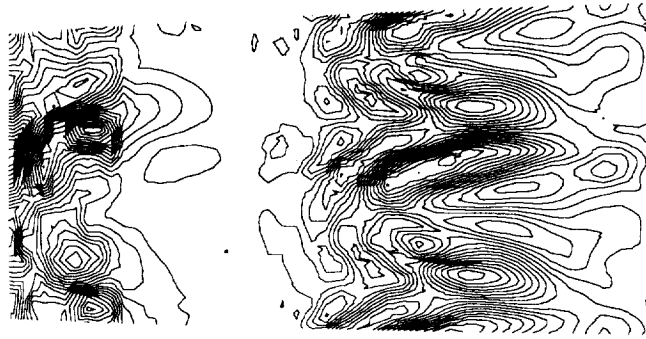


FIGURE 8. No sub-grid scale model simulation. Plan view spanwise velocity fluctuations at approximately 30 wall units away from the upper surface of the airfoil.

The first simulation was performed with no sub-grid scale model to establish a baseline case. The plan view of the spanwise velocity fluctuations at approximately 30 wall units away from the upper surface of the airfoil is shown in Fig. 8. Note the strong fluctuations beginning just after the nose, followed by a calm region and then continued fluctuations. The calm region is associated with a separation bubble which was not observed in the experiment. The calculation was discontinued after it became clear that the separation bubble was not a transient.

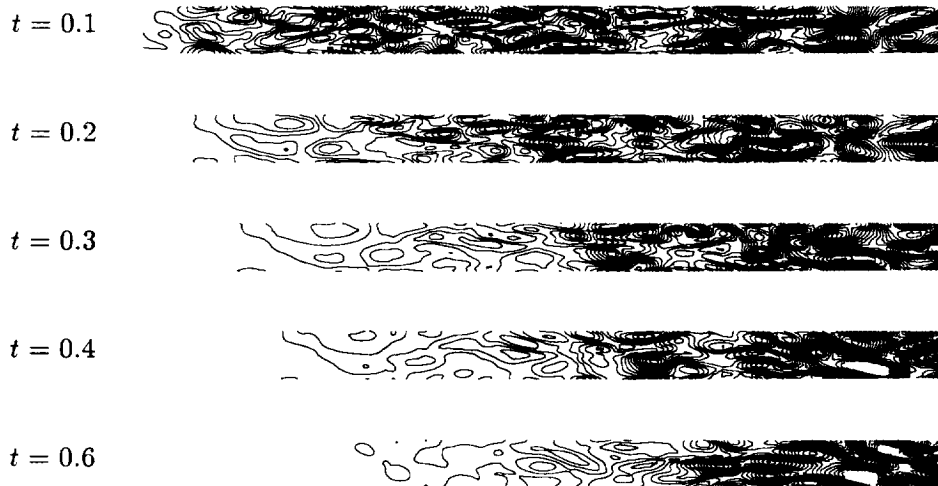


FIGURE 9. Constant-coefficient Smagorinsky model large-eddy simulation. Plan view spanwise velocity fluctuations at approximately 30 wall units away from the upper surface of the airfoil at various fractions of flow-over-chord times.

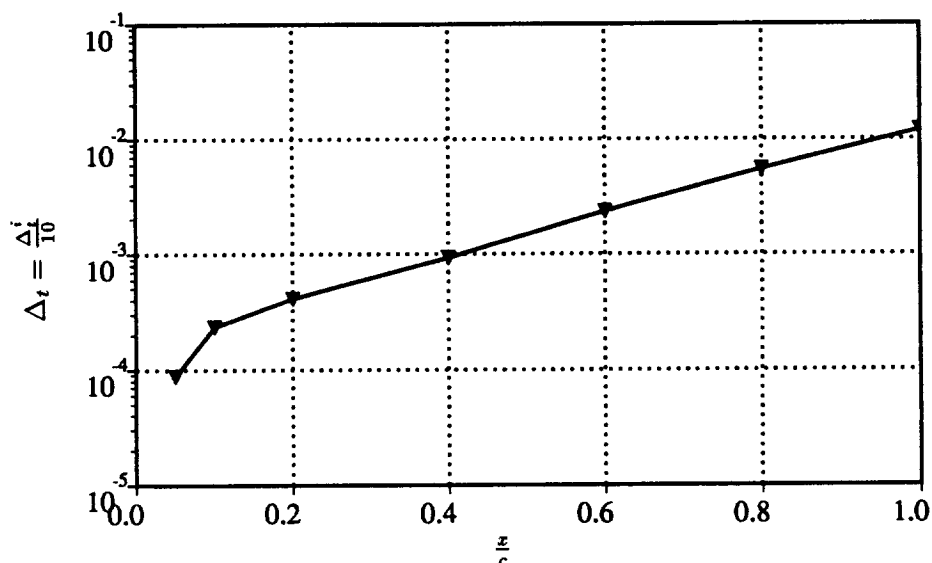


FIGURE 10. The time step which satisfies the one-tenth of an inertial time scale criterion as a function of position on the airfoil upper surface.

The second simulation performed utilized a constant-coefficient Smagorinsky model with wall damping. The additional eddy viscosity caused the flow to stay attached at the nose, but other difficulties were encountered. Fig. 9 shows a plan view of the fluctuating spanwise velocity field at approximately 30 wall units away from the upper surface. The full upper surface is shown at various fractions of flow-over-chord time. Note that the turbulence is convecting and interacting, but no new turbulence is being generated in the first two-thirds of the airfoil. The area of turbulent activity simply moves down the plate until it reaches the separation zone. Perhaps this should be the expected result as we have provided no disturbances to the boundary layer to sustain the turbulence. This simulation lacks the temporal and spatial resolution to undergo a natural transition. Strategies to force a cost-efficient transition will be investigated in future work. It is encouraging to note that the separated boundary layer maintains its turbulence as it should since it is an absolute instability (boundary layers are only convectively unstable).

A dynamic model simulation is under way. Preliminary results are quite promising. It seems that the laminar separation bubble at the leading edge that was observed in the coarse DNS is present at certain times in the dynamic model calculation. The highly transient separation seems to be causing enough of a disturbance to maintain turbulence over the entire airfoil upper surface. It is too early to tell if this disturbance is enough like the tripped boundary layer in the experiment to expect agreement further downstream. The calculation will be continued, and should it fail, more precise forcing strategies will be explored.

2.5 Time-step constraints

The current implementation of the code requires 10 seconds per non-linear iteration on the 128 node CM5. A real challenge in this flow is the very restrictive time step imposed by the flow in, and immediately following, transition. It is common when performing large-eddy simulations to choose the time step to be one tenth of an inertial time scale $\Delta_t^i = \frac{\delta}{u_e}$. In this problem, the boundary layer thickness, δ , and the boundary layer edge velocity, u_e , vary with x/c . The effect of this variation on the desired time step is plotted in Fig. 10. The simulations described above were calculated at a time step of 2.0×10^{-4} non-dimensional time units (normalized by chord and freestream velocity). This time step is only time accurate beyond $\frac{x}{c} = 0.1$. At this time step one flow over the chord requires 5000 time steps. It seems clear that time-accurate resolution of the transition process would be very expensive (experimental trip was placed at $x/c = .02$).

3. Future plans

3.1 Dynamic model

The new filtering operators developed in section 2.3 should be validated on simple, well understood flows such as decaying isotropic turbulence. This flow is very sensitive to errors in the filter width ratio as the decay rate is very sensitive to this quantity. Certain simple triangulation patterns may lend themselves to a closed form analysis of the filter width, but mixed triangulations occur in practice. While studying this problem, we might also examine the influence of the least-squares stabilization operator and the cost effectiveness of higher order elements.

3.2 Transition

The preliminary simulations have demonstrated a need to aid transition of the flow as was done in the experiment. It would be more efficient to do these studies on a flat plate where the mesh could be kept smaller. The goal here is not to give a spatially accurate transition, but rather to create and sustain turbulence beyond a certain percent of chord. An accurate resolution of the transition process is a costly alternative that hopefully may be avoided.

3.3 Improve code performance

New results from Aliabadi & Tezduyar (1994) indicate that further simplification of the least-squares stabilization operator may be possible. These ideas offer the potential to reduce the number of floating point operations per time step by a factor of two. The effect of these simplifications on accuracy must be studied.

3.4 Airfoil simulation

The airfoil simulation will continue to be the main focus of the unstructured-grid large-eddy simulation program. The above topics are parallel projects that are designed to constantly improve the quality of the airfoil simulation.

REFERENCES

- ALIABADI, S. K. & TEZDUYAR, T. E. 1994 Parallel fluid dynamics computations in aerospace applications. *University of Minnesota Supercomputer Institute Research Report UMSI 94/166*.
- CARATI, D. 1994 Private communication.
- CHAPMAN, D. R. 1979 Computational aerodynamics development and outlook. *AIAA J.* **17**, 1293.
- CHOI, H. 1994 Private communication.
- COLES, D., & WADCOCK, A. J. 1979 A flying-hot-wire study of two-dimensional mean flow past an NACA 4412 airfoil at maximum lift. *AIAA J.* **17**, 321.
- GERMANO, M., PIOMELLI, U., MOIN, P. & CABOT, W. H. 1991 A dynamic subgrid-scale eddy viscosity model. *Phys Fluids A.* **3**, 1760.
- GHOSAL, S., LUND, T. S., MOIN, P. & AKSELVOLL K. 1992 A dynamical localization model for large eddy simulation of turbulent flows. *J. Fluid Mech.* To appear.
- HASTINGS, R. C. & WILLIAMS B. R. 1987 Studies of the flow field near a NACA 4412 aerofoil at nearly maximum lift. *Aero. J.* **91**, 29.
- JANSEN, K. 1993 Unstructured grid large eddy simulation of wall bounded turbulent flows. *Annual Research Briefs 1993*. Center for Turbulence Research, NASA Ames/Stanford Univ.
- JANSEN, K., JOHAN, Z., & HUGHES, T. J. R. 1993 Implementation of a one-equation turbulence model within a stabilized finite element formulation of a symmetric advective-diffusive system. *Comp Meth Appl Mech Eng.* **105**, 405.
- JOHAN, Z., HUGHES, T. J. R., MATHUR, K. K., & JOHNSON, S. L. 1992 A data parallel finite element method for computational fluid dynamics on the Connection Machine system. *Comp Meth Appl Mech Eng.* **99**, 113.
- MOIN, P. & JIMENÉZ, J. 1993 Large-eddy simulation of complex turbulent flows. *AIAA-93-3099, AIAA 24th Fluid Dynamics Conference*.
- WADCOCK, A. J. 1987 Investigation of low-speed turbulent separated flow around airfoils. *NACA CR 177450*.

Large-eddy simulation of flow through a plane, asymmetric diffuser

By Hans-Jakob Kaltenbach

1. Motivation and objectives

A challenge for traditional turbulence modeling, based on the Reynolds averaged Navier-Stokes equations, remains the accurate prediction of 'mild', adverse pressure-gradient driven separation from a smooth surface. Durbin (1994) showed recently that his modified $k - \epsilon$ -model, which carries the wall-normal Reynolds stress as additional velocity scale, is superior to a variety of more complicated Reynolds stress models in its capability to predict 'mild' separation.

With this study we want to explore the capability of large-eddy simulation to predict the separation which occurs on the deflected wall of an asymmetric, plane diffuser with opening angle of 10° . Simpson (1989) points out that 'mild' separation of a boundary layer under the influence of an external pressure gradient leads to a growth of turbulent length scales and generally increases the turbulence level. He emphasizes the role of 'coherent' motion elements for the process of separation. Smoke visualization has revealed that the zone of mean backflow strongly interacts with the forward flow in the above layer. In the mean backflow region, the flow reverses sign quite often, indicating strong intermittency. These features are difficult to capture with statistical models which are based on mean velocity gradients such as mixing length approaches. Conversely, one can expect that LES which explicitly resolves the large motion elements should be able to correctly represent this aspect of separated flows.

The flow through the plane diffuser - which is depicted in Fig. 1- exhibits some additional interesting physical phenomena which make it a challenging test case. In addition to 'mild' separation about halfway down the deflected ramp, the flow is characterized by a small backflow zone with stalled fluid in the rear part of the expanding section. The turbulent flow entering the diffuser is subject to combined adverse and radial pressure gradients stemming from the convex curvature. Finally the flow recovers into a developed, turbulent channel flow in the outlet section.

Obi *et al.* (1993) provide measurements of mean flow, Reynolds stresses, and pressure recovery, which were obtained by means of LDV in a wind tunnel. The details of the experiment and the suitability of the measurements for validation purposes will be discussed in section 2.4.

The objective of this study is to investigate whether LES with the standard dynamic model is able to accurately predict the flow in the one-sided diffuser and to explore the resolution requirements and associated costs.

PRECEDING PAGE BLANK NOT FILLED

PAGE 174 INTENTIONALLY BLANK



FIGURE 1. Computational domain for the plane diffuser. Only a subset of the actual grid lines is plotted. All streamwise distances are measured as distance from the entrance of the expanding section in units of δ .

2. Accomplishments

2.1 Numerical method

The numerical method for solving the unsteady, incompressible Navier-Stokes equations is described in Choi *et al.* (1993). Second-order spatial central differences on a staggered mesh are combined with a fully-implicit time integration scheme (Crank-Nicholson) which uses Newton linearization along with approximate factorization. Approximately 4 iterations per time step are required to reduce the residual sufficiently when running the code at CFL ranging from 2 to 3. The cost is therefore comparable to an explicit scheme running at CFL smaller than 1. In this type of flow the CFL-limit is set through the wall-normal velocity in the vicinity of the rounded entrance corner. For a typical grid of $163 \times 64 \times 64$ cells the code runs at 350 Mflops and requires $20 \mu\text{s}$ per cell per time step on a Cray C-90.

Unsteady data, created in an independent LES of fully developed channel flow, are specified at the inflow plane. A convective boundary condition, i.e. $\partial u_i / \partial t + c \partial u_i / \partial x = 0$, is applied at the outflow plane, where c is the bulk velocity of the outlet channel. The upper and lower boundaries are no-slip walls.

A simple, robust version of the dynamic SGS model (Germano *et al.* 1991) in combination with least-square contraction (Lilly 1992) and spanwise averaging is used. The total viscosity is constrained to be positive through a clipping operation.

2.2 Grid spacing requirements

The dimensions of the computational domain are shown in Fig. 1. The diffuser geometry and the Reynolds number $Re_b = U_b \delta / \nu = 9000$ match the experimental configuration of Obi *et al.* (1993). Here, U_b denotes the bulk velocity of the incoming fully developed turbulent channel flow of height 2δ . The flow from the inlet channel of length 5δ enters an asymmetric diffuser with an expansion ratio of $a = 4.7$ and an opening angle of approximately 10° . The expanding section extends over 42δ . The outlet section is too short to cover the full recovery, but no measurements were reported beyond $x = 58\delta$. Both corners are rounded with a radius of 8.6δ . Due to the high resolution requirements in the spanwise direction, the computational domain could not be chosen larger than 4δ , resulting in aspect ratios of inlet and outlet channel of $1 : 2$ and $1 : 0.43$, respectively. The experiment had much higher aspect ratios of $1 : 35$ and $1 : 7.45$, respectively.

Previous studies have shown that proper simulation of the near-wall region without employing a near-wall model imposes severe limits on the spanwise grid-spacing.

With the present numerical method, a spanwise spacing of $\Delta z^+ = 15$ can be tolerated for a canonical boundary layer or a developed channel flow at this Reynolds number before results deteriorate significantly. Resolution requirements are highest in the inlet channel where the flow is attached. At $Re_b = 9000$ we expect Re_τ close to 500 and a wall-unit approximately 0.002δ . We therefore used 128 points in the span for a width of 4δ , corresponding to $\Delta z^+ = 15.5$, for the *inflow data creation run*, but not for the actual diffuser LES.

Span-wise resolution requirements decrease further downstream because of the increase of a wall-unit due to the channel expansion. Additionally, near-wall physics change under an adverse pressure gradient and resolution requirements become less severe. Therefore, the following approach can be justified: the inflow data are created on a fine mesh; at the inflow plane we use unsteady data which are filtered onto a mesh which has only half of the spanwise resolution of the inflow creation run ($\Delta z^+ = 30$). We find that this method works quite well and does not give significantly different results from a case where the fine spanwise resolution was carried through the whole diffuser. A similar approach was used by Akselvoll (1994) for simulation of flow over a backward-facing step.

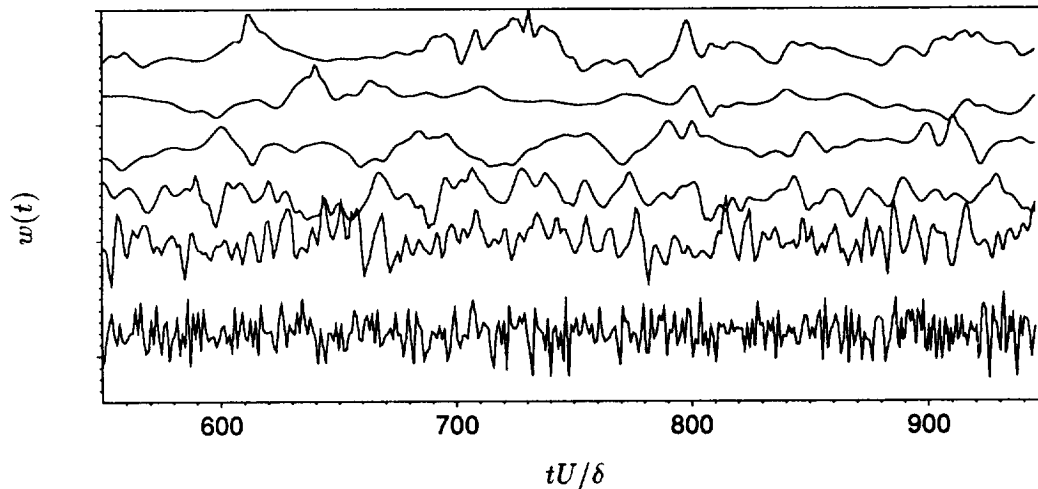


FIGURE 2. Time series of spanwise velocity fluctuations from LES at stations $x = 11, 20, 26, 35, 45,$ and 61 , from bottom to top, recorded close to the diffuser centerline.

2.3 Simulation time requirements

As was the case with the *spatial* resolution, we find that the flow inside the diffuser imposes very different requirements with respect to the *temporal* resolution in the inlet and outlet sections. The inertial time scale $\tau = 0.5h(x)/U_b(x)$, based on local diffuser height $h(x)$ and bulk velocity $U_b(x)$, increases with the square of the expansion ratio from the inlet to the outlet section, i.e. $\tau_{out} = a^2\tau_{in}$. In order to properly simulate the inlet turbulence and due to CFL-limits, the maximum

time-step is approximately $0.1\tau_{in}$. Statistics in the outlet section will converge after a minimum of $50\tau_{out}$ or 12000 time-steps. The total cost of one simulation is 100 CPU hours, of which 40% were spent reaching a statistical steady state. The order-of-magnitude time scale change which occurs as the flow slows down inside the expanding section becomes evident in the time series of spanwise velocity fluctuations measured at several streamwise locations (Fig. 2).

2.4 Assessment of the experiment for validation purposes

The experiment by Obiet *al.* (1993) was done in an open loop wind tunnel facility. The flow entered the diffuser after a rather long development section of 200δ . The wide aspect ratios of 1 : 35 and 1 : 7.45 for inlet and outlet duct guaranteed a spanwise homogeneous core flow over 90% of the inlet and 60% of the outlet span. An increase of mass-flow along the core section of the diffuser was found in the experiment, see Fig. 3. The rather strong increase (more than 10%) downstream of $x = 40$ indicates that a secondary flow develops in the outlet section. It is unclear whether the flow upstream of $x = 40\delta$ is affected by this phenomenon. If not, it can be used for validation purposes of a simulation which assumes spanwise homogeneity of turbulence to avoid explicitly accounting for side walls.

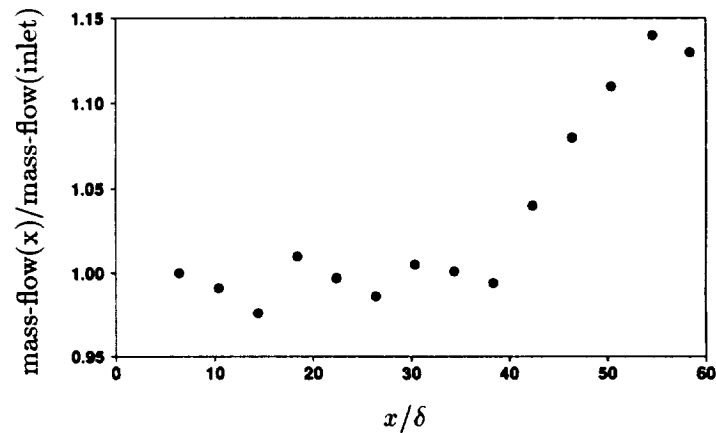


FIGURE 3. Mass-flow ratio as obtained from integrating measured velocity profiles over the local diffuser height.

Measurements have been rescaled individually for each streamwise location in order to make them consistent with a constant mass-flow through the inlet duct. It is probably safe to use data upstream of $x = 40$ for validation purposes. Flow separation occurs a substantial distance (20δ) upstream of the location with the mass-flow problem. It seems unlikely that the flow at this location is affected by the secondary flow in the outlet section. Additional support for this hypothesis comes from the fact that flow statistics did not change when we performed a simulation on a domain where the outflow boundary was inside the expanding section.

The secondary flow causes additional pressure losses, which would not be present in a spanwise homogeneous case. This becomes evident when a force balance for

a control volume formed by a vertical x, y cross-section and with unit depth is computed from the experimental data.

2.4.1 Force balance

An integral force balance indicates whether a simulation has reached statistical equilibrium and gives insight about the relative importance of frictional losses. Additionally, a force balance is a good check of the suitability of the pressure measurements for validation purposes.

The control volume for the force balance in the streamwise direction is formed by a plane through the inlet duct at x_{in} , a plane perpendicular to the flat wall somewhere inside the diffuser at x_{out} , and through cuts along upper and lower diffuser walls. The balance for a volume with unit depth and under the assumption of constant pressure across the diffuser reads

$$\sum F_x = -F_{pressure} - F_{friction} - F_{ramp} = \dot{J}|_{x_{out}} - \dot{J}|_{x_{in}}$$

with the (positive) forces defined as

$$F_{pressure} = (p_{x_{out}} - p_{x_{in}})h_{x_{in}}, \quad F_{friction} = \int_{x_{in}}^{x_{out}} \tau_w(l) \cos \alpha(l) dl,$$

$$F_{ramp} = \int_{x_{in}}^{x_{out}} (p_{x_{out}} - p(l)) \sin \alpha(l) dl, \quad \dot{J} = \rho \int_0^{h(x)} U(y)^2 \text{sign}(U) dy .$$

The angle formed by the wall and the horizontal is denoted α . Fig. 4 depicts the various contributions to the force balance as a function of location x_{out} . The inlet station was fixed at $x_{in} = -3$. For the experiment, no data were available for the inlet velocity profile and skin friction. We assumed a $y^{1/7}$ power law for the mean velocity at the inlet, which gives about the right ratio U_{cent}/U_b . For the skin friction we used data from the simulation. As will be shown later the frictional losses play a minor role in the force balance.

The terms of the right-hand side of the force balance are normalized with the left-hand side (l.h.s), i.e. the momentum flux difference across the control volume. Once steady state has been reached, the normalized l.h.s. should sum up to 100%, which is approximately the case for the simulation data, independently from where the control volume is located. A small residual of 2% stems from approximations involved in the evaluation of the individual forces. The difference in momentum flux is mainly balanced by the pressure gain throughout the diffuser. Roughly 30% of the momentum loss is converted into a force acting on the inclined wall. Friction from the top and bottom walls accounts for less than 5% of the momentum losses. Even a 20% change in the skin friction changes the overall balance by only 1%.

If we compute the force balance from the experimental data, we find a rather large residual in the range from 20% to 30% of the momentum flux difference. Possible

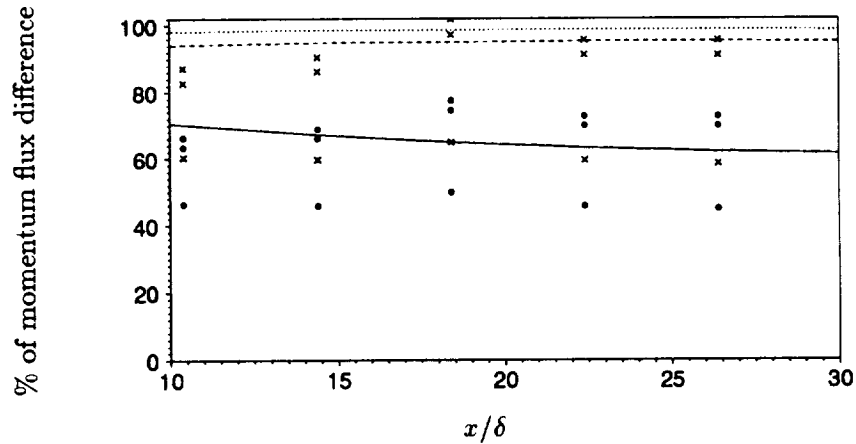


FIGURE 4. Force balance for plane diffuser: accumulated forces F_{press} (—), $F_{press} + F_{ramp}$ (---), and $F_{press} + F_{ramp} + F_{frict}$ (.....), from LES, normalized by the momentum flux difference as a function of the location of the downstream control volume face. The upstream face is fixed at $x = -3$. Balance computed from original data of Obiet *al.* (1993) (•) and with c_p enhanced by a factor of 1.3 (×).

reasons include measurement errors (wrong reference velocity or density for c_p), deviations from spanwise homogeneity, and additional pressure losses resulting from secondary flow in the diffuser outlet. The additional frictional losses which stem from the diffuser side walls can be neglected because the side wall surface area is rather small compared to the upper and lower walls of the experimental facility. The most likely source for the momentum deficit is the use of a wrong reference velocity for computation of c_p . In the original data set, mean velocities were scaled in such a way that the corresponding ratio of centerline to bulk velocity in the inlet section would be 1.05, which is quite different from the independently measured value for this ratio of 1.14. The source for this mismatch is obviously the use of devices (Pitot tube, hot-wire, LDA) which were not properly calibrated or aligned.

Possibly, the same problem appears with normalization of pressure measurements. However, as discussed earlier, the pressure rise inside the diffuser will be strongly affected by the presence of a secondary flow. Blockage from side wall boundary layers increases the velocity in the center of the duct and limits the pressure recovery. If the momentum deficit was purely caused by usage of a wrong reference velocity, a 'valid' c_p curve can be reconstructed by rescaling the measured c_p . The rescaling factor can be determined by requiring that the residual for the force balance vanish. Fig. 4 includes the force balance for the experimental data set, which was obtained when c_p was increased by 30%. This corresponds to a 14% decrease in reference velocity. With this correction, the residual drops below 5%.

Despite the problem with the pressure measurements, we think that the experiment is valuable and can be used for validation purposes, at least upstream of $x = 40$. From the close coupling between mean flow profile shape and c_p -curve,

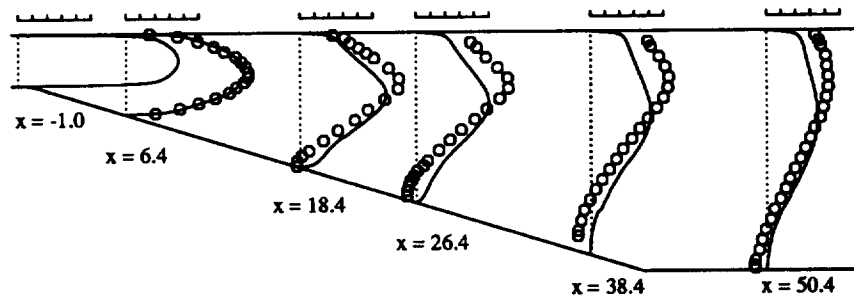


FIGURE 5. Mean velocity $U/U_{b,in}$ from LES (—) and experiment (o). Increments of the scales are 0.1.

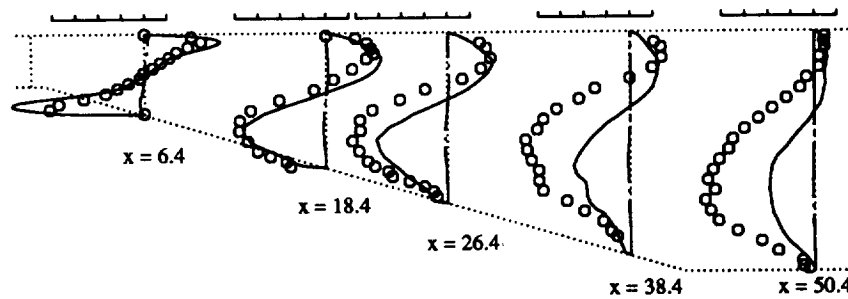


FIGURE 6. Turbulent shear stress $\overline{uv}/U_{b,in}^2$ from LES (—) and experiment (o) and SGS-stress τ_{12} (---). Increments of the scales are 0.001.

it follows that it is sufficient to either match the mean flow or the c_p -curve as an indicator for proper prediction of the flow if only one of these quantities is available.

2.5 Simulation results

Flow statistics were obtained by averaging simulation results in time and in the spanwise homogeneous direction. We compare results from a LES with measurements of Obi *et al.* (1993).

All data are scaled with the bulk velocity from the inlet channel, $U_{b,in}$. The ratio of centerline to bulk velocity in the inlet channel was 1.10 in the simulation and 1.14 ± 0.02 in the experiment. Profiles of mean velocity are strongly asymmetric inside of the expanding section, see Fig. 5. The flow remains attached on the flat wall and separates about halfway down the ramp. The LES exhibits only minimal backflow between $x = 30$ and $x = 50$ whereas measurements show significant backflow downstream of $x = 18$. Profiles of components of the Reynolds stress tensor are shown in Figs. 6, 7 and 8. We depict only the resolved motion part of the normal stresses \overline{uu} and \overline{vv} from the LES because the SGS kinetic energy is not explicitly known in our SGS-model. Fig. 6 shows that the off-diagonal components of the SGS-stresses are negligible when compared with the resolved scale turbulent shear stress \overline{uv} .

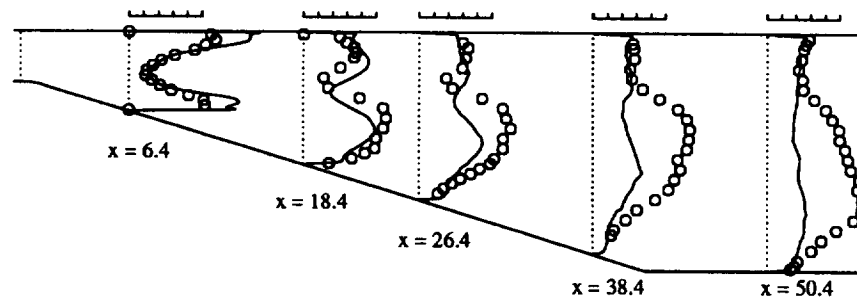


FIGURE 7. Streamwise velocity variance $\overline{u'u'}/U_{b,in}^2$ from LES (—) and experiment (o). Increments of the scales are 0.002.

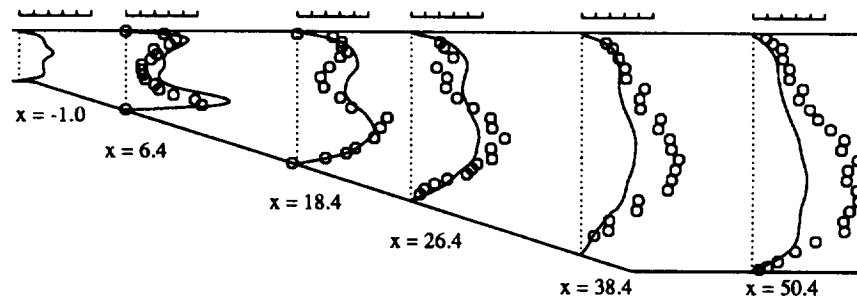


FIGURE 8. Vertical velocity variance $\overline{v'v'}/U_{b,in}^2$ from LES (—) and experiment (o). Increments of the scales are 0.001.

Simulated and measured Reynolds stresses agree within some scatter up to location $x = 14.4$ (not shown). Further downstream, the simulation exhibits a much lower core flow turbulence level than the experiment. Mean flow profiles begin to deviate at station $x = 10$. The satisfactory match of simulation and experiment in the entrance part of the diffuser indicates that the inlet condition for the simulation, i.e. fully developed channel flow, was adequate. Additionally, we found that this flow is not very sensitive to the quality of the inflow database. Underprediction of separation leads to a quicker pressure recovery in the simulation compared with the (rescaled) experimental data, see Fig. 9.

2.6 Discussion

The outcome of this simulation does not give a clear picture about the success or failure of LES to predict the flow inside the diffuser. The following discussion is based on more simulation data than presented in this report. We have performed a series of simulations on finer meshes where we varied the spacing in all three directions, for example Δz^+ between 12 and 40. A good measure for the role of the SGS model in this type of simulation is the contribution of the SGS stresses to the total energy dissipation rate, which varied from less than 50% on fine meshes to more than 80% on coarse meshes (see Fig. 10).

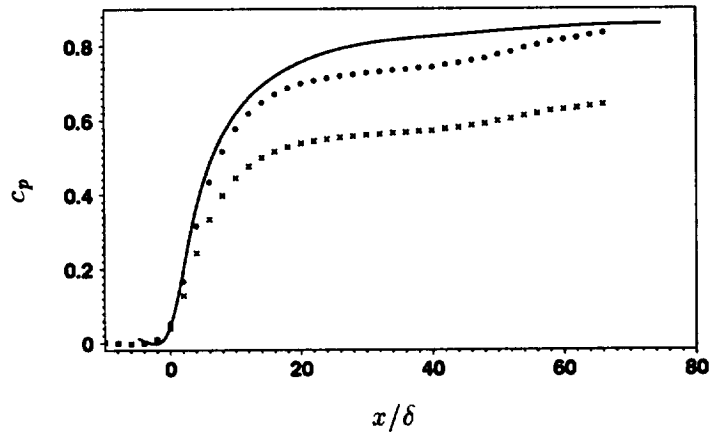


FIGURE 9. Pressure coefficient c_p , based on $U_{b,in}$, along lower diffuser wall. Results from LES (—), original experimental data (\times) and data scaled with 1.3 (\bullet).

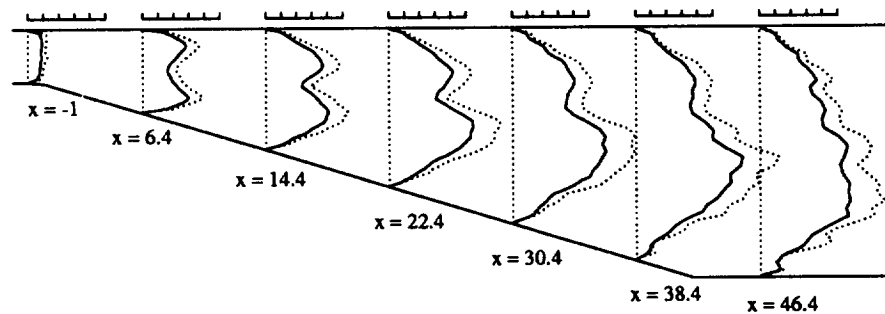


FIGURE 10. Ratio of SGS-eddy viscosity and molecular viscosity (—) and of corresponding dissipation rates (----) from LES. Scale increments are 1.

The LES solutions obtained on various meshes differ with respect to pressure recovery by less than 4% and overpredict c_p by roughly 10% when compared with the *rescaled* experimental data, see Fig. 9. This proves the capability of the dynamic procedure to adapt the role of the SGS model to a given grid resolution. Our simulations are in this sense ‘grid-independent’. We also found that the flow changes quite drastically (on the coarser meshes) when the SGS model is turned off, indicating the importance of an adequate SGS model for this type of simulation.

We also checked the sensitivity of results with respect to the spanwise domain size, which we varied between 4δ and 12δ . Again, the flow inside the diffuser turned out to be rather insensitive with respect to this parameter.

There is also the possibility of a non-adequate numerical scheme which might have an even stronger impact on the simulation than specific properties of the SGS model. Although the discretization of the non-linear term is strictly energy conserving on a

Cartesian mesh, this property might be violated on stretched meshes. This aspect is the topic of an ongoing evaluation of the numerical scheme.

3. Conclusions and future plans

We find that LES of flow through the plane diffuser gives a consistent, grid-independent result. The dynamic model seems to work fine in an adverse pressure gradient situation although the present simulation underpredicts separation when compared with measurements. The cost of the simulation is set by the high spatial resolution requirements of the inlet section and the rather long simulation time caused by the presence of a very wide range of time scales. Use of zonal techniques or unstructured meshes (see article by Ken Jansen in this volume) would be desirable and could strongly reduce the overall cost.

The cause for deviation between LES results and measurements has not been fully understood yet. The experimental data have some obvious flaws in terms of momentum balance and mass conservation. However, we are not so much concerned about the lack of reliable pressure measurements for validation purposes. For the present flow, the shape of the mean flow profiles is a very sensitive indicator for the quality of flow prediction and partially compensates for the lack of c_p .

A fully-resolved DNS for this case would be very costly (in the order of 1000 CPU hours) but could be done on present computers. This would eliminate all doubts about the 'right' flow to compare with. We will further investigate this case by improving the numerics, using schemes with higher-order truncation errors. As a further goal, we plan to investigate whether a LES with a near-wall model is able to describe this flow adequately at a much lower cost than the present simulation.

REFERENCES

- AKSELVOLL, K. 1994 Personal communication.
- CHOI, H., MOIN, P. & KIM, J. 1993 Direct numerical simulation of turbulent flow over riblets. *J. Fluid Mech.* **255**, 503-539.
- DURBIN, P. 1994 Separated flow computations with the $k - \epsilon - v^2$ model. *CTR Manuscript 152*. NASA Ames/Stanford Univ.
- GERMANO, M., PIOMELLI, U., MOIN, P. & CABOT, W. H. 1991 A dynamic subgrid-scale eddy viscosity model. *Phys. Fluids A*. **3**, 1760-1765.
- LILLY, D. K. 1992 A proposed modification of the Germano subgrid scale closure method. *Phys. Fluids A*. **3**, 2746-2757.
- OBI, S., AOKI, K. & MASUDA, S. 1993 Experimental and computational study of turbulent separating flow in an asymmetric plane diffuser; in: *Ninth Symposium on Turbulent Shear Flows*, Kyoto, Japan, August 16-19, 1993. p. 305.
- SIMPSON, R. L. 1989 Turbulent boundary-layer separation. *Ann. Rev. Fluid Mech.* **21**, 205-234.

Large-eddy simulation of a boundary layer with concave streamwise curvature

By T. S. Lund

1. Motivation and objectives

Turbulence modeling continues to be one of the most difficult problems in fluid mechanics. Existing prediction methods are well developed for certain classes of simple equilibrium flows, but are still not entirely satisfactory for a large category of complex non-equilibrium flows found in engineering practice. Direct and large-eddy simulation (LES) approaches have long been believed to have great potential for the accurate prediction of difficult turbulent flows, but the associated computational cost has been prohibitive for practical problems. This remains true for direct simulation but is no longer clear for large-eddy simulation. Advances in computer hardware, numerical methods, and subgrid-scale modeling have made it possible to conduct LES for flows of practical interest at Reynolds numbers in the range of laboratory experiments. A handful of these simulations have been performed over the last few years (*cf.* Akselvoll and Moin 1993, Zang *et al.* 1993, He and Song, 1993). Many of these recent simulations were performed to develop LES technology for complex flows and assess the accuracy of the dynamic subgrid-scale model. The indication from these first simulations is that LES in conjunction with the dynamic model is capable of accurately predicting high Reynolds number complex flows for which Reynolds-averaged techniques have not been able to produce satisfactory results. The validation and technology development phase for LES of complex flows is ongoing, and additional challenging test cases must be attempted. The objective of this work is to apply LES and the dynamic subgrid-scale model to the flow of a boundary layer over a concave surface.

Although the geometry of a concave wall is not very complex, the boundary layer that develops on its surface is difficult to model due to the presence of streamwise Taylor-Görtler vortices. These vortices arise as a result of a centrifugal instability associated with the concave curvature. The vortices are of the same scale as the boundary layer thickness, alternate in sense of rotation, and are strong enough to induce significant changes in the boundary layer statistics. Owing to their streamwise orientation and alternate signs, the Taylor-Görtler vortices induce alternating bands of flow toward and away from the wall. The induced upwash and downwash motions serve as effective agents to transport streamwise momentum normal to the wall, thereby increasing the skin friction. Reynolds-averaged prediction techniques are unable to resolve these vortices and must resort to *ad hoc* correction terms. Aside from Taylor-Görtler vortices, concave curvature affects the turbulent Reynolds stress budget. This effect is captured in full Reynolds stress models but is absent in the more commonly used algebraic, one- or two-equation models.

In contrast to Reynolds-averaged approaches, LES is well suited for the concave-wall boundary layer flow since the Taylor-Görtler vortices are simulated directly. In addition, the effects of curvature, not associated with vortices, are captured.

The simulations reported here are designed to match the laboratory experiments of Barlow and Johnston (1988) and Johnson and Johnston (1989). These experiments are an ideal test case since a rather complete set of velocity statistics are available for several streamwise stations.

2. Accomplishments

2.1 Numerical method

The computer code used for this project is based on the second-order staggered mesh finite difference algorithm described by Choi and Moin (1994). The incompressible Navier-Stokes equations are integrated in time with a fully implicit variant of the fractional step algorithm. Generalized curvilinear coordinates are used in two directions with the third direction (usually spanwise) restricted to be uniform. In the fractional step procedure, the dependent variables are advanced in a two-step process where an intermediate velocity field is first advanced without the pressure gradient term. The effect of the pressure gradient is then accounted for through a correction term obtained by solving a Poisson equation. In the current implementation, the intermediate velocity field is advanced with a fully-implicit scheme where Newton iteration is used to reduce the factorization error. By taking a Fourier transform in uniform mesh direction (spanwise), the Poisson equation is reduced to a series of two dimensional problems, one for each spanwise wavenumber. The lowest wavenumber system is solved with a direct inversion technique, whereas the higher wavenumber systems are treated with a Gauss-Seidel iteration scheme. Although the scheme is stable for CFL numbers of at least 5, the time step is usually dictated by accuracy requirements. In this work, the maximum CFL number is held below 2.0.

2.2 Computational domain and flow conditions

The simulations are designed to match the laboratory configuration of Barlow and Johnston (1988) and Johnson and Johnston (1989). The experimental facility is a water channel where a straight entry flow section is fitted to a 90° constant radius of curvature bend (see Fig. 1). The opposite wall is contoured in order to minimize the streamwise pressure gradient on the concave wall. Boundary layers develop on both channel walls; one experiences an abrupt transition to concave curvature while the other experiences a transition to convex curvature. Measurements are available only for the concave side. Both boundary layers are tripped early on the entry section and become fully turbulent by the beginning of the curved section. At this station, the two boundary layers are separated by about 1.5 boundary layer thicknesses of potential core in the center of the channel. The potential core diminishes with downstream distance, and the two boundary layers merge between the 75° and 90° stations. The momentum thickness Reynolds number at the beginning of the curve is $R_{\theta_0} = 1300$. At this station, the ratio of boundary layer thickness to radius of

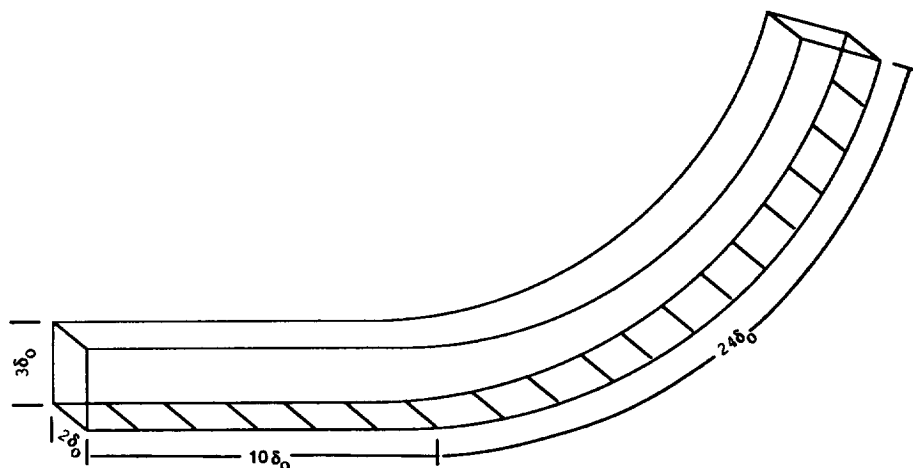


FIGURE 1. Computational domain. All dimensions are referred to the boundary layer thickness measured at the location where the curvature begins (δ_0). The radius of curvature is $R = 18.1\delta_0$.

curvature, δ_0/R , is 0.055, which is sufficiently large to create significant curvature effects.

The computational domain is an abbreviated version of the experimental geometry. A sketch is provided in Fig. 1. The calculation begins approximately 10 boundary layer thicknesses upstream of the curved section and ends at the 75° station (the boundary layer thickness measured at the onset of curvature, δ_0 is used as the normalizing length scale). Unsteady turbulent boundary layer data are supplied at the inflow boundary whereas a convective boundary condition is used at the outflow boundary. The domain extends $2\delta_0$ in the spanwise direction and periodic boundary conditions are used in this direction. According to the experimental measurements, the spanwise width is sufficient to enclose 4 streamwise Taylor-Görtler vortices. Only the concave boundary layer is simulated, and consequently the domain extends from the concave wall to the streamline that lies along the channel centerline. No slip conditions are applied at the solid wall whereas impermeable and no-stress conditions are applied at the upper boundary. The position of the streamline boundary is determined by conducting an inviscid analysis of the experimental geometry. The displacement effects of both boundary layers is accounted for in this analysis.

The computational grid contains $358 \times 44 \times 64$ points in the streamwise, wall-normal, and spanwise directions respectively. The mesh is stretched in the wall-normal direction and uniform in the other two. The grid spacings, based on wall units at the location where the curve begins, are $\Delta x^+ = 50$, $\Delta y_{\min}^+ = 1$, and

$$\Delta z^+ = 16.$$

2.3 Inflow boundary data

A spatially-evolving simulation such as this one requires the specification of instantaneous turbulent data at the inflow boundary. Accurate inflow data is required to insure that the boundary layer is fully turbulent and in equilibrium at the beginning of the curve. Instantaneous inflow data is generated via an auxiliary large-eddy simulation of a flat plate boundary layer. This simulation is also spatially evolving, but makes use of Spalart's method (1988) to generate its own inflow data by rescaling the data at the exit station. The resolution of the inflow simulation is identical to that of the main simulation. The inflow simulation is run in parallel with the main simulation in a time-synchronous fashion. At each time step, the velocity field is extracted from an appropriate $y - z$ plane in the inflow simulation. This data is used directly as the inflow boundary conditions. In practice, the inflow simulation can be either run at the same time as the main simulation or run ahead of time and the inflow data stored on disk. The inflow simulation increases the overall cost of the main simulation by about 10%.

2.4 Simulation results

Before sampling statistics, the simulation is run for an initial transient elimination period of 45 boundary layer inertial time scale units (1.2 flow-through times). Statistics are then sampled over a period of 150 inertial time scales (3.9 flow-through times). Mean quantities are formed by averaging over both the spanwise direction and time.

The pressure distribution on the concave wall is compared with the experimental measurements in Fig. 2. The curve begins at $x = 0$, and thus negative values of x correspond to the flat entry section. Overall, the pressure is reasonably constant. The largest pressure gradient occurs near the start of the curve. This is due to slight errors in the contour applied to the upper streamline. Since the streamline was determined through an inviscid analysis of the experimental configuration, it is quite likely that a similar pressure signature exists in the experiment. Unfortunately no detailed measurements are available in the region near the start of the curve. The maximum deviation from uniform pressure is roughly 2%, which probably has a negligible effect on the boundary layer development. Aside from the pressure variation near the start of the curve, there is a small uniform drop in pressure with streamwise distance. This is due to a slight acceleration of the core flow resulting from errors made in the estimate for the boundary layer displacement thickness used to determine the upper streamline. The enhanced pressure drop near the downstream boundary is due to inaccuracies in the outflow boundary condition.

Mean velocity profiles at several streamwise stations are compared with the experimental data in Fig. 3. The first station is on the flat inlet section, 8 boundary layer thicknesses ahead of the curved section. The next 4 stations are at 15° , 30° , 45° , and 60° (4.7, 9.5, 14.2, and 18.9 boundary layer thicknesses into the curved section). The velocity data are normalized with the velocity profile that would be developed by an inviscid flow through the curved section. To a good approximation,

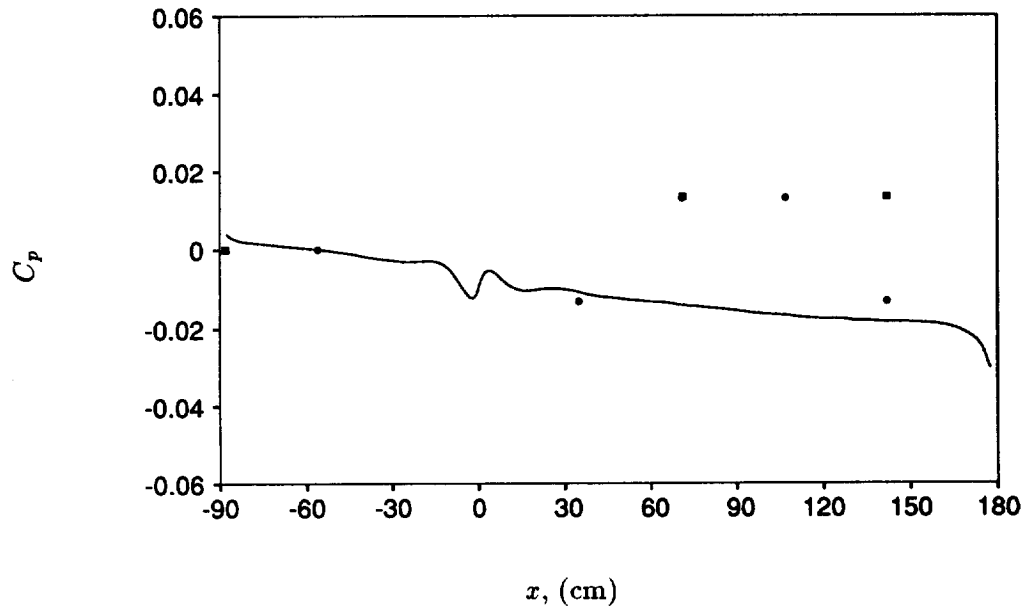


FIGURE 2. Pressure distribution on the concave wall. The curve begins at $x = 0$. δ_0 is the boundary layer thickness at $x = 0$. — : LES; ● : Johnson and Johnston (1989); ■ : Barlow and Johnston (1988). In the experiments, the pressure is determined indirectly from the velocity measured in the potential core region.

this profile varies linearly according to

$$U_p(y) \simeq U_{pw}(1 + y/R), \quad (1)$$

where U_{pw} is the inviscid velocity that would be achieved at the wall. Overall, the agreement between simulation and experiment is quite good. On the flat section, the simulation produces profiles that are a bit fuller near the wall as compared with the experiment. This discrepancy is related to the grid resolution and can be reduced by refining the streamwise and spanwise mesh spacings. The current level of agreement is deemed acceptable, however. The initial discrepancy fades in the curved section. Note the difference in the shape of the profile between the flat and 60° stations (first and last curves in Fig. 3). The effect of concave curvature is to create fuller profiles, especially close to the wall. This is due to enhanced mixing resulting from the effects of curvature.

Reynolds shear stress profiles are shown in as the solid lines in Fig. 4 (the dashed lines will be described below). Overall, the agreement with the experimental data is reasonable. The simulation does a good job of capturing the qualitative changes to the shear stress profile that result from concave curvature. The peak Reynolds stress increases and the profile develops a bulge in the central region of the profile. On a quantitative level, however, the simulation tends to under-predict the peak Reynolds stress, especially at the 45° and 60° stations. The reason for this discrepancy is not

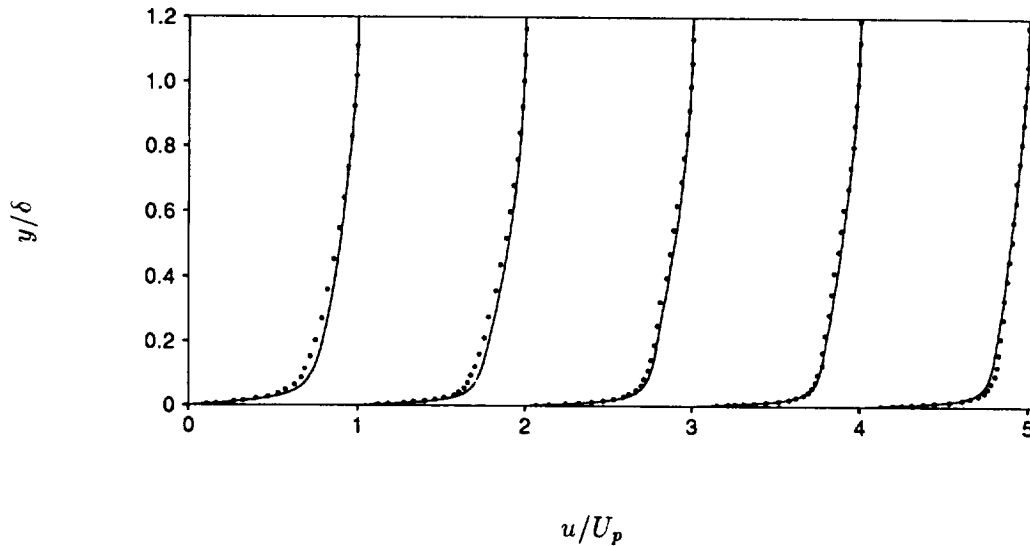


FIGURE 3. Mean streamwise velocity profiles. The velocity is scaled by $U_p(y)$ (Eq. (1)), the streamwise profile that would be developed in an inviscid flow through the curved section. The first station is on the flat inlet section, 8 boundary layer thicknesses ahead of the curve. The next 4 stations are at 15° , 30° , 45° , and 60° respectively. — : LES; • : Johnson and Johnston (1989).

fully understood, but there is some evidence that it is related to the details of the inflow conditions. An example of the sensitivity to inflow conditions is shown by the dashed lines in Fig. 4, where an alternative set of inflow data is used. In this case, inflow is generated from a parallel-flow boundary layer simulation. The instantaneous velocity data from this simulation is rescaled to yield statistics that are consistent with a spatially-evolving boundary layer. The rescaling operation is not sufficiently accurate to keep the boundary layer in equilibrium, and a transient develops near the inflow boundary. This effect is clearly visible in Fig. 4 where the Reynolds stress is over-predicted at the first measurement station. Although it may be fortuitous, higher levels of Reynolds stress on the flat section lead to considerably better agreement with the experimental data at the downstream stations. Future work will focus on a through understanding of this effect.

Velocity fluctuations are compared with the experiment in Fig. 5. Agreement with the experimental data is good. Again the qualitative changes to the profiles resulting from concave curvature are well reproduced. A bulge develops in the central portion of each profile. This effect is greatest for the wall-normal and spanwise fluctuations. On a quantitative level, minor differences exist between the simulation and experiment. Except for the near-wall region of the streamwise profile, all three velocity fluctuations are generally under-predicted in the simulation. The

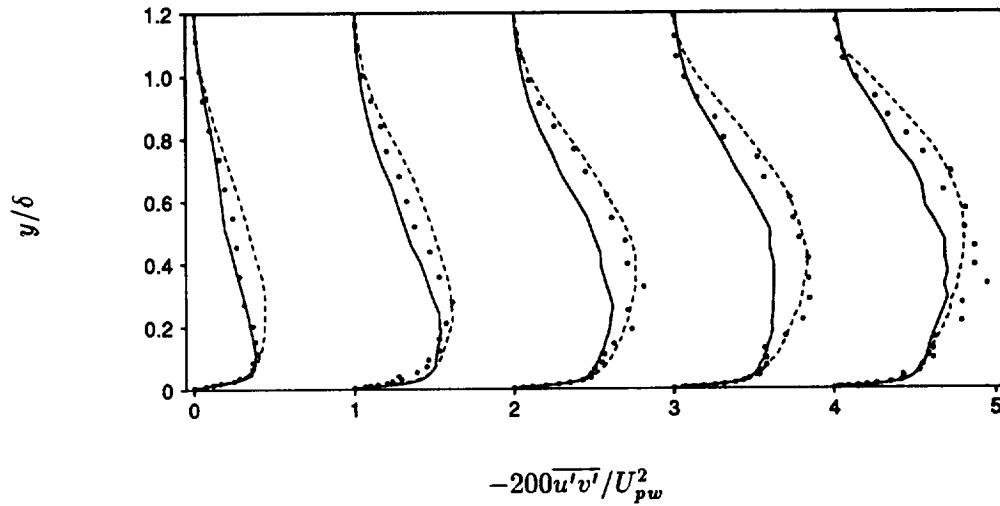


FIGURE 4. Reynolds shear stress profiles. — : LES, spatially evolving boundary layer inflow data; ---- : LES, rescaled parallel flow boundary layer inflow data; ● : experimental measurements of Johnson and Johnston (1989). The first station is on the flat inlet section, 8 boundary layer thicknesses ahead of the curve. The next 4 stations are at 15° , 30° , 45° , and 60° respectively. U_{pw} is an extrapolation of the core velocity to the wall assuming an inviscid profile.

reason for this discrepancy is not completely understood, but as in the case of the Reynolds shear stress, it is sensitive to the inflow conditions. Better agreement can be obtained at the downstream stations if the fluctuation levels are increased at the inlet. Aside from these differences, the velocity fluctuations are too anisotropic near the wall; the streamwise fluctuation is over-predicted whereas the wall-normal and especially spanwise fluctuations are under-predicted. This is a common symptom of marginal resolution in either a direct or large-eddy simulation. It is caused by an inability to resolve the inter-component energy transfer mechanism in this region of the flow. The discrepancy can be reduced by increasing the number of grid points, but current level of agreement is deemed acceptable.

The calculated skin friction is compared with experiment in Fig. 6. The skin friction is seen to increase significantly due to the effects of concave curvature. The simulation captures this trend but also exhibits some quantitative differences with the experimental data. The simulation results agree best with the experiment on the flat section ahead of the curve and beyond about 45° in the curved section. In the intermediate section, the simulated skin friction appears to respond more rapidly than the experiment downstream of the start of the curved section. The small excursion immediately upstream of the curved section is due to the residual pressure gradient in this region (see Fig. 2). Skin friction was determined in the experiment by fitting a log-law to the velocity profiles (Clauser chart approach). This method is accurate for equilibrium boundary layers but can be in significant

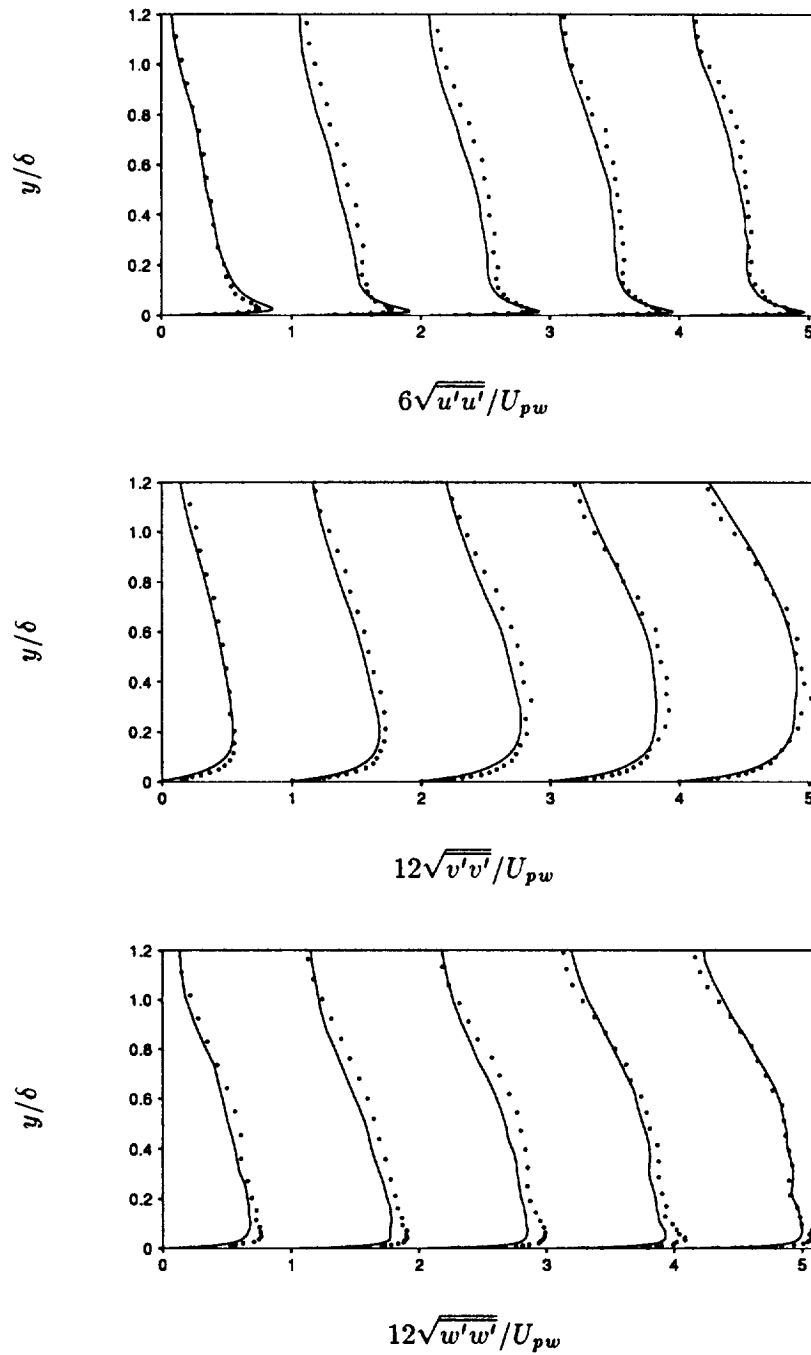


FIGURE 5. Velocity fluctuation profiles. The first station is on the flat inlet section, 8 boundary layer thicknesses ahead of the curve. The next 4 stations are at 15° , 30° , 45° , and 60° respectively. U_{pw} is an extrapolation of the core velocity to the wall assuming an inviscid profile. — : LES; • : experimental measurements of Johnson and Johnston (1989).

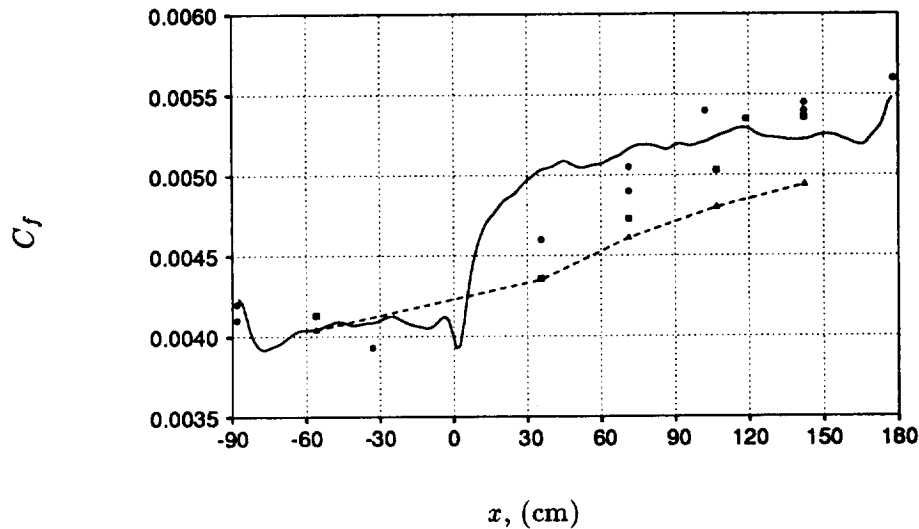


FIGURE 6. Skin friction coefficient. The curve begins at $x = 0$. — : LES, direct method; \bullet : experimental data of Johnson and Johnston; \blacksquare : experimental data of Barlow and Johnston; $-\triangle-$: LES, Clauser method.

error when applied in non-equilibrium situations. Since the boundary layer is displaced from equilibrium while transitioning from the flat to curved sections, the experimental skin friction measurements could be in error. In order to assess this possibility, skin friction was determined from the simulation data indirectly through use of the Clauser chart. The results of these measurements are shown as the triangles connected with a dashed line in Fig. 6. As expected, there are significant differences between the direct measurement and the Clauser method near the onset of curvature. In particular, the Clauser method measurements fall below the direct measurements near the onset of curvature and are actually in better agreement with the experimental data in this region. As the boundary layer comes into equilibrium further downstream, the Clauser and direct measurements appear to be converging.

2.5 Conclusions

Large-eddy simulations of a concave-wall boundary layer have been performed. The simulations make use of the dynamic subgrid-scale model which requires neither the tuning of model constants, nor the use of *ad hoc* corrections for curvature. Concave curvature results in large changes to the turbulent statistics, and LES does a good job of predicting the transition from a flat wall to a concave surface. Quantitative differences exist between the LES results and the experimental data, and these can be attributed in part to the details of the turbulent data supplied at the inflow boundary. The turbulent flow fields do not reveal strong Taylor-Görtler vortices, a feature that may also be related to the inflow data. In the experiment, streamwise vorticity is generated by the flow-conditioning devices and is amplified in the contraction leading to the channel. These vortices may act as effective nuclei

for the rapid development of Taylor-Görtler vortices in the curved section. In the simulations, coherent streamwise vorticity is absent from the outer regions of the spatially-evolving boundary layer inflow data. Stream-wise vortices are probably also absent in the outer portion of the parallel flow boundary layer data, although the rescaling operation results in higher fluctuations in this region of the profile. In any case, Taylor-Görtler vortices will develop eventually from the background turbulence, but the organization process may require a streamwise distance that is a function of the initial velocity fluctuation level. In order to avoid this uncertainty, it may be necessary to “seed” the outer regions of the inflow boundary layer with semi-coherent streamwise vorticity corresponding to the levels existing in the experiment.

3. Future plans

Future work will focus on a careful study of the influence of inflow conditions. In particular, streamwise vorticity will be introduced to the outer region of the inflow boundary layer. The flow fields will be examined for the presence of strong Taylor-Görtler vortices and the results compared with the existing runs. Once issues with the inflow data are resolved, the impact of the subgrid-scale model will be investigated. This will be done by repeating the simulation with no subgrid-scale model. Differences between the runs with and without the model will help elucidate the influence of the subgrid-scale model in this flow.

The LES results will also be compared with the predictions of Reynolds averaged Navier-Stokes (RANS) calculations. Aside from full Reynolds stress closure, RANS methods have no formal dependence on curvature. *Ad hoc* corrections are commonly used to account for curvature and the accuracy of a few of these will be investigated. Full Reynolds stress models do have a curvature-dependent production term, and the effect of this term will be investigated.

REFERENCES

- AKSELVOLL, K. & MOIN, P. 1993 Application of the dynamic localization model to large-eddy simulation of turbulent flow over a backward-facing step. In *Engineering applications of large-eddy simulations*, ed. by S. A. Ragab and U. Piomelli. Presented at the ASME fluid engineering conference, Washington D. C. June 20-24, 1993.
- BARLOW, R. S. & JOHNSTON, J. P. 1988 Structure of a turbulent boundary layer on a concave surface. *J. Fluid Mech.* **191**, 137-176.
- CHOI, H., MOIN, P. & KIM J. 1993 Direct numerical simulation of turbulent flow over riblets. *J. Fluid Mech.* **255**, 503-540.
- HE, J., & SONG, C. C. S., 1993 Some applications of large-eddy simulation to large-scale turbulent flows at small Mach number. In *Engineering applications of large-eddy simulations*, ed. by S. A. Ragab and U. Piomelli. Presented at the ASME fluid engineering conference, Washington D. C. June 20-24, 1993.

- JOHNSON, P. L., & JOHNSTON, J. P. 1989 The effects of grid-generated turbulence on a flat and concave turbulent boundary layer, Report MD-53, Thermosciences Division, Dept. of Mech. Eng., Stanford University.
- SPALART, P. R. 1988 Direct simulation of a turbulent boundary layer up to $R_\theta = 1410$. *J. Fluid Mech.* **187**, 61-98.
- ZANG, Y., STREET, R. L., & KOSEFF, J. R. 1993 A dynamic mixed subgrid-scale model and its application to recirculating flows. *Phys. Fluids A*. **5**, 3186-3196.

Experimental investigations of “on-demand” vortex generators

By Seyed G. Saddoughi

1. Motivation and background

Conventional vortex generators as found on many civil aircrafts are mainly for off-design conditions - e.g. suppression of separation or loss of aileron power when the Mach number accidentally rises above the design (cruise) value. In normal conditions they perform no useful function and exert a significant drag penalty. Recently there have been advances in new designs for passive vortex generators and boundary layer control. While traditionally the generators heights were of the order of the boundary layer thickness (δ), recent advances have been made where generators of the order of $\delta/4$ have been shown to be effective: see Gad-el-Hak & Bushnell (1991) for a review.

The advancement of Micro-Electro-Mechanical (MEM) devices has prompted several efforts in exploring the possibility of using such devices in turbulence control. These new devices offer the possibility of boundary layer manipulation through the production of vortices, momentum jets, or other features in the flow. However, the energy output of each device is low in general, but they can be used in large numbers. Therefore, the possibility of moving from passive vortex generators to active (on-demand) devices becomes of interest. Replacement of fixed rectangular or delta-wing generators by devices that could be activated when needed would produce substantial economies.

One example of an “on-demand” device is the vortex-generator jet originally proposed by Compton & Johnston (1992), in which an oblique jet is emitted from a nozzle flush with the surface. This is a simple device; however, it is likely to be economic only on or near engine nacelles where high-pressure air is available. Ducting to other parts of an aircraft is likely to involve so much extra weight and cost that there would be no net economic benefit.

An alternative form of “on-demand” vortex generator, requiring only an electrical power supply, has been developed by Jacobson & Reynolds (1993) at Stanford University. It consists of a surface cavity elongated in the stream direction (Fig. 1) and covered with a lid cantilevered at the upstream end. This kind of a vortex generator is also called a “springboard” actuator. The lid, which is a metal sheet with a sheet of piezoelectric ceramic bonded to it, lies flush with the boundary. On application of a voltage of the order of 10-100V, the ceramic expands or contracts; although the longitudinal strain is small, the induced bending strain is orders of magnitude larger. Even so, adequate amplitude can be obtained only by running at the cantilever resonance frequency and applying amplitude modulation: for 2.5 mm \times 20 mm cantilevered lids, they obtained tip displacements of the order of 100

RESEARCH PAGE BLANK NOT FILMED

RESEARCH PAGE BLANK NOT FILMED

P.196

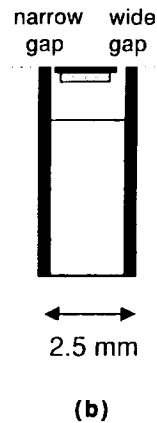
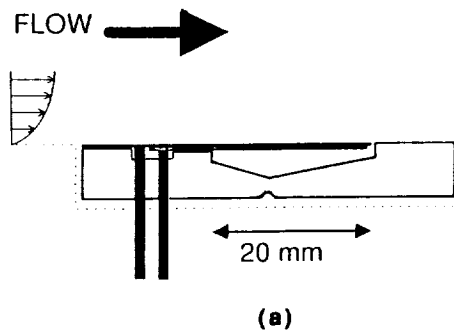


FIGURE 1. A schematic diagram of springboard piezo-ceramic actuator developed by Jacobson & Reynolds (1993). (a) Side view; (b) Front view.

to $150\ \mu\text{m}$. As the lid oscillates, fluid is expelled from the cavity through the gap around the lid on the downstroke.

The breakthrough innovation of the device was achieved using an asymmetrical gap configuration as shown in Fig. 1 (narrow gap ≈ 50 to $75\ \mu\text{m}$ and wide gap $\approx 250\ \mu\text{m}$). Their actuator was driven with a 25 V amplitude sine wave at a frequency of approximately 325 Hz in water. Jacobson & Reynolds found that periodic emerging jets on the narrow side induced periodic longitudinal vorticity into the boundary layer. With a vertical cavity wall a vortex pair with common flow upwards is formed (Fig. 2). The cavity-lid combination developed by them has the potential to be made using micro-fabrication techniques, which are ideally suited to mass production. Their device was used to modify the inner layer of the boundary layer for skin-friction reduction and is now being incorporated into an active-control feedback system.

Our proposed application is not strictly “active” control: the vortex generators would simply be switched on, all together, when needed (e.g. when the aircraft Mach

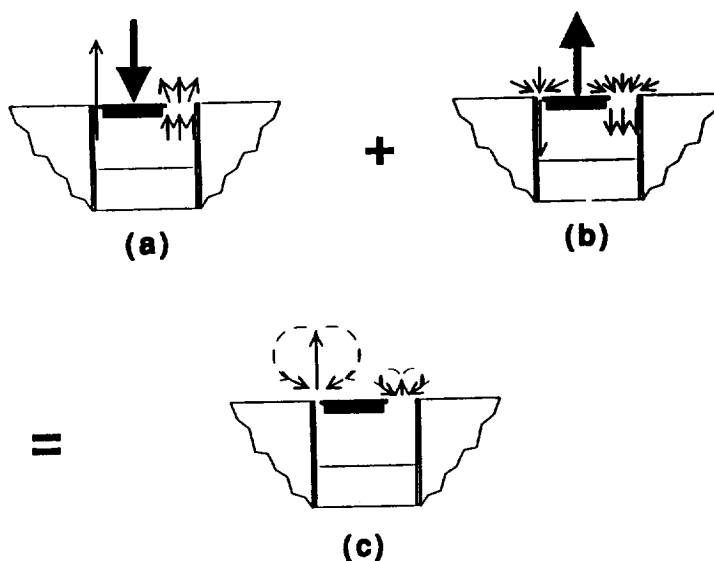


FIGURE 2. Induced actuator flow from Jacobson & Reynolds (1993). (a) Directed efflux; (b) Diffuse influx; (c) Superposition of (a) and (b).

number exceeded a certain limit). To this extent our scheme is simpler; however, to promote mixing and suppress separation we desire to deposit longitudinal vortices into the outer layer of the boundary layer as in conventional vortex generators. This requires a larger device although an alternative might be an array of smaller devices, for example, a longitudinal row with phase differences in the modulation signals so that the periodic vortices join up. The vortex pair with common flow up has the advantage that it will naturally drift away from the surface, but the disadvantage is that the net vorticity is zero so that the pair is eventually obliterated by turbulent mixing, rather than simply being diffused as in the case of a single vortex. It should be possible to devise alternative shapes of cavity wall so that the jet emerges obliquely and produces net longitudinal vorticity.

2. Accomplishments

2.1. Apparatus and measurement techniques

We have built a device with a mechanically driven cantilevered lid to avoid the restrictions of resonant forcing. Our device is made about ten times the size of Jacobson & Reynolds' device because intuition suggested that the optimum ratio of device size to boundary-layer thickness for our purpose would need to be larger than in the different task of control of inner-layer turbulence.

Our vortex generator is made so that shape or size of the cavity and lid (28 mm \times 250 mm) can be easily changed: for example the side walls of the cavity are the ends of inserts which can be moved in the spanwise direction to alter the gap-width on one or both sides. The cavity depth (20 mm) can be changed by placing inserts inside the cavity. The lid frequency can be changed easily by means of a variable speed DC motor; presently we can obtain a maximum frequency of about 60 Hz for the cantilever-tip displacement of approximately 10 mm.

As mentioned above, cavity wall inclination may have a large effect on the ejected vortex pair. Hence our vortex generator is mounted on a turntable so that its yaw angle can be changed; if the emerging jet sheet is regarded crudely as a solid blockage of the boundary-layer flow, the jet emerging from a yawed cavity might be a more effective vortex generator than an unyawed jet. Finally, tests over a range of ratios of vortex-generator size to boundary layer thickness can be carried out simply by changing the streamwise location of the device.

Our vortex generator was mounted on the top wall of the 76 cm \times 76 cm suction wind tunnel in the Mechanical Engineering Department at Stanford University. This wind tunnel is mainly used for flow-visualization purposes. The existing test section is about 3 m long so that fairly thick turbulent boundary layers can be obtained at downstream locations in this tunnel.

We conducted extensive flow-visualization experiments at two different free-stream velocities of $U_e \approx 1$ m/s and 5 m/s. Here we use a Cartesian coordinate system $x_i = (x, y, z)$ with x -axis along the flow direction, y -axis normal to the solid surface (top wall of the tunnel) and z -axis in the spanwise direction. The respective mean-velocity components in these directions are $U_i = (U, V, W)$.

Smoke was sucked into the flow by the boundary-layer fluid, through a slot located upstream of the vortex generator. A laser-light sheet was used to visualize the motion in cross-stream (y - z) planes. To document our results, we have taken photographs and films of the flow patterns around the vortex generator set at different orientations to the flow direction; the oscillating tip of the cantilevered lid was pointed in the (i) downstream, (ii) 45° to the downstream, (iii) upstream, and (iv) 45° to the upstream directions. Also, tests were conducted for different gap-width sizes and lid-oscillation frequencies at the above two free-stream velocities. Some of these flow-visualization results are presented and discussed below.

2.2. Results and discussion

For the first time, we are able to see the vortices that the "on-demand" vortex generator deposits into the boundary layer. As mentioned above we have taken a large number of photographs, three of which are shown in Figs. 3, 4, and 5, where all the pictures show flow patterns in y - z planes (flow out of page). Also, in these pictures, the wide-gap and the narrow-gap are 1 mm and 0.2 mm respectively. The lid frequencies were approximately 20 Hz and 50 Hz for the experiments conducted at $U_e \approx 1$ m/s and 5 m/s respectively.

In Fig. 3 the vortex generator is pointed in the downstream direction, and the wide gap in this case is located on the left-hand side of the picture. This is the flow pattern obtained at $U_e \approx 1$ m/s. Fig. 4 shows the flow visualization for the same

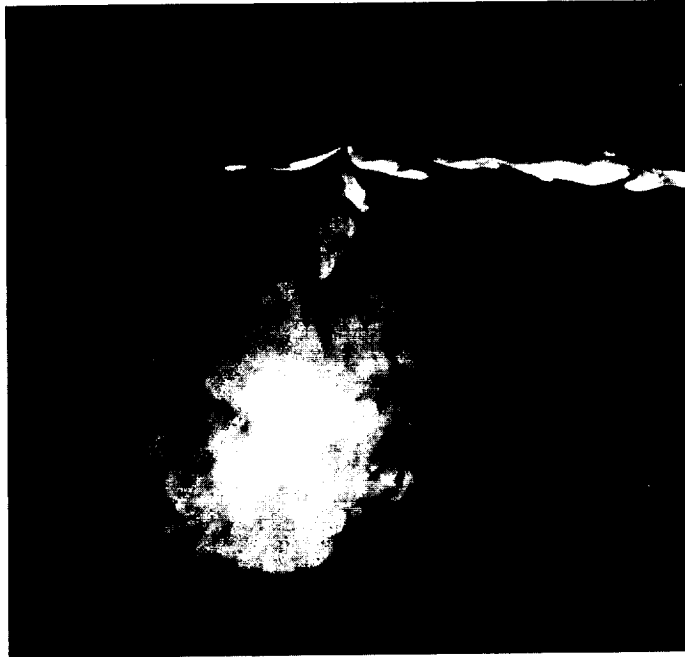


FIGURE 3. Jet sheet ejected from the wide gap at $U_e \approx 1$ m/s, when the vortex generator is pointed in the downstream direction.

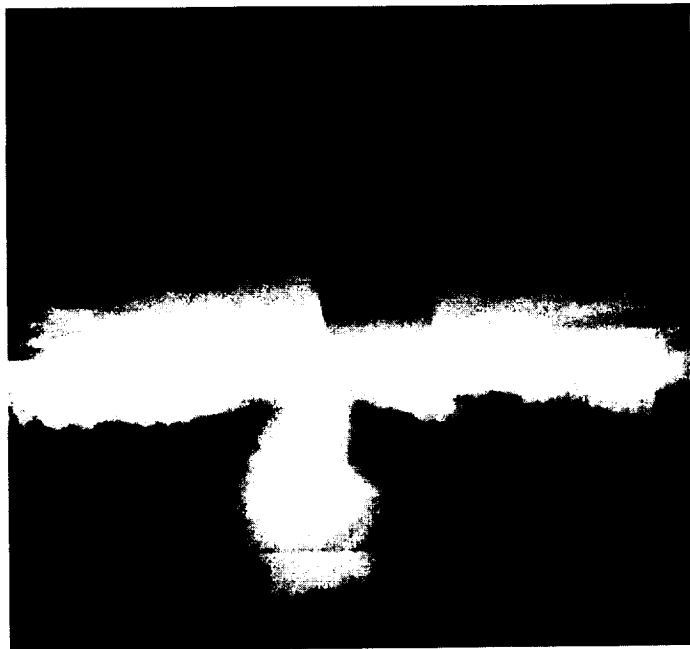


FIGURE 4. As Fig. 3 but at $U_e \approx 5$ m/s.

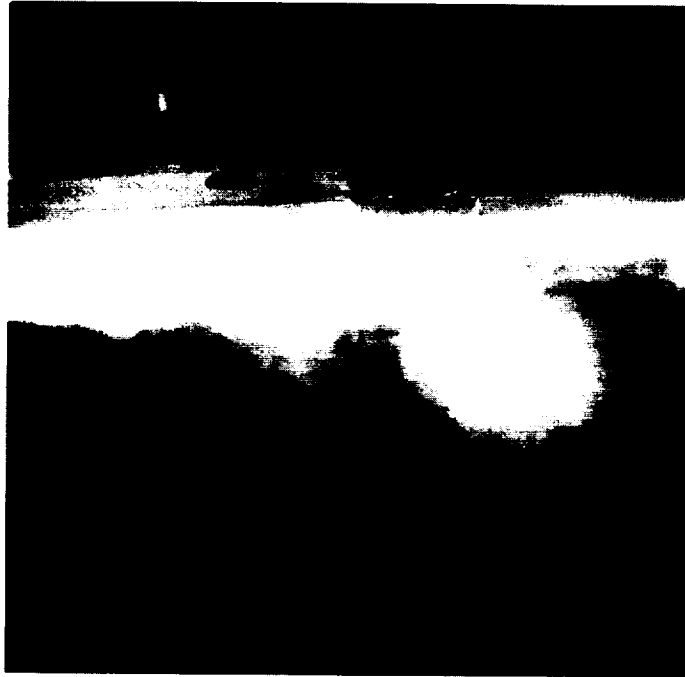


FIGURE 5. Vortical structure ejected from the wide gap at $U_e \approx 5$ m/s, when the vortex generator is pointed in the upstream direction.

orientation of the vortex generator, but at $U_e \approx 5$ m/s. It can be seen clearly that at both free-stream velocities, the jet sheets emerge from the wide gaps only, and for the high-speed case where the boundary layer thickness at the measurement location was about 20 mm, the jet sheet extends to approximately 3 to 4 times boundary-layer thicknesses into the flow.

Fig. 5 shows the flow pattern for $U_e \approx 5$ m/s, but in this case the vortex generator is pointed in the upstream direction; therefore, the wide gap is now located on the right-hand side of the picture. Here also we see large ejections from the wide gap only; however, in this case we can observe a better vortical structure than the one shown in Fig. 4. This suggests that a more efficient vortex generation may be achieved in this way. Our visualizations show that these vortical structures last for large distances downstream of the vortex generator.

In all of our experiments we observed that the stronger jet emerged from the wide-gap side rather than the narrow side. This is contrary to the finding of Jacobson & Reynolds. In order to explain this difference one may consider the Stokes' parameter, $St \equiv \sqrt{\frac{2\pi f d^2}{\nu}}$, (Rathnasingham, *et al.* 1994), where f is the frequency, d is the diameter of the circular hole for the "wall-jet" actuators, and ν is the kinematic viscosity. Based on dimensional analysis, Rathnasingham, *et al.* proposed that for this kind of actuator, $St > 1$ is required to prevent the blockage of the exit flow due to viscous effects.

In the case of the springboard actuators, one may assume d to represent the gap-width size. In our investigations, for the narrow gap at the highest lid-frequency of 50 Hz, $St < 1$. Therefore, it appears that for our narrow gap the exit flow is viscous dominated. This may be the reason that we do not see any flow out of the narrow gap. However, for the narrow gap of Jacobson & Reynolds' case, $St > 1$, since their experiments were conducted in water, and also in their case the lid frequency was larger than the present studies.

3. Future plans

In order to quantify our conclusions from the flow visualization experiments, we plan to conduct the following measurements:

(i) To check the efficiency of our device, we need to take spanwise measurements of skin friction at a few streamwise locations downstream of the vortex generator.

(ii) To obtain a measure of the mean longitudinal vorticity, $(\frac{\partial W}{\partial y} - \frac{\partial V}{\partial z})$, we will take X -wire measurements in x - y and x - z modes (at close enough spacing to obtain accurate derivatives) in a few cross-sectional locations downstream of the vortex generator.

(iii) If the above initial tests show strong vortex-generation effects, we will use our vortex generators in laboratory adverse-pressure-gradient boundary layers to suppress separation, and eventually we would test them on a full-scale aircraft in the 80' \times 120' wind tunnel at NASA Ames.

Acknowledgments

This work was carried out in collaborations with Dr. Nagi Mansour and Professors Peter Bradshaw and Bill Reynolds. We would like to thank Mr. Fritz Rinehart for his suggestions during the manufacturing of the vortex generator. We would also like to thank Don Bott, Carl Buice, and Pat Moriarty for their help during the experiments.

REFERENCES

- COMPTON, D. A. & JOHNSTON, J. P. 1992 Streamwise vortex production by pitched and skewed jets in turbulent boundary layer. *AIAA J.* **30**, 640.
- GAD-EL-HAK, M. & BUSHNELL, D. M. 1991 Separation control: Review. *J. Fluids Eng.* **113**, 5.
- JACOBSON, S. A. & REYNOLDS, W. C. 1993 Active boundary layer control using flush-mounted surface actuators. *Bulletin of the American Physical Society*, Vol. 38, No. 12, P. 2197.
- RATHNASINGHAM, R., PIEPSZ, O., GOLDBERG, H. D., SCHMIDT, M. A. & BREUER, K. S. 1994 Performance of sensors and actuators for turbulent flow control. *Bulletin of the American Physical Society*, Vol. 39, No. 9, P. 1909.

Direct numerical simulations of “on-demand” vortex generators — Mathematical formulation

By P. Koumoutsakos

1. Motivation and objectives

The objective of the present research is the development and application of efficient adaptive numerical algorithms for the study, via direct numerical simulations, of active vortex generators. We are using innovative computational schemes to investigate flows past complex configurations undergoing arbitrary motions. Some of the questions we try to answer are: Can and how may we control the dynamics of the wake? What is the importance of body shape and motion in the active control of the flow? What is the effect of three-dimensionality in laboratory experiments?

We are interested not only in coupling our results to ongoing, related experimental works, but furthermore to develop an extensive database relating the above mechanisms to the vortical wake structures with the long-range objective of developing feedback control mechanisms. This technology is very important to aircraft, ship, automotive, and other industries that require predictive capability for fluid mechanical problems. The results would have an impact in high angle of attack aerodynamics and help design ways to improve the efficiency of ships and submarines (maneuverability, vortex induced vibration, and noise).

2. Accomplishments

This is a preliminary report describing our numerical method and presenting results of direct numerical simulations of pertinent two-dimensional bluff body flows. Our final objective is the simulation of flows past the three dimensional configuration shown in Fig. 1a. At the first stage of this work, we are interested in the respective two-dimensional configuration (Fig. 1b). The results of these simulations would help us investigate the effects of three dimensionality in experiments and assess the role of two-dimensional vortical mechanisms.

2.1 Mathematical formulation - numerical method

Two-dimensional incompressible unsteady flow of a viscous fluid may be determined by the vorticity transport equation as

$$\frac{\partial \omega}{\partial t} + \mathbf{u} \cdot \nabla \omega = \nu \nabla^2 \omega \quad (1)$$

where $\mathbf{u}(\mathbf{x}, t)$ is the velocity, $\omega = \omega \hat{\mathbf{e}}_z = \nabla \times \mathbf{u}$ the vorticity, and ν denotes the kinematic viscosity. For flow around a non-rotating flat plate, translating with velocity $\mathbf{U}_b(t)$, the velocity of the fluid (\mathbf{u}) on the surface of the body (\mathbf{x}_s) is equal to the velocity of the body:

$$\mathbf{u}(\mathbf{x}_s, t) = \mathbf{U}_b(t) \quad (1a)$$

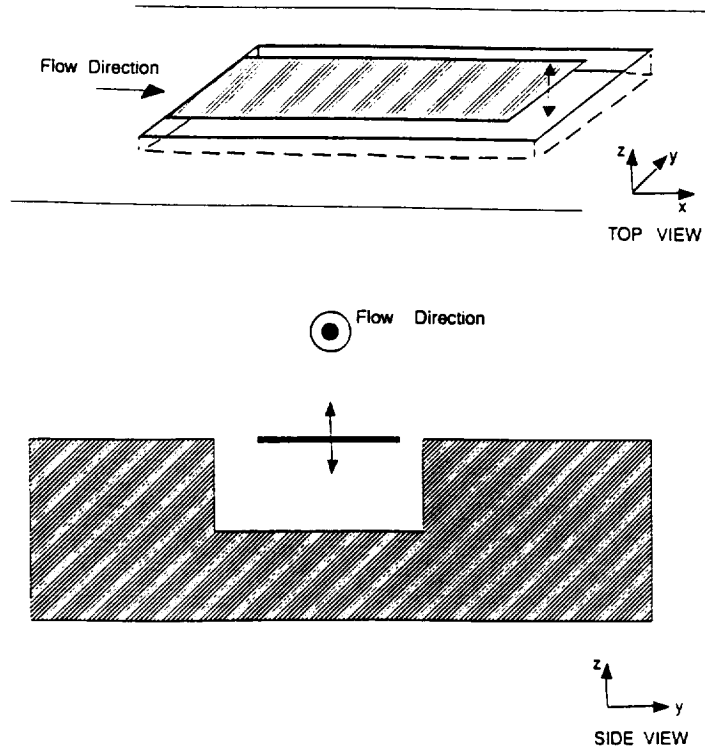


FIGURE 1. Definition sketch. Top view (a), front view (b).

At infinity we have:

$$\mathbf{u}(\mathbf{x}) \rightarrow \mathbf{U}_\infty \quad \text{as} \quad |\mathbf{x}| \rightarrow \infty \quad (1b)$$

where \mathbf{U}_∞ is the free stream velocity. Using the definition of the vorticity and the continuity ($\nabla \cdot \mathbf{u} = 0$), it can be shown that \mathbf{u} is related to $\boldsymbol{\omega}$ by the following Poisson equation:

$$\nabla^2 \mathbf{u} = -\nabla \times \boldsymbol{\omega}. \quad (2)$$

The velocity-vorticity formulation helps in eliminating the pressure from the unknowns of the equations. However, for bounded domains, it introduces additional constraints in the kinematics of the flow field and requires the transformation of the velocity boundary conditions to vorticity form.

2.1.1 Particle/vortex methods

The present numerical method is based on the discretization of the above equations in a Lagrangian frame using particle (vortex) methods. The vorticity equation

Eq. 1 may be expressed in a Lagrangian formulation by solving for the vorticity-carrying fluid elements (\mathbf{x}_a) based on the following set of equations:

$$\begin{aligned}\frac{d\mathbf{x}_a}{dt} &= \mathbf{u}(\mathbf{x}_a, t) \\ \frac{d\omega}{dt} &= \nu \nabla^2 \omega\end{aligned}\quad (3)$$

In the context of particle methods, it is desirable to replace the right-hand side of equations Eq. 3 by integral operators. These operators are discretized using the locations of the particles as quadrature points so that ultimately Eq. 3 is replaced by a set of O.D.E.'s whose solution is equivalent to the solution of the original set of equations. To this effect the velocity field may be determined by the vorticity field using the Green's function formulation for the solution of Poisson's equation (Eq. 2).

$$\mathbf{u} = -\frac{1}{2\pi} \int \mathbf{K}(\mathbf{x} - \mathbf{y}) \times \omega \, d\mathbf{y} + \mathbf{U}_0(\mathbf{x}, t) \quad (4)$$

where $\mathbf{U}_0(\mathbf{x}, t)$ contains the contribution from the solid body rotation and \mathbf{U}_∞ , and $\mathbf{K}(\mathbf{z}) = \mathbf{z}/|\mathbf{z}|^2$. The use of the Biot-Savart law to compute the velocity field guarantees the enforcement of the boundary condition at infinity.

The Laplacian operator may be approximated by an integral operator (Degond and Mas-Gallic, 1989) as well so that:

$$\nabla^2 \omega \approx \int G_\epsilon(|\mathbf{x} - \mathbf{y}|) [\omega(\mathbf{x}) - \omega(\mathbf{y})] \, d\mathbf{y} \quad (5)$$

where, in this paper, G_ϵ is taken to be $G_\epsilon(\mathbf{z}) = (2/\pi\epsilon^2) \exp(-|\mathbf{z}|^2/2\epsilon^2)$. The boundary condition Eq. 1a is enforced by formulating the physical mechanism it describes. The surface of the plate is the source of vorticity that enters the flow. A vorticity flux ($\partial\omega/\partial n$) may be determined on the boundary in a way that ensures Eq. 1a is satisfied. Here a fractional step algorithm is presented that allows for the calculation of this vorticity flux (see also Koumoutsakos *et al.* 1993). It is shown then that this mechanism of vorticity generation can be expressed by an integral operator as well:

$$\frac{d\omega}{dt} = \int H(\mathbf{x}, \mathbf{y}) \frac{\partial\omega}{\partial n}(\mathbf{y}) \, d\mathbf{y} \quad (6)$$

where the kernel H is developed in Section 3. Using the above integral representations for the right-hand side of Eq. 3, we obtain the following set of equations.

$$\begin{aligned}\frac{d\mathbf{x}_a}{dt} &= -\frac{1}{2\pi} \int \mathbf{K}(\mathbf{x}_a - \mathbf{y}) \times \omega \, d\mathbf{y} + \mathbf{U}_0(\mathbf{x}_a, t) \\ \frac{d\omega}{dt} &\approx \nu \int G_\epsilon(|\mathbf{x}_a - \mathbf{y}|) [\omega(\mathbf{x}_a) - \omega(\mathbf{y})] \, d\mathbf{y} \\ \frac{d\omega}{dt} &\approx \nu \int H(\mathbf{x}_a, \mathbf{y}) \frac{\partial\omega}{\partial n}(\mathbf{y}) \, d\mathbf{y}\end{aligned}\quad (7)$$

In vortex methods, the vorticity field is considered as a discrete sum of the individual vorticity fields of the particles, having core radius ϵ , strength $\Gamma(t)$, and an individual distribution of vorticity determined by the function η_ϵ so that:

$$\omega(\mathbf{x}, t) = \sum_{n=1}^N \Gamma_n(t) \eta_\epsilon(\mathbf{x} - \mathbf{x}_n(t)) \quad (8)$$

When this expression for the vorticity is substituted in Eq. 7, the singular integral operators K, G are convolved with the smooth function η_ϵ and are replaced by smooth operators K_ϵ, G_ϵ . These integrals are subsequently discretized using a quadrature having as quadrature points the locations of the particles. Assuming that each particle occupies a region of area h^2 and that the shape of the body is discretized by M panels, then algorithmically the method may be expressed as:

$$\begin{aligned} \frac{d\mathbf{x}_i}{dt} &= -\frac{1}{2\pi} \sum_{j=1}^N \Gamma_j K_\epsilon(\mathbf{x}_i - \mathbf{x}_j) + \mathbf{U}_0(\mathbf{x}_i, t) \\ \frac{d\Gamma_i}{dt} &= \nu \sum_{j=1}^N [\Gamma_j - \Gamma_i] G_\epsilon(|\mathbf{x}_i - \mathbf{x}_j|) \\ \frac{d\Gamma_i}{dt} &= \nu \sum_{m=1}^M H(\mathbf{x}_i, \mathbf{x}_m) \frac{\partial \omega}{\partial n}(\mathbf{x}_m) \\ \Gamma_i(0) &= \omega(\mathbf{x}_i, 0) h^2 \quad i = 1, 2, \dots, N \end{aligned} \quad (9)$$

The Lagrangian representation of the convective terms avoids many difficulties associated with its discretization on an Eulerian mesh such as excess numerical diffusion. However the straightforward method of computing the right-hand side of (Eq. 8), using (Eq. 9) for every particle, requires $\mathcal{O}(N^2)$ operations for N vortex elements. Recently fast methods have been developed that have operation counts of $\mathcal{O}(N)$ (Greengard and Rohklin, 1987). In the present scheme the efficient vectorization of the $\mathcal{O}(N)$ scheme allows for computations with one CPU minute per velocity evaluation for one million vortices on a single processor of a CRAY YMP. The accuracy of the method relies on the accuracy of the quadrature rule as information needs to be gathered from the possibly scattered particle positions. The convergence properties of vortex methods with a finite core dictate that the particles must overlap (i.e. $h < \epsilon$) at all times (Beale, 1986). However the local strain field of the flow may distort the particle locations, thus producing particle clustering in one direction accompanied by an expansion in another direction, similar to that which would occur around a hyperbolic stagnation point in a steady flow. When such a situation occurs the particle locations have to be re-initialized (remeshed) onto a uniform grid while interpolating the old vorticity on the new particle locations. In our algorithm we use a nine-point scheme to perform this remeshing, conserving the circulation as well as the linear and angular momentum of the vorticity field. See Koumoutsakos (1993) for further discussion.

2.2 A fractional step algorithm - boundary conditions

The no-slip boundary condition accounts for the generation of vorticity on the surface of the body. The surface of the body acts as a source of vorticity (Lighthill, 1963), and the task is to relate this vorticity flux on the surface of the body to the no-slip condition. This is achieved by appropriately coupling the kinematic and dynamic constraints of the flow. The present methodology was first proposed by Schmall and Kinney (1974) and is implemented here in a fractional step algorithm.

In the present formulation Eq. 9 are not integrated simultaneously in time, but instead a fractional step algorithm is employed. The governing equations are solved via a splitting scheme that accommodates the enforcement of the boundary conditions. For a non-zero thickness body the enforcement of the no-tangency flow implies the enforcement of the no-through flow as well (Koumoutsakos, 1993). This is not the case, however, for the zero thickness flat plate, as one has to account explicitly for the no-through flow boundary condition.

Let us assume that at the n -th time step (corresponding to time $t - \delta t$) the vorticity field has been computed (respecting the no-slip boundary condition) and we seek to advance the solution to the next time step (time t). The following two-step procedure is implemented:

- **Step 1:** Using as initial conditions $f(\mathbf{x}) = \omega^n(\mathbf{x}^n, n\delta t)$ we solve:

$$\begin{aligned} \omega_t + \mathbf{u} \cdot \nabla \omega &= \nu \nabla^2 \omega & \text{in } \mathcal{D} \times [t - \delta t, t] \\ \omega(\mathbf{x}, t - \delta t) &= f(\mathbf{x}) & \text{in } \mathcal{D} \end{aligned} \quad (10)$$

where \mathcal{D} denotes the flow domain exterior to the body surface $\partial\mathcal{D}$. Particles are advanced via the Biot-Savart law, and their strength is modified based on the scheme of Particle Strength Exchange.

Algorithmically then Step 1 may be expressed as:

$$\begin{aligned} \frac{d\mathbf{x}}{dt} &= \mathbf{u}^n(\mathbf{x}^n, n\delta t) \\ \frac{d\omega'_1}{dt} &= \nu \nabla^2 \omega'_1 \end{aligned} \quad (11)$$

At the end of Step 1 a vorticity field ω'_1 has been established in the fluid.

- **Step 2:**

The boundary conditions are enforced in this stage by a vorticity (not particle) creation algorithm.

2.2.1 Simply connected domain - flat plate

Without loss of generality we assume that the plate surface lies along the x -axis at $y = 0$ and between $-L/2 \leq x \leq L/2$. First, in order to enforce the **no-through** flow boundary condition, a vortex sheet of strength $\kappa(\xi)$ is distributed on the plate surface. The strength of this vortex sheet is then determined by the solution of the following integral equation:

$$\int_{-L/2}^{L/2} \frac{\kappa(\xi)}{x - \xi} d\xi = \mathbf{u}_n(x) \quad (12)$$

where $\mathbf{u}_n(x)$ is the velocity normal to the surface of the plate. The above integral equation is singular as it admits more than one solution. A unique solution is obtained by enforcing the conservation of circulation (note that in airfoil theory κ is uniquely determined by enforcing the Kutta condition)

$$\int_{-L/2}^{L/2} \kappa(\xi) d\xi = - \int \omega(\mathbf{x}) d\mathbf{x} \quad (13)$$

Introducing the transformation $\theta = \cos^{-1}(\frac{2y}{L})$ and using the orthogonality of a Fourier series expansion for $\kappa(\theta)$, (Batchelor, 1967) over the interval $[0, \pi]$, we obtain that at each instant of time:

$$\kappa(\theta) = -(A_0 + 2\sin\beta) \frac{\cos\theta}{\sin\theta} + \frac{C}{\sin\theta} + 2 \sum_{m=1}^{\infty} A_m \sin(m\theta) \quad (14)$$

where:

$$A_m = \frac{2}{\pi} \int_0^{\pi} u_n(\theta) \cos(m\theta) d\theta \quad \text{form } = 0, 1, \dots, \infty \quad (15)$$

and C is determined by enforcing the conservation of circulation (Eq. 13):

$$C = \frac{2\Gamma}{\pi L} + A_1 \quad (16)$$

A finite number of terms (P) is retained in the infinite series Eq. 14 in the numerical implementation of this method. Note also that the expression in Eq. 14 has built in the singularity of the vortex sheet at the tips of the plate. The enforcement of the no-through flow does not imply the enforcement of the no-slip condition for the zero thickness flat plate. A tangential velocity $u_t(x)$ may be computed along the plate surface due to the vortices in the wake. By taking the limit of Eq. 12 a vortex sheet of strength γ is observed on each side of the plate as:

$$\begin{aligned} \gamma(y = 0^-, x) &= -\frac{1}{2}\kappa(x) + u_t(x) \\ \gamma(y = 0^+, x) &= +\frac{1}{2}\kappa(x) + u_t(x) \end{aligned} \quad (17)$$

In order to enforce the **no-slip** condition then, in the context of the present algorithm we need to eliminate the spurious vortex sheet (κ) and the tangential velocity on the surface of the plate.

2.2.2 Doubly connected domain - vortex generators

For a doubly connected domain as that shown in Fig. 1b, the potential flow problem needs to be modified. For an open domain such as that exterior to the cavity (in the absence of the flat plate), in order to enforce the no-through flow boundary condition we require that the tangent flow on the interior surface of the boundary vanishes. Unlike the case of a closed body, no additional constraint needs

to be imposed for the solution of the respective integral equation (Koumoutsakos and Leonard, 1989).

For the combined configuration the resulting integral equation is then:

$$\int_{-L/2}^{L/2} \frac{\kappa(\xi)}{\mathbf{x}_p - \xi} d\xi + \int_{-\infty}^{\infty} \gamma_w(\zeta) \frac{\partial}{\partial s(\mathbf{x}_p)} \text{Log}|\zeta - \mathbf{x}_p| d\zeta = \mathbf{u}_n(\mathbf{x}_p) \quad (18a)$$

$$\int_{-L/2}^{L/2} \kappa(\xi, t) d\xi = -\nu \int_0^t \int_{-L/2}^{L/2} \frac{\partial \omega(\mathbf{x}_p, T)}{\partial n(\mathbf{x}_p)} d\mathbf{x}_p dT \quad (18b)$$

$$\int_{-L/2}^{L/2} \kappa(\xi) \frac{\partial}{\partial n(\xi)} \text{Log}|\zeta - \xi| d\xi + \int_{-\infty}^{\infty} \gamma_w(\zeta) \frac{\partial}{\partial n(\zeta)} \text{Log}|\zeta - \zeta'| d\zeta' = \mathbf{u}_t(\zeta) \quad (18c)$$

where $\kappa(\xi)$, \mathbf{x}_p and $\gamma_w(\zeta)$, ζ denote vortex sheets and location of points on the surface of the plate and the cavity respectively.

The above set of equations, when discretized using a panel method, results in a well posed system of equations which can be solved iteratively or by direct LU decomposition (if storage is not a limiting factor).

The spurious vortex sheet (γ) that is observed on the surface of the body may then be translated to a vorticity flux (Koumoutsakos and Leonard (1994)).

$$\nu \frac{\partial \omega}{\partial n}(x) = \frac{\gamma}{\delta t}(x) \quad \text{on } \partial \mathcal{D} \quad (19)$$

The computed vorticity flux generates vorticity in the fluid. The vorticity field is augmented by this viscous mechanism as described by the following set of equations:

$$\begin{aligned} \frac{\partial \omega'_2}{\partial t} - \nu \nabla^2 \omega'_2 &= 0 & \text{in } \mathcal{D} \times [t - \delta t, t] \\ \omega'_2(\mathbf{x}, t - \delta t) &= 0 & \text{in } \mathcal{D} \\ \nu \frac{\partial \omega'_2}{\partial n} &= \frac{\gamma(\omega'_1)}{\delta t} & \text{on } \partial \mathcal{D} \end{aligned} \quad (20)$$

Note that the diffusion equation is solved here with homogeneous initial conditions as the initial vorticity field was taken into account in the previous substep. The solution at Step 2 is a vorticity field ω'_2 , which we superimpose onto the solution of Step 1 to obtain the vorticity distribution at the next time step

$$\omega^{n+1} = \omega'_1 + \omega'_2 \quad (21)$$

3. Results

We have conducted a computational study of the unsteady flow behind a zero thickness plate started impulsively or uniformly accelerated normal to the flow.

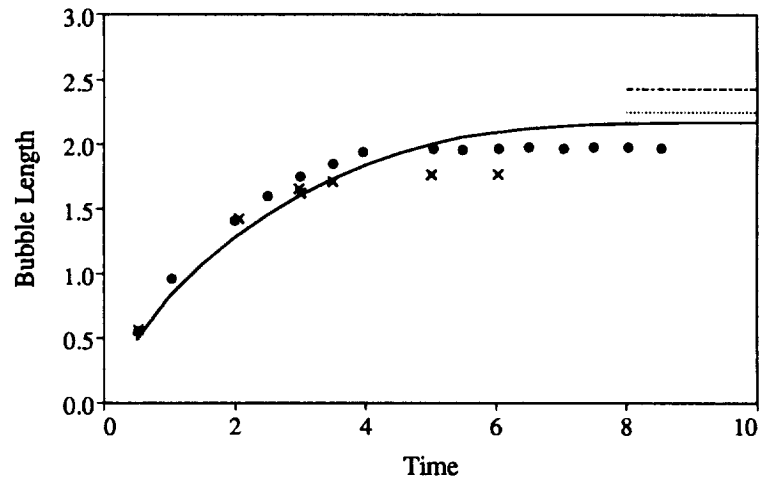


FIGURE 2. Evolution of the recirculating bubble for $Re = 20$. — : Present computations, \bullet , \times : Experiments (Coutanceau and Launay) for blockage ratios of 0.1 and 0.15 respectively. Theory (Steady State Results): --- : Dennis and Qiang, : Ingham and Tang.

For the impulsively started plate the present results complement related experimental works while providing quantities such as the vorticity of the flow field and the forces experienced by the body. The development of the flow is similar for all the Reynolds numbers that were simulated (20 to 1000). The separating shear layer rolls up into a vortex in the lee of the plate, inducing initially a region of secondary vorticity. Diffusion acts to increase the width of the shear layer and reduce the strength of the vortex resulting in a stable configuration. In Fig. 2 we present the results of the present computations for the length of the recirculating bubble for $Re=20$ and compare with existing experimental and theoretical works. The discrepancies may be attributed to the different treatment of the boundary conditions from the calculations of the steady state results and to the finite blockage ratio in the experiments. A different behavior is observed for the separating shear layer of a uniformly accelerated plate ($U = a t$). The continuous increase of the shear flow overcomes the effects of diffusion, increasing the strength of the separating shear layer and inducing a Kelvin-Helmholtz type instability. The wavelength and the onset of this instability depends on the acceleration of the plate. The present simulations are the first to confirm related experimental evidence on the formation of vortex centers along the separating shear layers of an accelerating flat plate (Fig.3). Such undulations have been attributed to experimental defects, but the present simulations suggest that this is an intrinsic behavior of the flow. Finally the drag coefficient of the plate is shown to scale due to the similarity in the inviscid development of the flow.

An extensive study of these flows for various Re numbers and acceleration rates may be found in Koumoutsakos (1994).

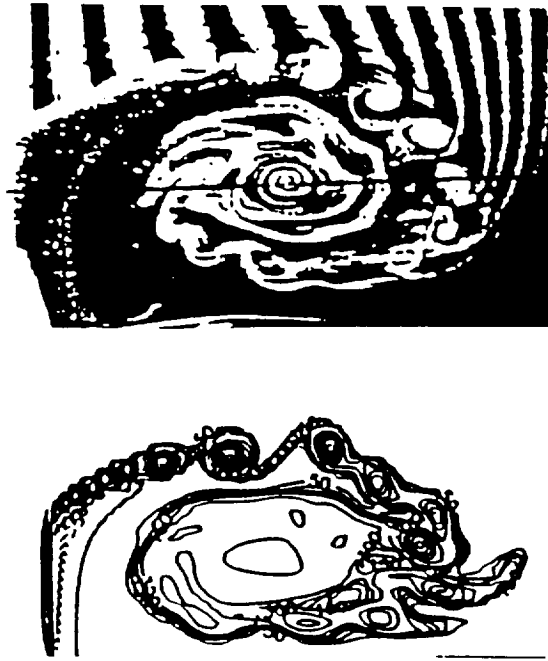


FIGURE 3. Flow past an accelerating flat plate. Top: Experimental results from Lian and Huang (1989) for $\alpha = aL^3/\nu^2 = 24.51 \times 10^6$ at $T^* = at^2/L = 4.37$. Bottom: Computational results. Equivorticity Contours for $\alpha = 1.68 \times 10^6$ at $T^* = 6.25$.

4. Future plans

We are currently at the final stages of development of our code for the study of flows involving the doubly connected configuration shown in Fig. 1b. We are interested in investigating the role of three dimensionality in the experiments and determining the role of two-dimensional vortical structures. We will be investigating possible control mechanisms with the long-range objective of developing feedback control mechanisms.

Our final goal is full three-dimensional direct numerical simulations to complement the ongoing experimental investigations. We may use existing algorithms or algorithms under development or proceed to extend the present computational technique to three-dimensional flows. In particular, research would be directed in the development of fast solutions of integral equations in three dimensions (with possible multi-disciplinary applications) and the process of restoring the Lagrangian computational grid. Of particular interest would be the coupling of the present Lagrangian method with large-eddy simulation (LES) methodologies.

Acknowledgments

I wish to acknowledge many extensive and enlightening discussions with Professor Anthony Leonard and Mr. Douglas Shiels of the Department of Aeronautics at the California Institute of Technology.

REFERENCES

- BEALE, J. T. 1994 On the accuracy of vortex methods at large times, *Proc. Workshop on Comp. Fluid Dyn. and React. Gas Flows*. IMA, Univ. of Minnesota.
- DENNIS, S. C. R., QIANG, W., COUTANCEAU, M., & LAUNAY, J-L. 1993 Viscous flow normal to a flat plate at moderate Reynolds numbers. *J. Fluid Mech.* **248**, 605-635.
- DEGOND, P. & MAS-GALLIC, S. 1989 The Weighted Particle Method for Convection-Diffusion Equations, Part I: The Case of an Isotropic Viscosity, Part II: The Anisotropic Case. *Math. Comput.* **53**, 485-526.
- GREENGARD, L. AND ROHKLIN, V. 1987 A fast algorithm for particle simulations. *J. Comput. Phys.* **73**, 325-348.
- INGHAM, T. B. AND TANG, T. 1991 Steady two-dimensional flow past a normal flat plate. *J. of Applied Math. and Phys. (ZAMP)*. **42**, 584.
- KOUMOUTSAKOS, P. AND LEONARD A. 1989 Improved Boundary Integral Method for Inviscid Boundary Condition Applications. *AIAA J.* **31(2)**, 401-404.
- KOUMOUTSAKOS, P. 1993 Direct Numerical Simulations of Unsteady Separated Flows Using Vortex Methods. *Ph.D. Thesis*. California Institute of Technology.
- KOUMOUTSAKOS, P., LEONARD, A. AND PEPIN, F. 1994 Boundary Conditions for Viscous Vortex Methods. *J. of Comput. Phys.* **113**, 52-61.
- KOUMOUTSAKOS, P. & LEONARD, A. 1994 High Resolution simulations of the flow past an impulsively started cylinder. *J. Fluid Mech.* To appear.
- KOUMOUTSAKOS, P. 1994 Simulations of the Viscous Flow Normal to a Zero Thickness Flat Plate. *J. Fluid Mech.* Submitted.
- LIGHTHILL, M. J. 1963 *Introduction. Boundary Layer Theory*. J. Rosenhead Ed., Oxford Univ. Press, NY. 54-61.
- LIAN, Q. X. & HUANG, Z. 1989 Starting flow and structures of the starting vortex behind bluff bodies with sharp edges. *Experiments in Fluids*. **8**, 95.
- SCHMALL, R. A. & KINNEY, R. B. 1974 Numerical Study of Unsteady Viscous Flow past a lifting plate. *AIAA J.* **12 (11)**, 1566.

Drag reduction strategies

By D. C. Hill

1. Motivation and objectives

In last year's Annual Research Briefs (Hill 1993) a description was given of an active control scheme using wall transpiration that leads to a 15% reduction in surface skin friction beneath a turbulent boundary layer, according to direct numerical simulation. In this research brief further details of that scheme and its variants are given together with some suggestions as to how sensor/actuator arrays could be configured to reduce surface drag. The research which is summarized here was performed during the first half of 1994.

This research is motivated by the need to understand better how the dynamics of near-wall turbulent flow can be modified so that skin friction is reduced. The reduction of turbulent skin friction is highly desirable in many engineering applications. Experiments and direct numerical simulations have led to an increased understanding of the cycle of turbulence production and transport in the boundary layer (Robinson 1991) and raised awareness of the possibility of disrupting the process with a subsequent reduction in turbulent skin friction (Bushnell & McGinley 1989, Blackwelder 1989). The implementation of active feedback control in a computational setting is a viable approach for the investigation of the modifications to the flow physics that can be achieved (Choi *et al.* 1994).

Bewley *et al.* (1993) and Hill (1993) describe how ideas from optimal control theory are employed to give "sub-optimal" drag reduction schemes. The objectives of the work reported here is to investigate in greater detail the assumptions implicit within such schemes and their limitations. It is also our objective to describe how an array of sensors and actuators could be arranged and interconnected to form a "smart" surface which has low skin friction.

2. Accomplishments

As before, the various schemes are aimed at reducing the mean drag upon a plane wall by the application of distributed or localized blowing and suction. There is no net mass flux through the wall, and an expense is associated with the control action. The simulations are performed for a channel flow with a constant mass flux through the channel. The Reynolds number based on friction velocity is of the order 100 for the tests.

2.1 Assumptions

The sub-optimal drag reduction scheme of Hill (1993) is based upon minimizing the drag by considering how the flow is most favorably influenced during consecutive short time intervals. In order to arrive at the relatively simple control law, several assumptions must be made about the flow field.

Only flow structures in a layer close to the wall are significant in deciding how control will modify the flow evolution. The characteristic thickness of this *layer of influence* is

$$L_T = \frac{4}{3} \sqrt{\frac{T}{\pi}} \text{ wall units,} \quad (1)$$

where T is the *control time interval* in wall units over which the local optimization is made. The layer of fluid between the wall and $y^+ = L_T$ will be referred to as the layer of influence. The dynamics of the flow within this layer guides the control force distribution.

One concern about the original derivation of the result reported last year was the assumption that there is no mean shear at the wall. The flow was taken to be uniform, and the effects of mean shear were assumed to be negligible. Following a considerable analytical effort, that assumption has been shown to be valid. A re-derivation of the scheme with mean shear effects included leads to the same result as that presented by Hill (1993).

Other assumptions made during the derivation have been clarified:

1. *Events far from the surface are not modified significantly by the effect of the surface control velocities.*

2. *On the control time interval, mixing within the layer of influence is sufficiently weak that it plays a negligible role in the transport of control signals.* There is an unsteady component in the near-wall flow field. The effect of unsteadiness in transporting the control signals has been neglected. Note that this does not mean that unsteadiness has been neglected.

3. *Those flow structures which govern the sensitivity of the immediate drag to changes in the control distribution do not evolve significantly on the control time interval.*

4. *The layer of influence is sufficiently thin that the mean and unsteady flow components within the layer are represented well by a low order Taylor expansion at the wall.* It is assumed that the differential scale in the wall-normal direction of the velocity fluctuations is much larger than the thickness of the layer of influence.

It is important to recognize that the present control theory deals only with efficient changes to the behavior of the viscous sub-layer region. The physics of the sweep events and turbulence production involves events further from the wall which have a much longer time scale than that of the optimization. Consequently, these flow characteristics are not necessarily modified in an optimal manner. They are influenced indirectly by the modifications which are applied in the viscous sub-layer.

2.2 Variants of the original scheme

Using the sensitivity function, two classes of scheme have been devised and tested by direct numerical simulation. The wall-normal velocity component at the n th time step is represented by its Fourier transform, $\hat{\Phi}^{(n)}(\alpha, \beta)$, where α and β are

streamwise and spanwise wave numbers ($\gamma = \sqrt{\alpha^2 + \beta^2}$). The Fourier transform of the streamwise velocity fluctuations is denoted by $\hat{u}^{(n)}(\alpha, \beta; y)$.

1. In the spirit of Choi *et al.* (1994), we considered the scheme

$$\hat{\Phi}^{(n+1)}(\alpha, \beta) = \frac{\hat{u}^{(n)}(\alpha, \beta; L_T)}{(\ell - \frac{i\alpha}{2\gamma}(1 - \gamma L_T))}. \quad (2)$$

This scheme uses information within the flow domain at $y^+ = L_T$. With $\ell = 1$ and $L_T = 10$, a drag reduction of 19% is achieved. The similar scheme of Choi *et al.*, which applies wall transpiration equal and opposite to the wall-normal velocity component at $y^+ = 10$, gives a reduction of about 23%.

2. The following relaxation scheme has been tried:

$$\hat{\Phi}^{(n+1)}(\alpha, \beta) = \frac{1}{1 + \mu(\ell - \frac{i\alpha}{2\gamma}(1 - \gamma L_T))} \left\{ \hat{\Phi}^{(n)}(\alpha, \beta) + \mu L_T \left(\frac{\partial \hat{u}^{(n)}}{\partial y} \right)_{y=0} \right\}, \quad (3)$$

where μ is a relaxation parameter. This scheme uses wall information only and leads to a drag reduction of about 14% ($\mu = 0.05, \ell = 1, L_T = 5$).

2.3 Implications for sensor and actuator arrays

In practice an active drag reduction system is likely to consist of an array of wall-mounted sensors and actuators. For the present scheme, the sensors must measure the streamwise component of wall shear, while the ‘‘actuators’’ are orifices through which fluid is injected and removed. The control velocity at a particular actuator is updated on the basis of information from the sensors in its neighborhood. The prior control velocities at neighboring actuators are also required.

Consider a rectangular array of locations on the wall at which the control velocity is specified. Variable $\Phi_{i,j}^{(n)}$ denotes the control velocity at the i th streamwise and j th spanwise position. Let h_x^a and h_z^a be the streamwise and spanwise spacing, respectively, between actuators. Suppose that the unsteady component of wall shear in the streamwise direction, $\sigma_{i,j}^{(n)}$, is measured at a similar array of sensor positions, which is offset from the actuator array. Let h_x^s and h_z^s be the streamwise and spanwise spacing of the sensors. In order to define the control update at the (i, j) th actuator, data from a number of neighboring actuators and sensors is employed. Let there be N_x^a streamwise and N_z^a spanwise actuators and N_x^s streamwise and N_z^s spanwise sensors.

The following scheme is proposed:

$$\Phi_{i,j}^{(n+1)} = \sum_{k=1}^{N_x^a} \sum_{l=1}^{N_z^a} W_{k,l}^a \Phi_{i+k,j+l}^{(n)} + \mu L_T \sum_{k=1}^{N_x^s} \sum_{l=1}^{N_z^s} W_{k,l}^s \sigma_{i+k,j+l}^{(n)}. \quad (4)$$

The weights are

$$\begin{aligned} W_{k,l}^a &= c(k, N_x^a) c(l, N_z^a) h_x^a h_z^a K(-x_{k,l}^a, -z_{k,l}^a), \\ W_{k,l}^s &= c(k, N_x^s) c(l, N_z^s) h_x^s h_z^s K(-x_{k,l}^s, -z_{k,l}^s), \\ c(k, N) &= 1/2, \text{ if } k = 1, N, \\ &= 1 \text{ otherwise,} \end{aligned} \quad (5)$$

where $(x_{k,l}^a, z_{k,l}^a)$ and $(x_{k,l}^s, z_{k,l}^s)$ are the locations of the actuators and sensors, respectively, measured relative to the location of the actuator for which the control velocity is being computed.

The function $K(x, z)$ is defined by

$$K(x, z) = \frac{1}{4\pi^2} \int_{-\alpha_0}^{\alpha_0} \int_{-\beta_0}^{\beta_0} \frac{e^{i(\alpha x + \beta z)}}{(1 + \mu(\ell - \frac{i\alpha}{2\gamma}(1 - \gamma L_T)))} d\beta d\alpha. \quad (6)$$

The wave number cutoffs α_0 and β_0 are introduced since the derivation for the analytical control law is not defined as α and β become very large. Preliminary experience suggests that the application of this cutoff does not have a detrimental effect.

It has been found that only a few neighboring points offer a significant contribution to the summation; the weight factors $W_{i,j}^{a,s}$ diminish rapidly in magnitude as $|i|$ and $|j|$ are increased. This is very encouraging since it suggests that a control stencil that employs information from nearby sensors and actuators alone may be quite effective. Experience with the spectral version of the control scheme suggests that the streamwise spacing between actuators/sensors should not exceed 12 wall units if the scheme is to be effective. The spanwise spacing should not exceed 4 wall units.

Once more the author is indebted to T. Bewley for his time, patience, and effort in the implementation of these rules in the direct numerical simulations.

REFERENCES

- BEWLEY, T., CHOI, H., TEMAM, R. & MOIN, P. 1993 Optimal feedback control of turbulent channel flow. *Annual Research Briefs-1993*. Center for Turbulence Research, NASA-Ames/Stanford Univ.
- BLACKWELDER, R. F. 1989 Some ideas on the control of near-wall eddies. *AIAA Paper No. 89-1009*.
- BUSHNELL, D. M., & MCGINLEY, C. B. 1989 Turbulence control in wall flows. *Ann. Rev. Fluid Mech.* **21**, 1-20.
- CHOI, H., MOIN, P., & KIM, J. 1994 Active turbulence control for drag reduction in wall-bounded flows. *J. Fluid Mech.* **262**, 75-110.
- HILL, D. C. 1993 Drag reduction at a plane wall. *Annual Research Briefs-1993*. Center for Turbulence Research, NASA Ames/Stanford Univ.
- ROBINSON, S. K. 1991 Coherent motions in the turbulent boundary layer. *Ann. Rev. Fluid Mech.* **23**, 601-639.

Optimal active control for Burgers equation

By Yutaka Ikeda¹

A method for active fluid flow control based on control theory is discussed. Dynamic programming and fixed point successive approximations are used to accommodate the nonlinear control problem. The long-term goal of this project is to establish an effective method applicable to complex flows such as turbulence and jets. However, in this report, the method is applied to stochastic Burgers equation as an intermediate step towards this goal. Numerical results are compared with those obtained by gradient search methods.

1. Motivation and objectives

There is current research at Stanford to develop active feedback control schemes based on optimal control theory to control turbulence. In particular, an optimal control method based on a gradient search algorithm is discussed in Choi, Teman and Moin (1993) and Bewley and Moin (1994). Such gradient schemes, however, are not guaranteed to converge to the global minimum of the cost functional and thus may suffer from degraded performance when compared with the "optimal" in a given situation.

The objective of the current research is to investigate an alternative method to the gradient search method without increasing computational complexity. The approach we take is to impose the convexity onto the cost functional and derive the analytical optimal controlled solutions for a set of linearized systems. This eliminates the minimization process of the cost functional. Then the optimal controlled solution for stochastic Burgers equation is found by Fixed Point Theorem. The resulting method is compared with the gradient method through numerical simulation, then assessments for applicability to more complex flow dynamics are made.

2. Scheme for optimal control

2.1 System model

We consider stochastic Burgers equation as a system model:

$$\frac{\partial u}{\partial t} = \frac{1}{Re} \frac{\partial^2 u}{\partial x^2} - \frac{\partial}{\partial x} \frac{u^2}{2} + F + \chi. \quad (1)$$

Initial condition and boundary conditions are given by $u(x, t_0) = u_0(x)$, $x \in (0, 1)$ and $u(0, t) = u(1, t) = 0$, $t \in [t_0, T]$. Also, Re , $F(x, t)$, and $\chi(x, t)$ denote Reynolds number, a forcing term, and a normally distributed random forcing term with zero mean and unit variance, respectively.

¹ McDonnell Douglas Aerospace

In order to control the velocity gradient $v = \partial u / \partial x$, we introduce the dynamics of the velocity gradient, which can be formally obtained by differentiating Burgers equation with respect to x such that

$$\frac{\partial v}{\partial t} = \frac{1}{Re} \frac{\partial^2 v}{\partial x^2} - u \frac{\partial v}{\partial x} - u_x v + f + \xi \quad (2)$$

where $f(x, t) = \partial F(x, t) / \partial x$ denotes the control forcing term for the differential form of Burgers equation and $\xi = \partial \chi(x, t) / \partial x$, a formally differentiated random forcing term.

2.2 Cost functional

We consider a control problem in which the cost functional to be minimized is given by

$$J = \frac{1}{2} E \left[\int_{t_0}^T \int_0^1 (m_d \left(\frac{\partial u}{\partial x} \right)^2 + l_d (f(x, t))^2) dx dt \right], \quad (3)$$

where $E[\cdot]$ denotes a mathematical expectation. In a more general setting, the state, control, and the cost functional can be formed by

$$X = \begin{pmatrix} u \\ \frac{\partial u}{\partial x} \end{pmatrix}, \quad U = \begin{pmatrix} F \\ f \end{pmatrix},$$

and

$$J = \frac{1}{2} E \left[\int_{t_0}^T \int_0^1 (m_d (X^T Q X) + l_d (U^T R U)) dx dt \right], \quad (4)$$

where

$$Q = \begin{pmatrix} q_1 & 0 \\ 0 & q_2 \end{pmatrix} \quad \text{and} \quad R = \begin{pmatrix} r_1 & 0 \\ 0 & r_2 \end{pmatrix}.$$

If we select q_1 small relative to q_2 and r_2 small relative to r_1 , we can formulate a problem similar to that discussed in Choi *et al.* (1993). However, this introduces a higher dimension of the system dynamics. For computational simplicity, control of the decoupled (1-D) system rather than the augmented (2-D) system is considered by selecting $q_1 = r_1 = 0$, which results in (3).

2.3 Optimal control strategy

A brief summary of the optimal control strategy is now given:

* *Linearize system:* Consider the system given by the linear equation

$$\frac{\partial v}{\partial t} = \frac{1}{Re} \frac{\partial^2 v}{\partial x^2} - u_{opt} \frac{\partial v}{\partial x} - (u_{opt})_x v + f + \xi, \quad (5)$$

where u_{opt} denotes the solution of Burgers equation (1) when the optimal control f_{opt} is applied to the system (2).

- * *Design a linear optimal controller:* The dynamic programming technique is applied to the linear distributed parameter system (5) to find the optimal control for the linear system (for detail, see Tzafestas and Nightingale 1968).
- * *Compute optimal controlled solution u_{opt} :* Once the optimal controller for (5) is found, integrate Eq. (5) with respect to x to yield:

$$\frac{\partial u}{\partial t} = \frac{1}{Re} \frac{\partial^2 u}{\partial x^2} - u_{opt} \frac{\partial u}{\partial x} + F + \chi. \quad (6)$$

To solve (6) for the optimal controlled solution, we need to know the optimal solution before it is solved. Hence, for the moment, we replace u_{opt} in (5) and (6) by a known function $w(x, t)$ and consider a mapping $G(w)$ defined on a function space which maps $w(x, t)$ to the solution $u(x, t)$ of (6). Notice that for each w the optimal controller is designed for the linearized system, and thus each image u of $G(w)$ forms an optimal solution for the corresponding system. Now, consider a family of optimal controlled solutions generated by $G(w)$. Then it is clear that the fixed point of $G(w)$ (if it exists) is the optimal controlled solution u_{opt} of Burgers equation (6). To find the fixed point of $G(w)$, a method of successive approximations is employed.

3. Numerical simulation

An early evaluation of this new optimal control formulation is important for determining the promise of the approach. To accomplish this, an evaluation through comparison is performed between the current method and the gradient method investigated by Choi *et al.* A numerical example was taken from Choi *et al.* (1993) for a comparison study (distributed control problem, case(ii), where the weights $l_d = 1$ and $m_d = 1/dx$ in the cost functional, $Re = 1500$ and $dx = 2047$). However, only qualitative comparison is meaningful in the current comparison study since the control problem is set up differently from the gradient method by Choi *et al.* in order to keep the computational complexity low. That is, the current method uses the cost functional (3) as one of the simplest cases of the more general form (4) (see discussion in 2.2), while the gradient method by Choi *et al.* uses the integrated control F instead of f in the cost functional (3). Another difference is that the cost functional in Choi *et al.* (1993) is formulated without the integral sign with respect to time; hence, the cost is minimized at each instance of time rather than over a duration of time.

Two different values for the ratio l_d/m_d were considered. Case-1: the weights l_d and m_d were set to be identical with those in the example. Case-2: the weight l_d was reduced by a factor of 1000 to allow more control power, keeping the weight m_d the same. In each case, the time histories of the cost functional, control power used, and gradient at the wall ($x = 0$) were computed. The results are shown in Figs. 1-3. The velocities at time 2 second are shown in Fig. 4. The corresponding figures from Choi *et al.* (1993) are also shown in Figs. 1, 2, and 4 for comparison.

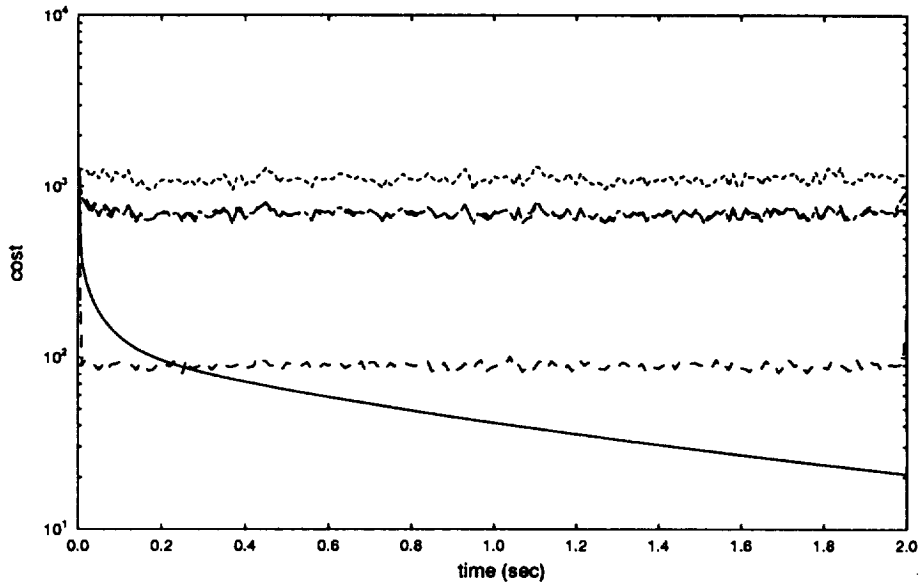


FIGURE 1. Time history of the cost functional. Legend: —, without forcing; ----, with random forcing and no control; - - -, with control and random forcing (case 1); - - -, with control and random forcing (case 2); — —, with control and random forcing (Choi *et. al.*).

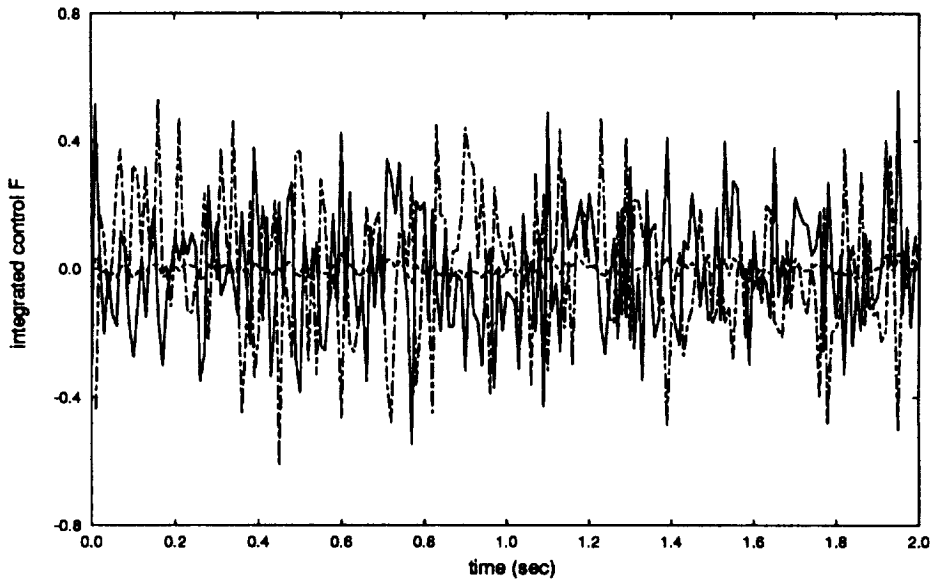


FIGURE 2. Time history of momentum forcing. Legend: —, control forcing (case 2); ----, control forcing (case 1); - - -, control forcing (Choi *et. al.*).

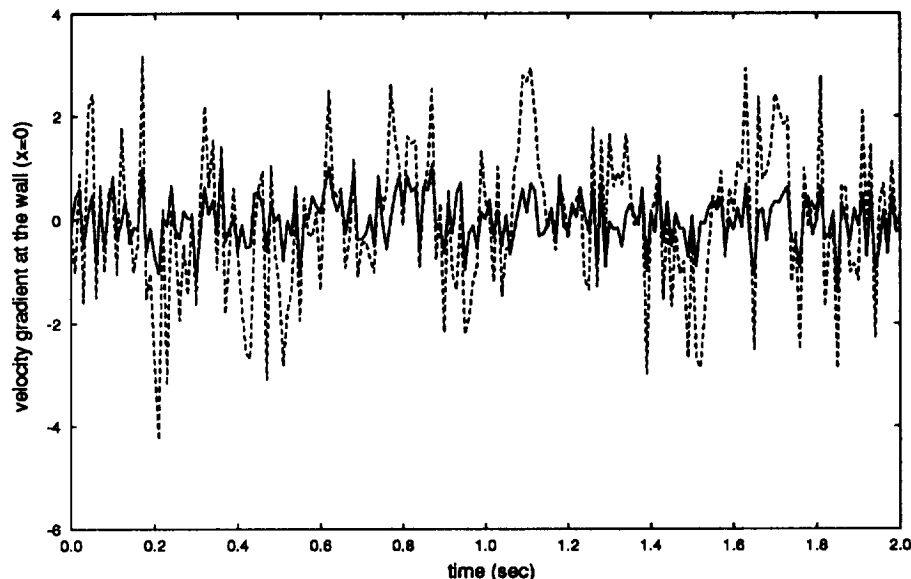


FIGURE 3. Wall velocity gradient at $x = 0$. Legend: —, with control and random forcing (case 2); ----, without control.

Fig. 1 shows that both methods reduced the cost functional significantly. The integrated control power F in each case of the current method and the gradient method are shown in Fig. 2. It shows that the amount of control F used in Case-1 is much less than that in Case-2 and the gradient method. Therefore, Case-2 seems more comparable to the example with the gradient method with respect to the momentum forcing added to Burgers equation. This seems natural since the velocity gradient becomes large in magnitude, particularly when the random noise is present. Hence, it requires more control power f when the velocity gradient is fed back than when the velocity is fed back. Fig. 3 shows that the current method controls the velocity gradient effectively if enough control power is allowed. Both Case-1 and the gradient method needed more control power to reduce the gradient at the wall significantly. From Fig. 4 it can be seen that the current method reduced the velocity magnitude as well as the velocity gradient while the gradient method did not reduce the velocity magnitude as much. This may be explained as follows: the current method seems to control the velocity gradient by regulating the gradient magnitude uniformly. Then, since the velocity at the boundaries are fixed to be zero, the velocity magnitude becomes small. On the other hand, the gradient method seems to control the velocity gradient by linearly scaling down. Hence, it reduces the absolute magnitude of the higher velocity gradient more significantly. One final observation is that the control formulated by the current method seems to respond more than a one order of magnitude faster than that by the gradient method (see Case-2 in Fig. 1, and Fig. 7(b) in Choi *et al.* 1993). This is a very important advantage for non-stationary applications.

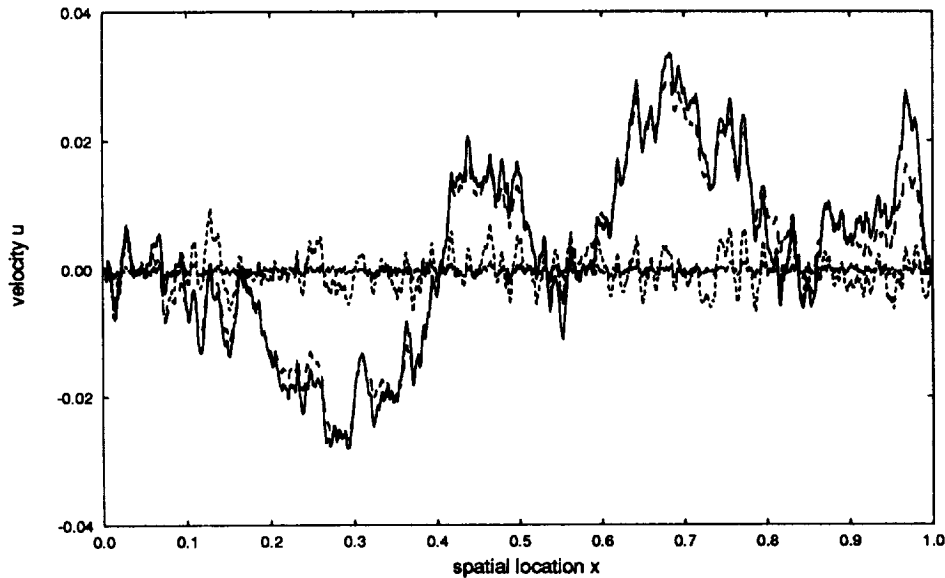


FIGURE 4. Velocity at $t = 2$. Legend: ———, with random forcing and no control; ----, with random forcing and control (case 1); - · - ·, with random forcing and control (case 2); · · · ·, with random forcing and control (Choi *et. al.*).

4. Conclusions

A method for active control of fluid flow dynamics was discussed. The simulation results show that the current control method works effectively and seems to be extendable to Navier-Stokes equations without major problems. Applications to turbulence and/or jet control will be attempted in the near future.

Acknowledgements

The author would like to acknowledge the financial support of McDonnell Douglas Corporation. The author also wishes to acknowledge Prof. Parviz Moin and Mr. Thomas Bewley for their helpful discussions and warm hospitality during the author's stay at CTR, and Prof. Hacheon Choi for providing useful information about the gradient method.

REFERENCES

- BEWLEY, T., & MOIN, P. 1994 Optimal control of turbulent channel flows. *ASME Winter Annual Meeting*, Chicago, 9 Nov. 94.
- CHOI, H., TEMAM, R., MOIN, P., & KIM, J. 1993 Feedback control for unsteady flow and its application to the stochastic Burgers equation. *J. Fluid Mech.* **253**, 509.
- TZAFESTAS, S., & NIGHTINGALE, J. 1968 Optimal control of a class of linear stochastic distributed-parameter systems. *Proc. IEE.* **115** (8), 1213, 1220.

593-34
400-13

Acoustics of laminar boundary layer breakdown

By Meng Wang

1. Motivation and objectives

Boundary layer flow transition has long been suggested as a potential noise source in both marine (sonar-dome self noise) and aeronautical (aircraft cabin noise) applications, owing to the highly transient nature of the process (Farabee *et al.* 1989). The design of effective noise control strategies relies upon a clear understanding of the source mechanisms associated with the unsteady flow dynamics during transition. Due to formidable mathematical difficulties, theoretical predictions either are limited to early linear and weakly nonlinear stages of transition (Haj-Hariri & Akylas 1986; Akylas & Toplosky 1986), or employ acoustic analogy theories based on approximate source field data, often in the form of empirical correlation.

In the present work, an approach which combines direct numerical simulation of the source field with the Lighthill acoustic analogy (Lighthill 1952) is utilized. This approach takes advantage of the recent advancement in computational capabilities to obtain detailed information about the flow-induced acoustic sources. The transitional boundary layer flow is computed by solving the incompressible Navier-Stokes equations without model assumptions, thus allowing a direct evaluation of the pseudosound as well as source functions, including the Lighthill stress tensor and the wall shear stress. The latter are used for calculating the radiated pressure field based on the Curle-Powell solution (Curle 1955; Powell 1960) of the Lighthill equation. This procedure allows a quantitative assessment of noise source mechanisms and the associated radiation characteristics during transition from primary instability up to the laminar breakdown stage. In particular, one is interested in comparing the roles played by the fluctuating volume Reynolds stresses and the wall-shear-stresses, and in identifying specific flow processes and structures that are effective noise generators.

Natural transition in a boundary layer starts with modulated Tollmien-Schlichting (T-S) wave trains initiated by random excitations from free-stream turbulence (Gaster 1993). The laminar breakdown process which destroys the smooth, orderly flow pattern is a localized event triggered by instability mechanisms (Kachanov 1994). These observations suggest that without loss of generality, one could simulate the transition phenomena by following the evolution of a T-S wave packet instead of a periodic wave series as in controlled experiments. This results in considerable savings in computer memory and CPU time due to the reduced domain size. Furthermore, the amplitude modulation allows the wave packet to evolve spontaneously into a turbulent spot, which cannot be achieved if the initial instability wave is strictly periodic (Kachanov 1994). From an acoustic viewpoint, tracking an isolated wave packet has the advantage that the linkage between the calculated sound signal and the specific transition stage is apparent. Once the sound generation properties from a single breakdown (burst) are determined, one could make

statistical inferences regarding the sound of a realistic transitional boundary layer where a large collection of spots are present.

This report summarizes work accomplished to date and the major findings. A longer and more complete version is available as a CTR manuscript (Wang *et al.* 1994).

2. Accomplishments

2.1. Numerical simulation of wave packet transition

The specific problem considered involves a strongly modulated T-S wave packet in a low Mach number, zero pressure gradient boundary layer formed on a rigid, flat plate. In the spirit of Lighthill's theory, the acoustic source functions can be approximated by considering an equivalent incompressible flow since the compressibility effect is negligibly weak. The incompressible Navier-Stokes and continuity equations are solved numerically on a staggered grid using a finite difference scheme developed by Le and Moin (1991). The grid spacing is uniform in the streamwise (x_1) and spanwise (x_3) directions, and non-uniform in the wall-normal direction (x_2). Time advancement is of semi-implicit, three-step Runge-Kutta type combined with a fractional step method. The Poisson equation is solved at the final sub-step to satisfy the divergence-free constraint. The numerical scheme is second order accurate in both space and time.

The domain of integration consists of a rectangular box parallel to the flow direction. A no-slip condition is applied on the wall. At the free-stream boundary a normal velocity distribution based on the Blasius solution and zero vorticity are prescribed. In the spanwise direction periodicity is assumed for all dependent variables. A convective boundary condition capable of maintaining the accurate steady (Blasius) velocity profiles (Wang *et al.* 1994) is used at the downstream boundary.

The unsteady wave packet is introduced into the computational domain from the upstream boundary by requiring that

$$\begin{aligned}
 u_i(x_1 = 0) = & u_i^B(x_2) + \text{Real} \left\{ \epsilon^{2D} u_i^{2D}(x_2) e^{-i\beta t} \right. \\
 & + \frac{1}{2} \epsilon^{3D} u_i^{3D+}(x_2) e^{i[(\alpha \sin \phi) x_3 - \beta t]} \\
 & \left. + \frac{1}{2} \epsilon^{3D} u_i^{3D-}(x_2) e^{i[-(\alpha \sin \phi) x_3 - \beta t]} \right\} e^{-\left(\frac{t-t_0}{\tau}\right)^4} g(x_3) \quad (1)
 \end{aligned}$$

where $u_i^B(x_2)$ represents the Blasius solution for a two-dimensional boundary layer. $u_i^{2D}(x_2)$ and $u_i^{3D\pm}(x_2)$ are the least stable eigenmodes and α is the corresponding eigenvalue, obtained by solving the Orr-Sommerfeld and Squire equations for given frequency $\beta = 0.094$ and oblique angle $\phi = \pi/4$. The eigenfunctions are normalized such that the maximum streamwise velocity has unit magnitude. The disturbance amplitudes are $\epsilon^{2D} = 0.025$ and $\epsilon^{3D} = 0.01$. The streamwise shape of the wave packet is determined by $\tau = 40$ and $t_0 = 120$ in the time-modulating envelope. In addition, symmetry relative to the spanwise center $x_3 = 0$ is destroyed by the

function $g(x_3) = 1 + 0.1(e^{-\left(\frac{x_3-1.73}{1.73}\right)^2} - e^{-\left(\frac{x_3+1.73}{1.73}\right)^2})$. As pointed out by Corral & Jiménez (1991), spanwise asymmetry accelerates the transition process and renders the simulation more manageable. The Reynolds number defined in terms of δ_0^* is $Re = 1000$, which is equivalent to $Re_x \approx 3.38 \times 10^5$ as measured in terms of distance from the leading edge.

In (1) and the subsequent descriptions, the velocities, spatial coordinates, and time are non-dimensionalized with respect to the free-stream velocity U'_∞ , the inflow boundary layer displacement thickness δ_0^* , and δ_0^*/U'_∞ , respectively. The thermodynamic variables are non-dimensionalized relative to their constant free-stream values.

Computations start out on a $514 \times 130 \times 66$ grid covering a computational domain defined in $0 \leq x_1 \leq 200$, $0 \leq x_2 \leq 20$ and $-\lambda_{x_3}/2 \leq x_3 \leq \lambda_{x_3}/2$, where $\lambda_{x_3} \approx 25.95$ is the spanwise wavelength for the oblique eigenmode pair. As simulation proceeds, resolution requirement becomes increasingly severe within the traveling disturbance region, whereas near the upstream boundary the flow becomes basically steady. Grid refinement is performed twice in conjunction with shifts in computational boundaries following the movement of the wave packet. A cubic-spline interpolation scheme is used to interpolate solutions onto new grids. By the end of the simulation, the computational grid consists of $1282 \times 130 \times 258$ points covering a shortened region $70 \leq x_1 \leq 210$. The entire simulation utilizes approximately 60 single processor CPU hours on CRAY-YMP-C90.

Figs. 1a-f depict a time sequence of the instantaneous contours of the negative spanwise vorticity $-\omega_{x_3}$, which is closely related to the normal shear $\partial u_1/\partial x_2$, at $x_3 \approx 1.1$. Solid lines denote positive contour values, and dashed lines denote negative ones. The plane $x_3 \approx 1.1$, which lies slightly off the spanwise center, is chosen because it corresponds to the approximate location of maximum shear. Notice that due to the slight asymmetry of the initial T-S wave packet, the peak-valley splitting along the spanwise direction during the secondary instability is not as clear-cut as for symmetric disturbances. Nonetheless, the transition is seen to follow closely the route that leads to fundamental (*K*-type) breakdown.

The complete wave packet enters the upstream boundary $x_1 = 0$ at $t \approx 185$. Through the action of primary and secondary instability mechanisms, it amplifies rapidly, evolving into a detached high shear layer as shown in Fig. 1a. Underneath the shear layer lie a pair of counter-rotating streamwise vortices (lambda vortex) whose structure will be shown later. The high shear layer intensifies to create a kink in Fig. 1b, which breaks down in Fig. 1c to form an eddy (presumably hairpin eddy) while a second kink develops. In Figs. 1d-1f the detached high shear layer continues to disintegrate, shedding eddies into the free stream. In the meantime, vortical activity intensifies in the near wall region, and a new generation of shear layers originates there. The new shear layers are expected to experience similar breakdown processes, known as turbulent "bursts". The flow field depicted in Fig. 1f already bears certain resemblance to turbulence. However, large scale high shear layers and streamwise vortices still dominate the overall flow structure, particularly in the rear part of the wave packet and away from the spanwise center.

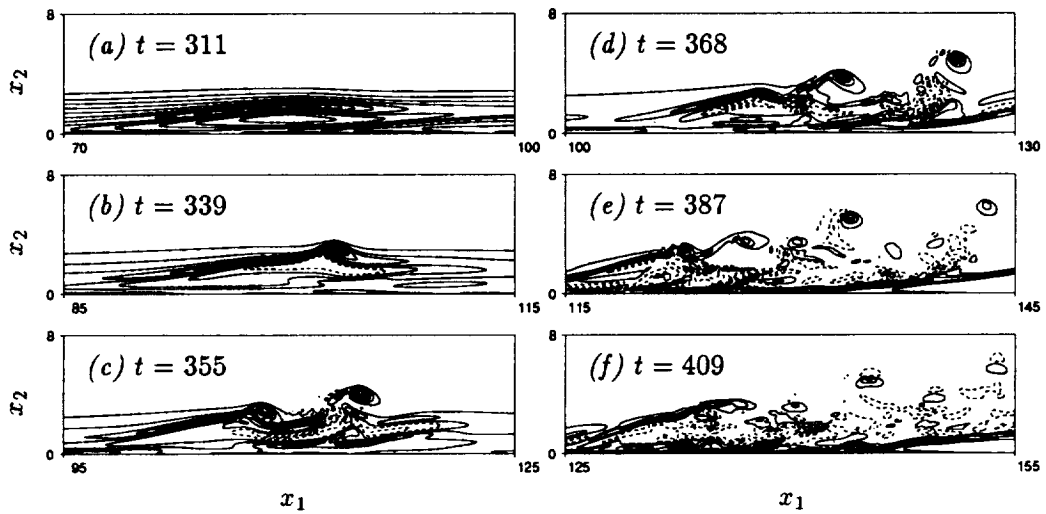


FIGURE 1. Contours of negative spanwise vorticity $-\omega_{x_3}$ at $x_3 \approx 1.1$ during laminar breakdown. Contour values: (a) 0 to 0.94, (b) -0.23 to 1.81, (c) -0.59 to 1.61, (d) -1.30 to 2.13, (e) -1.52 to 3.22, (f) -0.98 to 3.83.

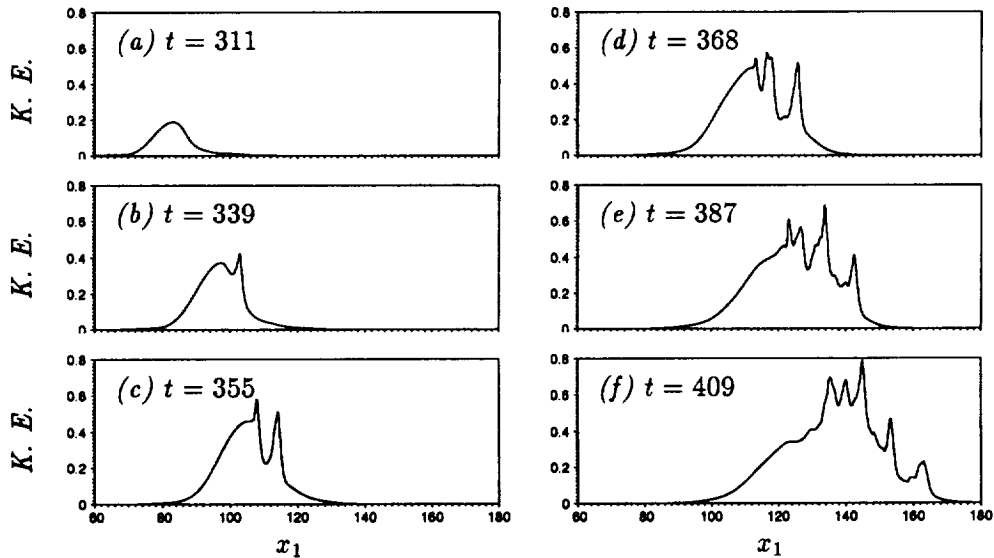


FIGURE 2. Evolution of disturbance kinetic energy integrated over the x_2 - x_3 plane during laminar breakdown.

Figs. 2a-f illustrate the streamwise distribution of the disturbance kinetic energy integrated over the x_2 - x_3 plane, at time instants corresponding to those in Figs. 1a-f. The energy is calculated based on the excess velocities relative to the steady solution. The snapshots show the nonlinear distortion of the energy waveform which leads to

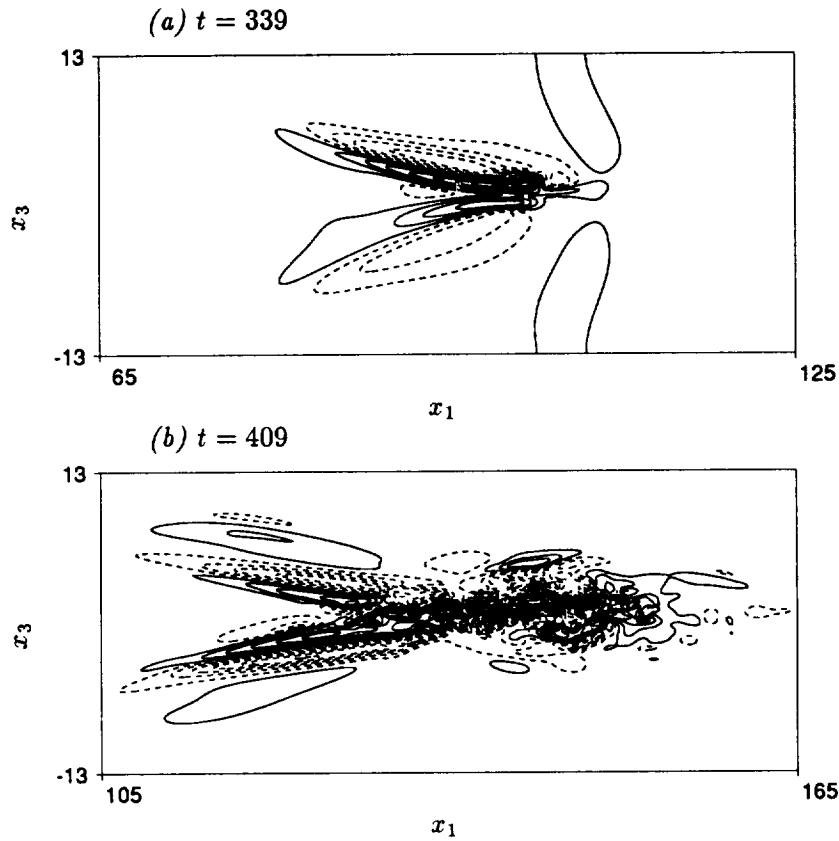


FIGURE 3. Contours of instantaneous normal velocity at $x_2 \approx 1.1$. (a) $t = 339$, contour spacing = 0.015; (b) $t = 409$, contour spacing = 0.02.

the formation of one, two, and multiple spikes, each corresponding to an eddy. These spikes are observed in experiments for the K -regime breakdown (Kachanov 1994) as high frequency flashes of disturbances on the streamwise-velocity oscilloscope traces. Kachanov notes that the velocity flashes do not disperse while they propagate downstream near the edge of the boundary layer, a feature identifiable with solitons. It is conceivable that the kinetic energy waveforms exhibited in Figs. 2a-f may be modeled by certain evolutionary equations within the framework of soliton theory. The spread of the nonlinear wave packet in the streamwise direction during laminar breakdown is apparent in Figs. 2a-f. The amplitude increase observed in the energy waveform reflects not only the growth in disturbance velocities, but also the spread of the wave packet in the spanwise direction.

In Figs. 3a-b the normal velocity contours in the plane $x_2 \approx 1.1$ are plotted for two time instants before and after laminar breakdown. Fig. 3a shows the two legs of the lambda vortex which merge gradually along the streamwise direction. The lambda vortex is "crippled" in the sense that it has unequal strength in the two legs, caused by the spanwise asymmetry prescribed in the initial disturbance. The

imbalance causes the two legs to become twisted near the tip of the vortex loop, accelerating the breakdown of the streamwise vortex structure and the high shear layer supported by it. This effect can be seen more clearly if one plots streamwise vorticity contours at certain x_2 - x_3 cross-sections. Similar observation has been made by Corral & Jiménez (1991). By the time depicted in Fig. 3b, the front portion of the primary lambda vortex has disintegrated, and regions of smaller streamwise vortices emerge. The disturbance region has been elongated since the turbulence-like small-scale structures travel at a faster speed than the lambda vortex. At the rear the lambda vortex legs are still recognizable. Fig. 3b also demonstrates that up to this stage, the disturbance region remains small in the spanwise direction relative to the width of the computational box. Interaction between the neighboring patches is negligible despite the periodicity imposed in the spanwise direction. Thus, the wave packet can be justifiably considered isolated.

The transition scenario described in this section is in qualitative agreement with experimental observations (Gaster 1993; Borodulin & Kachanov 1992). In particular, the coherent structures depicted in Figs. 1e and 1f are remarkably similar to the experimental measurements illustrated in Fig. 31 of Kachanov (1994). Quantitative comparisons are difficult because of disparity in parametric conditions. The results of the present simulation are also in keeping with those of earlier numerical studies (Zang & Hussaini 1990; Kleiser & Zang 1991, for example). The latter are based on a temporal formulation (assuming streamwise periodicity) and do not exceed the two-spike stage. The observed similarity between the two types of simulations confirms that as first suggested by Kachanov (1994), the laminar breakdown of a modulated wave packet proceeds in nearly the same way as that for a periodic T-S wave series. This illustrates the localized nature of resonant mechanisms that lead to laminar breakdown.

2.2. Computation of acoustic radiation

Acoustic computation based on Lighthill's theory is particularly simplified for a compact flow region. In this case the small retarded time effect can be approximated in the sense of multipole source expansions. Based on the integral results of Curle (1955) and Powell (1960), the far-field acoustic pressure can be shown to have the following asymptotic property as $M \rightarrow 0$; $|\vec{X}| \rightarrow \infty$:

$$\begin{aligned} \frac{4\pi}{\gamma} [p(\vec{X}, t) - 1] \approx & 2M^4 \frac{X_\alpha}{|\vec{X}|^2} \dot{R}_\alpha(t - |\vec{X}|) \\ & + M^5 \frac{X_i X_j + X_i^* X_j^*}{|\vec{X}|^3} \ddot{Q}_{ij}(t - |\vec{X}|) \\ & + 2M^5 \frac{X_\alpha X_\beta}{|\vec{X}|^3} \ddot{S}_{\alpha\beta}(t - |\vec{X}|) \end{aligned} \quad (2)$$

where M is the free-stream Mach number and $\vec{X} = M\vec{x}$ is the rescaled far-field position vector, whose image in the rigid wall $X_2 = 0$ is $\vec{X}^* = (X_1, -X_2, X_3)$. Repeated

indices i and j represent summation over 1 to 3, whereas α and β are summed over 1 and 3 only. The three terms on the right side of (2) represent contributions from, respectively, net surface dipoles due to fluctuating wall shear stresses, net volume quadrupoles (including wall reflection) dominated by fluctuating Reynolds stresses, and net surface quadrupoles due to finite spatial distribution of wall shear stresses. The dipole and quadrupole source strengths are determined by

$$\dot{R}_\alpha(t) = \frac{\partial}{\partial t} \int_{A_0} \tau_{\alpha 2}(\vec{y}, t) dA(\vec{y}), \quad (3)$$

$$\ddot{Q}_{ij}(t) = \frac{\partial^2}{\partial t^2} \int_{V_0} T_{ij}(\vec{y}, t) dV(\vec{y}), \quad (4)$$

$$\ddot{S}_{\alpha\beta}(t) = \frac{\partial^2}{\partial t^2} \int_{A_0} y_\beta \tau_{\alpha 2}(\vec{y}, t) dA(\vec{y}), \quad (5)$$

where the Lighthill stress tensor and the viscous stress tensor take the approximate values

$$T_{ij} \approx u_i u_j, \quad \tau_{ij} \approx \frac{1}{Re} \left(\frac{\partial u_i}{\partial x_j} + \frac{\partial u_j}{\partial x_i} \right), \quad (6)$$

given the small Mach number assumption. The volume integrations are taken over the entire unsteady flow region, and the surface integrals are evaluated on the wall.

A serious difficulty confronts computational acousticians when vortical structures enter or pass out of the computational domain, causing powerful dipole radiation which may mask the true physical sound (Crighton 1993; Wang 1993). This arises because, if the complete disturbance region is not included in the finite computational domain, the time variations of the volume (surface) integrated Q_{ij} , R_α , and $S_{\alpha\beta}$ (cf. (3)–(5)) tend to be dominated by the fluxes of their respective integrand across the integration boundaries rather than by the internal generation of these quantities within the control volume.

Steps have been taken in order to eliminate the non-physical boundary effects. First, the computational boundaries for Navier-Stokes simulation of the source field are maintained sufficiently far away from the region of significant disturbances, as is evident from a comparison of the computational box size ($140 \times 20 \times 25.95$) with the size of flow structures displayed in Figs. 1–3 (note that only part of the domain is plotted to magnify the main feature). This measure alone removes most of the boundary artifacts at the expense of increased computational cost. However, it is impossible to prevent small disturbances from reaching the downstream boundary even if a very long computational domain is used. The difficulty is illustrated in Fig. 4, which depicts contours of the instantaneous normal vorticity at $x_2 \approx 2.3$, $t = 292$. The primary structure at left is identified with the wave packet. The transient ripples induced by the wave packet extend all the way to the right because they are convected near the edge of the boundary layer at a faster speed.

The residual boundary artifacts caused by these ripples are removed by using the corrected quadrupole sources defined as

$$\ddot{Q}'_{ij} = \ddot{Q}_{ij} + \dot{F}_{ij}, \quad \dot{F}_{ij} = \frac{\partial}{\partial t} \int_S u_1^B T_{ij} dS, \quad (7)$$

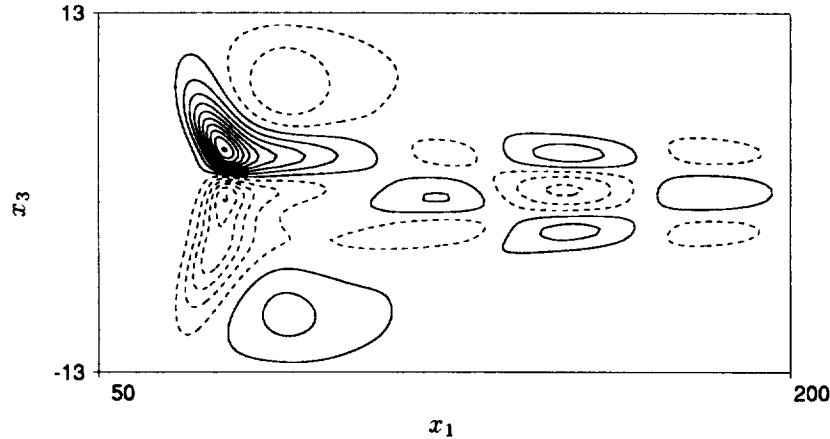


FIGURE 4. Contours of instantaneous normal vorticity at $x_2 \approx 2.3$, $t = 292$. Contour spacing = 0.0015.

where F_{ij} represents the flux of Lighthill stress components at the outflow boundary. Eq. (7) is derived based on a control-volume balance for T_{ij} , recognizing that the physical sound sources are associated only with the Lighthill stresses (predominantly Reynolds stresses) generated internally through nonlinear interactions. Eq. (7) is exact except for the evaluation of the surface flux F_{ij} , which assumes that T_{ij} is convected passively out of the outflow boundary at the local mean velocity. The approximation works well for the present problem, as demonstrated below, because the ripple disturbances are linear and travel at approximately the free-stream velocity. In general, however, the T_{ij} associated with large vortical structures involves nonlinear effects and travels at a phase velocity which is not known *a priori*. More accurate methods for estimating F_{ij} need to be developed, perhaps along the line of Fedorchenko (1986).

Fig. 5 illustrates the effect of flux correction for \ddot{Q}_{12} , the component with the largest boundary artifact. The dashed and dotted lines, representing the original quadrupole source and the time-derivative of the outflow boundary flux, respectively, show oscillations of similar magnitude but opposite phase for $t \leq 330$. As a result the corrected acoustic source (the solid line) remains nearly zero during this period. Had the spurious boundary contribution not been subtracted, one would predict incorrectly sound radiation when the wave packet transition is still in an early stage (cf. Figs. 1a-f). At later times, Fig. 5 shows that the boundary flux contribution continues to be significant although the physical source gradually becomes dominant. The vertical dotted line in the figure indicates the time when the computational domain is moved from $0 \leq x_1 \leq 200$ to $40 \leq x_1 \leq 180$. This causes a discontinuity in \ddot{Q}_{12} and \dot{F}_{12} , but \ddot{Q}'_{12} remains continuous since the physical source is completely contained within both domains.

In what follows the prime in \ddot{Q}'_{ij} is dropped to simplify notation, with the understanding that the quadrupole sources presented are free of boundary artifacts. Convergence of the quadrupole and dipole source terms is monitored by evaluating

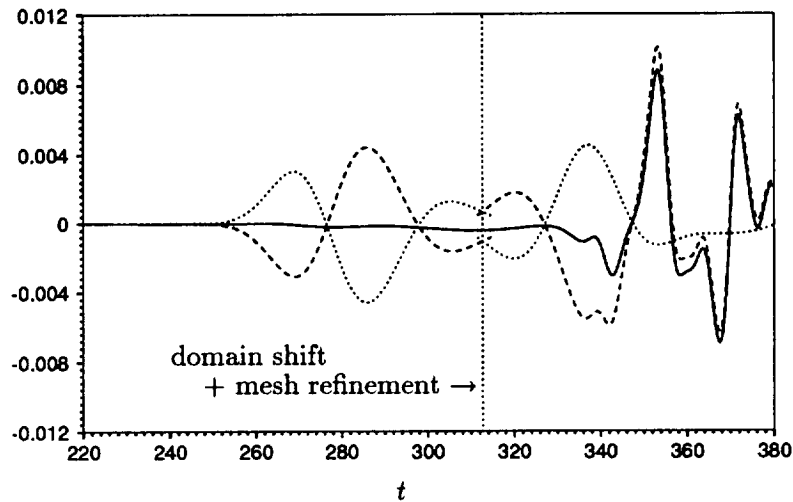


FIGURE 5. Time variation of a quadrupole source component, with and without correction for outflow boundary effect. ---- \ddot{Q}_{12} ; \dot{F}_{12} ; — $\ddot{Q}_{12} + \dot{F}_{12}$.

them in two domains of integration whose downstream boundaries are a short distance (~ 5) apart. Agreement between the two solutions indicates that no boundary effect is present. When the two solutions start to deviate, the computational box is moved to a new downstream location.

2.9. Results and discussion

Figs. 6 illustrate the time-variations of the volume quadrupole source terms \ddot{Q}_{ij} calculated from (4) with appropriate boundary flux corrections. The upper figure depicts the three longitudinal components, and the lower figure depicts the lateral ones. Since the Lighthill stress tensor is symmetric, only six components are needed to define \ddot{Q}_{ij} completely. The characteristics of source oscillations should be analyzed in conjunction with the flow structures shown in Figs. 1a-f. The quadrupole source signals generated by wave packet evolution are relatively weak initially, and then amplify dramatically as the shear layer begins to break down. Thereafter, the \ddot{Q}_{ij} curves are seen to develop oscillations dominated by frequencies 5 to 7 times the basic T-S wave frequency (T-S wave period ≈ 66.5).

A close examination of the \ddot{Q}_{11} curve and Figs. 1-2 indicates a strong correlation between source oscillation and vortex-shedding in the boundary layer. At $t = 409$, the number of spikes (eddies) shown in Figs. 2a-f is approximately equal to the number of cycles experienced by \ddot{Q}_{11} . Thus it appears that the dominant mechanism for generating quadrupole sound is the intermittent vortex shedding, or bursting, resulting from strong inflexional instability of the high shear layer. This is not unexpected since turbulent stress production occurs mainly during the bursts (Landahl 1975). In his experiments concerning instability of modulated T-S wave trains, Gaster (1993) observes a characteristic bursting frequency of 5 to 6 times the T-S wave frequency, coinciding with the dominant source frequencies

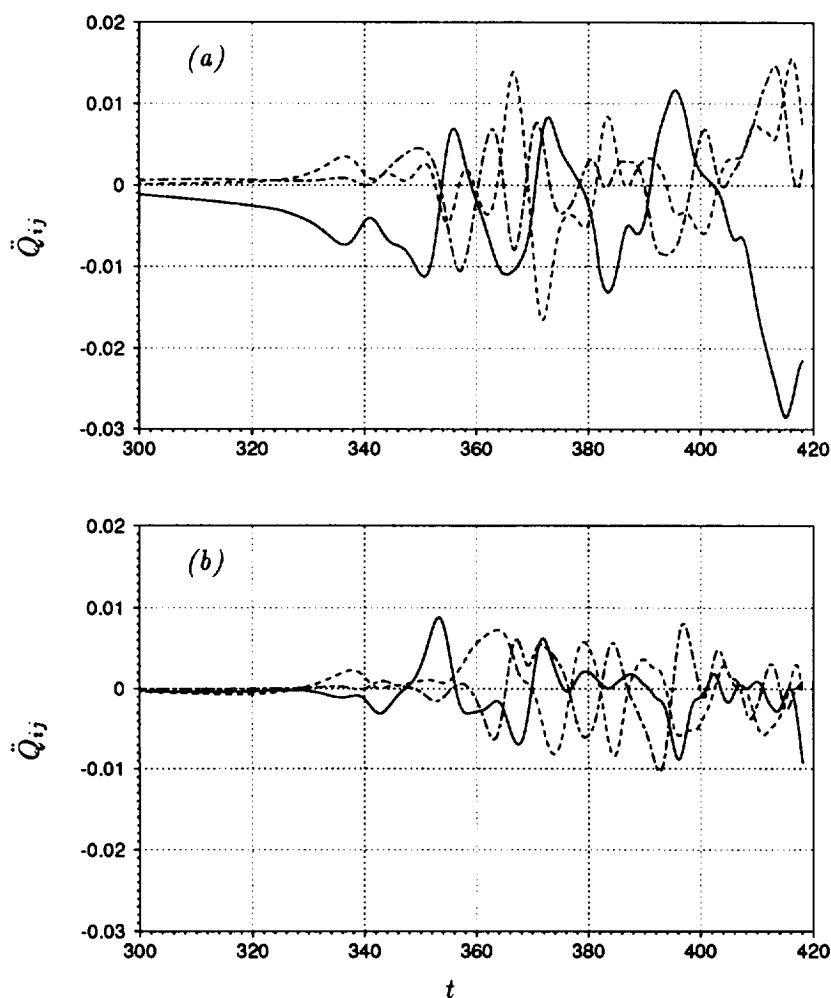


FIGURE 6. Time variations of volume quadrupole sources due to Reynolds stress fluctuation during local laminar breakdown. (a) Longitudinal components: — \ddot{Q}_{11} ; ---- \ddot{Q}_{22} ; - · - \ddot{Q}_{33} . (b) Lateral components: — \ddot{Q}_{12} ; ---- \ddot{Q}_{13} ; - · - \ddot{Q}_{23} .

calculated in the present study. Gaster further notes that the bursting frequency is independent of the Reynolds number. The agreement between the bursting and acoustic source frequencies supports the assertion that the large-scale shear layer instability is primarily responsible for the calculated quadrupole sound.

It is interesting to notice that no significant increase in higher frequency contents is observed in Figs. 6a-b as transition proceeds to create increasingly refined scales. Likewise, the amplitudes for \ddot{Q}_{ij} remain basically invariant with time, even though the total kinetic energy of the source region (the area under each curve in Figs. 2a-f)

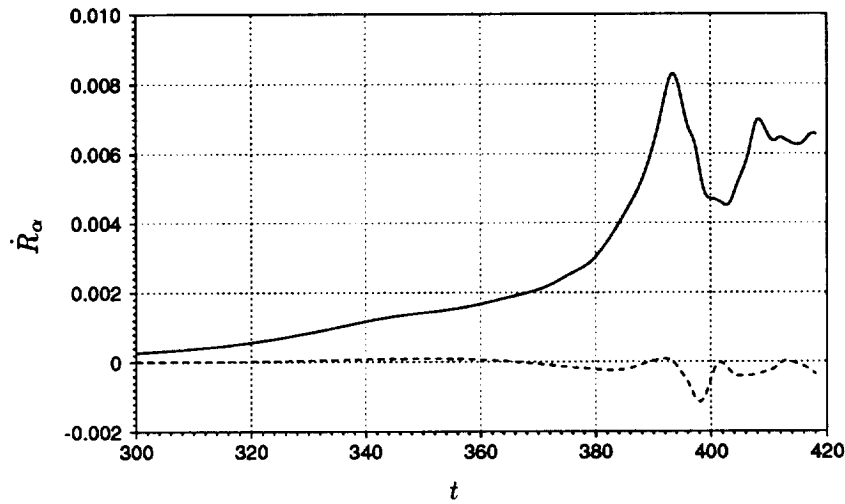


FIGURE 7. Time variations of surface dipole source terms due to viscous wall stress during local laminar breakdown. — \dot{R}_1 ; ---- \dot{R}_3 .

grows at an exponential rate. These observations can be explained in terms of the localized nature of bursting which dominates the instantaneous sound production. The small-scale features and the convected large eddies produced during previous bursts are less efficient as quadrupole acoustic sources, although they contain large amount of disturbance energy.

In Fig. 7 the two net acoustic dipoles caused by fluctuations of wall shear stress exerted on the fluid are plotted. They are dominated by low (T-S wave) frequency, small amplitude phenomena during the process of shear layer lift-up and the first three bursts. Figs. 1a-f show clearly that within this period, the near-wall region is little affected by the violent events outside. As the laminar wave packet approaches the turbulent spot stage, the near-wall shear intensifies, giving rise to a surge in higher frequency dipole strength. The magnitudes of \dot{R}_3 in Fig. 7, as well as \dot{Q}_{13} and \dot{Q}_{23} in Figs. 6a-b, reflect the extent of spanwise asymmetry during flow development. They would vanish if symmetry conditions were imposed for the simulation.

The surface quadrupole acoustic sources given by (5) are caused by the changing spatial distribution of wall shear stress. They represent an $O(M)$ correction to the wall-stress induced dipole radiation in the compact source limit. Like the dipole source terms, the surface quadrupole components are small until the inner boundary layer is excited at a late laminar breakdown stage as illustrated in Fig. 8. The segments of $\ddot{S}_{\alpha\beta}$ plotted have magnitudes comparable with those of the volume quadrupoles depicted in Figs. 6a-b, but at higher frequency. Before $t = 390$, however, contribution from \dot{S}_{ij} is insignificant.

Figs. 6-8 demonstrate that the acoustic emission level is very low at early stages of wave packet transition. At the earliest instant plotted ($t = 300$), the wave packet has already evolved into a lambda vortex-high shear layer structure. Prior to that, the acoustic source terms exhibit either monotonic growth or extremely low amplitude

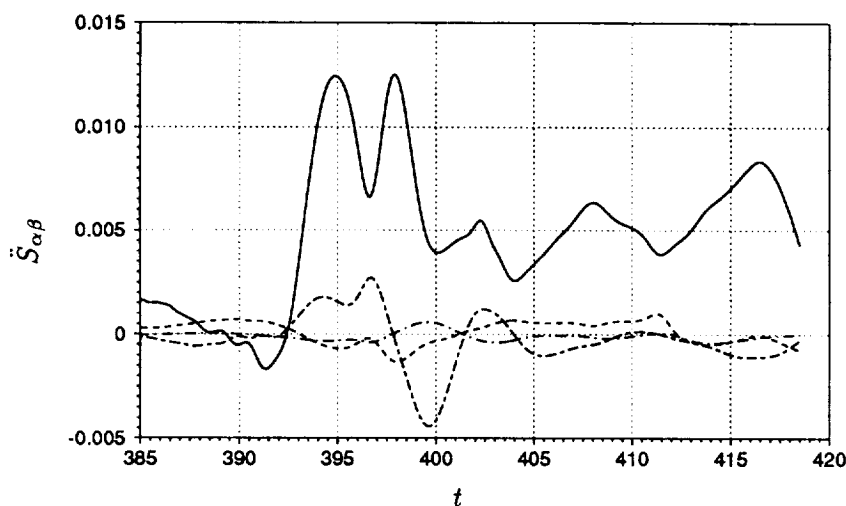


FIGURE 8. Time variations of surface quadrupole sources due to viscous wall stress during local laminar breakdown. — \ddot{S}_{11} ; ---- \ddot{S}_{13} ; - · - \ddot{S}_{31} ; — — \ddot{S}_{33} .

oscillations at the basic T-S wave frequency. Thus it can be concluded that linear and weakly nonlinear amplification of the T-S wave packet produces insignificant sound relative to the more violent bursting process later. Unfortunately, only the former regime is amenable to rigorous analytical treatment (*e.g.*, Ffowcs-Williams 1967; Akylas & Toplosky 1986; Haj-Hariri & Akylas 1986).

For flow-noise problems it is generally recognized that the energy-containing coherent structure provides the predominant noise source. The fine-scale structure associated with high frequency phenomenon is largely irrelevant (Crighton 1975), a conclusion supported by the lack of relatively high frequency components in Figs. 6–8. To test the sensitivity of quadrupole sources to the size of flow structure, the computed flow field is filtered in the x_1 – x_3 plane using a box filter of varying width before the volume integration in (4) is performed. The results for $\Delta_i = 2\Delta x_i$, $4\Delta x_i$, and $8\Delta x_i$, where Δ_i is the filter width in the i th direction and Δx_i is the mesh spacing, are compared in Fig. 9 with those without filtering. For brevity only the three longitudinal components are given; the three lateral ones behave in the same way. Clearly, the basic source characteristics are preserved after filtering the flow field with a filter of widths up to $4\Delta_i$ ($2\Delta_i$ for \ddot{Q}_{22}). With a filter width of $8\Delta_i$, the results are still in qualitative agreement with their unfiltered counterparts in terms of basic frequency and amplitude. This verifies that removing small-scale flow structures indeed has little impact on the distant-field sound radiation. Since the application of a box filter also alters the lower wavenumber (large-scale) components to some extent, the actual agreement between unfiltered and filtered source quantities might be even better had the large-scale motion been truthfully preserved.

The comparison made in Fig. 9 is also an indication of numerical convergence. It illustrates that the direct numerical simulation for the source field has adequately

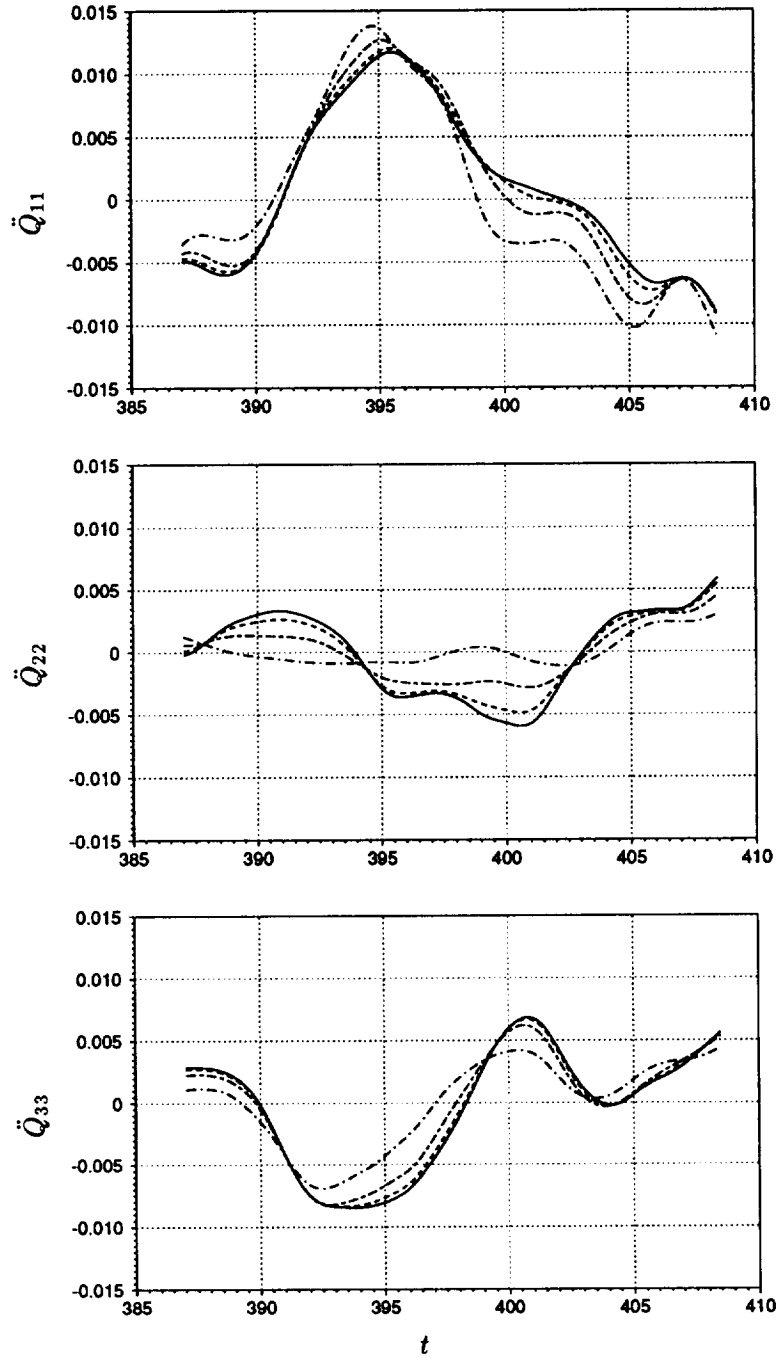


FIGURE 9. Longitudinal quadrupole sources calculated based on the velocity field filtered in the x_1 - x_3 plane with filter width Δ_i . — no filtering; ---- $\Delta_i = 2\Delta x_i$; - · - $\Delta_i = 4\Delta x_i$; - - - $\Delta_i = 8\Delta x_i$.

resolved the scales relevant to sound production. In fact, the simulation can be conducted on a coarser grid if the subgrid-scale stress can be modeled adequately. This suggests the promising role that can be played by the less expensive large-eddy simulation methods for flow-noise prediction.

An issue worthy of particular attention is the relative importance of wall-shear-stress radiation *vs.* volume Reynolds stress radiation. Eq. (2) and the numerical results in Figs. 6 and 7 indicate that at the late laminar breakdown stage, viscous dipole radiation is important or even dominant for low Mach number flows, in agreement with Landahl (1975) but at variance with conclusions of Howe (1979) and Haj-Hariri & Akylas (1985), who assert that surface stress contribution is in general negligible. The contradiction may arise because Howe's (1979) analysis is limited only to the low wavenumber (acoustic) components of the wavenumber-frequency spectrum, whereas the analysis of Haj-Hariri & Akylas (1985) fails to utilize the pertinent turbulence scales in estimating the Lighthill source terms at high Reynolds number. Furthermore, the three aforementioned studies are all concerned with fully turbulent boundary layers, although Landahl (1975) notes the qualitative similarities between the high shear layer breakdown during transition and the turbulent bursting in the inner layer of a turbulent boundary layer.

As an example, Figs 10a and 10b compare the distant sound field generated by, respectively, the inviscid Reynolds stress (volume quadrupoles) and viscous wall-stress (sum of surface dipoles and quadrupoles), in terms of iso-contours of the acoustic pressure \hat{p} ($= p - 1$) at $X_3 = 0$ and $t = 420$. The source region is centered at $\vec{X} = 0$, bearing in mind that \vec{X} is scaled relative to the acoustic length scale. The free-stream Mach number is $M = 0.02$, characteristic of underwater applications. At the time instant plotted, the shear-stress induced sound is mainly confined in a region close to the source (the latest signal depicted at $|\vec{X}| = 10$ is emitted at $t = 410$). The quadrupole radiation pattern suggests contributions from the longitudinal components, but not the lateral ones. The latter are identically zero due to both cancellations from wall reflection and the specific plane ($X_3 = 0$) selected for plotting (cf. (2)). Given the extremely low Mach number, the total radiated field obtained by summing the results in Figs. 10a and 10b is dominated by the surface stress contribution, as is evident from Fig. 10c. The relative effect of volume quadrupoles is, of course, also dependent on the orientation of the plotting plane. For instance, quadrupole radiation is felt more strongly in the $X_1 = 0$ plane than in the plane plotted. When the Mach number is increased to $M = 0.1$, the volume quadrupole sound is found to be comparable in strength with that due to wall-shear-stress, particularly in the plane $X_1 = 0$.

3. Conclusions and future directions

A computational study has been carried out concerning the sound emission from a localized disturbance as it undergoes transition to turbulence in a boundary layer formed on a flat, rigid surface. The flow is characterized by small free-stream Mach number and a Reynolds number of 1000 based on the displacement thickness. Direct numerical simulation is applied in conjunction with the Lighthill acoustic analogy

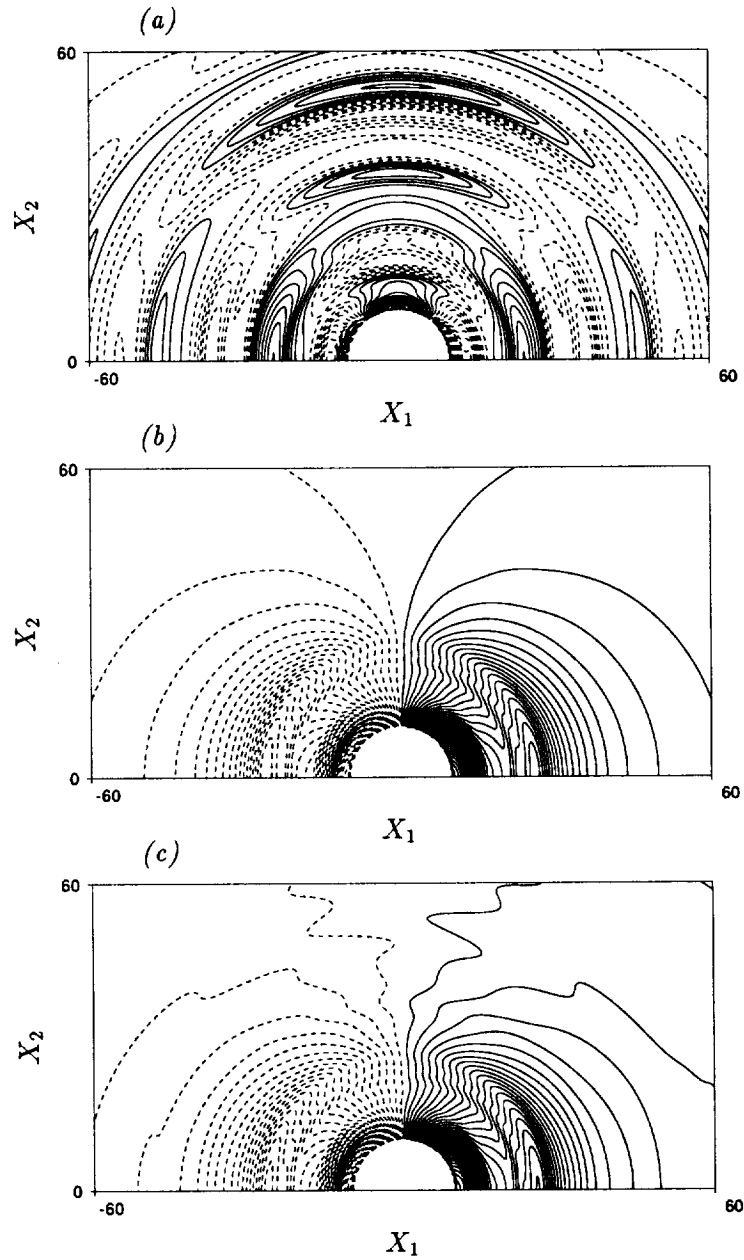


FIGURE 10. Iso-contours of the far-field acoustic pressure in the plane $X_3 = 0$ at $t = 420$, radiated during laminar breakdown of an isolated wave packet. The free-stream Mach number $M = 0.02$. (a) Volume Reynolds stress contribution (contour levels from -1.02×10^{-12} to 0.50×10^{-12}); (b) wall shear-stress contribution (contour levels from -2.25×10^{-11} to 2.31×10^{-11}); (c) total acoustic pressure (contour levels from -2.31×10^{-11} to 2.19×10^{-11}).

to determine the near-field flow dynamics and the far-field sound, respectively. The objectives are to establish a relationship between specific flow processes and the emitted acoustic signals, and to identify the primary noise source.

The boundary-layer disturbance initially consists of a modulated, three-dimensional T-S wave packet emulating that excited by free-stream turbulence in natural transition. Detailed accounts of the subsequent evolution, from the early linear stage to the final laminar breakdown, are obtained by solving the full incompressible Navier-Stokes equations. The simulation allows streamwise growth of the boundary layer thickness as well as spanwise asymmetry. The latter effect promotes interaction between the (unequal) lambda vortex legs and accelerates the high shear layer breakdown and the associated eddy shedding. The route to turbulence is seen to follow the usual sequence of events for the fundamental breakdown type. The flow structures are in qualitative agreement with the experimental observations of Borodulin and Kachanov (1992).

Acoustic computation based on the Lighthill theory is facilitated by a multipole Taylor series expansion in the compact source limit. The radiated far-field acoustic density (pressure) comprises of, to $O(M^5)$ relative to the mean, contributions from net surface dipoles caused by viscous wall shear stresses, net volume quadrupoles due to fluctuating Reynolds stresses, and net surface quadrupoles due to finite spatial distribution of wall shear stresses. All the sources produce negligible sound throughout the primary and secondary instability processes of the wave packet. As the detached high shear layer starts to disintegrate, dramatic amplification occurs for the volume quadrupole sound. The primary frequency (5–7 times the basic T-S wave frequency) of quadrupole radiation corresponds to the frequency of hairpin eddy (spike) generation in the near-field, indicating the latter to be the physical source. The surface dipole and quadrupole sources experience a surge in strength at a later breakdown stage caused by the activation of the high-shear wall layer as the disturbance region evolves to a turbulence spot.

This study suggests that for boundary layer transition at low Mach number, the fluctuation in viscous wall stress takes a significant part in radiating sound to the surrounding. It is in fact the primary sound source at later laminar breakdown stages.

An interesting extension of the present work would be to explore the suitability of large-eddy simulation (LES) techniques for simulating the laminar boundary layer breakdown process and calculating the acoustic source terms. LES possesses tremendous potential in terms of reducing the computational cost drastically while still capturing the energy-containing unsteady flow features essential to noise generation. An earlier study by Piomelli *et al.* (1990) suggests that the Smagorinsky subgrid-scale (SGS) model is excessively dissipative, resulting in less intense high shear layers and delayed transition. New SGS models developed at CTR, such as the dynamic SGS model (Germano *et al.* 1991), offer improved prospects for predicting the important transitional flow structures accurately.

A separate project commenced recently concerns noise radiation caused by turbulent flow past a hydrofoil/airfoil. Broadband noise is known to exist when turbulent

boundary layers interact with a sharp trailing edge as a result of hydrodynamic pressure scattering. In addition, high angles of attack and blunt trailing edges cause flow separation and vortex shedding, which are the source of distinct peaks in the noise spectra (Brooks & Hodgson 1981). A numerical noise-prediction method will be developed using LES in conjunction with aeroacoustic theories. The turbulent boundary layer and near-wake flows are simulated using LES, and the radiated far-field sound is calculated within the framework of the Lighthill theory, taking advantage of experiences gained through the present project. The prediction method can be validated by comparing the numerical results with the experimental data of Brooks & Hodgson (1981).

Acknowledgements

This work was produced in collaboration with Prof. S. K. Lele and Prof. P. Moin. We wish to thank Dr. K. Shariff and Mr. B. Mitchell for fruitful discussions during the course of this work. Appreciation is extended to Mr. Y. Na for providing the original Navier-Stokes code and related assistance, and to Mr. S. Collis for providing the Orr-Sommerfeld eigensolver. Computations were carried out on the NAS facilities at NASA Ames Research Center. This project was supported in part by the Office of Naval Research.

REFERENCES

- AKYLAS, T. R. & TOPLOSKY, N. 1986 The sound field of a Tollmien-Schlichting wave. *Phys. Fluids*, **29**, 685–689.
- BORODULIN, V. I. & KACHANOV, Y. S. 1992 Experimental study of soliton-like coherent structures. In *Eddy Structure Identification in Free Turbulent Shear Flows*. IUTAM Symposium, Poitiers, 1992.
- BROOKS, T. F. & HODGSON, T. H. 1981 Trailing edge noise prediction from measured surface pressures. *J. Sound & Vib.* **78**, 69–117.
- CORRAL, R. & JIMÉNEZ, J. 1991 *Direct Numerical Simulation of the Leading Edge Boundary Layer*, Technical Note ETSIA/MF-916, Dept. of Fluid Mech., Universidad Politécnica Madrid.
- CRIGHTON, D. G. 1975 Basic principles of aerodynamic noise generation. *Prog. Aerospace Sci.* **16**, 31–96.
- CRIGHTON, D. G. 1993 Computational aeroacoustics for low Mach number flows. In *Computational Aeroacoustics*. ICASE/NASA LaRC Series, (Hardin J. C. and Hussaini, M. Y. Eds.), Springer-Verlag.
- CURLE, N. 1955 The influence of solid boundaries upon aerodynamic sound. *Proc. Royal Soc. London Ser. A*. **231**, 505–514.
- FARABEE, T. M., HANSEN, R. J., & KELTIE, R. F. (Eds.) 1989 *Flow-Induced Noise Due to Laminar-Turbulence Transition Process*, ASME NCA-Vol. 5, Symposium for ASME Winter Annual Meeting, San Francisco, 1989.

- FEDORCHENKO, A. T. 1986 On vortex outflow through the permeable boundary of the computational domain of non-stationary subsonic flow. *U.S.S.R. Comput. Maths. Math. Phys.* **26**, 71–80.
- FFOWCS-WILLIAMS, J. E. 1967 Flow noise. In *Underwater Acoustics*, Vol. 2, Chap. 6, Plenum Press.
- GASTER, M. 1993 The origins of turbulence. In *New Approaches and Concepts in Turbulence*, Monte Verita Ser. (Dracos, T. A. & Tsinober, A. Eds.), Birkhauser Boston.
- GERMANO, M., PIOMELLI, U., MOIN, P. & CABOT, W. H. 1991 A dynamic subgrid-scale eddy viscosity model. *Phys. Fluids A*. **3**, 1760–1765.
- HAJ-HARIRI, H. & AKYLAS, T. R. 1985 The wall-shear-stress contribution to boundary-layer noise. *Phys. Fluids*. **28**, 2727–2729.
- HAJ-HARIRI, H. & AKYLAS, T. R. 1986 Sound radiation by instability wave packets in a boundary layer. *Stud. Appl. Math.* **75**, 57–76.
- HOWE, M. S. 1979 The role of surface shear stress fluctuations in the generation of boundary layer noise. *J. Sound & Vib.* **65**, 159–164.
- KACHANOV, Y. S. 1994 Physical mechanisms of laminar-boundary-layer transition. *Ann. Rev. Fluid Mech.* **26**, 411–482.
- KLEISER, L. & ZANG, T. A. 1991 Numerical simulations of transition in wall-bounded shear flows. *Ann. Rev. Fluid Mech.* **23**, 495–537.
- LANDAHL, M. T. 1975 Wave mechanics of boundary layer turbulence and noise. *J. Acoust. Soc. Am.* **57**, 824–831.
- LE, H. & MOIN, P. 1991 An improvement of fractional step methods for the incompressible Navier-Stokes equations. *J. Comput. Phys.* **92**, 369–379.
- LIGHTHILL, M. J. 1952 On sound generated aerodynamically; I. General theory. *Proc. Roy. Soc. London Ser. A*. **211**, 564–587.
- PIOMELLI, U., ZANG, T. A., SPEZIALE, C. G., & HUSSAINI, M. Y. 1990 On the large-eddy simulation of transitional wall-bounded flows. *Phys. Fluids A*. **2**, 257–265.
- POWELL A. 1960 Aerodynamic noise and the plane boundary. *J. Acoust Soc. Am.* **32**, 982–990.
- WANG, M. 1993 Sound radiation due to boundary layer transition. *Annual Research Briefs-1993* Center for Turbulence Research, NASA Ames/Stanford Univ., 299–312.
- WANG, M, LELE, S. K., & MOIN, P. 1994 Sound radiation during local laminar breakdown in a low Mach number boundary layer. *CTR Manuscript No. 153*, NASA Ames/Stanford Univ.
- ZANG, T. A. & HUSSAINI, M. Y. 1990 Multiple paths to subharmonic laminar breakdown in a boundary layer. *Phys. Rev. Lett.* **64**, 641–644.

Small-scale behavior in distorted turbulent boundary layers at low Reynolds number

By Seyed G. Saddoughi

1. Motivation and background

During the last three years (Saddoughi 1993a; Saddoughi 1993b; Saddoughi & Veeravalli 1994), we have conducted high- and low-Reynolds-number experiments, including hot-wire measurements of the velocity fluctuations, in the test-section-ceiling boundary layer of the 80- by 120-foot Full-Scale Aerodynamics Facility at NASA Ames Research Center, to test the local-isotropy predictions of Kolmogorov's (1941) universal equilibrium theory. This hypothesis, which states that at sufficiently high Reynolds numbers the small-scale structures of turbulent motions are independent of large-scale structures and mean deformations, has been used in theoretical studies of turbulence and computational methods such as large-eddy simulation: however, its range of validity in shear flows has been a subject of controversy. The present experiments were planned to enhance our understanding of the local-isotropy hypothesis.

Our experiments were divided into two sets. First, (Saddoughi & Veeravalli 1994) measurements were taken at different Reynolds numbers in a plane boundary layer, which is a "simple" shear flow with the basic mean strain rate $S \equiv \partial U / \partial y$. Here our results established the conditions under which local isotropy can be expected in simple shear flows. Detailed analyses of these data have been already presented in our previous reports. The main conclusions were that the lower-wavenumber limit of locally-isotropic behavior (negligible shear-stress cospectra) is given by $k_1 \sqrt{\epsilon / S^3} \approx 10$. Our investigation also indicated that for energy spectra this limit could be relaxed to $k_1 \sqrt{\epsilon / S^3} \approx 3$; this is Corrsin's (1958) criterion, with the numerical value obtained from our data. The existence of an isotropic inertial range requires that this wavenumber be much less than the wavenumber at the onset of viscous effects so that the combined condition (Corrsin 1958 and Uberoi 1957) is $S \sqrt{\nu / \epsilon} \ll 1$. Spectral "bumps" between the $-5/3$ inertial range and the dissipative range were observed on all the compensated energy spectra. The shear-stress cospectra rolled off with a $-7/3$ power law and scaled linearly with S (Lumley 1967). In summary, it was shown that one decade of inertial subrange with truly negligible shear-stress co-spectral density requires $S \sqrt{\nu / \epsilon}$ not more than about 0.01 (for a shear layer with turbulent kinetic energy production approximately equal to dissipation, this implies a microscale Reynolds number of about 1500).

Second, experiments were designed to address this question: will our criteria for the existence of local isotropy hold for "complex" non-equilibrium flows in which extra rates of mean strain are added to the basic mean shear. In our last report (Saddoughi 1993b) we showed that the small-scale data taken at different locations in a highly-distorted boundary layer at high microscale Reynolds numbers (1750

to 2000) behaved similarly to the simple shear flow case, and that they satisfied the local-isotropy predictions. In the current report the results of our experiments conducted in complex flows at low Reynolds numbers at a variety of extra mean strain rates are presented.

2. Accomplishments

2.1 Apparatus and measurement techniques

We have studied the plane-of-symmetry flow in front of a circular cylinder placed vertically in a fully developed two-dimensional turbulent boundary layer. In this type of flow, the pressure rises strongly as the obstacle is approached, and the boundary layer is also influenced by the effects of lateral divergence. Hence, in addition to the basic mean shear, $\partial U/\partial y$, the extra mean strain rates involved in the flow are $\partial U/\partial x$, $\partial V/\partial y$, and $\partial W/\partial z$. To obtain the desired effects, the size of the cylinder should be at least of the order of the thickness of the boundary layer. Since in our study the approaching boundary-layer thickness was approximately 1.1 m, the following dimensions were chosen for our test cylinder: $D = 1.22$ m and height $L = 1.83$ m. Our measurement location was fixed at $x/D \approx 0.85$ with respect to the front of the cylinder.

We presented (Saddoughi 1993b) a very brief review of the experimental investigations dealing with the large-scale structural changes that occur in this kind of flow, and also gave a detailed description of the test cylinder and other apparatus used in our experiments. The measurement strategy, instrumentation, and procedure were all similar to those explained by Saddoughi & Veeravalli (1994), and details will not be repeated here.

Our low-Reynolds-number complex-flow experiments are divided into two cases: boundary layers under the influence of (i) large and (ii) small, extra mean strain rates. These two flow cases are described below.

2.2 Distorted boundary layers: Large extra-strain-rate experiments

Fig. 1. shows a schematic diagram of the test cylinder attached to the ceiling of the $80' \times 120'$ wind tunnel. During our complex-flow measurements the tunnel runs were dedicated to our experiments; however, as shown in Fig. 1, a full-scale F-18 fighter aircraft set at an angle of attack of 50° was present in the central region of the working section for both the high- and low-Reynolds-number measurements. It will be shown later that the presence of the aircraft in the tunnel usefully increased the mean strain rate in front of the cylinder.

Our low-Reynolds-number measurements have been taken at a reference velocity, $U_{ref} = 10.75$ m/s. The mean-flow data for this case are compared with the data for the high-Reynolds-number large-extra-strain-rate case in Fig. 2.

The normalized profiles of the longitudinal mean velocity, U/U_{ref} , for the distorted boundary layers are compared with the profiles obtained for the plane boundary layer in Fig. 2(a), where y is the distance from the wall. The shapes of the velocity profiles for the distorted boundary layers are typical of the large adverse-pressure-gradient flows: note the flattening of the profiles in the middle of the layer.

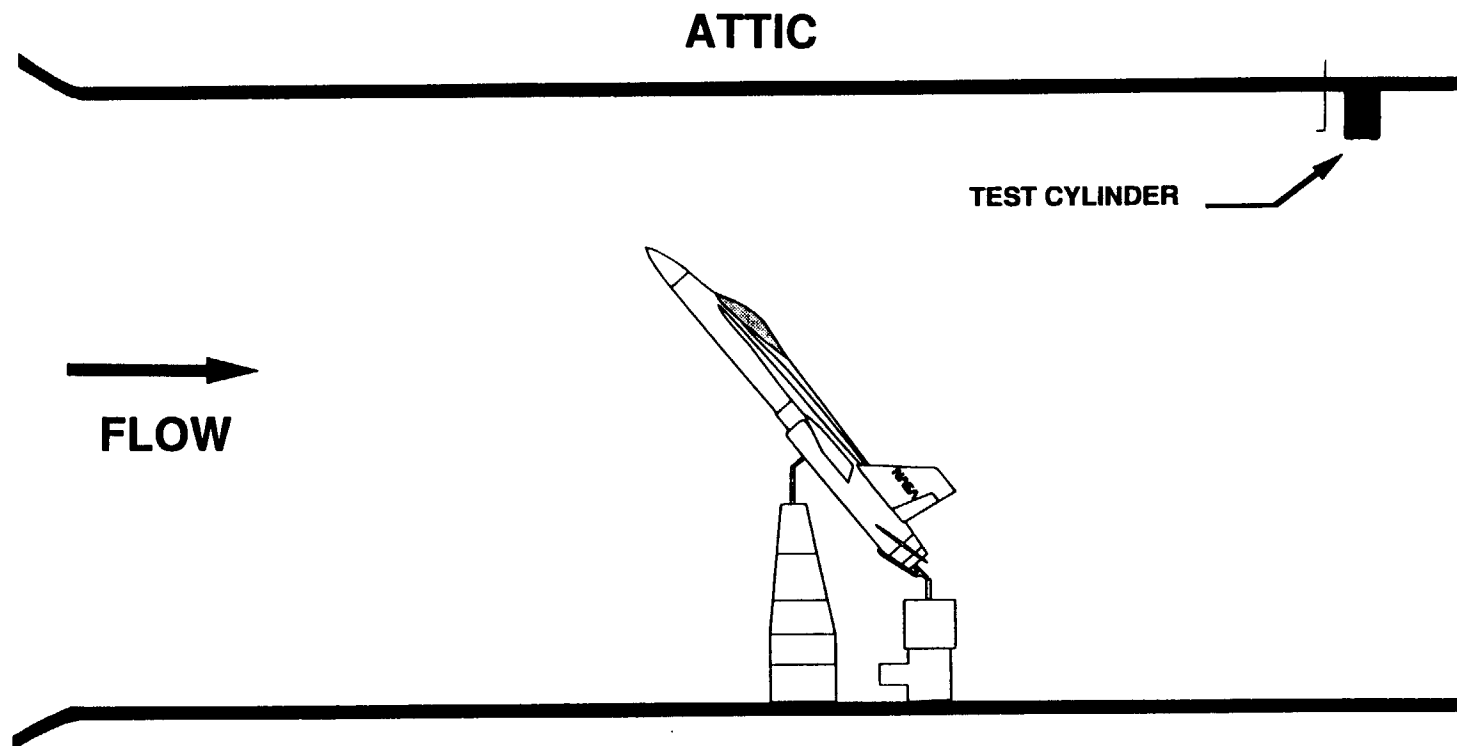


FIGURE 1. A schematic diagram for the large extra-strain-rate experiments, showing the relative position of the test cylinder with respect to the F-18 aircraft, which is set at an angle of attack $\alpha \approx 50^\circ$. The drawing is to scale.

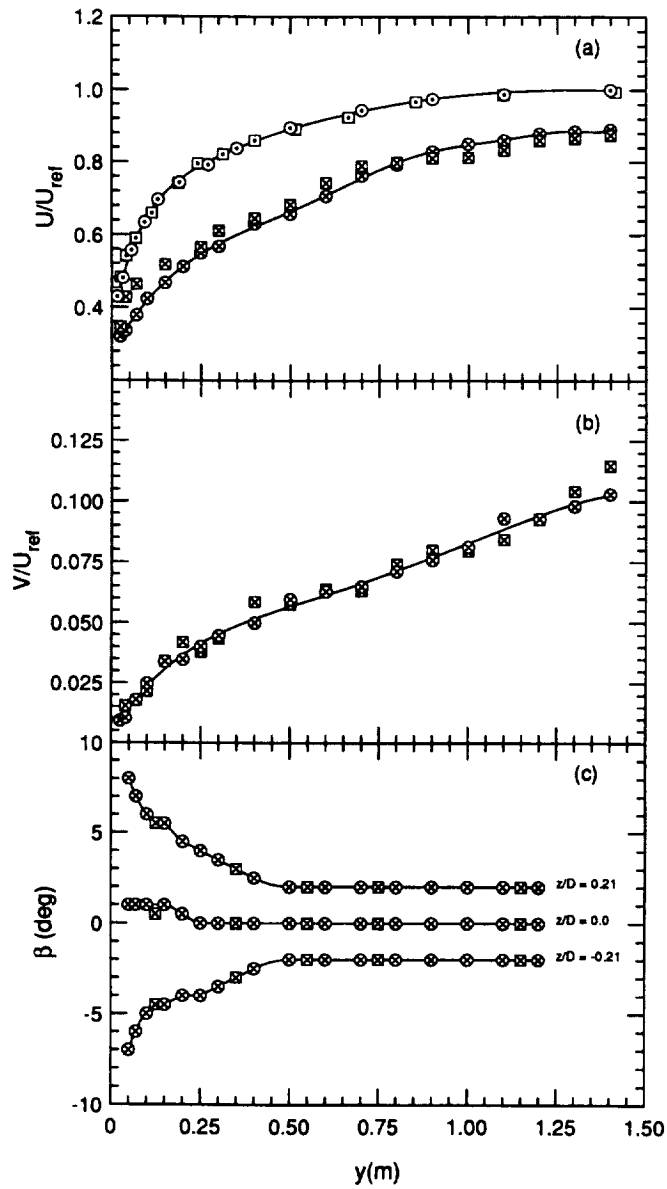


FIGURE 2. Mean-flow data at high and low Reynolds numbers. (a) Normalized longitudinal mean-velocity profiles, U/U_{ref} , measured in large extra-strain-rate and plane boundary layers. (b) Normalized vertical mean-velocity profiles, V/U_{ref} , measured in large extra-strain-rate boundary layers. (c) Flow yaw-angle profiles, β , measured in large extra-strain-rate boundary layers at different spanwise locations. \circ , $U_{ref} \approx 50$ m/s and \square , $U_{ref} \approx 10$ m/s plane boundary layer; \bullet , $U_{ref} \approx 51.25$ m/s and \blacksquare , $U_{ref} \approx 10.75$ m/s large extra-strain-rate boundary layer.

The boundary-layer thickness, δ (the point where $U/U_e = 0.995$), has increased to approximately 1250 mm in the distorted boundary layer. Here the shape factor $H \approx 1.85$, and at the edge of the boundary layer the pressure coefficient $C_p \approx 0.23$.

Fig. 2(b) shows the normalized profiles of the vertical velocity component, V/U_{ref} . A least-squares polynomial fit to the V profile was used to obtain the values of $\partial V/\partial y$.

The magnitudes of the extra strain rate due to the streamline divergence, $\partial W/\partial z$, influencing the plane of symmetry of the flow can be obtained from $(\partial W/\partial z) \equiv U(\partial\beta/\partial z)$ (see e.g. Saddoughi & Joubert 1991), where β is the flow yaw angle measured at different spanwise locations z . The profiles of β measured by a yaw-meter probe for three spanwise locations ($z/D = -0.21, 0$, and 0.21) through the boundary layers are shown in Fig. 2(c). It can be seen that, as expected, in the plane of symmetry of the flow the crossflow, W , is approximately equal to zero. The profiles are typical of three-dimensional boundary layers: larger flow yaw angles near the wall than the freestream.

Finally, the continuity equation was used to obtain the $\partial U/\partial x$ values. For both our high and low Reynolds number distorted boundary layers, typical values of $(\partial U/\partial x)/(\partial U/\partial y)$, $(\partial V/\partial y)/(\partial U/\partial y)$, and $(\partial W/\partial z)/(\partial U/\partial y)$ were larger than 0.1, 0.2, and 0.3 respectively. These large extra-mean-strain rates produce large non-linear effects on the large-scale structures of the boundary layers (Bradshaw 1973).

The profiles of the Reynolds normal stresses ($\overline{u_1^2}/U_{ref}^2, \overline{u_2^2}/U_{ref}^2, \overline{u_3^2}/U_{ref}^2$), and the shear stress, $-\overline{u_1 u_2}/U_{ref}^2$, for the distorted boundary layers at high and low Reynolds numbers are compared with the profiles for the plane boundary layers in Fig. 3. The profiles for the distorted boundary layers appear to be quite different from the plane flow case. The peaks of $\overline{u_2^2}$ and the shear stress, $-\overline{u_1 u_2}$, profiles have moved away from the wall to $y \approx 300$ mm, and in the outer part of the layer the values of all the Reynolds stresses have increased.

From Fig. 3(d) it can be deduced that at the wall $\tau/\rho U_{ref}^2 \approx 0.0003$. Also from Fig. 2(a) note that at the edge of the boundary layer $U/U_{ref} \approx 0.88$. Based on the above values, a $C_f \approx 0.00078$ can be obtained, which corresponds to shear velocities $U_\tau \approx 0.89$ m/s and 0.186 m/s for the high-Reynolds-number and low-Reynolds-number cases respectively. Using U_τ as the scaling velocity, the Reynolds shear-stress profiles are replotted in Fig. 4. These large changes in the large-scale structure of turbulence are due to the effects of large adverse pressure gradients (see Bradshaw 1967).

2.2.1 Analysis of small-scale data: low-Reynolds-number case

As mentioned earlier, the spectral measurements taken in this highly-distorted boundary layer at high Reynolds number were presented in our last report where it was shown that these data satisfied local-isotropy predictions. Hence, in the following we will concentrate only on the low-Reynolds-number experiments.

The spectral measurements of the three components of the velocity taken at $y = 100$ mm (inner-layer), 300 mm (maximum shear stress), 500 mm (around mid-layer), and 700 mm (outer-layer) for the low-speed case are analyzed here. In this case, the microscale Reynolds number range was about 850 to 650.

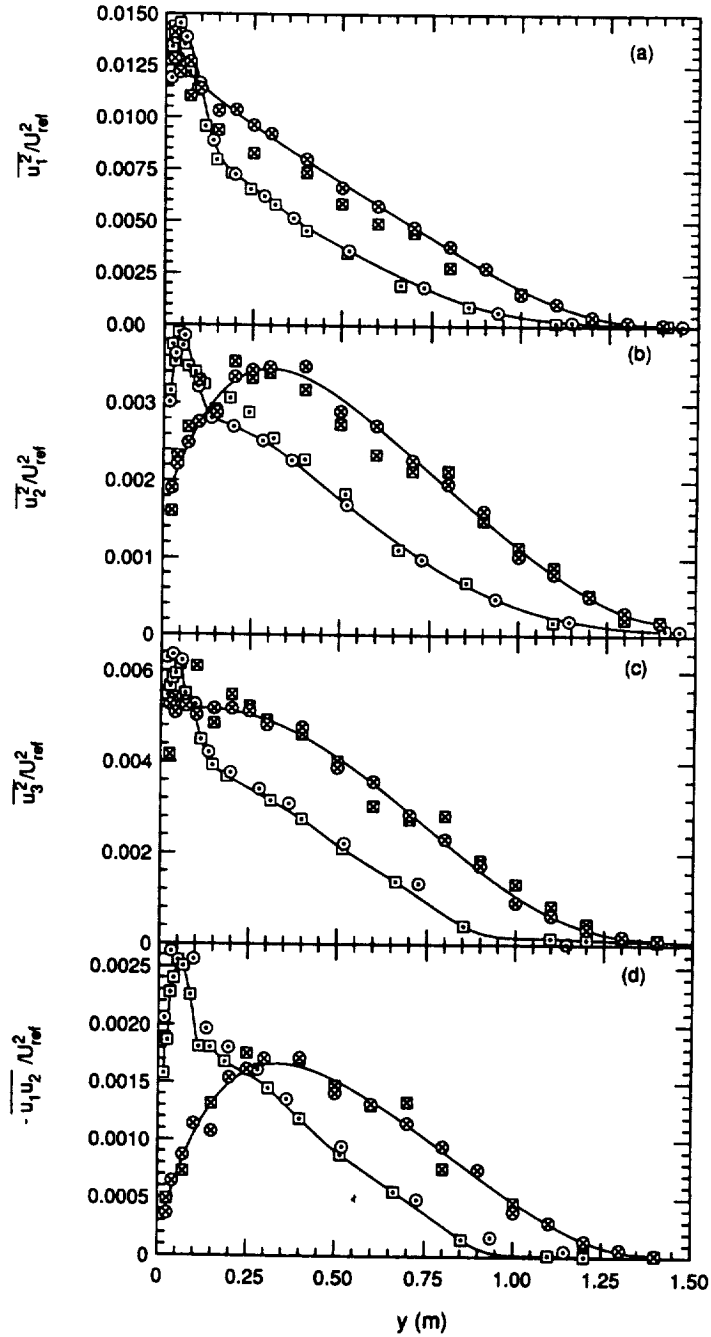


FIGURE 3. Profiles of Reynolds stresses measured in plane and large extra-strain-rate boundary layers at high and low Reynolds numbers: (a) $\overline{u_1^2}/U_{ref}^2$, (b) $\overline{u_2^2}/U_{ref}^2$, (c) $\overline{u_3^2}/U_{ref}^2$, (d) $-\overline{u_1 u_2}/U_{ref}^2$. For key to symbols see Fig. 2.

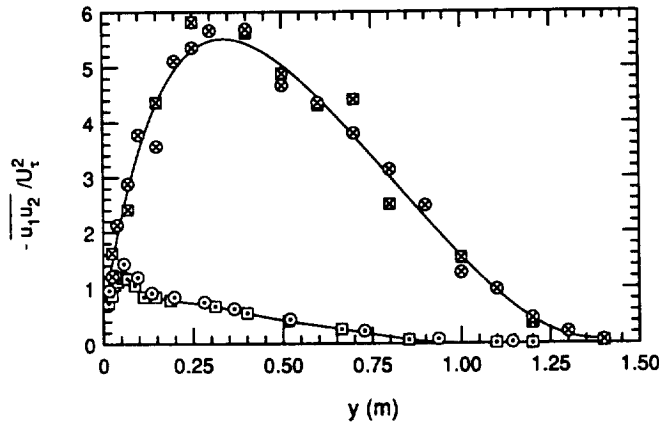


FIGURE 4. Scaling of the Reynolds shear-stress profiles (Fig. 3d) using U_τ as velocity scale. For key to symbols see Fig. 2.

Compensated spectra can be defined as $\varepsilon^{-2/3} k_1^{5/3} E_{\alpha\alpha}(k_1)$, where $\alpha = 1, 2$ or 3 (no summation over α). In the inertial subrange, these should be independent of wavenumber and equal to the Kolmogorov's constants for one-dimensional spectra.

In Fig. 5 the compensated longitudinal spectra at the four y -positions are plotted against $k_1\eta$. The compensated ninth-order, least-square log-log polynomial fits of $E_{11}(k_1)$ are also presented in this figure. Here the dissipation value at each measurement location was obtained from the isotropic relation $\varepsilon = 15\nu \int_0^\infty k_1^2 E_{11}(k_1) dk_1$ (e.g. Batchelor 1953). (For details see our previous reports.) As can be seen in this figure, the u_1 -spectra (single wire) at all the measurement locations have $-5/3$ ranges and the Kolmogorov constant $C = 1.5$ (i.e. $C_1 = 18C/55 = 0.491$) (Monin & Yaglom 1975; Saddoughi & Veeravalli 1994) agrees reasonably well with the present data.

The compensated u_2 - and u_3 -spectra are presented in Figs. 6 and 7 respectively. These two figures illustrate several points. (i) They show that the extent of $-5/3$ range of the transverse spectra reduces when the wall is approached. This is similar to the behavior of the spectra for the zero-pressure-gradient boundary layer. (ii) At the inner-layer position, isotropy is satisfied and the densities of the transverse spectra in the inertial subrange are equal to $4/3$ times that of the u_1 -spectrum. However, when the outer part of the boundary layer is approached, there is an increased deviation from isotropic behavior. (iii) All the compensated spectra at the outer-layer position ($y = 700$ mm) have a new "bump" between the large-scale range and the inertial subrange. (iv) At all the measurement positions, to within the accuracy of measurement, the u_3 - and u_2 -spectra are equal to each other in the inertial subrange and dissipation range. This is further illustrated in Fig. 8, where the ratio of the measured u_3 -spectrum to u_2 -spectrum, $E_{33}^{meas}(k_1)/E_{22}^{meas}(k_1)$, at each y location is plotted against $k_1\eta$.

All of the above measurements were repeated by taking data on different days with different hot-wire elements having different calibrations and using different anemometers. Also, the u_1 -spectra obtained by X -wires in x - y and x - z planes

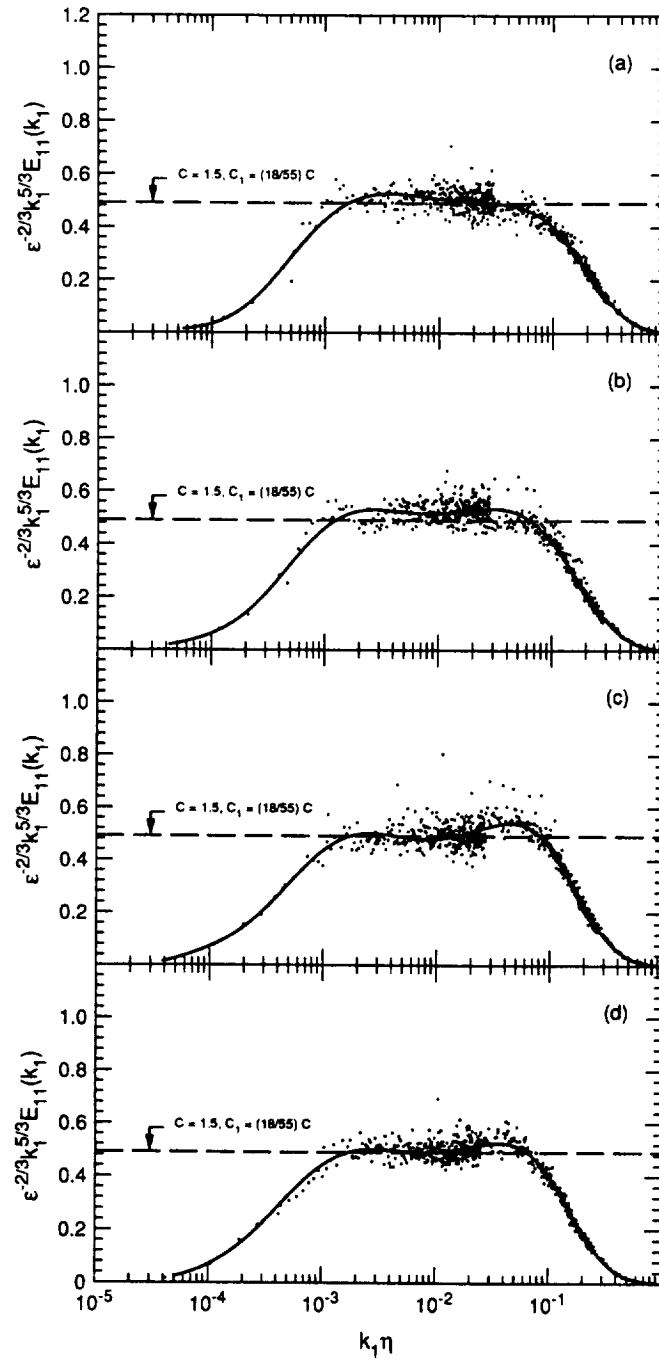


FIGURE 5. Compensated u_1 -spectra measured at different locations in the large extra-strain-rate boundary layer at low Reynolds number. Solid lines are the ninth-order, least-square, log-log polynomial fits to the spectral data. (a) $y = 700$ mm (outer-layer), $R_\lambda \approx 650$; (b) $y = 500$ mm (around mid-layer), $R_\lambda \approx 820$; (c) $y = 300$ mm (maximum shear stress), $R_\lambda \approx 800$; (d) $y = 100$ mm (inner-layer), $R_\lambda \approx 830$.

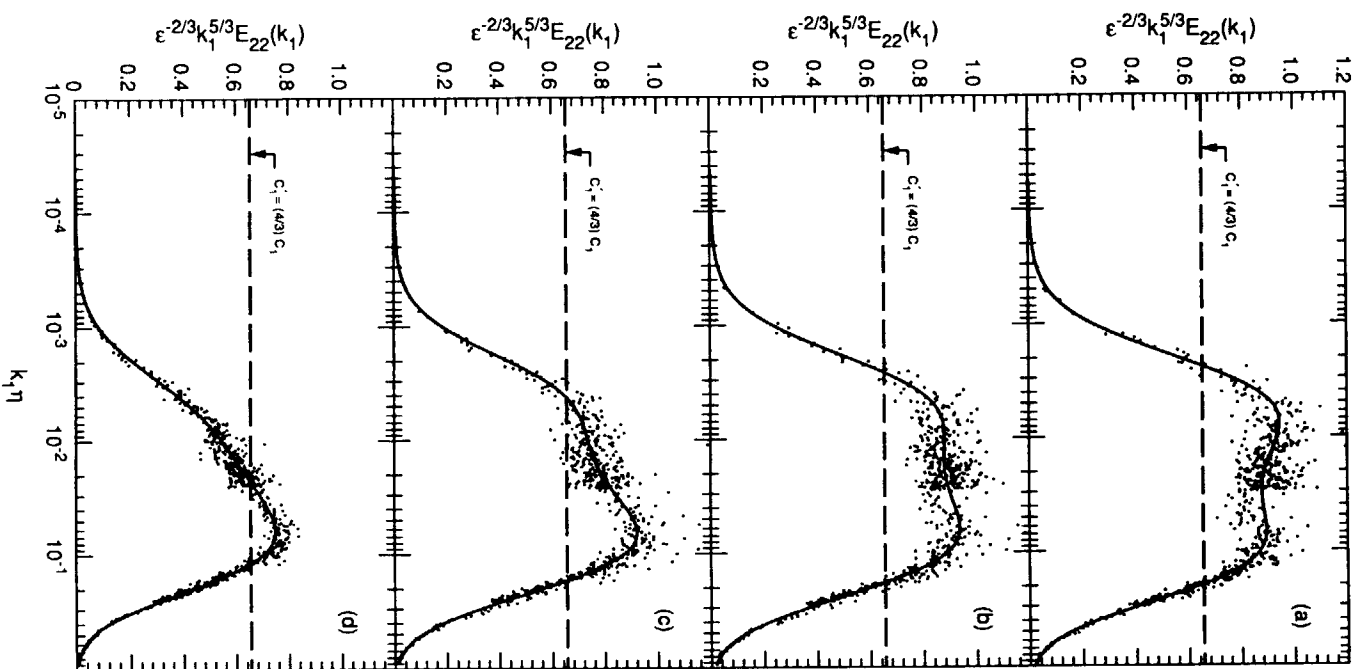


FIGURE 6. Compensated u_2 -spectra measured at different locations in the large extra-strain-rate boundary layer at low Reynolds number. Solid lines are the ninth-order, least-square, log-log polynomial fits to the spectral data. For key to captions for (a)-(d) see Fig. 5.

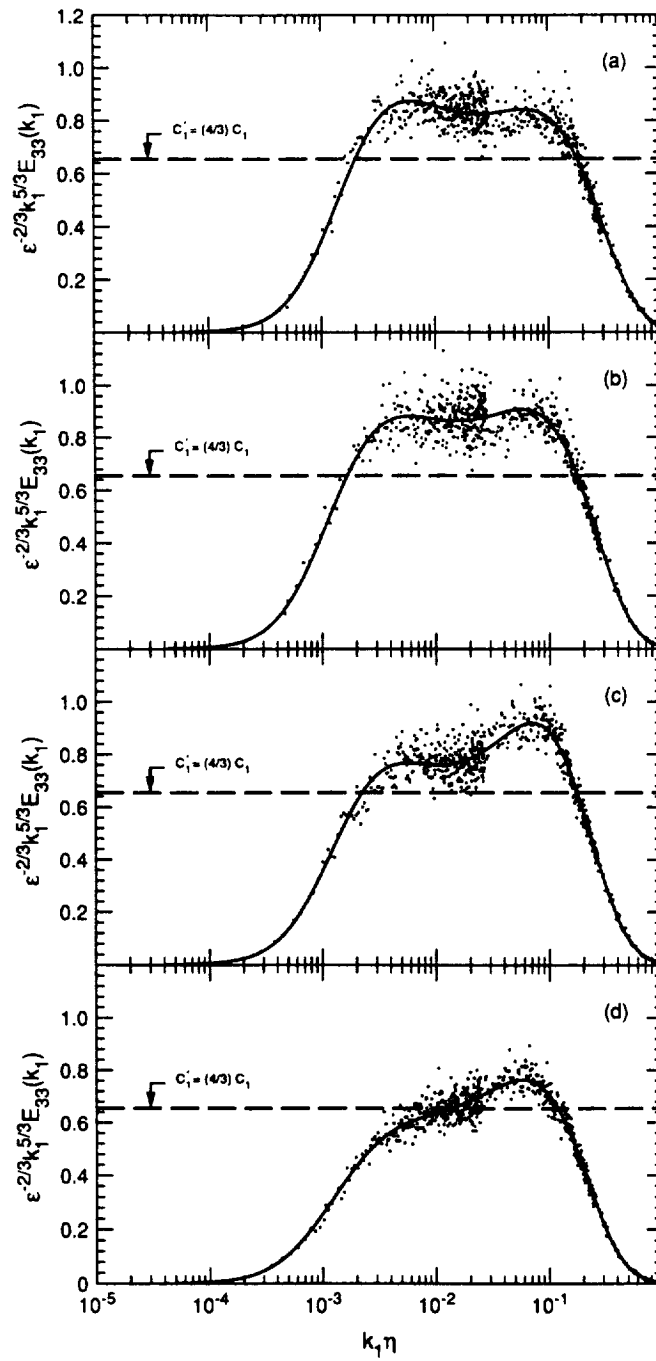


FIGURE 7. Compensated u_3 -spectra measured at different locations in the large extra-strain-rate boundary layer at low Reynolds number. Solid lines are the ninth-order, least-square, log-log polynomial fits to the spectral data. For key to captions for (a)-(d) see Fig. 5.

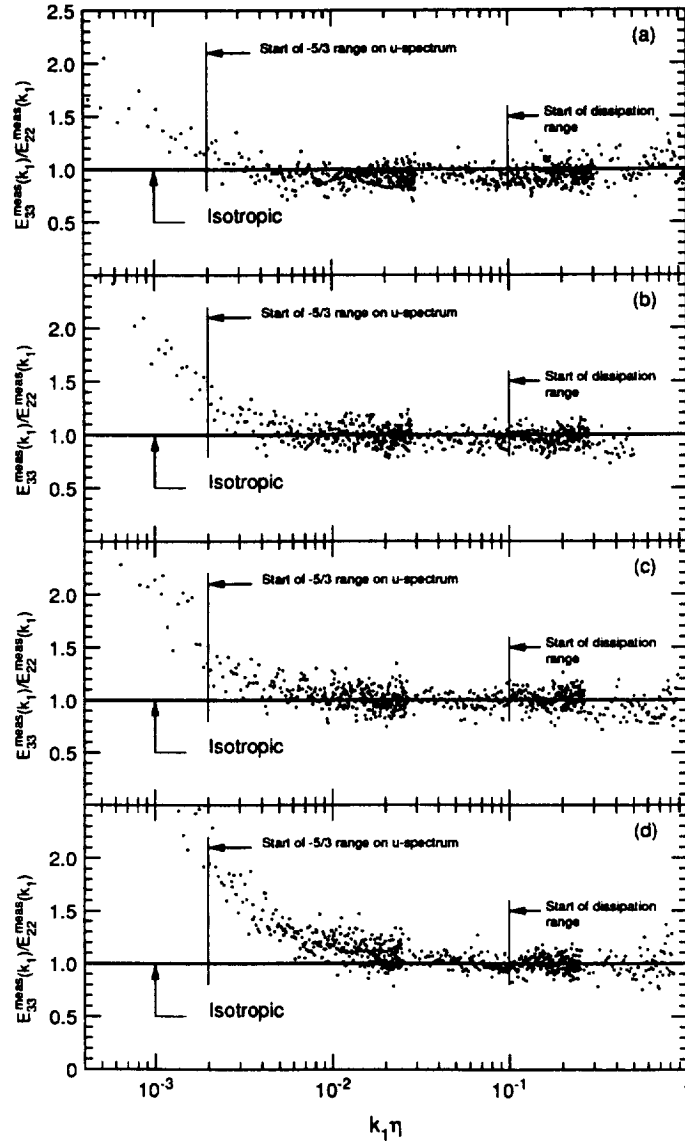


FIGURE 8. Ratios of the measured u_3 -spectra to u_2 -spectra at different locations in the large extra-strain-rate boundary layer at low Reynolds number. For key to captions for (a)-(d) see Fig. 5.

compared well with the spectra measured by single wires (shown in Fig. 5).

If the motion is isotropic, the transverse spectra $E_{22}(k_1)$ and $E_{33}(k_1)$ are uniquely determined by the longitudinal spectrum $E_{11}(k_1)$ (e.g. Batchelor 1953): $E_{22}(k_1) = E_{33}(k_1) = \frac{1}{2}(1 - k_1 \frac{\partial}{\partial k_1})E_{11}(k_1)$. The transverse spectra, $E_{22}^{calc}(k_1)$ and $E_{33}^{calc}(k_1)$, can be calculated from the measured longitudinal spectrum, $E_{11}^{meas}(k_1)$, using the above equation. An anisotropy measure may be defined as $E_{\alpha\alpha}^{calc}(k_1)/E_{\alpha\alpha}^{meas}(k_1)$, where $\alpha = 2$ or 3 corresponds to u_2 or u_3 respectively. These anisotropy measures

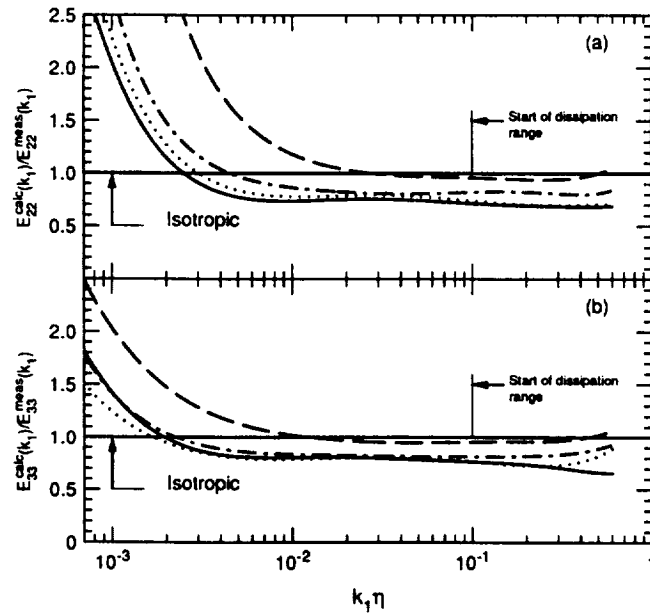


FIGURE 9. Ratios of the calculated to measured transverse spectra at different locations in the large extra-strain-rate boundary layer at low Reynolds number. (a) u_2 -ratio; (b) u_3 -ratio. —, $y = 700$ mm (outer-layer), $R_\lambda \approx 650$; ·····, $y = 500$ mm (around mid-layer), $R_\lambda \approx 820$; - - -, $y = 300$ mm (maximum shear stress), $R_\lambda \approx 800$; ----, $y = 100$ mm (inner-layer), $R_\lambda \approx 830$.

should be equal to 1.0 in an isotropic flow. We have used the least-squares fit data in Figs. 5, 6, and 7 to calculate these measures, which are plotted against $k_1\eta$ in Fig. 9. These measures clearly show that, as expected from our earlier observations of the compensated spectra, at the inner-layer position, isotropy is satisfied, and when the outer part of the boundary layer is approached, the transverse spectra deviate from the local-isotropy predictions.

We showed (Saddoughi 1993b) that our small-scale measurements in the highly-distorted boundary layer at high Reynolds number followed the local-isotropy predictions. For the same flow at low Reynolds number, isotropy is satisfied in the inner-layer position; however, it appears that in the outer parts of the boundary layer, the small-scale behavior is better described by local-axisymmetry assumption about the streamwise direction (Batchelor 1946) since the measured transverse spectra are equal to each other and they deviate from the isotropy predictions.

The correlation-coefficient spectra, $R_{12}(k_1) \equiv -E_{12}(k_1)/\sqrt{E_{11}(k_1)E_{22}(k_1)}$, are plotted in Fig. 10. In isotropic flow the shear-stress cospectrum, $E_{12}(k_1)$, which satisfies $\int_0^\infty E_{12}(k_1) dk_1 = -\overline{u_1 u_2}$, is equal to zero. This indicates that the correlation coefficient spectrum should fall to zero at high wavenumbers. This condition should also be satisfied for a locally-axisymmetric flow. As can be seen in Fig. 10, for all the measurement positions in this boundary layer the $R_{12}(k_1)$ spectra drop to zero at high wavenumbers, but as noted before (Saddoughi & Veeravalli 1994),

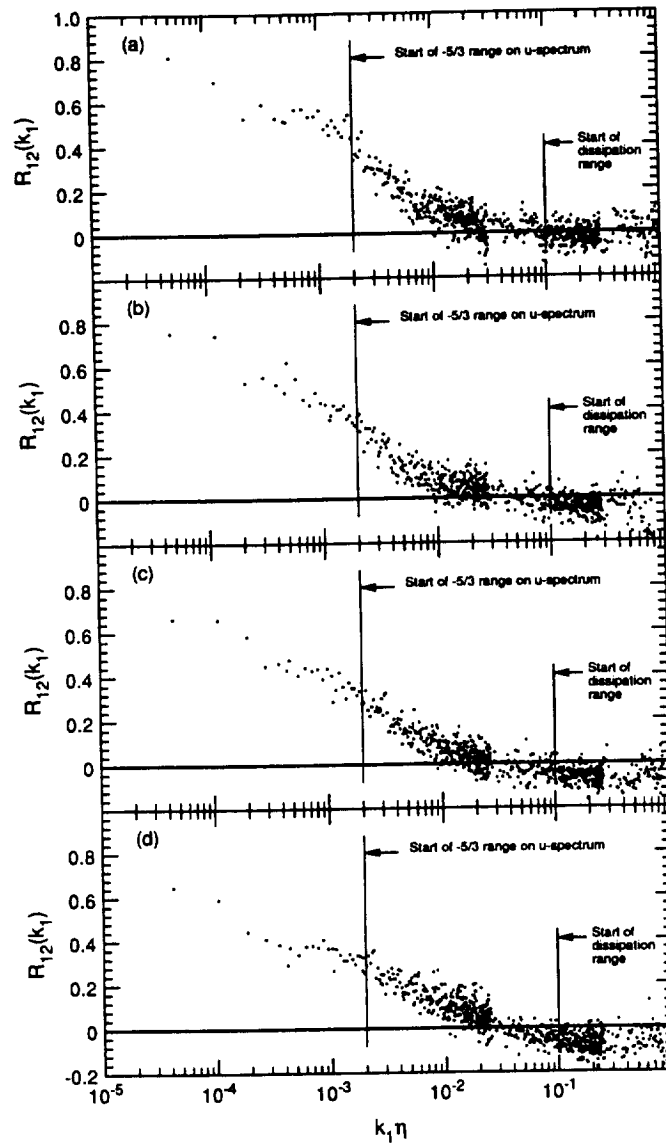


FIGURE 10. Correlation-coefficient spectra obtained at different locations in the large extra-strain-rate boundary layer at low Reynolds number. For key to captions for (a)-(d) see Fig. 5.

both positive and negative values are inferred from the measurements in the high-wavenumber ranges for all the measurement stations. However, in the dissipation ranges of the present case at the measurement locations close to the wall, average values of $R_{12}(k_1)$ appear to be slightly negative. Based on their model for Taylor-hypothesis correction, Wyngaard & Clifford (1977) suggested that the convection velocity fluctuations could alias enough spectral content into the measured cospectrum to make it appear to change sign at large k_1 . At the inner-layer station where

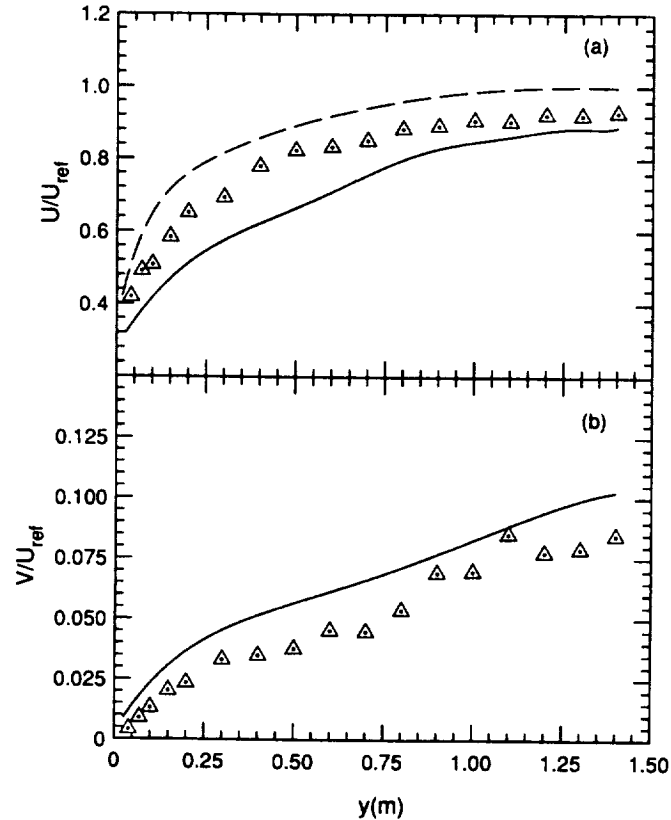


FIGURE 11. Normalized mean-velocity profiles for different boundary layers. (a) U/U_{ref} ; (b) V/U_{ref} . ----, plane boundary layer at low and high Reynolds numbers; —, large extra-strain-rate (with F-18) boundary layer at low and high Reynolds numbers; \triangle , small extra-strain-rate (without F-18) boundary layer at low Reynolds number.

the local turbulence intensity for the current experiment is approximately 0.2, the errors arising from the use of Taylor's hypothesis can be large in the dissipation range, and the present data appear to follow the trend suggested by Wyngaard & Clifford (1977).

2.3 Distorted boundary layers: Small extra-strain-rate experiments

In order to isolate the reasons for the deviations of the transverse spectra from the local-isotropy predictions in the outer parts of the distorted boundary layer at low Reynolds number, we repeated our measurements in front of the cylinder after the F-18 aircraft was removed from the $80' \times 120'$ wind tunnel.

The normalized profiles of the longitudinal mean velocity, U/U_{ref} , and the vertical velocity component, V/U_{ref} , for this case measured at low Reynolds number, are compared with the profiles obtained for the plane boundary layer and the large extra-strain-rate case (with F-18) in Fig. 11. It is clear that the removal of the F-18 from the wind tunnel reduces the magnitudes of the extra mean strain rates in

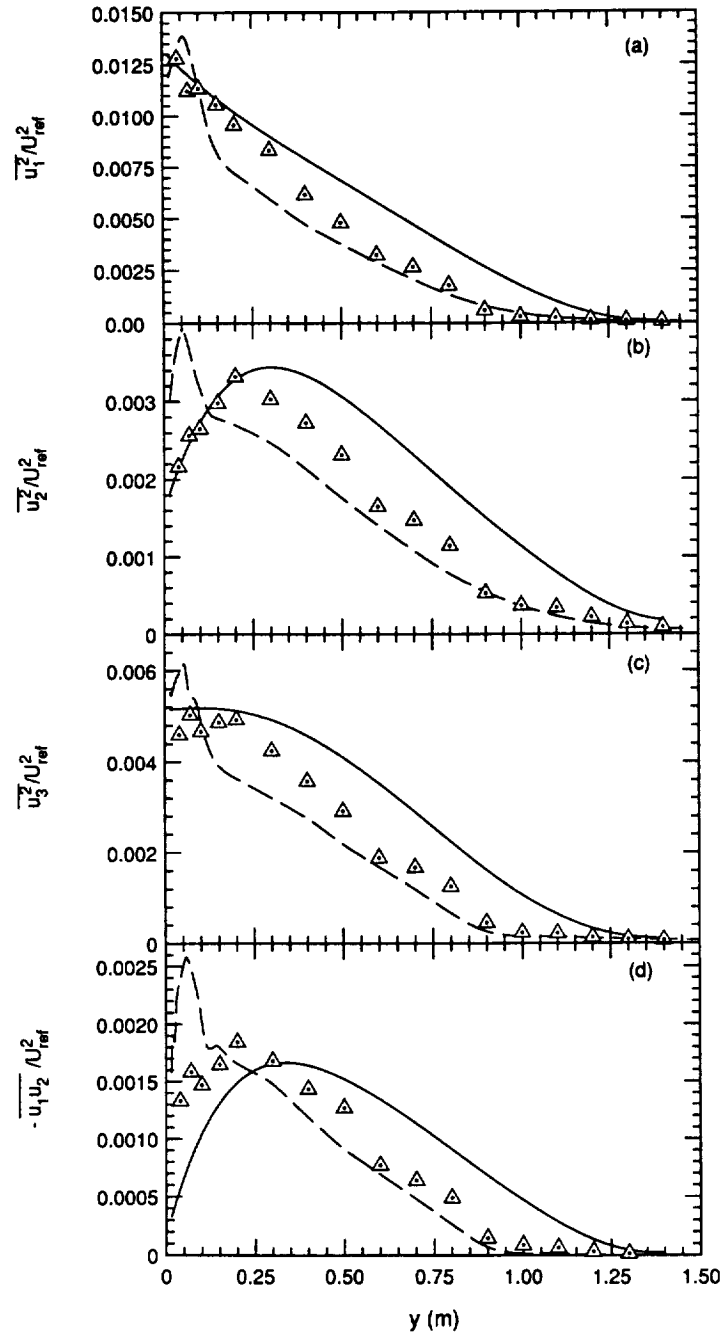


FIGURE 12. Normalized profiles of Reynolds stresses for different boundary layers. (a) $\overline{u_1^2}/U_{ref}^2$, (b) $\overline{u_2^2}/U_{ref}^2$, (c) $\overline{u_3^2}/U_{ref}^2$, (d) $-\overline{u_1 u_2}/U_{ref}^2$. For key to symbols see Fig. 11.

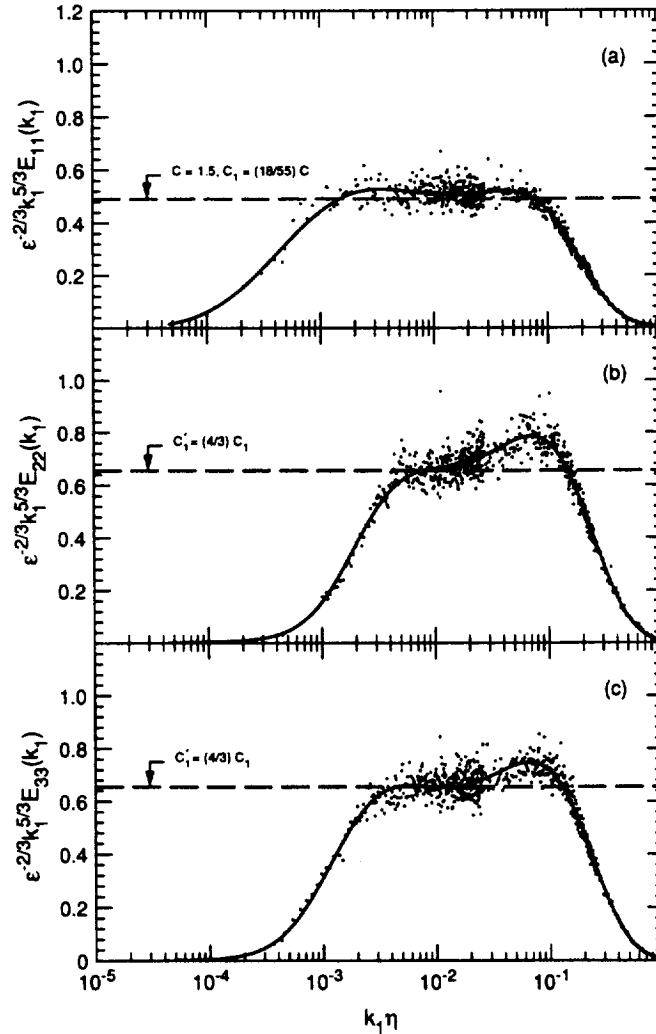


FIGURE 13. Compensated longitudinal and transverse spectra measured at $y = 300$ mm in the small extra-strain-rate boundary layer at low Reynolds number ($R_\lambda \approx 790$). Solid lines are the ninth-order, least-square, log-log polynomial fits to the spectral data. (a) u_1 -spectrum; (b) u_2 -spectrum; (c) u_3 -spectrum.

front of the cylinder. This reduction can be seen also on the profiles of the Reynolds stresses, shown in Fig. 12.

2.3.2 Analysis of small-scale data: low-Reynolds-number case

The compensated spectra of the three components of the velocity taken at $y = 300$ mm, 500 mm, and 700 mm for the low-Reynolds-number case are shown in Figs. 13, 14, and 15 respectively. Recall from Figs. 6 and 7 that the deviations from the

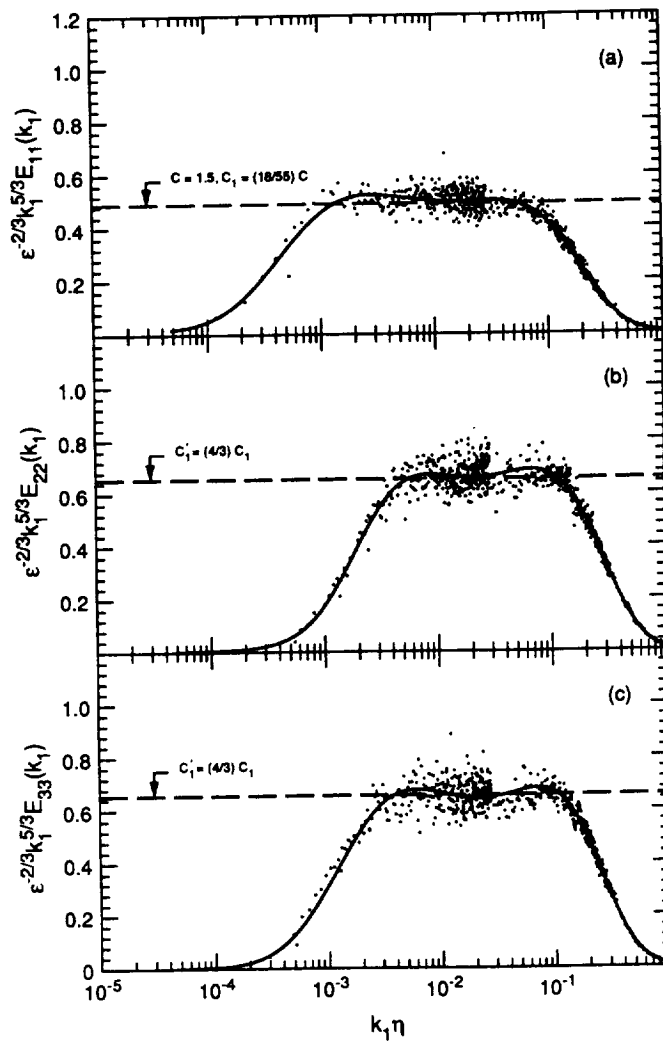


FIGURE 14. Compensated longitudinal and transverse spectra measured at $y = 500$ mm in the small extra-strain-rate boundary layer at low Reynolds number ($R_\lambda \approx 760$). Solid lines are the ninth-order, least-square, log-log polynomial fits to the spectral data. (a) u_1 -spectrum; (b) u_2 -spectrum; (c) u_3 -spectrum.

small-scale isotropy took place only at these three y locations. However, for the present case, without the presence of the F-18, the transverse spectra at all the measurement stations follow the local-isotropy predictions: i.e. at each station the transverse spectra are equal to each other and are larger than the u_1 -spectrum by the 4/3 factor.

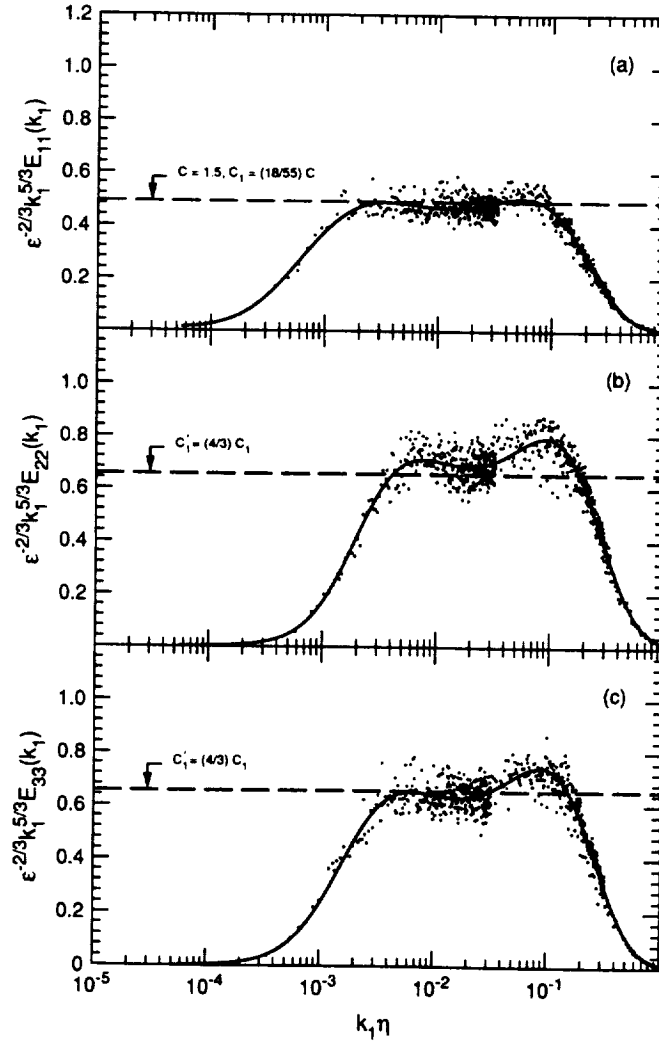


FIGURE 15. Compensated longitudinal and transverse spectra measured at $y = 700$ mm in the small extra-strain-rate boundary layer at low Reynolds number ($R_\lambda \approx 560$). Solid lines are the ninth-order, least-square, log-log polynomial fits to the spectral data. (a) u_1 -spectrum; (b) u_2 -spectrum; (c) u_3 -spectrum.

3. Closure

Further analysis of all the data taken in distorted boundary layers at high and low Reynolds numbers is in progress. However, our complex-flow experiments (see also Saddoughi 1993b) have again highlighted an important fact: as long as the high-Reynolds-number requirement – which is an intrinsic part of the local-isotropy hypothesis – is satisfied, the small-scale structures of turbulent motions become independent of large-scale structures and the mean deformation rate (Kolmogorov 1941).

Acknowledgments

We wish to thank Drs. Fredric Schmitz, James Ross, Wendy Lanser, Gavin Botha, Paul Askins, and Pet Zell of the Full-Scale Aerodynamics Research Division at NASA Ames for their kind cooperation during the experiments.

We wish to thank Professors Bill Reynolds, Parviz Moin, Peter Bradshaw, Bob Rogallo, Javier Jimenez, and Bill George for many valuable discussions of our results.

I am grateful to my wife, Elizabeth, who helped me with the measurements.

REFERENCES

- BATCHELOR, G. K. 1946 The theory of axisymmetric turbulence. *Proc R. Soc. Lond.* **A186**, 480-502.
- BATCHELOR, G. K. 1953 *The Theory of Homogeneous Turbulence*. Cambridge University Press.
- BRADSHAW, P. 1967 The turbulence structure of equilibrium boundary layers. *J. Fluid Mech.* **29**, 625-645.
- BRADSHAW, P. 1973 Effects of streamline curvature on turbulent flow. *AGARDograph* **169**.
- CORRSIN, S. 1958 On local isotropy in turbulent shear flow. *Report NACA R & M 58B11*.
- KOLMOGOROV, A. N. 1941 The local structure of turbulence in incompressible viscous fluid for very large Reynolds numbers. *C. R. Acad. Sci. U.R.S.S.* **30**, 301.
- LUMLEY, J. L. 1967 Similarity and the turbulent energy spectrum. *Phys. Fluids.* **10**, 855-858.
- MONIN, A. S. & YAGLOM, A. M. 1975 *Statistical Fluid Mechanics, vol. 2*. M.I.T. Press.
- SADDOUGHI, S. G. 1993a Local isotropy in high Reynolds number turbulent shear flows. *Annual Research Briefs-1992*, Center for Turbulence Research, Stanford University/NASA Ames. 237-262.
- SADDOUGHI, S. G. 1993b Local isotropy in distorted turbulent boundary layers at high Reynolds number. *Annual Research Briefs-1993*, Center for Turbulence Research, Stanford University/NASA Ames. 347-363.
- SADDOUGHI, S. G. & JOUBERT, P. N. 1991 Lateral straining of turbulent boundary layers. Part 1. Streamline divergence. *J. Fluid Mech.* **229**, 173-204.
- SADDOUGHI, S. G. & VEERAVALLI, S. V. 1994 Local isotropy in turbulent boundary layers at high Reynolds number. *J. Fluid Mech.* **268**, 333-372.
- UBEROI, M. S. 1957 Equipartition of energy and local isotropy in turbulent flows. *J. Appl. Phys.* **28**, 1165-1170.
- WYNGAARD, J. C. & CLIFFORD, S. F. 1977 Taylor's hypothesis and high-frequency turbulence spectra. *J. Atmos. Sci.* **34**, 922-929.

Transverse vorticity measurements in the NASA Ames 80x120 wind tunnel boundary layer

By J. F. Foss¹, D. G. Bohl¹, F. D. Bramkamp², AND J. G. Klewicki³

1. Motivation and objectives

The MSU compact four-wire transverse vorticity probe, see Fig. 1, permits $\omega_z(t)$ measurements in a nominally 1mm² domain. Note that a conventional coordinate system is used with x and y in the streamwise and normal directions respectively. The algorithms to extract $\omega(t)$ from the four simultaneously sampled voltages and the relevant uncertainty considerations are reported by Foss and Haw (1990). Typical results, from earlier studies can be found in Haw, *et al.* (1989), Bruns, *et al.* (1991) and Foss (1994).

The purpose of this investigation was to acquire time series data – in the same access port at the ceiling of the 80 ft x 120 ft wind tunnel (NASA Ames Research Center) as earlier used by the Wallace group from the University of Maryland – and to compare the present results with those of the three-component vorticity probe used in that earlier study. See Wallace, *et al.* (1992) and Wallace and Ong (1995) for this earlier investigation. Note that both these earlier and the present off-centerline results can also be compared with the centerline (at the same streamwise location) measurements reported by Saddoughi and Veeravalli (1994).

The technical objectives of the latter investigation, which were definitively achieved, were to examine the degrees to which local isotropy conditions describe the large turbulent Reynolds number ($R_\lambda = \bar{u}\lambda/\nu = 500$ and 600 at $y = 100$ and 515 mm from the wall respectively) conditions of this turbulent boundary layer. Their investigation provides an excellent framework for the evaluation of the data sets from the two complementary (and much briefer) studies.

The University of Maryland probe has a sample domain of approximately 1.5 mm diameter in the plane normal to the stream and a length characterized by the convected frame derivative evaluation (approximately 1 mm). Given these dimensions and given the approximately 1 mm² dimension for the MSU probe, it is advantageous to make measurements in as large a flow as possible. Hence the nominal boundary layer thickness of 1 m (at the NASA Ames tunnel) presented a most attractive measurement environment for these two research groups. Both sets of measurements were executed at $U_\infty = 10$ m/s.

From Saddoughi and Veeravalli (1994) the Kolmogorov microscales at 100 and 515 mm from the wall can be estimated for $U_\infty = 10$ m/s; viz., $\eta_k = 0.18$ mm ($y = 100$ mm) = 0.32 mm ($y = 515$ mm).

1 Michigan State University

2 RWTH, Aachen, Michigan State University

3 University of Utah

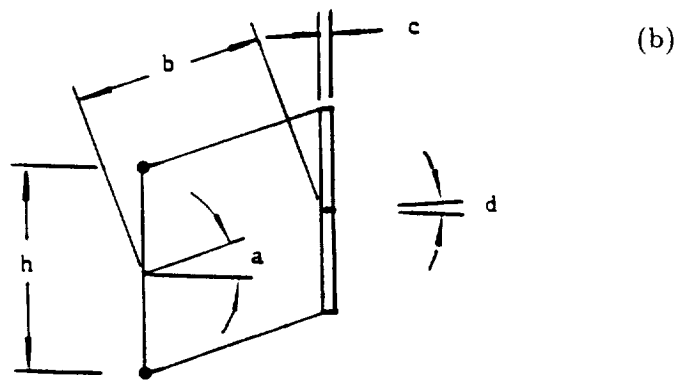
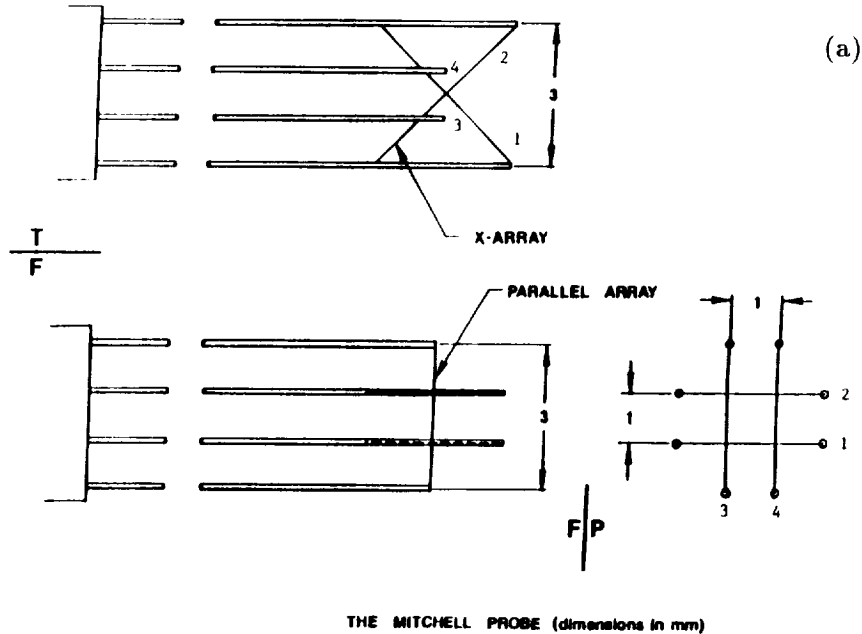


FIGURE 1. The MSU compact vorticity probe. a). Probe geometry; b) A schematic representation of the micro circulation domain. h = separation between parallel probes; a = average pitch angle associated with the time steps to reduce the connected length (b); d, c = angle and length (as above) for the next time step in the time series.

The latter permits the probe scale of 1 mm to satisfy the Wyngaard (1963) criterion of $h/\eta \approx 3$ to fully resolve the vorticity.

2. Accomplishments

The data processing for these experiments is in progress. Sufficient results are in hand to ensure a body of viable data (i.e., the pre- and post-calibrations show quite satisfactory agreement); however, no flow field results will be included in this

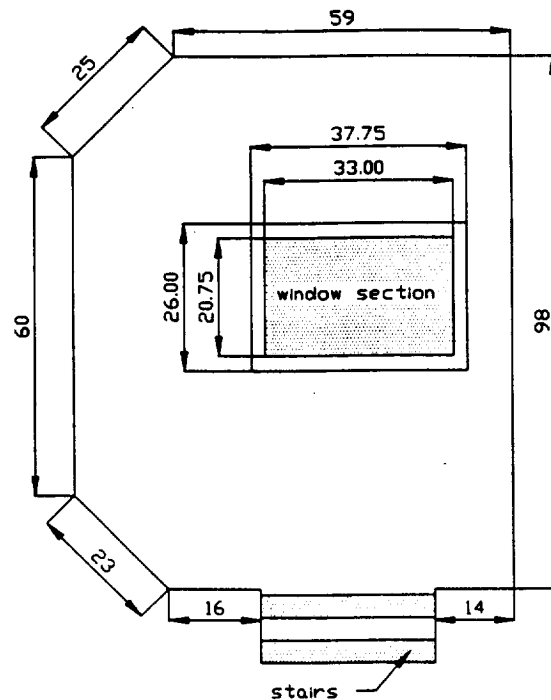


FIGURE 2. Work area-access port at the ceiling of the 80 ft×120 ft NASA Ames Wind Tunnel. All dimensions in inches.

report. It is anticipated that a full reporting of the velocity and transverse vorticity values will be available for the 1995 CTR Annual Research Briefs.

2.1 The experimental apparatus

The present co-author, F. Bramkamp, prepared his second Studienarbeit (see Bramkamp (1994)) on the basis of the design, implementation, and initial results evaluation for this project. The traverse system designed by him will be briefly noted herein.

There is a twofold significance of our reporting on this traverse device: i) the components are in storage at MSU; their loan can be arranged should they be useful to a subsequent investigator, and ii) the Bramkamp design is known to meet the strict safety requirements of the NASA test engineers and these specifications are detailed in his thesis.

Fig. 2 presents the work area for the access port at approximately 50 m from the end of the contraction; this site is at the 1/4 width location to the left (looking streamwise) of the tunnel centerline. Fig. 3 shows the traverse system that was fabricated for these measurements. A “trap door”, labeled 19a, b in Fig. 3, was opened to pass the probe holder assembly (17, 18) through the plane of the tunnel ceiling. The actual probe holder (18) was removed and the probe was attached to the portable traverse rig to accomplish the pitch-angle flow-speed calibration map (see Section 2.2).

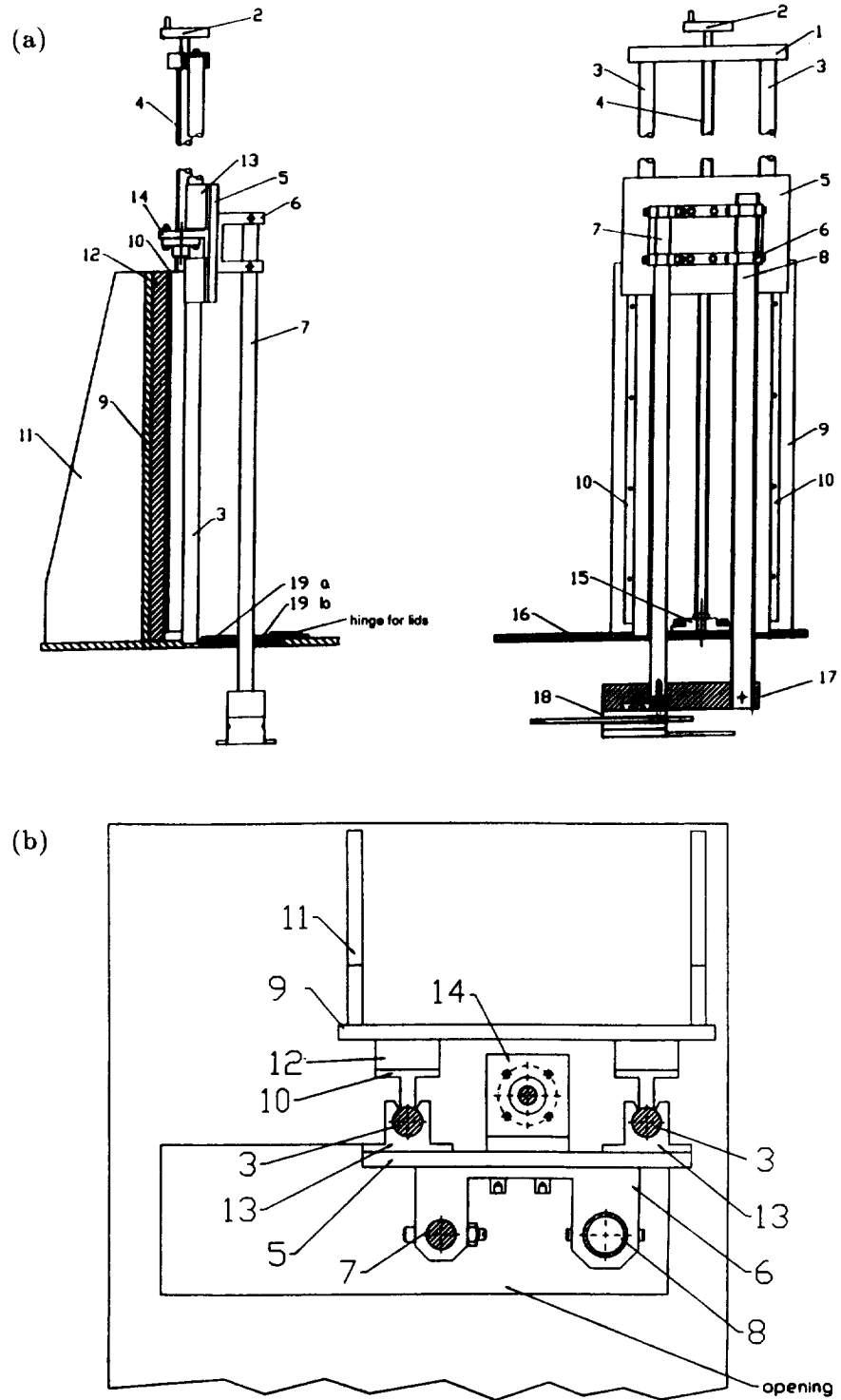


FIGURE 3. Traverse system. a) Elevation views; b) Top view.

Data time series from $y \approx 100$ mm to nearly the full extent (1.3 m) of the traverse system were acquired with this device. The top view (Fig. 3b), shows the open tube (8) that was used for the probe (hot-wire and thermistor) cables.

A portable calibration tunnel, with provision for orienting the probe at $\pm 36^\circ$ in pitch and providing a 2 to 12 m/s flow-speed range, was used before and after each approximately two-hour data session.

2.2 Calibration data

The pre- and post-calibration data sets have been subjected to comparative analysis by: i) fitting the form

$$E^2(Q, \gamma) = A(\gamma) + B(\gamma)Q^{n(\gamma)} \quad (1)$$

to each pitch angle (γ), and ii) comparing the separate calibrations to the A, B, n values of the combined calibration data set.

The first evaluation (i) is to ensure (by a sufficiently small standard deviation between measured and computed velocities) that the individual calibrations have integrity. The second evaluation (ii) is to ensure that any drift in the voltage-velocity transfer function for each wire was sufficiently small during the time period required for the measurements.

The single wire probe data at $y = 100, 112.6, 87.4$ mm and $y = 515, 549, 481$ mm were used to evaluate ϵ and η from the integral of $k^2, E(k)$. Specifically, the averaged coefficients in (1) agreed with the respective calibrations to within $\pm 0.3\%$.

The parallel array and one of the slant wires of the transverse vorticity probe showed quite satisfactory agreement using these criteria for the above y locations plus a second data session that provided data at $y = 100, 300, 515, \text{ and } 900$ mm from the wall.

If the pitch angles of the flow exhibit a sufficiently small range approximately $\pm 15^\circ$, then the single slant wire can adequately resolve the magnitude and direction of the velocity for the “three-wire” probe. Fortunately, preliminary data processing suggests that this situation is obtained.

2.3 Flow field data

Twelve time series data sets (E_1, E_2, E_3, E_4) were acquired at a rate of 30 kHz and for a time period of 13 seconds at the $y = 100 \pm 0, 12.6$ m locations. Eight data sets (same conditions) were acquired at $y = 515, \pm 0, 34$ mm before the tunnel was “shut down”. Note that the $\pm y$ positions are to provide an unambiguous value for the time mean vorticity; namely, $\bar{\omega}_z$.

The second acquisition session provided 85 data sets at each of the y locations (0.9 to 0.1 m) using a 30 kHz sample rate and a duration of 16.6 seconds per set.

3. Future plans

The flow field data will be processed using the viable calibration data. Direct comparisons with the results of Saddoughi and Veeravalli (1994) and with Wallace, *et al.* (1992) will then be made. The “activity intermittency”, introduced by Haw,

et al. (1989) will be used to interrogate the outer region signals. Comparisons with the intermittency data from the large two-stream shear layer at the University of Houston (using the same probe) will be of particular interest. See Foss, *et al.* (1994) for a brief indication of the latter.

The vorticity-vorticity correlation functions will be of particular interest at the minimum y position in the boundary layer. These correlations, in the large Re_θ condition of the one- and two-stream shear layers, show pronounced small- and large-scale effects. Specifically, the correlation function drops sharply for small displacements but retains significant values for unexpectedly large displacements. These free shear layer considerations have been identified by Foss, *et al.* (1993) and Foss (1994).

REFERENCES

- BRAMKAMP, F. D. 1994 The Design, Testing and Utilization of Wind Tunnel Measurement Equipment and Calibration Software. A Studienarbeit for the Aerodynamics Institute, RWTH Aachen, Executed at Michigan State Univ.
- BRUNS, J. M., HAW, R. C., & FOSS, J. F. 1991 The Velocity and Transverse Vorticity Fields in a Single Stream Shear Layer. Proc. Eighth Turbulent Shear Flows Conference, 3-1-1 to 3-1-6.
- FOSS, J. F. 1994 Vorticity Considerations and Planar Shear Layers. *Experimental Thermal and Fluid Sciences*. **8**, 260-270.
- FOSS, J. F., BOHL, D.G., & KLEIS, S. J. 1993 Vorticity-Vorticity Correlation Functions in a Two-Stream Mixing Layer. *Bull Am Phys Soc*. **38**.
- FOSS, J. F., & HAW, R. C. 1990 Transverse Vorticity Measurements Using a Compact Array of Four Sensors. *The Heuristics of Thermal Anemometry*. **97**, 71-76.
- HAW, R. C., FOSS, J. K., & FOSS, J. F. 1989 Vorticity Based Intermittency Measurements in a Single Stream Shear Layer. Proc. Second European Turb. Conf. Advances in Turbulence 2.
- SADDOUGHI, S. G., & VEERAVALLI, S. V. 1994 Local Isotropy in Turbulent Boundary Layers at High Reynolds Number. *J. Fluid Mech*. **268**, 333-372.
- WALLACE, J., & ONG, L. (In press) Local isotropy of the vorticity field in a boundary layer at high Reynolds number. Proc. of the 5th European Turbulence Conf.
- WALLACE, J., ONG, L., & BALINT, J.-L. 1992 An Investigation of small scale of turbulence in a boundary layer at high Reynolds number. *Annual Research Briefs 1992*. NASA Ames/Stanford University, 263-268.
- WYNGAARD, J. C. 1969 Spatial Resolution of the Vorticity Meter and Other Hot-Wire Arrays. *J. Sci. Instr. (J. Phys. E.)*, **2**, 983-87.

Experimental and numerical study of the intermittency exponent μ

By Alexander Praskovsky¹

1. Motivation, background, and objectives

After publication of the Kolmogorov (1962) refined similarity hypotheses, the small-scale intermittency of the energy dissipation field became a central problem in fully developed turbulence (FDT). This phenomena has been studied in many different ways, e.g. by searching for corrections to scaling exponents in the inertial range velocity structure functions (see reviews in Monin & Yaglom 1975, Kuznetsov & Sabelnikov 1990). A direct measure of this intermittency is, however, available by studying the local rate of energy dissipation, and it may be quantitatively characterized by the intermittency exponent μ (Nelkin 1981).

The first description of the intermittent field was proposed by Kolmogorov (1962), who introduced the energy dissipation ε_r averaged over a segment r :

$$\varepsilon_r(x) = \frac{1}{r} \int_0^r \varepsilon(x + \chi) d\chi, \quad (1)$$

where x is the longitudinal coordinate, and the local value of the energy dissipation $\varepsilon(x)$ is defined in the standard way as

$$\varepsilon(x) = \frac{\nu}{2} \left(\frac{\partial u_i}{\partial x_j} + \frac{\partial u_j}{\partial x_i} \right)^2, \quad (2)$$

where ν is the kinematic viscosity, and u_i , $i = 1, 2, 3$, denote the velocity components in the directions x_i . To analyze experimental data and compare them with numerical modeling, the one-dimensional sections of the energy dissipation field in the $x \equiv x_1$ direction will be considered throughout this paper.

It was assumed by Kolmogorov that ε_r has the normal probability density distribution (pdd) if r belongs to the inertial range, i.e., $\eta \ll r \ll L$ where L and η denote the integral and Kolmogorov viscous scales, respectively. This assumption is known as the log-normal model. Kolmogorov further assumed that the variation of $\ln \varepsilon_r$ obeys a logarithmic scaling

$$\sigma_{\ln \varepsilon_r}^2 = A + \mu_k \ln(L/r), \quad \eta \ll r \ll L, \quad (3)$$

where A is some function of the local flow conditions, and μ_k is the intermittency exponent which was assumed to be a universal constant (if there is no intermittency,

¹ National Center for Atmospheric Research, Boulder, Colorado 80307-3000

$\mu_k \equiv 0$). Different subscripts to μ are adopted to identify different definitions of the intermittency exponent.

Novikov & Stewart (1964) showed that

$$\langle \varepsilon_r^2(x) \rangle \propto r^{-\mu_r}, \quad \eta \ll r \ll L. \quad (4)$$

Hereafter the angular brackets denote average over x . Novikov (1990) demonstrated that under some weak assumptions $\mu_k = \mu_\varepsilon$.

It was also found (Monin & Yaglom 1975) that the correlation function of energy dissipation $R_\varepsilon(r)$ obeys the power-law scaling at separations r within the inertial range

$$R_\varepsilon(r) \equiv \langle \varepsilon(x) \varepsilon(x+r) \rangle = C_\varepsilon \langle \varepsilon \rangle^2 (r/L)^{-\mu_r}, \quad \eta \ll r \ll L, \quad (5)$$

where C_ε is assumed to be a universal constant, and $\mu_r = \mu_\varepsilon$.

Monin & Yaglom (1975) further assumed that at very high Reynolds numbers, where fluctuations of $\varepsilon(x)$ are much larger than $\langle \varepsilon \rangle$,

$$R_\varepsilon(r) \approx B_\varepsilon(r) \equiv \langle [\varepsilon(x) - \langle \varepsilon \rangle] [\varepsilon(x+r) - \langle \varepsilon \rangle] \rangle \propto r^{-\mu_b}, \quad \eta \ll r \ll L, \quad (6)$$

and the energy spectrum of ε (which is the Fourier transform of B_ε) should behave as

$$E_\varepsilon(k) = \frac{1}{\pi} \int_0^\infty B_\varepsilon(r) \cos(kr) dr \propto k^{-1+\mu_\varepsilon}, \quad 1/L \ll k \ll 1/\eta, \quad (7)$$

where k is the wave-number.

Relations (3)–(7) are commonly used to estimate μ . Several more methods for such an estimate are also well-known, e.g. by using the six-order velocity structure function (Monin & Yaglom 1975), the breakdown coefficients (Novikov 1990), etc. but in this brief paper only methods based on (3)–(7) are considered.

A diverse body of measurements of μ in different laboratory flows as well as in the atmosphere and ocean has been reported during the last three decades (for comprehensive review see Kuznetsov & Sabelnikov 1990, Gibson 1991, Nelkin 1994). The reported values of μ vary from 0.15 to 0.7, and this scatter certainly exceeds the measurement errors. Some theoretical considerations as well as the scatter in experimental results caused a doubt about universality of the exponent μ (e.g., Kraichnan 1974, Nelkin 1994). However, as far as we know, nobody has posed an obvious question: Is the intermittency exponent μ a **unique** constant, i.e., are the values μ_k , μ_ε , μ_r , μ_b , and μ_e the same at high Reynolds numbers, or do they create a set of different (and perhaps independent) exponents? This paper addresses the above question using the high Reynolds number experiments.

The second objective of this paper becomes clear from the following considerations. It is commonly assumed (e.g., Monin & Yaglom 1975, Nelkin 1981) that the

longitudinal component $\partial u/\partial x$ should contain most of the important dynamical information on the dissipation field. In other words, it is assumed that the exponents μ defined by Eqs. (3)–(7) would not be changed if the true local rate of energy dissipation $\varepsilon(x)$ were replaced by the one-dimensional surrogate

$$\tilde{\varepsilon}(x) = 15 \nu (\partial u/\partial x)^2. \tag{8}$$

Nelkin (1981) commented, “this rather weak assumption seems plausible, but is difficult to test experimentally”. We are not so optimistic about the “weakness” of this assumption. Indeed, it is well-known (e.g., Hosokawa and Yamamoto 1991) that pdd of $\varepsilon(x)$ and $\tilde{\varepsilon}(x)$ are qualitatively different. The second statement, namely “difficult to test experimentally”, is completely valid. In most experiments nothing more than $u(x)$ has been recorded, and in some experiments simultaneous measurements of $u(x)$ and $u_2(x)$ were executed. There are also a few experiments at low Reynolds numbers (see Tsinober *et al.* 1992, and references therein) where all terms in Eq. (2) were directly measured with multi-wire probes. However, the reliability of such measurements, especially at high Reynolds numbers, still seems to be rather questionable.

The remarkable success of direct numerical simulations (DNS) of FDT during the last decades offers another approach to such a test. In spite of well-known limitations (relatively low Reynolds numbers, somewhat arbitrary boundary conditions, etc.), DNS provides an exact solution of the Navier-Stokes equations and gives complete information on the three-dimensional flow field. Using the numerical data base, one can estimate (at least qualitatively) how adequately the true energy dissipation $\varepsilon(x)$ is represented by the one-dimensional surrogate $\tilde{\varepsilon}(x)$. To execute such a test is a second objective of this paper. This approach contradicts traditional belief that measurements give the “final truth”, and any theoretical or numerical result should be tested by comparison with experiment. We believe that numerical modeling (now fairly called numerical experiment) becomes so powerful and reliable that it can be used to test physical experiments. First results from this approach are reported in this paper.

2. Accomplishments

2.1 Experimental and numerical data bases

The experimental data base includes measurements in the atmospheric surface layer and in a large wind tunnel at very high Reynolds numbers.

The experiment in the atmospheric surface layer was executed by Dr. Steven Oncley from the National Center for Atmospheric Research (Oncley 1992). After preliminary processing, six time series were chosen from the total record (Praskovsky & Oncley 1994a). Four of these series are analyzed in the present work. The second experiment was executed in the large wind tunnel of the Central Aerohydrodynamic Institute (Moscow, Russia). Measurements have been done in the mixing layer and in the return channel of the wind tunnel (Praskovsky *et al.* 1993).

The main flow characteristics of the experimental data base are listed in Table 1 where the abbreviations ML, RC, and ASL denote the mixing layer, return channel,

and atmospheric surface layer, respectively, and numerals after ASL correspond to the sequence of the time series (in accordance with that in Praskovsky & Oncley 1994a). U is the mean longitudinal velocity, and σ_ϕ denotes the rms value of any quantity ϕ . The Taylor λ and Kolmogorov η scales, and the Reynolds number R_λ , are defined with standard formulas: $\lambda = \sigma_u / \sigma_{\partial u / \partial x}$, $\eta = (\nu^3 / \langle \varepsilon \rangle)^{1/4}$, and $R_\lambda = \sigma_u \lambda / \nu$. Other quantities in Table 1 will be defined later. Taylor's hypothesis was used to convert from temporal to spatial coordinates.

Time series	ML	RC	ASL-2	ASL-3	ASL-5	ASL-6
U , m/s	7.87	10.8	6.58	8.10	12.9	14.5
σ_u , m/s	1.67	1.03	0.693	1.10	1.82	2.08
L , m	1.3	4.8	42	51	99	77
$\langle \varepsilon \rangle$, m^2/s^3	1.90	0.115	0.0235	0.0322	0.140	0.128
λ , cm	1.8	4.6	6.5	9.0	7.0	8.3
$R_\lambda \times 10^{-3}$	2.0	3.2	3.3	6.9	9.2	12.7
η , mm	0.21	0.41	0.58	0.55	0.37	0.37
$\overline{\mu_r} \pm \sigma_{\mu_r}$	0.20±0.01	0.19±0.01	0.20±0.01	0.20±0.01	0.20±0.02	0.20±0.01
$\overline{\mu_b} \pm \sigma_{\mu_b}$	0.38±0.01	0.32±0.01	0.35±0.02	0.29±0.03	0.33±0.02	0.30±0.02
$\overline{\mu_e} \pm \sigma_{\mu_e}$	0.59±0.03	0.60±0.02	0.57±0.04	0.61±0.02	0.56±0.02	0.55±0.01
$\overline{\mu_k} \pm \sigma_{\mu_k}$	0.40±0.01	0.22±0.03	0.19±0.04	0.22±0.02	0.22±0.02	0.23±0.02
$\overline{\beta} \pm \sigma_\beta$	0.26±0.01	0.24±0.01	0.23±0.02	0.19±0.01	0.18±0.01	0.14±0.01
$\overline{\gamma_e} \pm \sigma_{\gamma_e}$	0.42±0.01	0.38±0.01	0.41±0.02	0.38±0.01	0.36±0.01	0.35±0.01

Table 1. Main turbulence characteristics of analyzed time series.

The DNS of homogeneous, isotropic, equilibrium flow fields were executed by Dr. Robert Rogallo from the NASA Ames Research Center. A description of this data base, covering a range of R_λ from 35 to 168 can be found in Jimenez *et al.* (1993). Two simulations at $R_\lambda = 94$ and 168 are analyzed in the present work.

2.2 Experimental results for $\tilde{\varepsilon}(x)$

2.2.1 Correlation functions and spectra

Two examples of the correlation functions $R_\varepsilon(r)$ and $B_\varepsilon(r)$ at the lowest and highest R_λ are presented in Fig. 1. The local values of scaling exponents are estimated using the logarithmic derivatives:

$$\mu_r(r) = -\frac{d[\lg R_\varepsilon(r)]}{d[\lg r]}, \quad \mu_b(r) = -\frac{d[\lg B_\varepsilon(r)]}{d[\lg r]}, \quad \mu_e(k) = 1 + \frac{d[\lg E_\varepsilon(k)]}{d[\lg k]}. \quad (9)$$

It follows from Eqs. (5)–(7) that μ_r , μ_b , and μ_e should be constants within the inertial range. The measured values of $\mu_r(r)$ and $\mu_b(r)$ are presented in Fig. 2. The constant-value regions of these exponents are ill-defined, especially for $\mu_b(r)$. However, for each time series one can choose a range of separations r where the exponents are *approximately* constant. Within these limits, deviations of μ from constant can be attributed to measurement uncertainty. The mean values $\overline{\mu_i}$ and

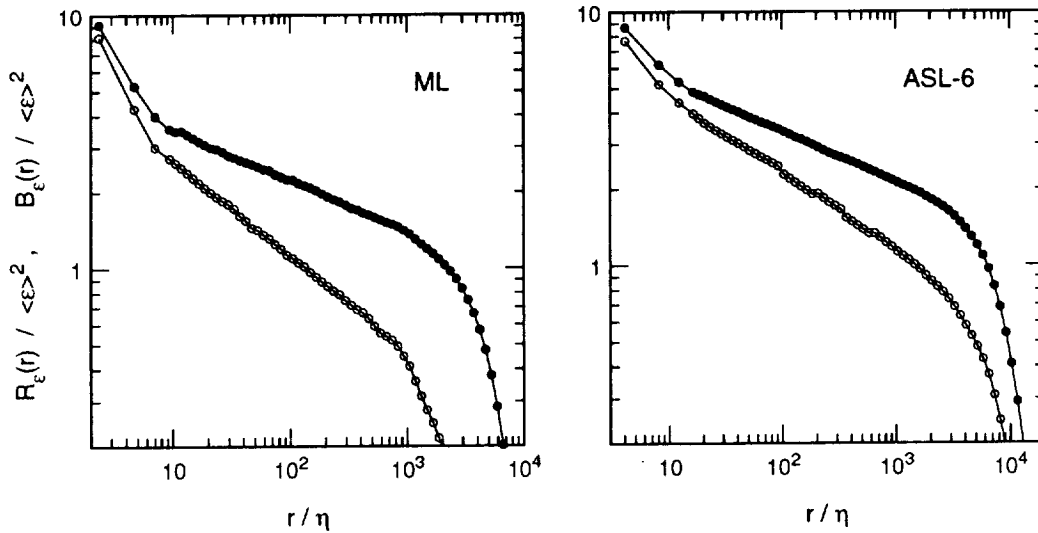


FIGURE 1. Correlation functions of the energy dissipation. \bullet , $R_\epsilon(r)$; \circ , $B_\epsilon(r)$.

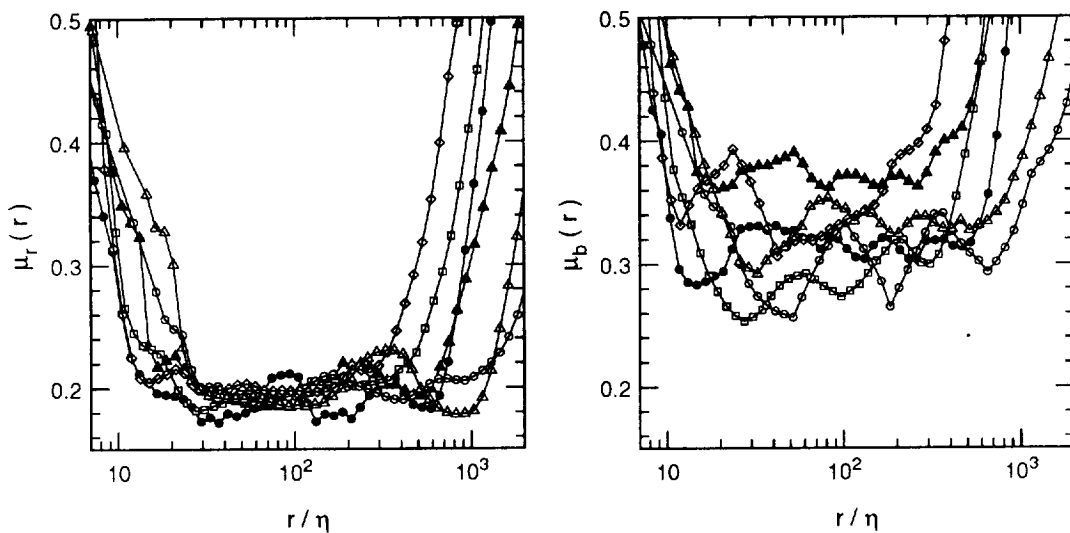


FIGURE 2. The local values of scaling exponents $\mu_r(r)$ and $\mu_b(r)$. Note the expanded linear scale of the ordinate at this and other similar figures. \blacktriangle , ML; \bullet , RC; \diamond , ASL-2; \square , ASL-3; \triangle , ASL-5; \circ , ASL-6.

standard deviations σ_{μ_i} , ($i = r, b$) were estimated by averaging over these ranges, and the results are listed in Table 1. It is seen that $\overline{\mu_r}$ is significantly smaller than $\overline{\mu_b}$. This result is not surprising. Anselmet *et al.* (1984) found $\mu_r = 0.18$ and $\mu_b = 0.48$ in the round jet at $R_\lambda = 536$. Kuznetsov *et al.* (1992) found $\mu_r \approx 0.14$, $\mu_b \approx 0.45$, and $\mu_\epsilon \approx 0.60$ in the mixing layer at $R_\lambda \approx 1700$. The equality $R_\epsilon(r) \approx B_\epsilon(r)$ is based on the assumption that both $R_\epsilon(r)$ and $B_\epsilon(r)$ are much larger than $\langle \epsilon \rangle^2$

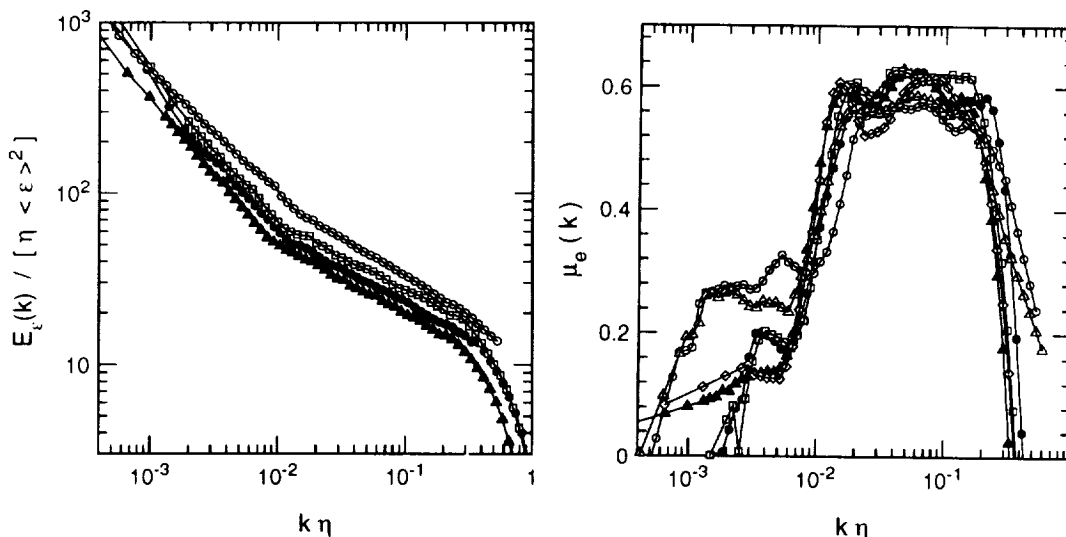


FIGURE 3. Spectra of the energy dissipation, and the local values of scaling exponent $\mu_\epsilon(k)$. For symbols see Fig. 2.

in the inertial range (Monin & Yaglom 1975). This assumption is not valid *at any finite Reynolds number*. It is seen in Fig. 1 that at big enough r , say at $r/\eta \approx 10^3$, $B_\epsilon(r)$ is smaller than $\langle \epsilon \rangle^2$. Hence one should always obtain $\mu_r < \mu_b$. There is a contradiction, recently noted by Praskovsky & Oncley (1994b). The correlation functions are connected by the exact relation:

$$B_\epsilon(r) \equiv R_\epsilon(r) - \langle \epsilon \rangle^2. \quad (10)$$

It obviously follows from this relation that at any finite R_λ where $\langle \epsilon \rangle^2$ is of the order of (or even larger than) $B_\epsilon(r)$ at $\eta \ll r \ll L$, only one of the functions, $R_\epsilon(r)$ or $B_\epsilon(r)$, may obey the power-law scaling. As was mentioned above, the constant-value regions for both $\mu_r(r)$ and $\mu_b(r)$ are ill-defined. Taking into consideration Eq. (10), one can suggest that the present experiments as well as all previous measurements *do not prove* power-law behavior of any correlation function. The results demonstrate that the power laws (5) and (6) *reasonably approximate* both correlators within the inertial range.

Typical energy spectra $E_\epsilon(k)$ and local values of the scaling exponents $\mu_\epsilon(k)$ are presented in Fig. 3. It is seen that at large enough k the power law (7) gives reasonable approximation of $E_\epsilon(k)$. The mean values $\overline{\mu_\epsilon}$ and the standard deviation σ_{μ_ϵ} are estimated over the ranges where $\mu_\epsilon(k)$ are approximately constant, and the results are listed in Table 1. It is seen that $\overline{\mu_\epsilon}$ are roughly twice $\overline{\mu_b}$. This result agrees with previous studies, and it is explained by Nelkin (1981). It follows from Eq. (7) that $\mu_b \equiv \mu_\epsilon$ if scaling (6) is valid for all r from 0 to infinity. In reality, $B_\epsilon(0)/\langle \epsilon \rangle^2$ increases with no limit as $R_\lambda \rightarrow \infty$ while the inertial range values of $B_\epsilon(r)/\langle \epsilon \rangle^2$ increase more slowly. In other words, $B_\epsilon(r)$ has a strong peak at $r \leq \eta$, and this peak increases as R_λ increases. As was shown by Kuznetsov

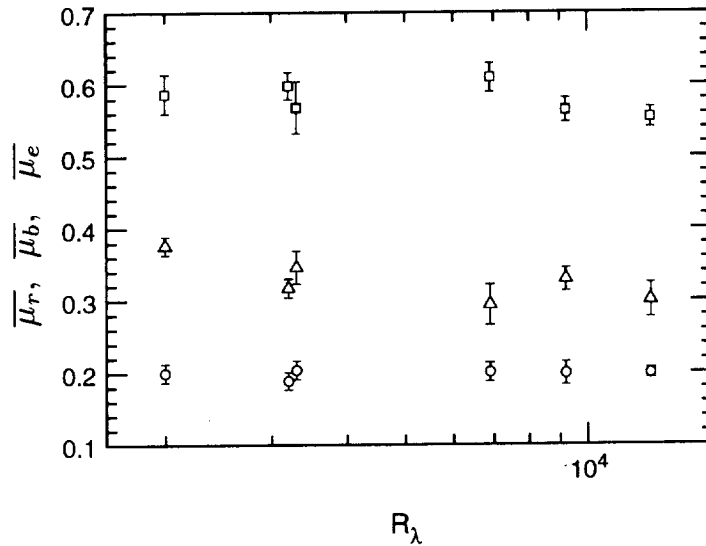


FIGURE 4. Scaling exponents averaged over the inertial range. Error bars at this and other similar figures correspond to the rms value of the exponent. \circ , $\overline{\mu_r}$; \triangle , $\overline{\mu_b}$; \square , $\overline{\mu_e}$.

et al. (1990), μ_b is always smaller than μ_e , and this difference may increase when R_λ increases.

The values of $\overline{\mu_r}$, $\overline{\mu_b}$, and $\overline{\mu_e}$ are plotted in Fig. 4. Beyond any doubt, μ_r , μ_b , and μ_e are different exponents at R_λ up to 12,700. Variation of these exponents with R_λ and the type of flow is quite small. As a first approximation, one can consider the exponents $\mu_r \approx 0.2$, $\mu_b \approx 0.3$, and $\mu_e \approx 0.55$ to be universal (but different!) constants at the highest Reynolds numbers currently attainable, say at $R_\lambda \geq 2 \times 10^3$. At Reynolds numbers too high to be attained on this planet, the different μ 's could still be the same.

2.2.2 Test of the log-normal model

The log-normal model includes the statement that $\ln \varepsilon_r$ has a normal distribution for $\eta \ll r \ll L$ (Kolmogorov 1962). Note that this assumption and Eq. (3) are two *independent* hypotheses, i.e., the log-normal model may be valid while Eq. (3) is not, and vice-versa (see Castaing *et al.* 1990 for more explanation).

The log-normality of $\ln \varepsilon_r$ was tested in numerous experiments (see reviews in Monin & Yaglom 1975, Gibson 1991), and this was found to give a reasonable approximation of reality in different turbulent flows. The present experiments give similar results. As an illustration, several distributions for segments r from the inertial range are presented in Fig. 5. It is surprising that deviations of experimental results from the log-normal model increase as R_λ increases.

Eq. (3) was also reported by many authors to be valid (see Gibson 1991 and references therein). However, Castaing *et al.* (1990) presented experimental and theoretical evidences that at small r (up to the viscous range) the variation of $\ln \varepsilon_r$ obeys the power-law scaling

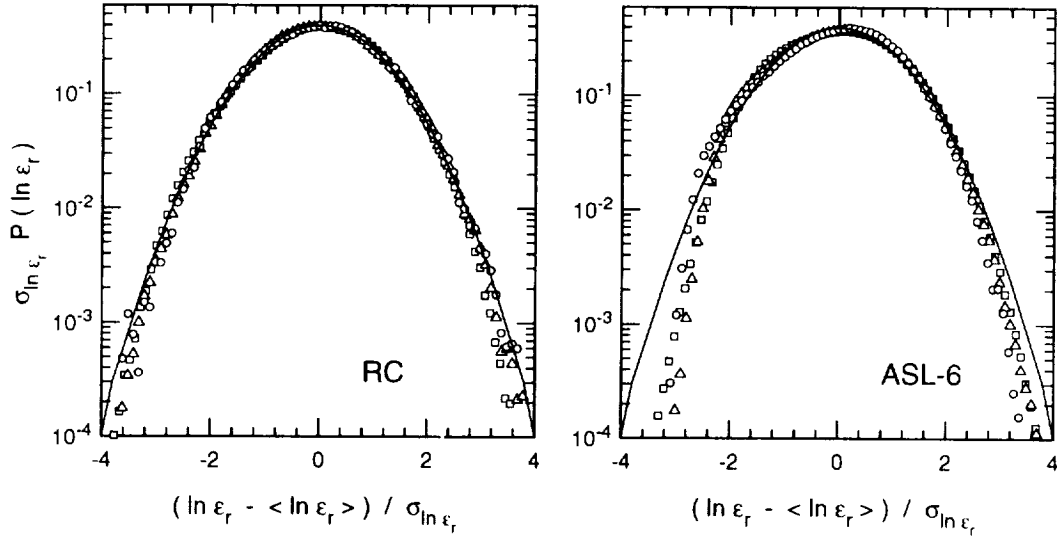


FIGURE 5. Pdd of $\ln \varepsilon_r$. Solid lines correspond to the normal distribution. RC: \square , $r/\eta = 23$; \triangle , 130; \circ , 927; ASL-6: \square , $r/\eta = 33$; \triangle , 180; \circ , 1025.

$$\sigma_{\ln \varepsilon_r}^2 \propto r^{-\beta}. \quad (11)$$

Hypotheses (3) and (11) are tested in Fig. 6. The local values of $\mu_k(r)$ and $\beta(r)$ are defined as

$$\mu_k(r) = -\frac{d[\sigma_{\ln \varepsilon_r}^2]}{d[\ln r]}, \quad \beta(r) = -\frac{d[\lg \sigma_{\ln \varepsilon_r}^2]}{d[\lg r]}. \quad (12)$$

It is seen that at large r , say $r/\eta \geq 200$, the Kolmogorov (1962) assumption (3) provides a good approximation of the experimental results. At small r Eq. (3) does not agree with the present experiments while the power-law scaling (11) works quite well. The values of $\overline{\mu_k}$ and $\overline{\beta}$ averaged over regions where they are approximately constant are listed in Table 1 and presented in Fig. 7. One can see that μ_k does not depend on R_λ and the type of flow at $R_\lambda \geq 3 \times 10^3$, and is approximately equal to 0.22. The exponent β in (11) does not reveal any dependence on the type of flow (measurements by Castaing *et al.* 1990 in the round jet at $R_\lambda = 852$ and in the Modane wind tunnel at $R_\lambda = 2720$ are also presented in Fig. 7). However, this exponent strongly depends on R_λ , and the dependence may be approximated as $\beta \propto R_\lambda^{-1/3}$, which is different from the relation $\beta \propto 1/\ln R_\lambda$ suggested by Castaing *et al.* (1990).

2.2.3 Measurements of the second-order moments

The measured values of $\langle \varepsilon_r^2(x) \rangle$ as well as the local values of scaling exponent $\mu_\varepsilon(r) = -d[\lg \langle \varepsilon_r^2 \rangle]/d[\ln r]$ are presented in Fig. 8. No region of power-law scaling is seen within the inertial range; i.e., $\mu_\varepsilon(r)$ decreases monotonically over the range of r/η from say 5 to 20,000. Contradiction of this result to all previous studies is

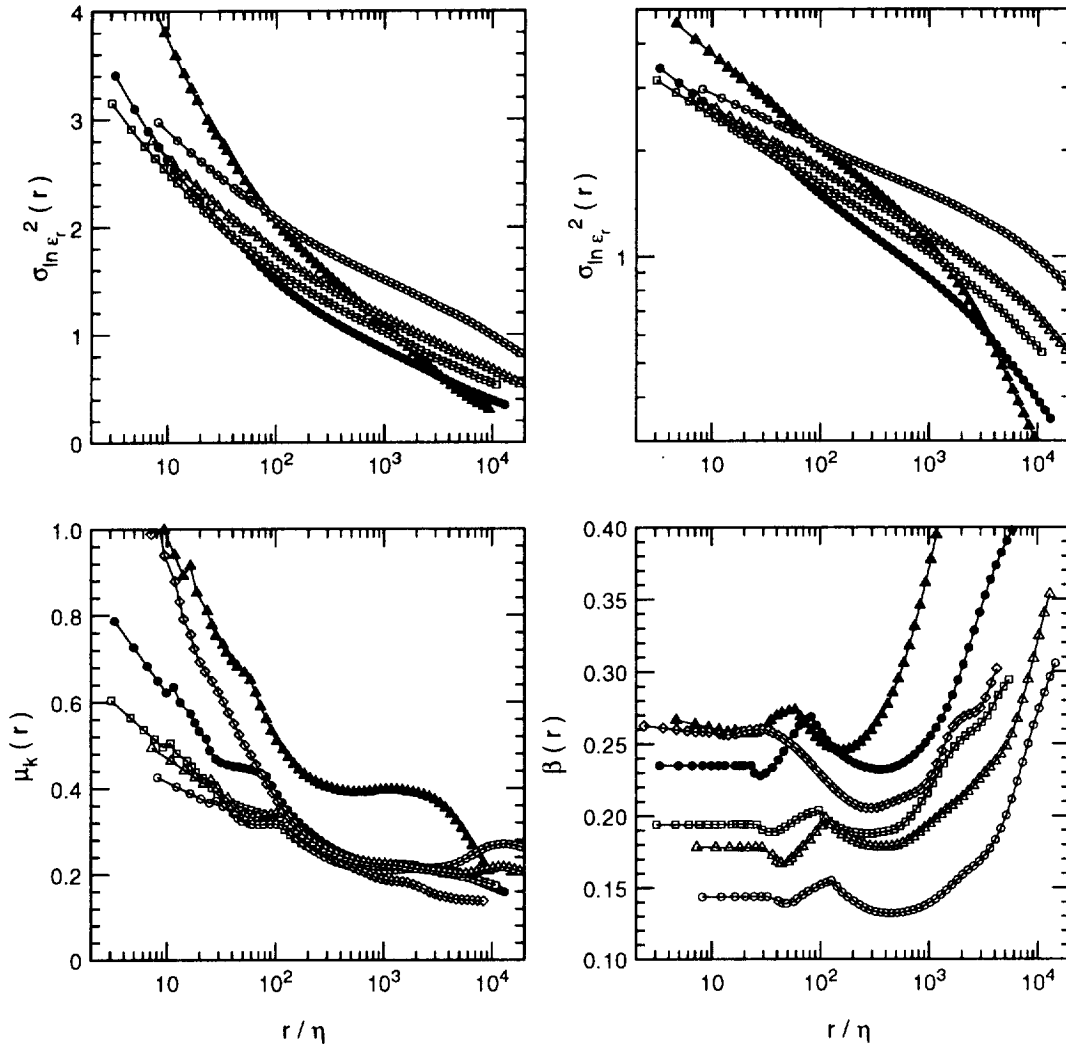


FIGURE 6. Variation of $\ln \varepsilon_r$, and the local values of $\mu_k(r)$ and $\beta(r)$.

apparent. No previous papers reported the local values $\mu_\varepsilon(r)$, but only log-log plots such as that in Fig. 8. Such plots may be deceptive; a range of slow change in $\mu_\varepsilon(r)$ may be erroneously considered as implying $\mu_\varepsilon(r) \approx \text{constant}$.

It was recently suggested by L'vov and Procaccia (1994) that scaling (4) should be applied to the centered second-order moment, i.e., the relation

$$\langle [\varepsilon_r(x) - \langle \varepsilon \rangle]^2 \rangle \propto r^{-\gamma_\varepsilon}, \quad \eta \ll r \ll L \tag{13}$$

should be used instead of (4). This suggestion is tested in Fig. 9. It is seen that $\gamma_\varepsilon(r) = d[\lg \langle (\varepsilon_r - \langle \varepsilon \rangle)^2 \rangle] / d[\lg r]$ does reveal some range of being approximately constant. The values of $\bar{\gamma}_\varepsilon$ averaged over these ranges are presented in Fig. 10. It is seen that γ_ε slightly depends on Reynolds number.

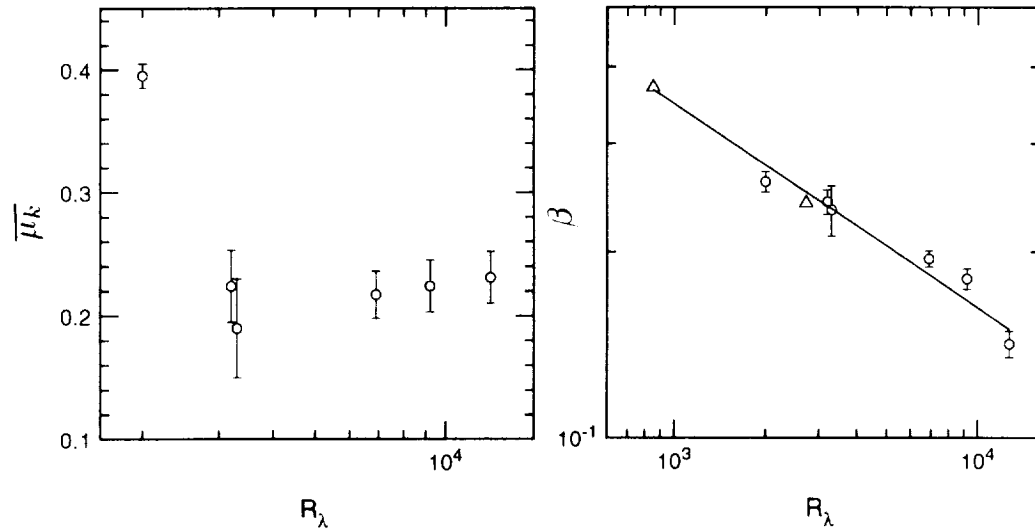


FIGURE 7. Averaged values of the exponents $\overline{\mu_k}$ and $\overline{\beta}$. — corresponds to $\beta \propto R_\lambda^{-1/3}$; \circ , the present results; \triangle , Castaing *et al.* (1990).

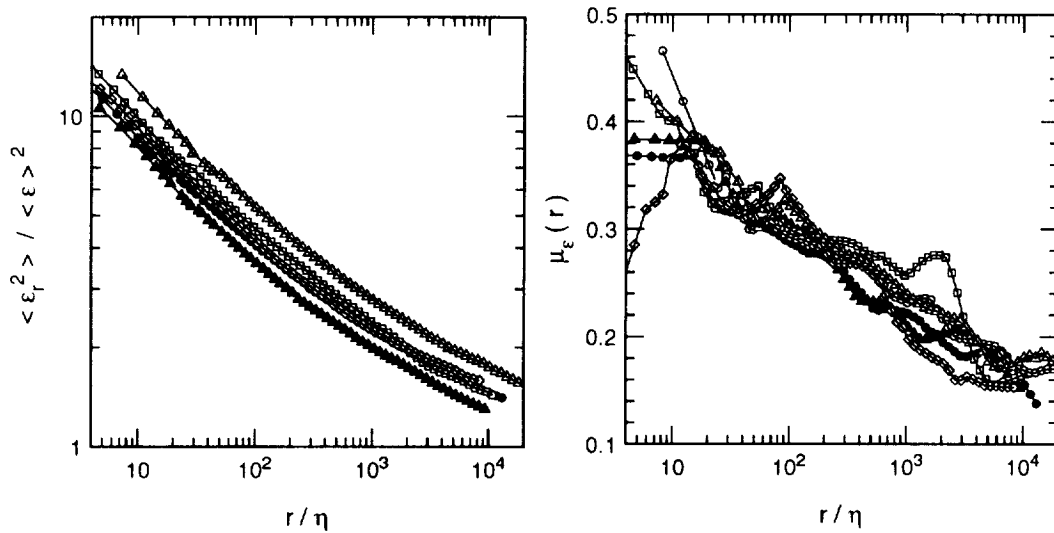


FIGURE 8. The second-order moments $\langle \varepsilon_r^2(x) \rangle$ and the local values of scaling exponent $\mu_\varepsilon(r)$. For symbols see Fig. 2.

2.3 Analysis of the DNS data base

Two DNS of isotropic homogeneous turbulence at $R_\lambda = 94$ and 168 (Jimenez *et al.* 1993) are analyzed. The purpose of this analysis is a comparison of statistical characteristics of the “true” energy dissipation field $\varepsilon(x)$, Eq. (2), and its one-dimensional surrogate $\tilde{\varepsilon}(x)$, Eq. (8). Significance of such a comparison is illustrated in Fig. 11 where pdd $P(\varepsilon)$ of $\varepsilon(x)$ and $P(\tilde{\varepsilon})$ of $\tilde{\varepsilon}(x)$ are presented. One can see a

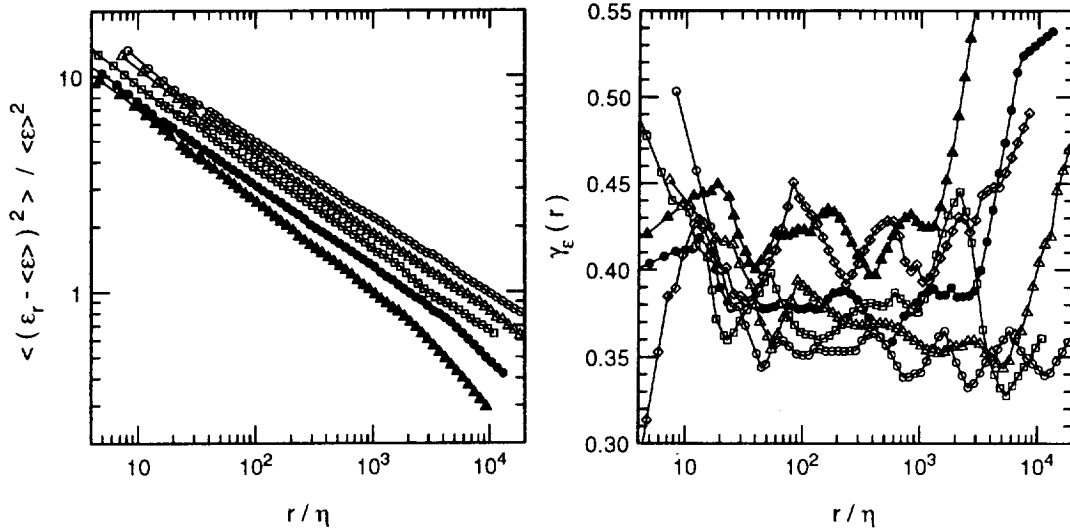


FIGURE 9. The centered second-order moments $\langle [\varepsilon_r(x) - \langle \varepsilon_r \rangle]^2 \rangle$, and the local values of scaling exponent $\gamma_\varepsilon(r)$. For symbols see Fig. 2.

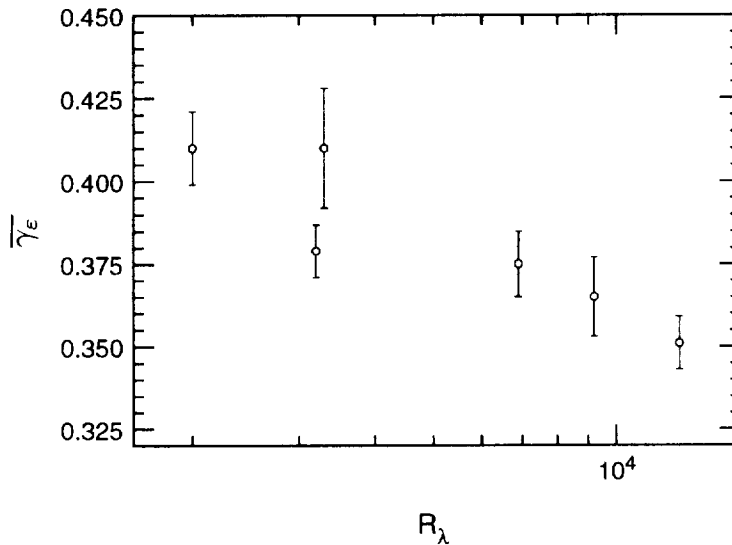


FIGURE 10. Exponent $\overline{\gamma_\varepsilon}$ averaged over the inertial range.

qualitative difference of these functions: $P(\varepsilon) \rightarrow 0$ as $\varepsilon \rightarrow 0$ while $P(\tilde{\varepsilon}) \rightarrow P_0 > 0$ as $\tilde{\varepsilon} \rightarrow 0$ (see also Hosokawa and Yamamoto 1991). In other words, we test a question: what of the results from Sec. 2.2 which are obtained for $\tilde{\varepsilon}(x)$ are valid for the true dissipation $\varepsilon(x)$? A comparison is executed in the following way. Using the DNS data base, each parameter is estimated for the true energy dissipation and one-dimensional surrogate by substituting in the same defining formula either $\varepsilon(x)$ or $\tilde{\varepsilon}(x)$, respectively.

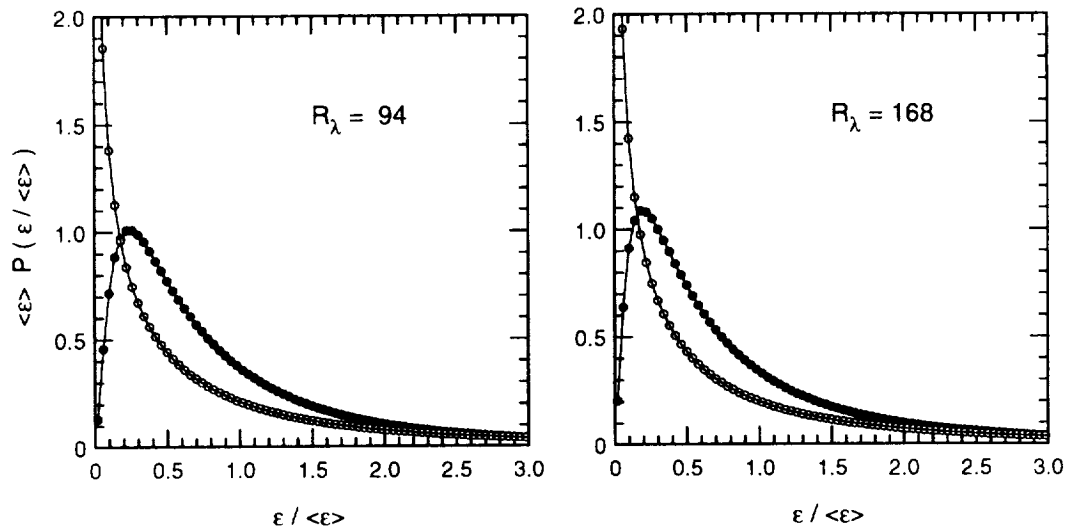


FIGURE 11. DNS: pdd of the energy dissipation. In this and the following figures the solid symbols correspond to the true dissipation $\epsilon(x)$, and the open symbols correspond to the one-dimensional surrogate $\tilde{\epsilon}(x)$.

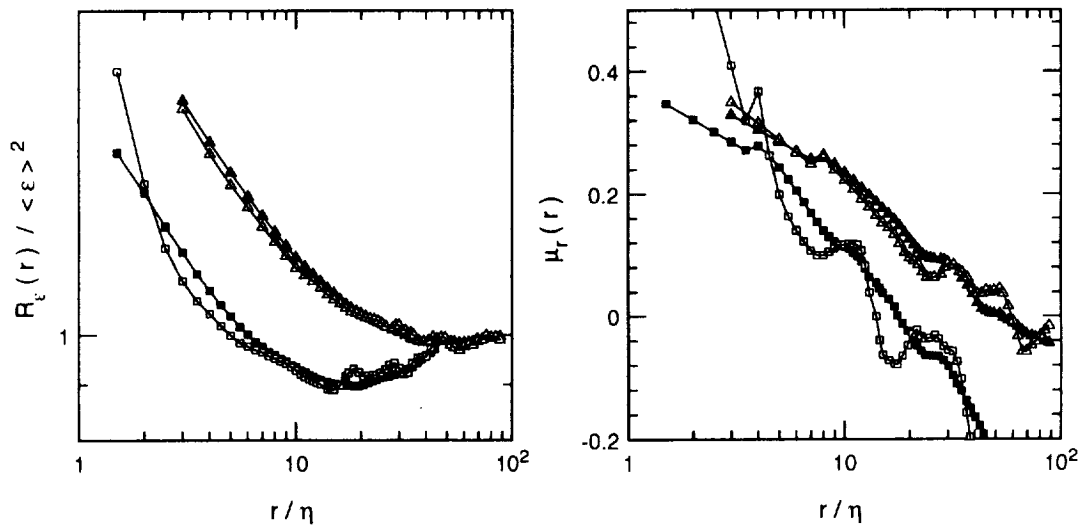


FIGURE 12. DNS: correlation functions of the energy dissipation, and the local values of scaling exponent $\mu_r(k)$. \square , $R_\lambda = 94$; \triangle , 168. See caption of Fig. 11.

The correlation functions $R_\epsilon(r)$ and the local values of scaling exponent $\mu_r(r)$ are presented in Fig. 12. No clearly defined inertial range is seen, i.e., there is no region where $\mu_r(r) \approx \text{constant}$. This is expected due to relatively low Reynolds number in the present DNS. In spite of different pdd (Fig. 11), a qualitative behavior of $R_\epsilon(r)$ for $\epsilon(x)$ and $\tilde{\epsilon}(x)$ is quite similar. Hence one can expect that results and conclusions

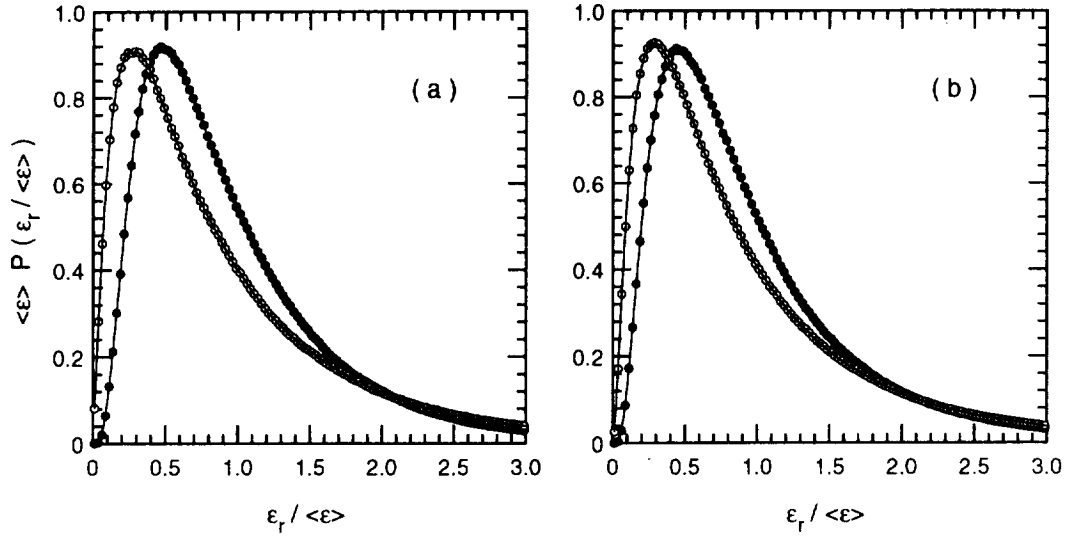


FIGURE 13. DNS: pdd of the energy dissipation averaged over a segment r . (a) $R_\lambda = 94, r/\eta = 10$; (b) $R_\lambda = 168, r/\eta = 15$. See caption of Fig. 11.

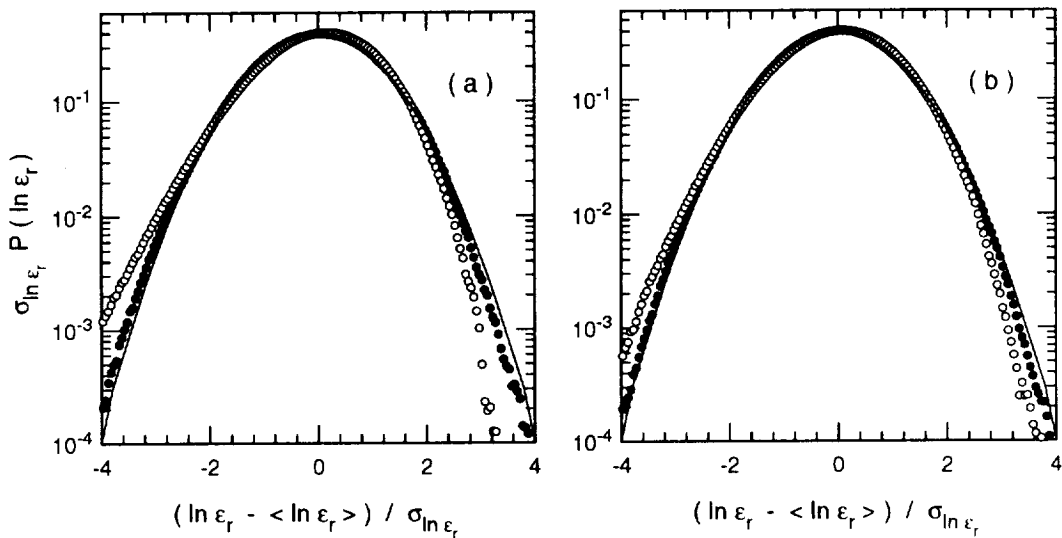


FIGURE 14. DNS: pdd of $\ln \epsilon_r$. Solid lines correspond to the normal distribution. (a) $R_\lambda = 94, r/\eta = 10$; (b) $R_\lambda = 168, r/\eta = 15$. See caption of Fig. 11.

of Sec. 2.2.1 are valid for the true energy dissipation field.

Pdd of energy dissipation averaged over a segment r are presented in Fig. 13. Variation of $\tilde{\epsilon}_r(x)$ is much larger than that of $\epsilon_r(x)$: the maxima of $P(\tilde{\epsilon}_r)$ are shifted to the smaller amplitudes while the tails of $P(\tilde{\epsilon}_r)$ at large amplitudes are higher than those of $P(\epsilon_r)$. The log-normal model is tested in Fig. 14. The true energy dissipation field agrees quite well with the model while $P(\ln \tilde{\epsilon}_r)$ reveals significant

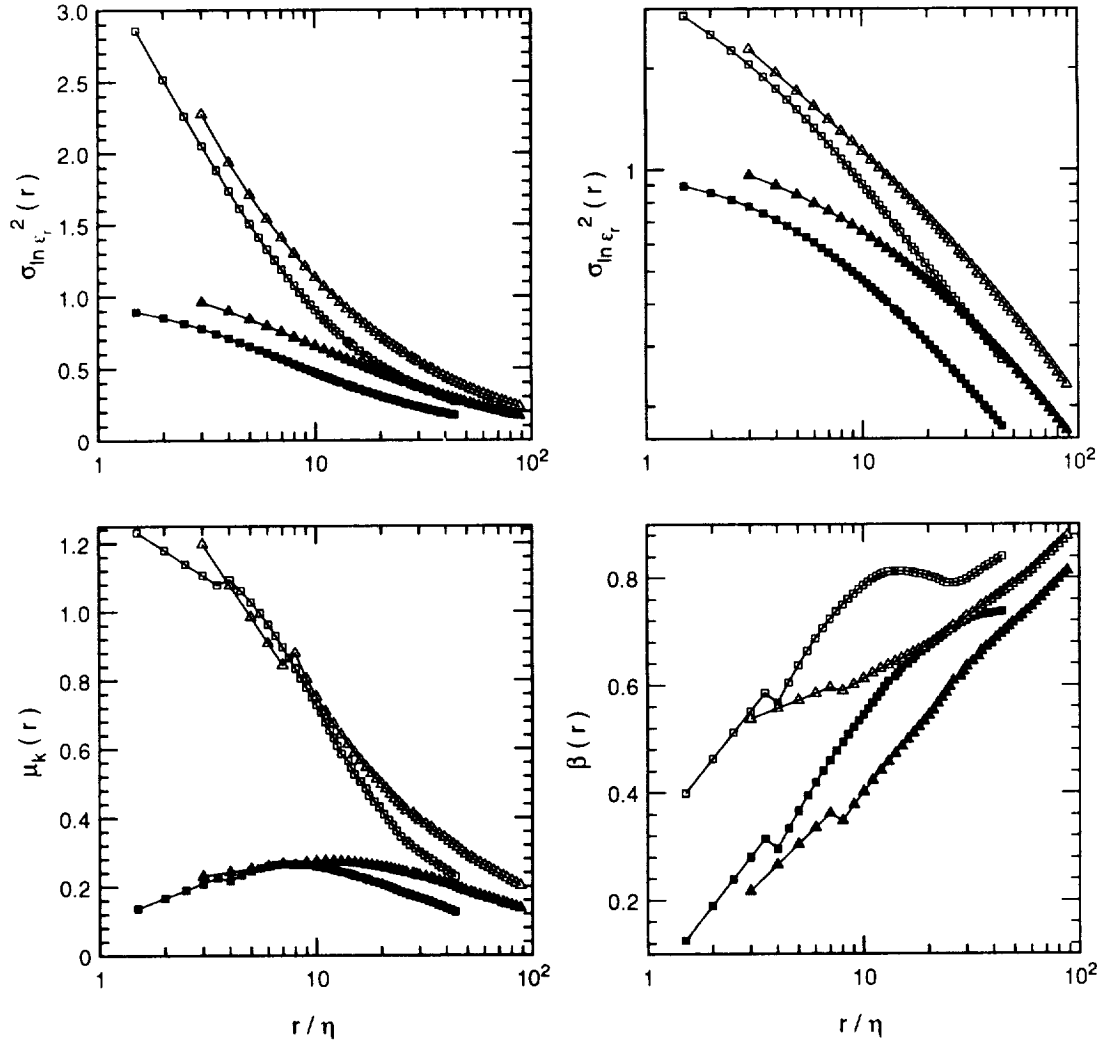


FIGURE 15. DNS: variation of $\ln \varepsilon_r$, and the local values of $\mu_k(r)$ and $\beta(r)$. \square , $R_\lambda = 94$; \triangle , 168. See caption of Fig. 11.

deviations similar to those in Fig. 5. One can suggest that the deviations from the log-normal model in Fig. 5 would be smaller (or even disappear) if the true energy dissipation was measured at high R_λ .

Eqs. (3) and (11) were tested, and the results are presented in Fig. 15 which is similar to Fig. 6 for experimental data. A qualitative behavior of $\sigma_{\ln \varepsilon_r}^2$ for the one-dimensional surrogate in the DNS is completely similar to that in the high Reynolds number experiments. The DNS results for $\tilde{\varepsilon}_r$ do not agree with Eq. (3) at $r/\eta \approx 7-20$ (this region is expected to model the inertial range) while they agree with Eq. (11). On the other hand, the true field $\varepsilon_r(x)$ is reasonably described by Eq. (3) in the vicinity of $r/\eta \approx 10$, and it does not agree with Eq. (11). Using DNS at

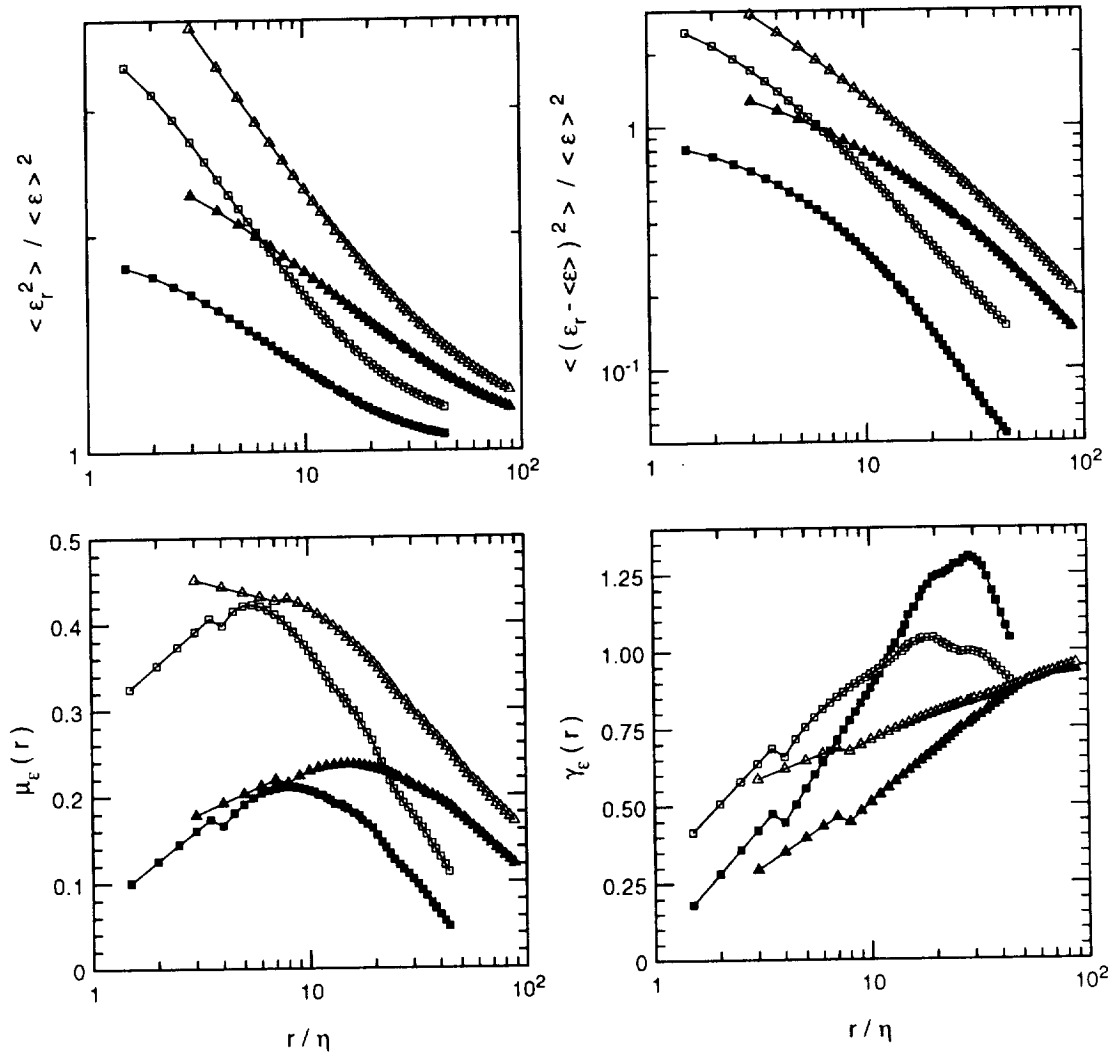


FIGURE 16. DNS: the non-centered and centered second-order moments of $\varepsilon_r(x)$, and the local values of scaling exponents $\mu_\varepsilon(r)$ and $\gamma_\varepsilon(r)$. \square , $R_\lambda = 94$; \triangle , 168. See caption of Fig. 11.

$R_\lambda = 68.1$ and 151, Wang *et al.* (1994) recently found the values of $\mu_k \approx 0.28$ for the true field $\varepsilon_r(x)$, and 0.34 for the surrogate $\tilde{\varepsilon}_r(x)$. In the present DNS the values of $\mu_k(r)$ for $\tilde{\varepsilon}_r$ are also larger than those for ε_r (Fig. 15). However, our results differ conceptually from those by Wang *et al.* (1994). We state that the surrogate field does not obey Eq. (3) in the vicinity of $r/\eta \approx 10$ –15, and no value of μ_k may be estimated. Perhaps, Wang *et al.* (1994) would draw the same conclusion if they used the logarithmic derivatives instead of the log-linear plots of $\sigma_{\ln \varepsilon_r}^2$ vs $\ln r$.

The DNS results for $\langle \varepsilon_r^2 \rangle$ (Fig. 16) are also similar to the experimental data (Figs. 8, 9). A functional behavior of the second-order moment $\langle \tilde{\varepsilon}_r^2 \rangle$ in the DNS

agrees with Eq. (13) at $r/\eta \approx 10$ -20 as that in experiments while $\langle \varepsilon_r^2 \rangle$ clearly agrees with Eq. (4).

It follows from the above results that the experimental findings of Sec. 2.2.2 and 2.2.3 may be valid only for $(\partial u/\partial x)^2$, and their application to the true dissipation field $\varepsilon(x)$ is quite questionable. Based on these preliminary results, we cannot draw any final conclusions. However, two suggestions may be stated. First, any experimental finding obtained for the surrogate $\tilde{\varepsilon}(x)$ should not be applied to the true dissipation field before similarity of this result to that for $\varepsilon(x)$ is proven. Second, DNS seems to be the most reliable (and perhaps a unique) tool for such a proof.

3. Future plans

The goal remains to understand what characteristics of the energy dissipation field are adequately represented by the one-dimensional surrogate. To further study this question, we are going to use the recent DNS data base with resolution 512^3 .

The second question may be formulated as follows: what is the minimum set of terms in Eq. (2) which adequately represents any statistical characteristic of $\varepsilon(x)$? An answer to this question will allow a proper design of the future high Reynolds number experiments.

Acknowledgments

The author is sincerely grateful to Dr. Steven Oncley for the experimental data in the atmospheric surface layer, to Dr. Robert Rogallo for the DNS data base, intensive help, and valuable discussions, and to Prof. Peter Bradshaw for comments on the draft. The experimental part of this work was supported by the National Center for Atmospheric Research, and the computational part by the Center for Turbulence Research. Personal encouragement and valuable comments by Prof. Parviz Moin are highly appreciated.

REFERENCES

- ANSELMET, F., GAGNE, Y., HOPFINGER, E. J. & ANTONIA, R. A. 1984 High-order velocity structure functions in turbulent shear flows. *J. Fluid Mech.* **140**, 63-89.
- CASTAING, B., GAGNE, Y. & HOPFINGER, E. J. 1990 Velocity probability density functions of high Reynolds number turbulence. *Physica D.* **46**, 177-200.
- GIBSON, C. H. 1991 Kolmogorov similarity hypotheses for scalar fields: sampling intermittent turbulent mixing in the ocean and galaxy. *Proc. R. Soc. Lond. A.* **434**, 149-164.
- HOSOKAWA, I. & YAMAMOTO, K. 1992 Evidence against the Kolmogorov refined similarity hypothesis. *Phys. Fluids A.* **4**, 457-459.
- JIMENEZ, J., WRAY, A.A., SAFFMAN, P.G. & ROGALLO, R.S. 1993 The structure of intense vorticity in isotropic turbulence. *J. Fluid Mech.* **255**, 65-90.

- KOLMOGOROV, A. N. 1962 A refinement of previous hypotheses concerning the local structure of turbulence in a viscous incompressible fluid at high Reynolds numbers. *J. Fluid Mech.* **13**, 82-85.
- KRAICHNAN, R. H. 1974 On Kolmogorov's inertial-range theories. *J. Fluid Mech.* **62**, 305-330.
- KUZNETSOV, V. R., PRASKOVSKY, A. A. & SABELNIKOV, V. A. 1990 Intermittency and fine-scale turbulence structure of shear flows. *Proc. Inst. of Thermophysics*. (Novosibirsk, Russia), 223-224.
- KUZNETSOV, V. R., PRASKOVSKY, A. A. & SABELNIKOV, V. A. 1992 Fine-scale turbulence structure of intermittent shear flows. *J. Fluid Mech.* **243**, 595-622.
- KUZNETSOV, V. R. & SABELNIKOV, V. A. 1990 *Turbulence and Combustion* (Hemisphere Publ.).
- L'VOV, V. S. & PROCACCIA, I. 1994 'Intermittency' in hydrodynamic turbulence as an intermediate asymptotic to Kolmogorov'41 scaling. Submitted to *Phys. Rev. Lett.*
- MONIN, A.S. & YAGLOM, A.M. 1975 *Statistical Fluid Mechanics*, **2**, (MIT Press).
- NELKIN, M. 1981 Do the dissipation fluctuations in high Reynolds number turbulence define a universal exponent? *Phys. Fluids* **24**, 556-557.
- NELKIN, M. 1994 Universality and scaling in fully developed turbulence. *Advances in Physics*, in press.
- NOVIKOV, E. A. 1990 The effect of intermittency on statistical characteristics of turbulence and scale similarity of breakdown coefficients. *Phys. Fluids A*, **2**, 814-820.
- NOVIKOV, E.A. & STEWART, R.W. 1964 The intermittency and the spectral distribution of energy dissipation. *Izv. Akad. Nauk SSSR, Ser. Geofiz.* **2**, 408-413.
- ONCLEY, S. 1992 TKE dissipation measurements during the FLAT experiment. In *Proc. of 10th Symp. on Turbulence and Diffusion*, 165-166 (AMS, Boston MA).
- PRASKOVSKY, A. A., GLEDZER, E. B., KARYAKIN, M. YU. & ZHOU, Y. 1993 The sweeping decorrelation hypothesis and energy-inertial scale interaction in high Reynolds number flows. *J. Fluid Mech.* **248**, 493-511.
- PRASKOVSKY, A. A. & ONCLEY, S. 1994a Measurements of the Kolmogorov constant and intermittency exponent at very high Reynolds numbers. *Phys. Fluids*, **6**, 2886-2888.
- PRASKOVSKY, A. A. & ONCLEY, S. 1994b Correlators of velocity differences and energy dissipation at very high Reynolds numbers. *Europhys. Lett.*, in press.
- TSINOBER, A., KIT, E. & DRACOS, T. 1992 Experimental investigation of the field of velocity gradients in turbulent flows. *J. Fluid Mech.* **242**, 169-192.

- WANG, L.-P., CHEN, S., BRASSEUR, J. G. & WYNGAARD, J. C. 1994 Examination of hypotheses in the Kolmogorov refined turbulence theory through high-resolution simulations. Submitted to *J. Fluid Mech.*

On the dynamics of small-scale vorticity in isotropic turbulence

By J. Jiménez¹ and A. A. Wray²

1. Motivation

In a previous report (Jiménez *et al.* 1993, referred from now on as JWSR), it was shown that the strong vorticity in isotropic turbulence is organized into tubular vortices (“worms”) whose properties were characterized through the use of full numerical simulations at several Reynolds numbers. That paper should be consulted for details as well as for the previous history of the subject. At the time most of the observations were kinematic, and several scaling laws were discovered for which there was no theoretical explanation. In the meantime, further analysis of the same fields yielded new information on the generation of the vortices, and it was realized that even if they have to be formed by stretching, they were at any given moment actually compressed at many points of their axes (Jiménez and Wray, 1994). This apparent contradiction was partially explained by postulating axial inertial waves induced by the nonuniformity of the vortex cores, which helped to “spread” the axial strain and allowed the vortices to remain compact even if not uniformly stretched. The existence of such solutions was recently proved numerically by (Verzicco, Jiménez & Orlandi 1994). The present report discusses a set of new numerical simulations of isotropic turbulence, and a re-analysis of the old ones, in an effort to prove or disprove the presence of these waves in actual turbulent flows and to understand the dynamics, as opposed to the kinematics, of the vortices.

One set of experiments use hyperviscous dissipation instead of regular viscosity. Since the strong vortices are known to be dissipative structures with characteristic radii in the range of the near dissipation range of the turbulence cascade, they can be considered as being forced by inertial range eddies, but to be dominated by viscous diffusion. The hope was that hyperviscosity would change the diffusion mechanism without changing the forcing and give us a better insight into the dynamics. This strategy was largely successful, but some unexpected consequences of hyperviscosity were found in the form of a strong bump in the upper inertial range of the spectrum, spanning at least one and a half decades in wavenumber, and which seems to be an evolution of the much weaker bump described in some experiments in real fluids. This bump is discussed below in detail and may be of some practical relevance since some sub-grid models in LES computations use eddy viscosity laws that resemble hyperviscosity, and the present result suggests that their effect might distort the spectrum across a range of scales comparable to that of most practical LES numerical grids.

¹ Also with School of Aeronautics, U. Politécnica, Madrid

² NASA Ames Research Center, Moffet Field, Ca. 94035

Finally, the study of strong vorticity leads directly to the question of intermittency. It appears that at the Reynolds numbers of our flows ($Re_\lambda \leq 170$), most of the extended tails in the probability density functions of the velocity gradients can be associated to the vortex filaments and scale with Reynolds number in the same way as they do. We show evidence that the volume ratio occupied by the filaments decreases with Re_λ while the intensity of the individual structures increases. This raises the question, already posed in JWSR, of their behavior in the infinite Reynolds number limit. It would appear that the mechanisms described here can not be extended indefinitely as $Re_\lambda \rightarrow \infty$ although the limitations of numerical resolution prevent us from giving a definite answer.

The simulations, both viscous and hyperviscous, are described first. The global flow statistics, especially those related to intermittency, are described next, followed by a description of worm properties and a short discussion of the results. The present is an interim report, and more work is needed, especially from the point of view of theoretical analysis.

2. Viscous simulations

The viscous simulations used in this report are essentially the same as in JWSR. The spectral numerical scheme (Rogallo 1981) and other parameters are described in that paper, which should also be consulted for the detailed definitions of the different quantities, which generally follow (Batchelor 1953). Some simulations were continued for a longer time to improve the statistics, and the two lower Reynolds numbers were repeated at higher resolution, $k_{\max}\eta = 4$ instead of $k_{\max}\eta = 2$, to check that the scalings reported in JWSR were not artifacts of the use of a uniform resolution in Kolmogorov units. No artifacts were found. These new simulations were also used in a separate study of the effect of resolution on both experiments and in simulations (Jiménez 1994b).

Since the time of the previous report, the fields corresponding to the highest Reynolds number ($Re_\lambda = 168$ on a 512^3 grid) became unavailable for further processing. To palliate this problem, a new simulation was run on a 384^3 grid, resulting in $Re_\lambda = 141$. All these simulations, including the older ones, are summarised in Table 1, which refers only to the numerical resolution $k_{\max}\eta = 2$.

As in the original study, all simulations were forced to reach a statistically stationary state with a given energy dissipation, adjusted to achieve a desired value for $k_{\max}\eta$. In particular, every Fourier velocity coefficient with a wave number such that $k = |\mathbf{k}| \leq 2.5$ was multiplied at each time step by a common real factor, chosen so that the extra energy introduced in that way was equal to the desired energy dissipation.

It was felt that forcing the flow at such low wave numbers could reduce excessively the statistics of the large scales and perhaps affect the flow. To check that effect, two simulations were performed in which the same type of forcing was applied to the spectral shell $3.5 < |\mathbf{k}| \leq 6.5$. In general, few differences were found between the two types of simulations although the new statistics should clearly be better

Re_λ	N	L_ϵ	L_ϵ/λ	L_ϵ/η	$\epsilon L/u'^3$	t/T	$-F_3$
35	64	1.8	2.3	27	1.09	54.2	0.49
63	128	2.2	4.2	65	0.80	9.3	0.50
94	256	2.0	6.3	120	0.72	8.2	0.52
142	384	2.4	9.5	222	0.73	5.9	0.52
168	512	2.4	11.2	286	0.69	5.9	0.52
26	128	0.6	1.7	18	0.96	11.2	0.50
48	256	0.7	3.2	44	0.62	15.1	0.51

TABLE 1. Numerical and flow parameters for the viscous cases analyzed in this paper. t/T is the total run time in eddy turnover units, F_3 is the skewness coefficient, L is the integral scale, and $L_\epsilon = u'^3/\epsilon$ is the eddy dissipation scale. The last two cases were forced at higher wavenumbers as explained in text.

than the older ones. Those differences that were found are discussed below in the corresponding sections, and the flows themselves are documented in Table 1. The better statistics were compensated by the possibility of reaching only much lower Reynolds numbers. Fig. 1 presents compensated spectra for the different flows.

3. Hyperviscosity

Hyperviscosity, the use of the iterated Laplacian in place of the usual dissipative operator, has been used often in the numerical simulation of turbulence in an effort to obtain longer inertial ranges out of a given resolution. The hope has been that its use would not affect the inviscid aspects of the turbulent flow although it clearly changes the characteristics of the dissipative scales. Since the vortices that concern us seem to be dissipative features, hyperviscous simulations were undertaken in the hope of clarifying their dynamics by changing their behavior. Define the hyperviscosity exponent α through the momentum equation,

$$\frac{D\mathbf{u}}{Dt} + \nabla p = (-1)^{\alpha+1} \nu \nabla^{2\alpha} \mathbf{u} \quad (1)$$

The regular Navier-Stokes equations correspond to $\alpha = 1$. In spectral calculations, the dissipative term is obtained by multiplying the Fourier coefficients of the velocity by $|\mathbf{k}|^{2\alpha}$, and there is no reason to restrict α to be an integer although the physical representation of the dissipation operator may be complicated for non-integer exponents.

The first difficulty in analyzing hyperviscous turbulence simulations is to find reasonable scaling quantities. Since the inertial cascade mechanism is not expected to change, the Kolmogorov dimensional arguments should apply, and the inner microscale should depend only on the viscosity coefficient, ν , and of the dissipation,

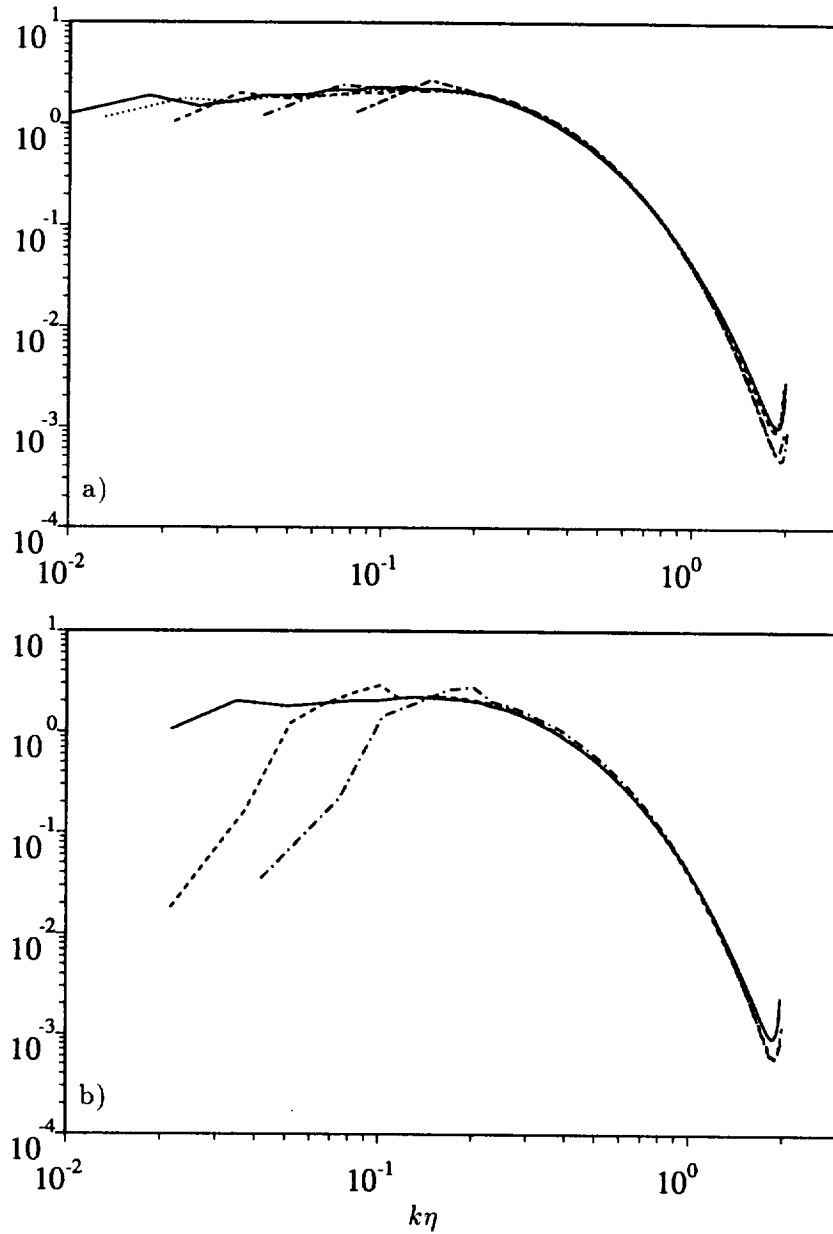


FIGURE 1. Three dimensional compensated energy spectra for the different viscous cases. Vertical axis is $\epsilon^{-2/3} k^{5/3} E(k)$ to enhance the inertial range. a) Forcing at low wavenumbers. — : $Re_\lambda = 168$; : 142; ---- : 94; - · - : 63; - - - : 36. b) Forcing at intermediate wavenumbers. ---- : $Re_\lambda = 48$; - · - : 26. — : $Re_\lambda = 94$ (from Fig. 1a, for comparison).

which is expressed in terms of the energy spectrum as

$$\epsilon = 2\nu \int k^{2\alpha} E(k) dk. \quad (2)$$

The inertial scaling is

$$E(k) = v^2 \eta f(k\eta),$$

where

$$v = (\epsilon\eta)^{1/3}, \quad \eta = (\nu^3/\epsilon)^{1/2(3\alpha-1)}. \quad (3)$$

Note that these definitions agree with the usual ones when $\alpha = 1$, but that ν should not be interpreted as a regular viscosity coefficient, even dimensionally.

There is no unique generalization for the Taylor microscale. In regular turbulence its most obvious use is in defining the microscale Reynolds number Re_λ , which is then related to the ratio of the different length scales as

$$L_\epsilon/\eta = 15^{-3/4} Re_\lambda^{3/2}, \quad \lambda/\eta = 15^{1/4} Re_\lambda^{1/2}, \quad (4)$$

where $L_\epsilon = u'^3/\epsilon$. If we take these two relations as defining λ and Re_λ , the result is

$$\lambda = \sqrt{15} (L_\epsilon \eta^2)^{1/3}, \quad Re_\lambda = 15^{(1-\alpha)/2\alpha} \left(\frac{u' \lambda^{2\alpha-1}}{\nu} \right)^{1/\alpha}, \quad (5)$$

which reduces to the usual one for regular viscosity.

The numerical experiments are listed in Table 2. All except one were conducted at the same numerical resolution, 128^3 and $k_{\max}\eta = 2$, and result in roughly similar Re_λ . A single case was repeated on a larger grid to check Reynolds number scaling. All the fields were forced at $|\mathbf{k}| \leq 2.5$ in the same way as in the viscous cases. One of the quantities listed in the table,

$$\epsilon^* = \epsilon/\nu^{1/\alpha} \omega'^{(3\alpha-1)/\alpha}$$

is a generalization of the equation $\epsilon/\nu\omega'^2 = 1$, which only holds for regular viscosity. The deviation of this coefficient away from unity measures the failure of the vorticity magnitude to represent dissipation in hyperviscous flows.

3.1 Numerics

There are special numerical problems associated with high hyperviscous exponents. The principal one is the limitation imposed to the time increment by the accuracy requirements of the dissipative term. Since most codes implement this substep by some unconditionally stable implicit scheme, the viscous parameter does not represent a stability limitation, but unless the time increment is chosen short enough, the evolution of the velocity due to dissipation will be represented inaccurately, and while the resulting system will usually be equivalent to some dissipative model, it would not be possible to claim that it represents a hyperviscosity of the intended order.

α	Re_λ	N	L_ϵ	L_ϵ/λ	L_ϵ/η	$\epsilon L/u^3$	ϵ^*	t/T	$-F_3$
1.	63	128	2.2	4.2	65	0.80	1.00	9.3	0.50
1.25	65	128	2.2	4.3	68	0.69	0.57	3.1	0.50
1.50	64	128	2.2	4.2	66	0.68	0.41	3.1	0.49
2.	68	128	2.4	4.5	73	0.66	0.27	3.4	0.49
2.50	68	128	2.5	4.5	74	0.65	0.21	9.5	0.49
4.	75	128	2.8	5.0	86	0.65	0.15	4.8	0.42
2.	95	256	2.0	6.3	121	0.84	0.28	1.5	0.52

TABLE 2. Numerical and flow parameters for the hyperviscous cases analyzed in this paper. The case $\alpha = 1$ is the same one described in Table 1, and is only included here for comparison. The quantity ϵ^* is defined in the text.

Consider a spectral code for the evolution equations (1). The accuracy and stability of the convective term is controlled by the usual CFL parameter, which is proportional to

$$c \sim u' k_{\max} \Delta t, \quad (6)$$

while that of the hyperviscous term is controlled by

$$\delta = \nu k_{\max}^{2\alpha} \Delta t. \quad (7)$$

In our code, which uses an integrating factor for the dissipative term (Rogallo 1981), the modes corresponding to k_{\max} are multiplied every time step by $\exp(-\delta)$, and the explicit integrator for the advection term assumes that this factor is close enough to unity for the accuracy of the nonlinear interactions not to be destroyed during the step. This requires that δ should not be too large. Other implicit schemes have different behaviors, but the accuracy requirement for the dissipative term is always that δ be at most $O(1)$.

The time increment Δt is usually adjusted by fixing the CFL, and the viscous parameter has to be measured. In our code, u' is given by the dissipation ϵ and by the form of the spectrum through the choice of the resolution parameter $k_{\max}\eta$. Assume that $\epsilon \sim u'^3/L \sim u'^3 k_0$, where k_0 is the center of our forcing band. It follows from our definition of the Kolmogorov scale that

$$u' \sim \nu \eta^{1-2\alpha} (k_0 \eta)^{-1/3}. \quad (8)$$

When Δt is obtained using this estimate in the CFL and is then substituted in δ , we obtain

$$\delta/c = \text{const.} (k_{\max}\eta)^{2\alpha-2/3} (k_0/k_{\max})^{1/3} \approx 1. \quad (9)$$

From our observations, the empirical constant is approximately 0.03.

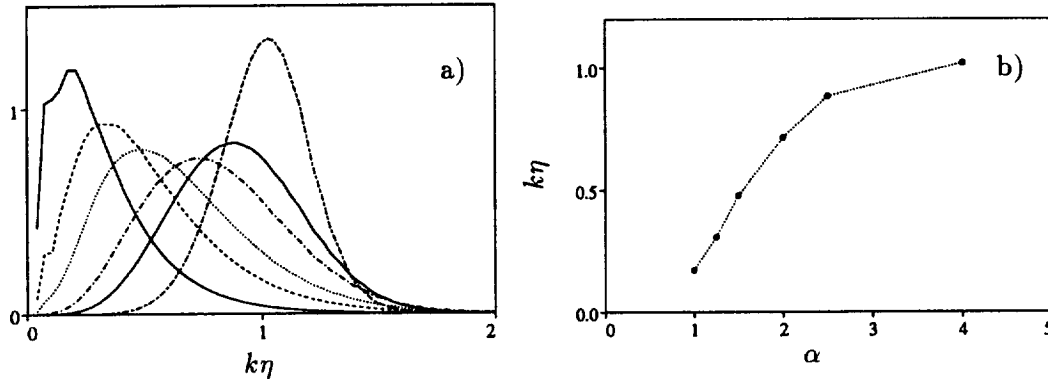


FIGURE 2. a) Dissipation spectra, $\epsilon^{-2/3}\eta^{-5/3}(k\eta)^{2\alpha}E(k)$, for different hyperviscosity exponents. From left to right: $\alpha = 1, 1.25, 1.5, 2.0, 2.5, 4.0$. b) Wavenumber of maximum dissipation.

Fig. 2a displays the hyperviscous dissipation spectra $k^{2\alpha}E(k)$, for various exponents, and Fig. 2b shows the position of the dissipation maximum for the different cases. It is clear from these figures that hyperviscosity succeeds in separating the forcing and dissipation ranges, even at moderate resolutions, although it will be seen below that this does not guarantee an inertial range in the usual sense. It is also clear that $k_{\max}\eta$ should be chosen somewhat larger than unity if the dissipative range is to be reasonably well represented, making the requirement expressed in Eq. (9) more restrictive as the hyperviscosity order increases. In practice, for our choice of $k_{\max}\eta = 2$ and for $k_0 = 2$, $k_{\max} = 60 - 120$ (128^3 or 256^3 grids), it limits our simulations to $\alpha \leq 4 - 5$.

3.2 The near dissipation spectrum

Compensated three-dimensional spectra for some of the hyperviscous fields are presented in Fig. 3a. There is no collapse in the dissipative range, and the qualitative shape of the spectra changes drastically as a function of the hyperviscosity exponent although it should be noted that the two spectra corresponding to the same exponent, $\alpha = 2$, collapse well. As the exponent increases, a large ‘‘bump’’ appears in the near-dissipation range that for the highest exponents and at these low Reynolds numbers, dominates the spectrum. In Fig. 3b, in which the spectrum is premultiplied by k , the bump is seen to behave approximately as k^{-1} .

Anomalous bumps in this region of the spectrum have been reported in experimental viscous flows (Mestayer 1982, She & Jackson 1993, Saddoughi & Veeravalli 1994), and the k^{-1} behavior was claimed by the second of these groups. A theoretical explanation for this power law, based on the depletion of nonlinearity in the near dissipation scales, was offered in (Yakhot & Sakharov 1993). An older explanation for the presence of the bump, although not for the power behavior, is that the outgoing energy cascade is inhibited in the dissipation range since energy has to move into spectral triads with much smaller amplitudes than those corresponding to the equilibrium $k^{-5/3}$ spectrum while the incoming energy is not subject to that

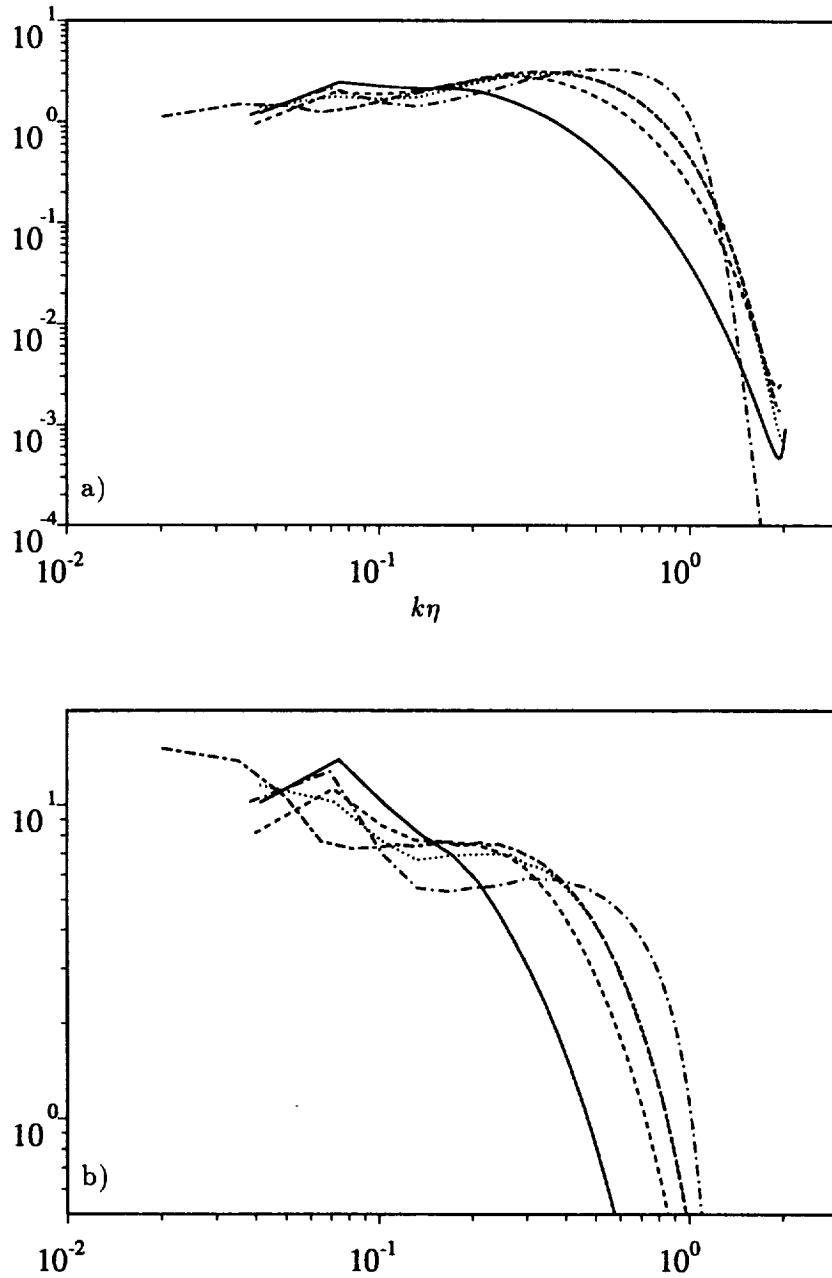


FIGURE 3. Three-dimensional energy spectra for different hyperviscosity exponents. a) $\epsilon^{-2/3} k^{5/3} E(k)$, to enhance inertial range. b) $(\epsilon\eta)^{-2/3} k E(k)$, to enhance the near dissipation bump. — : $\alpha = 1$; ---- : 1.5; : 2.0; —·— : 4.0. All at 128^3 resolution. —·— curve: $\alpha = 2.0$, 256^3 . This curve overlaps the dotted one in the dissipation range.

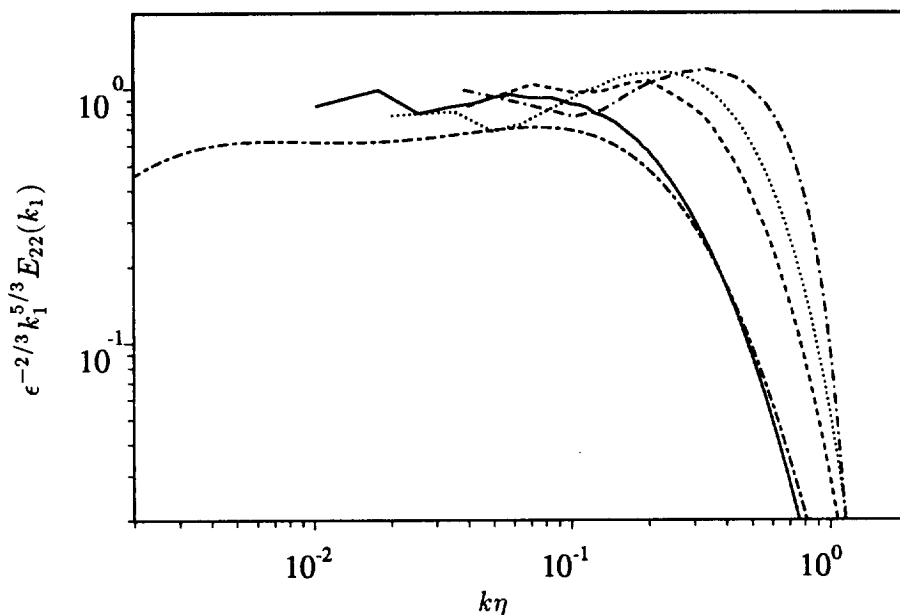


FIGURE 4. Compensated transverse spectra showing extent of near dissipation bump. — : $Re_\lambda = 168$, $\alpha = 1$; dashed: $Re_\lambda = 64$, $\alpha = 1.5$; : $Re_\lambda = 96$, $\alpha = 2$; - · - : $Re_\lambda = 64$, $\alpha = 4$; --- : $Re_\lambda = 600$, $\alpha = 1$, after (Saddoughi & Veeravalli 1994). The peak in the lowest wave numbers of all the numerical spectra is spurious due to forcing scheme.

inhibition. The bump is a consequence of the resulting energy “bottleneck” in the cross-over region (Falkovich 1994). The latter author has described the same spectral behavior in wave turbulence (Ryzhenkova & Falkovich 1990) and has remarked that it would become more pronounced in hyperviscous simulations as the damping becomes more abrupt. The effect is present in spectral turbulence models and has been observed in EDQNM based simulations (Mestayer, Chollet & Lesieur 1983). Finally, some recent hyperviscous simulations of isotropic turbulence, using $\alpha = 8$, have also reported the presence of a k^{-1} bump (Borue & Orszag 1994).

Since it is known that the near dissipation region contains strong vortex filaments, they may also provide an explanation for the k^{-1} behavior. That randomly oriented vortex filaments would generate a spectrum with this behavior was first noted by Townsend (1951) and observed directly in JWSR by computing the spectrum of a flow in which all the vorticity, except the one contained in the strong filaments, had been zeroed. Moreover, an (inviscid) infinite vortex filament is an equilibrium solution of the Euler equation for which, by definition, all the nonlinear interactions cancel identically, and for which the turbulent cascade is fully absent, even if the filament itself is usually formed by the cascade mechanism of vortex stretching. In this sense the three explanations are not necessarily incompatible, and the filament hypothesis merely points to a possible physical implementation of the two previous

ideas.

However, it will be shown below that in the course of the present investigation, we were not able to find significant differences between the structure or frequency of filaments in viscous and hyperviscous flows, which may explain the presence of stronger bumps in the latter. As a consequence the filament explanation remains unlikely. Also, our observations cast doubts on the -1 exponent as a preferred spectral law.

In Fig. 4 we present transverse compensated spectra from several simulations, including our highest Reynolds number regular viscosity case, together with an experimental spectrum from (Saddoughi & Veeravalli 1994). The bump is clearly seen in the experimental spectrum and, in retrospect, also in the regular viscous simulation, showing that even the highest Reynolds number computed by us is far from containing a true inertial range.

Figs. 5a-b display the local logarithmic slope, $d(\log E)/d(\log k)$, for the different spectra in the near dissipation region. They also include data from (Saddoughi & Veeravalli 1994) although in this case, to make it comparable to ours, it is in the form of a three-dimensional spectrum obtained from their data for E_{11} , using the assumption of isotropy. Fig. 5a, for the regular viscous cases, reinforces the conclusion that all our simulations are far from the real inertial range. Fig. 5b, which contains the hyperviscous cases, shows a steady climb of the least negative slope with increasing α with no sign of saturating at k^{-1} . Moreover, the two Reynolds numbers at $\alpha = 2$ show the same tendency as the regular viscous cases with the spectral hump extending further into the low wavenumber range, suggesting that these simulations are also far from reaching a true inertial range and that the extent of the bottleneck region is not shortened by the sharpening of the dissipation peak.

4. Velocity gradients

It has been known for a long time that the probability density functions for velocity differences become increasingly non-Gaussian at short distances, and that this leads to highly intermittent behavior of the velocity gradients, which becomes more pronounced at high Reynolds numbers. In JWSR we presented histograms for different combinations of gradients (vorticity and total strain magnitudes and local stretching, $\sigma = \omega S\omega/\omega^2$), which clearly showed this Reynolds number effect. A compact representation of this departure from Gaussianity is provided by the high order flatness and skewness $F_n(\zeta) = \langle \zeta^n \rangle / \langle \zeta^2 \rangle^{n/2}$, two of which are given in Fig. 6 for the viscous and hyperviscous cases. In each case the vertical origin of coordinates has been chosen to coincide with the Gaussian value ($F_4 = 3$, $F_6 = 15$). The tendency for both flatnesses to grow with Reynolds number is clear, as is the fact that the simulations forced at intermediate wave numbers do not differ significantly in this respect from those forced at low wave numbers. The values for the fourth order flatness of the longitudinal gradients agrees well with the compilation in (Van Atta & Antonia 1980) although our experiments cover a much narrower range of Reynolds numbers than theirs.

The variation of the flatness with the hyperviscosity exponent (Fig. 6b) is more

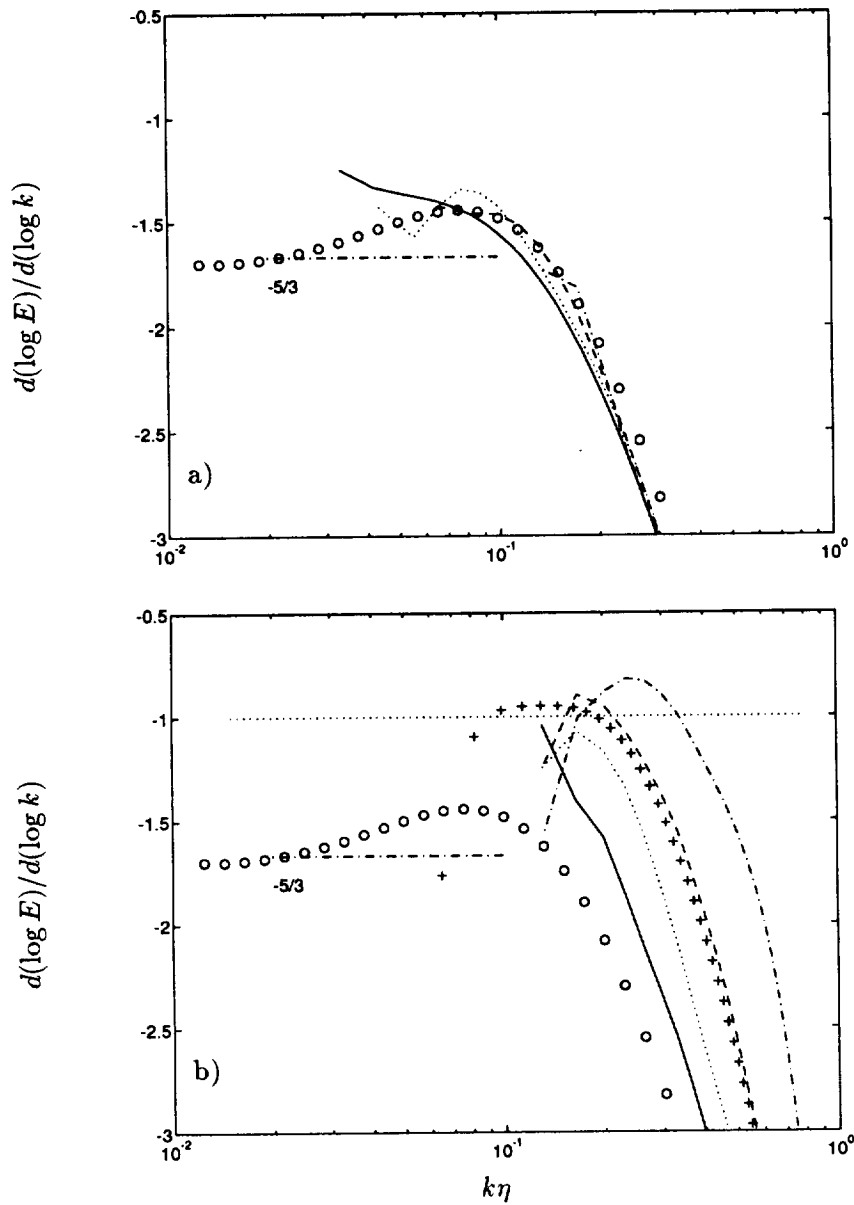


FIGURE 5. Logarithmic slope for the different three-dimensional energy spectra, in the near dissipation region. a) Regular viscosity. — : $Re_\lambda = 168$; : 141; ---- : 98; -·-· : 65. b) Hyperviscosity. — : $\alpha = 1.25$; : 1.5; ---- : 2. ($Re_\lambda = 68$); +: 2. ($Re_\lambda = 94$); -·-· : $\alpha = 4$. In both figures, open circles are experimental data from (Saddoughi & Veeravalli 1994) at $Re_\lambda = 600$.

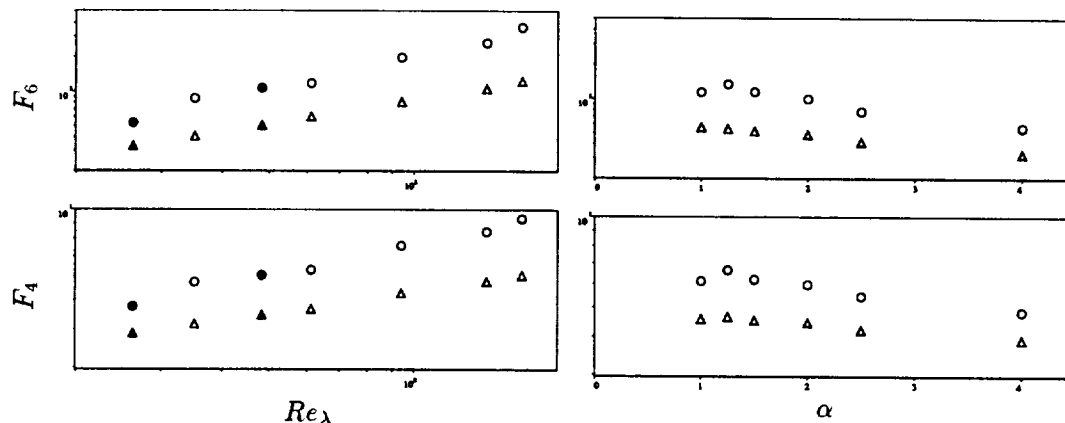


FIGURE 6. Fourth and sixth order flatness factors for velocity gradients. (a) Viscous simulations vs. Reynolds number. (b) Hyperviscous simulations vs. exponent; $Re_\lambda \approx 65$. \triangle : longitudinal gradients, $\partial u/\partial x$. \circ : transverse, $\partial u/\partial y$. Open symbols are flows forced at low wave numbers. Closed symbols are forced at intermediate wave numbers.

surprising. While it seems from table 2 that the equivalent Reynolds number increases slightly with increasing α and while the same conclusion could be reached from the increasing separation between the integral scales and the dissipation peak (Fig. 2a), the flatness is seen to decrease with α . The same behavior is observed in the histograms of almost all the gradient quantities, as can be seen for the vorticity magnitude in Fig. 7a. The exception is the stretching histogram (Fig. 7b) which shows a much weaker variation with α , essentially within the statistical uncertainty.

It should be stressed that the variation of the flatness with Re_λ is similar in the hyperviscous flows at constant α and in the viscous ones. This is clear from table 3, which contains flatness for the two Re_λ available at $\alpha = 2$. There is also a consistent, although much weaker, increase in the skewness, F_3 , with Re_λ which can be seen from tables 1 and 2, and which is also in general agreement with the data in (Van Atta & Antonia 1980).

5. Worms

An algorithm was developed in JWSR to track individual filaments and to measure their properties. The same algorithm has been used here to analyze the new flow fields and to obtain data which may be useful in understanding their dynamics. The axis of each filament is followed until some arbitrary definition of its end point is reached and the vortex radius, circulation, peak axial vorticity, and axial stretching are measured at each point and used to compile statistics over the fraction of the flow contained in the worms.

The axial stretching is defined as $n_i S_{ij} n_j$, where S_{ij} is the strain tensor and n_i is the unit vector in the direction of the axis. The condition to end a filament was

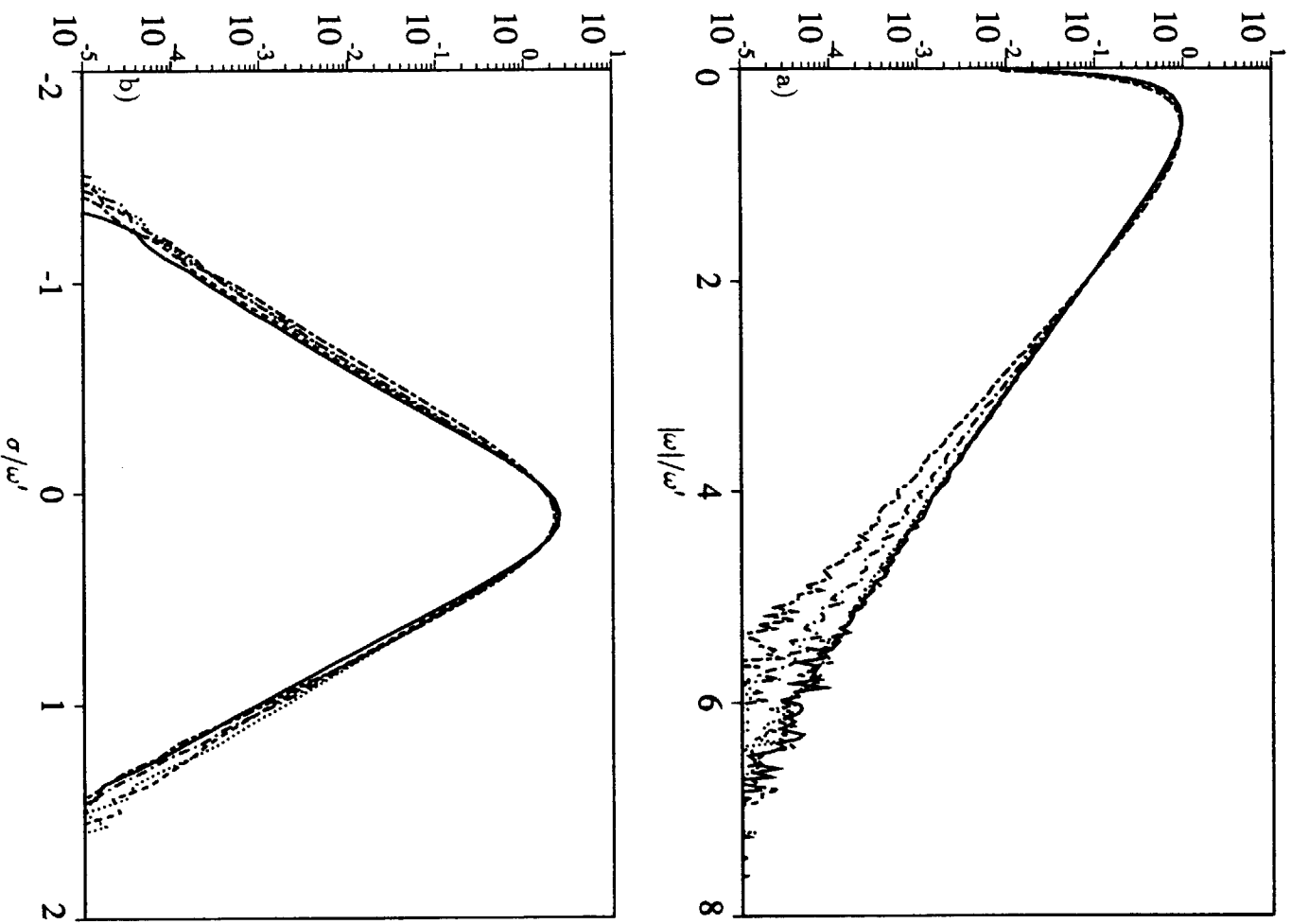


FIGURE 7. Probability density functions of (a) Vorticity. (b) Stretching rate. In all cases $Re_\lambda \approx 65$. — : $\alpha = 1$; - - - : 1.5; - · - · : 2; ····· : 2.5; — — — : 4.

Re_λ	F_{4t}	F_{4t}	F_{6t}	F_{6t}
68	4.5	5.9	49	100
95	4.8	6.5	62	131

TABLE 3. Flatness factor for the two hyperviscous cases with $\alpha = 2$. Subscript ℓ refers to longitudinal gradients, t to transverse ones.

described in detail in JWSR but depends essentially on the axial vorticity weakening below a given level.

The simplest statistic is the mean value of a given property over all the axial points of all the worms detected in a given flow. There are two groups of properties. Since filaments have to be formed by stretching of preexisting vorticity, the axial stretching can be considered as the driving force in the formation of the worms while all the other properties can be considered as the results of that forcing.

Both groups behave differently. The mean value of axial stretching, averaged over the axes of the worms, is shown in Fig. 8 normalized with the rms value of the vorticity over the whole flow, which is the natural scaling for the velocity gradients in the bulk of the flow. Except for a slight tendency to grow with Re_λ , the stretching scales well with ω' although the proportionality constant depends on the hyperviscosity exponent. It was shown in JWSR that the average stretching, conditioned on a given vorticity, depends only weakly on the conditioning value, and this was interpreted as an indication that the filament did not stretch itself appreciably. The present result reinforced that conclusion since it will be seen below that the mean vorticity in the worms is a fairly strong function of Re_λ while we have shown that the stretching is not.

This is further confirmed by Figs. 9 and 10, which show correlation functions and lengths for the axial distribution of the stretching along worms. The correlation length is a useful indication of the typical length scale of a given property, and we use it here as a less subjective indication of length than the one used in JWSR, which was based on the total length of the detected worms.

Consider a quantity, $\zeta(s)$, given as a function of arc length along the axis and assumed to have zero mean value, and define the correlation

$$R(s) = \langle \zeta(s')\zeta(s'+s) \rangle / \langle \zeta^2 \rangle, \quad (10)$$

where the average is taken over the axial position s' . This function has zero integral and $R(0) = 1$. It will first become negative at some point $s = s_0$ (Fig. 9). We define the correlation length as

$$\ell_\zeta = \int_0^{s_0} sR(s) ds / \int_0^{s_0} R(s) ds. \quad (11)$$

The same definition can be used on properties which are defined at all points in the flow for which the arc length s has to be substituted by a coordinate distance

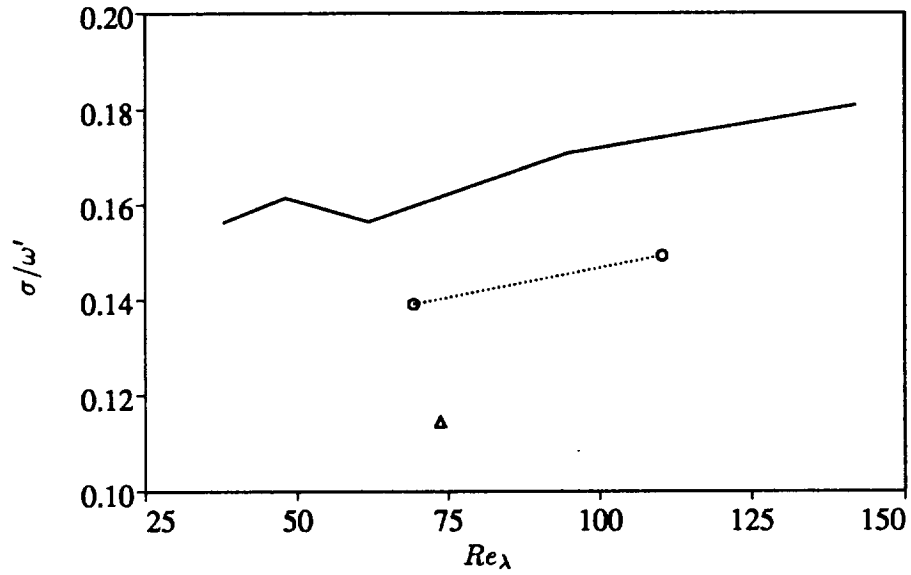


FIGURE 8. Average axial stretching along filament axes. — : viscous flows; o : $\alpha = 2$; Δ : $\alpha = 4$.

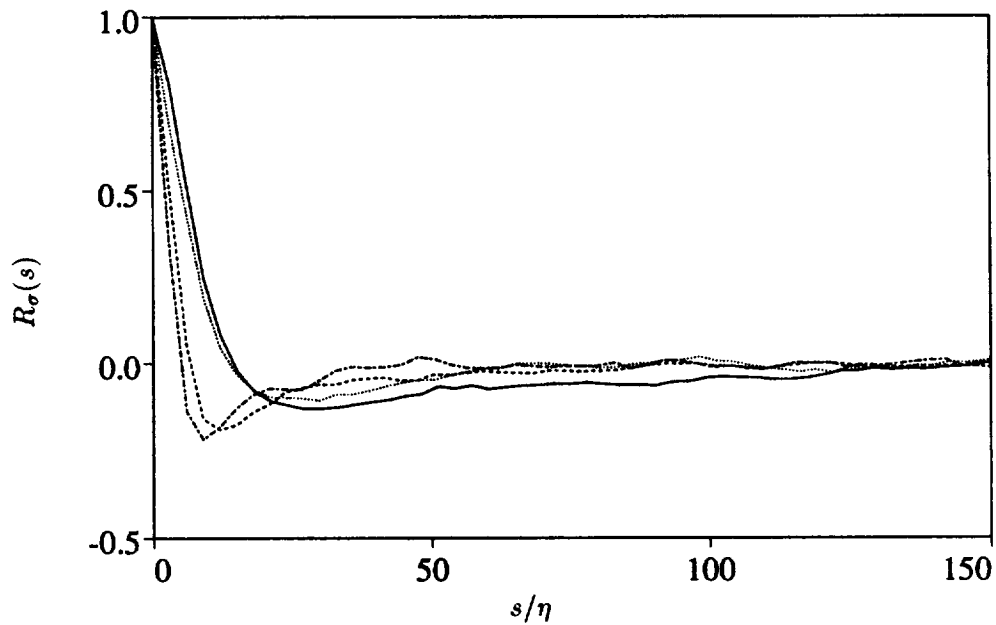


FIGURE 9. Correlation functions of axial stretching, against of the arc length along the worm axes. — : $\alpha = 1$, $Re_\lambda = 63$; : $Re_\lambda = 142$; ---- : $\alpha = 2$, $Re_\lambda = 68$; --- : $\alpha = 4$.

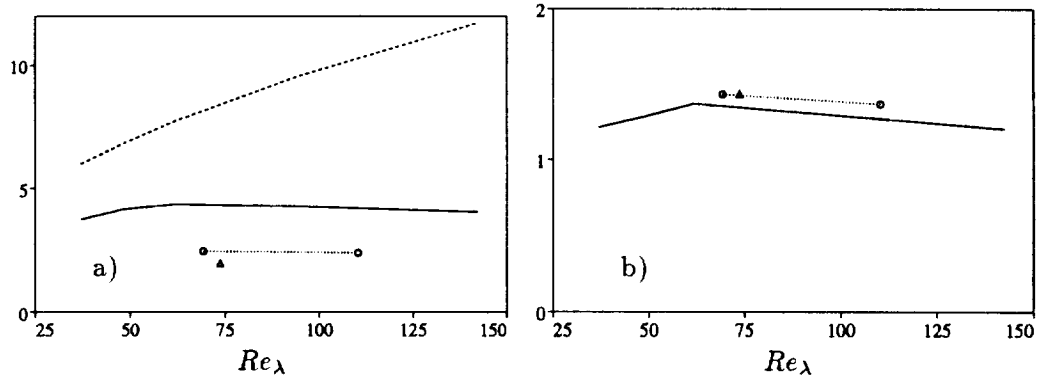


FIGURE 10. Axial correlation length of the stretching along the filament axes. (a) Normalized with the Kolmogorov length. (b) Normalized with the correlation length of longitudinal gradients over the whole flow. Symbols as in Fig. 8. The dashed line in (a) is the Taylor microscale, for comparison.

(e.g. x). This global correlation function can be computed as the inverse Fourier transform of the one-dimensional spectrum of the quantity (Batchelor 1953). From that, and since the power spectrum of the velocity gradients has its maximum at the near dissipation region, it follows that the correlation lengths for gradients when averaged over the whole flow should scale with η .

Fig. 10a shows the correlation length for the stretching along the worms, ℓ_σ , which scales well with η , although the scaling constant depends again on the hyperviscosity exponent. This is not surprising since we have shown that the shape of the near dissipation spectra depends on α and so does presumably the relation between the size of the gradient eddies and η . In Fig. 10b we show ℓ_σ normalized with the correlation length of the longitudinal gradients $\partial u/\partial x$ taken over the whole flow. Most of the dependence with α disappears, and the ratio is close to one, showing once again that the stretching along the worms is essentially indistinguishable from that at a generic point in the flow and that self stretching is not important.

It is therefore surprising that the axial correlation lengths of all the resulting worm properties are much larger than η and scale apparently on the integral scale of the flow (Fig. 11). This generalizes the observation in JWSR, which has been made by all the investigators that have studied these filaments, that their length is of the order of the integral scale. While the original observations were made on the basis of arbitrary visualization or termination criteria, the present result is a more objective characterization of the same phenomenon. In these last two figures we have included a curve for the Taylor microscale λ which is defined by Eq. (4). This is done mainly for comparison, but also because this scale has been suggested often as a natural scale for the turbulent eddies. In particular, it was observed in JWSR that if the characteristic stretching along worms was of $O(\omega')$ and since it is known that the velocity differences in a turbulent flow scale with u' without strong Reynolds number effects, the largest possible length scale for the stretching was $O(\omega'/u') = O(\lambda)$. It was felt at the time that this contradicted the observation

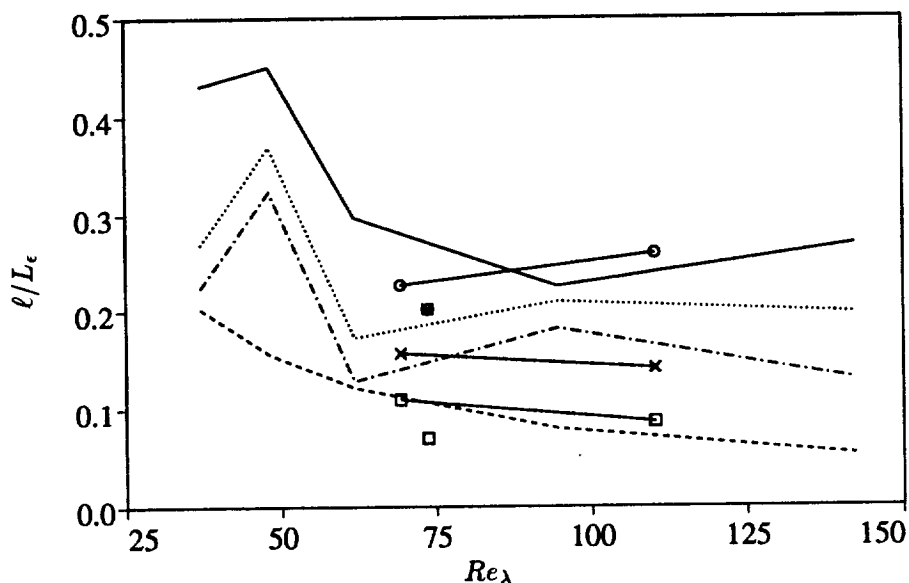


FIGURE 11. Axial correlation lengths along worms axes, normalized of the dissipation length L_ϵ . — and \circ : axial vorticity at axis; and \times : circulation; --- and \square : radius. Lines without symbols are viscous simulations. Lines with symbols are $\alpha = 2$. Isolated symbols are $\alpha = 4$.

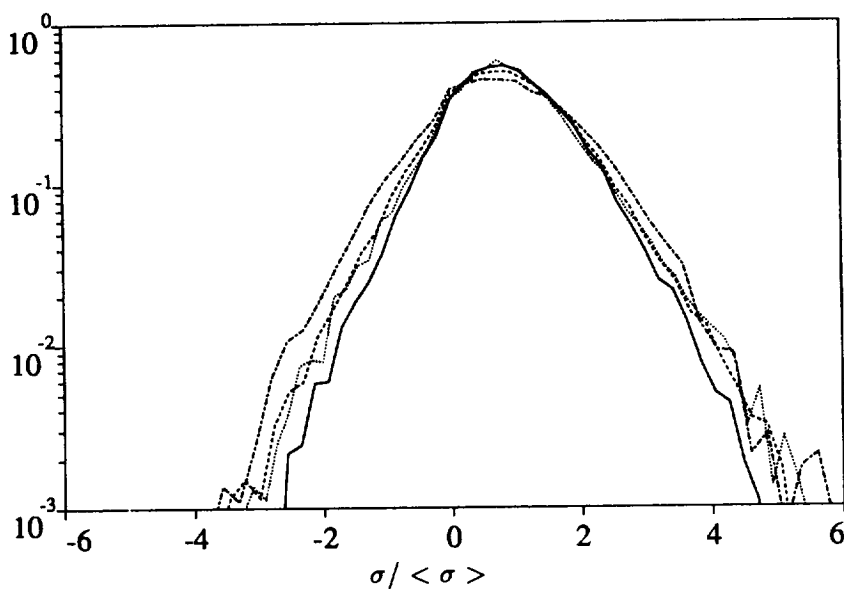


FIGURE 12. Probability density function for the stretching σ along the axes of the worms. Symbols as in Fig. 9. All histograms are normalized to unit mean value.

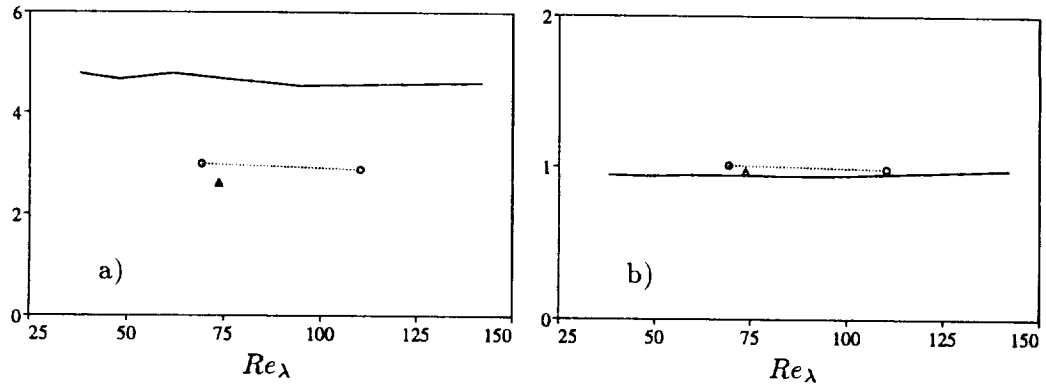


FIGURE 13. Mean worm radius. (a) Normalized with the Kolmogorov length. (b) Normalized with Burgers' radius for the average axial strain. Symbols as in Fig. 8.

that the length of the worms was $O(L_\epsilon)$ since it was assumed that vortices could only survive if stretched on the average. This proved to be false, and it was shown in (Jiménez & Wray 1994) that the strain along the worms is compressive over a large fraction of the axis (Fig. 12). Verzicco, Jiménez and Orlandi (1994) have shown recently by direct computation that vortices subject to spatially nonuniform axial strain, even one with zero axial average stretching, can reach a steady state thanks to the presence of axial inertial waves which "smooth" the strain over the compressive parts.

It is still interesting to note that although the L_ϵ scaling seems to be a better representation of the data in Fig. 11, especially at the higher Re_λ , a scaling of a few Taylor microscales is not completely incompatible with them.

In (Jiménez & Wray 1994) the equivalent to Fig. 12 was plotted together with probability density functions of the same quantity computed over the whole flow field. The differences between the two were shown to be small, stressing again that the forcing of the filaments is not different from that of the rest of the flow. Note however that the collapse of the stretching pdf's over the full field for different values of α (Fig. 7b) is better than those of the same quantity over the worms (Fig. 12), suggesting either that there is a selection mechanism for the location of worms in terms of stretching or a dynamical feedback from the worms into the structure of the stretching itself. The same conclusion can be drawn from the dependence of the average worm stretching on α , shown in Fig. 10.

The average radius of the worms is given in Fig. 13a. It scales with the Kolmogorov scale although there is again a different proportionality constant for different hyperviscosity exponents. A better collapse is possible if we assume that the filaments are Burgers' vortices driven by the mean axial strain. For viscous flows, the Burgers' radius due to a strain ω' is $2(\nu/\omega')^{1/2} = 2\eta$, which agrees with the approximate Kolmogorov scaling for these flows in Fig. 13a.

Hyperviscous Burgers' vortices were computed in (Jiménez 1994a). Although their outer tails are different from the viscous ones and actually change sign before

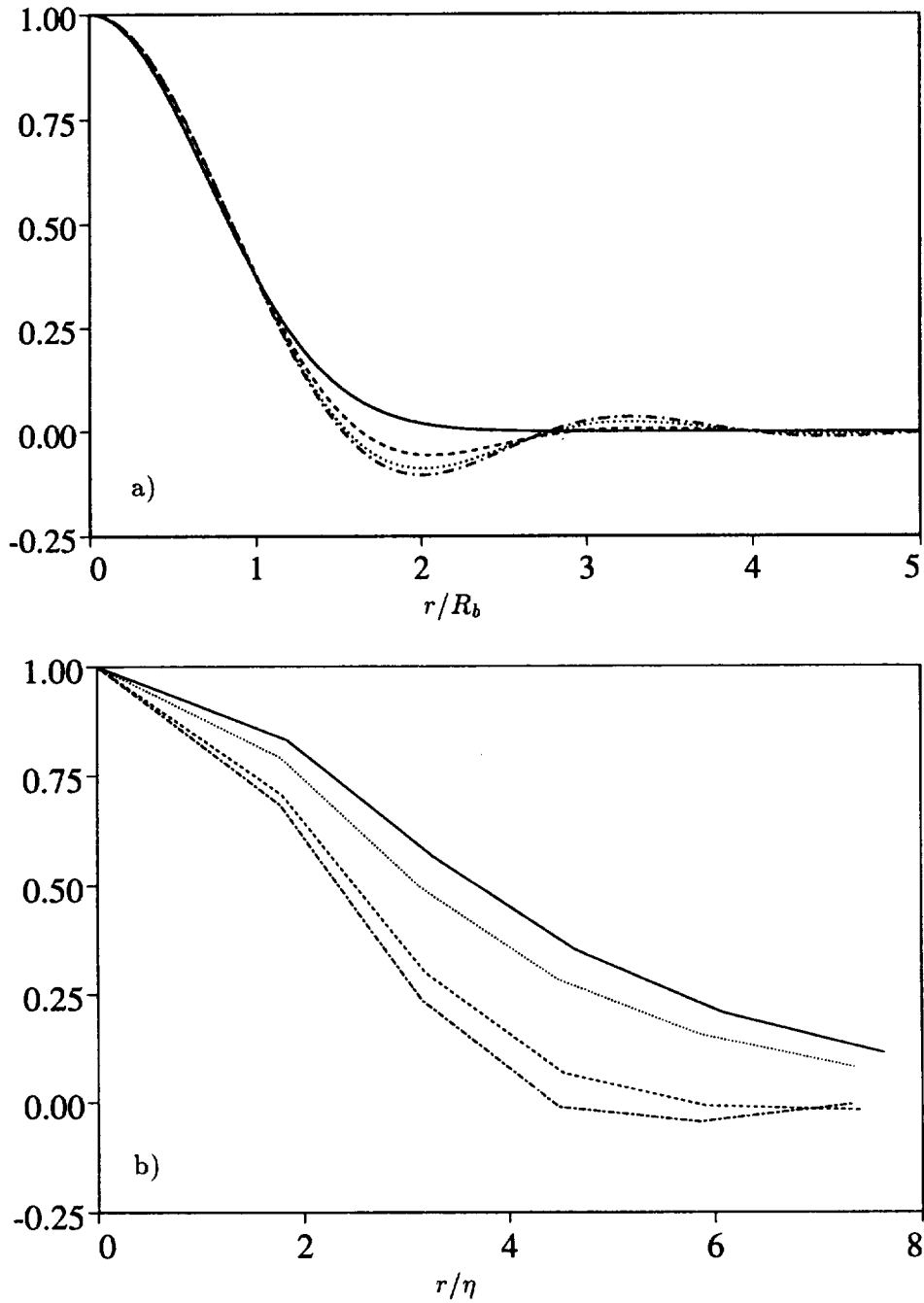


FIGURE 14. (a) Radial vorticity distribution for hyperviscous Burgers' vortices, normalized using Eq. (12). — : $\alpha = 1$; - - - : 2; ····· : 3; — · — : 4. (adapted from Jiménez 1994a). (b) Mean radial distribution of axial vorticity in worms. Symbols as in Fig. 9.

they settle to zero, their cores are approximately Gaussian (Fig. 14a) with a $1/e$ radius which can be approximated for $\alpha \leq 5$ by

$$R_b = (2.022 - 0.0843\alpha + 0.0688\alpha^2 - 0.0086\alpha^3)(\nu/\sigma)^{1/2\alpha}, \quad (12)$$

where the coefficient is the result of a polynomial fit to the solution of an ordinary differential equation. When this formula is used to compute the Burgers' radius associated to the measured mean stretching from Fig. 8, the results are the normalized radii in Fig. 13b, in which the effect of hyperviscosity is essentially absent.

Fig. 14.b contains vorticity profiles averaged along the axes of all the worms in a given flow. The profiles are also approximately Gaussian, and it is interesting to note that the more hyperviscous profiles show signs of negative vorticity at the edges, which may be a reflection of the oscillations in the tails of the theoretical solutions.

Full probability density functions for the local radius and for the radius divided by the *local* Burgers' radius are given in Fig. 15. To avoid effects related to the variations of the mean values, the averages of all those distributions are adjusted to unity. The collapse of the Burgers' plot is excellent, but there is some differences between the pdf's of the raw radii in viscous and in hyperviscous flows, probably reflecting the differences in the structure of the local stretching that were discussed above.

The mean values of the vorticity at the axes of the worms are given in Fig. 16a. It was suggested in JWSR that ω/ω' increases with Reynolds number as $Re_\lambda^{1/2}$ and that same normalization is used in the figure. Except for the case at $Re_\lambda = 48$ in which the forcing was done at higher wave numbers, it seems to work correctly. The intermediate forcing seems to work differently from all the other flows for all quantities which scale with the integral length as can also be observed in Fig. 11. The large scales are different from those of the flows forced at lower wave numbers, and it appears that the axial distribution of vorticity in the worms is controlled by them. A line corresponding to $\omega \sim \omega'$ is also included in the figure and is incompatible with the data. In Fig. 16b we have represented the mean value of the vortex circulation, normalized with the mean vorticity and radius for each flow. It clusters around unity in what is essentially a consistency check for the averages, but which also reflects that the statistical distribution of vorticity and radius are relatively independent of the dissipation model. A few representative pdf's are given in Fig. 17, normalized to unit mean. The sharp cut-off of the vorticity pdf is artificial. The tracking algorithm terminates a worm whenever its axial vorticity falls below ω' .

It is finally interesting to enquire which is the relative importance of worms with respect to the bulk of the flow. This is largely a matter of definition, but a volume fraction can be defined by taking the mean vorticity detected at the axes by our algorithm and defining as worms all the points whose vorticity magnitude is above that threshold. This, although arbitrary, seems justified since it appears from Fig. 17a that our threshold is below the maximum of the distribution and is probably not distorting the mean value too much. When this is done, a volume fraction can

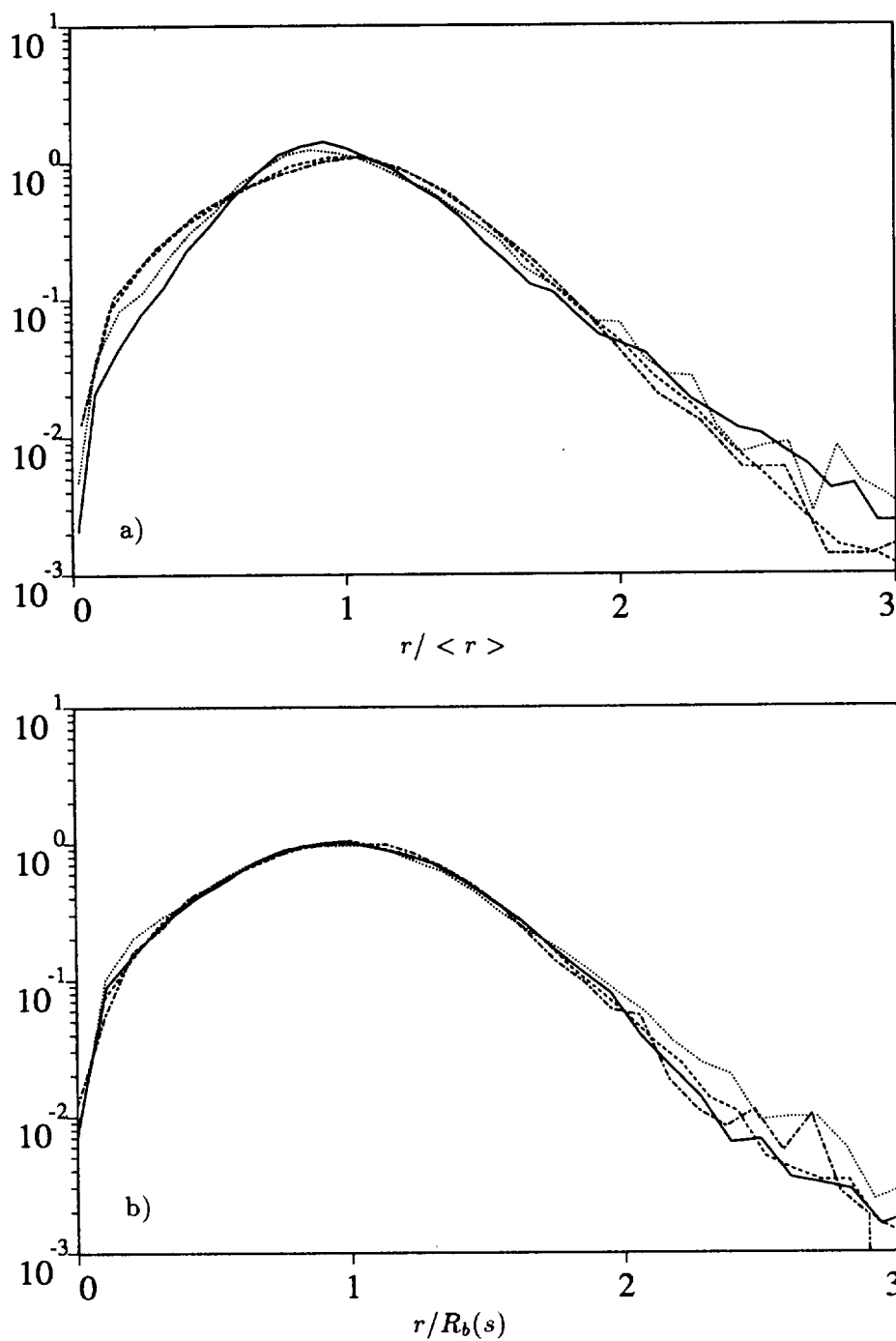


FIGURE 15. Probability density functions for the radius of worms, adjusted in each case to unit average. (a) Radius. (b) Radius divided by local Burgers' radius. Symbols as in Fig. 9.

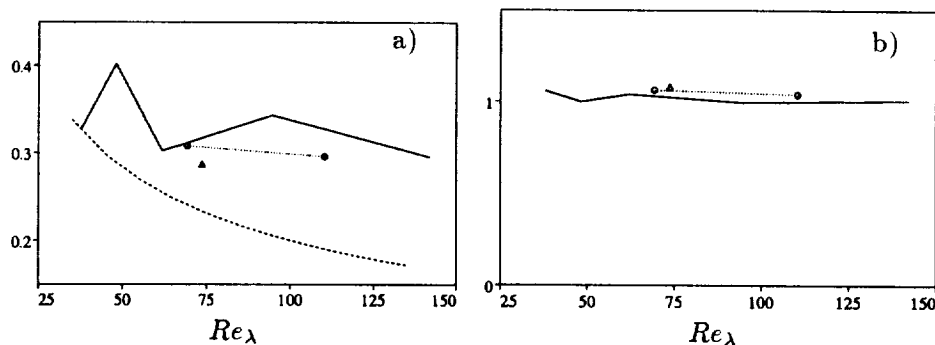


FIGURE 16. (a) Mean vorticity along worm axes, normalized with $\omega' Re_\lambda^{1/2}$. Symbols as in Fig. 8. Dashed line corresponds to $\omega \sim \omega'$, without Reynolds number dependence. (b) Mean value of filament circulation, normalized with mean vorticity and vortex radius, $\langle \gamma \rangle / \pi \langle \omega \rangle \langle r \rangle^2$.

be read from the vorticity histogram of the flow (Fig. 7a) and is represented in Fig. 18. The volume occupied by the worms decreases with Reynolds number as Re_λ^{-2} . Since their characteristic vorticity increases only with $Re_\lambda^{1/2}$, this implies that not only the volume, but also the enstrophy contained in them decreases rapidly as the Reynolds number increases.

6. Conclusions and future work

We have shown that the vortex strong filaments in isotropic turbulence have lengths and axial correlation lengths of the order of the integral scale of the flow, even if the stretching along their axes has a spatial scale of the order of the Kolmogorov length and seems essentially indistinguishable from the strain in the bulk of the flow. We have also shown that the average radius of the vortices is very close to the Burgers' radius corresponding to the mean axial strain, even if large segments of the axes are actually under compression. We have suggested that this is accomplished through the action of axial waves, which distribute the effective strain along the axes. All these observations hold for hyperviscous flows with the obvious modifications needed to accommodate the different core structure of the vortices.

We can think of few mechanisms to generate coherent vortices of such lengths in turbulent flows. The obvious one, in which vortices form by roll-up of the large scale vorticity layers in between large eddies, is unlikely because it can readily be shown that the large-scale stretching is at most able to collapse vortices to radii of the order of the Taylor microscale, and it is difficult to think of a way in which straining motions of the observed scales, η , could further collapse these cores, much thicker than themselves, into more compact cores.

Another possibility, and the one that we favor at the moment, is a mechanism by which short vortex "sticks" form individually and are later patched by the axial waves into longer units. This mechanism has been demonstrated in simpler situations in (Verzicco, Jiménez and Orlandi 1994). Note that from Figs. 10 and 11, the

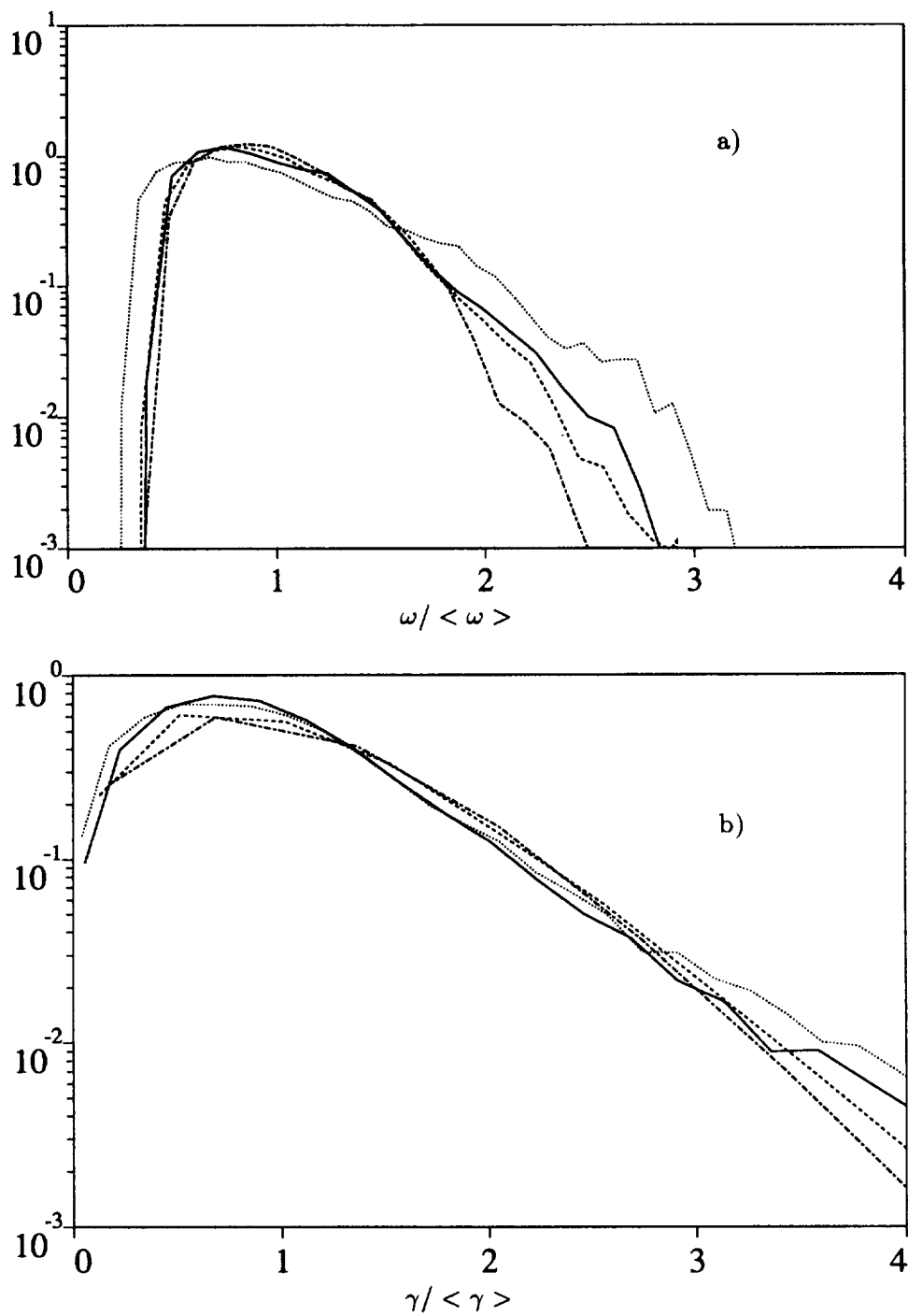


FIGURE 17. Probability density functions for (a) vorticity at worm axis. (b) Circulation, adjusted in each case to unit average. Symbols as in Fig. 9.

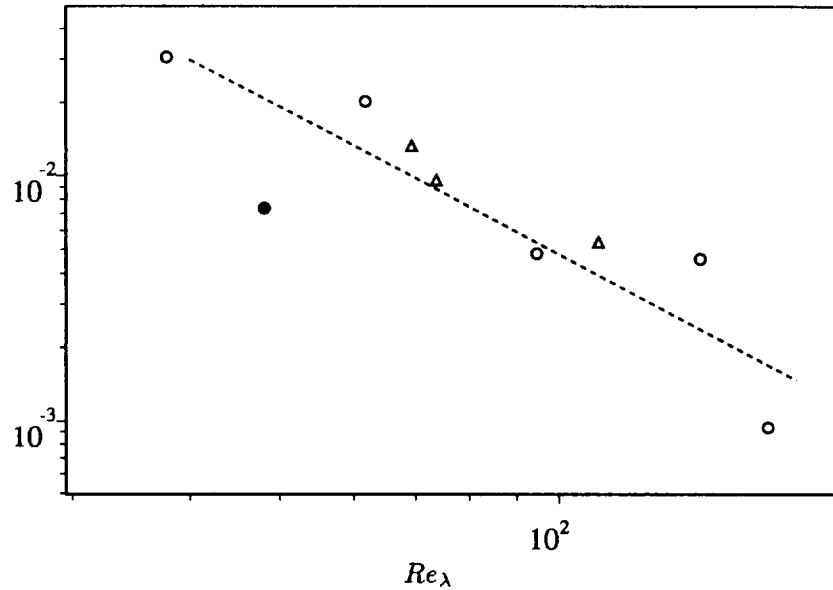


FIGURE 18. Volume fraction occupied by vorticity above the average detected in worms. \circ : viscous simulations, low wave number forcing; \bullet : viscous, middle wave number forcing; \triangle : hyperviscous; dashed line has slope -2.

elongation of the worms, $\ell_r / \langle r \rangle$, although large and increasing with Re_λ , never exceeds 10–20 in our range of Reynolds numbers.

A remaining problem is the growth of the circulation of the vortices with Re_λ . It was noted in JWSR that this implies an increase of the Reynolds number of the azimuthal motion of the individual structures and that at some point those structures should become unstable. We still feel that way, but we have no way of predicting the conditions for this instability.

We have also shown that the volume fraction occupied by worms decreases as Re_λ^{-2} . This is somewhat misleading and should be understood in relation to the decrease of their radii. If we remember that $\eta \sim Re_\lambda^{-3/2}$, it follows that the accumulated length of the structures grows like $L_\epsilon Re_\lambda$, and their total “number” per unit volume, as Re_λ . This is difficult to reconcile with their increasing instability as their Reynolds number increases. It has been proposed recently that an internal structural transition might exist in turbulence at $Re_\lambda \approx 10^3$, resulting in a decrease of intermittency (Tabeling *et al.* 1994). If this is confirmed, it could possibly resolve the present dilemma.

Finally, we have described the effect of hyperviscosity in isotropic simulations. The resulting spectra are dominated by large humps in the near dissipation region, which extend to the last wave number decade of the inertial range. They seem to be generated by the energy “bottleneck” produced by the inhibition of the energy cascade by viscosity.

Acknowledgments

The simulations were carried out on the Intel hypercube at NASA Ames Research Center and on the Intel Paragon at Wright Patterson AFB. The assistance of these computer centers' personnel is also gratefully acknowledged.

REFERENCES

- BATCHELOR, G. K. 1953 *The theory of homogeneous turbulence*. Cambridge Univ. Press.
- BORUE, V. & ORSZAG, S. A. 1994 Forced three-dimensional homogeneous turbulence with hyperviscosity. Preprint.
- FALKOVICH, G. 1994 Bottleneck phenomenon in developed turbulence. *Phys. Fluids*, **6**, 1411-1414.
- JIMÉNEZ, J. 1994a Hyperviscous vortices. *J. Fluid Mech.* **279**, 169-176.
- JIMÉNEZ J. 1994b Resolution requirements in turbulence. *CTR Annual Res. Briefs*
- JIMÉNEZ, J. & WRAY, A. A. 1994 Columnar vortices in isotropic turbulence. *Meccanica*. to appear.
- JIMÉNEZ, J., WRAY, A. A., SAFFMAN, P. G. & ROGALLO, R. S. 1993 The structure of intense vorticity in isotropic turbulence. *J. Fluid Mech.* **255**, 65-90.
- MESTAYER, P. 1982 Local isotropy and anisotropy in a high-Reynolds-number turbulent boundary layer. *J. Fluid Mech.* **125**, 475-503.
- MESTAYER, P., CHOLLET, J. P. & LESIEUR, M. 1983 Inertial subrange of velocity and scalar variance spectra in high-Reynolds-number three-dimensional turbulence, in *Turbulence and chaotic phenomena in fluids* (T. Tatsumi, ed.), 285-.
- ROGALLO, R. S. 1981 Numerical experiments in homogeneous turbulence. *NASA Tech. Mem.* **81315**, see also Canuto, C., Hussaini, M. Y., Quarteroni, A. and Zang, T. A., *Spectral methods in fluid dynamics*. Springer (1981), pp. 85-86.
- RYZHENKOVA, I. V. & FALKOVICH, G. E. 1990 Effect of dissipation on the structure of a stationary wave turbulence spectrum. *Sov. Phys. JETP*. **71**, 1085-1090.
- SADDOUGHI, S. G. & VEERAVALLI, S. V. 1994 Local isotropy in turbulent boundary layers at high Reynolds number. *J. Fluid Mech.* **268**, 333-372.
- SHE, Z-S. & JACKSON, E. 1993 On the universal form of the energy spectrum in fully developed turbulence. *Phys. Fluids A*, **5**, 1526-1528.
- TABELING, P., ZOCCHI, G., BELIN, F., MAURER, J. & WILLAIME, H. 1994 Probability density functions, skewness and flatness in large Reynolds number turbulence. Preprint.
- TOWNSEND, A. A. 1951 On the fine scale structure of turbulence. *Proc. Roy. Soc. London*. **A 208**, 534-542.

- VAN ATTA, C. W. & ANTONIA, R. A. 1980 Reynolds number dependence of skewness and flatness factors of turbulent velocity derivatives. *Phys. Fluids*. **23**, 252-257.
- VERZICCO, R., JIMÉNEZ, J. & ORLANDI, P. 1994 On steady columnar vortices under local compression. Preprint.
- YAKHOT, V. & ZAKHAROV, V. 1993 Hidden conservation laws in hydrodynamics: energy and dissipation rate fluctuation spectra in strong turbulence. *Physica*. **D 64**, 379-394.

Forced free-shear layer measurements

By R. L. LeBoeuf

Detailed three-dimensional three-component phase averaged measurements of the spanwise and streamwise vorticity formation and evolution in acoustically forced plane free-shear flows have been obtained. For the first time, phase-averaged measurements of all three velocity components have been obtained in both a mixing layer and a wake on three-dimensional grids, yielding the spanwise and streamwise vorticity distributions *without invoking Taylor's hypothesis*. Initially, two-frequency forcing was used to phase-lock the roll-up and first pairing of the spanwise vortical structures in a plane mixing layer. The objective of this study was to measure the near-field vortical structure morphology in a mixing layer with "natural" laminar initial boundary layers. For the second experiment the second and third subharmonics of the fundamental roll-up frequency were added to the previous two-frequency forcing in order to phase-lock the roll-up and first *three* pairings of the spanwise rollers in the mixing layer. The objective of this study was to determine the details of spanwise scale changes observed in previous time-averaged measurements and flow visualization of unforced mixing layers. For the final experiment, single-frequency forcing was used to phase-lock the Karman vortex street in a plane wake developing from nominally two-dimensional laminar initial boundary layers. The objective of this study was to compare measurements of the three-dimensional structure in a wake developing from "natural" initial boundary layers to existing models of wake vortical structure.

Part 1: Forced mixing layers

1. Motivation and objectives

The three-dimensional structure of plane transitioning mixing layers has been the subject of many experimental and computational studies since the early seventies when it was realized that, in addition to spanwise vortices ("rollers") which arise as a result of the Kelvin-Helmholtz instability, a secondary structure was also generated. The secondary structure took the form of "spatially-stationary" streamwise vortices which were soon identified in flow visualization studies and in velocity measurements. These earlier results showed that the streamwise structures ("ribs") first formed in the *braid* region, a region connecting adjacent spanwise vortices, and that their locations were related to the strength and position of (weak) incoming disturbances.

The presence and role of these "naturally-occurring" streamwise structures were recently investigated through detailed time-averaged measurements (Bell and Mehta 1992). A plane, two-stream mixing layer was generated with nominally two-dimensional laminar initial boundary layers. The measurements indicated that

small spanwise disturbances originating upstream in the boundary layer flow were amplified, leading to the formation of spatially-stationary streamwise vortices. Based on mean velocity measurements in the near-field region, it was concluded that this amplification occurred just downstream of the first spanwise vortex roll-up. The mean vorticity first appeared in "clusters" containing vorticity of both signs, but further downstream, it "re-aligned" to form counter-rotating pairs in a nominally linear arrangement. The vortex structure was found to grow in size with downstream distance, the spanwise wavelength associated with them increasing in a stepwise fashion. In contrast to some other experimental results, however, a jump in spanwise wavelength was *not* observed at *every* estimated roller pairing location and the spanwise wavelength remained constant over fairly large streamwise distances. Since the jumps in spanwise scale were correlated with local increases in the average streamwise circulation per vortex, Bell & Mehta (1992) suggested that at least one mechanism for the increase in spanwise scale was amalgamation of vortices of the same sign.

Although the secondary structure in a plane mixing layer has already received considerable attention, all issues regarding the three-dimensional structure in "natural" mixing layers have not yet been addressed. In terms of the computations, limits imposed by boundary conditions and the expense associated with grid size and computation time make it difficult to evaluate the structure of a (natural) spatially-developing mixing layer. Of course, details and interactions of the secondary structure are lost through time-averaging while the use of partial vorticity and Taylor's hypothesis, which were commonly used to interpret previous measurements, obviously add to the uncertainty in experimental results. In fact, the measurements described in this report were used to show that the use of Taylor's hypothesis introduces large errors both in the shapes and levels of the vorticity contours, especially in the roller pairing regions (LeBoeuf & Mehta 1994*a*). The issue of spanwise scale change of the streamwise vortical structures in mixing layers has also already received considerable attention, but it is still not clear when and how such a scale change will occur in a "natural" mixing layer. In particular, details of the streamwise structure scale change have not been studied quantitatively in experiments.

The main objective of the first study described in this report was to investigate the development of three-dimensionality and evolution through a spanwise roller pairing in a forced plane two-stream mixing layer developing from "natural" laminar boundary layers. Acoustic forcing was used to phase-lock the initial roll-up and first-pairing, which would otherwise occur randomly in an unforced mixing layer. Phase-averaged measurements were then used to quantify the resulting vorticity development and interaction (LeBoeuf & Mehta 1994*b*). Since a spanwise scale change was not observed through the first pairing, a second study was conducted in which acoustic forcing was used to phase-lock the formation and first *three* pairings of the spanwise rollers. Phase-averaged vorticity measurements were then used to identify the regions and details of the spanwise scale changes. The mechanisms responsible for the scale changes in this "natural" mixing layer have also been

identified (LeBoeuf & Mehta 1994c).

2. Accomplishments

2.1 The experiment

The experimental apparatus was essentially the same as that described in LeBoeuf (1993) and has been further described in detail in LeBoeuf & Mehta (1994b); only a brief description is therefore given here. The experiments were conducted in a mixing layer wind tunnel with the two free-stream velocities set to 12 m/s and 7.2 m/s. The boundary layers on the splitter plate were laminar and nominally two-dimensional with these operating velocities. Velocity measurements were made using a single cross-wire probe which was rotated in order to obtain data in two-coordinate planes (uv and uw).

The forcing signals used to obtain the results described in this report consisted of the sum of a sine wave at the fundamental “most-probable” roll-up frequency (500 Hz, obtained from centerline spectra in the unforced layer) and its first subharmonic (250 Hz). Two additional subharmonics (125 Hz and 62.5 Hz) were added for the second (spanwise scale change) study. The forcing signal relative phase angles were optimized in order to induce rolling-type interactions for all pairings. The individual sine waves were combined using a simple summing circuit and output via an audio amplifier to speakers which were placed directly across from the splitter plate trailing edge at a side-wall slot location. The amplitude (volume) of the output signal from the amplifier was set to the absolute minimum level that still gave adequate coherence in the phase-locking.

For the phase-averages obtained in the first study, 768 ensembles of 16 samples per cycle were measured. The measurement grid consisted of 55 uniformly spaced X locations in the range 1 to 28 cm and 20 uniformly spaced Y locations distributed over a linearly increasing range of -1 to 1 cm at $X = 1$ cm to -2.5 to 2.5 cm at $X = 28$ cm. In the spanwise direction, the three-dimensional grid ranged from $Z = -5$ to 5 cm with 41 uniformly spaced locations. For the phase-averages obtained in the second study, 768 ensembles of 32 samples per cycle were measured. The measurement grid consisted of 155 uniformly spaced X locations in the range 1 to 78 cm and 11 uniformly spaced Y locations distributed over a linearly increasing range of $-$ to 1 cm at $X = 1$ cm to -6.2 to 4.4 cm at $X = 78$ cm. In the spanwise direction, the three-dimensional grid ranged from $Z = 0$ to 5 cm with 21 uniformly spaced locations.

2.2 Results and discussion

2.2.1 Two-frequency forcing: initial roll-up and first pairing

The streamwise evolution of spanwise vorticity along the mixing layer centerline ($Z = 0$) is depicted in Figs. 1(a-d) for four phases (or times). In effect, every fourth phase out of the 16 measured phases per subharmonic cycle is presented. The evolution and pairing of sets of primary rollers can be easily tracked through the four phases shown. The initial spanwise vortex roll-up occurs at $X \approx 5$ cm. Clearly, signs of subharmonic forcing are present early in the mixing layer development

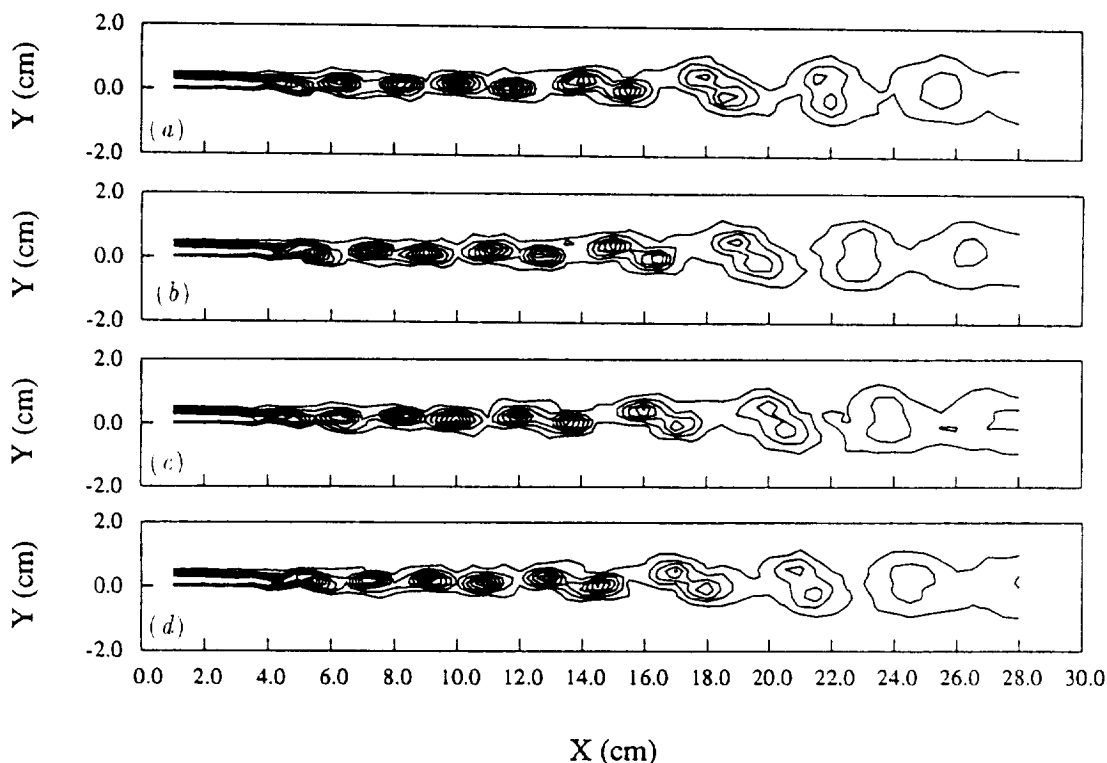


FIGURE 1. Centerplane phase-averaged spanwise vorticity ($\langle \Omega_z \rangle / U_0$, cm^{-1}) contours at various phases. Lowest level = -0.25 , increment = -0.5 . (a) phase 1; (b) phase 5; (c) phase 9; (d) phase 13.

since distinguishable *pairs* of primary rollers are discernable from the onset of their development. Spanwise vortices of each pair start to move closer together between $X \approx 10$ and 15 cm, begin to corotate at $X \approx 15$ cm, and complete the first pairing by $X \approx 25$ cm. The peak phase-averaged spanwise vorticity levels drop by an order of magnitude during the pairing process.

Details of the vortical structures can be examined in detail by using two-dimensional "cuts" through the three-dimensional data. To maintain figure legibility, the figures and discussion thereof was divided into two parts: the initial spanwise vortex roll-up region and the pairing region. In the initial roll-up region, spanwise vorticity contours in XY -planes which intersect ribs (Figs. 2a and c) and those between ribs (e.g. Fig. 2b) appear quite similar both in terms of qualitative (structural) features and vorticity levels. The cups of intense spanwise vorticity observed by Buell & Mansour (1989a) and Rogers & Moser (1992) in their direct numerical simulation studies were not found in the present investigation. The formation of cups was attributed to the effects of alternating stretching and compression of the primary rollers by collapsed rib vortices.

The XY -planes of streamwise vorticity through the ribs and between them, on

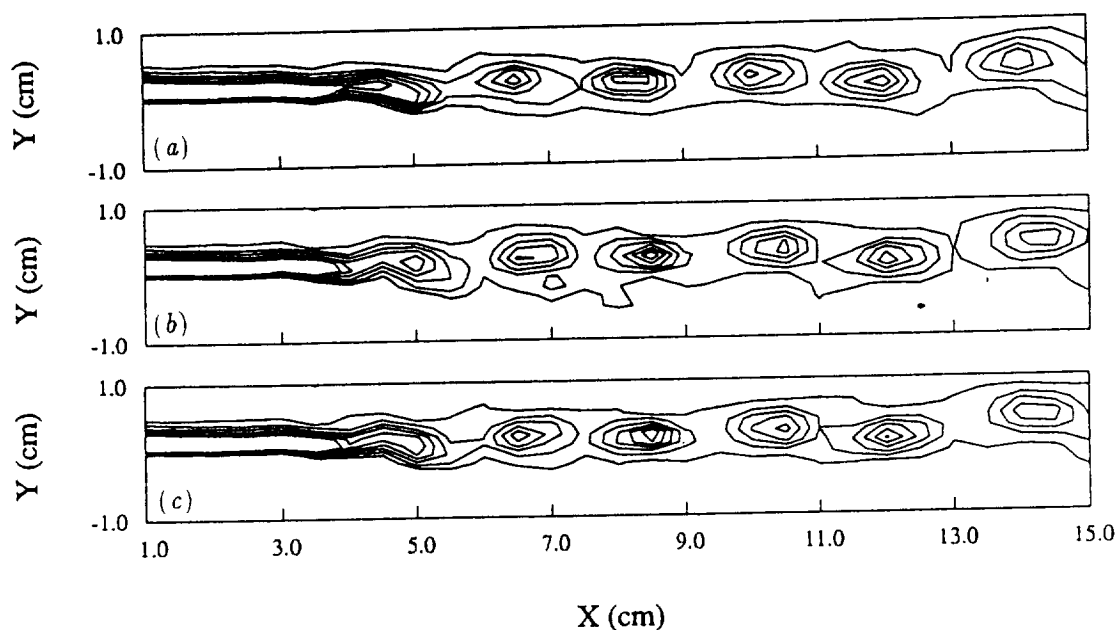


FIGURE 2. Phase-averaged spanwise vorticity ($\langle \Omega_z \rangle / U_0$, cm^{-1}) contours at phase 1. Lowest level = -0.25 , increment = -0.75 . (a) *RP* through positive rib, $Z = 0.25$ cm; (b) *BP*, $Z = 1.25$ cm; (c) *RP* through negative rib, $Z = 2$ cm.

the other hand, certainly show some obvious differences. In addition to the rib vortices, *opposite-sign* streamwise vorticity peaks appear within the spanwise roller core in planes intersecting the ribs (Figs. 3*a* and *c*). This effect is attributable to (streamwise) kinking of the spanwise roller, and its appearance here is consistent with the simulation results of Buell & Mansour (1989*a*) and Rogers & Moser (1992) and with the measurements of Lasheras & Choi (1988), Tung (1992) and Nygaard & Glezer (1991). This production of opposite-signed streamwise vorticity has been explained in vortex stretching terms in the streamwise vorticity equation by Buell (1991) and Rogers & Moser (1991). Since the deflection of the spanwise roller reaches a maximum and therefore has only a spanwise component between the ribs ($Z = 1.25$ cm), its contribution is absent in that plane (Fig. 3*b*). The arrangement of rib vortices and streamwise vorticity within the spanwise roller yields a three-tier arrangement of streamwise vorticity in cross-stream (YZ)-planes which intersect the primary rollers (Fig. 4*a*), whereas only the rib vortices are apparent in the cross-stream planes which intersect the braid regions (Fig. 4*b*).

In the pairing region, evolution of the streamwise vorticity was first examined through cross-stream (YZ -plane) cuts. Figs. 5(*a*) and (*b*) correspond to planes which intersect the primary (paired) rollers at $X = 22$ and 26 cm, respectively. It is evident from Fig. 1 that pairing is occurring between approximately $X = 17$ cm and $X = 24$ cm. A comparison of Figs. 5(*a*) and (*b*) indicates that reorganization

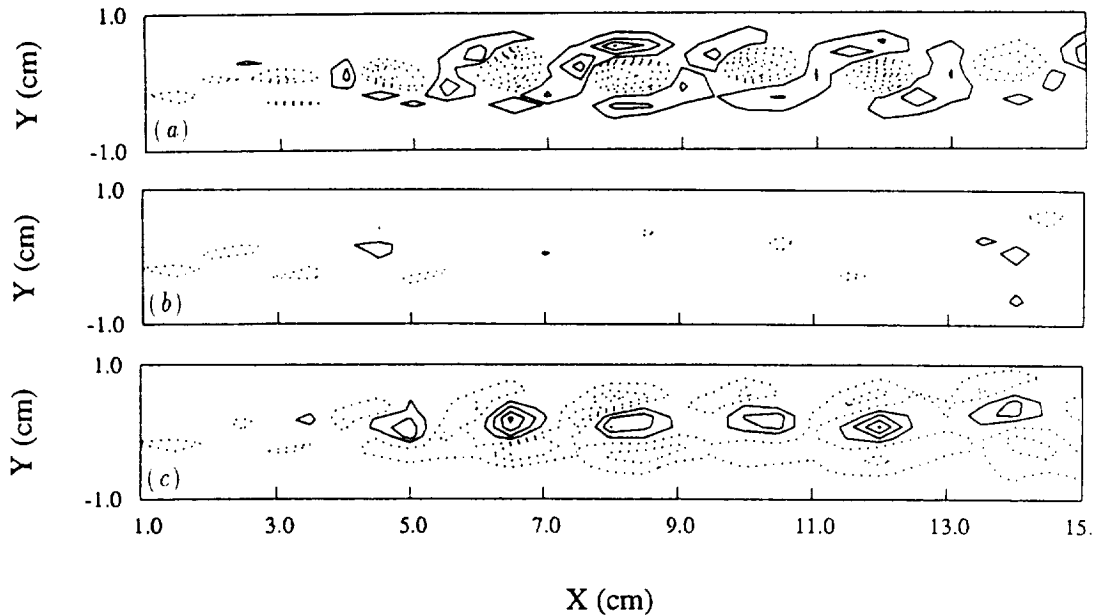


FIGURE 3. Phase-averaged streamwise vorticity ($\langle \Omega_x \rangle / U_0$, cm^{-1}) contours at phase 1. Negative \cdots , positive --- , lowest level = ± 0.2 , increment = ± 0.3 . (a) *RP* through positive rib, $Z = 0.25$ cm; (b) *BP*, $Z = 1.25$ cm; (c) *RP* through negative rib, $Z = 2$ cm.

(interaction) of the secondary vorticity continues to take place even towards the final stages of pairing. In particular, it appears that the streamwise vorticity arrangement is tending toward the three-tier arrangement within a cycle after pairing occurs (Fig. 5*b*).

Figs. 6(*a*) and (*b*) correspond to YZ -planes which intersect the braid regions at $X = 20.5$ and 23.5 cm, respectively. In contrast to the near-field downstream of $X \approx 20$ cm, the peak streamwise vorticity levels become higher in the braid region. Most importantly, the spanwise scale or spacing of the rib vortices has *not* increased through this first pairing. Thus, compared to the near-field value, the spanwise to streamwise wavelength ratio was decreased from about 1.3 to 0.65.

In the pairing and post-pairing stages of the mixing layer, exemplary XY -plane cuts of spanwise and streamwise vorticity through ribs and between ribs are shown in Figs. 7 and 8, respectively. As in the upstream domain, cuts showing spanwise vorticity contours through the ribs and between them appear very similar and, even in this region, there are no signs of the cups of relatively strong spanwise vorticity reported for the simulation results (Buell & Mansour 1989*a*; Rogers & Moser 1992).

As expected, the streamwise vorticity is significantly weaker in planes between ribs compared to those through the ribs. The two rollers undergoing pairing clearly exhibit the three-tier distribution as they start to rotate about each other. As

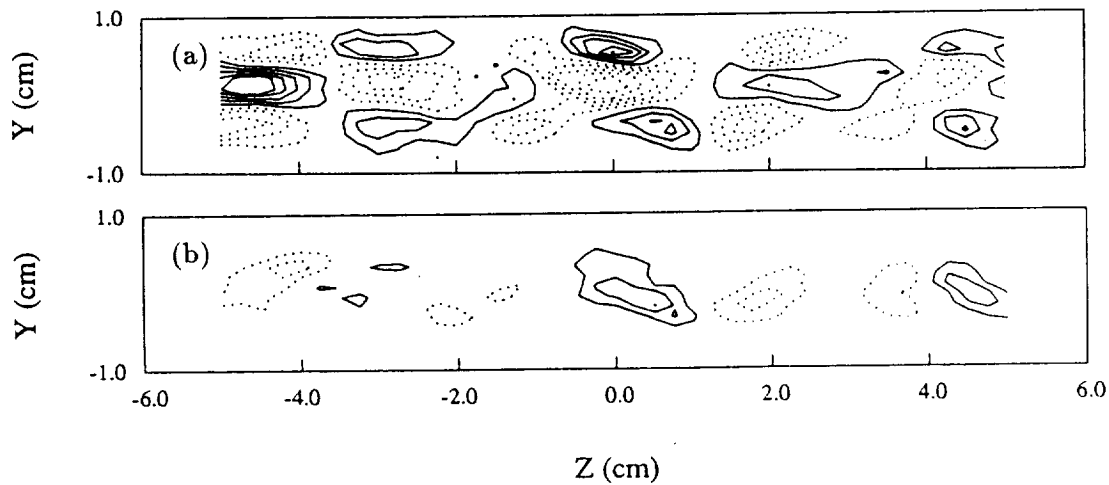


FIGURE 4. Cross-stream plane phase-averaged streamwise vorticity ($\langle \Omega_x \rangle / U_0$, cm^{-1}) contours at phase 1. Negative \cdots , positive — , lowest level = ± 0.2 , increment = ± 0.2 . (a) $X = 8$ cm; (b) $X = 5.5$ cm.

they pair, the two regions of spanwise roller core vorticity eventually coalesce, thus forming the contribution from the new core. In following the evolution of the perishing braid regions, the rib vorticity in between the two pairing rollers seemed to “disappear”. Simulation results suggest that this vorticity is destroyed by intense vortex stretching in this region (Moser & Rogers 1993).

Note that once the pairing process is complete ($X \approx 25$ cm), the streamwise vorticity of the rib vortices is substantially higher than that due to kinking of the primary rollers. In addition, the rib contribution to the streamwise vorticity is higher in the braid than it is in the primary roller YZ -planes. This is in sharp contrast to the initial roll-up region, where the streamwise vorticity levels in the primary roller cores due to their kinking are comparable to those of the rib contribution, which in turn is higher in the rollers compared to its magnitude in the braids. The same trends were apparent in the experimental results of Tung (1992) and in the temporal simulation results of Moser & Rogers (1993). Decreased kinking of the rollers is at least partly responsible for this observed effect since the paired structure is more two-dimensional than the pre-paired rollers. On examining XY -plane cuts in the region surrounding the ribs, it was found that the ribs are still wrapped around the rollers, but the ends are skewed in the spanwise direction, thus reducing their streamwise vorticity contribution in YZ -planes which intersect the primary rollers.

The phase-averaged vorticity measurements confirm that relatively strong streamwise vorticity appears in mixing layers as a result of an amplification of small incoming disturbances — it is *not* just directly fed-in from the boundary layers. The streamwise vorticity is first observed in the form of ribs just upstream of where the

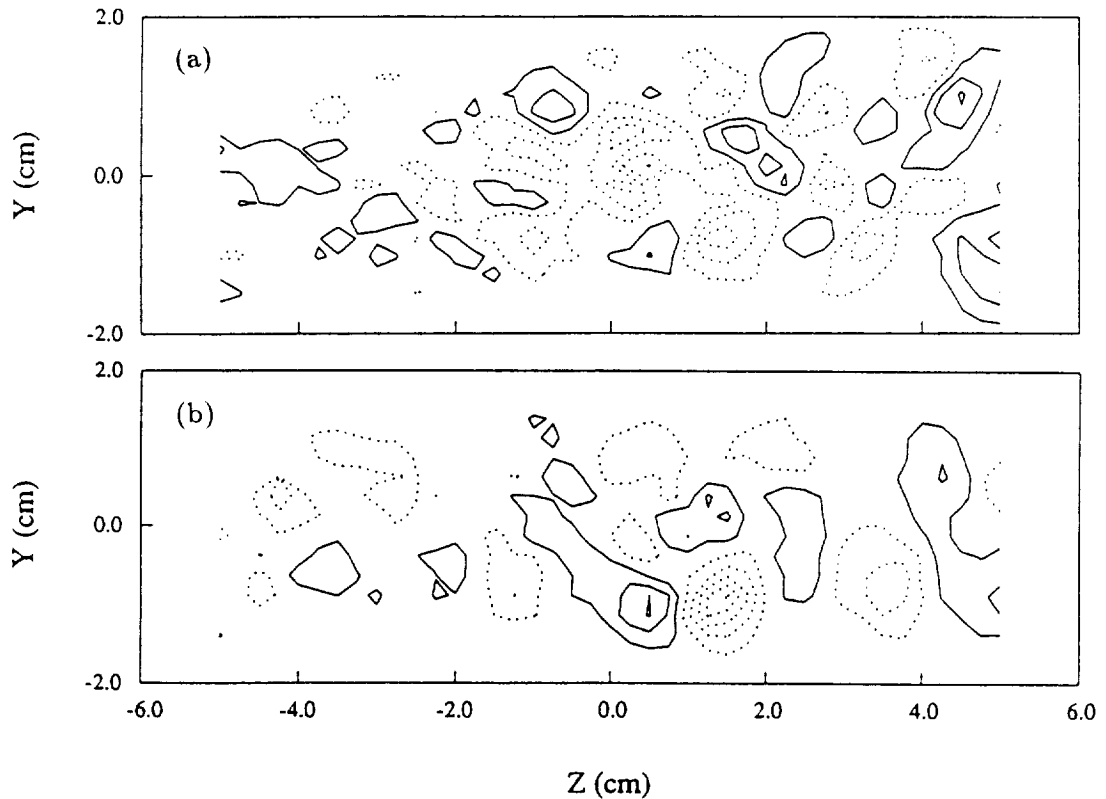


FIGURE 5. Cross-stream plane phase-averaged streamwise vorticity ($\langle \Omega_x \rangle / U_0$, cm^{-1}) contours at phase 1 through CPs. Negative \cdots , positive — , lowest level = ± 0.075 , increment = ± 0.15 . (a) $X = 22$ cm; (b) $X = 26$ cm.

first spanwise vortex is rolling-up. At the same time, the first spanwise roller becomes kinked, thus also contributing to the streamwise vorticity. As a result, cross-stream cuts through the braid regions show the familiar row of counter-rotating streamwise vortex pairs while those through the spanwise rollers exhibit a three-tier distribution consisting of the rib vortices aligned vertically with an opposite-signed contribution from the roller between them. This type of behavior and distribution are in agreement with previous observations in experiments (Tung 1992) and simulations (Buell & Mansour 1989a; Rogers & Moser 1992).

Because of the relatively strong contribution of the kinked rollers and the fact that the rib vortices are more aligned with the mean flow around the rollers, the highest levels of phase-averaged streamwise vorticity and circulation were observed in the spanwise vortex cores in the near-field region. The strong kinking of the spanwise rollers by the rib vortices was also observed in numerical simulations (Buell & Mansour 1989a; Rogers & Moser 1992). However, cups of relatively strong spanwise vorticity (also a result of the rib induced effects) reported for the simulation results

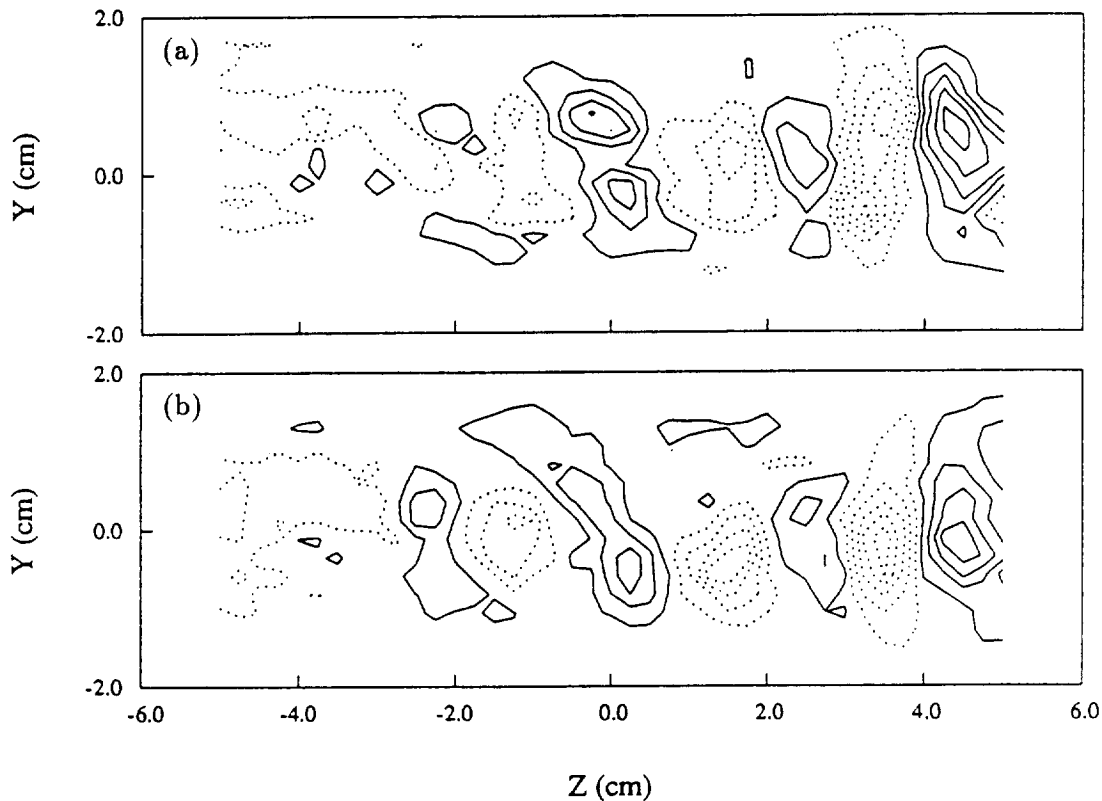


FIGURE 6. Cross-stream plane phase-averaged streamwise vorticity ($\langle \Omega_x \rangle / U_0$, cm^{-1}) contours at phase 1 through *MPs*. Negative , positive ——— , lowest level = ± 0.075 , increment = ± 0.15 . (a) $X = 20.5$ cm; (b) $X = 23.5$ cm.

were not observed in the present measurements. This is particularly surprising since the initial rib circulation in the present experiments is comparable to that used in the temporal simulations of Rogers & Moser (1992).

The morphology of the surviving braid region rib vortices was not significantly affected by the spanwise vortex pairing. In particular, their spanwise spacing did not increase after the pairing. This result is consistent with previous time-averaged measurements (Bell & Mehta 1992) which showed that the first increase in spacing did not occur until $X \approx 50$ cm, well downstream of the present measurement domain and after an estimated two spanwise vortex pairings had occurred. It also supports the findings of Rogers & Moser (1993), who suggested that the details of the spanwise scale change are dependent on the nature of the initial disturbance environment. The main effect noted in the post-pairing region is that the levels of streamwise vorticity in the roller core planes are reduced such that the highest levels are now found in the braid region. The smaller relative contribution due to kinking of the spanwise rollers is related to both, a reduction in roller kinking and a faster

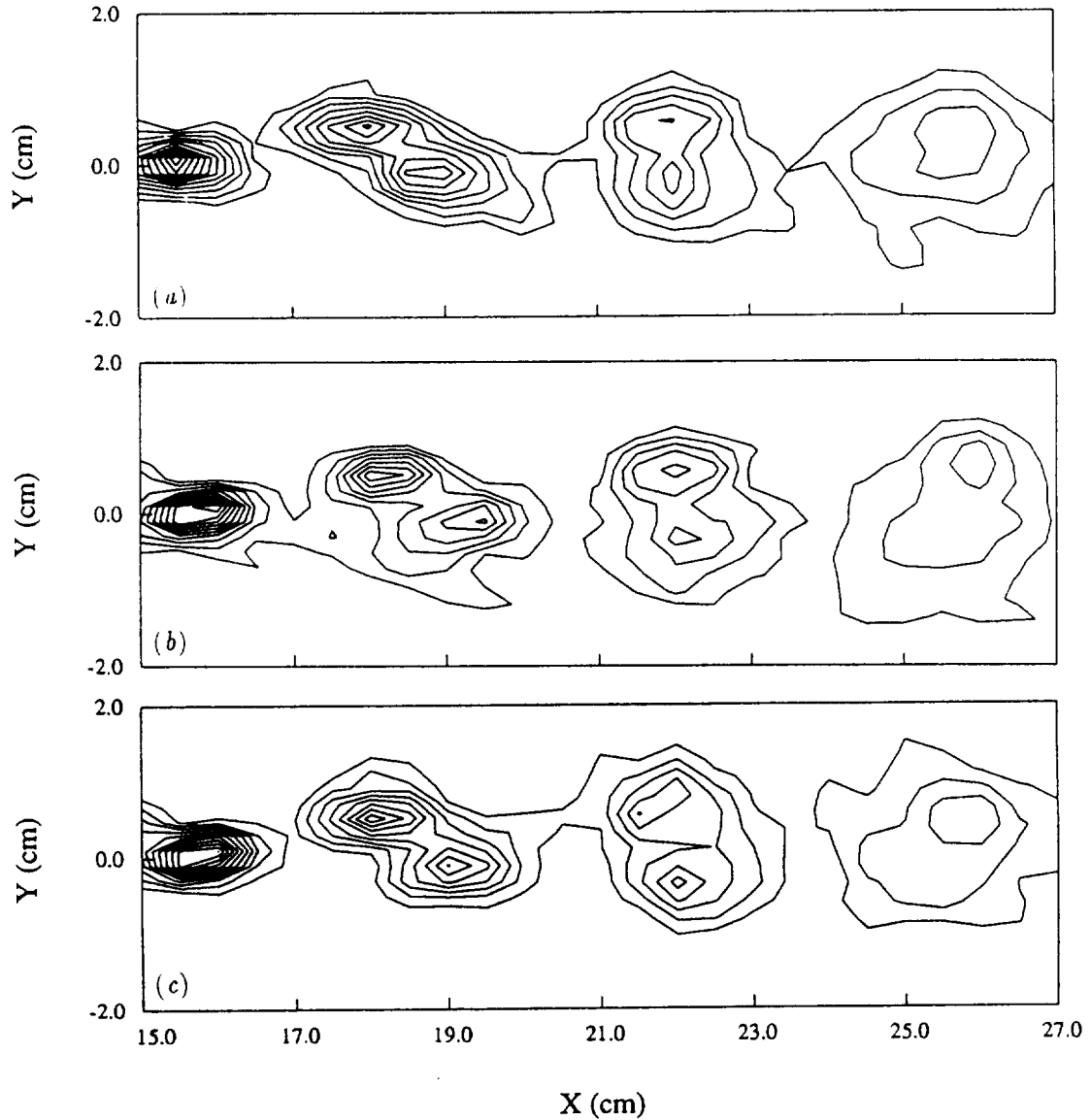


FIGURE 7. Phase-averaged spanwise vorticity ($\langle \Omega_z \rangle / U_0$, cm^{-1}) contours at phase 1. Lowest level = -0.25 , increment = -0.25 . (a) *RP* through positive rib, $Z = 0.25$ cm; (b) *BP*, $Z = 1$ cm; (c) *RP* through negative rib, $Z = 1.75$ cm.

rate of decay of the spanwise vorticity compared to that of the streamwise vorticity. The ribs make a smaller contribution in the roller planes because its ends are tilted in the spanwise direction. This change in the relative contributions is the reason why in the time-averaged measurements, the three-tier distribution observed in the near-field region soon “re-aligned” into a single row of mean streamwise vorticity (Bell & Mehta 1992).

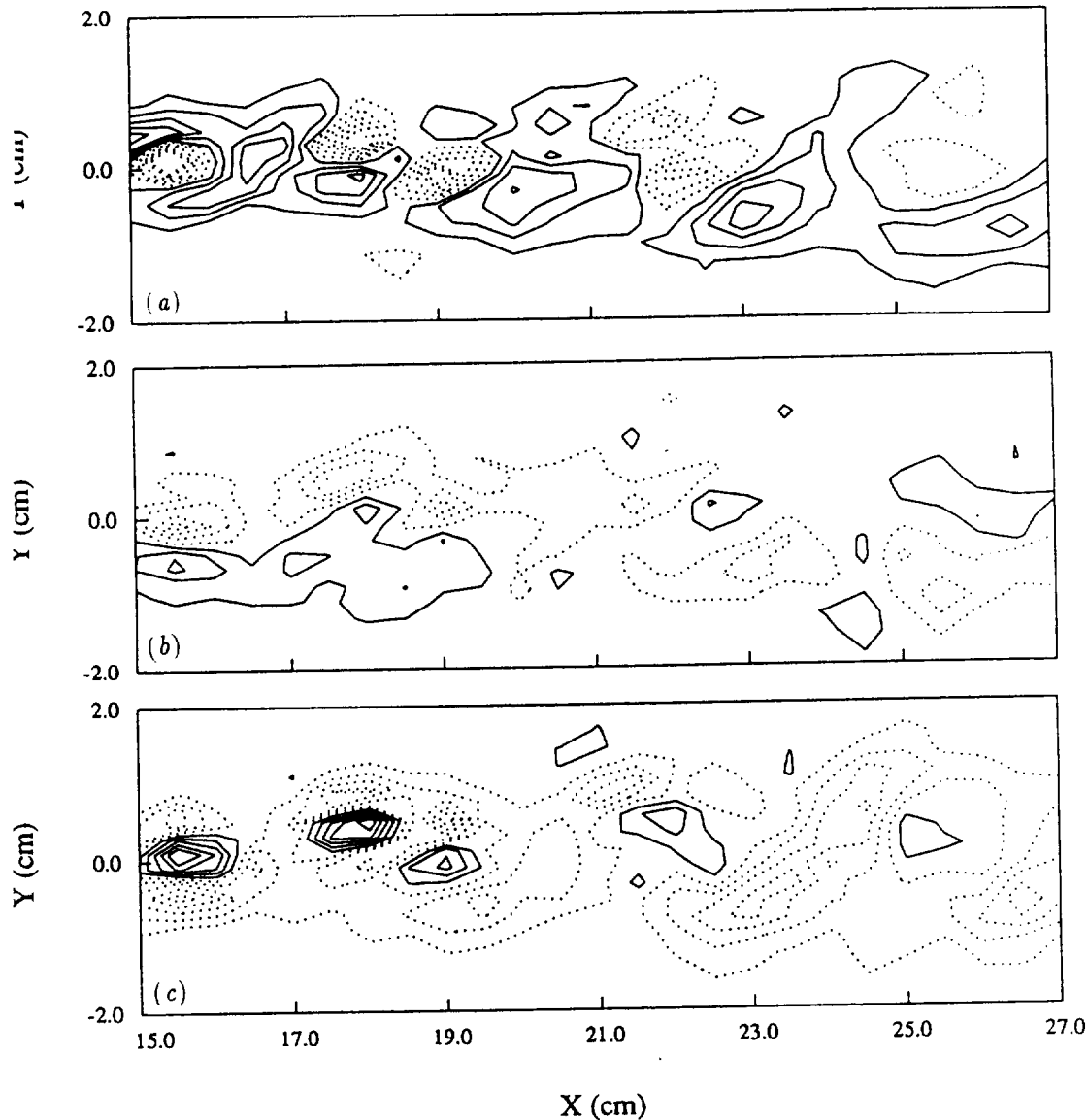


FIGURE 8. Phase-averaged streamwise vorticity ($\langle \Omega_x \rangle / U_0$, cm^{-1}) contours at phase 1. Negative \cdots , positive — , lowest level = ± 0.075 , increment = ± 0.15 . (a) *RP* through positive rib, $Z = 0.25$ cm; (b) *BP*, $Z = 1$ cm; (c) *RP* through negative rib, $Z = 1.75$ cm.

The present results clearly show that a plane mixing layer originating from laminar boundary layers will develop a three-dimensional structure in the form of streamwise vorticity as soon as the Kelvin-Helmholtz instability generates spanwise vortex rollers. Although in practice the details of the streamwise vortical structures will be facility dependent, they will generally appear in the form of an array of counter-rotating vortex pairs. The present data are consistent with existing models of the

secondary structure: rib vortices are formed in the braid region which wrap around the spanwise rollers (from the bottom of one roller to the top of the next). The streamwise vorticity and its associated effects on the mixing layer properties decay slowly with streamwise distance. This secondary structure therefore forms an integral and important part of the structural morphology of a transitioning mixing layer.

2.2.1 Four-frequency forcing: measurements of a spanwise scale change

The streamwise evolution of spanwise vorticity ($\langle \Omega_z \rangle / U_0$, cm^{-1}) along the mixing layer centerline ($Z = 0$) is depicted in Figs. 9(a-d) for four phases (or times). In effect, every eighth phase out of the 32 measured phases per lowest (third) subharmonic cycle is presented. The evolution and pairings of sets of primary rollers can be easily tracked through the four phases shown. The initial spanwise vortex roll-up occurs at $X \approx 5$ cm and the spanwise rollers are shed with an initial streamwise wavelength of about 1.75 cm. Clearly, signs of subharmonic forcing are present early in the mixing layer development since distinguishable *sets* of primary rollers are discernable at the onset of their development. Spanwise vortices of each pair start to move closer together between $X \approx 10$ and 15 cm, begin to corotate between $X \approx 15$ and 20 cm, and complete the first pairing by $X \approx 25$ cm. The second pairing is initiated immediately after the first pairing is complete, beginning between $X \approx 25$ and 30 cm and ending at $X \approx 50$ cm. The third pairing, which immediately follows, remains in progress up to the end of the measurement domain at $X = 78$ cm. The peak phase-averaged spanwise vorticity levels drop from 4 cm^{-1} to 1 cm^{-1} during the first pairing, down to 0.5 cm^{-1} during the second pairing, and finally down to 0.4 cm^{-1} during the third pairing.

Since the objective of the present study was to investigate spanwise scale changes associated with the rib structures, the spatial evolution of surviving rib structures was observed as they evolved through the three spanwise roller pairings. This is achieved by marching in X and phase at the same time. With 32 phases per third subharmonic forcing cycle ($1/62.5 \text{ Hz} = 0.016$ seconds duration), this gives a streamwise evolution of 0.48 cm per phase, based on an average convection velocity, $(U_1 + U_2)/2 = 9.6 \text{ m/s}$. Of course, as adjacent rollers pair, the braid region between them is engulfed into the new roller. Therefore, the so-called “surviving” braid region was chosen for examination of its streamwise evolution through the three roller pairings. The surviving braid region selected for the present scrutiny is marked by the first vertical line in Fig. 1(a). The location of that particular surviving braid region can then be followed by tracking the streamwise displacement of the vertical line through the four phases. Of course, to continue tracking the surviving braid region beyond the location indicated by a line in Fig. 9(d), it is necessary to go back to Fig. 9(a) and follow the next downstream location indicated, and so on.

In order to investigate the spanwise scale of the rib structures, cross-stream (YZ) plane cuts through the selected surviving braid region are presented in Figs. 10(a-h) as this region evolves through the first, second, and third primary roller pairings. At $X = 7$ cm (Fig. 10a), approximately two pairs of streamwise vortex pairs are apparent, with the stronger pair on the left ($0 < Z < 2.5$ cm) and a weaker, less

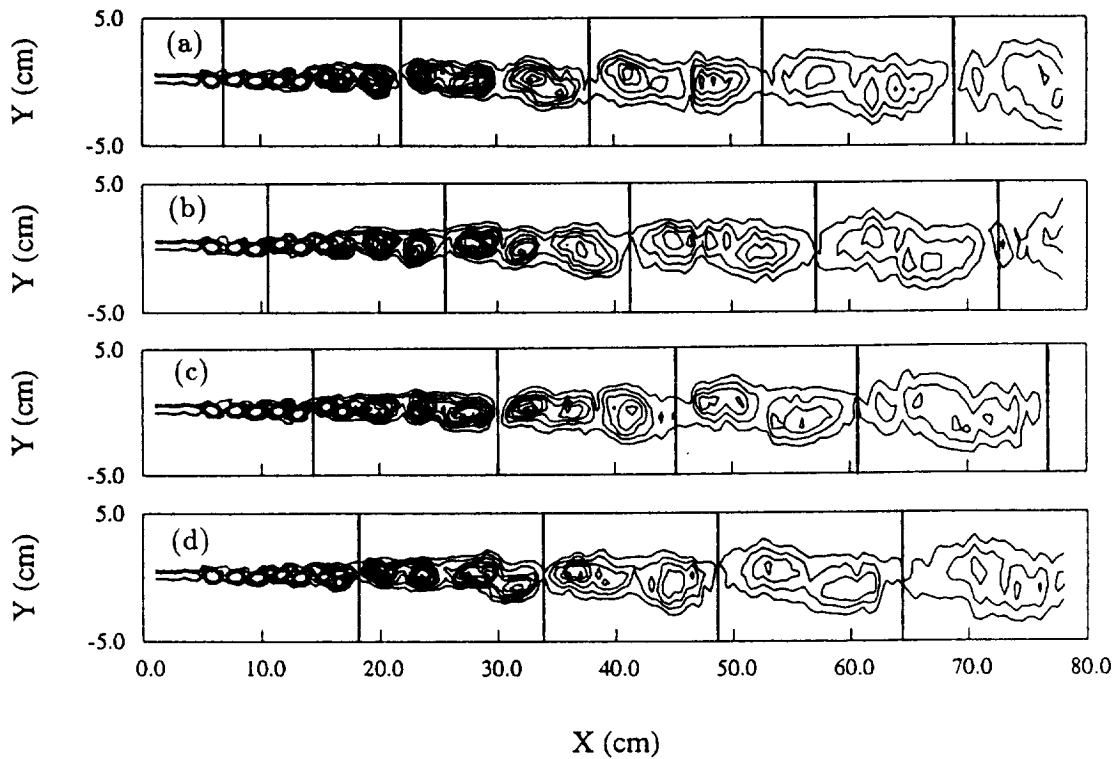


FIGURE 9. Centerplane phase-averaged spanwise vorticity ($\langle \Omega_z \rangle / U_0$, cm^{-1}) contours at various phases. Vertical lines mark the location of the surviving braid region tracked in Fig. 2. Lowest contour level = -0.113 , increment = -0.1 . (a) phase 1; (b) phase 9; (c) phase 17; (d) phase 25.

organized one on the right ($2.5 < Z < 5$ cm). In particular, the positive vortex at $Z \approx 3$ cm appears to be split into two smaller structures and the negative one at $Z \approx 4.5$ cm is considerably weaker than its counterpart at $Z \approx 2$ cm. The average spacing between the streamwise vortices is about 1.5 cm, which gives an initial spanwise to streamwise wavelength ratio of about 1.7. Further downstream, by $X = 17$ cm (Fig. 10*b*), the two weak positive structures have merged into one. Somewhat surprisingly, at $X = 18$ cm (Fig. 10*c*), the weak positive structure starts to split up again and the negative region above it has broken away from the stronger negative structure. Fig. 9(*d*) shows that at this location and phase, the selected braid region is right in the middle of the first roller pairing process. The upstream pair is in the process of rolling-up while the downstream pair has almost completely merged together.

Further downstream, the split positive pair merges together again and by $X = 25$ cm, at a time (phase) at which the braid is located between two paired rollers, two complete pairs of streamwise vortices are apparent (Fig. 10*d*). So while there is no scale change in the region of the first roller pairing as such, the weaker vortices do

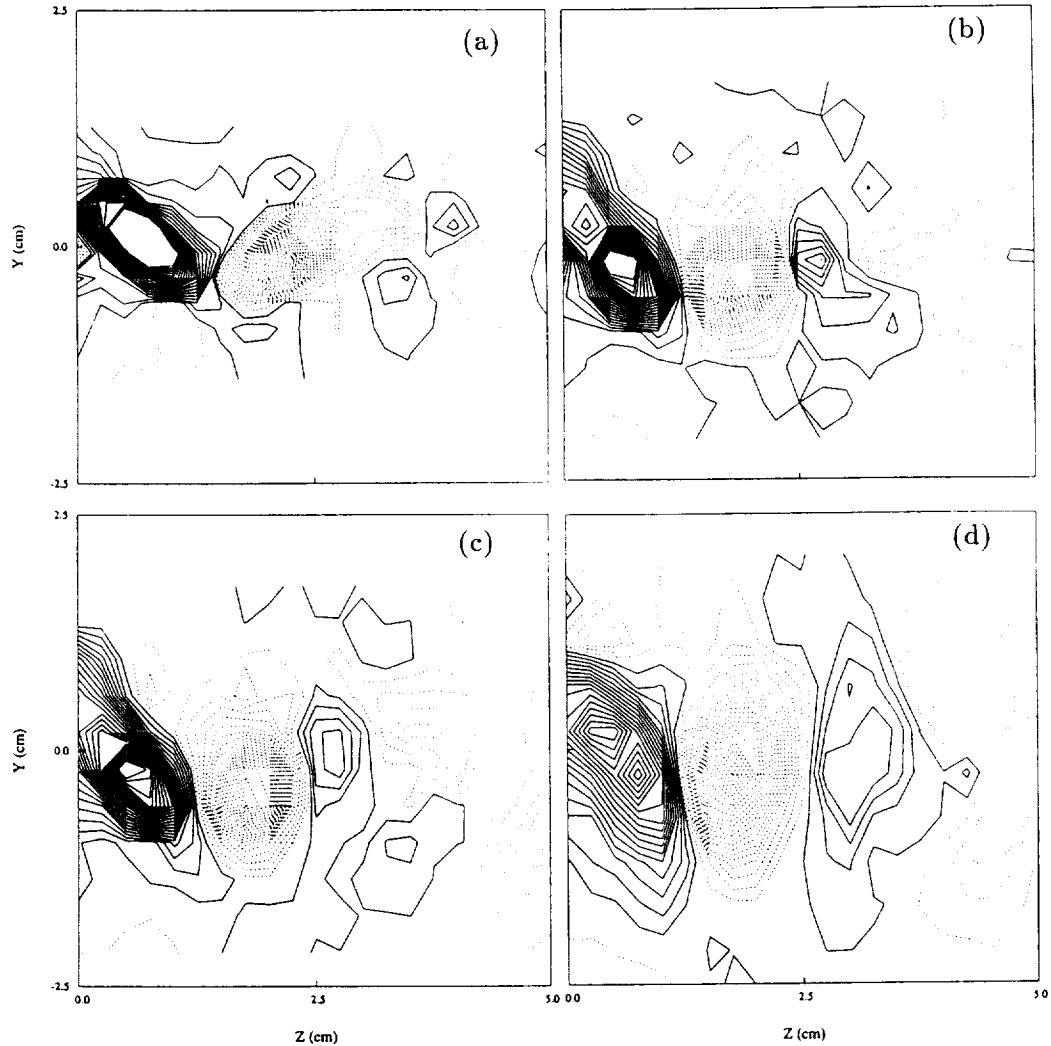


FIGURE 10. Cross-stream plane phase-averaged streamwise vorticity ($\langle \Omega_x \rangle / U_0$, cm^{-1}) contours. Negative \cdots , positive — , lowest level = ± 0.013 , increment = ± 0.025 . (a) $X = 7$ cm, phase 1; (b) $X = 17$ cm, phase 23; (c) $X = 18$ cm, phase 25; (d) $X = 25$ cm, phase 7.

undergo some temporary changes in structure and/or position. A similar behavior of the weaker vortices in this region was also observed in our two-frequency forcing results (LeBoeuf & Mehta 1994b).

The trends observed in the region of the first pairing continue during the second pairing. Following the weak positive vortex at $Z \approx 3$ cm, between $X = 25$ cm (Fig. 10d) and $X = 44.5$ cm (Fig. 10e), the vortex splits and recombines three more times. The split always occurs at the onset of an upstream or downstream

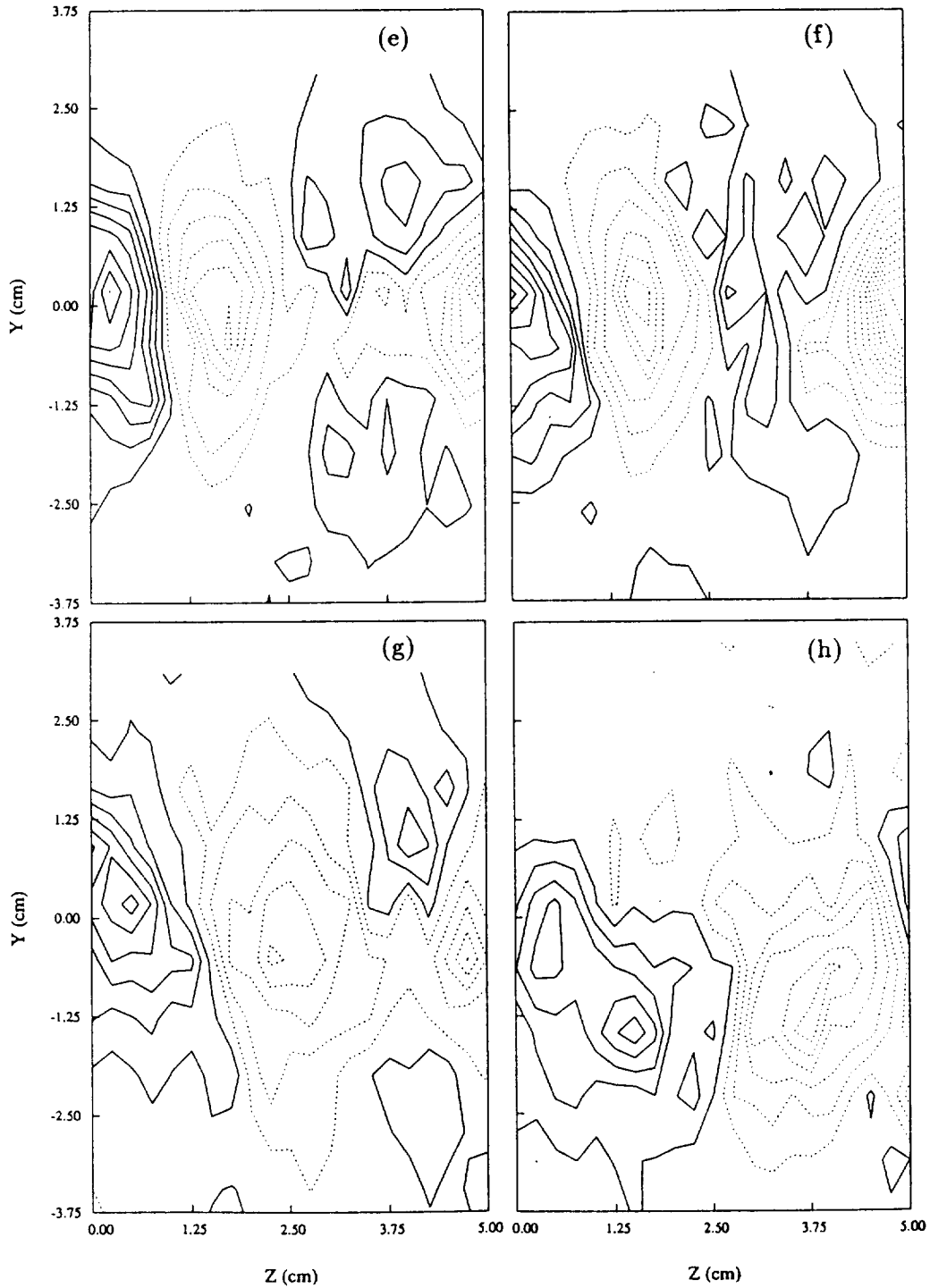


FIGURE 10 (CONTINUED). Cross-stream plane phase-averaged streamwise vorticity ($\langle \Omega_x \rangle / U_0$, cm^{-1}) contours. Negative , positive ———, lowest level = ± 0.013 , increment = ± 0.025 . (e) $X = 44.5$ cm, phase 14; (f) $X = 46$ cm, phase 17; (g) $X = 48.5$ cm, phase 23; (h) $X = 57$ cm, phase 9.

roller pairing. The weak vortex at $Z \approx 3$ cm recombines for the last time at $X = 46$ cm during the beginning of the third pairing (Fig. 10f). Note that throughout its evolution through the first and second pairing, the stronger pair on the left ($0 < Z < 2.5$ cm) does not change much, except that the vorticity levels drop with streamwise distance as the vortices diffuse and thus enlarge. However, the enlargement only takes place in the vertical (Y) direction; the spanwise growth is presumably restricted by the neighboring streamwise vortices. In fact, the spacing between the two vortices *does not change* at all in the region, $X = 7$ to 46 cm.

By $X = 48$ cm (Fig. 10g), the weak positive vortex at $Z \approx 3$ cm splits again, but this time the two neighboring negative vortices move closer together into the area vacated by the weak positive vortex and start to amalgamate. The fragments of the shredded positive vortex appear to move out of the measurement domain. At $X = 57$ cm (Fig. 10h), only a *single* pair of streamwise vortices is clearly visible with the distance between the pair *doubled*. This single pair persists to the end of the measurement domain ($X = 78$ cm). The spacing between the pair is about 3.6 cm, which gives a spanwise to streamwise wavelength ratio of about 0.5.

Clearly the mechanism for the increase in spanwise scale is that the weakest (positive) vortex splits up and moves out of the array, the two neighboring vortices (both negative) move closer together and amalgamate, and the spanwise spacing is hence readjusted. Apparently there was a tendency for the weakest vortex to split and thereby permit merging of the two like-signed adjacent vortices during both the first and second pairing; however, the merging finally occurred during the third primary roller pairing. If this was a true amalgamation of two vortices of the same sign, then one would expect the circulation of the new (merged) vortex to be higher than those of the original vortical structures. And indeed, in the present results, the circulation of the merged negative structure in Fig. 10(h) is twice that of one of the original negative structures (that at $Z \approx 2$ cm in Fig. 10f).

In order to confirm that the observed scale change was not an artifact of the imposed forcing signal, time-averaged streamwise vorticity measurements for the forced mixing layers (averaged over all 32 phases) were compared to those obtained in the same mixing layer, but with the forcing turned off. All other initial and operating conditions were maintained exactly the same in this *unforced* mixing layer. In both cases, the spanwise scale observed in the mean streamwise vorticity measurements was constant out to $X \approx 50$ cm, after which it doubled abruptly. Therefore, the forcing is obviously *not* responsible for the location of the observed scale change.

The present results agree, in particular, with many of the observations and notions of Bell & Mehta (1992) developed from their time-averaged measurements. They also observed the first rapid scale change at $X \approx 50$ cm, which was estimated to be the location of the third roller pairing. As in the present study, the spanwise scale was found to double in this region. Since the locations of the scale changes were correlated with local increases in the average streamwise circulation per vortex, Bell & Mehta suggested that the mechanism for the increase in spanwise scale was amalgamation of vortices of the same sign, which is exactly what is observed here.

Tung (1992) also reported seeing some (local) pairings of streamwise vortices of the same sign. While the other proposed mechanisms, such as viscous annihilation and amalgamation of opposite sign vortex pairs (Jimenez 1983, Rogers & Moser 1993), have not been observed in the present direct measurements, in principle there is no reason why they should not occur, providing the local circumstances (such as streamwise vortex strength and spacing, for example) are right.

The balance of experimental evidence suggests that the spanwise wavelength of the streamwise structures will increase, scaling approximately with the mixing layer vorticity thickness. However, the increase will in general be non-linear (stepwise) with the jumps coinciding with *some* pairing locations. An increase in spanwise wavelength has not been observed experimentally in the absence of spanwise roller pairings. However, it is quite clear that the spanwise scale does not have to increase at every spanwise roller pairing location, although it can, as shown by Huang & Ho (1990). This means that, in general, a constant ratio of spanwise to streamwise wavelength will not be maintained. At least one (measured) mechanism for the increase in spanwise scale is amalgamation of streamwise vortices of the same sign. As Rogers & Moser (1993) suggested, in practice the details of the spanwise scale change will probably be determined by the incoming disturbance environment.

Part 2: Forced wake

1. Motivation and objectives

The effects of (passive) spanwise perturbations on the wake three-dimensionality have been investigated in a few studies. Meiburg & Lasheras (1988) investigated the structure of a perturbed splitter plate wake through inviscid vortex simulations and low Reynolds number flow visualization experiments and found that the redistribution, reorientation, and stretching of vorticity produced counter-rotating pairs of streamwise vortices which were superimposed onto the spanwise vortices. These streamwise vortices were in the form of lambda-shaped structures and resided in the braid regions connecting adjacent (opposite-signed) spanwise vortices. Subsequent interaction of the streamwise and spanwise structures led to the formation of closed vortex loops.

Although the secondary structure in a plane wake has already received some attention both experimentally and computationally, all issues regarding the three-dimensional structure of a wake developing from “natural” initial conditions have not yet been addressed. The appearance of mean streamwise vorticity in time-averaged measurements confirmed the existence of coherent spatially-stationary secondary vorticity in wakes (Weygandt & Mehta 1993). However, the details of the secondary structure are lost through the averaging process. The popular use of Taylor’s hypothesis in the past in interpreting three-dimensional measurements can obviously add to the uncertainty. As for the computations, limits imposed by boundary conditions and the expense associated with grid size and computation time make it difficult to evaluate the structure of a “natural” spatially-developing wake.

The main objective of this study was to investigate the formation of three-dimensionality and its evolution in a forced plane wake developing from laminar boundary layers. Acoustic forcing was used to phase-lock the shedding of the Karman vortices. Phase-averaged measurements were then used to quantify the resulting vorticity development and interaction. These measurements, coupled with previous experimental and simulation results, shed new light on the structural development of spatially-evolving wakes with “natural” initial conditions (LeBoeuf & Mehta 1994*d*).

2. Accomplishments

2.1 The experiment

The experiments were conducted using the same equipment as that used for the aforementioned mixing layer experiments. Therefore a complete description will not be repeated here. Of course, there were differences in operating conditions, namely that the two sides of the wake were set to 9 m/s and the forcing consisted of a single sine wave at the fundamental roll-up frequency (450 Hz, obtained from centerline spectra in the unforced wake). The boundary layers on the splitter plate were laminar and nominally two-dimensional at these operating conditions. Again, the amplitude of the output signal from the amplifier was set to the absolute minimum level which still gave adequate coherence in the phase-locking.

For the phase-averages shown in the next section, 768 ensembles of 16 samples per cycle were measured. The measurement grid consisted of 29 uniformly spaced X locations in the range 1 to 15 cm and 20 uniformly spaced Y locations distributed over a linearly increasing range of -1 to 1 cm at $X = 1$ cm to -1.8 to 1.8 cm at $X = 15$ cm. In the spanwise direction, the three-dimensional grid ranged from $Z = -5$ to 5 cm with 41 uniformly spaced locations, thus occupying the central ninth of the total test section span.

2.2 Results and discussion

The streamwise evolution of phase-averaged spanwise vorticity ($\langle \Omega_z \rangle / U_e$, cm^{-1}) along the wake centerline ($Z = 0$) is depicted in Figs. 11(*a-d*) for four phases (or times). In effect, every fourth phase out of the 16 measured phases per forcing cycle is presented. The formation and evolution of the two rows of opposite-signed vortices forming the familiar Karman street can be easily tracked through the four phases shown. The initial spanwise instability leading to the first spanwise vortex roll-up occurs at $X \approx 3$ cm. This coincides with the location at which significant streamwise vorticity was first measured.

Details of the vortical structures were examined more closely by using two-dimensional “cuts” through the three-dimensional data. The first signs of any significant streamwise vorticity at phase 1 were found at $X = 3$ cm. This location is just *upstream* of the first positive spanwise roller, which at this phase has not yet peeled away from the initial shear layer (see Fig. 11*a*). It also coincides with the location where the instability leading to the formation of the spanwise rollers first appears. The fact that significant streamwise vorticity is not measured in the

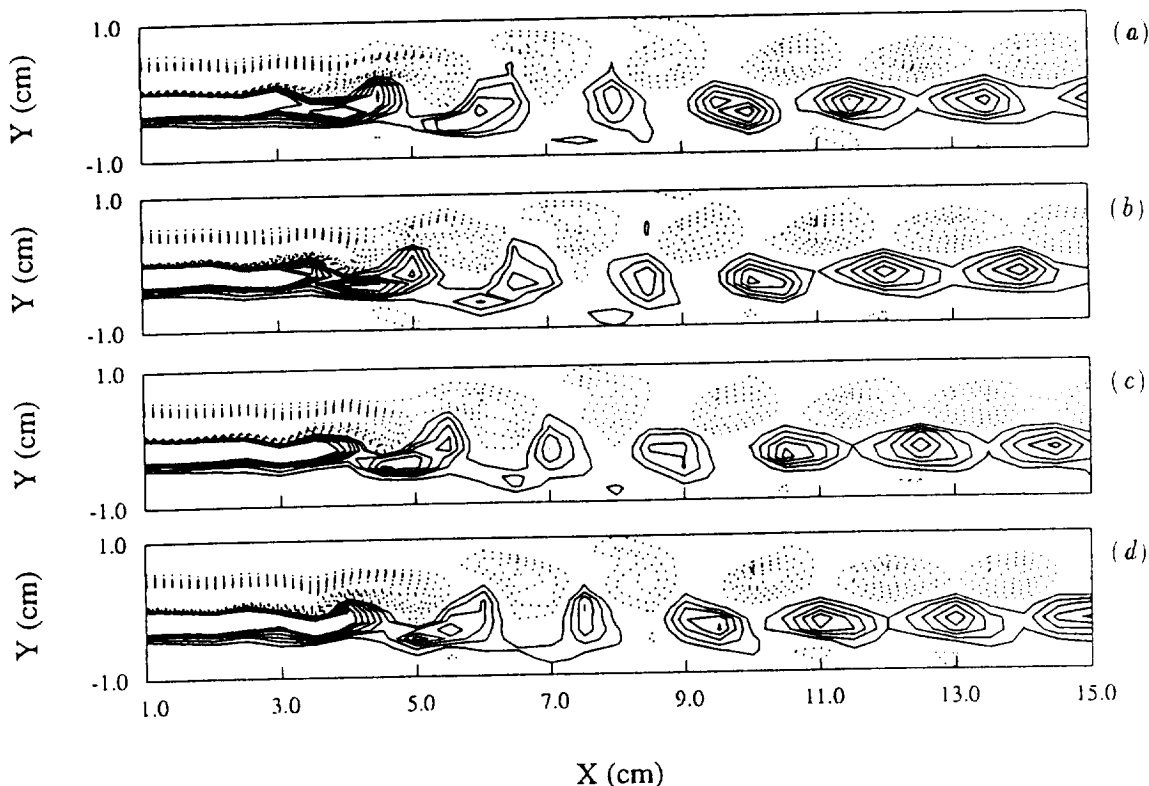


FIGURE 11. Centerplane phase-averaged spanwise vorticity ($\langle \Omega_z \rangle / U_e$, cm^{-1}) contours at various phases. Lowest level = ± 0.15 , increment = ± 0.15 . (a) phase 1; (b) phase 5; (c) phase 9; (d) phase 13.

very near-field region ($1 < X < 2.5$ cm) of the present wake supports the view that the appearance of streamwise vorticity further downstream is due to an amplification of weak incoming disturbances — it is not just a simple case of *relatively strong* streamwise vorticity being fed in directly from the boundary layers. In this study, perceptible amplification occurs as soon as the first spanwise vortices start to roll up. Since the (upstream) braid undergoes streamwise stretching during this phase, it is presumed that this is the mechanism by which weak incoming disturbances (weak longitudinal vortices) are amplified. Details of the initial streamwise structures are not uniform across the span because the “natural” disturbance environment of the incoming flow field is not expected to be uniform.

In order to investigate the incoming disturbance field and initial formation region in more detail, the cross-stream plane streamwise vorticity contours at $X = 3$ cm are presented in Figs. 12(a) and (b) for phases 5 and 9. These figures show that the incoming disturbance field is in the form of an approximate single row of counter-rotating streamwise vortices whose cross-stream (Y) location changes with phase. On comparing Figs. 12(a) and (b), which are exactly one half cycle apart, it is evident that a single row appears on the lower half of the wake at phase 5, but on

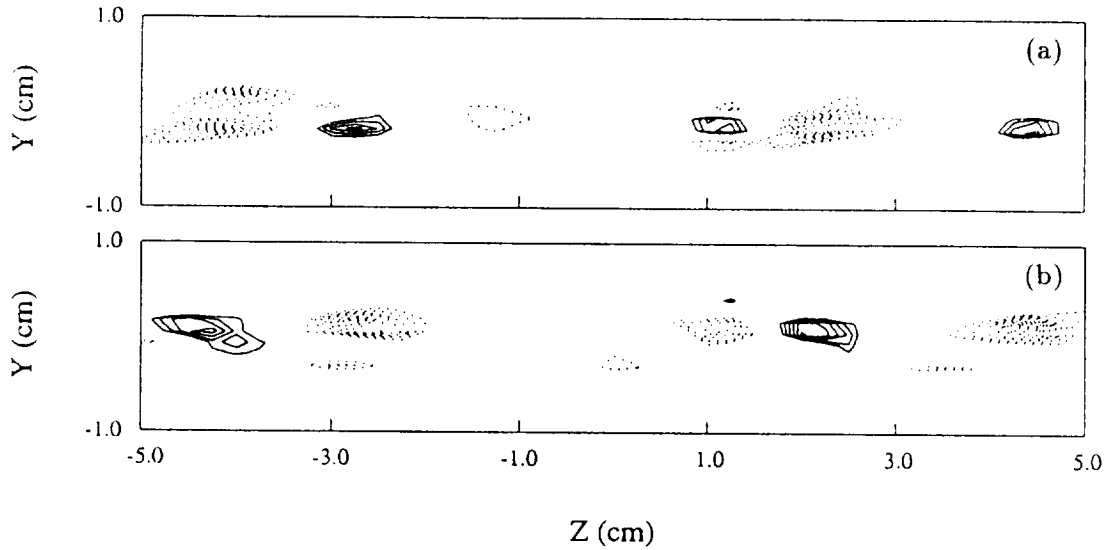


FIGURE 12. Phase-averaged streamwise vorticity ($\langle \Omega_x \rangle / U_e$, cm^{-1}) contours at $X = 3$ cm for various phases. Negative $\cdots\cdots$, positive — , lowest level = ± 0.015 , increment = ± 0.05 . (a) phase 5; (b) phase 9.

the upper half at phase 9. On inspecting Figs. 11(b) and (d), it is apparent that at phase 5 the lower spanwise vortex is rolling-up prior to shedding, whereas at phase 9 the same situation is true for the upper roller. So it appears as though disturbances from both boundary layers are fed into the wake and amplified. At a given phase, depending on which (positive or negative) spanwise vortex is rolling up, the disturbances fed into that vortex sheet are amplified as the sheet is stretched. Thus, an alternating-signed array of streamwise vorticity is generated for every half cycle. This explains why the time-averaged measurements of Weygandt & Mehta (1993) exhibited two rows of mean streamwise vorticity arranged in quadrupoles.

The alternating-signed inlet streamwise vorticity development for every half cycle is characteristic of the “mode 2” disturbance field of Lasheras & Meiburg (1990). In their simulations, this mode resulted in out-of-phase undulations of the primary rollers. These roller distortions were easily recognizable in the current data set. For example, their imprint was evident in YZ -plane contours of streamwise velocity (not shown here), which exhibited a pinching and cresting behavior in the spanwise direction. The same type of behavior was also noted by Weygandt & Mehta (1993) in their mean velocity contours.

It is not clear from the present study if it will always be the alternating-signed streamwise vorticity of mode 2 that is generated when the wake develops from “natural” laminar boundary layers. It has been shown in both simulations and experiments that the “mode 1” perturbation can also be sustained if the corresponding disturbance field is introduced at the wake origin (Buell & Mansour 1989*b*; Lasheras

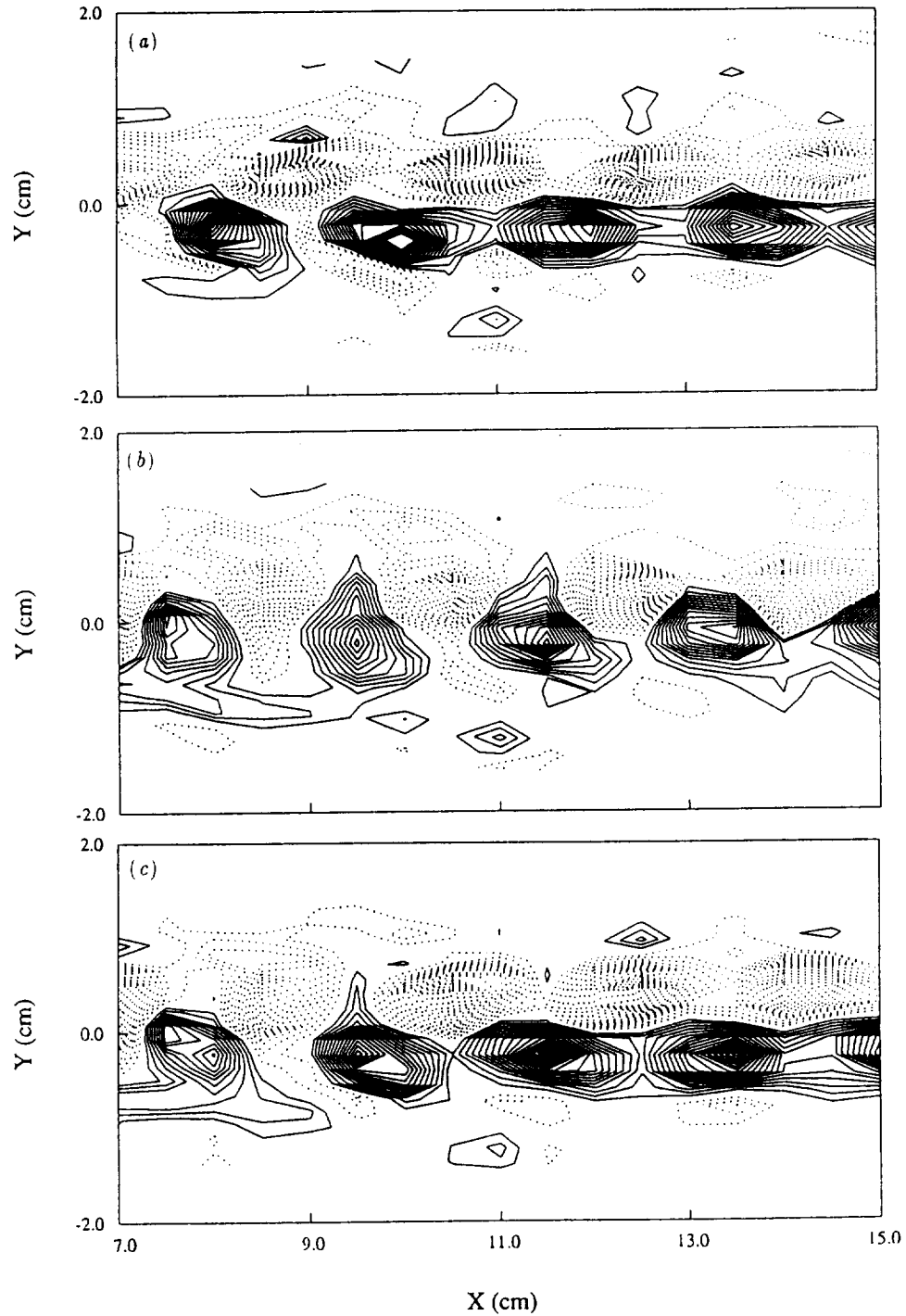


FIGURE 13. Phase-averaged spanwise vorticity ($\langle \Omega_z \rangle / U_e, \text{cm}^{-1}$) contours at phase 1. Negative $\cdots\cdots$, positive --- , lowest level = ± 0.05 , increment = ± 0.05 . (a) Cut through a rib at $Z = 2.25$ cm; (b) Cut through a region between ribs, $Z = 3.25$ cm; (c) Cut through a rib at $Z = 4.25$ cm.

& Meiburg 1990). The mode 1 disturbance field consists of the same-signed streamwise vorticity for every half-cycle and leads to an in-phase undulation of the primary rollers. In the present study, the results suggest that disturbances from both boundary layers are fed into the wake as discussed above. It is fair to assume that, at least upstream of the splitter plate trailing edge, the disturbance fields in the two boundary layers are fully independent of each other. So it is either a coincidence that the inlet disturbance field corresponds to mode 2, or there must be some realignment of the disturbances in the region immediately downstream of the splitter plate trailing edge ($0 < X < 3$ cm) which reorganizes a random field into one corresponding to mode 2. Since the initial disturbance field is typically too weak to measure directly, this issue cannot be easily settled in experimental studies.

In order to examine the details of the vorticity morphology, longitudinal (XY) cuts in the Karman vortex street region ($X = 7$ to 15 cm) showing spanwise and streamwise vorticity contours are presented in Figs. 13 and 14, respectively. The XY -planes are chosen based on the spanwise locations of the streamwise structures, as shown, for example, in the cross-stream contours of streamwise vorticity included as Fig. 15. Two of the planes cut through adjacent rib structures at $Z = 2.25$ cm (Figs. 13*a* and 14*a*) and 4.25 cm (Figs. 13*c* and 14*c*) and the third ($Z = 3.25$ cm) represents the plane in between the two streamwise structures (Figs. 13*b* and 14*b*).

Of course, in the plane between the legs of the loops ($Z = 3.25$ cm), no significant streamwise vorticity is measured (Fig. 14*b*). However, in the rib-planes, it is clear from Figs. 14(*a*) and (*c*) that apart from rib vorticity connecting the spanwise rollers, the rollers themselves also make a significant contribution to the streamwise vorticity. This is a result of the rollers becoming kinked (along the span) in the streamwise direction. Note that on a given side of the wake (positive or negative Y), the streamwise vorticity contribution due to roller kinking is of opposite sign to that of the ribs. This effect has also been noted in numerical simulations of wakes (Buell & Mansour 1989*b*), and it is attributed to vortex stretching terms in the streamwise vorticity equation (Buell 1991). The streamwise vorticity due to the roller kinking is staggered relative to the ribs in the Y -direction, thus forming the four-tier structure observed in YZ -planes (Fig. 15).

The main difference between the cuts at $Z = 2.25$ cm and $Z = 4.25$ cm is that regarding the sign of the ribs; the upper ribs are negative and the lower ribs are positive in Fig. 14(*a*) whereas in Fig. 14(*c*) the upper ribs are negative and the lower positive. This configuration strongly suggests the vortex loop structure proposed by Lasheras & Meiburg (1990) for their mode 2 perturbation. If the present three-dimensional structure indeed consists of vortex loops, then the “heads” of the loops should be visible in the spanwise vorticity contours at $Z = 3.25$ cm, the plane separating the rib structures at $Z = 2.25$ and $Z = 4.25$ cm. Small spanwise vorticity peaks, relative to the primary Karman vortex street, are certainly discernible in Fig. 13(*b*). It is noteworthy that the peaks appear on *both* sides of the wake, implying that it is indeed the mode 2 configuration — the mode 1 perturbation would only produce peaks on one side of the wake. Local spanwise vorticity peaks are also observed in Figs. 13(*a*) and (*c*), the planes cutting through the rib vortices.

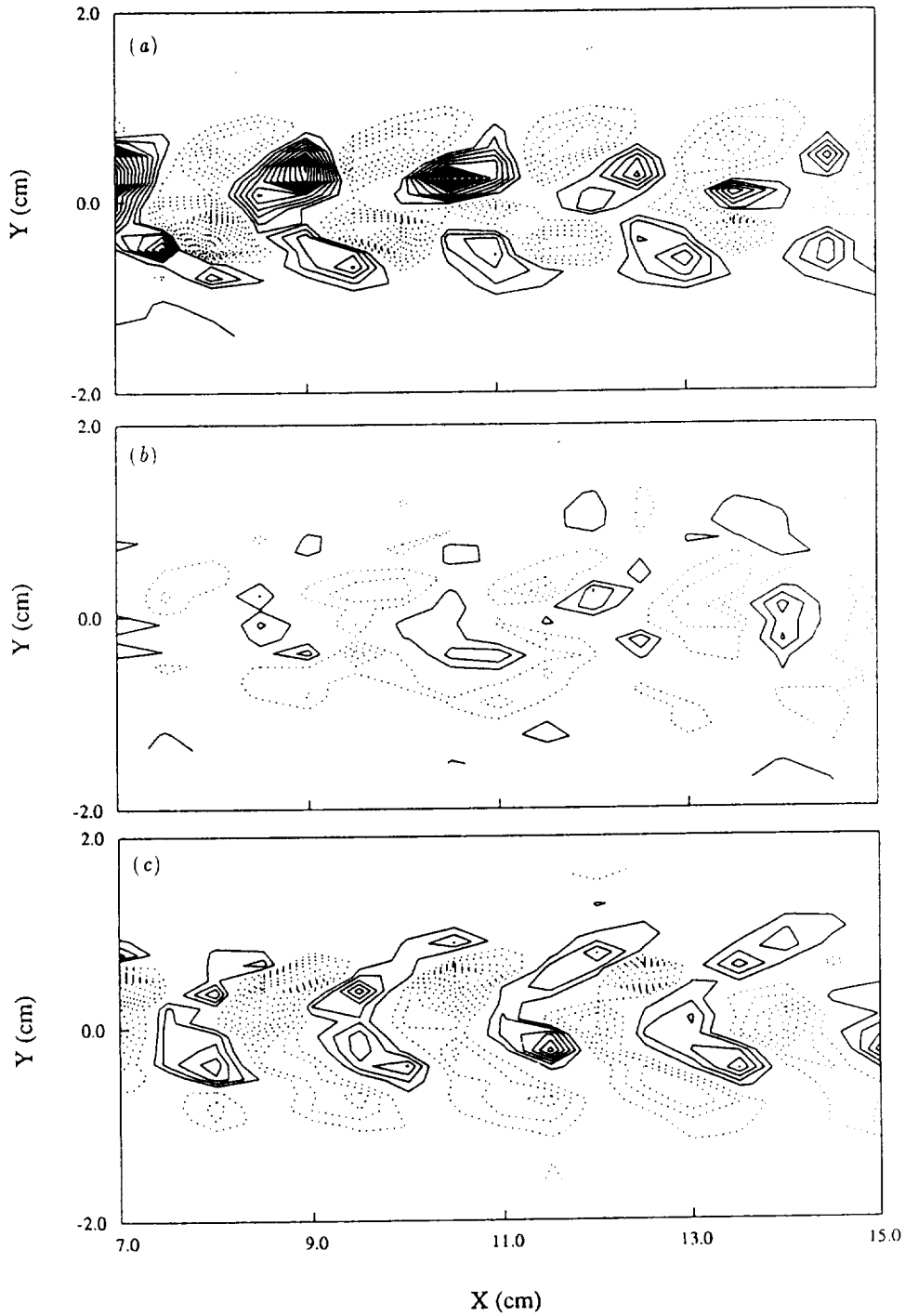


FIGURE 14. Phase-averaged streamwise vorticity ($\langle \Omega_x \rangle / U_e$, cm^{-1}) contours at phase 1. Negative , positive ———, lowest level = ± 0.05 , increment = ± 0.05 . (a) Cut through a rib at $Z = 2.25$ cm; (b) Cut through a region between ribs, $Z = 3.25$ cm; (c) Cut through a rib at $Z = 4.25$ cm.

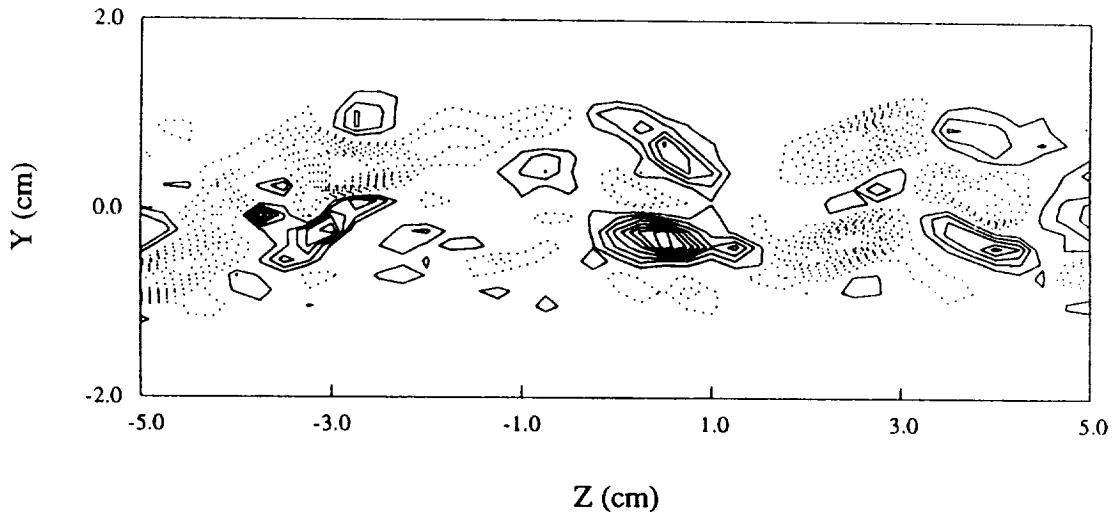


FIGURE 15. Cross-stream plane phase-averaged streamwise vorticity ($\langle \Omega_x \rangle / U_e$, cm^{-1}) contours in the Karman vortex street region at phase 1 and $X = 10$ cm. Negative \cdots , positive — , lowest level = ± 0.05 , increment = ± 0.05 .

This observation implies that the ends of the vortex loops wrapping around the spanwise rollers are inclined in the spanwise direction.

The present results clearly show that a plane wake originating from laminar boundary layers will develop a three-dimensional structure in the form of streamwise vorticity as soon as the primary instability generates spanwise vortex rollers. The secondary structure takes the form of vortex loops which connect opposite-signed spanwise rollers. The details of the vortex loop structures are dependent on the initial disturbance field. This secondary structure topology forms an integral and important part of a transitioning wake, and it must be accounted for in all modeling and wake control studies.

Acknowledgements

This work was performed in the Fluid Mechanics Laboratory, NASA Ames Research Center in collaboration with Dr. R. D. Mehta. We are grateful to Drs. R. D. Moser and M. M. Rogers for many helpful discussions. We would like to thank Dr. J. H. Watmuff for sharing his digital sine-wave generator design and also for many invaluable suggestions.

REFERENCES

- BELL, J. H. AND MEHTA, R. D. 1992 Measurements of the streamwise vortical structures in a plane mixing layer. *J. Fluid Mech.* **239**, 213.
- BUELL, J. C. 1991 A hybrid numerical method for three-dimensional spatially-developing free-shear flows. *J. Comp. Phys.* **95**, 313-338.

- BUELL, J. C. & MANSOUR, N. N. 1989a Asymmetric effects in three-dimensional spatially-developing mixing layers. *Proc. Seventh Symp. Turbulent Shear Flows, Stanford University, August, 9.2.1-9.2.6.*
- BUELL, J. C. & MANSOUR, N. N. 1989b Near-field structures in three-dimensional spatially-developing wakes. *Proc. Tenth Australasian Fluid Mechanics Conference, Melbourne, Australia, 9.21-9.24.*
- HUANG, L. S. & HO, C. M. 1990 Small-scale transition in a plane mixing layer. *J. Fluid Mech.* **210**, 475-500.
- JIMENEZ, J. 1983 A spanwise structure in the plane mixing layer. *J. Fluid Mech.* **132**, 319-326.
- LASHERAS, J. C. & CHOI, H. 1988 Three-dimensional instability of a plane free shear layer: an experimental study of the formation and evolution of streamwise vortices. *J. Fluid Mech.* **189**, 53-86.
- LASHERAS, J. C. & MEIBURG, E. 1990 Three-dimensional vorticity modes in the wake of a flat plate. *Phys. Fluids A.* **12**, 371-380.
- LEBOEUF, R. L. 1993 Vortical structure in a forced plane mixing layer. *Annual Research Briefs - 1993*, Center for Turbulence Research, NASA Ames Research Center - Stanford University, 285-298.
- LEBOEUF, R. L. & MEHTA, R. D. 1994a On using Taylor's hypothesis for three-dimensional mixing layers. Submitted to *Phys. Fluids*.
- LEBOEUF, R. L. & MEHTA, R. D. 1994b Vortical structure morphology in a forced mixing layer: initial roll-up and pairing. Submitted to *J. Fluid Mech.*
- LEBOEUF, R. L. & MEHTA, R. D. 1994c Measurements of spanwise scale change in a forced mixing layer. Submitted to *J. Fluid Mech.*
- LEBOEUF, R. L. & MEHTA, R. D. 1994d Topology of the near-field vortical structures in a three-dimensional wake. Submitted to *J. Fluid Mech.*
- MEIBURG, E. & LASHERAS, J. C. 1988 Experimental and numerical investigation of the three-dimensional transition in plane wakes. *J. Fluid Mech.* **190**, 1-37.
- MOSER, R. D. & ROGERS, M. M. 1993 The three-dimensional evolution of a plane mixing layer: pairing and transition to turbulence. *J. Fluid Mech.* **247**, 275-320.
- NYGAARD, K. J. & GLEZER, A. 1991 Evolution of streamwise vortices and generation of small-scale motion in a plane mixing layer. *J. Fluid Mech.* **231**, 257-301.
- ROGERS, M. M. & MOSER, R. D. 1991 The three-dimensional evolution of a plane mixing layer. Part 1. The Kelvin-Helmholtz rollup. *NASA T-M 103856.*
- ROGERS, M. M. & MOSER, R. D. 1992 The three-dimensional evolution of a plane mixing layer: the Kelvin-Helmholtz rollup. *J. Fluid Mech.* **243**, 183-226.
- ROGERS, M. M. & MOSER, R. D. 1993 Spanwise scale selection in plane mixing layers. *J. Fluid Mech.* **247**, 321-337.

- TUNG, C. H. 1992 Initial streamwise vorticity formation in a two-stream mixing layer. *PhD Dissertation*, University of Houston.
- WEYGANDT, J. H. & MEHTA, R. D. 1993 Three-dimensional structure of straight and curved plane wakes.. *JIAA Rep. TR-110*. Dept. of Aeronautics and Astronautics, Stanford University. Shortened version to appear in *J. Fluid Mech.*

Numerical study of boundary layer interaction with shocks - method and code validation

By N. A. Adams

1. Motivation and objectives

A major problem in modeling of turbulent supersonic flows is the correct assessment of viscous-inviscid interaction problems. Of particular interest is the interaction of boundary layers with shocks. Present turbulence models give in most cases unsatisfactory results in the region of rapid distortion and in the separation region (if one is present) in particular with regard to mean flow profiles and turbulence quantities (cf. Kline *et al.*, 1981).

Recent direct numerical simulations (DNS) at moderate supersonic Mach numbers of boundary layers without interaction show that the effect of compressibility in those cases is rather small (Guo & Adams, 1994). Even at those Mach numbers, however, compressibility can have a significant effect in case viscous-inviscid interaction is present.

Compression corner flows are of great practical interest since they appear to be omnipresent in aeronautical configurations (aircraft fuselage, fuselage-wing junction, engine inlet, etc.). On the other hand, they also give rise to a particularly interesting combination of phenomena, which all are more or less confined to a relatively narrow region about the corner. First, the turbulence in the oncoming boundary layer responds to a rapid distortion. This is a generalization of the problem of isotropic turbulence interacting with normal shocks (e.g. Lee, 1993) to anisotropic turbulence with inhomogeneous mean shear. Second, for large enough Mach numbers and deflection angles there is a shock-induced unsteady separation. The separation bubble is contained by a detached curved shear layer, and fluctuations in this shear layer, subject to high strain, are strongly amplified. Some experiments report evidence for Görtler-like vortices in the detached shear layer (Smits & Muck, 1987). Third, there is unsteady shock motion, which is suspected to be triggered by bursting events in the oncoming turbulent boundary layer (Andreopoulos & Muck, 1987). And finally, the shock is generated at the wall. This is favorable for direct numerical simulations since it relieves the need to accurately introduce a shock at the outer boundaries.

The objective of the present work is the direct numerical simulation of shock boundary layer interaction. This report summarizes the first phase during which a numerical method suitable for this problem has been developed and a computer code has been written and tested.

2. Accomplishments

The first part of this work focuses on the development of a new type of spatial discretization scheme which combines the spectral-like wave-representation of symmetric compact finite difference schemes (Lele, 1992) with a suppression of aliasing

errors by implicit dissipation at non-resolved wavenumbers and increased robustness against generation of spurious waves at the boundaries. In an additional step the scheme is made shock capturing by switching locally to an essentially non-oscillatory (ENO) scheme near discontinuities (in case of weak solutions). In this report the numerical method is merely outlined; for details the reader is referred to Adams & Shariff (1994).

The newly developed spatial scheme is used to discretize the reduced hyperbolic part of the Navier-Stokes equations while for the parabolic part a symmetric compact finite difference scheme is used (cf. Adams, 1993). This report summarizes the status after implementation and validation of the according computer code.

The performance of the present working code lies in between about 200 MFLOPS and about $140\mu s$ per grid point and time step (pure 3rd order ENO, 2D) and about 500 MFLOPS and roughly $20\mu s$ per grid point and time step (pure compact-FD, 3D) on a single CRAY Y-MP C90 CPU. These relations reflect the increased number of logical instructions required for the non-linear ENO scheme.

2.1 Numerical method

Generalizing the formulation of compact finite-difference schemes (Lele, 1992), a family of centered upwind-biased compact schemes of 5th order is introduced. Numerical dissipation is used to suppress unresolved wavenumbers while an accurate representation of the dispersion relation for resolved wavenumbers is required. This requirement is formulated as a constrained optimization problem. A parameter study allows for the generation of a whole family of locally optimal schemes, one member of which, called P455/1, we are using in this study. The general formula of the schemes is

$$\sum_{\mu=-\mu_l}^{\mu_r} \alpha_{\mu} f_{j+\mu}^{(\sigma)} = \frac{1}{h^{\sigma}} \sum_{\nu=-\nu_l}^{\nu_r} a_{\nu} f_{j+\nu}. \quad (1)$$

In this equation $f_j = f(x_j)$ is the grid function, the derivative of order σ of which is searched for. For scheme P455/1 it is $\sigma = 1$, $\mu_l = \mu_r = \nu_l = \nu_r = 2$ for interior schemes, $\mu_l = \nu_l = 1$, $\mu_r = 2$, $\nu_r = 3$ for the left next-to-boundary scheme and $\mu_l = \nu_l = 0$, $\mu_r = 2$, $\nu_r = 4$ for the left boundary scheme (accordingly for the schemes at the right boundary). The coefficients α_{μ} and a_{ν} are determined from order conditions and the abovementioned optimization problem. For the numerical values see Adams & Shariff (1994).

The discrete derivative operator for a semi-discretized scalar advection equation on a strip consists of interior and boundary schemes whose frequency responses are shown in Fig. 1. It should be noted that the dispersion, Fig. 1a, is well approximated up to wavenumbers larger than 2, significantly increasing the resolved-wavenumber domain when compared with non-compact finite-difference schemes (e.g. that of Rai & Moin, 1993). The numerical dissipation is shown in Fig. 1b.

Moreover, the compact formulation allows for stable high-order boundary closures avoiding the order-drop at the boundary as in Rai & Moin (1993). Note that it has been shown by Gustafsson (1975) that for hyperbolic equations the boundary closures must not be of order less than $(r - 1)$ to maintain a global order r of

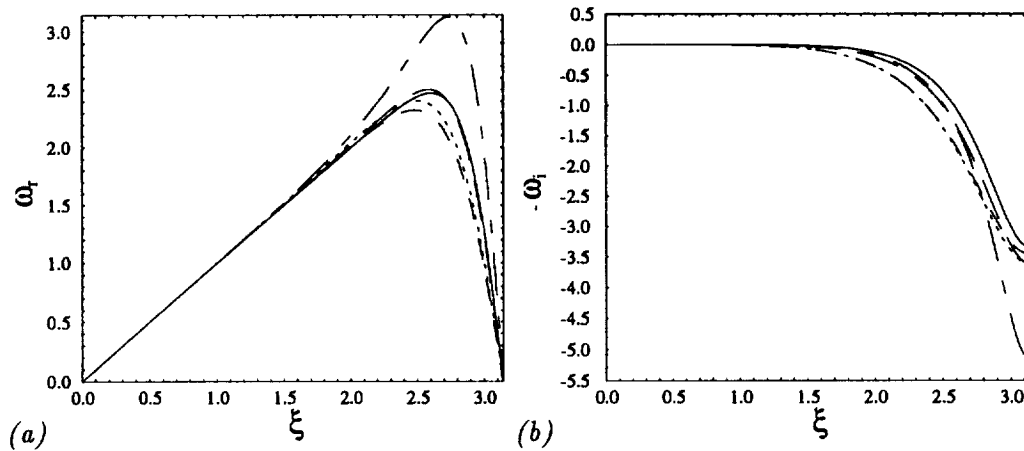


FIGURE 1. Frequency response ω_r of scheme P455/1, (a) real part, (b) imaginary part. scheme at left boundary; ---- scheme next to left boundary; — interior scheme; - - - scheme at right boundary; — — scheme next to right boundary. ξ is the wavenumber normalized with the grid spacing.

the semidiscretization. The linear stability of this scheme is analyzed in Adams & Shariff (1994).

Two different approaches of making an underlying compact scheme shock capturing (nonlinearly stable) have been pursued initially. The first followed the approach of Cockburn & Shu (1994), which required some minor modifications to be applicable for our general type of upwind compact schemes. Numerical tests, however, showed an unsatisfactory shock resolution. A Gibbs-like phenomenon could not be suppressed satisfactorily without a significant smearing of the shock. The second follows the guideline of Hou & Le Floch (1994), who gave evidence that a nonconservative scheme converges to a weak solution (so a solution exists) if in the neighborhood of discontinuities a conservative scheme is used. In our case scheme P455/1 is used in the smooth regions, while a 5th order ENO scheme in finite-difference form (Shu & Osher, 1989) using Roe fluxes on local characteristics with entropy-fix by switching to a local Lax-Friedrichs flux formulation is used near discontinuities. Without being able to give theoretical evidence, numerical tests reported in Adams & Shariff (1994) demonstrate that the hybrid scheme possesses the ENO property.

For integration in time two different 3rd order Runge-Kutta methods are used. A pure ENO scheme as spatial discretization is combined with a TVD Runge Kutta scheme (Shu, 1988). The hybrid scheme is combined with a low-storage explicit Runge Kutta scheme (Williamson, 1980, case 7). The admissible time step is calculated from an estimated bound for the discrete convective and the discrete viscous operator using a CFL (Courant-Friedrichs-Lewy) condition.

2.2 Discretization of the compressible conservation equations

The fundamental equations are the volume-specific conservation equations for

mass momentum and energy

$$\frac{\partial \mathbf{U}}{\partial t} = \frac{\partial \mathbf{F}}{\partial x} + \frac{\partial \mathbf{G}}{\partial y} + \frac{\partial \mathbf{H}}{\partial z} + \mathbf{Z} . \quad (1)$$

The flux vectors \mathbf{F} , \mathbf{G} , and \mathbf{H} are given, for example, in Anderson *et al.*(1984). The viscosity μ is calculated from Sutherland's law. \mathbf{Z} is a distributed forcing which can be used to cancel the residual of a given basic flow (this is done in the calculations of sections 2.4.1 and 2.4.2, otherwise $\mathbf{Z} = 0$). For a discussion of this term see, for instance, Adams (1993).

The fundamental systems of PDE are discretized in a method of lines manner, i.e. the spatial derivatives of the fluxes are approximated by a spatial discretization. The system thus becomes an ODE in t in terms of the grid point values and is projected forward in time with a Runge-Kutta integration method.

The viscous fluxes are discretized in conservative form by a symmetric P346-scheme used in Adams (1993). Note that although a conservative discretization of a linear heat equation with this scheme would be asymptotically unstable (Adams, 1993), this kind of discretization remains bounded in the present case with an upwind discretization of the convective terms. Since a conservative discretization has significantly less operations, it has been given the preference over the non-conservative discretization used in Adams (1993).

The discretization of the convective terms has been a major objective. For the details the reader is referred to Adams & Shariff (1994). Here, it is summarized in a few words. At each t the fluxes calculated from the instantaneous solution are processed by a discontinuity detector algorithm, and cells are marked for treatment by the ENO scheme. In the present code this is done in each index space component, and a whole plane is marked if at least one cell of this plane contains a transition. This is favorable for vectorization but has the disadvantage that the ENO scheme may be used in smooth regions, too. For the marked cells the fluxes are projected on the local characteristics by a transformation with the left-eigenvector modal matrix of the cell's Roe matrix. The flux derivatives at the cell faces (i.e. the nodes) are reconstructed from the cell-centered numerical fluxes on local characteristics obtained with a 5th order ENO scheme using a Roe-flux formulation with a local Lax-Friedrichs flux as entropy fix. The numerical fluxes (after application of the ENO procedure) are then projected back onto the computational space basis by a transformation with the corresponding right-eigenvector modal matrix.

The flux derivatives in the smooth regions are calculated with the positive biased and the negative biased compact schemes. This is done by projecting the fluxes with the respective right-hand side matrices of the schemes onto a local average, where the entries at the grid points at which the solution is to be taken from the ENO procedure are replaced with the already known flux derivatives. The left-hand side is modified accordingly by setting the respective submatrix to unity. In the reconstruction step the so obtained linear equation systems (pentadiagonal) are solved for the positive and negative biased fluxes. The upwinding is done by choosing the flux derivative in upwind direction according to the direction of the local

characteristics at each grid point. In case of a vanishing eigenvalue, the arithmetic mean is taken as is for the flux derivatives obtained by ENO since they are already upwinded. The advantage of this non-building block (though straight forward) flux splitting is that the flux-approximation is smooth up to the order of the scheme at sonic points. This would not be the case in general if split fluxes would be used.

2.3 Outflow boundary treatment

A major concern of direct numerical simulation methods for spatially evolving convective problems is the correct formulation at the outflow boundary. Since this boundary is artificial a prescription of the correct conditions would require the knowledge about the solution at this plane. Several approaches are now in more or less standard use. For incompressible flows there is the relaminarization method of Kloker *et al.*(1993). In compressible flow Pruett *et al.*(1994) use a buffer domain approach. Guo *et al.*(1994) suggested a much simpler method with the same efficiency as the buffer domain approach. In this work we adopt the latter, though in a different formulation, to account for the non-perturbation form of the equations solved here since the basic flow residual is not compensated by a forcing term as in Pruett *et al.*, 1994, and Guo *et al.*, 1994. Simpler approaches, for instance non-reflecting conditions (e.g. Poinso & Lele, 1992), treat viscous wave forms within the boundary layer improperly and give rise to spurious reflected waves.

The basic idea follows closely the concept of a *sponge layer* according to Israeli & Orszag (1981). From a simple model equation as

$$\frac{\partial v}{\partial t} = \frac{\partial v}{\partial x} - \sigma(x)v \quad (2)$$

it is seen that $\sigma(x)$ in the last term of the right-hand side has the character of a *Newtonian cooling* coefficient.

We choose the following damping function (cf. Israeli & Orszag, 1981)

$$\sigma(x) = A_s(N_s + 1)(N_s + 2) \frac{(x - x_s)^{N_s}(L_x - x)}{(L_x - x_s)^{N_s+2}} \quad (3)$$

for $x_s < x \leq L_x$. It has the properties: (i) $\int_{x_s}^{L_x} \sigma(x)dx = A_s$ and (ii) $\sigma(L_x) = 0$.

The implementation is done readily by adding a term

$$\mathbf{Z}_s = -\sigma(x)(U - U_0)$$

for $x_s < x \leq L_x$ to the fundamental equations (1). Herein U denotes the vector of conservative variables and $U_0 = U|_{t=0}$. From property (ii) of σ it is clear that the fundamental equations (1) are recovered at $x = L_x$ where a perfect non-reflecting condition is prescribed (Thompson, 1987).

2.4 Code validation

The computer code is validated using two kind of tests. The first is typical for DNS codes where a known mean flow is enforced and the correct representation of a

TABLE 1. Flow parameters.

Case	M_∞	Re_{δ_1}	T_w/T_∞	α	β	L_z
A	2.5	12773	2.041	0.26	0.43	15
B	4.5	10000	4.38	2.25	0	10

linear eigensolution is required. The second is typical for CFD codes where a mean flow is to be found.

In the first case we check for the efficiency and correct implementation of derivative and integration routines by marching eigensolutions of a temporally evolving boundary layer (streamwise periodic) in time. The global growth rate (defined from the mode energy Eq. (4)) is required to match the real part of the eigenvalue. Also, since the amplitude function is only a function of the wall normal coordinate z , frequency and growth rate at a given z should be close to the imaginary and real part of the eigenvalue locally in z . Inflow and outflow boundary conditions are examined by considering spatial instability in a parallel boundary layer. The spatial growth rate is required to be sufficiently accurately represented and the outflow boundary condition should have a limited upstream effect.

In the second test the steady problem of a shock impinging on a flat plate boundary layer is investigated. Though none of the methods used here is suitable to obtain steady state solutions efficiently, evidence is given that the (quasi time dependent) solution marches toward a steady state. After a reasonable number of iterations the computations are halted and compared with reference data.

2.4.1 Eigensolutions of temporally evolving boundary layer

As test cases we choose cases B and C from Adams (1993, section 6.1). For completeness the flow parameters are given in table 1. A combined algebraic- \sinh mapping is used in z ; see Adams, 1993, section 6.1 for parameters. Boundary conditions are periodic in x and y , non-reflecting at $z = L_z$, and isothermal no-slip at the wall with the wall temperature set to the adiabatic wall temperature (Mack, 1984).

The unperturbed mean flow is calculated from the compressible similarity equations (Stewartson, 1964) with a shooting method (Adams, 1993). An unstable eigenmode with streamwise and spanwise wavenumbers α and β , respectively, as given in table 1 calculated from a spectral solution method (Simen, 1993) (used earlier in Adams, 1993) is superimposed. For case A the eigensolution is an oblique vortical mode, for case B a two dimensional Mack mode (mixed vortical/acoustic). In both cases the initial amplitude is $A = 10^{-4}$. The grid spacing in x and y is uniform, the box dimensions are chosen consistently with the wavenumbers such that the eigenmodes become $(\pm 1, \pm 1)$ and $(\pm 1, 0)$ Fourier modes, respectively.

For the calculations scheme P455/1 is used. Since the solution is smooth the

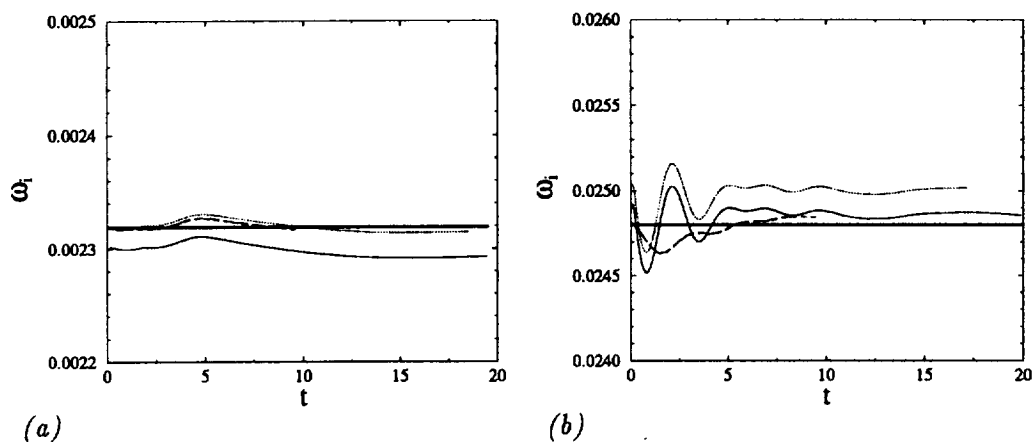


FIGURE 2. Global growth rate. (a) test case A, — (10 × 10 × 50), (20 × 20 × 50), ---- (20 × 20 × 100), — (40 × 40 × 100), — linear theory. (b) test case B, — (10 × 50), (20 × 50), ---- (20 × 100), — (40 × 100), — linear theory.

ENO scheme is inactive. We define a modal energy as

$$E(k_x, k_y; t) = \int_0^{L_z} \bar{\rho}(z) \hat{u}_j(k_x, k_y; t) \hat{u}_j^*(k_x, k_y; t) dz \quad (4)$$

u_j stands for the three velocity components (sum over j).

Fig. 2 shows the growth-rate obtained from the modal energy for different discretizations for 1100 time steps each. The initial transient is an effect of different solution methods and different meshes used for the initial eigenmode and for the DNS.

Figs. 3 and 4 show the local growth rate and frequency across the boundary layer for test cases A and B, respectively, making use of the fact that the eigenfunction maintain their shape in a parallel boundary layer. The improvement from a discretization 10 × 50 to 20 × 100 is mainly due to the refinement in z which allows for a better resolution of the region around the critical layer which is also a region of high curvature of the mean-flow profiles.

2.4.2 Eigensolutions of spatially evolving boundary layer

Since the y -discretization remains unchanged compared to the test cases in section 2.4.1, we can restrict ourselves here to 2D-problems. The main concern is the correct formulation of the inflow boundary condition and the efficiency of the outflow-boundary condition given in section 2.3. The test case is the spatially evolving equivalent of case B of section 2.4.1. Also, since it has been found in section 2.4.1 that $N_z = 51$ is about sufficient to resolve the eigenfunctions in z , we focus on the effect of changing N_x and the outflow boundary condition parameters. At the inflow all primitive variables are prescribed (as function of t) according to the

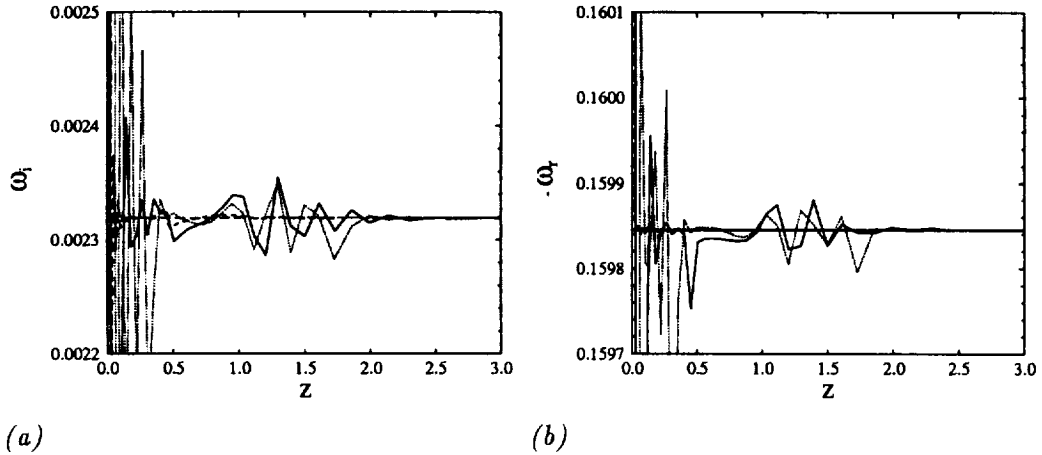


FIGURE 3. Local growth rate and frequency test case A. (a) growth rate ω_i . (b) frequency ω_r . — ρ , (20 × 50), u , (20 × 20 × 50), ---- ρ , (40 × 40 × 100), — — u , (40 × 40 × 100), ——— linear theory.

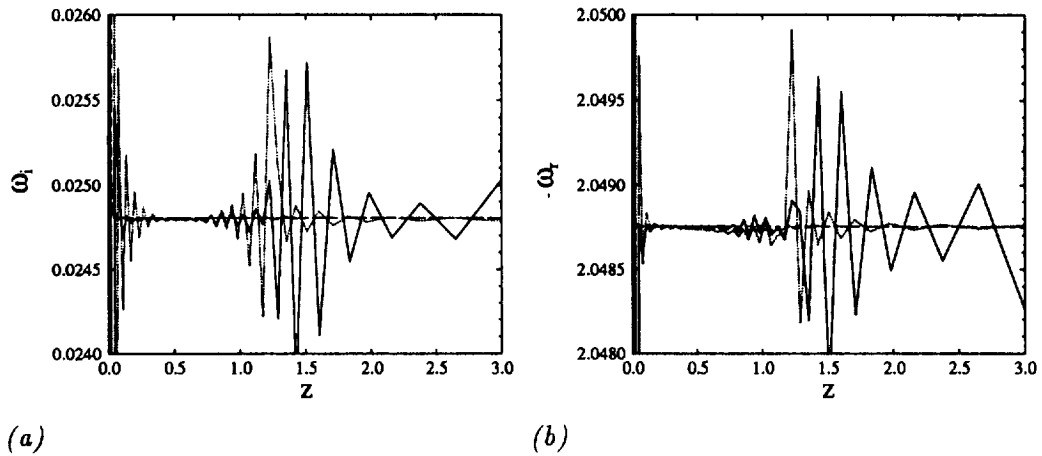


FIGURE 4. Local growth rate and frequency, test case B, (a) growth rate ω_i . (b) frequency ω_r . — ρ , (20), u , (20 × 50), ---- ρ , (40 × 100), — — u , (40 × 100), ——— linear theory.

well-posedness requirement (Oliger & Sundström, 1978); at the outflow the sponge layer of section 2.3 together with a non-reflecting condition at $x = L_x$ is used. As validation-test we check for the correct spatial growth rates in terms of primitive variables at an arbitrary position z . The growth rates are obtained from the coefficients of the solution's Fourier transform in y and t . These coefficients assume the form

$$\hat{a}_{\hat{y}i}(x, z) = \hat{A}(z)e^{i\alpha x} \quad (5)$$

where $\hat{A}(z)$ is the complex amplitude function of the linear eigensolution. From two

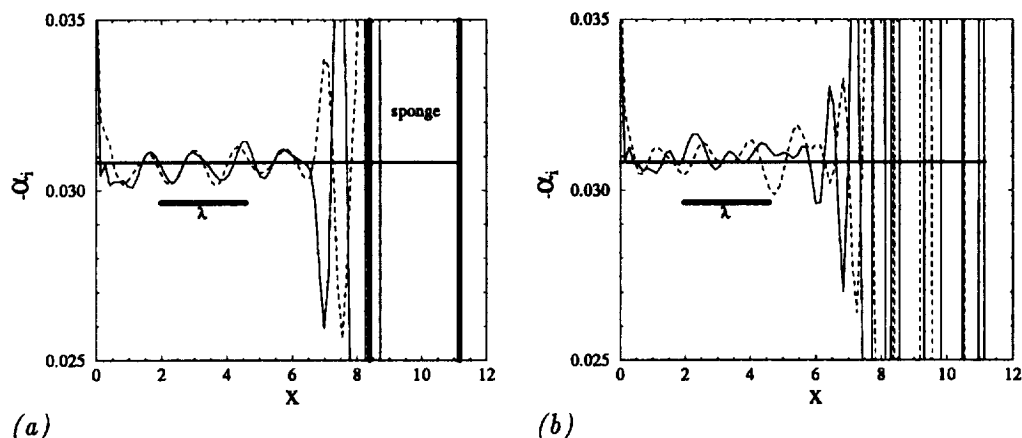


FIGURE 5. Local growth rate, $N_x = 81$, $A_s = 4$, $N_s = 3$, $z = 0.48$, $\delta t = 4\pi/\omega$. (a) sponge layer and non-reflecting boundary condition. (b) non-reflecting boundary condition only. — ρ , ---- u , ——— linear theory.

successive x -stations the complex α can then be obtained by

$$\alpha = -i \frac{\ln[\hat{a}_{y_i}(x_2, z)] - \ln[\hat{a}_{y_i}(x_1, z)]}{x_2 - x_1}, \quad (6)$$

so that the growth rate is $-\text{Im}(\alpha)$ and the frequency $\text{Re}(\alpha)$.

Fig. 5 shows the effect of the sponge layer. From the experience with a symmetric compact scheme (Guo *et al.*, 1994) we choose the sponge layer thickness to be one wavelength of the eigenmode. The minimum necessary sponge-layer thickness is problem dependent and is therefore not further investigated here. Spurious reflected waves penetrate into the computational domain further upstream in the case of a pure non-reflecting boundary condition, Fig. 5b, than in the case of a non-reflecting boundary condition plus a sponge layer, Fig. 5a. Though this effect is not so pronounced for the low amplitude linear perturbation in the present case, it is expected to be stronger for large amplitude turbulent fluctuations. Note that non-reflecting boundary conditions are not consistent with the evolution of a boundary layer eigensolution. This reflects in large oscillations near the outflow boundary of a sensitive measure as the local growth rate, Fig. 5b.

From Fig. 6 it is evident that increasing the order N_s of the cooling function polynomial in Eq. (3), (making the damping more localized) or increasing the cooling intensity A_s has no noticeable effect on the growth rate or the extent of the valid domain. Thus it is expected that an increased damping is able to extinguish stronger turbulent fluctuation efficiently without increasing the invalid part of the domain.

Fig. 7a shows the same case as Fig. 5a, but the integration time is increased to seven periods so that the wave can travel about two times the width of the computational box. Obviously the region of upstream influence of the boundary

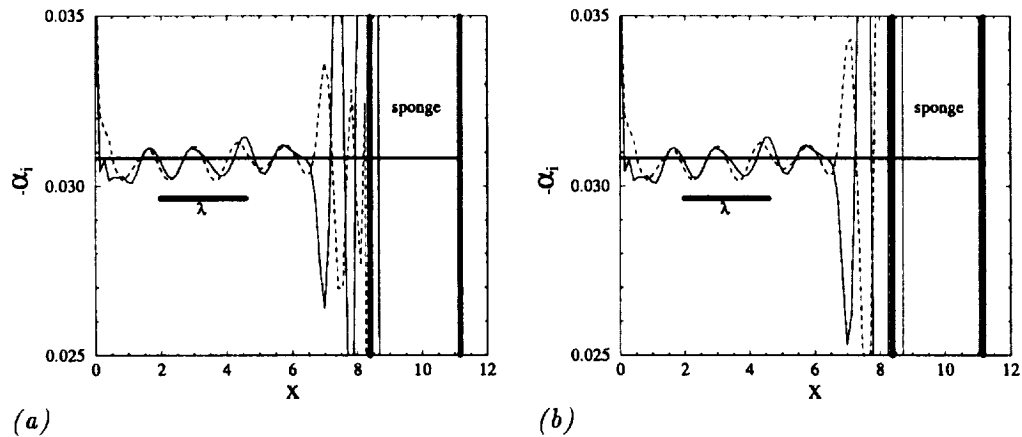


FIGURE 6. Local growth rate, $N_x = 81$, $\delta t = 4\pi/\omega$. (a) $A_s = 4$, $N_s = 7$. (b) $A_s = 10$, $N_s = 3$. — ρ , - - - u , — linear theory.

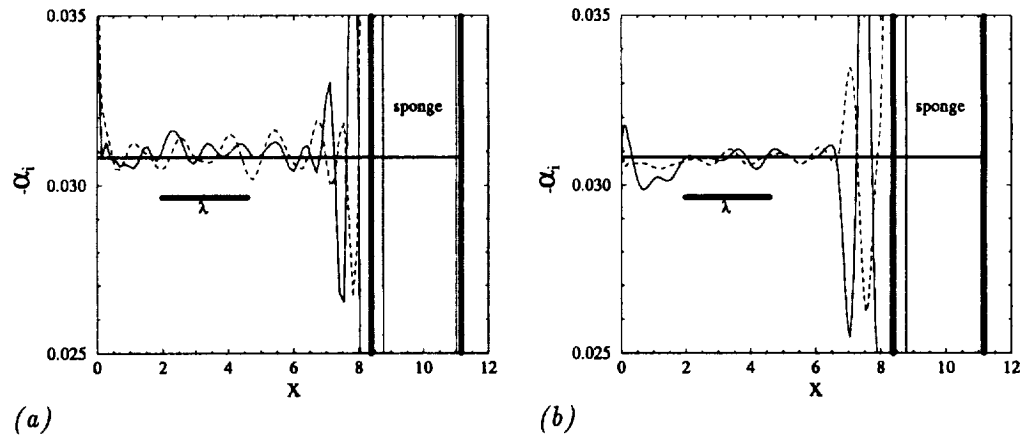


FIGURE 7. Local growth rate. (a) $N_x = 81$, $N_z = 51$, $\delta t = 14\pi/\omega$. (b) $N_x = 161$, $N_z = 101$, $\delta t = 4\pi/\omega$. — ρ , - - - u , — linear theory.

condition did not increase, so that the shorter integration times used before lead to correct conclusions about the upstream extent of the invalid part of the domain. In Fig. 7b both streamwise and vertical number of grid points are doubled, which results in a more accurate approximation of the growth rate as expected.

Two remarks are in order. Firstly we note that the setup used in the above test calculations is quite severe, allowing for only 4 wavelengths λ of the primary wave in x , which finally results in about 2.5λ for the extent of the valid part of the domain. Second, inflow transients are apparently unavoidable (as the initial transients were in the preceding section) since the inflow perturbation is taken from a linear stability solution obtained with a different method and on a different

TABLE 2. Flow parameters.

quantity	value	comment
T_{∞}^*	221.6K	estimated
M_{∞}	2	
p_{∞}^*	9178.79Pa	estimated
Pr	0.72	
κ	1.4	
R	287.03	
μ_{∞}^*	$1.449 \cdot 10^{-5}$ kg/m/s	
S^*	110.4K	
Re_{ξ_0}	140000	
Re_{ξ_1}	450000	
Re_{δ_1}	909.9053	
δ_1^*	$1.5309 \cdot 10^{-4}$ m	at ξ_0 , from sim. sol.
δ_0^*	$4.7325 \cdot 10^{-4}$ m	99.9% thickness
ξ_0	82.7559	
L_x	415	
L_z	200	

mesh. Other DNS results (e.g. Pruett *et al.*, 1994, Guo *et al.*, 1994) confirm this observation.

It can be concluded that the outflow boundary treatment has no upstream effect further than roughly 1.5λ upstream of L_x for $(L_x - x_s) = \lambda$. The findings in this section resemble the experiences made by Guo *et al.*(1994) with a different spatial discretization and a different cooling term. Pruett *et al.*(1994) report that their buffer domain approach spoils an upstream region of about 2λ . The sponge layer approach thus allows for a much simpler formulation with a comparable performance of a well-tuned buffer-domain approach.

2.4.3 Laminar boundary layer interacting with an impinging shock

The following test example is a standard case for the validation of steady state Navier-Stokes solvers. Experimental data are provided by Hakkinen *et al.*(1959). Although the experimental evaluation is limited and the comparison suffers from incompletely reported flow parameters, the experiment's favorable feature is that the flow is laminar, although it should be noted that the test section extends into the region where the laminar flat plate boundary layer is unstable.

An extensive numerical investigation of this particular problem has been done by Katzer (1989). We emphasize here that for the results presented in this section time-accurate and low-dissipation methods have been used. The computations have thus been halted before a true steady state has been reached. The flow parameters are given in table 2 (reference length is δ_1^* , dimensional quantities are marked with a star).

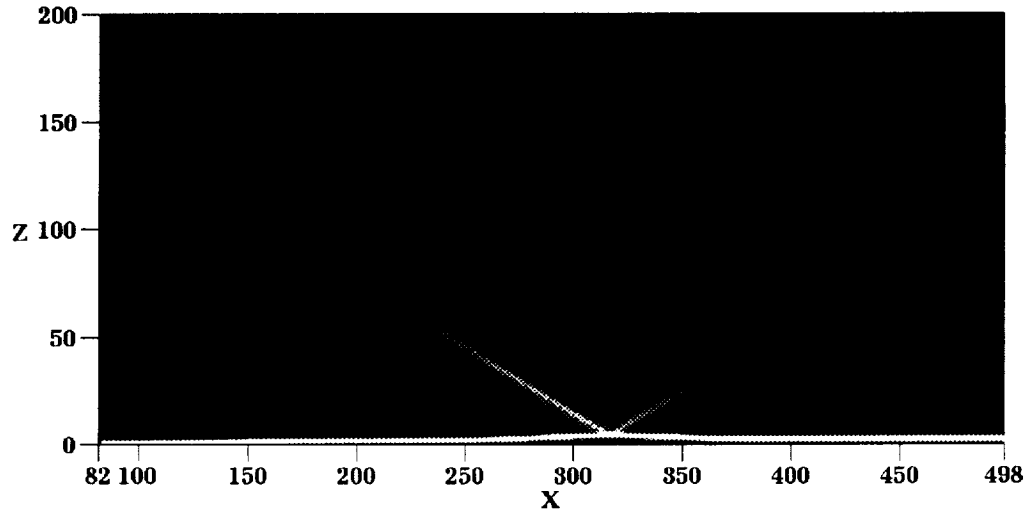


FIGURE 8. Quasi-Schlieren plot (intensity proportional to norm of density gradient).

Fig. 8 shows a quasi-Schlieren plot (merely the norm of the density gradient) when the computations were halted. A shock, introduced at the inflow boundary, impinges at $\beta = 32.6^\circ$ on the laminar boundary layer along a flat plate. At the boundary layer edge it is reflected as a decompression wave. The shock-induced boundary layer separation gives rise to a compression wave in front of the separation region and a compression wave behind.

As initial condition we take the solution of the inviscid shock-reflection problem outside of the boundary layer, while near the wall a boundary layer from a similarity solution is given. The shock is to impinge on the plate at $x_{sh} = 325.2041$ for the inviscid problem.

As boundary conditions we fix at the inflow the initial condition for all primitive variables (giving the correct number of 5 conditions for the Navier-Stokes equations according to Olinger & Sundström, 1978). At the outflow we prescribe perfectly non-reflecting boundary conditions (Thompson, 1987), and no viscous conditions are imposed. In fact the imposition of weak viscous boundary conditions in terms of derivatives of the viscous fluxes (Poinsot & Lele, 1992) was found to have no effect, while the imposition of boundary conditions in terms of stresses (Dutt, 1988) resulted in an outflow boundary-layer due to the inconsistency between boundary condition and solution. At the wall we prescribe a no-slip adiabatic condition. At the upper boundary all flow variables are prescribed corresponding to the state behind the impinging shock. Non-reflecting conditions at the upper boundary (Thompson, 1987) were found to give rise to a viscous (heat-equation like) instability emerging from the corner between inflow and upper boundary. The reason for that behavior is that the presence of the shock close to the upper boundary at the inflow leads to non-negligible viscous terms near the edge of the computational box, and inflow

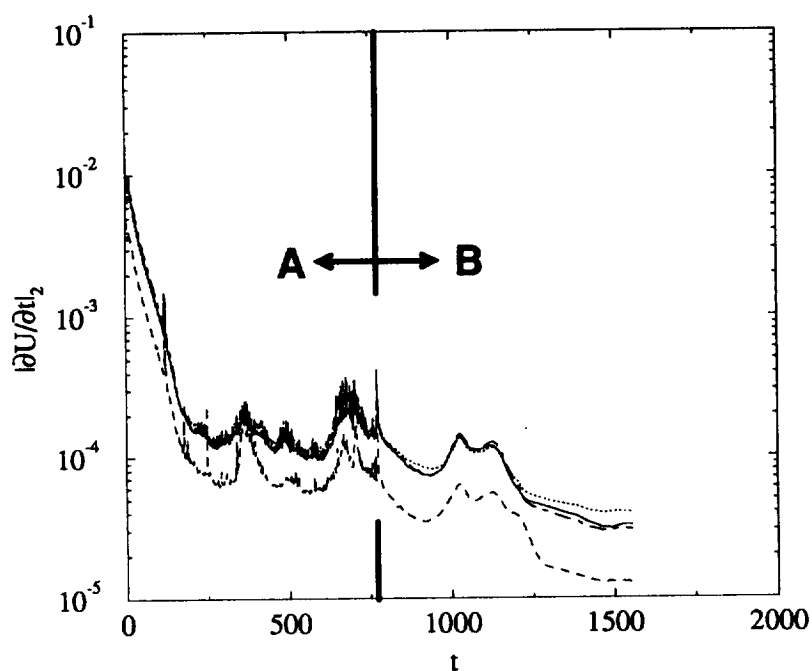


FIGURE 9. Residual. Method A: 3rd order ENO; method B: 5th order hybrid.
 — ρ , ρu , ---- ρw , -.- E .

and boundary conditions which are well posed only in the inviscid limit become invalid.

We perform a calculation with $N_x = 151$ and $N_y = 100$. First, the meaningless transient caused by the initial condition is spanned by marching a 3rd order ENO scheme 5500 iterations in time (method A). Note that since we use a time accurate solution procedure and since the ENO-stencil changes in time, the residual does not reach machine zero but merely the truncation error of the spatial discretization. This has been confirmed by continuing the calculation with method A for 5500 additional iterations (not shown). After the residual settled down the computation is continued for another 5500 iterations with the hybrid scheme (method B). Since the Reynolds number is small, the shock is resolvable by the scheme and the ENO-scheme is only active in z in the outer 4.95% of the domain (in the average over all iterations), where the grid spacing is wide (shock detector parameter settings: $\beta_x = 1$, $\beta_z = 0.05$). Fig. 9 shows the evolution of the residual for the four conservative variables.

Figs. 10 and 11 show pressure contours after 5500 iterations with method A and method B, respectively. The hybrid scheme appears to represent the reflected compression and decompression waves more accurately than the pure ENO scheme. This suggests that the internal phenomena of the boundary layer are better represented.

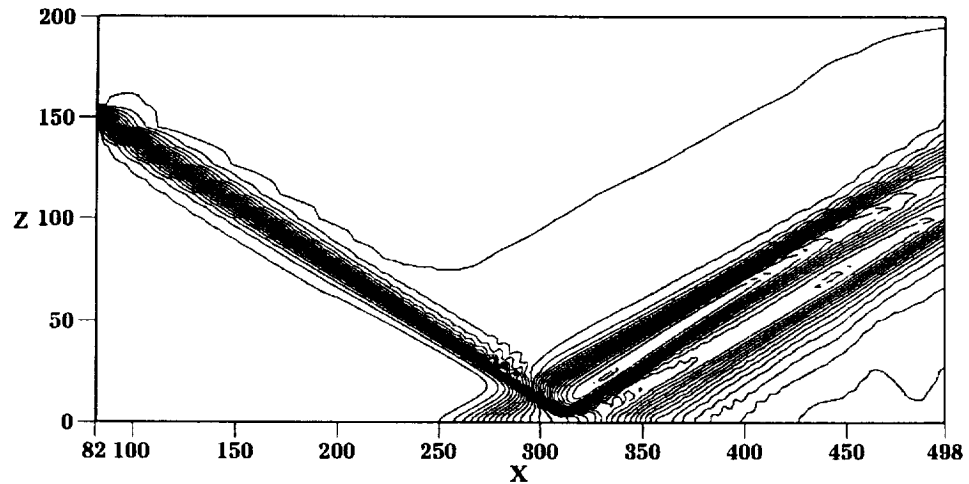


FIGURE 10. Pressure contours after 5500 iterations, method A ($min = 0.16$, $max = 0.26$, $inc = 0.002$).

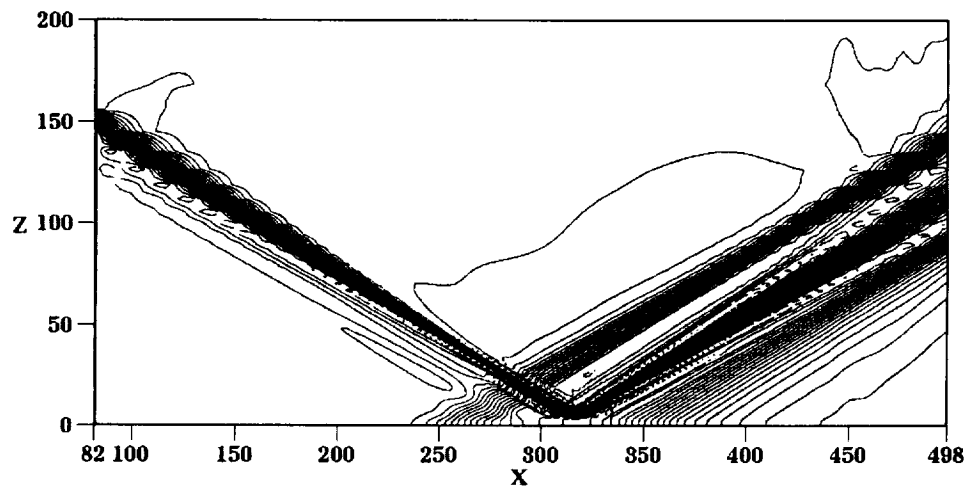


FIGURE 11. Pressure contours after 5500 additional iterations, method B ($min = 0.16$, $max = 0.26$, $inc = 0.002$).

This finding is confirmed if we compare numerical and experimental results. Fig. 12 shows surface pressure and skin friction. In both cases method B gives a better representation. Note that the experimental values downstream of the separation region appear to be affected by the particular method of measuring the skin friction with a pressure probe (Hakkinen, 1959). The accurate numerical solutions of Katzer (1989) show that the experimental values in this region are somewhat too large.

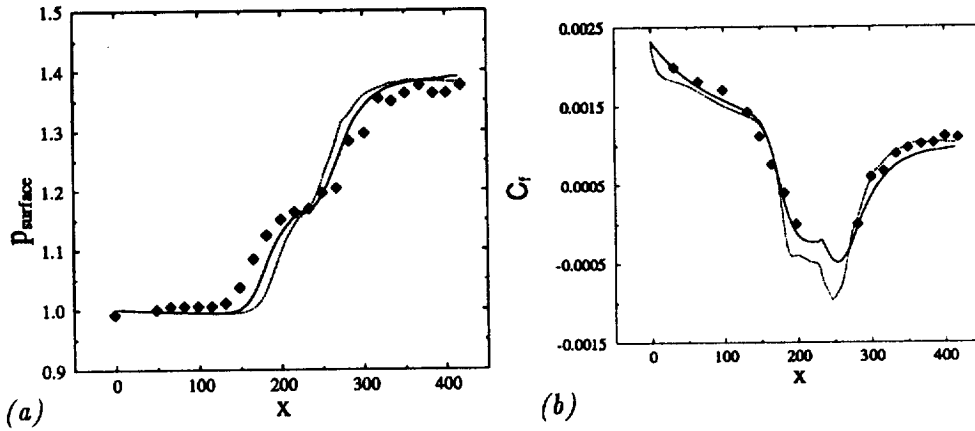


FIGURE 12. Surface pressure (a) and skin friction (b). symbols experiment, after A — after B.

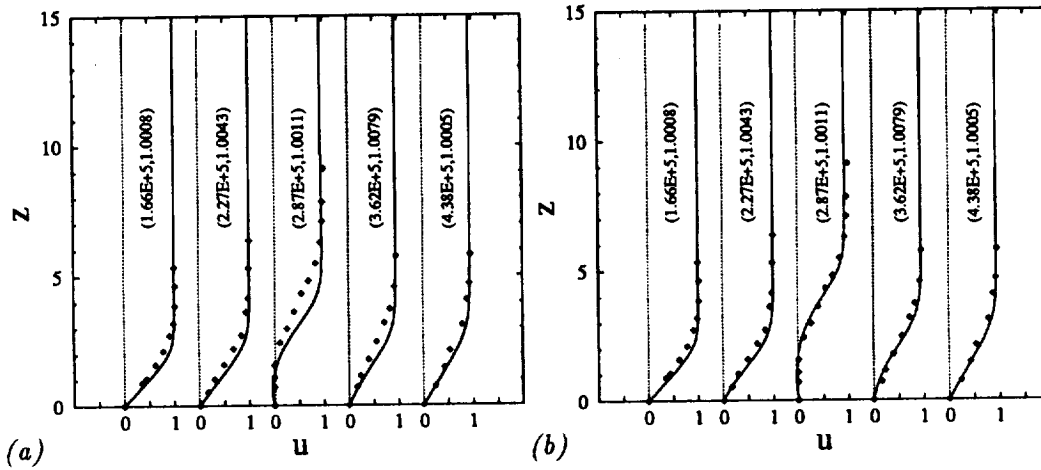


FIGURE 13. Velocity profiles. (a) after A (b) after B. The number-pairs on the curves give Re_{xexp} (first entry) and Re_{xexp}/Re_{xnum} (second entry). symbols experiment, — computation.

The correspondence between experimentally and numerically obtained velocity profiles is reasonable for method B and less satisfactory for method A, figure 13.

Two remarks are in order. First, as can be seen from Fig. 9, the residual is still decreasing when the computation with method B was halted, though with a shallow slope as expected for a time-accurate method. Thus the results should not be considered as converged. Second, the residual level after the computation with method A was halted does not decrease if the computation is continued with method A. The further decrease of the residual and the improvement of the solution is due to method B.

We finally note that for the present 2D calculations the code performance of the

pure 3rd order ENO scheme was 228 MFLOPS and $143 \mu s$ per grid point and time step, while the 5th order hybrid scheme performed at 354 MFLOPS and $23 \mu s$ per grid point and time step (CRAY fpp and cft77 optimization only, single processor Y-MP C90).

3. Future plans

In the next step the computational code will be extended to generalized coordinates (in (x, z)). This requires the characteristic transformation routines to be adapted and an extension of the flux calculation routines.

The final objective is to simulate a compression corner flow according to a suitable experiment. Experiments presently considered are those of Smits & Muck (1987) (having the advantage of relatively detailed turbulence data, the disadvantage of a quite large Reynolds number $Re_{\delta_2} = 78000$) of Ardonceau *et al.* (lacking the details of the previous one but having a smaller Reynolds number of roughly $Re_{\delta_2} = 7700$), and of Zheltovodov *et al.* (at about $Re_{\delta_2} = 9720$ for the incoming boundary layer with the problem that mean flow and turbulence data have been obtained in different wind tunnels). The Mach number range of those experiments is between 2.25 and 3, the turning angles go from 8° to 25° .

Acknowledgments

I acknowledge the preparatory work of K. Shariff, NASA ARC, concerning hybrid schemes, and his help by reviewing a draft of this report. For graphics postprocessing the package COMADI by H. Vollmers, DLR Göttingen, has been used.

REFERENCES

- ADAMS, N. A. 1993 Numerische Simulation von Transitionsmechanismen in kompressiblen Grenzschichten. *Doctoral Dissertation*, Technical University of Munich, Germany. Also *DLR-FB 93-29*, DLR, Germany (in German).
- ADAMS, N. A. & SHARIFF, K. 1994 A high-resolution hybrid compact-ENO scheme for shock-turbulence interaction problems. *CTR Manuscript* in preparation.
- ANDERSON, D. A., TANNEHILL, J. C. & PLETCHER, R. H. 1984 *Computational Fluid Mechanics and Heat Transfer*. Hemisphere Publ. Corp., New York.
- ANDREOPOULOS, J. & MUCK K. C. 1987 Some new aspects of the shock-wave / boundary-layer interaction in compression-ramp flows. *J. Fluid Mech.* **180**, 405-428.
- ARDONCEAU, P., LEE, D. H., ALZIARY DE ROQUEFORT, T. & GOETHALS, R. 1979 Turbulence behavior in shock wave / boundary layer interaction. *AGARD CP-271*, paper 8.
- COCKBURN, B. & SHU, C.-W. 1994 Nonlinearly stable compact schemes for shock calculations. *SIAM J. Numer. Anal.* **31**, 607-627.

- DUTT, P. 1988 Stable boundary conditions and difference schemes for Navier-Stokes equations. *SIAM J. Numer. Anal.* **25**, 245–267.
- GUO, Y. & ADAMS, N. A. 1994 Numerical investigation of supersonic turbulent boundary layers with high wall temperature. *Proc. 1992 Summer Program*, CTR, Stanford Univ. - NASA ARC.
- GUO, Y., KLEISER, L. & ADAMS, N. A. 1994 A comparison study of an improved temporal DNS and spatial DNS of compressible boundary layer transition. *AIAA-paper 94-2371* (sub. to *AIAA Journal*).
- GUSTAFSSON, B. 1975 The convergence rate of difference approximations to mixed initial boundary value problems. *Math. Comput.* **29**, 396–406.
- HAKKINEN, R. J., GREBER, I., TRILLING, L. & ABARBANEL, S. S. 1959 The interaction of an oblique shock wave with a laminar boundary layer. *NASA Memorandum 2-18-59W*.
- HOU, T. Y. & LE FLOCH, P. G. 1994 Why nonconservative schemes converge to wrong solutions: error analysis. *Math. Comput.* **62**, 497–530.
- ISRAELI, M. & ORSZAG, S. A. 1981 Approximation of radiation boundary conditions. *J. Comp. Phys.* **41**, 115–135.
- KATZER, E. 1989 On the length scales of laminar shock/boundary-layer interaction. *J. Fluid Mech.* **206**, 477–496.
- KLINE, S. J., CANTWELL, B. J. & LILLEY, G. M. (EDS) 1981 *Proc. 1980-81 AFOSR-HTTM Stanford Conf. Complex Turbul. Flow, Vol. III*. Thermosci. Div., Stanford Univ., CA.
- KLOKER, M., KONZELMANN, U. & FASEL, H. 1993 Outflow boundary conditions or spatial Navier-Stokes simulations of transition boundary layers. *AIAA Journal* **31**, pp. 620–628.
- LEE, S. S. 1993 Effects of shock strength on shock turbulence interaction. In *Annual Research Briefs - 1993*. CTR, Stanford Univ. - NASA ARC, 329–345.
- LELE, S. K. 1992 Compact finite difference schemes with spectral-like resolution. *J. Comp. Phys.* **103**, 16–42.
- MACK, L. M. 1984 Boundary-layer stability theory. In *Special Course on Stability and Transition of Laminar Flow*. AGARD Rep. No. 709, 3-1–3-81.
- OLIGER, J. & SUNDSTRÖM, A. 1978 Theoretical and practical aspects of some initial boundary value problems in fluid dynamics. *SIAM J. Appl. Math.* **35**, 419–446.
- POINSOT, T. J. & LELE, S. K. 1992 Boundary conditions for direct simulations of compressible viscous flows. *J. Comp. Phys.* **101**, 104–129.
- PRUETT, C. D., ZANG, T. A., CHANG, C.-L. & CARPENTER, M. H. 1994 Spatial direct numerical simulation of high-speed boundary-layer flows – part I: algorithmic considerations and validation. *Theor. Comput. Fluid Dyn.* **6**.

- RAI, M. M. & MOIN, P. 1993 Direct numerical simulation of transition and turbulence in a spatially evolving boundary layer. *J. Comp. Phys.* **109**, 169–192.
- SHU, C.-W. 1988 Total-variation-diminishing time discretizations. *SIAM J. Sci. Stat. Comput.* **9**, 1073–1084.
- SHU, C.-W., & OSHER, S. 1989 Efficient implementation of essentially non-oscillatory shock-capturing schemes. II. *J. Comp. Phys.* **83**, 32–78.
- SIMEN, M. 1993 Lokale und nichtlokale Instabilität hypersonischer Grenzschichtströmungen *Doctoral Dissertation*, University of Stuttgart, Germany. Also *DLR-FB 93-31*, DLR, Germany (in German).
- SMITS, A. J. & MUCK, K.-C. 1987 Experimental study of three shock wave / turbulent boundary layer interactions. *J. Fluid Mech.* **182**, 291–214.
- STEWARTSON, K. 1964 *The Theory of Laminar Boundary Layers in Compressible Fluids*. Oxford University Press, London.
- THOMPSON, K. W. 1987 Time dependent boundary conditions for hyperbolic systems. *J. Comput. Phys.* **68**, 1–24.
- WILLIAMSON, J. H. 1980 Low-storage Runge-Kutta schemes. *J. Comp. Phys.* **35**, 48–56.
- ZHELTOVODOV, A. A., ZAYLICHNY, E. G., TROFIMOV, V. M. & YAKOVLEV, V. N. 1990 An experimental documentation of supersonic turbulent flows in the vicinity of sloping forward and backward facing steps. In Settles, G. S., & Dodson, L. J. 1994 Supersonic and hypersonic shock / boundary-layer interaction database. *AIAA Journal* **32**, 1377–1383.

Resolution requirements for velocity gradients in turbulence

By J. Jiménez¹

1. Motivation

Since high resolution numerical simulations of turbulent flows, or experiments at high Reynolds numbers, represent a substantial investment in resources, the estimation of the minimum resolution required for the study of a given property has been the subject of continued interest. Early results include the papers by Wyngaard (1968, 1969) on the maximum hot wire length allowed for the resolution of the dissipative range of the energy spectrum in isotropic turbulence, and the more recent one by Klewicki and Falco (1990) for wall bounded flows. Both studies conclude that an adequate measurement of the spectrum requires hot wires sensors smaller than approximately three times the Kolmogorov length, $\eta = (\nu^3/\epsilon)^{1/4}$. The latter paper also treats the measurement of velocity gradients and concludes that the same resolution is needed for reliable estimates of the variance of $\partial u/\partial t$, and is probably sufficient for its skewness. From the numerical point of view it has been estimated that the resolution required in a properly de-aliased spectral code for the study of the vorticity structure in the near wall region of a turbulent channel is about 5 Kolmogorov lengths (Kim, Moin and Moser, 1987), although even in that case, the grid spacing in the direction normal to the wall, in which gradients are highest, is usually taken much smaller. The study of the dynamics of intense vorticity structures in isotropic turbulence requires $k_{\max}\eta \geq 2$, where k_{\max} is the largest resolved wavenumber, corresponding to a distance between collocation points $\Delta x/\eta \leq 1.5$ (Jiménez *et al.* 1993).

Different properties require, in general, different resolutions, and the present paper is dedicated to the requirements for the measurement of the probability distribution functions of the velocity gradients and, in particular, of their low order moments. The deviation of these quantities from the values corresponding to a Gaussian distribution was one of the first indications of the presence of Reynolds number-dependent intermittency (Batchelor and Townsend 1949) and has been the object of recent interest as numerical simulations have become able to explore the distribution of gradients in the low Reynolds number range, while new experiments have extended the range to increasingly high Reynolds numbers (Van Atta and Antonia 1980, Saddoughi and Veeravalli 1994). We will use progressive filtering of the results of numerical simulations of isotropic turbulence as a model for the effect of a sensor of finite size (Wyngaard 1968). The numerical issues will be addressed first to insure that the simulations are fully resolved from the point of view of the

¹ Also with School of Aeronautics, U. Politécnica, Madrid.

Re_λ	N	$k_{\max}\eta$	$\Delta x/\eta$	$-F_{3\ell}$	$F_{4\ell}$	$F_{6\ell}$	F_{4t}	F_{6t}
66	256	4	0.78	0.47	4.7	60	6.3	120
94	256	2	1.57	0.52	5.3	80	7.6	200

TABLE 1. Numerical and statistical parameters for the cases analyzed in the paper.

velocity gradients. This will also give us an estimate for the numerical resolution required for the different quantities.

2. The numerical fields

The numerical flow fields are the same used in (Jiménez *et al.* 1993) and are extensively discussed there. They are direct numerical simulations of isotropic homogeneous turbulence in triply periodic boxes at two different Reynolds numbers in the low end of the range for which dissipation first becomes independent of Reynolds number. They are summarized in Table 1.

The numerical method is fully spectral, using primitive variables, \mathbf{u} , p , with dealiasing achieved by a spherical mask and phase shifting (Rogallo 1981, Canuto *et al.* 1987). The resolution N given in Table 1 reflects the number of real Fourier modes in each direction before dealiasing. A more practical measure of resolution is the largest useful wavenumber after de-aliasing, $k_{\max} = \sqrt{2}N/3$. In terms of distance between “effective” collocation points, the grid spacing is $\Delta x = \pi/k_{\max}$. All simulations are forced to achieve a statistically stationary steady state. Forcing is achieved by introducing, for all the modes with wave numbers $k = |\mathbf{k}| \leq 2.5$, a negative viscosity coefficient whose magnitude is adjusted every few time steps so as to keep constant the product $k_{\max}\eta$. The instantaneous energy dissipation rate, ϵ , the one-component r.m.s. velocity, u' , and the Taylor and integral length scales, λ and L , are computed in terms of the three dimensional energy spectrum $E(k)$, as explained in (Jiménez *et al.* 1993). The microscale Reynolds number is defined as $Re_\lambda = u'\lambda/\nu$, and the large-eddy turnover time as $T = L/u'$.

Throughout this paper the probability density functions are often characterized by their generalized flatness factors

$$F_n = \mu_n/\mu_2^{n/2}, \quad \mu_n = \int y^n p(y) dy.$$

Flatness factors with subscript ℓ refer to the pdf of the longitudinal velocity derivatives, $\partial u/\partial x$, while those with subscript t refer to transversal derivatives, $\partial u/\partial y$. In all cases, equivalence was assumed for the three coordinate directions and used to augment the statistics.

The parameters in Table 1 represent the highest resolution available for each Reynolds number. For each run the pdf's of the velocity components and gradients

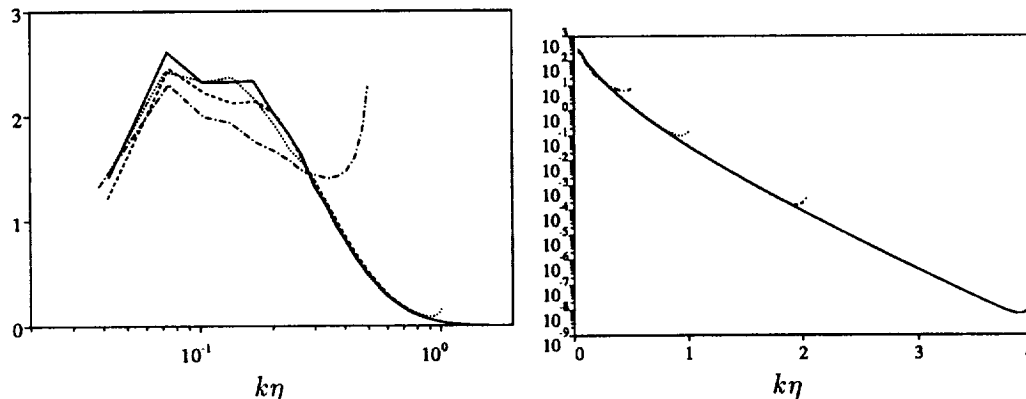


FIGURE 1. Three-dimensional energy spectra for the $Re_\lambda = 66$ simulation at four different resolutions. Left: $\epsilon^{-2/3} k^{5/3} E(k)$, to enhance the “inertial” range. Right: $\epsilon^{-2/3} \eta^{-5/3} E(k)$, to display the dissipation range. — : $k_{\max} \eta = 4$, ---- : 2, : 1, - · - : 0.5.

were computed periodically and accumulated. For all but the highest resolution cases, this was done “on the fly” while the simulation was advanced, and the statistics represent several tens of fields spaced at least by $0.1T$. For $N = 256$ the time step was too small to generate a sufficient number of fields in a single simulation, and the statistics were accumulated using the restart files from different runs. The number of fields used in this case is smaller, $O(10)$. The restart fields were also used for the filtering experiments described later.

There is considerable temporal variability in the extreme tails of the distributions, and the values for the different moments given in Table 1 are subject to appreciable statistical uncertainty. The number of significant figures given in the table is intended to give a rough indication of the reliability of the different figures, derived from the variability among different flow fields.

The same simulations were run at lower resolutions to check for numerical convergence. The three dimensional spectra for $Re_\lambda = 62$ at four different values of $k_{\max} \eta$ are given in Fig. 1, and the pdf’s for the velocity and for the longitudinal and transverse velocity gradients are given in Fig. 2. It is clear that there is little difference in any of these properties for resolutions better than $k_{\max} \eta \approx 2$, while there is some divergence in the pdf’s at $k_{\max} \eta \approx 1$ and a rapid deterioration thereafter. Since higher moments are dominated by the extreme probability tails of the pdf’s, Fig. 2d shows that those tails are the first ones affected by the lack of resolution, which is also consistent with the qualitative aspects of the other three parts of Fig. 2. It is noteworthy that even the velocity pdf, which is usually assumed to be dominated by large-scale events, is slightly affected by low resolution. The sub-Gaussian character of that distribution has been observed by other investigators at different Reynolds numbers, and is believed to be real (Anselmet *et al.* 1984, Vincent and Meneguzzi 1991).

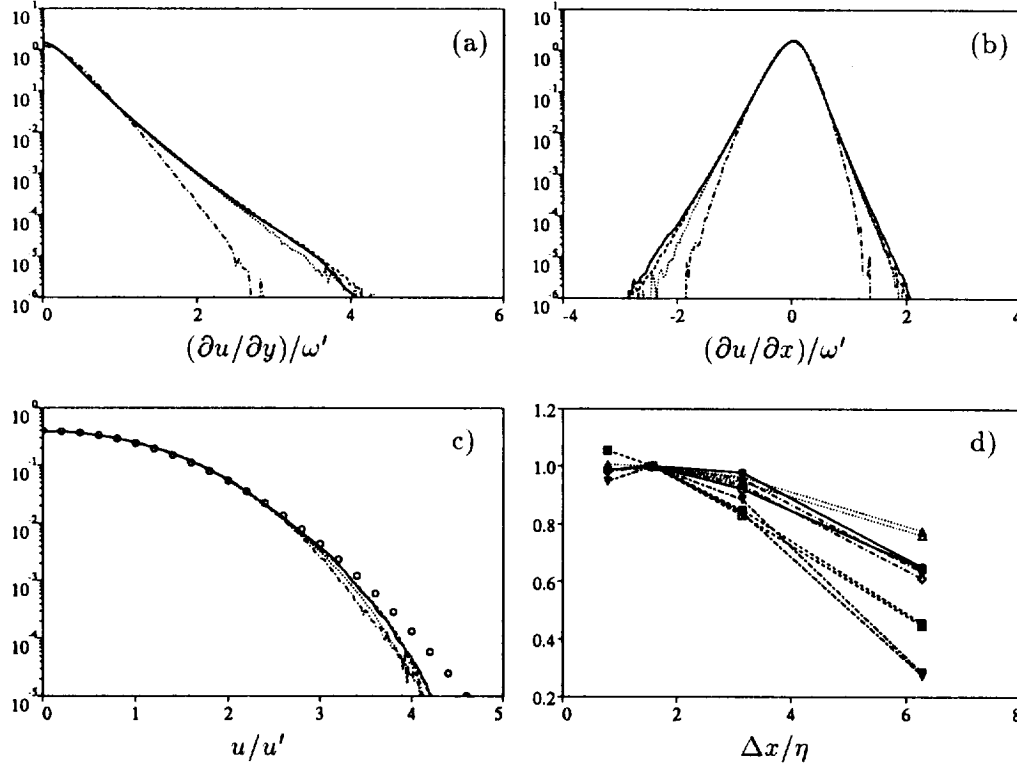


FIGURE 2. Dependence of the probability distributions on numerical resolution. (a-c) Pdf's of velocity and velocity gradients, $Re_\lambda = 66$. Lines are as in Fig. 1 and symbols in (c) are the Gaussian distribution. (d) Dependence of the velocity gradient flatness factors on $\Delta x/\eta = \pi/k_{\max}\eta$. All moments are normalized with their value at $k_{\max}\eta = 2$. \circ : $F_{3\ell}$, \triangle : $F_{4\ell}$, \square : $F_{6\ell}$, \diamond : F_{4t} , ∇ : F_{6t} . Solid symbols are $Re_\lambda = 66$, open ones, $Re_\lambda = 92$.

3. Probe size effects

The resolution effects documented above represented a more strict test than the effect of observing the flow with a probe of finite size. While in the former case the dynamics of the small scales are presumably disrupted by the lack of resolution, that is not true in the latter, in which the only effect is a smoothing of “properly computed” quantities. The classical model for the effect of a hot wire of finite length is that in (Wyngaard 1968). It is assumed that the hot wire is only sensitive to one velocity component and that it averages the true velocity signal along its length. No other measurement errors are considered. Whenever a spatial derivative is needed, it is computed as a centered difference from the signal at two neighboring wires. If homogeneous turbulence is assumed and the velocity is represented by its Fourier components,

$$u(\mathbf{x}) = \sum \hat{u}_{\mathbf{k}} e^{i\mathbf{k}\cdot\mathbf{x}},$$

the averaging effect of a hot wire of length h , oriented along z , is equivalent to

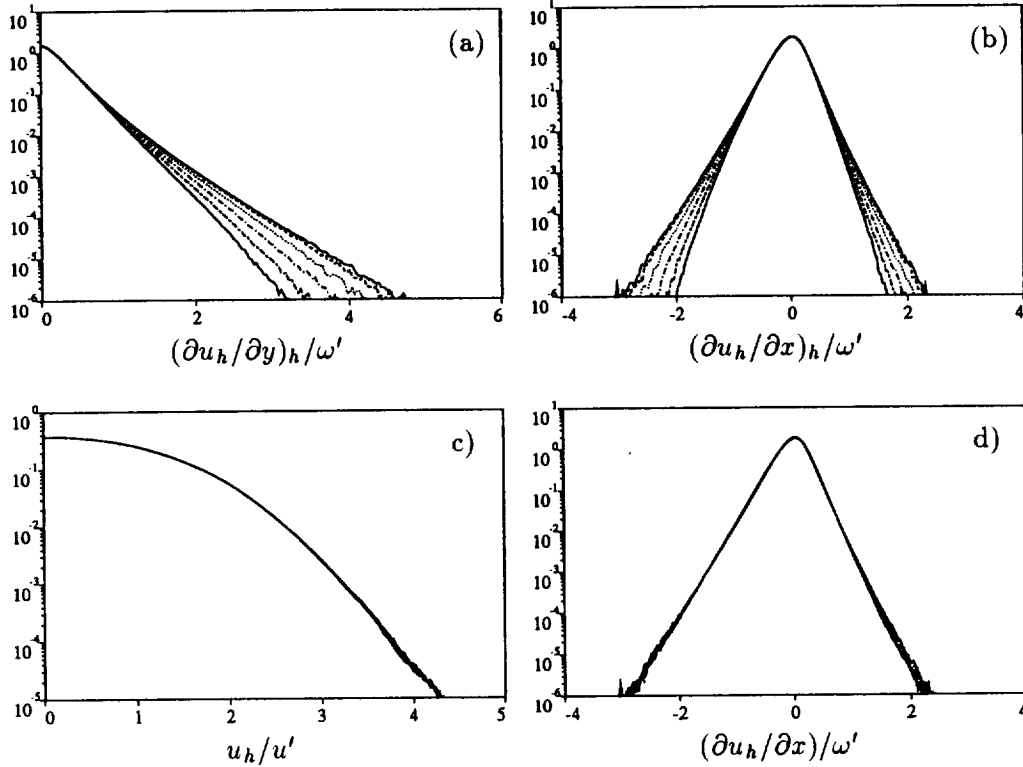


FIGURE 3. Dependence of the probability distributions on experimental resolution. Lines correspond to $h/\eta = 0(1.5)7.5$, in order of decreasing intermittency of distributions. $Re_\lambda = 92$. (a) Filtered transversal derivatives of filtered velocity. (b) Filtered longitudinal derivatives of filtered velocity. (c) Filtered velocity. (d) True longitudinal derivatives of filtered velocity.

multiplying each Fourier components by a filter (Wyngaard 1968)

$$F(\mathbf{k}) = \frac{\sin(k_z h/2)}{k_z h/2}.$$

In the same way, the effect of taking a derivative over a finite distance h is equivalent to multiplying the Fourier components of the derivative by the same filter function (Wyngaard 1969).

We applied this procedure to our numerical fields, using for each Reynolds number the highest available resolution. First the "wire" was oriented along the x -axis and used to obtain filtered values for v and w . The transverse derivatives, $\partial v / \partial z$ and $\partial w / \partial y$, were obtained by filtering the derivatives obtained from the filtered velocities. This was intended to model the effect of two parallel sensors of length h spaced by the same distance. The longitudinal derivatives, $\partial v / \partial y$ and $\partial w / \partial z$, were obtained in two different ways. In experimental practice these derivatives are usually not derived from two separate sensors, but deduced from a single time trace

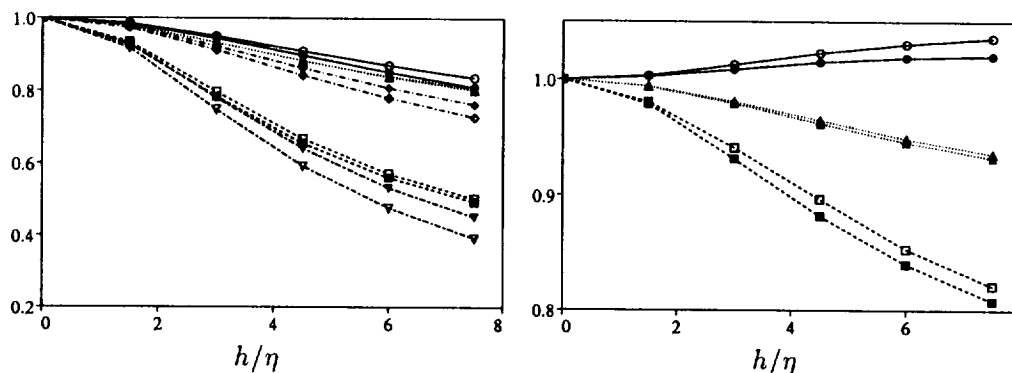


FIGURE 4. Dependence of the velocity gradient flatness factors on the experimental resolution. Left: Filtered derivatives of filtered velocities. Right: True longitudinal derivatives of filtered velocities. Symbols as in Fig. 2d.

using Taylor's approximation. Without taking into account the errors introduced by that procedure, it is in principle possible to sample the time trace fast enough to obtain "true" time derivatives of the signal. The sampling rate is limited by factors such as thermal inertia of the hot wire, seeding density in an LDV signal, or electronic limitations, all of which are essentially unrelated to sensor size. Two sets of longitudinal derivatives were thus obtained. The first one contains "true" derivatives of the filtered velocities, while the second one uses filtered derivatives with a sampling interval h , to make them comparable to the transversal gradients. The whole procedure was repeated with the "wire" oriented along the y and z axis, and pdf's were compiled for all the quantities. The results, as a function of sensor length relative to the Kolmogorov scale, are shown in Figs. 3 and 4.

There are several interesting aspects in those figures. First, as expected, the effect of experimental averaging is somewhat milder than that of numerical underresolution, but the magnitude of the effect is different for the different moments. While the degradation of the sixth order moments is comparable for a wire of length 8η and for a grid pitch of 5η , the third and fourth order moments are never degraded too much by filtering and remain with 20% of their true values even for the longest wire tested in our computations. Also, Wyngaard's criterion for wire length, $h \leq 3\eta$, is seen to be reasonable for the lowest order moments, but to lead to sizable errors for the sixth order flatness.

Perhaps the most unexpected results of Figs. 3 and 4 is the very mild degradation of the longitudinal gradients when only the velocities are filtered while the gradients themselves are computed with spectral accuracy. This indicates that the extreme tails of the pdf's are dominated by events, fronts, or filaments whose size in the direction normal to the gradient is comparatively large. This is of course consistent with modern observations of vorticity filaments in turbulent flows and suggests that reasonably accurate measurements of longitudinal gradients can be obtained by rapid sampling of velocity signals from fairly large sensors.

Another totally unexpected result was the tendency in Fig. 4b for the skewness

of the longitudinal derivatives of the filtered velocity to *increase* with the size of the filter. We have no explanation for this puzzling phenomenon, although it brings to mind the recent observations of persistent skewness in passive scalar fields associated with sharp fronts whose scale is similar to the integral length of the flow (Holtzer and Siggia 1994, Pumir 1994).

4. Conclusions

We have shown that the numerical resolution needed to simulate isotropic turbulence to the level of the sixth moment of the velocity gradient probability distributions is $\Delta x/\eta \approx 1.5$, for properly de-aliased spectral simulations at $Re_\lambda \sim O(100)$.

Using post-processing filtering of fully resolved numerical fields, we have shown that the classical limit on the size of experimental sensors (3η) is sufficient for third or fourth order moments of longitudinal or transverse velocity gradients, but that the sixth order moments require shorter wires. It is shown that most of the degradation in the higher moments results from the discretization of the differential operator and that fairly accurate longitudinal gradients can be obtained from large sensors by rapidly discretizing the time signal. As the discretization distance is extended into the inertial range ($h/\eta \approx 10$), the computation of the gradients merges into that of the normalized structure functions (see Anselmet *et al.* 1984, for a review), whose variation with distance is associated with the intermittency properties of the turbulent field. Our experiments show, however, that the degradation of the higher moments ($n \leq 6$) is substantial even when the discretization distance is kept in the dissipation range.

Finally, we have observed that the skewness of the filtered fields tends to increase with decreasing resolution, suggesting a large-scale origin for this quantity.

Acknowledgments

I have benefited from discussions with S. Saddoughi on experimental technique. The simulations were carried out at the Intel hypercube at NASA Ames and at the Paragon at Wright Patterson AFB. Much of the parallel code development is due to A. A. Wray and R. S. Rogallo. Work was funded by the Center for Turbulence Research and by the Office of Naval Research.

REFERENCES

- ANSELMET, F., GAGNE, Y. & HOPFINGER, E. J. & ANTONIA, R. A. 1984 High order velocity structure functions in turbulent shear flows. *J. Fluid Mech.* **140**, 63-89.
- BATCHELOR, G. K. & TOWNSEND, A. A. 1949 The nature of turbulent motion at large wave numbers. *Proc. Roy. Soc. London.* **A 199**, 238-255.
- CANUTO, C., HUSSAINI, M. Y., QUARTERONI, A. & ZANG, T. A. 1987 *Spectral methods in fluid dynamics*. Springer, pp. 85-86.
- HOLTZER, M. & SIGGIA, E. D. 1994 Turbulent mixing of a passive scalar. *Phys. Fluids.* **6**, 1820-1836.

- JIMÉNEZ, J., WRAY, A., SAFFMAN, P. G. & ROGALLO, R. S. 1993 The structure of intense vorticity in isotropic turbulence. *J. Fluid Mech.* **255**, 65-90.
- KIM, J., MOIN, P. & MOSER, R. 1987 Turbulence statistics in fully developed channel flow at low Reynolds number. *J. Fluid Mech.* **177**, 133-166.
- KLEWICKI, J. C. & FALCO, R. E. 1990 On accurately measuring statistics associated with small-scale structure in turbulent boundary layers using hot wire probes. *J. Fluid Mech.* **219**, 119-142.
- KOLMOGOROV, A. N. 1941 The local structure of turbulence in incompressible viscous fluids at very large Reynolds numbers. *Dokl. Nauk. SSSR.* **30**, 301-305 (see e.g. L. D. Landau & E. M. Lifshitz, 1959, *Fluid mechanics*, Pergamon, pp. 116-123).
- PUMIR, A. 1994 A numerical study of the mixing of a passive scalar in three dimensions in the presence of a mean gradient. *Phys. Fluids.* **6**, 2118-2132.
- ROGALLO, R. S. 1981 Numerical experiments in homogeneous turbulence. *NASA Tech. Mem.* **81315**.
- SADDOUGHI, S. G. & VEERAVALLI, S. V. 1994 Local isotropy in turbulent boundary layers at high Reynolds numbers. *J. Fluid Mech.* **268**, 333-372.
- VAN ATTA, C. W. & ANTONIA, R. A. 1980 Reynolds number dependence of skewness and flatness factors of turbulent velocity derivatives. *Phys. Fluids.* **23**, 252-257.
- VINCENT, A. & MENEGUZZI, M. 1991 The spatial structure and statistical properties of homogeneous turbulence. *J. Fluid Mech.* **225**, 1-20.
- WYNGAARD, J. C. 1968 Measurements of small-scale turbulence structure with hot wires. *J. Physics E: Sci. Instrum.* **1**, 1105-1108.
- WYNGAARD, J. C. 1969 Spatial resolution of the vorticity meter and other hot wire arrays. *J. Physics E: Sci. Instrum.* **2**, 983-987.

A method for obtaining a statistically stationary turbulent free shear flow

By S. F. Timson, S. K. Lele AND R. D. Moser

1. Motivation and objectives

The long-term goal of the current research is the study of Large-Eddy Simulation (LES) as a tool for aeroacoustics. New algorithms and developments in computer hardware are making possible a new generation of tools for aeroacoustic predictions, which rely on the physics of the flow rather than empirical knowledge. LES, in conjunction with an acoustic analogy (Lighthill 1952), holds the promise of predicting the statistics of noise radiated to the far-field of a turbulent flow.

While there have been preliminary studies where LES was used in aeroacoustic calculations, a thorough examination of LES's predictive capabilities has not been undertaken. Recent advances in subgrid-scale models (Ghosal *et al.* 1992) have shown promising results, but accurate acoustic predictions present a far more stringent test of LES's fidelity. LES does not resolve all scales in the simulated flow, and results of a given simulation depend on the subgrid-scale model employed. Previous verification of LES results has focused on one point statistics. The application of an acoustic analogy requires a two point space-time correlation, and it is unclear how accurately LES will reproduce this quantity.

It has been shown that the dominant features of far-field noise are associated with the energy containing range of scales in the near-field, offering hope that LES can supply accurate predictions. However, in practical applications, the subgrid-scale energy can represent a significant fraction of the total. Further, as Crighton (1988) points out, care must be taken when applying acoustic analogies. Computationally, spurious but efficient low order acoustic sources may result from discretization errors, boundary conditions, etc. It is important to assess whether or not the subgrid-scale model acts as such a low order acoustic source.

LES's predictive ability will be tested through extensive comparison of acoustic predictions based on a Direct Numerical Simulation (DNS) and LES of the same flow, as well as *a priori* testing of DNS results. The method presented here is aimed at allowing simulation of a turbulent flow field that is both simple and amenable to acoustic predictions. A free shear flow that is homogeneous in both the streamwise and spanwise directions and which is statistically stationary will be simulated using equations based on the Navier Stokes equations with a small number of added terms. Studying a free shear flow eliminates the need to consider flow-surface interactions as an acoustic source. The homogeneous directions and the flow's statistically stationary nature greatly simplify the application of an acoustic analogy.

2. Accomplishments

A method allowing simulation of a statistically stationary free shear flow has been developed. The method is an extension of that presented by Spalart (1988) to the

case of a wake or coflowing jet in the small deficit limit. The results are similar to those for the sink-flow boundary-layer presented in Spalart (1986). The derivation is more rigorous than either of the above analyses due to the simplification introduced by explicitly considering the small deficit limit. Some limited testing of the method has been carried out, and a more detailed validation is in progress.

2.1 Mathematical formulation

The flow to be simulated is that of a plane wake or coflowing jet. Self similar behavior is assumed and forms the basis for the rest of the analysis. The classical conditions necessary for self-similarity in a plane wake (in the small deficit limit) are

$$\delta \propto \sqrt{x} \quad (1)$$

$$U_o \propto \frac{1}{\delta} \propto \frac{1}{\sqrt{x}} \quad (2)$$

where δ is the wake thickness, $U_o = \Delta u_{max}$ is the maximum velocity deficit, and x denotes the streamwise direction.

A coordinate transformation is defined such that

$$(x, y, z, t) \rightarrow (x, \eta, z, t) \quad (3)$$

where $\eta = y/\delta(x)$. The spatial coordinates have been normalized by some initial length scale L_o , and time is normalized by some initial time scale t_o . Thus all quantities are non-dimensional. In the new set of coordinates, the profile thickness is independent of x . Lines of constant η have slope S where for the above coordinate system

$$S = \eta \frac{d\delta}{dx}. \quad (4)$$

The Jacobian of the coordinate transformation in space may then be written

$$J = \begin{pmatrix} 1 & 0 & 0 \\ S & T & 0 \\ 0 & 0 & 1 \end{pmatrix} \quad (5)$$

where $T = \delta$ for the coordinate change given in (3). The actual Jacobian is a 4x4 matrix, but as no transformation is carried out in time, the extra elements are deleted for simplicity.

Following Spalart (1988), a transformation is made to the dependent variables as well. Let the Cartesian velocity components be denoted by (u^*, v^*, w^*) , then the contravariant velocity components will be denoted by $(\tilde{u}, \tilde{v}, \tilde{w})$. The two sets are related through J^{-1} , giving

$$\begin{pmatrix} \tilde{u} \\ T\tilde{v} \\ \tilde{w} \end{pmatrix} = \begin{pmatrix} 1 & 0 & 0 \\ -S & 1 & 0 \\ 0 & 0 & 1 \end{pmatrix} \begin{pmatrix} u^* \\ v^* \\ w^* \end{pmatrix}. \quad (6)$$

Use of the contravariant velocity components preserves the form of the transport terms in the new coordinate system, i.e.

$$u^* \frac{\partial}{\partial x} + v^* \frac{\partial}{\partial y} + w^* \frac{\partial}{\partial z} = \tilde{u} \frac{\partial}{\partial x} + \tilde{v} \frac{\partial}{\partial \eta} + \tilde{w} \frac{\partial}{\partial z}. \quad (7)$$

As Spalart shows, the continuity equation becomes

$$\tilde{u}_x + \tilde{v}_\eta + \tilde{w}_z + \frac{S_\eta}{T} \tilde{u} + \frac{T_\eta}{T} \tilde{v} = 0. \quad (8)$$

The x-momentum equation becomes

$$\begin{aligned} \tilde{u}_t + \tilde{u}\tilde{u}_x + \tilde{v}\tilde{u}_\eta + \tilde{w}\tilde{u}_z = & -p_x + \frac{S}{T} p_\eta \\ & + \frac{1}{Re} \left(\left(-\frac{S_x}{T} + \frac{2SS_\eta}{T^2} - \frac{(1+S^2)T_\eta}{T^3} \right) \tilde{u}_\eta + \tilde{u}_{xx} \right. \\ & \left. + \frac{1+S^2}{T^2} \tilde{u}_{\eta\eta} - \frac{2S}{T} \tilde{u}_{x\eta} + \tilde{u}_{zz} \right). \end{aligned} \quad (9)$$

where p is the kinematic pressure.

Normalized velocity components are introduced, and the equations are expressed in terms of the velocity deficit. The variable change is

$$\begin{pmatrix} \tilde{u}(x, \eta, z, t) \\ \tilde{v}(x, \eta, z, t) \\ \tilde{w}(x, \eta, z, t) \\ p(x, \eta, z, t) \end{pmatrix} \rightarrow \begin{pmatrix} U_\infty + U_o(x)u(x, \eta, z, t) \\ U_o(x)v(x, \eta, z, t) \\ U_o(x)w(x, \eta, z, t) \\ U_o^2(x)p(x, \eta, z, t) \end{pmatrix} \quad (10)$$

The maximum deficit is used to scale the velocity components so that the mean and r.m.s of the velocity components are independent of downstream location in the new coordinate system.

The resulting equations are not presented as they are quite cumbersome. One should note that new terms involving x derivatives of the velocity scale are introduced. These terms are recast in terms of the undifferentiated velocity deficit using the assumed self-similar streamwise evolution. Using Eqs. (2) and (4) and recalling that $T = \delta$, it can be shown that

$$\frac{dU_o}{dx} = -\frac{S_\eta}{T} U_o, \quad (11)$$

and

$$\frac{d^2 U_o}{dx^2} = \left(2\frac{S_\eta^2}{T^2} - \frac{S_{x\eta}}{T} \right) U_o. \quad (12)$$

The equations are further simplified by choosing the length scale L_o to be δ_o , the dimensional value of the layer thickness at the downstream station to be simulated.

This implies the dimensionless quantity δ is 1. Then $T = 1$, η derivatives of T are zero, and x derivatives are removed through the identity

$$T_x = S_\eta. \quad (13)$$

Further, if δ is unity, η and y become equivalent, and all instances of η in the equations may be replaced with y . Then defining the parameter

$$\epsilon = \frac{U_o}{U_\infty}, \quad (14)$$

the continuity equation becomes

$$\frac{S_y}{\epsilon} + u_x + v_y + w_z = 0. \quad (15)$$

The x -momentum equation becomes

$$u_t + uu_x + vu_y + wu_z + \left(\frac{u_x}{\epsilon} - \frac{S_y u}{\epsilon} - S_y u^2 \right) = -p_x + Sp_y + \text{viscous terms}. \quad (16)$$

The viscous terms are quite complicated and are omitted for simplicity.

A Galilean transformation is now applied. A new coordinate x' is defined such that

$$x' = x - U_\infty t. \quad (17)$$

Applying this transformation, the terms in the momentum equations resulting from convection at U_∞ (e.g. the u_x/ϵ term in (16)) vanish.

The slope of the new coordinate lines S will now be expressed in the new coordinate system. Returning to the unmoving coordinate system, using (2) and (4) it can be shown that

$$S = \frac{U_o^2 \delta}{2} \frac{d}{dx} \left(\frac{1}{U_o^2} \right) y. \quad (18)$$

A quantity that was only a function of x in the stationary frame becomes a function of both x' and t in the moving frame, i.e.

$$F(x) = F(x' + U_\infty t). \quad (19)$$

Differentiating with respect to time in the new frame shows

$$\frac{1}{U_\infty} \frac{\partial F}{\partial t} = F' = \frac{dF}{dx}. \quad (20)$$

Applying (20) to (18) gives S in the new coordinate system as

$$S = \frac{U_o \delta}{2} \frac{\partial}{\partial t} \left(\frac{1}{U_o^2} \right) \epsilon y. \quad (21)$$

A parameter α is defined by

$$\alpha = \frac{U_o \delta}{2} \frac{\partial}{\partial t} \left(\frac{1}{U_o^2} \right), \quad (22)$$

and the scaling of U_o in (2) implies that α is constant. It follows that $S = \alpha \epsilon y$.

The small deficit limit is then enforced, letting $\epsilon \rightarrow 0$, giving for the continuity and momentum equations

$$\nabla \cdot \vec{u} = -\alpha, \quad (23)$$

and

$$\vec{u}_t + \vec{\omega} \times \vec{u} = -\nabla p + \alpha \begin{pmatrix} u \\ -v \\ w \end{pmatrix} + \frac{1}{Re} \nabla^2 \vec{u}. \quad (24)$$

These are the equations that will be integrated to yield the turbulent flow field. Note that (20) indicates that $V = -\alpha y$, and that the fluctuating velocity components are divergence free. Also note that all added viscous terms dropped out when the limit was taken.

2.2 Implementation

The modified equation set was implemented in the spectral code used by Rogers and Moser (1993) in their study of self-similar turbulent mixing layers. The numerical method (Spalart, Moser and Rogers 1991) employs Fourier analysis in conjunction with periodic boundary conditions in both the streamwise and spanwise directions. The application of periodic conditions in the streamwise direction is an approximation as the length and time scales for the fluctuating quantities are x dependent. The approximation should be a good one for the normalized components in this coordinate system as the variation of these scales is slow compared with the variation of δ . The non-homogeneous direction is handled through the use of rapidly decaying spectral basis functions in conjunction with two slowly decaying additional functions that exactly represent the irrotational component of the solution far from the vortical region.

The major question in implementing the modified equations is how to evaluate α . An initial value may be calculated for α by taking the second moment of the mean x -momentum equation, setting U_t to zero, and solving for α . Making use of the fact that the mean field is a function only of y , and integrating by parts, discarding the boundary terms, gives

$$\alpha = \frac{\int \frac{1}{2} y^2 (\overline{\vec{u} \times \vec{\omega}})_x + \frac{1}{Re} U dy}{\int y^2 U dy} \quad (25)$$

This value is then held, and the mean flow is allowed to evolve until a statistical steady state is reached. The flow in the interim has no physical meaning.

It may appear that a similar scheme may be used to constantly update α as the flow is evolving, in effect setting α to the value it would have if the flow was stationary at that moment, hopefully speeding evolution to the stationary state. In practice, however, this presents problems. It appears that a feedback loop involving

the Reynolds stresses results. Further investigation in this area is clearly needed. For the present work this is not critical as the initial conditions to be used are fully developed wakes simulated by Moser and Rogers (1994). Calculating α based on the initial condition and fixing it should not result in a significant evolutionary period.

2.3 Testing

The first test case was a laminar wake. The initial condition was simply a Gaussian. The flow evolved into a shape that was nearly Gaussian (a Gaussian does not solve the modified equation set) and remained stationary. A second test consisted of an initial condition of y^2 times a Gaussian, such that the profile had the same mass flow and second moment. The flow evolved to the same steady solution as was reached starting with a Gaussian.

The first turbulent test case is that of a low Reynolds number turbulent wake. This test is currently underway. The initial condition was taken from a temporally evolving simulation done by Moser and Rogers (1994). The results will be compared qualitatively to the results obtained from the temporal simulation to ensure that the results produced by the modified equation set are reasonable.

3. Future plans

Upon completion of the testing with the low Reynolds number wake, a higher Reynolds number DNS will be carried out, building the database necessary for aeroacoustic predictions. *A priori* testing of the DNS results will be carried out, comparing the acoustic prediction from the DNS data and a filtered version of the same flow-field. It has been seen previously that LES simulations are capable of producing better results than indicated by *a priori* tests. Therefore, the code will also be modified, and an LES of the same flow will be carried out. Using these databases, the issues discussed in section 1 will be investigated.

REFERENCES

- CRIGHTON, D. G. 1988 Goals for computational aeroacoustics, in *Computational Acoustics: Algorithms and Applications*. Elsevier Science Publishers B. V., IMACS, 1988.
- LIGHTHILL, M. J. 1952 On sound generated aerodynamically I. General Theory. *Proc. Roy. Soc. (A)*. **211**, 564-587.
- GHOSAL, S., LUND, T. S. & MOIN, P. 1992 A dynamic localization model for large-eddy simulation of turbulent flows. *Center For Turbulence Research Manuscript 189*.
- MOSER, R. D. & ROGERS, M. M. 1994 Direct Simulation of a Self-Similar Plane Wake. *NASA TM 108815*
- ROGERS, M. M. & MOSER, R. D. 1994 Direct simulation of a self-similar turbulent mixing layer. *Phys. Fluids*. **6**, 903-923.
- SPALART, P. R. 1986 Numerical study of sink flow boundary layers. *J. Fluid Mech.* **172**, 306-328.

SPALART, P. R. 1988 Direct Simulation of a turbulent boundary layer up to $R_\theta = 1410$. *J. Fluid Mech.* **187**, 61-98.

SPALART, P. R., MOSER, R. D. & ROGERS, M. M. 1991 Spectral methods for the Navier-Stokes equations with one infinite and two periodic directions. *J. Comput. Phys.* **96**, 297-324.

Direct numerical simulation of incompressible axisymmetric flows

By Patrick Loulou¹

1. Motivation and objectives

In the present work, we propose to conduct direct numerical simulations (DNS) of incompressible turbulent axisymmetric jets and wakes. The objectives of the study are to understand the fundamental behavior of axisymmetric jets and wakes, which are perhaps the most technologically relevant free shear flows (e.g. combustor injectors, propulsion jet). Among the data to be generated are various statistical quantities of importance in turbulence modeling, like the mean velocity, turbulent stresses, and all the terms in the Reynolds-stress balance equations. In addition, we will be interested in the evolution of large-scale structures that are common in free shear flows.

The axisymmetric jet or wake is also a good problem in which to try the newly developed b-spline numerical method. Using b-splines as interpolating functions in the non-periodic direction offers many advantages. B-splines have local support, which leads to sparse matrices that can be efficiently stored and solved. Also, they offer spectral-like accuracy and are C^{O-1} continuous, where O is the order of the spline used; this means that derivatives of the velocity such as the vorticity are smoothly and accurately represented. For purposes of validation against existing results, the present code will also be able to simulate internal flows (ones that require a no-slip boundary condition). Implementation of no-slip boundary condition is trivial in the context of the b-splines.

2. Accomplishments

To simulate these flows, we follow the procedure described in Moser *et al.* (1983) and Leonard *et al.* (1982), with b-splines replacing the Jacobi or Tchebyshev polynomials used in the radial direction.

2.1 Navier-Stokes equation

The starting point for the simulations are the incompressible Navier-Stokes equations:

$$\frac{\partial \mathbf{u}}{\partial t} - \mathbf{u} \times \boldsymbol{\omega} = -\nabla P - \frac{1}{Re} \Delta \mathbf{u} \quad (1a)$$

$$\nabla \cdot \mathbf{u} = 0 \quad (1b)$$

Let \mathbf{v} be our numerical approximation to \mathbf{u} , which will consist of a truncated expansion in terms of divergence-free vector functions (i.e. $\nabla \cdot \mathbf{v} = 0$). Furthermore,

¹ Department of Aeronautics and Astronautics, Stanford University

let ξ be any vector function representable by another finite set of divergence-free vector functions ($\nabla \cdot \xi = 0$), satisfying $\xi = 0$ on ∂G , the boundary of the domain. By substituting \mathbf{v} for \mathbf{u} in (1a) and using the standard weighted residual technique with ξ as the weight functions, we obtain the discrete weak form of the Navier-Stokes equations.

$$\int_G \xi \cdot \frac{\partial \mathbf{v}}{\partial t} dV - \int_G \xi \cdot \mathbf{v} \times \boldsymbol{\omega} dV = -\frac{1}{Re} \int_G \xi \cdot \Delta \mathbf{v} dV \quad (2)$$

By enforcing (2) for each ξ making up a basis for the weight functions, a coupled system of ordinary differential equations for the coefficients in the expansion for \mathbf{v} are obtained, which can be solved using standard time-advance techniques (see sect. 3). This formulation has the advantage of automatically satisfying the continuity equation (1b) and eliminating the pressure.

2.2 Velocity representation and vector shape functions

Given the formulation in (2), all that remains is to select the basis vectors to represent \mathbf{v} and ξ . This is facilitated by approximating the spatially developing jet or wake of interest as a time developing flow. In this case, the streamwise (axial or z) direction is homogeneous and we can approximate the flow as periodic in z with period L_z . This and the natural periodicity in θ allow the following representation of \mathbf{v} and ξ :

$$\mathbf{v}(r, \theta, z, t) = \sum_j \sum_{k_z} \sum_l \alpha_{jml}(t) \mathbf{u}_l(r; j, k_z) e^{ij\theta} e^{ik_z z} \quad (3)$$

$$\xi_{j'm'l'}(r, \theta, z) = \mathbf{w}_{l'}(r; j', k_z') e^{-ij'\theta} e^{-ik_z' z} \quad (4)$$

where

$$k_z = \frac{2\pi m}{L_z}, \quad -J \leq j \leq J, \quad -M \leq m \leq M$$

Due to the continuity constraint, there are only two degrees of freedom associated with each Fourier/b-spline mode. It is therefore convenient to divide the expansion and weight vectors, \mathbf{u}_l and $\mathbf{w}_{l'}$, into two distinct classes of vectors (\mathbf{u}_l^+ and \mathbf{u}_l^-) and ($\mathbf{w}_{l'}^+$ and $\mathbf{w}_{l'}^-$), with coefficients $\alpha_{jml}^+(t)$ and $\alpha_{jml}^-(t)$.

The expansion and weight vectors must be constructed such that they are divergence free and have the proper *regularity* properties at $r = 0$ (Shariff 1993). The following vectors meet both these requirements provided that $g_l(r)$ satisfy the appropriate condition at $r = 0$ (see below):

$$\mathbf{u}_l^+(r; j, k_z) = \begin{pmatrix} u_r^+ \\ u_\theta^+ \\ u_z^+ \end{pmatrix} = \hat{\nabla} \times \begin{pmatrix} ig_l(r) \\ g_l(r) \\ 0 \end{pmatrix}, \quad \mathbf{u}_l^- = \hat{\nabla} \times \begin{pmatrix} -ig_l(r) \\ g_l(r) \\ 0 \end{pmatrix} \quad (5)$$

$$\mathbf{w}_{l'}^+(r; j', k_z') = \hat{\nabla}^* \times \hat{\nabla}^* \times \begin{pmatrix} -ig_{l'}(r) \\ g_{l'}(r) \\ 0 \end{pmatrix}, \quad \mathbf{w}_{l'}^- = \hat{\nabla}^* \times \hat{\nabla}^* \times \begin{pmatrix} ig_{l'}(r) \\ g_{l'}(r) \\ 0 \end{pmatrix} \quad (6)$$

where $\widehat{\nabla} \times$ is the Fourier transformed curl operator and $\widehat{\nabla}^* \times$ is its complex conjugate. The $g_l(r)$ are b-splines expansion functions as described by de Boor (1978).

The above representation is incomplete when $k_z = 0$; so in this case, the following special representation is used:

$$\mathbf{u}_l^+ = \begin{pmatrix} \frac{-ijg_l(r)}{r} \\ g_l'(r) \\ 0 \end{pmatrix}, \quad \mathbf{u}_l^- = \begin{pmatrix} 0 \\ 0 \\ g_l(r) \end{pmatrix} \quad (7)$$

$$\mathbf{w}_{l'}^+ = \begin{pmatrix} \frac{ij'g_{l'}(r)}{r} \\ g_{l'}'(r) \\ 0 \end{pmatrix}, \quad \mathbf{w}_{l'}^- = \begin{pmatrix} 0 \\ 0 \\ g_{l'}(r) \end{pmatrix} \quad (8)$$

And when $j = 0$, these vectors are incomplete; so for that case ($k_z = j = 0$), we use:

$$\mathbf{u}_l^+ = \begin{pmatrix} 0 \\ g_l(r) \\ 0 \end{pmatrix}, \quad \mathbf{u}_l^- = \begin{pmatrix} 0 \\ 0 \\ g_l(r) \end{pmatrix} \quad (9)$$

$$\mathbf{w}_{l'}^+ = \begin{pmatrix} 0 \\ g_{l'}(r) \\ 0 \end{pmatrix}, \quad \mathbf{w}_{l'}^- = \begin{pmatrix} 0 \\ 0 \\ g_{l'}(r) \end{pmatrix} \quad (10)$$

All these additional vectors are also divergence-free and satisfy the regularity requirement.

In order to have the correct regularity property, depending on the azimuthal wave number j , $g_l(r)$ and some of its derivatives (Shariff 1993) must vanish when $r = 0$. Since this is not automatically satisfied by all the b-splines, some of the coefficients (α^+ and α^-) must be zero. In particular, for $j \geq 0$

$$\alpha_l^+ = 0, \quad 1 \leq l \leq \min(O, j) + 1 \quad \text{or} \quad lj \quad \text{is odd, while} \quad j + 3 \leq l \leq O + 1$$

and

$$\alpha_l^- = 0, \quad 1 \leq l \leq \min(O + 1, |j - 1|) \quad \text{or} \quad lj \quad \text{odd} \quad |j - 1| + 2 \leq l \leq O + 1$$

but with α_1^- unconstrained.

2.3 Boundary conditions

The present method is designed to treat both no-slip boundaries and potential boundaries (free shear flows).

2.3.1 No-slip boundary condition

Enforcing the boundary condition that $\mathbf{u}_l(R_2) = 0$, where R_2 is the outer edge of the domain, requires that

$$g_l(r = R_2) = 0, \quad g'_l(r = R_2) = 0 \quad (11)$$

But if the g_l are the b-splines as defined by de Boor, (11) is not satisfied for $l = L$ or $l = L - 1$ (the two functions closest to the boundaries). Therefore, we impose

$$\alpha_L^+ = \alpha_L^- = \alpha_{L-1}^+ = \alpha_{L-1}^- = 0 \quad (12)$$

However, for the shape functions in (5), (11) also implies

$$\frac{\partial u_\theta}{\partial r} = 0 \quad (13)$$

at the boundary, which is too restrictive. To alleviate this, we augment (5) and (6) with the additional vectors (Moser *et al.*, 1983):

$$\mathbf{u}_{L-1}^0 = \begin{pmatrix} 0 \\ -2k_z g_{L-1}(r) \\ \frac{2j g_{L-1}(r)}{r} \end{pmatrix}, \quad \mathbf{w}_{L-1}^0 = \begin{pmatrix} ij' g_{L-1}(r) \\ r g'_{L-1}(r) + g_{L-1}(r) \\ 0 \end{pmatrix} \quad (14)$$

With this, $\partial u_\theta / \partial r$ is unconstrained at the boundary.

2.3.2 Potential boundary condition

When simulating free shear flows, we follow the approach of Corral *et al.* (1993) and Sondergaard *et al.* (1994), where it is assumed that the vorticity in the flow is confined to a small region ($r < R_\omega$) which is to be computed. In the outer region of the flow ($r > R_\omega$), the vorticity is zero, so the velocity is a potential ($\mathbf{u} = \nabla \phi$ and $\Delta \phi = 0$).

For each Fourier mode, the potential $\hat{\phi}$ is given by:

$$\hat{\phi}(r; j, k_z) \sim K_j(k_z r)$$

where $K_j(x)$ is the modified Bessel function of the second kind. At the boundary of the computational domain, $r = R_2 > R_\omega$, the following relations are satisfied since \mathbf{u} is a potential:

$$u_\theta = \frac{ij}{qR_2} u_r, \quad u_z = \frac{ik_z}{q} u_r, \quad \text{where} \quad q = k_z \frac{K'_j(k_z R_2)}{K_j(k_z R_2)} \quad (15)$$

In addition, for the vorticity to be zero at $r = R_2$, u_r must satisfy

$$\gamma \frac{\partial u_r}{\partial r} + u_r = 0, \quad \text{where} \quad \gamma = \frac{-K'_j(k_z R_2)}{k_z K''_j(k_z R_2)} \quad (16)$$

Given the representation in (5), to satisfy (15) and (16), the coefficients must satisfy:

$$\alpha_L^+ \left[\frac{j}{qR_2} + 1 \right] + \alpha_L^- \left[\frac{j}{qR_2} - 1 \right] = 0 \quad (17)$$

$$(\alpha_{L-1}^+ + \alpha_{L-1}^-) - (\alpha_L^+ + \alpha_L^-) \left[1 + \frac{1}{\gamma g_L'(R_2)} \right] = 0 \quad (18)$$

where we made use of the following identities:

$$g_L(R_2) = 1, \quad g'_{L-1}(R_2) = -g'_L(R_2), \quad \frac{1}{\gamma} = \frac{1}{R_2} - \frac{j^2}{qR_2^2} - \frac{k_z^2}{q}$$

There are three boundary conditions in (15) and (16) but they are redundant with the continuity equation at the boundary. Since continuity is built into our expansions, only two conditions (17) and (18) are required.

For the $k_z = 0$ case, the conditions in (15) and (16) are satisfied when:

$$\alpha_L^- = 0 \quad (19)$$

$$\alpha_{L-1}^+ - \alpha_L^+ \left[1 + \frac{j}{R_2 g_L'(R_2)} \right] = 0 \quad (20)$$

3. Future plans

The only major parts of the code that remain to be implemented are the time integration scheme and the non-linear convective term. To time march the equations, we propose to use the method of Spalart *et al.* (1991) which is a mixed implicit/explicit scheme. The linear viscous term is time-marched implicitly using a Crank-Nicholson scheme and the non-linear terms are time-marched explicitly using a third order Runge-Kutta scheme. To compute the non-linear term, we revert back to physical space, take the cross product, integrate exactly by Gauss quadratures (doing the integrals exactly takes care of aliasing), and revert back to wave-space.

There are two types of free shear flow simulations that are of interest. First, a fully turbulent jet that can be simulated using a turbulent pipe simulation result as the initial condition (obtained from the same code). This is similar to the turbulent mixing layer and wake simulations of Moser and Rogers (1994). Second, a transitional jet or wake simulated using different initial conditions, similar to the work of Sondergaard *et al.* (1994) on wakes.

Acknowledgements

The author would like to thank Dr. Robert D. Moser for his seemingly endless patience in discussing the different relevant issues to this work.

REFERENCES

- CORRAL, R. & JIMÉNEZ, J. 1993 Fourier/Chebyshev methods for the incompressible Navier-Stokes Equations in Infinite Domains. *J. Comp. Phys.* To appear.
 DE BOOR, C. 1978 *A Practical Guide to Splines*. Springer-Verlag,

- LEONARD, A. & WRAY, A. 1982 A New Numerical Method for the Simulation of Three-Dimensional Flow in a Pipe. *NASA Technical Memorandum*. 84267.
- MOSER, R. D., MOIN, P. & LEONARD, A. 1983 A Spectral Numerical Method for the Navier-Stokes Equations with Applications to Taylor-Couette Flow. *J. Comp. Phys.* **52** (3), 524-544.
- MOSER, R. D. & ROGERS, M. M. 1994 Direct Simulation of a Self-Similar Plane Wake. *AGARD Symposium on Application of Direct and Large-Eddy Simulation*. Chania, Crete, Greece, April 18-21, 1994.
- ROGERS, M. M. & MOSER, R. D. 1994 Direct simulation of a self-similar turbulent mixing layer. *Phys. Fluids*. **6** (2), 903-923.
- SHARIFF, K. 1993 Comment on "Coordinate singularities" by P. R. Spalart. Notes from the author.
- SONDERGAARD, R., MANSOUR, N. N. & CANTWELL, B. J. 1994 The Effect of Initial Conditions on the Development of Temporally Evolving Planar Three Dimensional Incompressible Wakes. *AGARD Symposium on Application of Direct and Large-Eddy Simulation*.
- SPALART, P. R., MOSER, R. D. & ROGERS, M. M. 1991 Spectral Methods for the Navier-Stokes Equations with One Infinite and Two Periodic Directions. *J. Comp. Phys.* **96** (2), 297-324.

Database post-processing in Tensoral

By Eliot Dresselhaus

The CTR post-processing effort aims to make turbulence simulations and data more readily and usefully available to the research and industrial communities. The *Tensoral* language, introduced in this document and currently existing in prototype form, is the foundation of this effort. *Tensoral* provides a convenient and powerful protocol to connect users who wish to analyze fluids databases with the authors who generate them.

In this document we introduce *Tensoral* and its prototype implementation in the form of a user's guide. This guide focuses on use of *Tensoral* for post-processing turbulence databases. The corresponding document — the *Tensoral* “author's guide” — which focuses on how authors can make databases available to users via the *Tensoral* system — is currently unwritten.

Section 1 of this user's guide defines *Tensoral*'s basic notions: we explain the class of problems at hand and how *Tensoral* abstracts them. Section 2 defines *Tensoral* syntax for mathematical expressions. Section 3 shows how these expressions make up *Tensoral statements*. Section 4 shows how *Tensoral* statements and expressions are embedded into other computer languages (such as C or *Vectoral*) to make *Tensoral* programs. We conclude with a complete example program.

1. Basic notions

Post-processing in the abstract

The post-processing of fluids data entails computing quantities derived from base quantities such as the velocity vector field $\vec{u}(\vec{x}, t)$, scalar field $\phi(\vec{x}, t)$, or vorticity field $\vec{\omega}(\vec{x}, t) = \nabla \times \vec{u}$. Base quantities are those found in the databases output by simulation codes and may vary from simulation to simulation. Derived quantities are typically those commonly arising in theories of fluid mechanics, turbulence, and in practical problems such as velocity profiles, Reynolds' stresses, probability densities, etc.

The canonical post-processor starts with one or more base fields, computes one or more derived quantities, and outputs the results of these computations. An example post-processor might, given a velocity field, calculate pressure, strain, vorticity, strain times vorticity, mean and mean square velocity, Reynold's stresses, or skin friction, and generate tables or graphs of these quantities. In general terms, post-processing involves calculus and statistics applied to numerical tensor data.

1.1 Tensoral in the abstract

Tensoral has been designed to apply to a very general class of numerical problems. *Tensoral* applies whenever it is useful to separate the high-level coding and low-level implementation of calculus and statistics operations on numerical data. Applied to

turbulence databases *Tensoral* programs can flexibly and efficiently serve as post-processors. This user's guide will focus on such post-processing applications of the *Tensoral* language.

Tensoral, like other computer languages, provides abstractions to aid the user in understanding and using the system. There are three basic abstractions in *Tensoral*: a type of variable called a *tensor*, *operators* which *operate* on tensors and produce new tensors, and a general and programmable notion of *state* in which tensors exist and in which operators act. These basic abstractions when combined make up the description of a data type which is defined by an author's *back-end*.

1.2 Tensors

All mathematical quantities in *Tensoral* are represented by *tensors*. *Tensoral tensors* correspond (loosely) to mathematical tensor fields. They are more usefully thought of as "computational" tensors — that is, as indexed numerical arrays (e.g. $a_{ij}(xyz)$) with two sets of indices: a set of tensor or array indices (ij) and a set of *coordinate* indices (xyz). Each coordinate value (e.g. (xyz)) corresponds to an array of numbers (e.g. a_{ij}) which may or may not be indexed like a mathematical tensor.

1.3 Operators

Mathematical and other operations on tensors are represented by *Tensoral operators*. Certain *standard* operators are invoked by elements of *Tensoral* syntax (e.g. $a+b$ invokes the addition operator). Non-standard operators may be introduced by back-end authors to extend the functionality coded into *Tensoral* syntax. Standard operators in *Tensoral* include tensor assignment, algebraic operations (addition, subtraction, multiplication, division, exponentiation), differentiation, integration, and averaging. *Tensoral* also provides standard operators for the reading and writing of files in various formats. Standardization is intended to allow mathematically similar operations to be coded with the same syntax even if such operations have different back-end numerical implementations. Ideally, such standardization would allow post-processing codes for different back-ends to be identical. In addition to standard operators *Tensoral* provides a highly flexible mechanism for integrating new operators into the language. Such operators, as well as re-implementations of standard operators, may be provided at will by database authors.

Typically *Tensoral* operators apply to tensors as arrays: that is, they apply to all tensor (or array) indices and coordinate indices unless explicitly instructed otherwise. Thus, *Tensoral* is an array language. Adding two tensors, for example, adds array values for all tensor indices and at all spatial points (i.e. grid points) defined for a given simulation. Explicit tensor or coordinate indices can be specified with tensor indexing and coordinate indexing.

The implementation specifics of tensors and (potentially all) operators that act upon them are also provided by database authors. The numerical representation of an abstract tensor (e.g. as an array in memory, across processors in a multi-computer, split between memory and disk, etc.) and how operators operate (e.g. derivatives as finite differences or as multiplication in wave space, etc.) is completely

determined by a database author's *back-end*. Such back-ends provide all of the information necessary for the *Tensoral* compiler to convert high-level post-processors into an executable computer programs. Back-ends and especially back-end programming will not be covered in this document.

1.4 State

Every tensor at every stage in a computation is in a certain *state*. This state controls how back-ends represent tensor references and operations on them in terms of executable computer code. The state of a tensor is represented by a set of *state variables* taking a specified set of values (possibly Boolean true or false, integer, floating point, string, or otherwise). For example, each tensor has pre-defined integer valued state variables `rank` and `dim` which respectively define the number and range of tensor indices that may be validly used to index a tensor. Thus, `a_ij` is valid reference to a rank 2 tensor with indices `i` and `j` taking integral values from 1 to `dim`, the dimension of `a` (which must be an integer). Similarly, a tensor's coordinate dependencies are given by a built-in state called `dep`. Such dependencies change when variables are averaged over or new coordinates are introduced in an expression. Thus, the tensor `a_ij(xyz)` has state `{rank 2, dim 3, dep xyz}` — we shall use this notation throughout to denote state variables (here `rank`, `dim` and `dep`) with values (here 2, 3 and `xyz`) of a tensor's state. Other state variables can be introduced at will by database authors to encode specification of a simulation's grid, how a tensor is currently being represented (e.g. in physical or wave space), the state and type of a tensor's data management (e.g. three-dimensional tensor in `xy` planes), etc.

2. Expression syntax

Tensoral syntax is introduced here from bottom to top. First we show how to reference tensor variables. Tensor references are the building blocks of mathematical expressions. Such expressions are themselves the building blocks of *Tensoral* statements. *Tensoral* statements may introduce new tensors, assign tensors to expressions, read and write files, perform back-end specific operations, etc.

2.1 Tensor variables

Tensor references — for example, `a_12(xyz)` — have up to three components: a required tensor name `a`, optional array (tensor) indices `_12` and optional coordinates indices `(xyz)`. The notation `a_12(xyz)` corresponds to the mathematical notation $a_{ij}(\vec{x})$ for a tensor field of rank 2. Both array and coordinate indexing specialize a tensor reference. That is, `a` refers to $a_{ij}(\vec{x})$ for all indices ij and spatial points \vec{x} ; `a_12` refers to $a_{12}(\vec{x})$ for all spatial points \vec{x} ; `a_12(x=10)` corresponds to all values of $a_{12}(10, y, z)$ for all y and z . Array and coordinate indexing will be detailed below.

Tensor variable names are given by sequences of lower and upper case letters, underscores `_`, and primes `'`. Digits may also be used in tensor names but not as the first character. The following are all valid distinct tensor names: `u`, `U`, `v'`, `velocity`, `u1`, `u1'`, `long_name`, `str'ange_na'me`. Tensor indices are introduced by the final `_` character in a tensor name, but only if the preceding characters actually

refer to a tensor variable. Thus, `long_name_ij` either refers to an unindexed tensor named `long_name_ij` or refers to the `ij` component of a tensor named `long_name` depending on which alternative has been declared to be a tensor variable.

2.2 Coordinates

Coordinates are notated by single lower or upper case letters, optionally followed by prime ' characters. Thus, the following are valid and distinct *Tensoral* coordinates: `x`, `y`, `z`, `x'`, `X`, `X'`, `r`, `k` — as long as they have been provided for by back-end authors.

Tensors may depend on any unique combination of coordinates — as long as they have been defined by a back-end. A back-end author can provide various coordinate systems for a single simulation as appropriate and physically meaningful. For example, coordinates on a Cartesian grid are typically

<code>x y z</code>	Cartesian coordinates x , y and z ,
<code>r</code>	the radial coordinate $r^2 = x^2 + y^2 + z^2$.

Coordinates in *Tensoral* are special tensors of {rank 0} which depend on themselves and when referenced in expressions generate corresponding coordinate values. The values taken on by coordinates are defined by back-end authors. Thus, a `z` coordinate might go from 0 to 2π for isotropic turbulence and from 0 to ∞ for a boundary layer.

2.3 Tensor indexing

Tensor indices, introduced by the underscore character `_`, consist of a sequence of coordinates or single digits or dummy indices (*explicit* indexing) or may not be present at all (*implicit* indexing).

Explicit index values (e.g. `a_12` or `a_xy`) may be either digits or coordinates. No spaces are allowed before or after indices or the leading `_`: indexed expressions are atomic variable references which contain no white space. If a coordinate `c` is used to index a tensor, the tensor must depend on `c` (i.e. `c` must be present in the tensor's dep state) — otherwise a compiler error is issued; the value of a coordinate index is the position that `c` takes in the dependency state of the tensor. The value of a digit index is the specified number between 1 and `dim` (the tensor's dimension). Thus, if `a` has {rank 2, dep xyz} state, then `a_12`, `a_xy`, `a_1y`, and `a_x2` are all valid and equivalent indexed expressions.

Any tensor index which is not a digit or a coordinate direction (as defined in a particular simulation back-end) is assumed to be a dummy index. Dummy indices in *Tensoral* aim for the same semantics as in standard mathematical tensor notation. Thus, a dummy indexed expression `a_ij` (assuming neither `i` or `j` are coordinates) refers to all 9 components of `a` (assumed to be {rank 2}). Dummy indices label how tensor indices are to be repeated and combined in an expression — for example, distinguishing the assignment statements `a_ij = b_j c_i` and `a_ij = b_i c_j`. Dummy indices are also used in conjunction with the summation convention: namely, that repeated dummy indices in a product are summed over. We defer further details of dummy indexing until we introduce the operators which control their interpretation.

Tensor references need not have explicit indices; they may be indexed *implicitly*. If indices are not specified, dummy indices are introduced in a standard way. Currently, this standard has not been fully decided upon. The user is encouraged (for now) to use explicit dummy indices.

2.4 Coordinate indexing

Indexing is also supported for the coordinates a tensor depends on. A tensor u depending on coordinates xyz can be evaluated at particular x , y or z values — for example, at $x = 17$ planes with $u(17, y, z)$ (or equivalently, $u(x=17)$), at $x = 17$, $z = 69$ pencils as $u(17, y, 69)$ (or $u(x=17, z=69)$), or at a single point $x = y = z = 0$ as $u(0, 0, 0)$ (or $u(x=y=z=0)$). If a coordinate is either not specified or is specified only by name (with no explicit value given), this coordinate is assumed to take on all possible values. Thus, $u(17, y, z)$ refers to an array indexed by coordinates yz .

2.5 Algebraic notation

Mathematical notation in *Tensoral* is a super-set of *Vectoral* notation and as with *Vectoral* aims to present a syntax as close as possible to standard mathematical notation. Numerical constants (which are tensors of rank 0 with no coordinate dependencies) are entered as in *Vectoral*: as sequences of base ten digits and optional decimal point, followed with an optional e or E for exponent and optional i or I for the imaginary unit ($\sqrt{-1}$). Numerical constants can be thought of as tensors with zero rank and no coordinate dependencies (i.e. state {rank 0, dep 0}). Given expressions a and b , we have the following operators:

$a+b$, $a-b$	addition, subtraction,
a/b	division,
$a b$, $a.b$, $a*b$,	multiplication: juxtaposition, dot, star
a^b	exponentiation,
$a\$$	complex conjugate,
$-a$	negation,
$ a $	absolute value.

Any balanced parenthesis ($()$, $\{\}$ or $[\]$) may be used for grouping mathematical expressions. These operators — like most operators in *Tensoral*— apply to tensors as arrays: that is, they apply to all array and coordinate indices which have not been explicitly specified.

Precedence of operations in the above table increases from left to right, top to bottom. To avoid ambiguity between $a-b$ being subtraction ($a-b$) and juxtaposition (a) ($-b$) negation is not allowed with juxtaposition: juxtaposition may be used, however, with all other operators of lower precedence. Also, all non-commutative operations (i.e. subtraction, division, multiplication of tensors, and exponentiation) are left-associative. Thus, the exponentiation a^b^c is grouped as $(a^b)^c$, etc.

2.6 Three types of multiplication?

There are three types of binary multiplication in *Tensoral*: star $*$, dot $.$ and juxtaposition (which has no symbol). These three forms of multiplication differ in how they treat array indices.

Explicitly indexed, `.` and juxtaposition both imply the summation convention — that is, repeated indices are summed, for example making `a_ij b_j` or `a_ij . b_j` equivalent to matrix multiplication. Explicitly indexed multiplication with `*` does not sum repeated indices: Thus, `u_i * u_j` is the outer (tensor) product of `u` with itself. This convention roughly corresponds to the usual tensor notation: `.` is an inner (dot) product (contracts indices) and `*` is an outer (tensor) product.

In connection with use of the summation convention, *Tensoral* provides the standard tensors `delta` and `epsilon`. `delta_ij` is the totally symmetric unit tensor (Kronecker delta) and `epsilon_i1...iN` is the totally anti-symmetric unit tensor: equal to 1 for even permutations of `1...N`, -1 for odd permutations, 0 otherwise).

Here are some illustrative examples of explicitly indexed multiplications:

<code>c_k = epsilon_ijk a_i b_j</code>	cross product of rank 1 <code>a</code> and <code>b</code> .
<code>c = a_i b_i</code>	dot product of rank 1 <code>a</code> and <code>b</code> .
<code>c_ik = a_ij b_jk</code>	matrix multiplication of rank 2 <code>a</code> and <code>b</code> .
<code>c_ij = a_i * b_j</code>	outer product of rank 1 <code>a</code> and <code>b</code> .

(Implicit indexing will in the future be different for the three multiplications. The details of this difference is currently unresolved and are not given here.)

2.7 Operator notation

Algebraic operations and mathematical functions (e.g. sine, cosine, log, exponential), differentiation, Laplace inversion and curl operator inversion, among others, all invoke *Tensoral* operators. Such operators which are a part of standard *Tensoral* syntax, as well as those that are non-standard, can all be invoked explicitly with operator notation.

Operators in *Tensoral* act from the left and apply to operand expressions on the right. Operands are flanked by parentheses (one of `()`, `{}` or `[]`), and operands beyond the first are separated by commas as in standard mathematical notation. Additionally, if an operator takes one or zero operands these parenthesis and commas may be omitted so that the operator and operand are juxtaposed. Operators are specially introduced to *Tensoral*, so that it is possible to syntactically differentiate operator notation (e.g. `o` or `o(0,0,0)` for operator `o`) from tensor references (e.g. `a` or `a(0,0,0)` for tensor `a`). The following are examples of both types of *Tensoral* operator expressions:

<code>sqrt(x)</code>	<code>random</code>	<code>sqrt x</code>	<code>f(x,y)</code>	<code>sqrt x + y</code>
----------------------	---------------------	---------------------	---------------------	-------------------------

The last expression above is equivalent to `sqrt(x) + y` since juxtaposition of operands has higher precedence than addition (and other operators in the above table).

The standard mathematical functions in *Tensoral* are as in *Vectoral* and are listed in the following table:

<code>random</code>	A random number between 0 and 1,
<code>conj z</code>	Complex conjugate,
<code>exp z, log z, log10 z</code>	Exponential, log, log base 10,

<code>sqrt z</code>	Square root,
<code>sin z, cos z, tan z</code>	Trigonometric functions,
<code>arcsin z, arccos z</code>	
<code>arctan z</code>	Trigonometric inverse functions.

All functions taking arguments z in the above table may operate on either real or complex quantities.

2.8 Calculus, statistics, indexed operators

Like tensors, operators also have state and, therefore, rank and can be indexed. Standard indexed operators are:

<code>grad</code>	numerical differentiation,
<code>int</code>	numerical integration,
<code>ave, sum</code>	averaging, summation,
<code>min, max</code>	minimum, maximum.

Differentiation `grad` mimics the gradient operator ∇ : it has rank 1 and can be explicitly indexed as if it were a tensor (e.g. `grad_y u_x` for $\partial_y u_x$). As with products, the summation convention applies to repeated indices. In addition, a special indexed shorthand is available for derivatives: any dummy indices following a comma are taken as derivatives. Thus, `u_i,j` is short hand for `grad_j u_i`, and `v_j,ii` generates the Laplacian $\nabla^2 v_j$.

The remaining indexed operators mentioned above do not have fixed rank. That is, their operation is determined by how they are indexed. Consider `ave` as a typical example. `ave_x` performs an average over the x coordinate direction (as defined by the database back-end); `ave_xy` performs averaging over both x and y coordinate directions. The remainder of the average-like operators (`int`, `min`, `max`) behave in a similar fashion: operator indices determine which coordinates are to be integrated and minimized or maximized over.

2.9 Operators and back-ends

Currently, new operators may only be defined or re-defined (for standard operators) by back-ends. At some point the introduction of new operators will become standard *Tensoral*. The isotropic turbulence back-end `iso`, for example, re-defines the three product operators `*`, `.`, and juxtaposition. For `iso` tensors, multiplication can either be in physical or wave (Fourier) space. To select between these two possibilities, the back-end author (in this case E. D.) has defined `*` to imply wave space and juxtaposition `...` to imply physical space operands: that is, if any operand of `*` is not in wave space it is transformed into wave space (and similarly for physical space and juxtaposition). This mimics the notation $f \star g$ for convolution which, of course, is multiplication in wave space. The third multiplication `.` implies nothing about the wave and physical space representations of its operands.

3. Statement syntax

There are three kinds of statement in *Tensoral*: declarations, assignments, and statement level operator expressions. Declarations introduce new tensors to the

compiler. Assignments alter the value and state of existing tensors. Statement level operator expressions — whose syntax is identical to the operator expressions described above — allow for non-standard (i.e. back-end specific) operations to be performed.

3.1 Declarations

As in *Vectoral* or *C*, all variables in *Tensoral* must be declared. A declaration introduces a certain variable name (whose syntax is defined above) to be a tensor of a certain *type*. The type of a tensor corresponds to a back-end which describes this type. For example, the isotropic turbulence back-end defines a tensor type called *iso*. Tensors may have more than one type. For example, an *iso* tensor *a_{ij}* may be declared to be *symmetric*, indicating to the compiler that it may equate *a_{ij}* with *a_{ji}*.

The type or types in a tensor declaration define all of the state variables which may control how an abstract tensor is represented by a numerical tensor field. For example, *iso* tensors represent fields either in physical or in Fourier space and have a corresponding state variable called *wave* which is true or false depending on whether a given tensor is in wave or physical space at a given point in a program. (This state variable could have more complex semantics to represent tensors in mixed wave and physical space.) Other types may introduce other state variables or may override those already defined. For example, if a tensor is declared *symmetric iso*, *symmetric* states and operators have higher precedence than *iso* states and operators. (Such type precedence allows for back-ends to be constructed in a modular fashion — minimizing the duplication of effort.)

When a tensor is declared its initial state must also be declared. In particular, declarations may give values for the standard *Tensoral* state variables *rank*, *dimension dim*, and coordinate dependency *dep*. Other back-end specific state information may also be initialized, for example, declaring a tensor to have a certain back-end specific mesh parameters, to be in wave or physical space, etc. All state variables have *default* values. The standard states, for example, might default to values {*rank* 0}, {*dim* 3}, and {*dep* 0}. Back-end specific defaults are provided and documented by back-end authors.

The general syntax of *Tensoral* declarations is as follows:

$$type_1 \dots type_L \{init_1, \dots, init_M\} tensor_1, \dots, tensor_N$$

This declares $N > 0$ tensors all having the specified $L > 0$ types with decreasing state precedence from left to right and initial state specified by $M \geq 0$ initializations. Each initialization field may have two forms:

$$variable \ value \quad \text{or} \quad tensor$$

This first form explicitly initializes a given state variable to an optionally given value (which defaults to *true*); the second uses the current state of a tensor to initialize the state of another. In addition a tensor name (e.g. *T(xyz)*) may be followed by a list

of coordinates in parentheses (), {}, or [] to initialize its coordinate dependencies (e.g. to `xyz`). Uninitialized state variables take on their default values.

An author may declare certain tensors which can themselves be referenced to initialize other tensors. Such tensors are *templates* for other tensors and do not correspond to variables in *Tensoral* programs. All turbulence simulations are likely to have definitions of the velocity and/or scalar fields (for example, called `velocity` and `scalar`), which can be inherited by other tensors. This allows for simple declarations of derived quantities, for example, the declaration

```
iso {velocity} u, {rank 2} du, {rank 0} p
```

which might declare an `iso` velocity field `u`, its derivative `du`, and pressure `p`, a scalar.

3.2 Assignments

Tensoral assignments assign tensors on the left-hand side of an equals sign = to an expression on its right-hand side. Assignments can use multiple left-hand sides as long as they are tensors whose rank is mutually compatible with the right-hand side rank. Multiple assignments may be performed in parallel (as in *Vectoral*) with the `&` character joining the multiple assignments. In parallel assignment, right hand sides of all assignments linked with `&` characters are evaluated *before* any assignments are performed, so that the statement `a = b & b = a`, for example, swaps tensors `a` and `b`. Assignments transfer both the state and value of tensors.

In addition tensors may be read from and written to files with assignment notation. File names in *Tensoral* are delimited by double quotes "`restart10`" if constant or by angle brackets `<file>` if variable. Files are read if they occur on the right-hand side of assignments and are written if they occur on the left-hand side of assignments. Currently, file operations may not be mixed with other expressions. This may change in the future.

4. Program syntax

Tensoral statements exist *inside* of a *host* language. *Tensoral* itself was designed to be minimal: *Tensoral* supports tensors and operations on them — no more, no less. The host language is relied upon for everything else. The semantics of how programs are organized, say into different files and different subroutines, how variables are scoped (global versus local), etc. are all lifted from the host language. A user is not forced to learn another computer language; instead the user must only learn how to combine *Tensoral* and host code.

Back-ends also use host language code to implement operators, tensor references, declarations, file operations, etc. Thus, eventually a *Tensoral* program is transformed into a host language program which can then be compiled by the host-language compiler.

4.1 Tensoral in C

In the current *Tensoral* prototype, C is used as the host language. This is referred to as *Tensoral* in C. For the remainder of this section, we will take C as the host language to explain how *Tensoral* codes fits into host code.

Tensor variables and *Tensoral* containing functions may be introduced anywhere that C variables and functions may be introduced. *Tensoral* containing functions have the same syntax as C functions except their declared names are prefixed by tensor types just as they would appear in a regular tensor declaration. These types — with the usual precedence rule — make up the environment of back-end template tensors, state variables, coordinates, and operators available to the *Tensoral* code in the function. Tensors as arguments to functions and as local (called “automatic” in C) variables as in C are local to the {} block of their definition. (The user must be careful to keep distinct names for C and *Tensoral* variables — use of the same C and *Tensoral* variable names can cause confusing results!)

Tensoral statements may appear wherever C statements may. Since all tensor variables are specifically introduced as tensors, *Tensoral* code may be differentiated from C code. Because of this differentiation *Tensoral* expressions and statements may appear anywhere C expressions and statements may. The presence of *Tensoral* expressions may change the semantics of C code. *Tensoral* code may involve array operations and hence imply iteration over coordinates. This iteration also includes iteration over the C statement which contains the *Tensoral* array operation. For example, the function call `printf ("%g", f(xyz))`; will print `f` for all coordinate values `xyz`. On the other hand, some C statements such as the looping constructs `for` and `while` are not iterated over *Tensoral* coordinates; others (`switch`, `if`, function calls, etc.) are iterated.

4.2 Example: the isotropic turbulence back-end

Rogallo's isotropic turbulence simulation and the corresponding `iso` *Tensoral* back-end represent tensors on a uniform computational mesh of size N^3 . Since N here is desired to be as large as possible, tensors must have their data *managed* — that is, since arrays of size N^3 are potentially too large to fit into a computer's main memory, all tensors are split up into data plane groups of size MN^2 or into groups of lines of size $M'N$. At one time only M planes or M' lines of a tensor's data is operated on; the remainder of the tensor is kept on backing store (i.e. disk or other processors of a multi-computer). Data management code is automatically generated by the `iso` back-end.

Derivatives are computed by transforming into wave space; certain products are formed in physical space. Fourier transforms (whether 1, 2, or 3 dimensional) are automatically coded when derivatives are taken or when physical space products are requested. For `iso` tensors recall that star `*` implies wave space, juxtaposition implies physical space, and dot `.` implies neither. Thus, `a * b` will transform `a` and `b` to wave space if necessary before multiplying them; `a b` will transform both to physical space (as necessary); `a . b` will simply multiply `a` and `b` as is.

`iso` tensors have special state variables associated with them. The standard states `rank`, `dep`, and `dim` default to 0, 0 and 3 — by default, tensors are scalars, are not dependent on any of the coordinates, and have indices that range from 1 to 3. Tensors can be either in wave space (for state `{wave true}`) or in physical space (`{wave false}`). Currently, tensors are represented either in groups of `xy` planes (for state `{memxy true}`) or `xz` planes (`{memxy false}`).

The mesh size and planing factor are given by the state variables `mesh` (which corresponds to N above) and `plane` (which corresponds to M). These state variables may take on integer values, specifying a constant size mesh and constant planing factors; for example,

```
iso {rank 1, mesh 32, plane 2, wave} u
```

declares a 32^3 wave-space velocity field which is split into groups of data planes of size 2×32^2 . Similarly, `mesh` and `plane` may take on values that are the names of external C variables which contain the mesh size and planing factors at run time; for example,

```
iso {rank 1, mesh N, plane M} u
```

declares `u` to get its run time size and planing from C variables `N` and `M` (which had better exist!). Also, mesh and planing factors can be initialized when a field is read from a restart file.

The `iso` back-end also provides template tensors which can be used to initialize tensors in user's programs. The tensor `velocity` sets up a velocity field which can be read from a simulation restart file.

4.8 A complete example

Here we illustrate a simple post-processor written in *Tensoral*. Let's suppose — for the sake of example — we want to compute pressure statistics for a series of restart files `run1`, `run2`, One codes the following *Tensoral* (in C) program in a file `p.tlc`:

```
1  iso main (int argc, char * argv[]) {
2    int f;
3    iso {velocity} u, {u, rank 2} A, {u, rank 0} p;
4    iso {} mean, rms;
5    for (f = 1; f < argc; f++) {
6      u = <argv[f]>;
7      A_ij = u_i,j;
8      p = -unlaplacian (A_ij A_ji);
9      mean = ave_xyz (p);
10     rms = sqrt (ave_xyz (p^2) - mean^2);
11     printf ("pressure:  min %g, max %g, mean %g, rms %g\n",
12           min_xyz (p), max_xyz (p), mean, rms);
13   }
14 }
```

According to C standards `main` is the function which is called by the operating system with string arguments `argv` of size `argc`. `main` has been declared with type `iso` to indicate that it contains *Tensoral* code; `iso` has been previously introduced to the compiler as part of its library of back-end types. Line 2 declares a C integer variable which is used to loop through the restart files assumed to be given on the command line array `argv`. Line 3 declares the tensor variables we need. The velocity field `u` is initialized using the `iso` template `velocity`. `A` is the velocity

derivative tensor, declared to be like `u` but with `rank 2`. `p` is the pressure and `mean` and `rms` are both scalars (`{rank 0, dep 0}`) used for statistics. Line 5 loops over restart files; array operations inside this loop are iterated inside the loop (as for all `for` and `while` statements). Line 6 reads in a velocity field from the command line argument `argv[f]`. Line 7 forms the velocity gradients and line 8 forms the pressure. Lines 9 and 10 compute simple statistics and lines 11 and 12 print them out.

To execute this *Tensoral* program one first compiles it with the command

```
t1 -o p p.tlc
```

This produces an executable file `p` (the `-o f` flag names compiler output). Now `p` can be applied to the restart files `run1`, `run2`, ...

```
p run1 run2 ...
```

and will output the desired statistics.

Appendix

ROSTER

<u>NAME/TERM</u>		<u>AREA OF RESEARCH</u>
POSTDOCTORAL FELLOWS		
ADAMS, Dr. Nikolaus 10/93-present	(Ph.D, Theoretical Fluid Mechanics, 1993, DLR, Göttingen)	Boundary layer interaction with shocks
CARATI, Dr. Daniele 10/93-9/94	(Ph.D. Physics, 1991, University of Belgium)	Large-eddy simulation/RNG
CHOI, Dr. Haecheon 1/94-8/94	(Ph.D. Mechanical Engr., 1992, Stanford)	Large-eddy simulation of complex flows
GHOSAL, Dr. Sandip 2/92-present	(Ph.D. Physics, 1992, Columbia University)	Subgrid-scale modeling
JANSEN, Dr. Kenneth 9/93-present	(Ph.D. Mechanical Engr., 1993, Stanford)	Large-eddy simulation of complex flows
KALTENBACH, Dr. Hans-Jakob 9/92-present	(Ph.D. Atmospheric Physics, 1992, DLR)	Large-eddy simulation
KOUMOUTSAKOS, Dr. Petros 8/94-present	(Ph.D. Aero & Applied Mathematics, 1992, CALTECH)	Numerical simulation via vortex methods
LEBOEUF, Dr. Richard L. 9/91-5/94	(Ph.D. Mechanical Engr., 1991, SUNY at Buffalo)	Experimental study of turbulent mixing layer
MANTEL, Dr. Thierry 7/93-10/94	(Ph.D. Physics, 1993, University Rouen)	Turbulent combustion
RUETSCH, Dr. Gregory 9/93-present	(Ph.D. Applied Mathematics, 1991, Brown University)	Turbulent combustion

SADDOUGHI, Dr. Seyed G. 6/91-present	(Ph.D. Mechanical Engr., 1989, Univ. of Melbourne)	Experimental investigation of local isotropy in high- Reynolds-number turbulence
SAMANIEGO, Dr. Jean-Michel 4/92-12/94	(Ph.D. Combustion, 1992, Ecole Centrale Paris)	Reacting flows
WANG, Dr. Meng 9/92-present	(Ph.D. Mechanical Engr., 1989, Univ. of Colorado)	Aerodynamic noise

RESEARCH ASSOCIATES

CABOT, Dr. William H. 3/88-present	(Ph.D. Physics, 1983, University of Rochester)	Large-eddy simulation and convection
DRESSELHAUS, Dr. Eliot 9/91-present	(Ph.D. Applied Mathematics, 1991, Columbia University)	Postprocessing and computer languages
LUND, Dr. Thomas S. 11/90-present	(Ph.D. Aero-Astro, 1987, Stanford)	Large-eddy simulation

SR. VISITING FELLOWS

BILGER, Prof. Robert W. 1/94	University of Sydney	Turbulence combustion
BLACKWELDER, Prof. Ron F. 9/94-12/94	University of Southern California	Control of bounded shear flows
FOSS, Prof. John F. 11/93	Michigan State University	80x120 wind tunnel measurements
GEORGE, Prof. William K. 9/94	SUNY-Buffalo	80x120 wind tunnel measurements

SR. RESEARCH FELLOWS

BROADWELL, Dr. James E. 1/94-present		Turbulence combustion
DURBIN, Dr. Paul 1/90-present		Turbulence modeling

HILL, Dr. D. Christopher
5/92-5/94

Flow control

JIMENEZ, Prof. Javier
7/94-11/94

Small scales in turbulence

ZEMAN, Dr. Otto
3/1/89-9/94

Turbulence modeling

GRADUATE STUDENTS

LOULOU, Patrick
1/94-12/94

DNS of incompressible
axisymmetric flows

TIMSON, Stephen
10/93-9/94

LES of a statistically
stationary turbulent free
shear flow

1994 ADVISORY COMMITTEE

Prof. Ronald J. Adrian (Co-Chair)
University of Illinois

Prof. George K. Batchelor
DAMTP, Univ. of Cambridge

Dr. Richard G. Bradley, Jr.
Lockheed

Dr. Dennis M. Bushnell
NASA Langley Research Center

Prof. Eugene Covert (Co-Chair)
Massachusetts Institute of Technology

Dr. Coleman Donaldson
Gloucester, VA

Dr. Marvin E. Goldstein
NASA Lewis Research Center

Dr. Spiro Lekoudis
Office of Naval Research

Dr. James M. McMichael
Air Force Office of Scientific Research

Dr. Robert Melnik
Grumman Corporation

Prof. Norbert Peters
RWTH - Aachen

Prof. Stephen B. Pope
Cornell University

Prof. Richard A. Seebass
Univ. Colorado at Boulder

Dr. Ron Bailey (Ex-officio)
NASA Ames Research Center

Mr. John T. Howe (Ex-officio)
NASA Ames Research Center

1994 STEERING COMMITTEE

Prof. Dean R. Chapman
Dept. of Aeronautics & Astronautics
and Mechanical Engineering, Stanford

Dr. Dochan Kwak
Chief, Computational Algorithms and
Applications Branch
NASA Ames Research Center

Prof. Javier Jimenez
Senior Visiting Fellow, 7/94-11/94
Center for Turbulence Research,
Professor, Fluid Mechanics, University of
Madrid

Dr. N. N. Mansour
Turbulence Physics Section
NASA Ames Research Center

Mr. Joseph G. Marvin
Chief, Modeling & Experimental
Validation Branch,
NASA Ames Research Center

Prof. Parviz Moin
Director, Center for Turbulence Research
Professor, Mechanical Engineering,
Stanford,
Sr. Staff Scientist, NASA Ames Research
Center

Prof. William C. Reynolds
Program Coordinator, Center for
Turbulence Research,
Professor, Mechanical Engineering,
Stanford,
Sr. Staff Scientist, NASA Ames Research
Center